V. 122, NO. 5
SEPTEMBER 2025

ACI STRUCTURAL JOURNAL

A JOURNAL OF THE AMERICAN CONCRETE INSTITUTE



a. Drilling hole



b. Threading in hole



c. Fixing bolts



d. Tack welding

American Concrete Institute

CONTENTS

Editorial Board

Michael Kreger, Editor-in-Chief
University of Alabama

Liberato Ferrara,
Polytechnic University of Milan
Raissa Ferron,
The University of Texas at Austin
O. Burkan Isgor,
Oregon State University
Prannoy Suraneni,
University of Miami

Board of Direction

President
Maria Juenger

Vice Presidents
Scott M. Anderson
Matthew R. Sherman

Directors
Michael Ahern
Corina-Maria Aldea
Oscar R. Antommattei
Peter Barlow
Arturo Gaytan Covarrubias
James H. Hanson
Carol Hayek
Werner K. Hellmer
Mary Beth Deisz Hueste
Kimberly Waggle Kramer
Enrique Pasquel
Xiomara Sapón-Roldán

Past President Board Members
Charles K. Nmai
Antonio Nanni
Michael J. Paul

Executive Vice President
Frederick H. Grubbe

Staff

Publisher
John C. Glumb

Managing Director, Engineering and Professional Development
Michael L. Tholen

Engineers
Will J. Gold
Matthew R. Senecal
Michael L. Tholen
Gregory M. Zeisler

Managing Editor
Lauren E. Mentz

Associate Editor
Kimberly K. Olesky

Editors
Erin N. Azzopardi
Lauren C. Brown
Kaitlyn J. Dobberteen
Tiesha Elam
Angela R. Noelker
Kelli R. Slayden

ACI Structural Journal

September 2025, V. 122, No. 5

A JOURNAL OF THE AMERICAN CONCRETE INSTITUTE
AN INTERNATIONAL TECHNICAL SOCIETY

3 **Load-Carrying Capacity of Degraded Dapped-End Beams in Reinforced Concrete Bridges**, by Giuseppe Campione and Maria Zizzo

17 **Debonding and Control of Shield Tunnel Strengthened with Thin Plate**, by Dejun Liu, Xiaoyun Yao, Qingqing Dai, Cong Tian, and Jiangwen Zheng

29 **Progressive Collapse Performance of Unbonded Prestressed Reinforced Concrete Beam-Column Subassemblages under Column Removal Scenarios**, by Wen-Liu Xu, Li-Cheng Wang, Yong-Qin Liang, and Fei-Fan Feng

45 **Cyclic Loading Test for Precast Columns Using Slag-Based Concrete and Sleeve Splices**, by H.-S. Moon, K.-W. Jo, H.-J. Hwang, C.-S. Kim, J.-H. Jeong, C.-K. Park, and H.-G. Park

57 **Structural Assessment of Cracked Concrete Members by Digital Image Random Nonlinear Finite Element**, by Abdalla Elhadi Alhashmi and Fadi Oudah

71 **Behavior of Exterior Beam-Column Connections with Headed Bars under Nonreversible Cyclic Loading**, by Gustavo J. Parra-Montesinos and Jacob Zeuske

83 **Tensile Cracking and Flexure-Shear Capacity of Recycled Aggregate Concrete**, by Sourav Chakraborty and Kolluru V. L. Subramaniam

97 **Lightweight Alternative Machine Learning Model for Automating Concrete Crack Image Classification**, by Sang Min Lee, Hyeon-Sik Choi, Chanho Kim, and Thomas H.-K. Kang

107 **Efficient Seismic-Resistant Vertical Dry Connections in Precast Walls**, by A Selva Ganesa Moorthi and G. Appa Rao

123 **Novel Post-Tensioning Anchorage Solution with Ultra-High-Performance Concrete for Seismic Retrofit of Nonductile Reinforced Concrete Walls**, by Sumedh Sharma, Sriram Aaleti, and Pinar Okumus

139 **Stiffness Modifiers to Support Seismic Design of Reinforced Concrete Circular Columns**, by Mario E. Rodriguez and José I. Restrepo

153 **Behavior of Low-Carbon Fabric-Formed Reinforced Concrete Beams with Varying Shapes**, by Jared Mason, Neil A. Hoult, Joshua E. Woods, Evan C. Bentz, Cody Somers, and John Orr

Contents continued on next page

ACI Structural Journal
© 2025 American Concrete Institute. All rights reserved.

This material may not be reproduced or copied, in whole or in part, in any form or by any means, including making copies by any photo process, or by electronic or mechanical device, printed, written, graphic, or oral, or recording for sound or visual reproduction for use in any knowledge or retrieval system or device, without the written consent of ACI. This material may not be used by data mining, robots, screen scraping, or similar data gathering and extraction tools such as artificial intelligence ("AI") for purposes of developing or training a machine learning or AI model, conducting computer analysis or creating derivatives of this material, without the written consent of ACI.

American Concrete Institute®, ACI®, Always Advancing®, *ACI Structural Journal*®, and *ACI Materials Journal*® are registered trademarks of American Concrete Institute.

The *ACI Structural Journal* (ISSN 0889-3241) is published bimonthly by the American Concrete Institute. Publication office: 38800 Country Club Drive, Farmington Hills, MI 48331. Periodicals postage paid at Farmington, MI, and at additional mailing offices. Subscription rates: $210 per year, payable in advance. POSTMASTER: Send address changes to: *ACI Structural Journal*, 38800 Country Club Drive, Farmington Hills, MI 48331.

Canadian GST: R 1226213149.

Direct correspondence to 38800 Country Club Drive, Farmington Hills, MI 48331. Telephone: +1.248.848.3700. Facsimile (FAX): +1.248.848.3701. **Website: http://www.concrete.org.**

PRINTED WITH SOY INK®

CONTENTS

165 **Geopolymer Composites: Potential as Repair and Strengthening Materials for Concrete Structures**, by Giwan Noh, Uksun Kim, Myoungsu Shin, Woo-Young Lim, and Thomas H.-K. Kang

MEETINGS

SEPTEMBER 2025

10-13—ASCC Annual Conference 2025, Indianapolis, IN, https://ascconline.org/events

11-12—2nd International RILEM Conference on Early-Age and Long-Term Cracking in RC Structures (CRC2025), Katowice, Poland, https://crc2025.org

15-16—44th Cement & Concrete Science Conference, Leeds, UK, www.iom3.org/events-awards/44th-cement-concrete-science-conference.html

15-19—19th World Conference on Seismic Isolation, Energy Dissipation and Active Vibration Control of Structures (19WCSI), Berkeley, CA, https://19wcsi.org

16-18—3rd International Workshop on Durability and Sustainability of Concrete Structures (DSCS 2025), Naples, Italy, www.rilem.net/agenda/3rd-international-workshop-on-durability-and-sustainability-of-concrete-structures-dscs-2025-1613

16-20—2025 PCI Committee Days, Rosemont, IL, www.pci.org/CommitteeDays

18-19—6th Ibero-American Congress on Special Concretes – Concrete and Sustainability (HACBAC2025), Faro, Portugal, https://hacbac2025.ualg.pt/en

18-19—8th International RILEM Workshop on Concrete Behaviour Due to Fire Exposure, Kraków, Poland, www.rilem.net/agenda/8th-international-workshop-on-concrete-behaviour-due-to-fire-exposure-1707

ACI CONCRETE CONVENTION: FUTURE DATES

2025—Oct. 26-29, Hilton Baltimore & Marriott Baltimore Inner Harbor, Baltimore, MD
2026—Mar. 29-Apr. 1, Hyatt Regency O'Hare, Rosemont/Chicago, IL
2026—Oct. 11-14, Hilton Atlanta, Atlanta, GA

For additional information, contact:
Event Services, ACI
38800 Country Club Drive
Farmington Hills, MI 48331
Telephone: +1.248.848.3795
email: conventions@concrete.org

ON FRONT COVER: 122-S73, p. 112, Fig. 6—Process involved in making embedded plate.

Permission is granted by the American Concrete Institute for libraries and other users registered with the Copyright Clearance Center (CCC) to photocopy any article contained herein for a fee of $3.00 per copy of the article. Payments should be sent directly to the Copyright Clearance Center, 21 Congress Street, Salem, MA 01970. ISSN 0889-3241/98 $3.00. Copying done for other than personal or internal reference use without the express written permission of the American Concrete Institute is prohibited. Requests for special permission or bulk copying should be addressed to the Managing Editor, *ACI Structural Journal*, American Concrete Institute.

The Institute is not responsible for statements or opinions expressed in its publications. Institute publications are not able to, nor intend to, supplant individual training, responsibility, or judgment of the user, or the supplier, of the information presented.

Papers appearing in the *ACI Structural Journal* are reviewed according to the Institute's Publication Policy by individual experts in the subject area of the papers.

Contributions to *ACI Structural Journal*

The *ACI Structural Journal* is an open forum on concrete technology and papers related to this field are always welcome. All material submitted for possible publication must meet the requirements of the "American Concrete Institute Publication Policy" and "Author Guidelines and Submission Procedures." Prospective authors should request a copy of the Policy and Guidelines from ACI or visit ACI's website at **www.concrete.org** prior to submitting contributions.

Papers reporting research must include a statement indicating the significance of the research.

The Institute reserves the right to return, without review, contributions not meeting the requirements of the Publication Policy.

All materials conforming to the Policy requirements will be reviewed for editorial quality and technical content, and every effort will be made to put all acceptable papers into the information channel. However, potentially good papers may be returned to authors when it is not possible to publish them in a reasonable time.

Discussion

All technical material appearing in the *ACI Structural Journal* may be discussed. If the discussion is received within four months of the paper's print publication, it will appear in the issue dated ten months from this journal's date. Discussion material received after specified dates will be considered individually for publication or private response. ACI Standards published in ACI Journals for public comment have discussion due dates printed with the Standard. Discussion should be complete and ready for publication, including finished, reproducible illustrations. Discussion must be confined to the scope of the paper and meet the ACI Publication Policy.

Follow the style of the current issue. Discussions should not exceed 1800-word equivalents (illustrations and tables count as 300 words each). References should be complete. Do not repeat references cited in original paper; cite them by original number. Numbering of additional references, figures, tables, and equations should follow sequentially from the original manuscript throughout the discussion. The discusser must indicate the month, year, volume number, issue number, authors' names, and manuscript number of the original manuscript. Closures responding to a single discussion should not exceed 1800-word equivalents in length, and to multiple discussions, approximately one half of the combined lengths of all discussions. Closures are published together with the discussions.

Discuss the paper, not some new or outside work on the same subject. Use references wherever possible instead of repeating available information.

Discussion offered for publication should offer some benefit to the general reader. Discussion which does not meet this requirement will be returned or referred to the author for private reply.

Send manuscripts to:
http://mc.manuscriptcentral.com/aci
Send discussions to:
Journals.Manuscripts@concrete.org

ACI STRUCTURAL JOURNAL TECHNICAL PAPER

Title No. 122-S65

Load-Carrying Capacity of Degraded Dapped-End Beams in Reinforced Concrete Bridges

by Giuseppe Campione and Maria Zizzo

Sudden failure of reinforced concrete (RC) dapped-end beams of bridges and viaducts has occurred all around the world in the last few years due to corrosion of steel bars. The danger of sudden and brittle failure is often due to pitting corrosion of steel bars, concrete crushing, and loss of bond in steel bars. In this paper, the risk of failure of reinforced dapped-end supports at the ultimate state under vertical and lateral loads is investigated, focusing on the consequences of pitting corrosion and loss of bond in steel bars. A simplified strut-and-tie model was developed to predict the load-carrying capacity of dapped-end supports. The model includes the effects of corrosion of steel bars, loss of bond, and concrete crushing due to the biaxial state of stresses. Several laboratory experimental tests regarding the flexural behavior of RC beams with dapped-end supports were collected to validate the proposed model.

Keywords: corrosion; dapped-end beams; steel bars; strut-and-tie model (STM); viaduct.

INTRODUCTION

A very common type of bridge is one in which the main structure is made up of girders, and the beams are dapped ends. Dapped-end beams, also called Gerber-type saddles or half-joints, are used to have a more balanced distribution of internal moment in the structure without sacrificing the advantages of the isostatic structure.

Two main approaches are generally used to design the dapped ends: the shear-friction (PCI) method, and strut-and-tie modeling (STM). Both approaches require investigation of the potential failure mode, which depends very much on the arrangement of the steel reinforcements.

STM, widely adopted in several international codes (including ACI 318-19[1] and Eurocode 2[2]), consists of three main components: struts, ties, and nodes. The struts carry the compressive forces, and the ties, constituted by steel bars, are the tension members in the model. Nodes, or nodal areas, represent the points where the struts and ties meet. For a given half-joint, there is not a unique STM: numerous STMs can be mapped onto it. The STM to be adopted mainly depends on the reinforcement layout. There are diagonal, orthogonal, and combination models.

Cook and Mitchell[3] suggested adopting the truss model shown in Fig. 1(a), which is also adopted in ACI 318-19.[1]

Sanders[4] suggested adopting the truss model shown in Fig. 1(b), which was also adopted in the *fib*[5] recommendations, while Mattock,[6] based on his experimental results on dapped-end beams, suggested adopting the truss model of Fig. 1(c).

All three models refer to the arrangements of steel reinforcements shown in Fig. 1(d). The details of steel reinforcements are the following: horizontal bars of area A_s, constituting the tie AD in Fig. 1(a) to (c); and hanger reinforcement, constituted by closed vertical stirrups of area $A_{shanger}$ needed to develop a tension force to withstand the inclined compressive force of concrete in the dapped end, constituting the tie CB in Fig. 1(a) to (c). In addition, horizontal ties made up of horizontal stirrups of area A_h and vertical ties made up of vertical stirrups of area A_v are used to give an additional strength contribution (refer to Fig. 1(d)). It must be stressed that the tie AD of Fig. 1(c) should have sufficient extension to be anchored by struts between both the flexural reinforcement at the bottom of the beam and the flexural compression zone at the top of the beam.

According to Eurocode 2,[2] two different strut-and-tie schemes, shown in Fig. 2(a) and (b), are adopted. Eurocode 2[2] allows one to use only one of the two trusses shown in Fig. 2 or allows use of the two combined schemes by assigning, for example, 50% of the reaction of the saddle to each scheme. In the models in Fig. 1 and 2, the dashed lines indicate the compressed concrete zones of the equivalent truss, and the solid lines indicate the zone in tension of the equivalent trusses, which are the steel reinforcements placed in the dapped-end beams.

Figures 3(a) and (b) show typical steel reinforcements corresponding to the truss structures shown in Fig. 2(a) and (b). The diagonal reinforcements of Fig. 3(a) constitute the tie T_1 in the truss model in Fig. 2(a).

Dapped-end beams with reinforcements placed as shown in Fig. 1(d) or Fig. 2(b) can be characterized at rupture by different failure modes (refer to Fig. 4), which include: premature failure due to flexure or shear (mid-flexure crack and nib-inclined crack), direct shear crack for a very low shear span-depth ratio (between 0.2 and 0.4), and diagonal tension crack and resulting corner crack for shear failure in dapped ends with a low shear span-depth ratio (between 0.4 and 1.0).

If the girders of bridges with Gerber saddles suffer degradation of materials—for example, corrosion of steel bars induced by the presence of salt and poor watertightness, producing pitting and general corrosion—this leads to the typical degradation conditions shown in Fig. 5, which shows real cases of existing bridges in Europe.

ACI Structural Journal, V. 122, No. 5, September 2025.
MS No. S-2021-496.R3, doi: 10.14359/51746819, received June 27, 2022, and reviewed under Institute publication policies. Copyright © 2025, American Concrete Institute. All rights reserved, including the making of copies unless permission is obtained from the copyright proprietors. Pertinent discussion including author's closure, if any, will be published ten months from this journal's date if the discussion is received within four months of the paper's print publication.

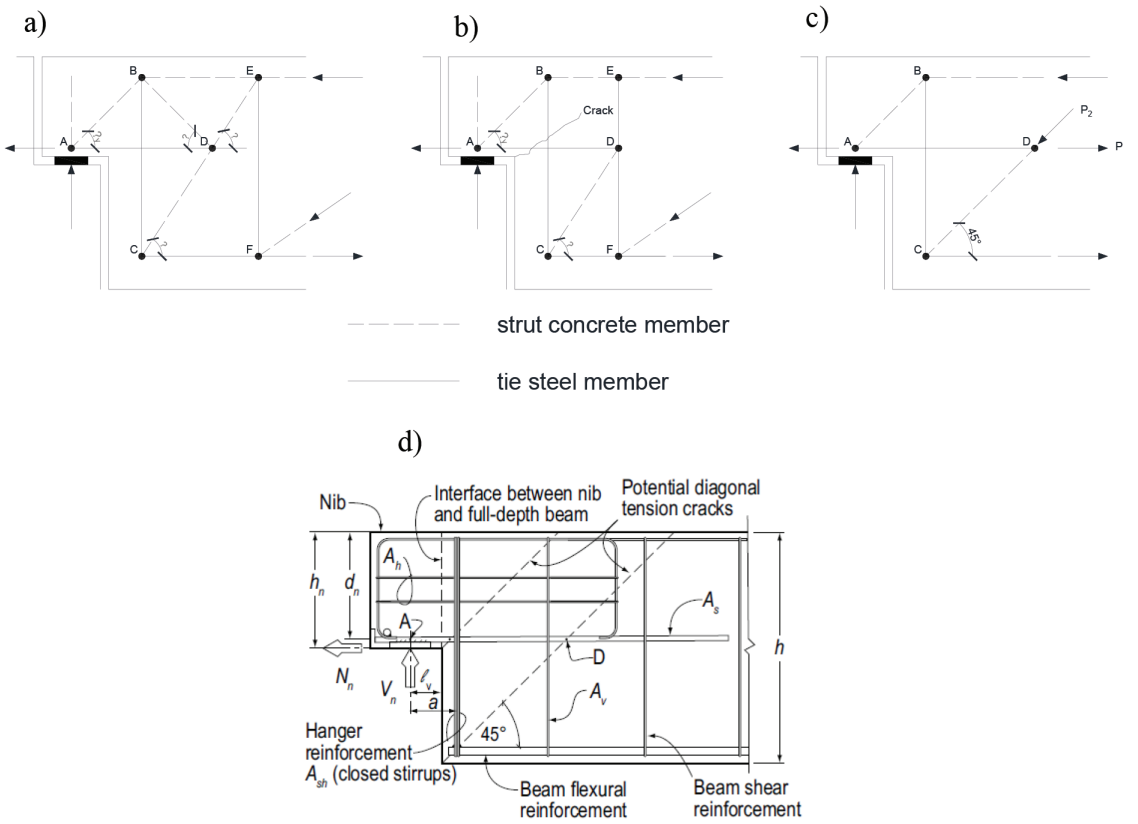


Fig. 1—Strut-and-tie models of dapped-end beams: (a) ACI 318-19[1]; (b) fib *recommendations[5]; (c) simplified STM, proposed by Mattock[6]; and (d) details of reinforcements.*

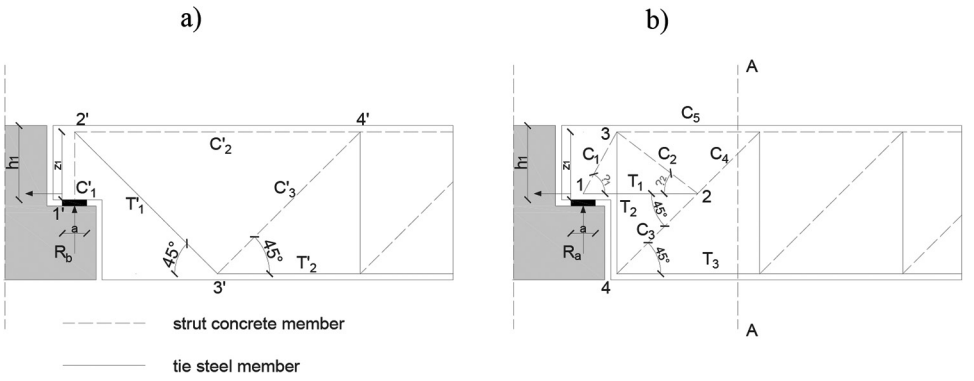


Fig. 2—Strut-and-tie mechanisms proposed by Eurocode 2.[2]

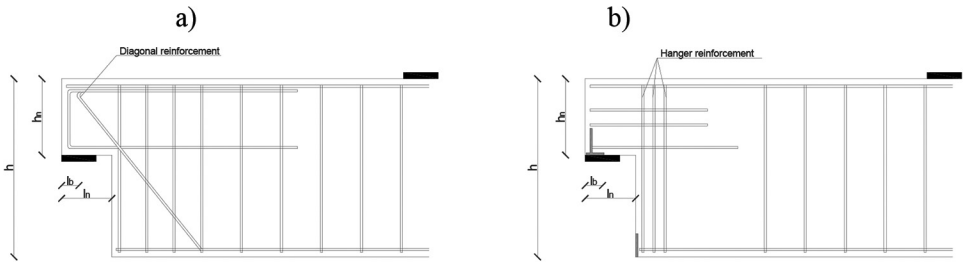


Fig. 3—Details of steel reinforcements proposed by Eurocode 2.[2]

In these structures, the joints are important portions of the beams to be investigated to verify the safety conditions where there is degradation of material due to corrosion or carbonation processes.

Bridge inspection reports can provide information about the integrity of the concrete and the potential location of struts. Existing crack patterns can also be used to identify the principal tensile and compressive stress directions at certain points in the half-joint, and hence the potential orientation and location of compressive struts.

Semi-destructive and nondestructive testing techniques are generally used to investigate corrosion effects. From these

tests, it emerges that degradation due to general and pitting corrosion of steel bars produces a reduction in the diameter of the main and secondary reinforcing bars (horizontal and vertical stirrups), and rust formation between the reinforcing bars and the surrounding concrete, causing cracking of the concrete and cover spalling and/or delamination.

Shear failure in these reinforced concrete (RC) members can be sudden and catastrophic in nature and should be avoided. Corrosion of steel stirrups may affect the shear capacity of concrete members and result in undesirable premature shear failures. Given the location of stirrups as an outer reinforcement, they are more susceptible to corrosion and may be subjected to related deterioration, which reduces the service life of the structure. In addition, the diameter of steel stirrups is generally small compared to that of longitudinal reinforcing bars, so relative loss of cross-sectional area due to corrosion in the stirrups is expected to be much more significant than that in the longitudinal bars.

Therefore, Gerber saddles, if degraded, represent a critical point in the girders, and a very important problem is the measurement of the structural safety of existing infrastructures equipped with such support devices.

In this paper, a simplified strut-and-tie calculation model is developed, which considers the influence of horizontal and vertical stirrups on the compressive strength of compressed struts and the share of yield stress available for the loss of bond induced by corrosion, to determine the load-carrying capacity of degraded Gerber saddles. The analytical results generated are compared with other existing models and available experimental data, giving good agreement.

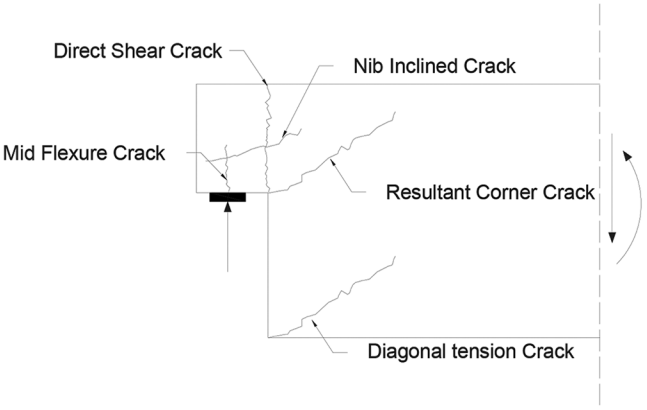


Fig. 4—Possible failure modes for dapped-end beams.

RESEARCH SIGNIFICANCE

Sudden failure of RC dapped-end beams of bridges and viaducts has occurred all around the world in the last few years due to corrosion of steel bars. STMs are the most widely used calculus model to predict the load-carrying capacity of uncorroded dapped-end beams.

In this paper, a simple STM that includes the effect of corrosion of steel bars and the presence of horizontal and vertical secondary steel bars is developed. The model was validated and proved satisfactory compared to available experimental data.

EFFECTS OF CORROSION ON MECHANICAL PROPERTIES OF MATERIALS

General and pitting corrosion are two possible corrosion types for the steel bars considered here. General corrosion affects a substantial area of longitudinal and transverse reinforcements, with uniform metal loss over the perimeter of reinforcing bars. It also causes cracking, cover spalling, and delamination of the concrete cover and produces rust staining on the concrete surface. Pitting is a localized corrosion type, concentrated over small areas of reinforcement; it does not cause spalling of the concrete cover and produces little or no rust staining on the concrete surface, so it may be difficult to discover during inspection. By contrast, general corrosion is evident during inspection.

To verify whether general corrosion induced by carbonation processes is present, it can be useful to calculate the evolution of the depth of carbonation S (mm) with time, which can be expressed as

$$S = K \cdot \sqrt{t} \tag{1}$$

where K is an experimental constant depending on several factors; and t is the time.

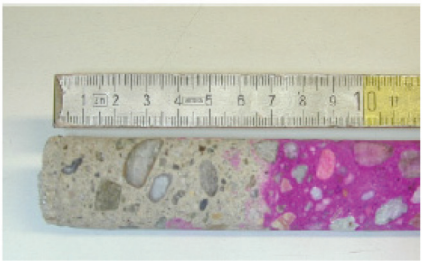
By setting S equal to the cover thickness c, Eq. (1) gives the time necessary for carbonation to reach the steel bars

$$t = (c/K)^2 \tag{2}$$



Fig. 5—Examples of degradation conditions in Gerber supports: (a) moderate; and (b) severe.

Table 1—Laboratory test for corrosion process determination

Phenomenon	Visual aspect	Information from test
Carbonation attack		Depth of layer of carbonation
Chloride attack		Content of chlorides
General corrosion		Reduction in diameter of bar through gravimetric method
Localized corrosion (pit)		Geometrical measurement on pit

By using Eq. (2) for $K = 5$ and $c = 20$ and 40 mm (0.787 and 1.575 in.), the result obtained is $t = 16$ and 64 years. Therefore, in most existing structures having low cover thickness and concrete with high porosity ($K = 5$), the corrosion process begins almost 20 years after initiation of the carbonation process. For pitting attacks, measurement of the chloride content in the cement paste allows one to establish whether localized corrosion on steel bars is in progress.

To calculate the load-carrying capacity of dapped-end beams, it is necessary to know how the geometrical and mechanical parameters of concrete and steel change during corrosion processes. This information can be obtained in two ways: the first one, shown in Table 1, is applicable when detailed experimental information is available (for example, carbonation test, chloride content, gravimetric method for general corrosion, measurement of the pitting in the bar); and the second one is based on a theoretical approach that can be applied simply by knowing the corrosion current density measured experimentally on the bar, for example, by using linear polarization resistance (LPR) measurement. Table 2 gives the qualitative correlation between corrosion current ($\mu A/cm^2$) and corrosion of the reinforcing bar obtained with the LPR method.

Mechanical properties of corroded bars

Several authors,[7-10] based on available experimental data, have suggested reducing yield stress and ultimate strain as the loss of mass increases.

According to Imperatore,[7] the yield stresses f_y and the ultimate strain ε_u of steel bars (and consequently the ductility reduction μ) decrease as the loss of mass X_p increases in the form

$$\beta = (f_{ycorr}/f_y) = 1 - 0.0138 \cdot X_p \quad (3)$$

Table 2—Corrosion current versus condition of reinforcing bar

Corrosion current, μA/cm^2	Condition of reinforcing bar
≤0.1	Passive
0.1 ÷ 0.5	Low to moderate
0.5 ÷ 1.0	Moderate to high
≥1.0	High corrosion rate

$$\mu = \frac{\varepsilon_{sucorr}}{\varepsilon_{su}} = e^{(-0.035 \cdot X_p)} \quad (4)$$

Zhang and Li[8] suggested the following equation

$$\beta = 1 - \alpha_1 \cdot X_p \quad (5)$$

with α_1 = 0.0124 and 0.0198 for uniform corrosion and pitting corrosion, respectively.

According to Zhang et al.,[10] the reduction in the yield stress and the reduction of the cross-sectional area of steel bars due to uniform corrosion prove to be

$$\beta = \frac{1 - 0.0123 \cdot X_p}{1 - 0.01 \cdot X_p} \quad (6)$$

Figure 6 shows the reduction in yield stress with the loss of mass for the aforementioned models. In the same graph, experimental data from the literature,[11-14] referring to uniform corrosion, are plotted. Equation (5) gives the safest prediction of experimental data and will therefore be adopted in the next section. Figure 7 shows a comparison in terms of the reduction of ductility with the loss of mass for the aforementioned models. Literature data[7,13-15] are plotted. All data refer to uniform and pitting corrosion. In the same graph, Eq. (4), with the 0.035 coefficient replaced with 0.07, is given. The comparison shows that Eq. (4) with the coefficient of 0.07 gives the best and safest prediction, which is in line with the experimental results.

Loss of area of steel bars

Corrosion of steel produces two different types of reduction of the cross-sectional area: uniform and localized. In this paper, uniform general corrosion was assumed along the entire length of the bar, and the reduction of area was related to the loss of mass X_p measured through gravimetric tests or determined analytically through Faraday's law. The reduction of the area of a steel bar of initial value A_s and the diameter of single bars ϕ can be calculated with the following expression (Campione and Cannella[15])

$$\alpha_g = (A_{scorroded}/A_s) = 1 - 0.01 \cdot X_p \quad (7)$$

Ghods et al.[16] suggested adopting

$$\alpha_g = 1 - A \cdot \left(\frac{0.01 \cdot X_p}{2}\right)^2 \quad (8)$$

where A = 2 for general corrosion, and A is between 4 and 6 for pitting attack (a value of 5 was assumed herein).

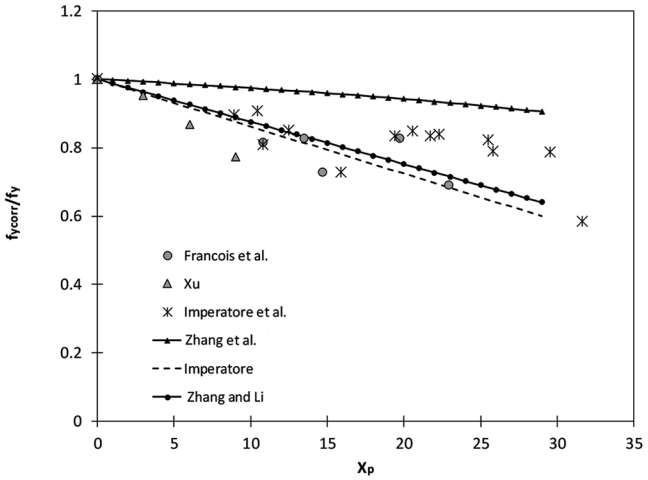


Fig. 6—Reduction of yield stress with loss of mass.

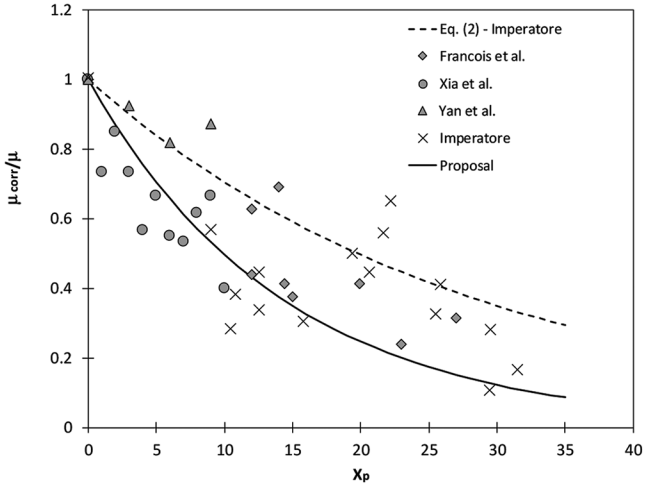


Fig. 7—Reduction of ductility with loss of mass.

For pitting corrosion, the sectional loss can be considered in a similar way to general corrosion. Vecchi et al.[17] suggested preliminarily estimating the presence of pitting through a visual inspection of extracted corroded steel bars. Vecchi et al.[17] operate an initial classification of the corrosion level, based on visual inspection, distinguishing three different levels of corrosion corresponding to: a loss of mass lower than 2%, characterized by the presence of small and localized pits; a medium level, characterized by bigger and widespread pits, corresponding to a loss of mass between 2 and 10%; and a high level of corrosion, identified by the presence of deeper and oversized pits, corresponding to a loss of mass higher than 10%. Vecchi et al.[17] showed that it is possible to reliably correlate the pit depth with the loss of mass for the low, medium, and high levels of corrosion. They suggested assuming correlation coefficients equal to 0.0601, 0.2804, and 0.1206, respectively, for loss of mass lower than 2%, between 2 and 10%, and higher than 10%. The pit attack depth p can also be measured experimentally, as was done in di Prisco et al.[18]

Val[19] proposed a theoretical model to estimate pitting attacks through a geometric pit configuration and the following expression for the area of pitting

$$A_{pit} = \frac{\phi^2}{4} \cdot \left[\arccos\left(1 - \frac{2 \cdot p}{\phi}\right)\right] \cdot \left\{\arccos\left(1 - \frac{2 \cdot p}{\phi}\right) - \sin\left(\arccos\left(1 - \frac{2 \cdot p}{\phi}\right)\right) \cdot \cos\left(\arccos\left(1 - \frac{2 \cdot p}{\phi}\right)\right)\right\} \quad (9)$$

The pit depth p can also be determined analytically by adopting the expression revised by Campione and Cannella[15] in terms of loss of mass in the form

$$p(t) = R \cdot \left(0.01 \cdot X_p \cdot \frac{\phi}{2}\right) \quad (10)$$

where R is assumed to be 4 and 9 for steel bars and stirrups, respectively.

Knowing the pit area, the area reduction factor due to a pitting attack proves to be

$$\alpha_{pitting} = \frac{A_s - A_{pi}}{A_s} \quad (11)$$

The reduced area due to general and pitting corrosion proves to be

$$A_{scorr} = \frac{\pi \cdot \phi^2}{4} \cdot (1 - 0.01 \cdot X_p)^2 - A_p \quad (12)$$

Figure 8 shows the reduction of steel area with the loss of mass for the aforementioned models. In the same graph, experimental data from the literature[13,20] referring to uniform corrosion are plotted. The comparison shows that Eq. (6) gives the best prediction of experimental results; therefore, it will be adopted in the following sections.

Compressive strength

Concrete geometry is influenced by the corrosion of steel stirrups and main bars. Corrosion of shear reinforcement causes cracking, delamination, and spalling. Cracking of concrete, due to expansion of the corroded longitudinal bars in the compressed zone (rust effect) of the beam, reduces its compressive strength. The lateral strain ε_1, which causes longitudinal microcracks, was assumed to be smeared on w_{cr} and to reduce the compressive strength. According to these concepts, following the approach of Coronelli and Gambarova,[21] the reduced compressive strength of concrete can be expressed as

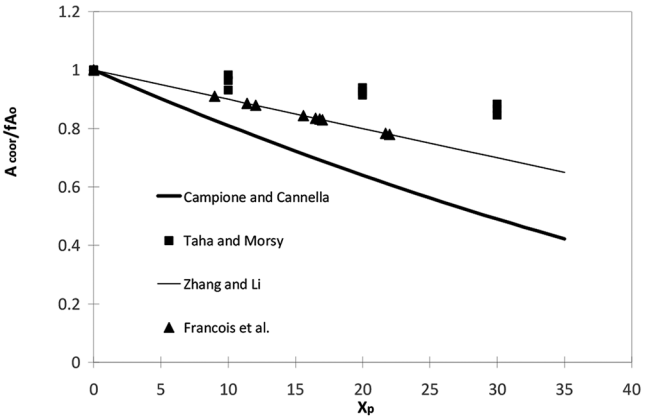


Fig. 8—Reduction of steel area with loss of mass.

$$\psi = \frac{f_c^*}{f_c} = \frac{1}{1 + k \cdot \frac{\varepsilon_1}{\varepsilon_0}} \quad (13)$$

with

$$\varepsilon_1(t) = \frac{b_f - b}{b} = \frac{n_{bars} \cdot w_{cr}}{b} = \frac{1 \cdot \pi \cdot n_{bars} \cdot (v_{rs} - 1) \cdot X(t)}{b} \quad (14)$$

where v_{rs} is the volume expansion ratio between rust and steel. According to Coronelli and Gambarova,[21] v_{rs} is in the range of 1.7 to 6.1, and its value depends on the practical application of the structure. Here, 2 was assumed, as in Campione and Cannella.[15] In most practical cases, the core can be cracked before corrosion; therefore, w_{cr}, used in the proposed model, considers both the effects of w_{cr} due to the previously evaluated loading conditions through a visual inspection and a caliber. The depth of the corrosion attack, X, can be related to the loss of mass X_p with the expression

$$X = 0.01 \cdot X_p \cdot (\phi/2) \quad (15)$$

Moreover, X can be related to the time t and the current intensity due to corrosion processes through Faraday's law in the form

$$X = 0.0116 \cdot i_{corr} \cdot t \quad (16)$$

where i_{corr} is the corrosion current density in the reinforcing bar, expressed in μA/cm^2; and t is the time in years.

Equations (13) and (14) are herein rearranged in the form

$$\psi = \frac{f_c^*}{f_c} = \frac{1}{1 + 1.57 \cdot \frac{n_{bars} \cdot X_p \cdot \phi}{b}} \quad (17)$$

The strength reduction given by Eq. (17) will be applied in the next section in the compressed zone of the beam having width b. In this study, to consider the effects of corrosion on the concrete section at the ultimate stage, the section width b will be purged from the concrete cover thickness.

Bond strength

Several researchers have shown that bond strength decreases with an increase in corrosion attack penetration.

Bhargava et al.[22] suggested reducing the bond strength of the uncorroded concrete by adopting the following

$$\gamma = \frac{\tau_{corr}}{\tau_o} = 1.192 \cdot e^{(-0.117 \cdot X_p)} \text{ for } X_p > 1.5\% \quad (18)$$

El Maaddawy et al.[23] adopted the following equation

$$\gamma = (A_1 + A_2 \cdot X_p) \quad (19)$$

where the values of A_1 and A_2 are given in the literature.[23]

The expression used herein is the one suggested by Coronelli and Gambarova[21] in the form

$$q_{res} = 0.6 \cdot \left(0.5 + \frac{c}{\phi}\right) \cdot f_{ct} \cdot \left[1 - 0.40 \cdot \left(0.01 \cdot X_p \cdot \frac{\phi}{2}\right)^{0.1}\right] + \frac{0.16 \cdot A_{st} \cdot f_{yt}}{s \cdot \phi} \quad (20)$$

where c is the cover thickness; and f_{ct} is the tensile strength of the concrete, assumed to be $f_{ct} = 0.4\sqrt{f_c}$ (in MPa) as in ACI 318-19.[1]

The reduction coefficient of concrete bond strength, in the absence of stirrups, results from Eq. (18) in the form

$$\gamma = 1 - 0.40 \cdot \left(0.01 \cdot X_p \cdot \frac{D}{2}\right)^{0.1} \quad (21)$$

Figure 9 shows the reduction of bond strength with loss of mass. Data from the literature[9,24-27] are plotted. All data refer to elements without stirrups. In the same graph, Eq. (18) to (20) are also plotted. A comparison shows that Eq. (18) and (19) give similar results. In all cases examined, the experimental data had high scatter. When referring to bond tests in the presence of stirrups,[24,28] the model by Coronelli and Gambarova[21] gives an accurate prediction of available data, as shown in Fig. 9. In the following section, Eq. (20) will be adopted with Eq. (21) because all cases examined in this paper refer to RC members with stirrups.

CALCULUS MODELS FOR LOAD-CARRYING CAPACITY

Existing models

An extended review of analytical expressions for the prediction of the load-carrying capacity of dapped-end beams can be found in the literature.[25]

Adopting the shear-friction design procedure based on a simple system of equilibrium conditions (flexural model) adopted for $a/d < 1$, the load-carrying capacity of dapped-end beams proves to be

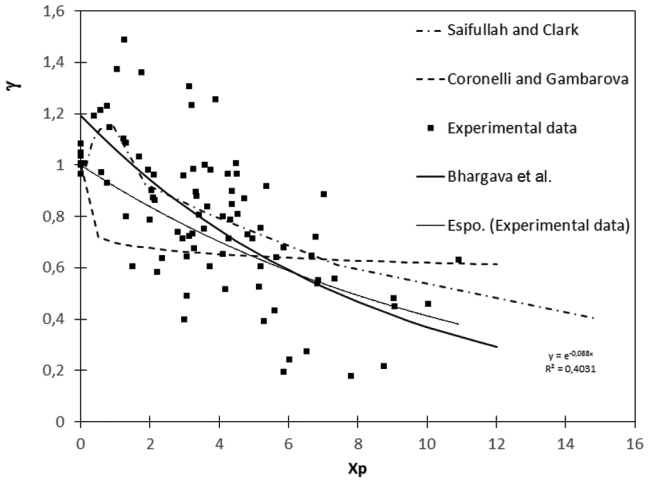


Fig. 9—Bond reduction with loss of mass for specimens without stirrups.

$$V_u = \min\begin{pmatrix} 0.2 \cdot f_c, \frac{a}{d} \cdot \left(d - \frac{A_s \cdot f_y}{1.7 \cdot b \cdot f_c}\right); \\ A_{vhanger} \cdot f_{yhanger};\ 0.8 \cdot A_v \cdot f_y + 0.5 \cdot b \cdot d \end{pmatrix} \quad (22)$$

Equation (22) considers shear failure due to compression crushing of the compressed strut, flexural mode of failure, shear constraint, and yielding of hanger bars.

Adopting the ACI 318-19[1] and Eurocode 2[2] STMs suggested referred to typical layouts of steel reinforcements already shown in Fig. 1(a) and (b).

The design codes do not provide specific guidance on suitable STMs for different cases, and designers usually have more than one choice of STM for the same problem to carry the imposed loads through the D-regions to the supports.

Desnerck et al.[29] proposed a specific STM for a corroded half-joint with main steel reinforcements, which is not described in detail here but is used in the next section to compare the available experimental data and the proposed model. Other authors also give a clear indication on how to apply the STM for dapped-end beams, not considering the presence of secondary reinforcements.[30,31]

The Lu et al.[25] model, shown in Fig. 10, is the truss model that explicitly considers the presence of horizontal and vertical steel reinforcements.

The presence of horizontal and vertical ties produces additional strength mechanisms. The horizontal mechanism consists of one horizontal tie and two flat struts. The horizontal tie is made up of horizontal stirrups. When computing the area of the horizontal tie, A_{th}, it is roughly assumed that horizontal stirrups within the center half are fully effective, while the rest are only 50% effective. If the horizontal stirrups are uniformly distributed in the two-thirds of the effective depth closest to the main bars, then $A_{th} = 0.8A_h$, where A_h is the area of the horizontal stirrups.

The vertical mechanism consists of one vertical tie and two steep struts. The vertical tie is made up of vertical stirrups. The area of the vertical tie, A_{tv}, is computed in the same way as that of the horizontal tie. If the vertical stirrups are uniformly distributed within the shear span, then A_{tv} =

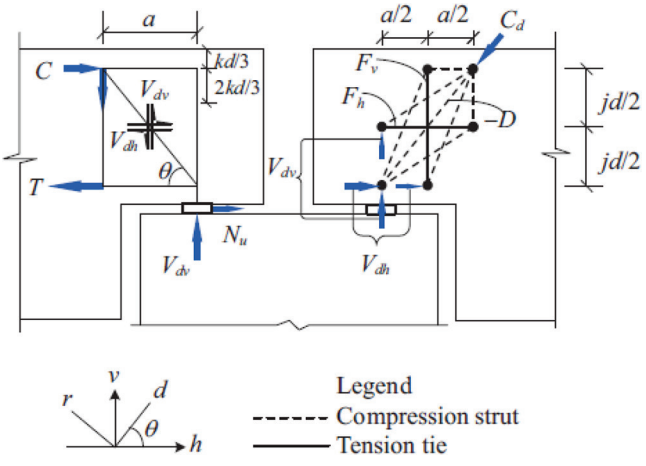


Fig. 10—Model of dapped ends according to Lu et al.[25]

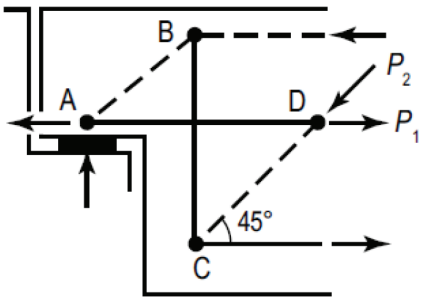


Fig. 11—Truss model adopted as in Mattock.[6]

$0.75A_v$, where A_v is the area of vertical stirrups within the shear span.

According to Lu et al.,[25] the diagonal compressive strength of dapped ends can be estimated as follows

$$C_u = (k_h + k_v - 1) \cdot \xi \cdot f_c \cdot A_{str} \tag{23}$$

where k_h is the horizontal tie index; k_v is the vertical tie index; f_c is the compressive strength of concrete; and ξ is the softening coefficient of concrete in compression.

The horizontal tie index can be estimated as follows

$$k_h = 1 + \left(\frac{1}{1 - 0.2 \cdot (\gamma_h + \gamma_h^2)} - 1\right) \cdot \frac{A_{th} \cdot f_{yh} \cdot \left[1 - 0.2 \cdot (\gamma_h + \gamma_h^2)\right]}{\gamma_h \cdot \xi \cdot f_c \cdot A_{str} \cdot \cos\theta} \le \frac{1}{1 - 0.2 \cdot (\gamma_h + \gamma_h^2)} \tag{24}$$

$$\gamma_h = \frac{2 \cdot \tan\theta - 1}{3}; \xi = \frac{3.35}{\sqrt{f_c}} \le 0.52 \tag{25}$$

where f_{yh} is the yield stress of horizontal stirrups; and γ is the fraction of horizontal shear transferred by the horizontal tie in the absence of the vertical tie.

The vertical tie index can be estimated as follows

$$k_v = 1 + \left(\frac{1}{1 - 0.2 \cdot (\gamma_v + \gamma_v^2)} - 1\right) \cdot \frac{A_{thv} \cdot f_{yhv} \cdot \left[1 - 0.2 \cdot (\gamma_v + \gamma_v^2)\right]}{\gamma_{hv} \cdot \xi \cdot f_c \cdot A_{str} \cdot \cos\theta} \le \frac{1}{1 - 0.2 \cdot (\gamma_v + \gamma_v^2)} \tag{26}$$

$$\gamma_v = \frac{2 \cdot \cot g\theta - 1}{3} \tag{27}$$

where f_{yv} is the yield stress of the vertical stirrups; and γ_v is the fraction of vertical shear transferred by the vertical tie in the absence of the horizontal tie.

The shear strength of dapped ends according to diagonal compression failure can be calculated as follows

$$V_u = C_u \cdot \sin\theta \tag{28}$$

Proposed model

The static scheme for the STM adopted herein is shown in Fig. 11. The nodes are those of applying the reactive force V and H of the CCT type (compression-compression-traction) and the convergence of the compressed strut of the CCC type (compression-compression-compression). In the STM, reinforcing bars are assumed to have a constant force over the length of the tie. Hence, full anchorage of a reinforcing bar is necessary to assume that yield will occur. If an insufficient bond length is provided, the tie cannot develop its full capacity, and a limit should be applied to the maximum force that can be taken by the tie in the range of 0.15 to 0.40.

One important aspect to remember is that the STM is based on the lower-bound theorem of plasticity and hence is only valid when adequate ductility can develop within the structure. Enough ductility of the concrete should be confirmed, and a check on the reinforcing steel quality during the assessment (regardless of its corroded state) is advised.

According to the linear bending theory, the position of the neutral axis and the lever arm $z = jd$ can be estimated as

$$\frac{x_c}{d} = \sqrt{(n \cdot \rho)^2 + 2 \cdot n \cdot \rho} - n \cdot \rho \tag{29}$$

$$z = j \cdot d = d \cdot \left(1 - \frac{1}{3} \cdot \sqrt{(n \cdot \rho)^2 + 2 \cdot n \cdot \rho} - n \cdot \rho\right) \tag{30}$$

where d is the effective depth of the dapped end; n is the modular ratio of elasticity; and ρ is the ratio of flexural tensile reinforcement.

$$\rho = \frac{A_s - \frac{H}{f_y}}{b \cdot d} \tag{31}$$

The diagonal compression strut had an angle of inclination θ. The horizontal and vertical mechanisms were considered by means of the increases in the compressive strength of the confined compressed strut f_{cc}, calculated adopting the confinement model of Mander et al.[26]

The inclination θ was defined as

$$\theta = \tan^{-1} \cdot (jd/a) \tag{32}$$

The effective area of the diagonal strut, A_{str}, can be estimated as

$$A_{str} = b_s \cdot \sqrt{x_c^2 + t_b^2} \tag{33}$$

where t_b is the thickness of the hanger zone; and $b_s = b - 2c$ (where c is the cover thickness) is the width of the diagonal strut, which can also be taken as the width of the dapped end.

The diagonal compressive strength of dapped ends can be estimated as follows

$$C_d = \xi \cdot f_{cc} \cdot A_{str} \tag{34}$$

with

$$\frac{f_{cc}}{f_c} = 1 + \frac{4.1}{f_c} \cdot \frac{A_{sh} f_{yh} + A_{sv} f_{yb}}{b \cdot a} \cdot \sin\theta \tag{35}$$

The efficiency factor k_e of the Mander et al.[26] model was assumed here to be 1 because of the presence of vertical and horizontal stirrups, and ξ was the softening coefficient in compression, calculated as suggested by Campione[27] in the form

$$\xi = \frac{1}{1 + 0.66 \cdot \left(\frac{a}{z}\right)^2} \tag{36}$$

The shear forces occurring at the yielding of the main area A_s are

$$V_y = A_s \cdot f_y \cdot (z/a) \tag{37}$$

A reduction factor γ (refer to Eq. (21)) was applied to all the tension ties within an STM based on their anchorage conditions. The factor γ was calculated as the ratio of the actual bond length to the required anchorage length (if enough anchorage is provided, λ was taken as equal to 1.0). It is emphasized that this method does not strictly satisfy the requirements of a lower-bound method but does provide a simplified approach.

The shear forces occurring at the concrete strut crushing prove to be

$$V_d = \xi \cdot f_{cc} \cdot A_{str} \cdot \sin\theta \tag{38}$$

Also, considering possible failure due to the flexural and yield strengths of the hanger, the shear strength of the dapped-end beams is the lowest among the aforementioned strength values.

The predicted shear strength of the dapped end according to flexure failure can be determined as follows

$$V_{flexural} = \frac{A_s \cdot f_y}{a} \cdot \left(d - \frac{A_s \cdot f_y}{1.7 \cdot b \cdot f_c}\right) \tag{39}$$

The shear force according to the tensile strength provided by the hanger bars can be estimated as follows

$$V_{dhanger} = A_{vhanger} \cdot f_{yhanger} \tag{40}$$

where A_{vh} and f_{yvh} are the area and yield strength of the hanger bars, respectively.

The increases in compressive strength of the concrete strut f_{cc}/f_c due to horizontal and vertical stirrups give the same results as the parameter $k_h + (k_v - 1)$ given in Lu et al.[25]

The expressions calculated previously can easily be rewritten considering corrosion effects, in dimensionless form, as

$$v_y = \frac{V_y}{b \cdot d \cdot f_c} = \frac{\alpha \cdot A_s \cdot \beta \cdot f_y}{b \cdot d \cdot \psi \cdot f_c} \cdot \frac{z(\alpha)}{a} = \omega \cdot \frac{z(\alpha)}{a} \cdot \frac{\alpha \cdot \beta}{\psi} \tag{41}$$

$$v_d = \frac{V_d}{b \cdot d \cdot f_c} = \frac{1}{1 + 0.66 \cdot \left(\frac{a}{z(\alpha)}\right)^2} \cdot \left(1 + 4.1 \cdot \frac{k_e}{f_c} \cdot \frac{\alpha A_{sh} \beta f_{yh} + \alpha A_v \beta f_{yb}}{b \cdot a}\right) \cdot \sqrt{\left(\frac{x_c(\alpha)}{d}\right)^2 + \left(\frac{t_b}{d}\right)^2} \cdot \sin\theta(\alpha) \tag{42}$$

$$v_{flexural} = \frac{V_{flexural}}{b \cdot d \cdot f_c} = \frac{\alpha \cdot \beta}{\psi} \cdot \omega \cdot \frac{d}{a} \cdot \left(1 - \frac{1}{1.7} \cdot \omega \cdot \frac{\alpha \cdot \beta}{\psi}\right) \tag{43}$$

Figures 12(a) and (b) show the variation of dimensionless shear strength versus ρf_y and a/d for x_m = 0.20 and 40%. It is evident that with an increase in the loss of mass, there is a reduction of load-carrying capacity, with a larger effect for lower values of the a/d.

COMPARISON WITH AVAILABLE EXPERIMENTAL DATA

In this section, a comparison with available experimental data given in the literature is made in terms of load-carrying capacity. The first research is that reported in extended form in the literature,[26] which refers to third-point bending tests on dapped-end beams having an a/d between 0.59 and 1.51, compressive strength between 27.7 and 69.2 MPa (4 and 10.34 ksi), ρf_y between 1.22 and 10.14 MPa

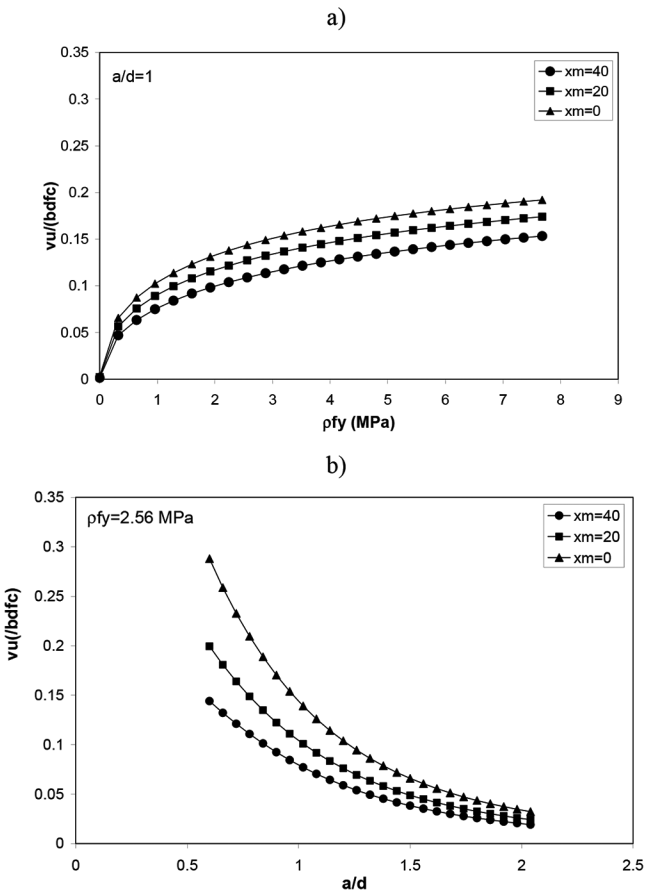


Fig. 12—Variation of shear strength with variation of: (a) ρf_y*; and (b)* a/d.

(0.176 and 1.47 ksi), $\rho_v f_{yv}$ between 0 and 6.45 MPa (0.93 ksi), and $\rho_h f_{yh}$ between 0 and 4.35 MPa (0.63 ksi).

The second research examined was that of Abdul-Jawad,[32] and it was used here for comparison with the analytical and numerical results obtained with ABAQUS in Abdul-Jawad.[32] In this research, three RC beams with a shear span-depth ratio of 1.2 were tested under a vertical load. The variables considered were compressive strength of concrete, main dapped-end reinforcement, and horizontal and vertical stirrups. The beams were formed on opposite ends of rectangular prismatic beams 3600 mm (141.73 in.) long. All the nibs were 500 mm (19.68 in.) long and had an overall height of 260 mm (10.23 in.). The reinforcement of the nibs contained main bars and horizontal and vertical stirrups, as shown in Fig. 12. The sizes and amounts of the main bars, horizontal stirrups, vertical stirrups, and hanger bars in each specimen can be found in Abdul-Jawad.[32]

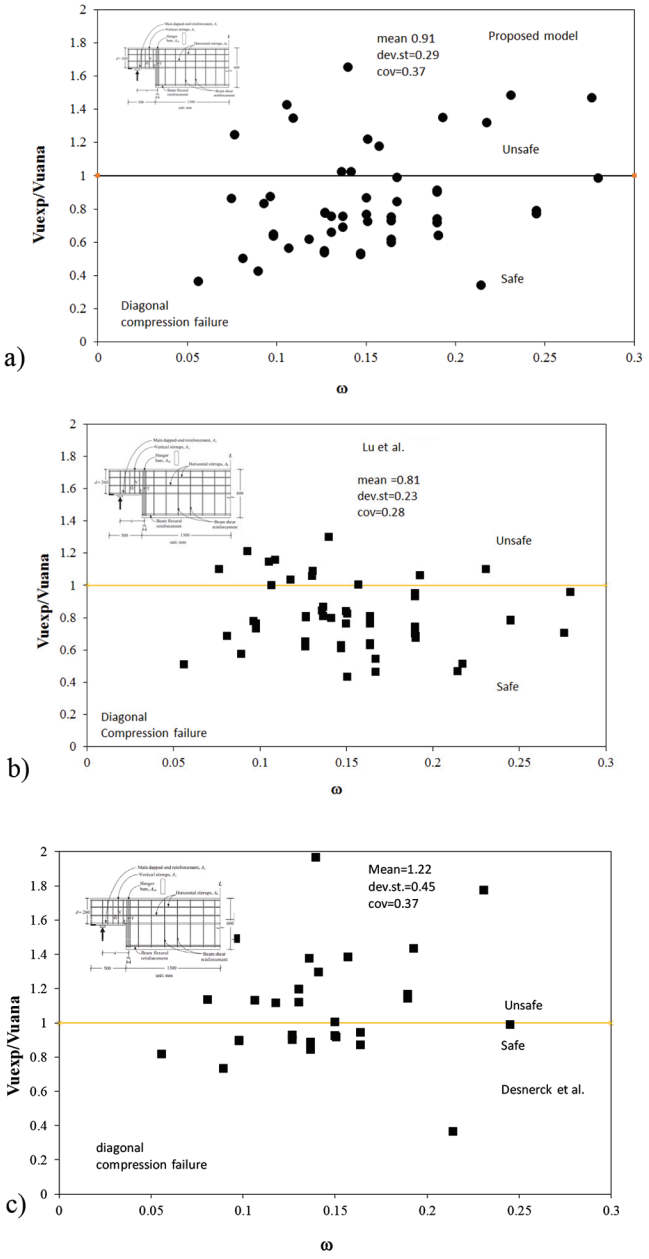


Fig. 13—Comparison between analytical and experimental results: (a) current model; (b) Lu et al.[25] model; and (c) Desnerck et al.[29]

Figure 13 shows the variation in the ratio between the experimental and the analytical prediction of load-carrying capacity with the variation in ω values according to the current model (Fig. 13(a)) and the model proposed by Lu et al.[25] (Fig. 13(b)). Both models give mean, standard deviation, and correlation factor values that are very close to one another, with the advantage that the proposed model is simpler to use to determine the strength contribution in the strut-and-tie mechanisms due to the presence of horizontal and vertical stirrups.

Figure 14 shows the variation of dimensionless shear stress with the variation of the mechanical ratio of longitudinal reinforcements. In the same graph, the analytical curves obtained with the current model, the Lu et al. model,[25] and the ACI 318-19[1] model are shown. The comparison highlights that the proposed model is the most conservative, while ACI 318-19[1] is sometimes unsafe for high values of a/d (1.2 and 1.5). The Lu et al.[25] model seems the most accurate for $a/d = 0.66$ and 1.20, while it seems unsafe for $a/d = 1.5$.

Figure 15 shows the influence of the a/d and the ratio of longitudinal reinforcement ρf_y stress on the ultimate load for the B3 specimen. It is observed that the maximum strength of the specimen declines with an increase in the a/d. In the same graph, numerical prediction with ABAQUS, the analytical proposed model, and the Lu et al.[25] model are given. A comparison between numerical and proposed models proves satisfactory, while in some cases, the Lu et al.[25] model is unsafe.

Finally, the experimental research of di Prisco et al.,[18] referring to a real case of degraded dapped-end beams with corroded bars that failed recently in a bridge in Italy, was used for a further comparison. The object of the collapse was the Annone overpass, which occurred in October 2016. The tests carried out to identify the characteristics of the materials used for the construction, the verification calculations that led to the identification of the critical mechanism in the collapse, and the test on the structural element deemed critical at the time of collapse are summarized. The bridge was built between 1960 and 1962. As shown by the original project, the deck consists of three longitudinal girders, for a total length of 56.10 m (2209 in.). Transversely, the deck consists of an ordinary RC slab, cast on site on cupels, with a total width of 7.40 m (291 in.), resting on five prefabricated beams in RC, placed at a distance of 1.35 m (53 in.). The two lateral girders constrained at the shoulders are placed on the intermediate piers (with a distance between their centers of 24.60 m [969 in.]) and project, with respect to the latter, 2.80 m (110 in.). The central girder rests on the two lateral girders by means of an indirect Gerber saddle support, to be isostatic. The span of the central beam, which is isostatic, is equal to 18.70 m (736 in.). Figure 16(a) shows an image of the breaking of the Gerber saddle of the collapsed bridge. A part of the unsized beam was cut and subjected to bending tests according to the scheme of Fig. 16(b). The reinforcements of the Gerber saddles that are considerably corroded are those indicated in Fig. 16(c). The model also included the contribution of diagonal bars by considering the horizontal

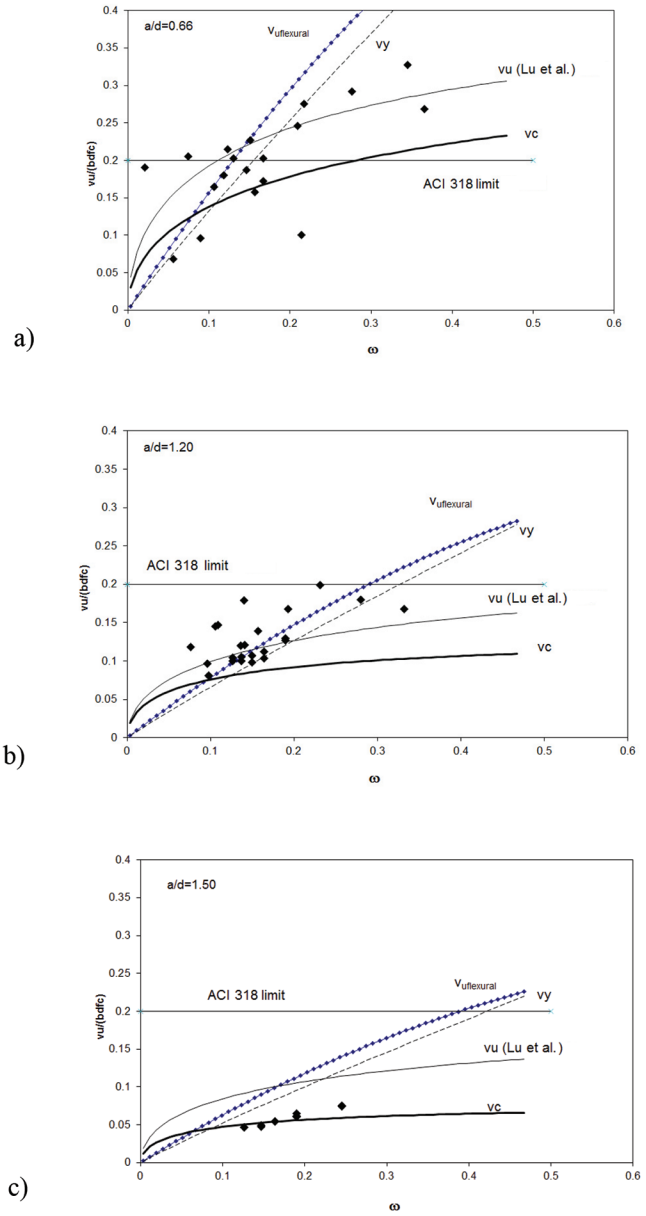


Fig. 14—Variation of dimensionless shear strength versus mechanical ratio of main steel for a/d*: (a) 0.66; (b) 1.20; and (c) 1.50.*

contribution in addition to the contribution of the main steel bars along the strut direction in reducing the compressive force.

The degradation induced by corrosion due to pitting was calculated theoretically with the proposed model, supposing a loss of mass that was measured experimentally; a loss of mass of 19% was calculated. The area of steel corrosion considered here was measured experimentally. The yield stress assumed was also that determined experimentally. The comparison is satisfactory in terms of maximum load.

CONCLUSIONS

The design of disturbed regions in reinforced concrete (RC) half-joints is traditionally performed by means of strut-and-tie modeling (STM) or nonlinear finite element modeling. The international design provisions found in standards and codes can be used for the assessment of existing structures

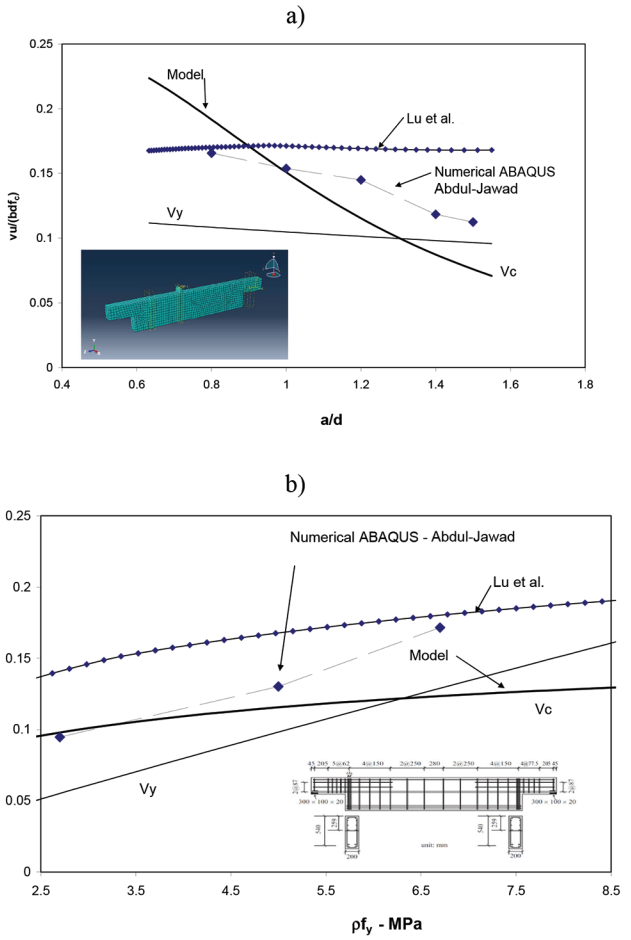


Fig. 15—Effects of: (a) a/d*; and (b)* ρf_y *on shear strength of dapped-end beams.*

with minor adjustments, but they give limited guidance on the incorporation of deterioration aspects such as corrosion, insufficient anchorage lengths, and crack formation.

A simplified STM was developed to predict the flexural response of the Gerber support, including the effects of corrosion of steel bars due to general and pitting corrosion. Loss of area, reduction in yield stress and ductility of steel bars, loss of bond and reduction in the anchorage length, and reduction in the compressed regions due to cracking of concrete were considered in the model and related to loss of mass of bars and crack width measured experimentally. Reduction of the width of the cross section was also considered to account for spalling of the concrete, while the effective concrete strength was reduced to account for the corrosion. The proposed STM was checked against experimental data available in the literature for dapped-end beams with corroded bars (main bars and transverse stirrups) and other existing models. The results of this comparison indicated that the proposed STM reasonably predicted the residual shear strength of the corroded dapped end-beams, and it is easy to include in the existing models given in the codes.

AUTHOR BIOS

Giuseppe Campione *is a Professor at the University of Palermo, Palermo, Italy, where he received his BS, MS, and PhD in civil engineering in 1988 and 1995. His research interests include shear strength and seismic design of fiber-reinforced concrete and fiber-reinforced polymer (FRP) structures.*

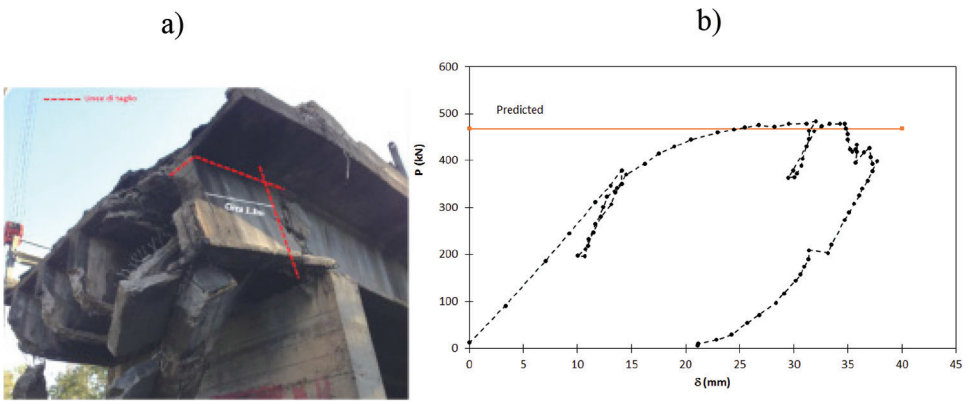


Fig. 16—(a) Failed overpass in Annone, Italy; and (b) load-deflection curves.

Maria Zizzo *is a Civil Engineer. She received her BS and MS in civil engineering in 2016 and her PhD in 2023 from the University of Palermo. Her research interests include the structural behavior of direct foundations and the influence of material degradation in structural members of reinforced concrete bridges.*

NOTATION

A_s = initial area of horizontal steel bars of Gerber saddle
$A_{scorroded}$ = corroded area of main steel of Gerber saddle
A_{sh} = area of horizontal stirrups
a = shear span
b = width of saddle
C = compressive force in strut
c = cover thickness
f_c = compressive strength of concrete
f_{cc} = compressive strength of confined concrete
f_y = yield stress of steel bars
f_{yw} = yield stress of stirrups
H = horizontal force
n = number of horizontal bars in tension
p = pitting depth
T = tensile force in horizontal bars
V = vertical force
V_c = shear strength at concrete crushing
V_y = shear strength at yielding
X = depth of attack penetration
X_m = loss of mass
x_c = neutral axis position
z = arm of internal forces
$\alpha_{pitting}$ = reduction factor of area of steel bars for pitting corrosion
$\alpha_{uniform}$ = reduction factor of area of steel bars for general corrosion
β = reduction factor of steel properties
ϕ = diameter of horizontal steel bars of Gerber saddle
γ = reduction factor of bond
θ = inclination of strut
ξ = softening coefficient in compression
ψ = reduction factor of compressive strength

REFERENCES

1. ACI Committee 318, "Building Code Requirements for Structural Concrete (ACI 318-19) and Commentary (ACI 318R-19) (Reapproved 2022)," American Concrete Institute, Farmington Hills, MI, 2019, 624 pp.

2. EN 1992-1-1:2004, "Eurocode 2: Design of Concrete Structures – Part 1-1: General Rules and Rules for Buildings," European Committee for Standardization, Brussels, Belgium, 2004, 227 pp.

3. Cook, W. D., and Mitchell, D., "Studies of Disturbed Regions near Discontinuities in Reinforced Concrete Members," *ACI Structural Journal*, V. 85, No. 2, Mar.-Apr. 1988, pp. 206-216.

4. Sanders, D. H., "Example 2: Dapped-End T-beam Supported by an Inverted T-beam," *Examples for the Design of Structural Concrete with Strut-and-Tie Models*, SP-208, K.-H. Reineck, ed., American Concrete Institute, Farmington Hills, MI, 2002, pp. 91-103.

5. *fib*, "CEB-FIP Model Code 1990," International Federation for Structural Concrete, Lausanne, Switzerland, 1993, 460 pp.

6. Mattock, A. H., "Behavior and Design of Dapped-End Members," *Proceedings of the U.S.-Japan Seminar on Precast Concrete Construction in Seismic Zones*, N. M. Hawkins and R. E. Englekirk, eds., Tokyo, Japan, Oct.-Nov. 1986, pp. 81-100.

7. Imperatore, S., "Influence of the Bond-Slip Relationship on the Flexural Capacity of R.C. Joints Damaged by Corrosion," *AIP Conference Proceedings*, V. 1738, No. 1, June 2016, Article No. 270021. doi: 10.1063/1.4952060

8. Zhang, X., and Li, B., "Shear-Strength Capacity Assessment of Corroded Reinforced Concrete Beam-Column Joints," *Journal of Performance of Constructed Facilities*, ASCE, V. 32, No. 5, Oct. 2018, p. 04018067. doi: 10.1061/(ASCE)CF.1943-5509.0001216

9. Lee, H.-S.; Noguchi, T.; and Tomosawa, F., "Evaluation of the Bond Properties Between Concrete and Reinforcement as a Function of the Degree of Reinforcement Corrosion," *Cement and Concrete Research*, V. 32, No. 8, Aug. 2002, pp. 1313-1318.

10. Zhang, X.; Wang, L.; Zhang, J.; and Liu, Y., "Model for Flexural Strength Calculation of Corroded RC Beams Considering Bond–Slip Behavior," *Journal of Engineering Mechanics*, ASCE, V. 142, No. 7, July 2016, p. 04016038. doi: 10.1061/(ASCE)EM.1943-7889.0001079

11. Almusallam, A. A., "Effect of Degree of Corrosion on the Properties of Reinforcing Steel Bars," *Construction and Building Materials*, V. 15, No. 8, Dec. 2001, pp. 361-368. doi: 10.1016/S0950-0618(01)00009-5

12. Imperatore, S.; Leonardi, A.; and Rinaldi, Z., "Mechanical Behaviour of Corroded Rebars in Reinforced Concrete Elements," *Mechanics, Models and Methods in Civil Engineering*, M. Frémond and F. Maceri, eds., Springer-Verlag GmbH, Heidelberg, Germany, 2012, pp. 207-220.

13. François, R.; Khan, I.; and Dang, V. H., "Impact of Corrosion on Mechanical Properties of Steel Embedded in 27-Year-Old Corroded Reinforced Concrete Beams," *Materials and Structures*, V. 46, No. 6, June 2013, pp. 899-910. doi: 10.1617/s11527-012-9941-z

14. Yan, X.; Di, W.; Yingfeng, T.; Minqiu, H.; and Hai, S., "Experimental Studies on Mechanical Properties of Corroded Steel Bars After Elevated Temperature," *Procedia Engineering*, V. 210, 2017, pp. 622-629. doi: 10.1016/j.proeng.2017.11.122

15. Campione, G., and Cannella, F., "Engineering Failure Analysis of Corroded R.C. Beams in Flexure and Shear," *Engineering Failure Analysis*, V. 86, Apr. 2018, pp. 100-114. doi: 10.1016/j.engfailanal.2017.12.015

16. Ghods, P.; Isgor, O. B.; and Pour-Ghaz, M., "A Practical Method for Calculating the Corrosion Rate of Uniformly Depassivated Reinforcing Bars in Concrete," *Materials and Corrosion*, V. 58, No. 4, Apr. 2007, pp. 265-272. doi: 10.1002/maco.200604010

17. Vecchi, F.; Franceschini, L.; Tondolo, F.; Belletti, B.; Sánchez Montero, J.; and Minetola, P., "Corrosion Morphology of Prestressing Steel Strands in Naturally Corroded PC Beams," *Construction and Building Materials*, V. 296, Aug. 2021, Article No. 123720. doi: 10.1016/j.conbuildmat.2021.123720

18. di Prisco, M.; Colombo, M.; Martinelli, P.; and Coronelli, D., "The Technical Causes of the Collapse of Annone Overpass on SS.36," *Structural Concrete Today: Theory, Uses, Materials, Techniques: Proceedings of AICAP/CTE Italian Concrete Conference*, M. di Prisco and M. Menegotto, eds., Naples, Italy, Sept. 20-22, 2018, 16 pp. (in Italian)

19. Val, D. V., "Deterioration of Strength of RC Beams due to Corrosion and Its Influence on Beam Reliability," *Journal of Structural Engineering*, ASCE, V. 133, No. 9, Sept. 2007, pp. 1297-1306. doi: 10.1061/(ASCE)0733-9445(2007)133:9(1297)

20. Taha, N. A., and Morsy, M., "Study of the Behavior of Corroded Steel Bar and Convenient Method of Repairing," *HBRC Journal*, V. 12, No. 2, Aug. 2016, pp. 107-113. doi: 10.1016/j.hbrcj.2014.11.004

21. Coronelli, D., and Gambarova, P., "Structural Assessment of Corroded Reinforced Concrete Beams: Modeling Guidelines," *Journal of Structural Engineering*, ASCE, V. 130, No. 8, Aug. 2004, pp. 1214-1224. doi: 10.1061/(ASCE)0733-9445(2004)130:8(1214)

22. Bhargava, K.; Ghosh, A. K.; Mori, Y.; and Ramanujam, S., "Suggested Empirical Models for Corrosion-Induced Bond Degradation in Reinforced Concrete," *Journal of Structural Engineering*, ASCE, V. 134, No. 2, Feb. 2008, pp. 221-230.

23. El Maaddawy, T.; Soudki, K.; and Topper, T., "Analytical Model to Predict Nonlinear Flexural Behavior of Corroded Reinforced Concrete Beams," *ACI Structural Journal*, V. 102, No. 4, July-Aug. 2005, pp. 550-559.

24. Kearsley, E. P., and Joyce, A., "Effect of Corrosion Products on Bond Strength and Flexural Behaviour of Reinforced Concrete Slabs," *Journal of the South African Institution of Civil Engineering*, V. 56, No. 2, Aug. 2014, pp. 21-29.

25. Lu, W.-Y.; Chen, T.-C.; and Lin, I.-J., "Shear Strength of Reinforced Concrete Dapped-end Beams with Shear Span-to-Depth Ratios Larger than Unity," *Journal of Marine Science and Technology*, V. 23, No. 4, 2015, pp. 431-442.

26. Mander, J. B.; Priestley, M. J. N.; and Park, R., "Theoretical Stress-Strain Model for Confined Concrete," *Journal of Structural Engineering*, ASCE, V. 114, No. 8, Sept. 1988, pp. 1804-1826. doi: 10.1061/(ASCE)0733-9445(1988)114:8(1804)

27. Campione, G., "Performance of Steel Fibrous Reinforced Concrete Corbels Subjected to Vertical and Horizontal Loads," *Journal of Structural Engineering*, ASCE, V. 135, No. 5, May 2009, pp. 519-529. doi: 10.1061/(ASCE)0733-9445(2009)135:5(519)

28. Mancini, G., and Tondolo, F., "Effect of Bond Degradation Due to Corrosion – A Literature Survey," *Structural Concrete*, V. 15, No. 3, Sept. 2014, pp. 408-418. doi: 10.1002/suco.201300009

29. Desnerck, P.; Lees, J. M.; and Morley, C. T., "Strut-and-Tie Models for Deteriorated Reinforced Concrete Half-Joints," *Engineering Structures*, V. 161, Apr. 2018, pp. 41-54. doi: 10.1016/j.engstruct.2018.01.013

30. Chen, H.; Yi, W.-J.; and Hwang, H.-J., "Cracking Strut-and-Tie Model for Shear Strength Evaluation of Reinforced Concrete Deep Beams," *Engineering Structures*, V. 163, May 2018, pp. 396-408. doi: 10.1016/j.engstruct.2018.02.077

31. El-Sayed, A. K., "Strut-and-Tie Modeling for RC Short Beams with Corroded Stirrups," *Latin American Journal of Solids and Structures*, V. 11, No. 12, 2014, pp. 2255-2270. doi: 10.1590/S1679-78252014001200008

32. Abdul-Jawad, H. M., "Modelling of Dapped-End Beams Using ABAQUS Software," *International Journal of Civil Engineering and Technology (IJCIET)*, V. 9, No. 1, Jan. 2018, pp. 1-10.

JOIN AN ACI Chapter!

The American Concrete Institute has Chapters and Student Chapters located throughout the world. Participation in a local chapter can be extremely rewarding in terms of gaining greater technical knowledge and networking with leaders in the concrete community.

Because chapters are distinct and independent legal entities, membership includes both ACI members and non-ACI members and is made up of a diverse blend of architects, engineers, consultants, contractors, educators, material suppliers, equipment suppliers, owners, and students—basically anyone interested in concrete. Many active ACI members initially became involved in ACI through their local chapter. In addition to technical programs and publications, many chapters sponsor ACI Certification programs, ACI educational seminars, project award recognition programs, and social events with the goal of advancing concrete knowledge.

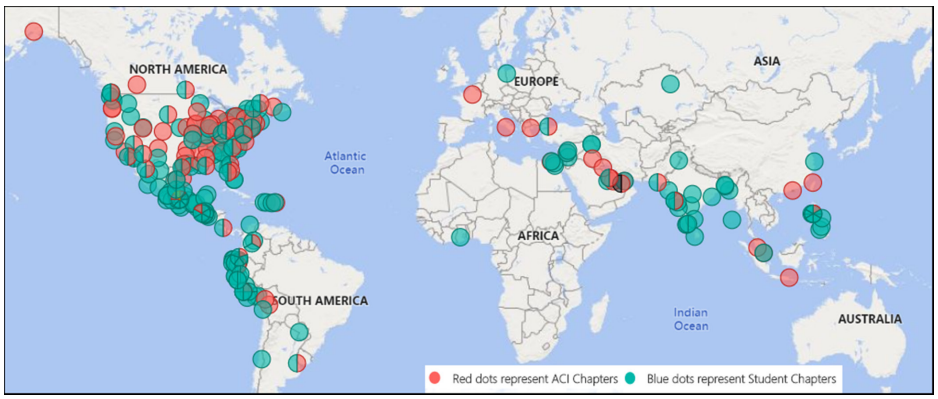
To find a chapter near you, go to: https://www.concrete.org/getinvolved/chapters.aspx

---

Student Chapters

Join or form an ACI Student Chapter to maximize your influence, knowledge sharing, and camaraderie! ACI has 240+ student chapters located throughout the world, each providing opportunities for students to:

- Connect with their peers and participate in concrete-related activities such as: student competitions, ACI Conventions, ACI Certification Programs, ACI Educational Seminars, local chapter meetings, social events, and community service projects;
- Network with members of local chapters, many of whom have been in the industry for decades and can help to develop professional relationships and offer career advice;
- Win recognition for their universities through the University Award; and
- Learn about the many scholarships and fellowships offered by the ACI Foundation and by ACI's local chapters.



ACI STRUCTURAL JOURNAL TECHNICAL PAPER

Title No. 122-S66

Debonding and Control of Shield Tunnel Strengthened with Thin Plate

by Dejun Liu, Xiaoyun Yao, Qingqing Dai, Cong Tian, and Jiangwen Zheng

Inner surface reinforcement is one of the most widely adopted techniques for upgrading or strengthening shield tunnels. An important failure mode in this method is the debonding of the thin plates from the segments, resulting in less reinforcement effect than expected. A shield tunnel lining is a discontinuous curved structure formed by connecting segments with bolts, and its structural form and internal force state are essentially different from reinforced concrete beams. However, there are few reports on the evolution process of debonding failure of similar structures. Therefore, to develop a thorough understanding of the debonding failure, a three-dimensional refined numerical model for a shield tunnel strengthened by a thin plate at the inner surface based on the mixed-mode cohesive method was proposed. The validity and rationality of the model were corroborated by a full-scale experiment. Then, the model was applied to other inner surface reinforcement schemes commonly used in practice to explore the debonding mechanism of the adhesive layer. Finally, anti-debonding measures were proposed, and their effectiveness was elucidated by numerical analysis. The results show that the proposed numerical model can accurately predict the failure process of the adhesive interface of the shield tunnel strengthened by a thin plate. There are obvious interfacial stress concentrations at the joints and the plate ends, which are the essential reasons for the debonding failure initiating from those places. Anchoring the thin plate only at the plate ends and joints can significantly and sufficiently increase the debonding load. Therefore, it is not necessary to add anchoring measures elsewhere.

Keywords: anti-debonding measures; cohesive zone model; inner surface reinforcement; interface debonding; numerical analysis; shield tunnel.

INTRODUCTION

With the rapid development in urban traffic infrastructure, more and more underground tunnels have been constructed in recent years. More recently, shield tunnels have become an important component of urban infrastructure. As a one-dimensional ultra-long linear assembly structure built in complex and uncertain stratum, there are many uncertain factors in the design, construction, and service environment of shield tunnels. Therefore, structural defects are prevalent in the lining segments, such as differential settlement, water leakage, concrete spalling, steel bar corrosion, and even bolt yielding.[1-3] Those issues are rooted in the structural deformation of shield tunnel segments.[2] Various remedial measures (Fig. 1) have been developed to address structural deformations,[4-10] among which inner surface reinforcement is the most commonly adopted method. However, many experiments and field practice have shown that debonding failure is the primary failure mode for such reinforcement,[11-13] which often leads to insufficient use of reinforcement materials and fails to achieve the desired purpose. Therefore, considering the deformation and stress characteristics of shield tunnels and the influence of joints, bolts, and other structures, it is imperative to clarify the debonding mechanism and propose effective anti-debonding measures.

When the reinforced concrete structure is retrofitted by bonding a thin plate to its soffit, the debonding failure largely depends on the interfacial stresses. Research findings on the interfacial stresses of such strengthened structures have been extensively reported. Theoretically, the most commonly used assumption was simplifying the adhesive layer as a shear layer. The normal and shear stresses in the adhesive layer were constant along the thickness direction. Thus, the simple approximate solution of the interfacial stresses was derived.[14-17] However, this assumption leads to the extreme value of shear stress at the end of the adhesive layer, contradicting the free boundary condition at the end of the adhesive layer.[18,19] When the bending stiffness of the thin plate is much less than that of the strengthened member, the interfacial stresses obtained by the simple approximate solution are consistent with the finite element results, except for the ends of the adhesive layer—for example, the case of reinforced concrete (RC) beams strengthened with fiber-reinforced polymer (FRP) sheets. However, when the bending stiffness of the thin plate is large, the assumption that the normal and shear stresses are constant along the thickness direction of the adhesive layer does not hold well. Therefore, to overcome the limitations of the simple approximate solution, researchers have considered the deformation compatibility conditions in the normal direction of the adhesive layer, and a more accurate high-order analytical model of the interfacial stresses has been obtained.[20-22] Further, some researchers developed the bond-slip model based on "interfacial fracture energy,"[23-25] which reflected the response of interfacial shear stress and normal stress during the complete loading process. However, those theoretical solutions primarily focus on continuous structures, and the nonlinear behavior of materials is also not considered. Therefore, such models are unsuitable for the solution of interfacial stresses of shield tunnels strengthened by thin plates at the inner surface.

In terms of numerical analysis, Teng et al.[26] presented the influence of the mesh size on the interfacial stresses and the stress mutation phenomena in the adhesive layer. Zhang

ACI Structural Journal, V. 122, No. 5, September 2025.

MS No. S-2022-355.R2, doi: 10.14359/51746813, received January 10, 2024, and reviewed under Institute publication policies. Copyright © 2025, American Concrete Institute. All rights reserved, including the making of copies unless permission is obtained from the copyright proprietors. Pertinent discussion including author's closure, if any, will be published ten months from this journal's date if the discussion is received within four months of the paper's print publication.



Fig.1(a)



Fig.1(b)



Fig.1 (c)



Fig.1(d)



Fig.1 (e)



Fig.1(f)

Fig. 1—Common control methods for deformation of shield tunnels: (a) grouting in tunnel[4]; (b) grouting from ground surface[5]; (c) FRP[5]; (d) FRP grid[6]; (e) steel plate[4]; and (f) corrugated steel.

and Teng[27] discussed different finite element (FE) modeling approaches for RC beams strengthened with thin plates, in which the adhesive layer was simulated by plane stress and spring elements. It was assumed that the bonding interface would remain intact, and the main purpose was to explore the distribution law of the interfacial stresses under different structural parameters. Teng et al.[28] showed the first FE approach capable of accurately predicting debonding failure, focusing on plate-end debonding. The mixed-mode cohesive law was employed to depict interfacial behavior under a combination of normal and shear stress in the proposed FE method. In the work of Deng et al.,[29] notched steel beams strengthened with CFRP plates were simulated by the FE method, where the mixed-mode cohesive law was employed to determine the interfacial stresses, and the initiation, propagation, and debonding of interfacial cracks were accurately simulated.

Taking the typical segment structure of Shanghai subway tunnels as the research focus, Liu et al.[11] investigated the bearing capacity and failure mechanism of a shield tunnel strengthened with full-ring and half-ring steel plates by a full-scale test. The test results showed that the stiffness and bearing capacity of shield tunnels could be significantly enhanced by bonding steel plates on the inner surface. Still, the debonding failure between the steel plates and tunnel segments was the governing failure mode of such a strengthened structure. Liu et al.[30] evaluated the influence of steel plates on the stiffness and bearing capacity of shield tunnels by numerical analysis, in which the tie contact was adopted for the adhesive layer without considering the debonding failure. A simplified numerical model of the shield tunnel strengthened with thin plates was proposed by Zhao et al.,[13] in which segments and thin plates were simulated by beam elements, whereas the adhesive layer was simulated by spring elements. In the study by Liu et al.,[31] the shield tunnel was regarded as a homogeneous curved beam, while shield tunnel members and reinforcement materials were treated as elastic materials. Thus, the relation for the interfacial stresses was developed, and the distribution law of interfacial stresses at the end of the thin plate was preliminarily discussed. However, the influence of joints on the interfacial stresses was not considered in the study, and the analysis of the evolution process of the debonding failure could not be realized.

Therefore, it is of great significance to accurately simulate the bonding behavior for a thorough understanding of debonding failure mechanism of thin-plate reinforced shield tunnels. To that end, the present study proposes a FE approach for the shield tunnel strengthened with thin plates, focusing on the accurate modeling of the interfacial behavior using the mixed-mode cohesive method. Then, the rationality of the proposed FE approach was validated by a full-scale test. Further, the evolution process of the debonding failure under commonly employed reinforcement schemes in practice was analyzed through the proposed numerical model—that is, shield tunnels strengthened with half-ring steel plates and CFRP along the crown at an angle of 30 degrees. Finally, reasonable anti-debonding measures were suggested, and their corresponding effects were determined by numerical analysis.

RESEARCH SIGNIFICANCE

The load-carrying capacity of the shield tunnel strengthened with thin plates on inner surface depends on the contribution of the thin plate at the time of debonding. However, previous studies have focused on the strengthening gain of the bearing capacity of the shield tunnel improved by the thin plate, either ignoring debonding failure or blindly increasing anchoring measures to avoid interface failure. The purpose of the present study was to develop a numerical method to

simulate the debonding failure of shield tunnels strengthened with thin plates on its inner surface and to provide useful information for proposing the reasonable anti-debonding measures. The debonding process of shield tunnels strengthened with thin plates can be accurately simulated by the proposed numerical model, where the mixed-mode cohesive law was employed to represent the stress distribution and debonding process. For shield tunnels strengthened with thin plates on the inner surface, debonding initiates from the presence of discontinuities, such as joints or ends of thin plates with concentrated interfacial stress. Therefore, the joints of the segments and ends of the thin plate are the key parts for controlling interface failure. The findings in this study are important for the development of debonding prevention measures. Although the numerical model was established with the Shanghai tunnel as the engineering background, the method proposed in this paper can also be used for reinforcement simulation of other tunnels.

FAILURE CRITERION OF BONDING INTERFACE

An important failure mode in the inner surface reinforcement of the shield tunnel is the debonding of the thin plate from the segments. The load-carrying capacity of such strengthened structures depends on the contribution of the thin plate at the time of debonding, which in turn depends on the interfacial stress transfer of the adhesive layer. The successful prediction of debonding failure in thin-plate-strengthened shield tunnels requires a reasonable model for the adhesive interface between the segment lining and the thin plate. Therefore, it is particularly important to accurately simulate the bonding behavior, which requires an appropriate model for the damage behavior of the adhesive interface. There are three failure modes of the adhesive layer—namely, opening, shear cracking, and tear cracking.[32] The final failure mode is also a mixture of opening and shear cracking. For accurate prediction of debonding, the mixed-mode cohesive law was proposed for numerical simulation,[28,29] in which all three failure modes can be simulated. For the adhesive layer of thin-plate-strengthened shield tunnels, there is a concurrency of the normal and shear stress that interact with each other on damage propagation along the bonding interface.[30,31] Therefore, the mixed-mode cohesive model was adopted for modeling of the adhesive layer, which has been proven to provide accurate predictions for interfacial debonding behavior. More details of the mixed-mode cohesive model can be found in the references.[28,29,32]

THREE-DIMENSIONAL REFINED FE MODEL

General information

The typical shield tunnel structure of the Shanghai metro was taken as the research object. The cross section of the lining structure is shown in Fig. 2. The inner and outer diameters of the lining ring are 5.5 and 6.2 m, respectively. The ring width is 1.2 m. Each lining ring consists of a top block K (16 degrees), two adjacent blocks L1 and L2 (65 degrees each), two standard blocks B1 and B2 (65 degrees each), and a bottom block D (84 degrees). These blocks are assembled along the longitudinal direction with M30 steel bolts of 5.8 grade at each longitudinal joint. The bolt length is

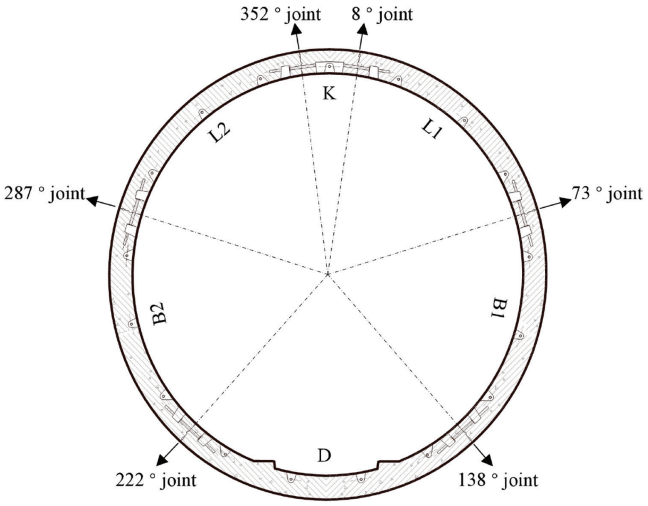


Fig. 2—Typical cross section of shield lining in Shanghai.

400 mm, and the diameter of the bolt hole is 42 mm. The bolt hole is located at $t/3$ from the inner surface of the lining segment (t is the thickness of the segment).

Finite element (FE) model

The general FE software ABAQUS was used in this study. A refined numerical model for a shield lining strengthened with a thin plate on the inner surface was proposed, focusing on the accurate modeling of the bond behavior of the adhesive layer. In this study, the crown of the tunnel was set to 0 degrees, and clockwise rotation was considered positive. Due to the symmetry of the structure and boundary conditions, only a quarter of a lining ring was simulated considering the computational efficiency—that is, from 180 to 360 degrees in the circumferential direction and half in the longitudinal direction, as shown in Fig. 3. In the numerical model, 222-, 287-, and 352-degree joints were resolved. The thin plate was symmetrically pasted on the tunnel inner surface along the crown using epoxy resin. Epoxy resin thickness was assumed to be 2 mm.

In the ABAQUS element library, each node of the C3D8R element (eight-node linear hexahedral element, reduced integral, hourglass control element) has a degree of freedom in each axis, which is conducive to the solution of three-dimensional (3-D) stress and strain. Therefore, the segments, bolts, and thin plates were all simulated in the numerical model with C3D8R elements. The longitudinal joints were connected by 5.8 grade M30 straight bolts, and the interaction between adjacent lining segments was set. The hard contact was employed in the normal direction, whereas friction contact was adopted in the tangential direction, and the coefficient of friction was taken as 0.4. The adhesive layer plays a vital role in the stress transfer between the lining and the thin plate, which is the key point of the numerical model. The COH3D8 element (eight-node 3-D cohesive element) in ABAQUS is developed based on the traction-separation criterion, which was employed to simulate the adhesive layer. In the FE model, the top and bottom surfaces of the adhesive layer were tied with the inner surface of the lining and the outer surface of the thin plate, respectively.

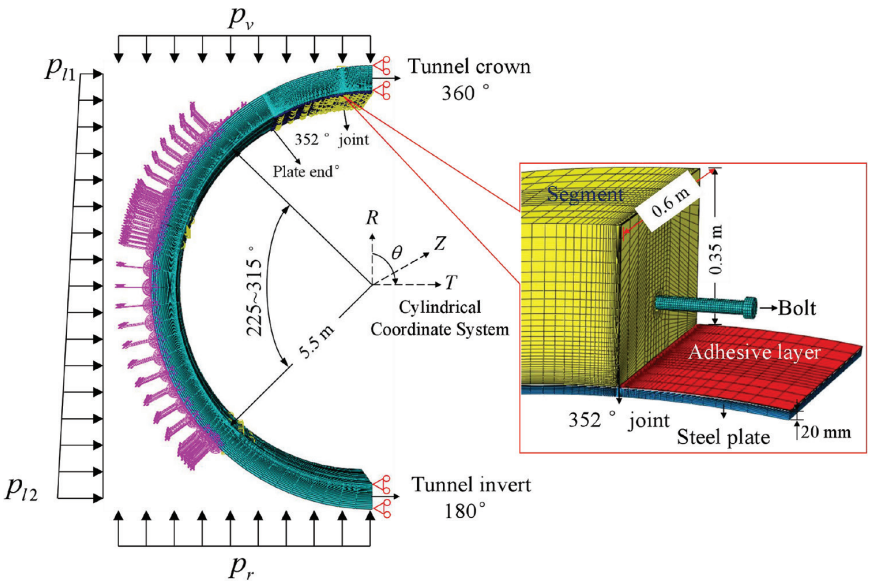


Fig. 3—Details of numerical model.

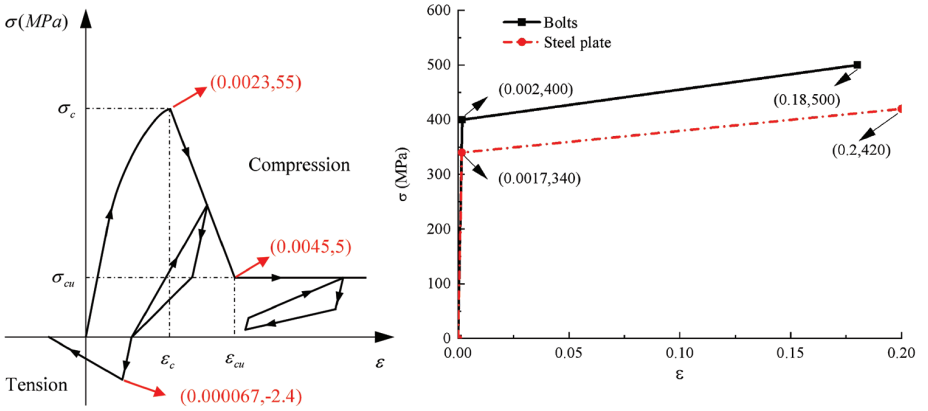


Fig. 4(a) **Fig. 4(b)**

Fig. 4—Constitutive relationship of components: (a) concrete; and (b) steel plate and bolts.

The same mesh division was adopted in the circumferential direction for the lining, adhesive layer, and thin plate. The mesh was encrypted at the ends of the plate and near the joint. Concerning the convergence of the FE model, the relationship between the principal bond stress and the mesh size was analyzed. When the mesh size of the cohesive element in the encryption area was 0.25 mm, the FE model reached convergence. The detail of the mesh is shown in Fig. 3.

Constitutive model

The constitutive models of the concrete, bolts, and steel plates are shown in Fig. 4. The constitutive model of the concrete was consistent with that proposed by Park and Paulay,[33] which had been widely used in the FE simulation of the shield tunnel lining. In the compression process, the stress-strain response follows the parabolic relationship until the stress reaches the compressive strength σ_c, and then the stress decreases linearly with the strain until the stress reaches the ultimate strength σ_{cu}. Before reaching the tensile strength, the stress-strain behavior is assumed to be linear during the tensile process, and the key point values are shown in Fig. 4(a). A bilinear constitutive model (Fig. 4(b)) was employed for the steel plate and bolts.[34] The mixed-mode cohesive law introduced in section "Failure Criterion of Bonding Interface" was adopted for the failure criterion of the adhesive layer. The key parameters of the traction-separation model used in the present study are given in Table 1.

Table 1—Parameters of traction-separation model[12]

Parameters / Direction	Ultimate strength, MPa	Ultimate displacement, mm	Interfacial fracture energy, N/mm
Normal direction	1.65	0.00165	0.225
Shear direction	6.83	0.01886	1.81

Load and boundary conditions

The loads acting on the tunnel segment are shown in Fig. 3, where p_v is the vertical earth pressure at the top of the tunnel; p_{l1} and p_{l2} are the lateral earth pressure at the crown and the invert of the tunnel, respectively; and p_r is the reaction pressure at the bottom of the tunnel. The load between p_{l1} and p_{l2} is linearly distributed. Those pressures can be calculated from the equations presented by Liu et al.[31]

and Zhang et al.[35] In addition, nonlinear ground springs were employed in the range of 225 to 315 degrees along the tunnel circumferential direction to simulate the soil resistance pressure caused by the transverse deformation of the lining. The spring resistance coefficient was set to 15,000 kN/m^3. The nodes at the crown and invert of the lining were constrained in normal translation and rotation.

Validation of proposed 3-D refined model

The experimental results of the full-scale test conducted by Liu et al.[11] were used to validate the 3-D refined model proposed earlier. The tunnel lining was strengthened by a full-ring steel plate fixed up along the segmental circumferential midline. The steel plate thickness and width were 20 and 850 mm, respectively. The structural dimensions, the modeling approach, and material parameters were the same as those described earlier.

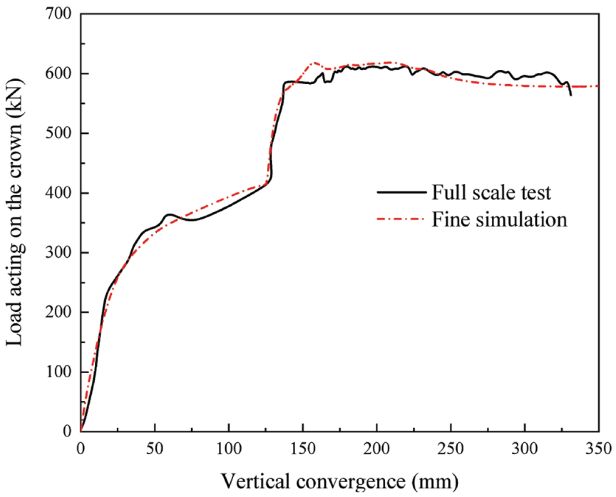


Fig. 5—Comparison of load-displacement curves between numerical analysis and experiment.

As shown in Fig. 5, when the steel plate was activated, as the load continued to increase, there was almost no change in the vertical convergence, and the curve was almost vertical. It is thus inferred that the steel plate significantly improved the stiffness of the lining structure. Overall, the curves of load versus deformation obtained by the numerical analysis and the scale test showed good consistency. For the strengthening point, where the vertical convergence reached 120 mm, the load acting on the crown obtained by the scale test and the numerical analysis were 418 and 413.73 kN, respectively, with an error of only 1.02%. When the lining structure reached the ultimate capacity, the value obtained by the numerical analysis was 611.6 kN, which was very close to the measured value of 603.4 kN—that is, an error of merely 1.36%.

Figure 6 shows the stiffness degradation (SDEG) of the adhesive layer under different vertical convergences. When the vertical convergence of the lining was 136.18 mm, the adhesive layer near the 287-degree joint first began to damage (Fig. 6(a)). With the continuous increase of the vertical convergence, the damage of the adhesive layer at 287- and 352-degree joints increased significantly, but the damage at the 352-degree joint developed faster. When the vertical convergence reached 157.70 mm, SDEG near the 352-degree joint was 1 (Fig. 6(b))—that is, the debonding failure started. When the vertical convergence increased to 167.02 mm, the interface element near the 352-degree joint completely failed, and the steel plate debonded from the segment (Fig. 6(c)). When

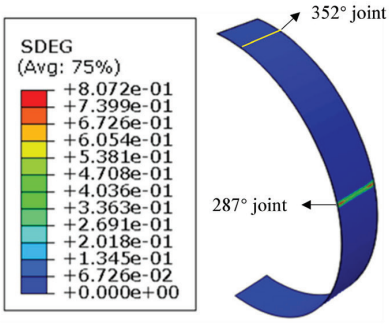


Fig. 6(a)

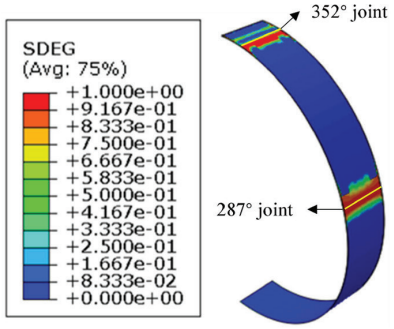


Fig. 6 (b)

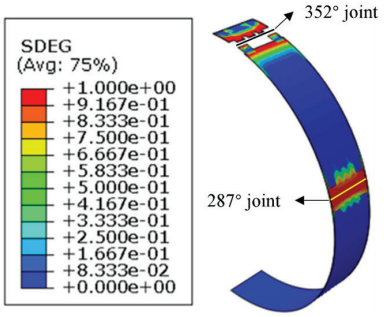


Fig. 6 (c)

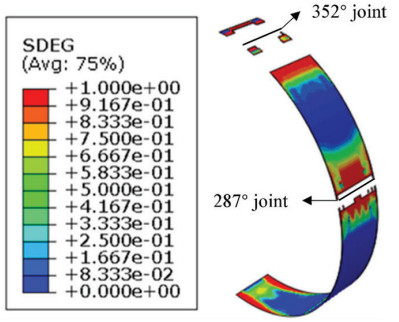


Fig. 6 (d)

Fig. 6—SDEG of adhesive layer: (a) initiation of damage (136.18 mm); (b) initiation of debonding failure (157.70 mm); (c) extension of debonding failure (167.02 mm); and (d) final failure mode (305.24 mm). (Note: numbers in brackets are vertical convergence.)

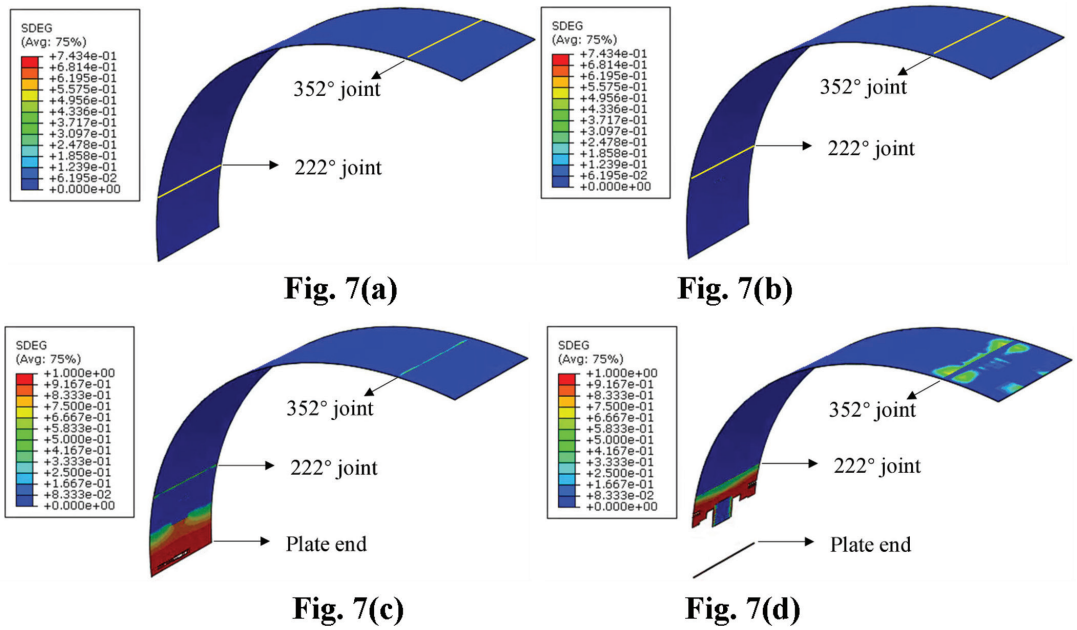


Fig. 7—SDEG of adhesive layer: (a) 3 mm; (b) 5 mm; (c) 24 mm (initiation of debonding failure); and (d) 47 mm.

the vertical convergence reached 305.24 mm, the debonding failure range of the interface near the 352-degree joint continued to expand, and there also was obvious debonding failure near the 287-degree joint (Fig. 6(d)). However, the debonding failure range near the 352-degree joint was much larger than that near the 287-degree joint. The interface failure process described previously was consistent with that observed in the scale test. The detailed results of the full-scale test can be found in Liu et al.[11]

The aforementioned analysis shows that the proposed 3-D refined numerical model has excellent prediction accuracy for the bearing performance and debonding failure of the thin-plate strengthened shield lining. Consequently, the proposed 3-D refined model can be used for the subsequent analysis of interface failure.

FAILURE EVOLUTION OF ADHESIVE LAYER

Reinforcement of half-ring steel plate

In practice, two methods are commonly employed to reinforce shield tunnels with steel plates: full-ring steel plate and half-ring steel plate. When the shield lining was strengthened by a half-ring steel plate, the SDEG of the adhesive layer under different vertical convergences is shown in Fig. 7. When the vertical convergence was small, the adhesive layer was intact (Fig. 7(a)). With the increase of vertical convergence, first, there was a damage concentration area in the 287-degree joint (Fig. 7(b)). As the vertical convergence continued to increase, the damage near the end of the steel plate increased rapidly and extended to the 287-degree joint (Fig. 7(c)). When the adhesive layer at the end of the steel plate completely failed, there was an obvious damage concentration area in the 352-degree joint, but there was no debonding failure (Fig. 7(d)).

To further understand the interfacial failure, the normal and shear stress of the adhesive layer from the plate end to the 287-degree joint under different vertical convergences were extracted, as shown in Fig. 8 and 9. In the two figures, the position of the end of the thin plate is defined as 0, and the distance from the joint to the end of the thin plate is equal to the corresponding arc length of the inner surface of the tunnel. That is, the radius of the inner surface of the tunnel is multiplied by the radians between the joint and the end of the thin plate. It can be seen that the plate end and the 287-degree joint are located at 0 and 816 mm on the horizontal axis, respectively. There were obvious interfacial stress concentrations at the end of the steel plate and the 287-degree joint. The end of the steel plate was in compression, whereas one side of the 287-degree joint was in tension and the other was in compression (Fig. 8). There was also an interfacial stress concentration near the bolt hole. However, the stress was significantly smaller than that at the 287-degree joint and the end of the steel plate. Due to the discontinuity in the boundary conditions, the interfacial stresses near the bolt hole noticeably fluctuated, especially the normal stress. When the vertical convergence was less than 5 mm (Fig. 8(b) and 9(b)), the normal and shear stress of the adhesive layer increased with the vertical convergence. When the vertical convergence increased to 24 mm—that is, the debonding vertical convergence—the shear and normal stress near the plate end became zero, indicating that the adhesive layer near the plate end failed (Fig. 8(c) and 9(c)). Then, the peak value of interfacial stresses moved from the plate end to the 287-degree joint, and the normal stress at the plate end decreased (Fig. 8(c)). When the vertical convergence increased to 47 mm, the peak value of interfacial stresses moved to the vicinity of the 287-degree joint (Fig. 8(d) and 9(d)). Besides, the length of "zero stress" was consistent with the SDEG of the adhesive layer.

Reinforcement of CFRP with 30-degree arrangement

Carbon FRP (CFRP) is another commonly used material for shield tunnel reinforcement. In this study, the 30-degree arrangement range of CFRP along the crown was selected

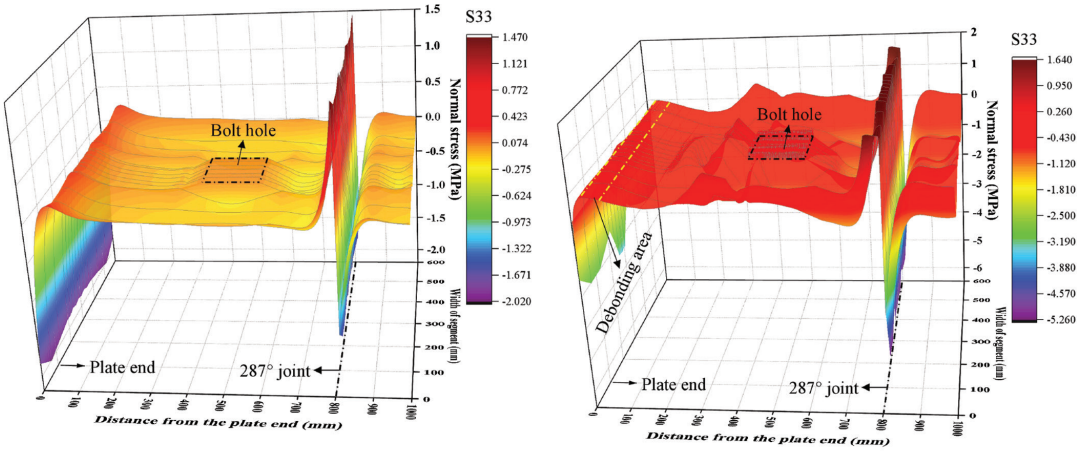


Fig. 8(a) Fig. 8(c)

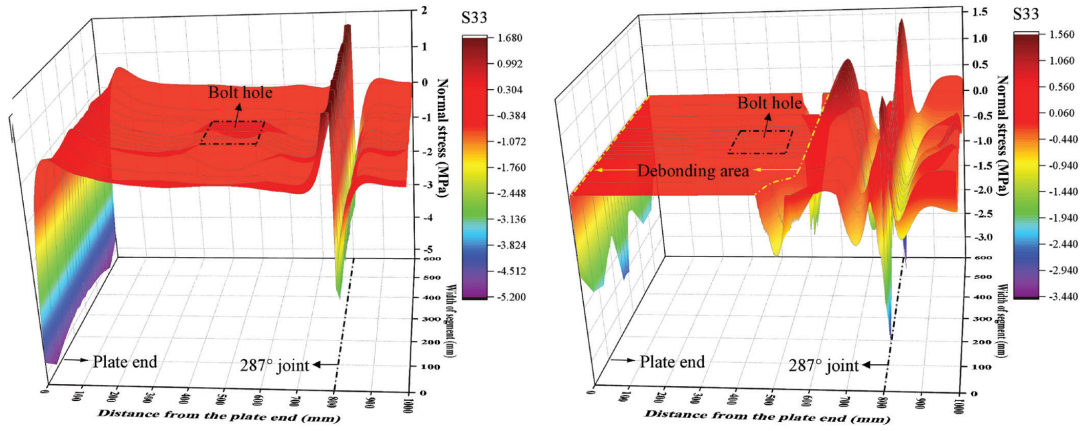


Fig. 8(b) Fig. 8(d)

Fig. 8—Normal stress distribution from plate end to 287-degree joint: (a) 3 mm; (b) 5 mm; (c) 24 mm (initiation of debonding failure); and (d) 47 mm.

as the reinforced scheme, which is also the most commonly adopted in practical applications. In the FE model, CFRP was regarded as an orthotropic material with a 2 mm thickness. According to Teng et al.[28] and Deng et al.,[36] the elastic modulus and Poisson's ratio in the fiber direction were 212 GPa and 0.3, respectively, while these parameters in the other two directions were 10 GPa and 0.0058, respectively.

In such a strengthening scheme, there is only the 352-degree joint of the shield tunnel within the scope of reinforcement. Figure 10 shows the SDEG of the adhesive layer under different vertical convergences. It can be concluded from the figure that there was a damage concentration in the adhesive layer near the 352-degree joint and the bolt hole (Fig. 10(a)), which significantly increased with the vertical convergence (Fig. 10(b) and (c)). When the vertical convergence reached 21.355 mm, the adhesive layer near the 352-degree joint started failing and expanding to both sides (Fig. 10(d) and (e)). However, it expanded faster towards the crown (Fig. 10(e)).

Figure 11 shows the distribution of the shear stress and the normal stress in the adhesive layer at different vertical convergences. There was stress concentration at the 352-degree joint. When the vertical convergence was 7.518 mm, the adhesive layer was all in an elastic state, and the peak value of the interfacial stresses was located at the 352-degree joint. As the vertical convergence increased to 13.882 mm, part of the adhesive layer near the 352-degree joint entered the soft stage, and the peak value of the interfacial stresses moved towards both sides. The interfacial stresses fluctuated in the softened part of the adhesive layer, especially the normal stress (Fig. 11(a)). The length of the soft stage increased with further increase of the vertical convergence until initiation of debonding failure of the adhesive layer (the vertical convergence was 21.355 mm). Then the debonding failure initiated at the 352-degree joint and propagated rapidly to both sides of the joint, as shown in the curves of 27.650 and 31.840 mm in Fig. 11. When the adhesive layer entered the debonding stage, the stress curve no longer changed with the increase in vertical convergence but moved to both sides as a whole. The interfacial stress distribution also showed that the debonding expanded faster towards the crown, which was consistent with the SDEG of the adhesive layer.

CONTROL MEASURES OF INTERFACIAL FAILURE

The previous analysis showed that the debonding failure of the adhesive layer initiated near the plate ends or the joints. Based on the model of the shield tunnel strengthened by the half-ring steel plate introduced in the subsection

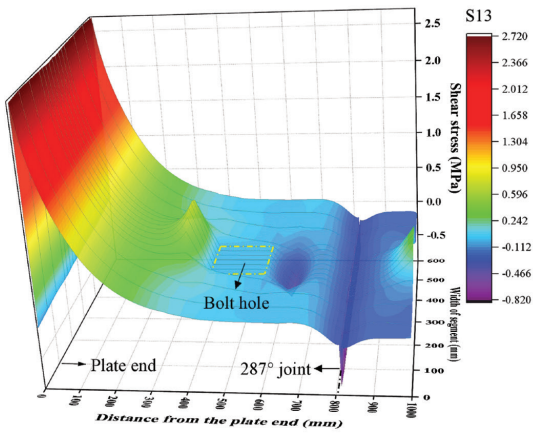


Fig. 9 (a)

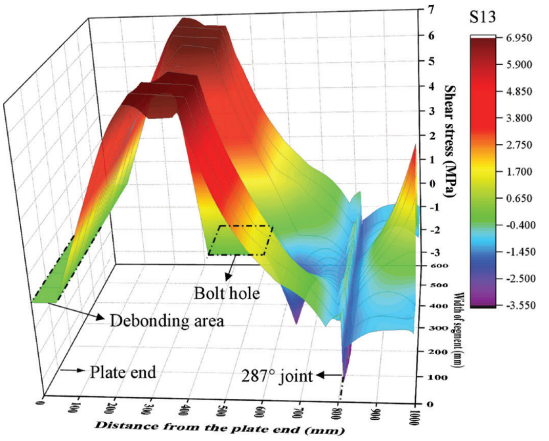


Fig. 9 (c)

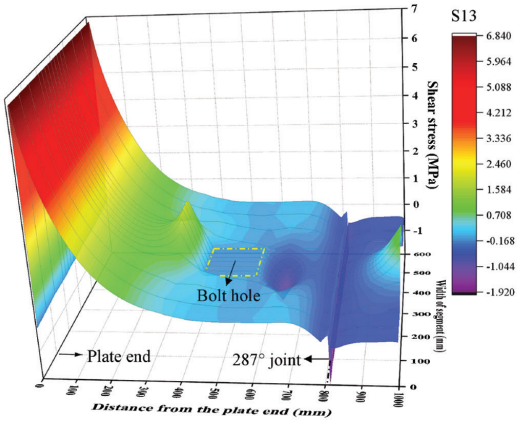


Fig. 9 (b)

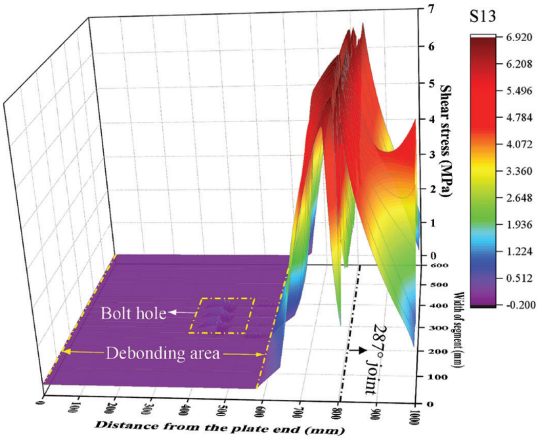


Fig. 9 (d)

Fig. 9—Shear stress distribution from plate end to 287-degree joint: (a) 3 mm; (b) 5 mm; (c) 24 mm (initiation of debonding failure); and (d) 47 mm.

"Reinforcement of half-ring steel plate," the influence of the anchoring measures and the end shape of the steel plate on the interfacial stresses is discussed in this section. Also, reasonable control measures for preventing interfacial failure are put forward.

Anchoring measures

In the FE model, it was assumed that the part of the adhesive layer anchored with bolts did not fail, and its upper and lower surfaces were tied with the segment and the steel plate, respectively. The simulation method of the other components was the same as that described in the section "Three-Dimensional Refined FE Model," while the load and boundary conditions were the same as those shown in Fig. 3. In practical application, bolts are employed to anchor the steel plate to avoid interfacial debonding. In Fig. 12, the shield tunnel is strengthened with a half-ring steel plate, and 22 rows of anchor bolts are uniformly arranged along the circumferential direction. Thus, holes need to be drilled on the segments before installing bolts. The more bolts there are, the more damage to the concrete will be induced. Therefore, clarifying the necessity of arranging so many anchor bolts to prevent interface failure is imperative. The numerical results show an interfacial stress concentration at the plate ends and the joints, resulting in the interfacial debonding occurring at these parts and then gradually expanding. Consequently, preventing interfacial debonding at the plate ends and the joints is critical. In this part, the failure modes of the interface were compared under two cases: uniform anchorage employed in practice, and stress concentration anchorage where bolts are only arranged at the plate ends and the joints.

The SDEG of the adhesive layer under uniform anchorage is shown in Fig. 13. There was also damage concentration at the plate ends and the joints (Fig. 13(a) and (b)). At the initial loading stage, the interface damage near the plate end was more obvious (Fig. 13(b)). With the load increase, the interface damage at the 352-degree joint developed rapidly, and interface failure occurred first (Fig. 13(c)). Compared with the scheme without anchoring measures (as shown in the subsection "Reinforcement of half-ring steel plate"), the initial position of interfacial failure under uniform anchorage shifted from the end of the steel plate to the vicinity of the 352-degree joint (Fig. 13(c)), and the debonding load increased by 59.70 kN with an increase of 21%. In the complete loading process, under the scheme of uniform anchorage, there was no interface failure at the plate end (Fig. 13(d)), indicating that the bolt arranged at the plate end is effective in preventing the interface failure.

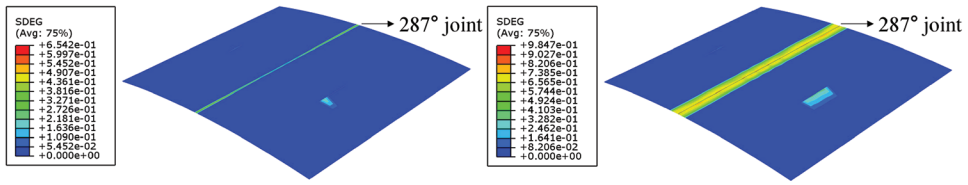


Fig. 10(a) **Fig. 10(b)**

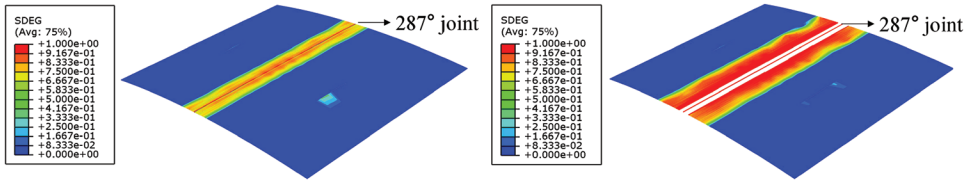


Fig. 10(c) **Fig. 10(d)**

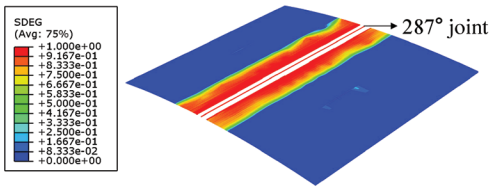


Fig. 10(e)

Fig. 10—SDEG of adhesive layer: (a) 7.518 mm; (b) 13.882 mm; (c) 21.355 mm; (d) 27.650 mm (initiation of debonding failure); and (e) 31.840 mm.

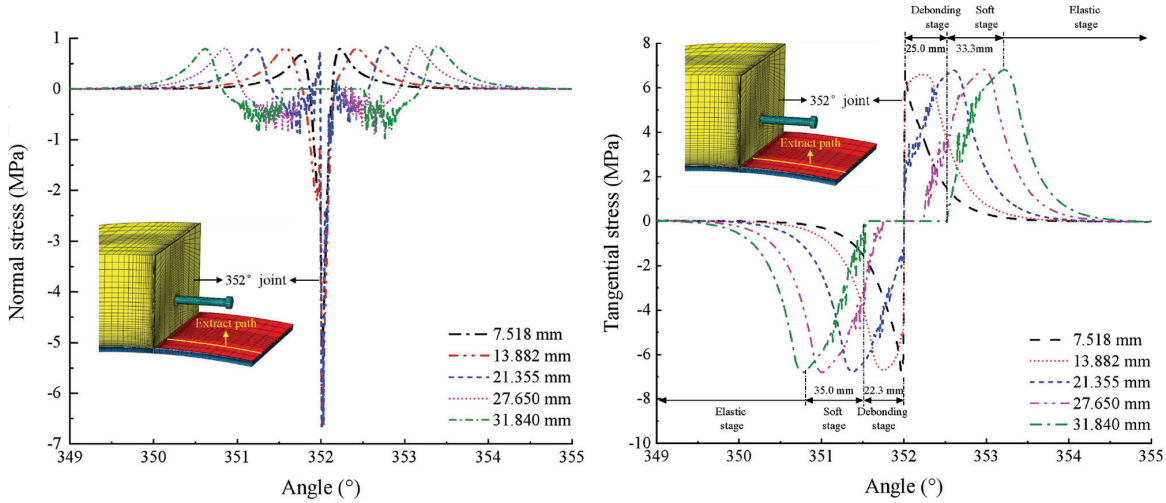


Fig. 11(a) **Fig. 11(b)**

Fig. 11—Distribution of interfacial stresses near 352-degree joint: (a) normal stress; and (b) shear stress.

The SDEG of the adhesive layer under stress concentration anchorage is shown in Fig. 14. The failure mode of the stress concentration anchorage was the same as that of the uniform anchorage—that is, interface failure occurred at the 352-degree joint—and there was obvious damage concentration at the plate end. Compared with the scheme without anchoring measures (as presented in the subsection "Reinforcement of half-ring steel plate"), the debonding load increased from 284.04 to 343.35 kN, with an increase of 20.9%.

The previous analysis shows that the debonding load of the scheme of the stress concentration anchorage is merely 0.38 kN less than that of uniform anchorage, indicating that the effects of uniform anchorage and stress concentration anchorage on controlling interface failure are the same. Uniform anchorage does not only cause a waste of bolts, but also results in additional damage to tunnel segments due to drilling. Therefore, it is recommended that bolts are arranged only at the plate ends and joints are sufficient to prevent interfacial failure.

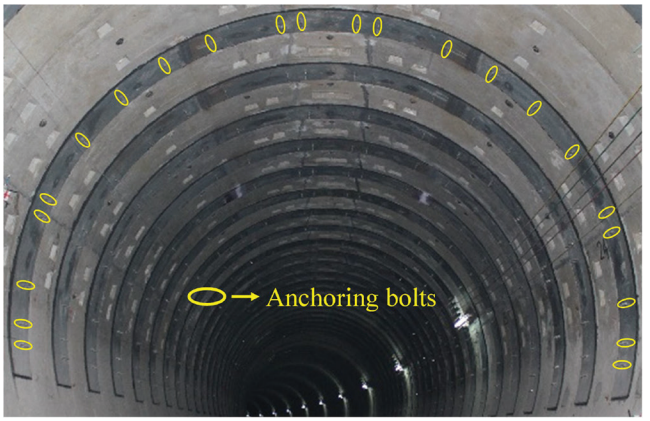


Fig. 12—Anchoring measures of steel plate adopted in practice.

Shape of plate ends

Previous studies have shown that the steel plate thickness significantly impacts the magnitude and distribution of the interfacial stresses. Specifically, the thicker the steel plate, the greater the interfacial stresses, and the easier the adhesive layer is to debond.[31] When the shield tunnel was strengthened by the half-ring steel plate, there was stress concentration at the plate end, which led to debonding failure. Consequently, the influence of the end shape of the steel plate on the interfacial failure was also analyzed. In the FE model, the end shape of the steel plate was changed from upright to conical (Fig. 15), while the other conditions were the same as that introduced in the subsection "Reinforcement of half-ring steel plate." The SDEG of the adhesive layer with the conical end is displayed in Fig. 16. The initiation and propagation process of the interfacial failure

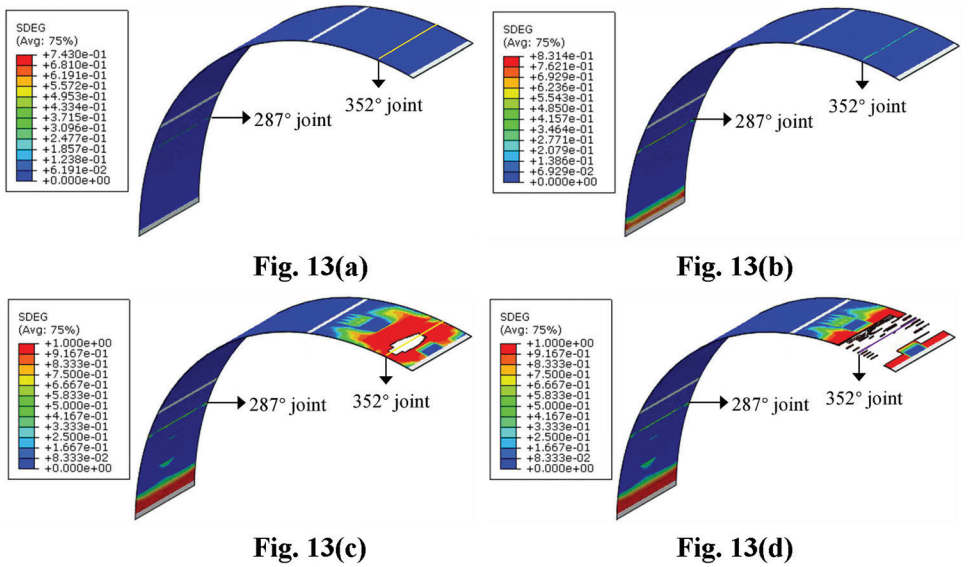


Fig. 13—SDEG of adhesive layer under uniform anchorage: (a) 102.69 kN; (b) 284.04 kN; (c) 343.74 kN (debonding load); and (d) 349.18 kN.

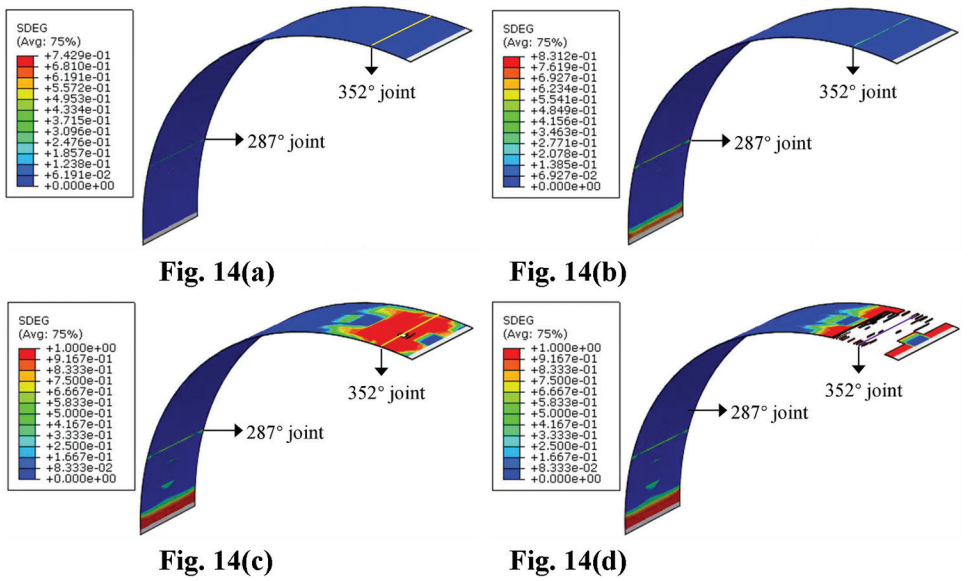


Fig. 14—SDEG of adhesive layer under stress concentration anchorage: (a) 102.69 kN; (b) 284.04 kN; (c) 343.35 kN (debonding load); and (d) 349.19 kN.

under the conical plate end and the upright plate end were the same. However, compared with the upright plate end, the debonding load of the conical plate end increased by 6.4%, from 284.04 to 302.14 kN. Therefore, the conical plate end is a useful measure to prevent debonding failure.

CONCLUSIONS

To deepen the understanding of the debonding failure of the adhesive interface of the shield tunnel strengthened by bonding a thin plate at the inner surface, a three-dimensional (3-D) refined numerical model focusing on the simulation of the adhesive interface was proposed. The rationality of the proposed model was validated by a full-scale experiment. The model was then extended to other cases to explore the debonding mechanism of the adhesive layer and propose reasonable anti-debonding measures. The main conclusions drawn from the study are as follows.

1. The mixed-mode cohesive method can accurately predict the interface failure process of a shield tunnel reinforced with a thin plate at its inner surface.
2. There are interfacial stress concentrations at the joints and plate ends. When the shield tunnel is reinforced with a full-ring steel plate, the debonding failure initiates from the 352-degree joint, followed by the 287-degree joint; meanwhile, when a shield tunnel is reinforced with a half-ring steel plate, the debonding failure begins at the end of the steel plate and rapidly expands to the 287-degree joint. When the shield tunnel is reinforced with carbon fiber-reinforced polymer (CFRP) along the crown with an arrangement range of 30 degrees, the debonding failure initiates at the 352-degree joint and rapidly propagates to both ends of the joint.
3. Anchorage measures can significantly increase the debonding load. Compared with the scheme without anchorage measures, the increase of debonding load for uniform anchorage and the stress concentration anchorage is the same. Therefore, it is sufficient to anchor the thin plate at the plate ends and the joints in practical applications. A plate end with a conical shape can also improve the debonding load, but it is not as effective as the anchoring measure.

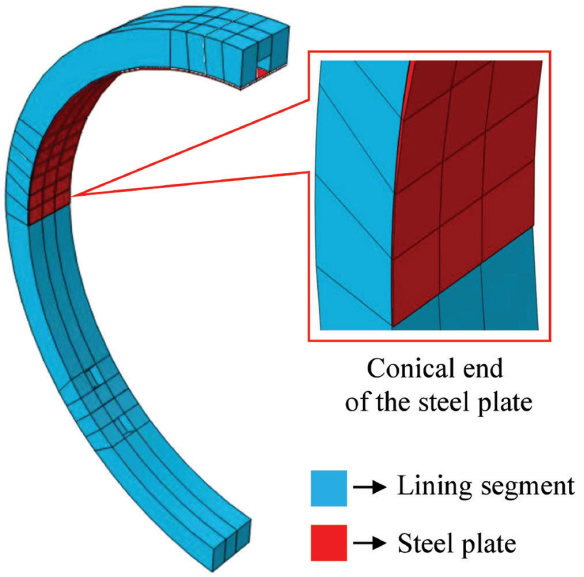


Fig. 15—Detail of conical end of steel plate.

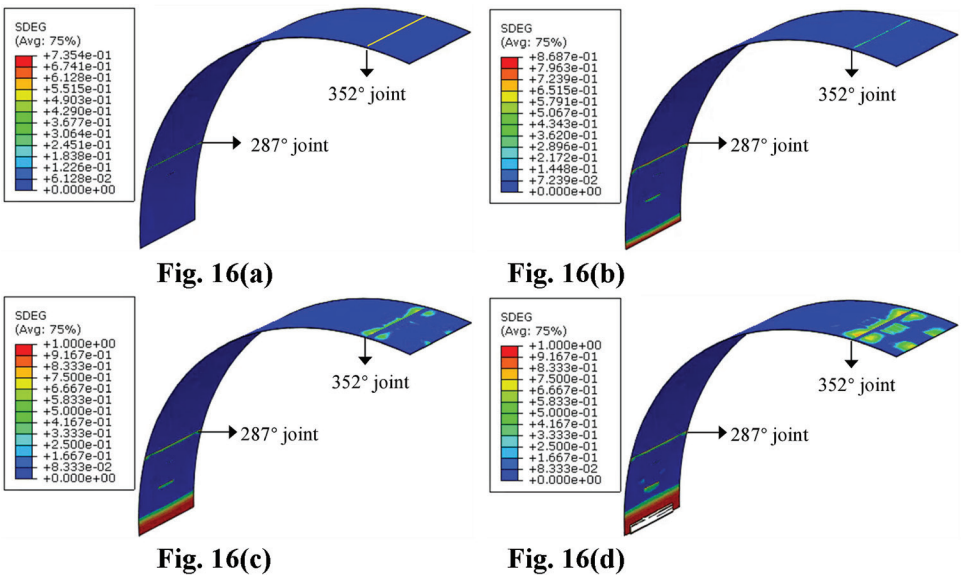


Fig. 16—SDEG of adhesive layer of scheme for steel plate with tapered end: (a) 102.69 kN; (b) 284.04 kN; (c) 302.14 kN (debonding load); and (d) 309.24 kN.

AUTHOR BIOS

Dejun Liu *is a Professor at School of Mechanics and Civil Engineering, China University of Mining and Technology, Beijing, Beijing, China. He received his BS and MS from Shandong University, Jinan, China, and his PhD from Tongji University, Shanghai, China. His research interests include reinforcement of reinforced concrete structures, textile-reinforced concrete, and fiber-reinforced polymer grid.*

Xiaoyun Yao *is a Master's Student at School of Mechanics and Civil Engineering, China University of Mining and Technology, Beijing. She received her BS from Jinggangshan University, Ji'an, China. Her research interests include nonlinear analysis of reinforced concrete structures.*

Qingqing Dai *is a Master's Student at School of Mechanics and Civil Engineering, China University of Mining and Technology, Beijing. He received his BS from Henan Polytechnic University, Jiaozuo, China. His research interests include stability analysis and control of underground structures.*

Cong Tian *is a Master's Student at School of Mechanics and Civil Engineering, China University of Mining and Technology, Beijing. He received his BS from Anhui University of Science and Technology, Huainan, China. His research interests include the numerical method of underground structures.*

Jiangwen Zheng *is an Undergraduate Student at School of Mechanics and Civil Engineering, China University of Mining and Technology, Beijing. His research interests include the numerical method of underground structures.*

ACKNOWLEDGMENTS

This study was substantially supported by the National Key R&D Program of China (No. 2023YFB2390300), the National Natural Science Foundation of China (Nos. 52478423), and the Fundamental Research Funds for the Central Universities (Grant no. 2024ZKPYLJ03).

REFERENCES

1. Shao, H.; Huang, H.; Zhang, D.; and Wang, R., "Case Study on Repair Work for Excessively Deformed Shield Tunnel under Accidental Surface Surcharge in Soft Clay," *Yantu Gongcheng Xuebao*, V. 38, No. 6, 2016, pp. 1036-1043.

2. Liu, D.; Huang, H.; Zuo, J.; Xue, Y.; and Li, Y., "Control Method and Mechanism of Large Transverse Deformation of Shield Segment Using TRC," *Yanshi Lixue Yu Gongcheng Xuebao*, V. 36, No. 8, 2017, pp. 1889-1898.

3. Liu, D.; Tian, C.; Wang, F.; Hu, Q.; and Zuo, J., "Longitudinal Structural Deformation Mechanism of Shield Tunnel Linings Considering Shearing Dislocation of Circumferential Joints," *Computers and Geotechnics*, V. 139, 2021, p. 104384. doi: 10.1016/j.compgeo.2021.104384

4. Liu, D.; Wang, F.; Hu, Q.; Huang, H.; Zuo, J.; Tian, C.; and Zhang, D., "Structural Responses and Treatments of Shield Tunnel Due to Leakage: A Case Study," *Tunnelling and Underground Space Technology*, V. 103, 2020, p. 103471. doi: 10.1016/j.tust.2020.103471

5. Huang, H., and Zhang, D., "Resilience Analysis of Shield Tunnel Lining under Extreme Surcharge: Characterization and Field Application," *Tunnelling and Underground Space Technology*, V. 51, 2016, pp. 301-312. doi: 10.1016/j.tust.2015.10.044

6. Liu, D.; Zhong, F.; Huang, H.; Zuo, J.; Xue, Y.; and Zhang, D., "Present Status and Development Trend of Diagnosis and Treatment of Tunnel Lining Diseases," *Zhongguo Gonglu Xuebao*, V. 34, No. 11, 2021, pp. 178-199.

7. Chang, C. T.; Wang, M. J.; Chang, C. T.; and Sun, C. W., "Repair of Displaced Shield Tunnel of the Taipei Rapid Transit System," *Tunnelling and Underground Space Technology*, V. 16, No. 3, 2001, pp. 167-173. doi: 10.1016/S0886-7798(01)00050-5

8. Liu, D.; Huang, H.; Yue, Q.; Xue, Y.; and Wang, M., "Behaviour of Tunnel Lining Strengthened by Textile-Reinforced Concrete," *Structure and Infrastructure Engineering*, V. 12, No. 8, 2016, pp. 964-976. doi: 10.1080/15732479.2015.1076009

9. Ai, Q.; Yuan, Y.; Mahadevan, S.; and Jiang, X., "Maintenance Strategies Optimisation of Metro Tunnels in Soft Soil," *Structure and Infrastructure Engineering*, V. 13, No. 8, 2017, pp. 1093-1103. doi: 10.1080/15732479.2016.1243564

10. Liu, D.; Shang, Q.; Li, M.; Zuo, J.; Gao, Y.; and Xu, F., "Cracking Behaviour of Tunnel Lining under Bias Pressure Strengthened Using FRP Grid-PCM Method," *Tunnelling and Underground Space Technology*, V. 123, 2022, p. 104436. doi: 10.1016/j.tust.2022.104436

11. Liu, X.; Jiang, Z.; Yuan, Y.; and Mang, H. A., "Experimental Investigation of the Ultimate Bearing Capacity of Deformed Segmental Tunnel Linings Strengthened by Epoxy-Bonded Steel Plates," *Structure and Infrastructure Engineering*, V. 14, No. 6, 2018, pp. 685-700. doi: 10.1080/15732479.2017.1354892

12. Liu, X.; Jiang, Z.; Yuan, Y.; and Mang, H. A., "Numerical Investigation of the Mechanical Behavior of Deformed Segmental Tunnel Linings, Strengthened by Epoxy-Bonded Filament Wound Profiles," *Tunnelling and Underground Space Technology*, V. 78, 2018, pp. 231-244. doi: 10.1016/j.tust.2018.04.033

13. Zhao, H.; Liu, X.; Bao, Y.; Yuan, Y.; and Bai, Y., "Simplified Nonlinear Simulation of Shield Tunnel Lining Reinforced by Epoxy Bonded Steel Plates," *Tunnelling and Underground Space Technology*, V. 51, 2016, pp. 362-371. doi: 10.1016/j.tust.2015.10.004

14. Smith, S. T., and Teng, J. G., "Interfacial Stresses in Plated Beams," *Engineering Structures*, V. 23, No. 7, 2001, pp. 857-871. doi: 10.1016/S0141-0296(00)00090-0

15. Abdelouahed, T., "Improved Theoretical Solution for Interfacial Stresses in Concrete Beams Strengthened with FRP Plate," *International Journal of Solids and Structures*, V. 43, No. 14-15, 2006, pp. 4154-4174. doi: 10.1016/j.ijsolstr.2005.03.074

16. Benachour, A.; Benyoucef, S.; Tounsi, A.; and Adda Bedia, E. A., "Interfacial Stresses Analysis of Steel Beams Reinforced with Bonded Prestressed FRP Plate," *Engineering Structures*, V. 30, No. 11, 2008, pp. 3305-3315. doi: 10.1016/j.engstruct.2008.05.007

17. De Lorenzis, L., and Zavarise, G., "Interfacial Stress Analysis and Prediction of Debonding for a Thin Plate Bonded to a Curved Substrate," *International Journal of Non-Linear Mechanics*, V. 44, No. 4, 2009, pp. 358-370. doi: 10.1016/j.ijnonlinmec.2009.01.002

18. Mostafa, A. A. B., and Razaqpur, A. G., "Finite Element Model for Predicting Post Delamination Behaviour in FRP-Retrofitted Beams in Flexure," *Construction and Building Materials*, V. 131, 2017, pp. 195-204. doi: 10.1016/j.conbuildmat.2016.11.066

19. De Lorenzis, L., and Zavarise, G., "Cohesive Zone Modeling of Interfacial Stresses in Plated Beams," *International Journal of Solids and Structures*, V. 46, No. 24, 2009, pp. 4181-4191. doi: 10.1016/j.ijsolstr.2009.08.010

20. Yang, J.; Teng, J. G.; and Chen, J. F., "Interfacial Stresses in Soffit-Plated Reinforced Concrete Beams," *Proceedings of the Institution of Civil Engineers - Structures and Buildings*, V. 157, No. 1, 2004, pp. 77-89. doi: 10.1680/stbu.2004.157.1.77

21. Stratford, T., and Cadei, J., "Elastic Analysis of Adhesion Stresses for the Design of a Strengthening Plate Bonded to a Beam," *Construction and Building Materials*, V. 20, No. 1-2, 2006, pp. 34-45. doi: 10.1016/j.conbuildmat.2005.06.041

22. Yang, J., and Ye, J., "An Improved Closed-Form Solution to Interfacial Stresses in Plated Beams Using a Two-Stage Approach," *International Journal of Mechanical Sciences*, V. 52, No. 1, 2010, pp. 13-30. doi: 10.1016/j.ijmecsci.2009.09.041

23. Rabinovitch, O., "Fracture-Mechanics Failure Criteria for RC Beams Strengthened with FRP Strips - A Simplified Approach," *Composite Structures*, V. 64, No. 3-4, 2004, pp. 479-492. doi: 10.1016/j.compstruct.2003.09.048

24. Carpinteri, A.; Cornetti, P.; and Pugno, N., "Edge Debonding in FRP Strengthened Beams: Stress versus Energy Failure Criteria," *Engineering Structures*, V. 31, No. 10, 2009, pp. 2436-2447. doi: 10.1016/j.engstruct.2009.05.015

25. De Lorenzis, L.; Fernando, D.; and Teng, J.-G., "Coupled Mixed-Mode Cohesive Zone Modeling of Interfacial Debonding in Simply Supported Plated Beams," *International Journal of Solids and Structures*, V. 50, No. 14-15, 2013, pp. 2477-2494. doi: 10.1016/j.ijsolstr.2013.03.035

26. Teng, J. G.; Zhang, J. W.; and Smith, S. T., "Interfacial Stresses in Reinforced Concrete Beams Bonded with a Soffit Plate: A Finite Element Study," *Construction and Building Materials*, V. 16, No. 1, 2002, pp. 1-14. doi: 10.1016/S0950-0618(01)00029-0

27. Zhang, L., and Teng, J. G., "Finite Element Prediction of Interfacial Stresses in Structural Members Bonded with a Thin Plate," *Engineering Structures*, V. 32, No. 2, 2010, pp. 459-471. doi: 10.1016/j.engstruct.2009.10.008

28. Teng, J. G.; Fernando, D.; and Yu, T., "Finite Element Modelling of Debonding Failures in Steel Beams Flexurally Strengthened with CFRP Laminates," *Engineering Structures*, V. 86, 2015, pp. 213-224. doi: 10.1016/j.engstruct.2015.01.003

29. Deng, J.; Li, J.; Wang, Y.; and Xie, W., "Numerical Study on Notched Steel Beams Strengthened by CFRP Plates," *Construction and Building Materials*, V. 163, 2018, pp. 622-633. doi: 10.1016/j.conbuildmat.2017.12.110

30. Liu, T.; Huang, H.; Xu, R.; and Yang, X., "Research on Load-Bearing Capacity of Metro Shield Tunnel Lining Strengthened by Bonded Steel Plates," *Zhongguo Gonglu Xuebao*, V. 30, No. 8, 2017, pp. 91-99.

31. Liu, D.; Wang, F.; Zhang, D.; and Duan, K., "Interfacial Stresses of Shield Tunnel Strengthened by a Thin Plate at Inner Surface," *Tunnelling and Underground Space Technology*, V. 91, 2019, p. 103021. doi: 10.1016/j.tust.2019.103021

32. Camanho, P. P.; Davila, C. G.; and de Moura, M. F., "Numerical Simulation of Mixed-Mode Progressive Delamination in Composite Materials," *Journal of Composite Materials*, V. 37, No. 16, 2003, pp. 1415-1438. doi: 10.1177/0021998303034505

33. Park, R., and Paulay, T., *Reinforced Concrete Structures*, Wiley, New York, NY, 1975.

34. Moser, T. C., "Rotational Stiffness of Single-Bolt Sleeve Connections," doctoral dissertation, Milwaukee School of Engineering, Milwaukee, WI, 2010.

35. Zhang, D. M.; Huang, Z. K.; Yin, Z. Y.; Ran, L. Z.; and Huang, H. W., "Predicting the Grouting Effect on Leakage-Induced Tunnels and Ground Response in Saturated Soils," *Tunnelling and Underground Space Technology*, V. 65, 2017, pp. 76-90. doi: 10.1016/j.tust.2017.02.005

36. Deng, J.; Lee, M. M. K.; and Moy, S. S. J., "Stress Analysis of Steel Beams Reinforced with a Bonded CFRP Plate," *Composite Structures*, V. 65, No. 2, 2004, pp. 205-215. doi: 10.1016/j.compstruct.2003.10.017

ACI STRUCTURAL JOURNAL TECHNICAL PAPER

Title No. 122-S67

Progressive Collapse Performance of Unbonded Prestressed Reinforced Concrete Beam-Column Subassemblages under Column Removal Scenarios

by Wen-Liu Xu, Li-Cheng Wang, Yong-Qin Liang, and Fei-Fan Feng

An approach to improve the progressive collapse resistance of conventional reinforced concrete (RC) frame structures was put forth by using unbonded post-tensioning strand (UPS). Two UPSs with straight profiles were mounted at the bottom of the beam section. A static loading test was conducted on an unbonded prestressed RC (UPRC) beam-column subassemblage under a column removal scenario. The structural behaviors of the test specimen such as load-carrying capacity, failure mode, post-tensioning force of the UPSs, and reinforcing bar strain were captured. By analyzing the results of the tested substructure, it was found that the compressive arch action (CAA) and catenary action (CTA) were sequentially mobilized in the UPRC subassemblage to avert its progressive collapse. The presence of UPSs could significantly improve the load-carrying capacity of conventional RC structures to defend against progressive collapse. Moreover, a high-fidelity finite element (FE) model of the test specimen was built using the software ABAQUS. The FE model was validated by experimental results in terms of the variation of vertical load, horizontal reaction force, and post-tensioning force of the UPSs against middle joint displacement (MJD). Finally, a theoretical model was proposed to evaluate the anti-progressive collapse capacities of UPRC subassemblages. It was validated by the test results as well as the FE models of the UPRC subassemblages, which were calibrated using the available experimental data.

Keywords: finite element (FE) model; progressive collapse performance; reinforced concrete (RC) frame structure; theoretical model; unbonded post-tensioning strand (UPS).

INTRODUCTION

Reinforced concrete (RC) frame structures may be subjected to accidental loads (explosions, fires, impacts, and so on) during their service life, resulting in local damage of these structures. As the initial local failure develops from one component to another, it may eventually lead to the collapse of the entire structure or a disproportionately large part of it.[1-5] The alternative load path (ALP) method has been extensively employed to estimate the anti-progressive collapse performance of RC frame structure under column removal scenarios.[6-9] In the ALP method, primary components of the structure system are notionally removed, and the progressive collapse resistance of the remaining structure is evaluated through structural analysis.[10,11] For example, Sasani et al.[12] conducted an in-place dynamic test on an actual 11-story RC frame structure following the explosion of several exterior columns. Their experimental results illustrated that the bidirectional Vierendeel action was recognized as the principal mechanism to mitigate progressive collapse risk of the residual structure.[13,14] Qian and Li[15] experimentally studied the dynamic behavior of multi-bay beam-column slab substructures under a column removal scenario. They found that the tested substructures could survive because catenary action (CTA) could develop in beams and tensile membrane action (TMC) in slabs, and their residual behaviors were also assessed by subsequent push-down tests. Adam et al.[16] performed a test to explore the progressive collapse-resistant behavior of a full-scale RC cast-in-place building structure after a corner column removal. It was observed that the effective load-transferred paths could activate in the structure after the sudden removal of a corner column, and as a result, extensive damage in the structures was avoided. Xiao et al.[17] presented the test results of a three-by-three bay and three-story half-scale RC frame structure subjected to a series of sudden column removals. The study showed that the compressive arch action (CAA) formed in the beams was only the predominant source of the load-resisting capacity if the corner or inner columns were removed. However, in the scenario of two-sided column removal, the structure experienced a transition from moment frame-resisting mechanism to catenary mechanism.

Izzuddin et al.[18] developed a simplified framework to estimate the potential of RC structures to collapse under the scenario of sudden column removal. In the framework, the anti-progressive collapse response on the beam level is essential for assessing progressive collapse resistance of a real-scale RC structure. Orton and Kirby[19] tested a one-quarter-scale two bay-by-two story RC planar frame following the sudden removal of the middle column. The test results revealed that the collapse-resistant capacity of the tested structures was chiefly attributed to the CTA mobilized in the beams. Yi et al.[20] carried out a progressive collapse test on a one-third-scale four bay-by-three story RC planar frame under a middle-column-removal scenario. Their experimental results demonstrated that the CAA formed in beams could markedly improve the progressive collapse resistance of the structure at the small deflection stage, and subsequently the development of the CTA at large deformation stage was conducive to mitigating its progressive collapse.

ACI Structural Journal, V. 122, No. 5, September 2025.

MS No. S-2023-205.R3, doi: 10.14359/51746754, received December 29, 2023, and reviewed under Institute publication policies. Copyright © 2025, American Concrete Institute. All rights reserved, including the making of copies unless permission is obtained from the copyright proprietors. Pertinent discussion including author's closure, if any, will be published ten months from this journal's date if the discussion is received within four months of the paper's print publication.

In addition, the effects of infill walls upon the progressive collapse behavior of RC planar frame were experimentally evaluated by many researchers.[21-24] It was found that the collapse-resistant capacity of the infilled frame could be significantly increased at both CAA and CTA stages. Moreover, extensive experimental studies[25-31] on RC beam-column subassemblage incorporating two-span beams and the middle column over column removal have been conducted, both statically and dynamically. These experimental results highlighted that the load-carrying capacity of RC subassemblages at the small deformation stage was primarily sustained by CAA, whereas under the large deformation stage, CTA developed to prevent catastrophic collapse of the subassemblages. In these tests, the drops of collapse-resistant capacity were attributed to the rupture of the beam bottom reinforcing bars near the middle column or the beam top reinforcing bars adjacent to the end column stubs. Once premature rupture of the reinforcing bars occurred at relatively small deformation, the anti-progressive collapse capacities of the structures sharply decreased and even triggered structural collapse.[32,33]

For this reason, many researchers recommended that steel strand be used to provide an alternative load path for RC frame structures to arrest progressive collapse in light of their higher tensile strength. For instance, Qian et al.[34] experimentally investigated whether one unbonded post-tensioning strand (UPS) with a parabolic curve could improve the collapse-resistant capacity of RC structure. The experimental results found that the UPS almost had no contribution to the CAA strength but could substantially upgrade its progressive collapse performance at the CTA stage. In a study by Deng et al.,[35] influences of bonded and unbonded strands with a parabolic profile on the progressive collapse response of an RC structure were explored experimentally. From the test results, it was observed that the load-carrying capacity of the RC substructure with bonded strand at the CAA stage was slightly higher than that of the RC substructure with unbonded strand, whereas their ultimate strength at CTA stage manifested a contrary trend. Yang et al.[36] experimentally studied the effects of span-depth ratios and prestress action modes (bonded prestress and unbonded prestress) on the progressive collapse behaviors of prestressed concrete substructures with parabolic strand curves. Observations during the tests indicated that prestress was proven to be effective to mobilize and maintain the CTA in the beams to avert the structural progressive collapse. Zhang et al.[37] experimentally estimated the dynamic responses of half-scaled post-tensioned substructures with parabolic strand profile after the sudden removal of a single interior column. Their test results showed that the post-tensioned strand can not only substantially increase the damping ratio and initial stiffness of RC substructures but can also increase the CTA capacity. Moreover, Qian et al.,[38] Lin et al.,[39] and Li et al.[40] also incorporated unbonded strand into prefabricated concrete structures to upgrade their anti-progressive collapse ability.

From the experimental results stated previously, it was confirmed that bonded or unbonded strands with a parabolic profile are useful for improving the load-bearing capacity of RC structures at the CTA stage. However, limited studies have been conducted on the anti-progressive collapse response of unbonded prestressed RC (UPRC) structures with two UPSs placed on the bottom of the beam cross section with a straight curve. It is imperative to study the progressive collapse performance of the UPRC structure under a sudden column removal scenario. Hence, the static progressive collapse test for the UPRC beam-column subassemblage was performed to study the effects of UPSs on improving the collapse-resistant capacity of RC structure. Subsequently, a three-dimensional finite element (FE) model of the UPRC subassemblage was created using ABAQUS software and was validated by the progressive collapse test results. Afterward, the validated FE model was extended to calibrate a theoretical model that is proposed in this study to predict the anti-progressive collapse capacity of UPRC subassemblage.

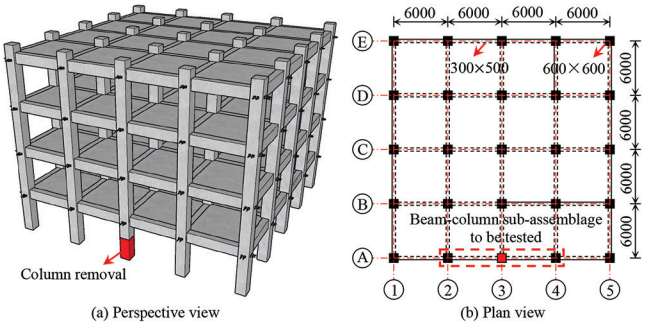


Fig. 1—Prototype structure of five-story UPRC frame. (Note: Units in mm; 1 mm = 0.0394 in.)

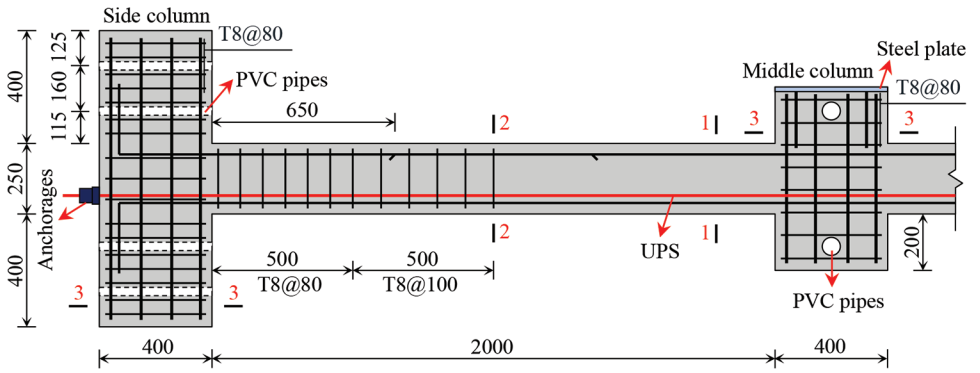
RESEARCH SIGNIFICANCE

Two UPSs installed on the bottom of a beam section with a straight profile were applied to improve the progressive collapse resistance of a traditional RC frame structure. Compared with other arrangements of bonded or unbonded strands in the form of a parabolic curve,[35-37] higher tensile strength and deformation capacity of the UPS can be fully used to mitigate the structural progressive collapse, and is easier to process installing, tensioning, and anchoring. By employing experimental methods, computational modeling, and analytical approach, a comprehensive study was conducted to investigate the progressive collapse performance of the UPRC beam-column subassemblage.

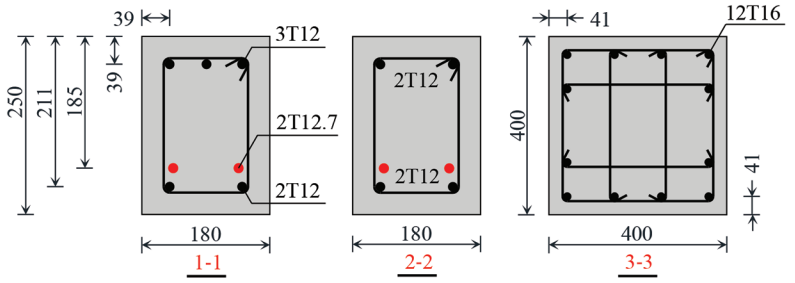
EXPERIMENTAL PROGRAM

Test specimen and material properties

The full-scale four-story UPRC frame structure with 6 x 6 m (236.2 x 236.2 in.) spans in two orthogonal directions was first designed to meet the requirements of the Code for Design of Concrete Structures,[41] as illustrated in Fig. 1. One UPRC beam-column subassemblage extracted from the prototype structure marked with a red dashed-line (illustrated in Fig. 1(b)) was scaled down to one half. The specimen consisted of two-bay bridging beams, two side columns, and a middle column over column removal; the specimen was named UPRC600. The designation of UPRC represents an unbonded prestressed RC frame structure with



(a) Reinforcement details of UPRC600



(b) Profiles of Sections 1-1 to 3-3

Fig. 2—Reinforcement details and sectional profiles of UPRC600. (Note: Units in mm; 1 mm = 0.0394 in.)

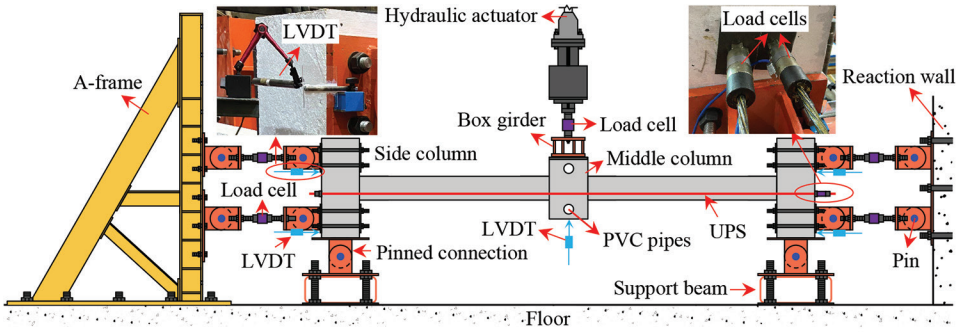
two UPSs mounted at the bottom of the beam section with a straight curve. Here, the number "600" denotes the effective prestress level of 600 MPa (87.02 ksi) applied to the UPSs. Figure 2 shows the reinforcement details of the specimen UPRC600. It should be noted that the cross-sectional area of the two side columns was intentionally augmented to 400 x 400 mm (15.75 x 15.75 in.) to ensure that the beam ends had sufficient boundary constraints. Meanwhile, the width of the bridging beams was broadened to 180 mm (7.09 in.) to conveniently impose an initial preload on the specimen by hydraulic jack. The length of the single-span beam was shortened to 2000 mm (78.74 in.) due to limited space of the test site. The total heights of the side and middle columns were 1050 and 650 mm (41.34 and 25.59 in.), respectively. The thickness of concrete cover of both beams and columns of the specimen was 25 mm (0.98 in.). In addition, a steel plate of 16 mm (0.63 in.) thickness was seated on top of the middle column to ensure that no local bearing failure occurred here under static loading. The cross-sectional area of the steel plate was the same as that of the middle column.

Table 1 shows the material properties of specimen UPRC600. Ready-mixed concrete was adopted for the tested substructure. The measured compressive strength f_{cp} and secant modulus E_{cs} of the concrete tubes were 63.9 MPa and 36.4 GPa (9.27 ksi and 5279.37 ksi), respectively. Hot-rolled ribbed steel bars with diameters of 12 and 16 mm (0.47 and 0.63 in.) were used for longitudinal reinforcement in the beam and column, respectively, and a round bar with a diameter of 8 mm (0.31 in.) was used for hoops. Two UPSs with diameters of 12.7 mm (0.5 in.) and cross-section areas of 98.7 mm^2 (0.15 in.^{2}) were used. Their yield and tensile strengths were 1816.2 and 1987.6 MPa (263.42 and 288.28 ksi), respectively.

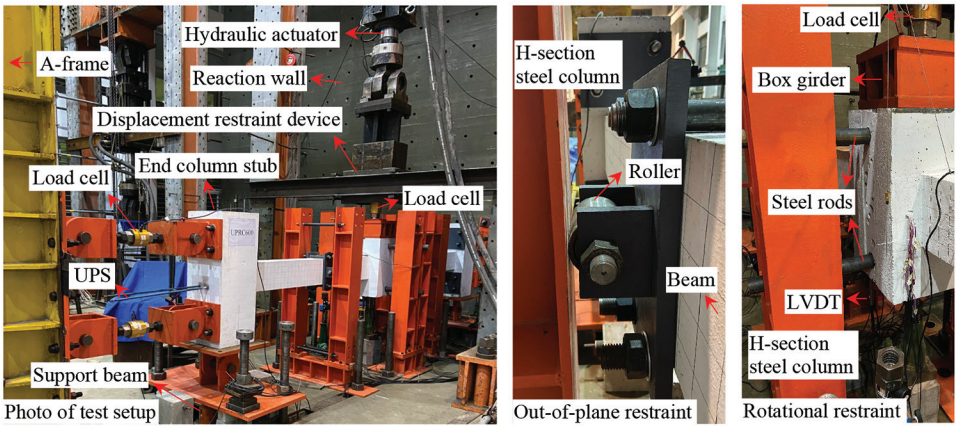
Test setup and instrumentation

As shown in Fig. 3, each two horizontal restraints from the A-frame and reaction wall were respectively fixed to the side column close to them, and a pinned connection which served as the vertical restraint was installed at the bottom of each side column. Out-of-plane deflection of the double-span beams under vertical loading was prevented by two sets of single H-section steel columns seated on each side of the beams, as illustrated in Fig. 3(b). The rotation of the middle column was addressed by two pairs of double H-section steel columns installed at front and behind the middle column. Note that a displacement-control load at a rate of 3 mm/min (0.12 in./min) on the middle column was achieved by a displacement-restraint device incorporating two U-steel beams and one steel jacket.

Tension-compression load cells were mounted at each horizontal restraint to measure their horizontal reaction forces. Linear variable differential transformers (LVDTs) were installed to record horizontal displacements of each horizontal restraint. When specimen UPRC600 was subjected to initial post-tensioning force, an LVDT was positioned at the bottom of the middle column to capture its reverse cambers (shown in Fig. 3(b)). After that, it was removed before the test began. The vertical load of the test specimen and the post-tensioning force of the UPSs were measured by load cells seated at the top of the box girder and placed on the side of end column stub (shown in Fig. 3(a)), respectively. Many strain gauges were attached to the beam longitudinal reinforcing bars to measure their strain variation, as shown in Fig. 4.



(a) Elevation view



(b) Photos of test setup

Fig. 3—Test setup for UPRC600 and instrumentation.

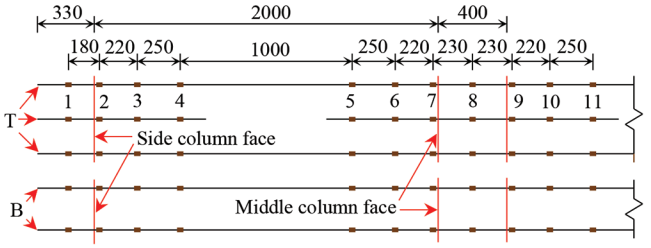


Fig. 4—Layout of strain gauges on longitudinal reinforcing bars. (Note: Units in mm; 1 mm = 0.0394 in.)

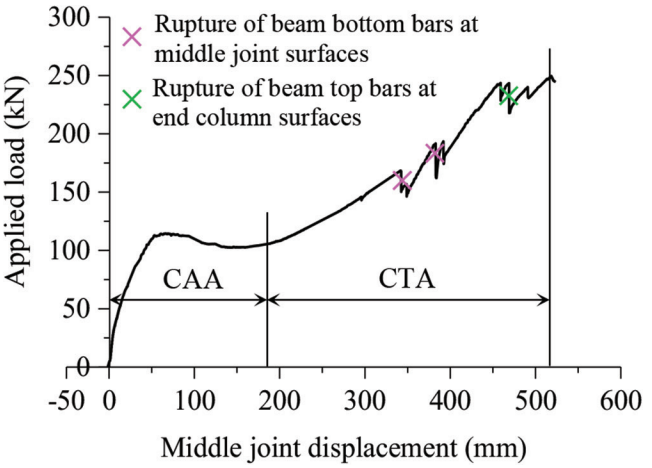


Fig. 5—Curve of applied vertical load versus MJD of UPRC600. (Note: 1 mm = 0.0394 in.; 1 kN = 0.225 kip.)

EXPERIMENTAL RESULTS

Force-displacement curves and failure mode

Figure 5 shows the variation of the applied vertical load with middle joint displacement (MJD). Figures 6 and 7 plot the variation of the horizontal reaction forces on the specimen UPRC600 versus MJD. It is worth noting that the total horizontal reaction forces were calculated by summing up the forces in the top and bottom horizontal load cells on each side column. The reverse arch effect of the tested substructure was initially observed when it was subjected to the initial pretensioning force. The measured reverse camber is 1.66 mm (0.07 in.) in height.

At small deformation, compressive arch action (CAA) was mobilized in the UPRC beam-column subassemblage (seen in Fig. 5). From Fig. 6, it was discovered that the horizontal compressive forces developed in the bridging beams were primarily transferred to the bottom restraints close to the A-frame and reaction wall, whereas forces in the top restraints were very small. This reveals that the bottom restraints played a significant pivotal role in forming the CAA in the double-span beams. When the first peak vertical force (CAA capacity) was reached, the horizontal reaction forces continued to increase. The CAA strength and maximum horizontal compressive force at the A-frame were 114.6 and –126.5 kN (25.76 and –28.44 kip), respectively. The crack modes of the test specimen under the CAA capacity are presented in Fig. 8. The tensile cracks

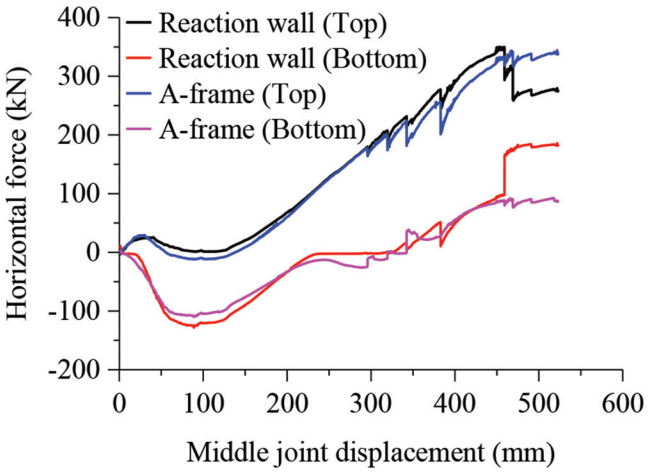


Fig. 6—Horizontal forces in top and bottom load cells close to A-frame and reaction wall. (Note: 1 mm = 0.0394 in.; 1 kN = 0.225 kip.)

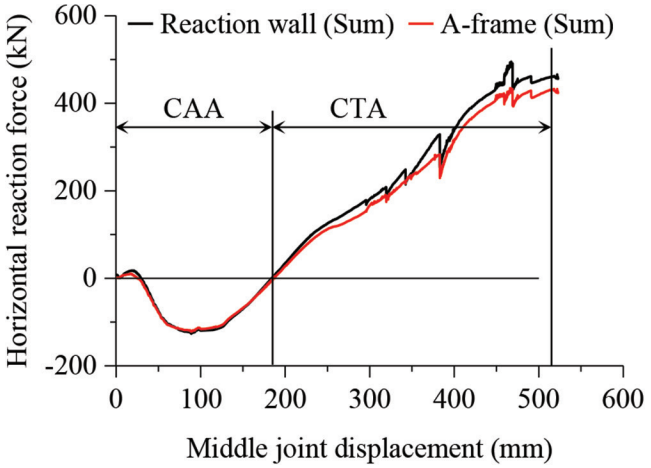


Fig. 7—Curves of horizontal reaction force versus MJD of UPRC600. (Note: 1 mm = 0.0394 in.; 1 kN = 0.225 kip.)

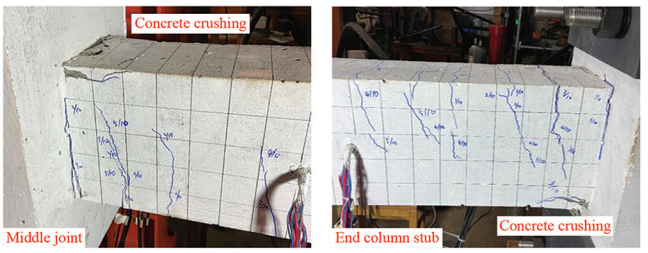


Fig. 8—Crack patterns of concrete at middle joint and end-column stub when tested substructure reached CAA capacity.

were initially observed in the beam ends and then developed along the beam height. After that, due to the crushing of cover concrete in the compression zone of both beam ends, the vertical force and horizontal reaction forces began to decrease with increasing MJD. When the horizontal reaction force of the tested substructure changed from compression to tension, the CTA was activated in the UPRC subassemblage. The vertical force was sustained by the tensile strength of the beam. As exhibited in Fig. 6, the top horizontal restraints connected to the A-frame and reaction wall contributed a significant portion to the total horizontal tension force. This demonstrated that the top restraints were more critical at the CTA stage. When the MJD reached 342 mm (13.46 in.), rupture of the bottom reinforcing bars adjacent to the middle joint interfaces was observed from Fig. 9, leading to the sudden drop of vertical force marked by crosses in Fig. 5. However, the reinforcing fracture imposed a minor effect on the horizontal tension force. Afterwards, the collapse-resistant capacity of the test specimen was sustained by the tensile strength of the UPSs and top reinforcing bars near the middle joint and end-column stubs until rupture of the top reinforcing bars at the end column stub interfaces. The measured CTA capacity of UPRC600 was 249.5 kN (56.09 kip). With the increase of MJD, the load-carrying capacity of the tested substructure maintained a continuously developing trend due to no rupture of the UPSs observed throughout the loading process. When the hydraulic actuator reached the maximum stroke limitation, the test was stopped. The finial failure mode of the test specimen is presented in Fig. 9.

Variation of post-tensioning force of UPSs with MJD

Figure 10 plots the variation of post-tensioning force of the UPSs against MJD. Note that the post-tensioning forces of the UPSs are average results of the two load cells mounted at the side of end column stub (illustrated in Fig. 3(a)). The initial post-tensioning force imposed on the UPSs was 61.2 kN (13.76 kip). The measured maximum post-tensioning force was 182.2 kN (40.96 kip). From Fig. 10, it could be found that before the MJD reached approximately 300 mm (11.81 in.), the post-tensioning force of the UPSs developed faster, which varied almost linearly with the MJD. After the UPSs reached their yield strengths, the ascent curve flattened out. This process demonstrated that the CAA and CTA provided by the UPSs could be mobilized to upgrade the load-carry capacity of the UPRC subassemblage to resist progressive collapse. Moreover, rupture of the

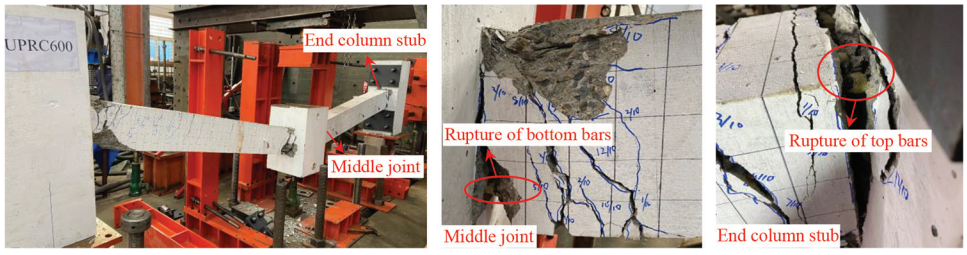


Fig. 9—Failure mode of UPRC600.

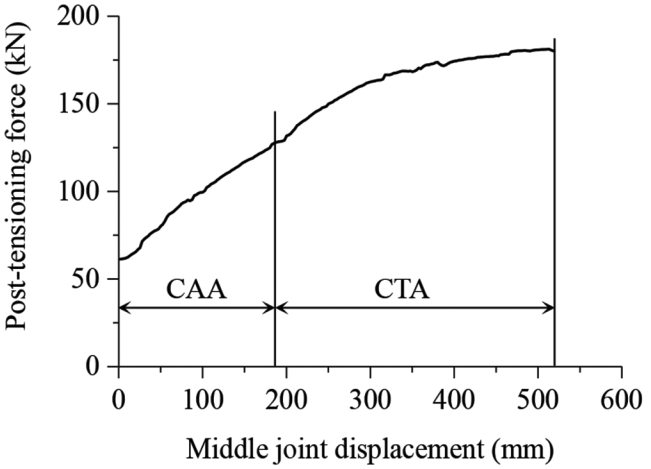
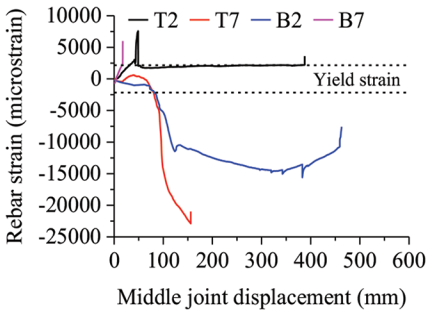


Fig. 10—Curve of post-tensioning force of UPSs versus MJD of UPRC600. (Note: 1 mm = 0.0394 in.; 1 kN = 0.225 kip.)

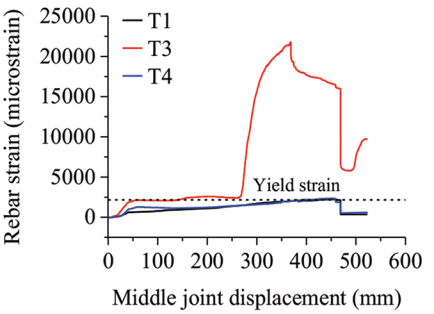
UPSs in Specimen UPRC600 were not observed throughout the test.

Variation of steel reinforcement strains with MJD

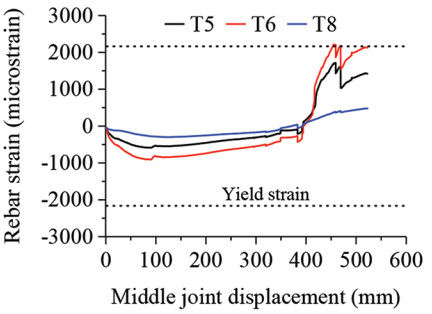
Considering the symmetrical characteristic of the test specimen, only strains of the longitudinal reinforcing bars in the left half were discussed. Figure 11 shows the strain variation with MJD. In the picture, "T2" and "B2" represent the mean strain readings of the beam top and bottom longitudinal bars at the side column surface (illustrated in Fig. 4). At small deformation, the tensile strain of beam-bottom reinforcement at the middle joint surface is greater than that of the top reinforcing bar at the end column stub surface, and soon afterwards, they attained the yielding stress state (seen in Fig. 11(a)). When the vertical force reached its peak value at the CAA stage, the tensile strains of the beam bottom reinforcing bar near the middle joint and top reinforcement close to the end column stub began to decrease gradually



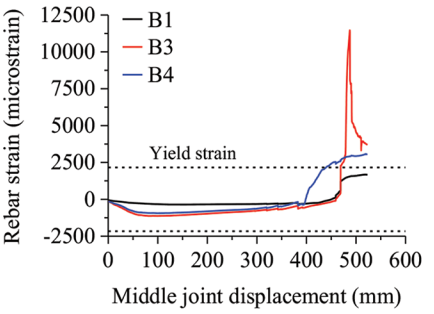
(a) Rebar strains at the beam ends



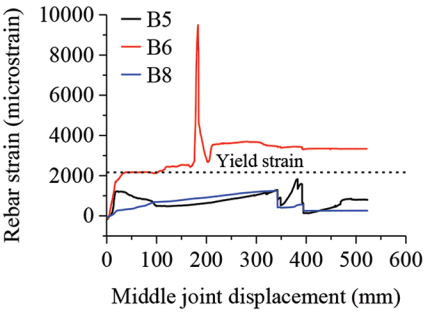
(b) Strains of beam top rebars near side column



(c) Strains of beam top rebars near middle column



(d) Strains of beam bottom rebars near side column



(e) Strains of beam bottom rebars near middle column

Fig. 11—Curves of strains of top and bottom longitudinal reinforcing bars in left half of test specimen UPRC600 against MJD. (Note: 1 mm = 0.0394 in.)

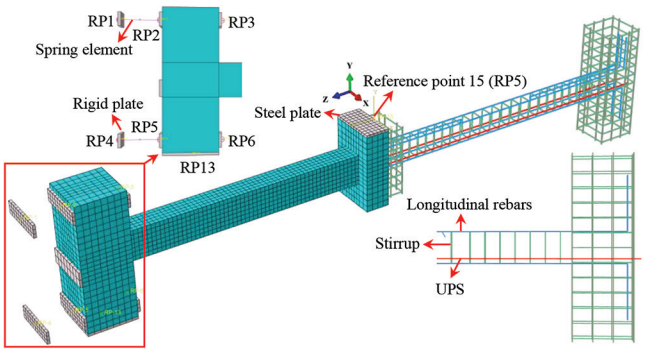


Fig. 12—Three-dimensional FE model of UPRC600.

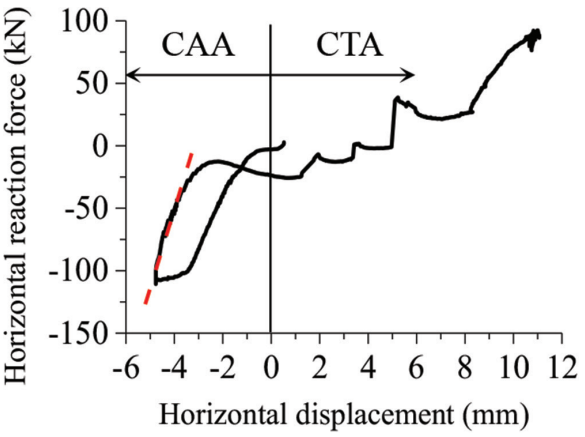


Fig. 13—Curve of horizontal reaction force versus MJD of UPRC600. (Note: 1 mm = 0.0394 in.; 1 kN = 0.225 kip.)

(presented in Fig. 11(b) and (e)). That can be attributed to the bond strength degradation between reinforcing bar and concrete in tensile zones of the beam resulting from the concrete cracking. As can be seen in Fig. 11, the tensile strains of T1 and B8 in the beam-column joint zones continued to increase as their bond strengths did not decay. The compressive strains were observed at the beam top bars near the middle joint and bottom reinforcing bars close to the side column (plotted in Fig. 11(c) and (d)), respectively. Afterwards, they were transformed to tensile strains due to the subsequent mobilization of CTA. When the MJD reached 342 mm (13.46 in.), the tensile strains of the beam bottom steel bars adjacent to the middle joint suddenly decreased due to reinforcing bar fracture. However, it had no influence on the development of strains of other reinforcements near the middle joint and end column stub. With continuing the increase of the MJD, strains in the beam kept increasing until the rupture of the top reinforcing bars at the end column stub surfaces. Therefore, it can be concluded that the measured strains of the top and bottom longitudinal reinforcing bars in the beam match well with the crack patterns and failure mode of the tested substructure.

FE SIMULATION

Establishment of FE model

The high-fidelity FE model of the specimen UPRC600, as exhibited in Fig. 12, was developed by means of the FE software ABAQUS. In the FE model, the axial stiffness of the side column was simulated by spring elements, whereas the

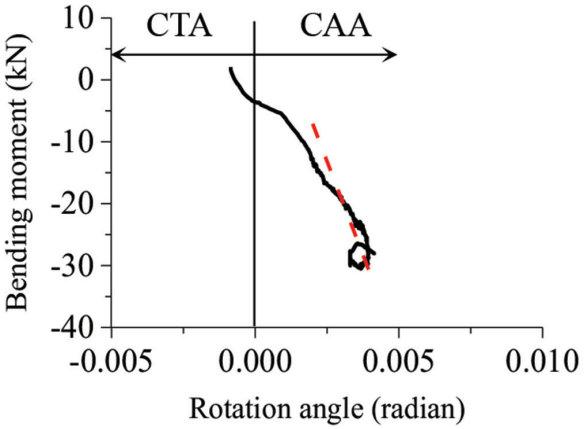


Fig. 14—Curves of bending moment versus rotation angle of UPRC600. (Note: 1 kN = 0.225 kip.)

Table 1—Horizontal and rotational stiffnesses of UPRC600

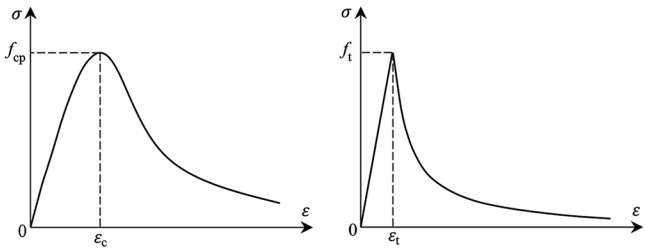
Specimen	Horizontal stiffness, N/mm	Connection gap, mm	Rotational stiffness, kN·m/rad	Free rotation, rad
UPRC600	63,144	0.33	12,114	0.001

distance between reference points 1 and 4 is adjusted to fit its rotational stiffness in the test (presented in Fig. 12). To determine the horizontal and rotational stiffnesses of the tested substructure, the method developed by Xu and Wang[42] was adopted. In this method, the horizontal and rotational stiffnesses of the end support stubs at CAA and CTA stages are assumed to be identical. The relationship between the horizontal reaction force and MJD, as well as that between the bending moment and rotation angle, are needed, as presented in Fig. 13 and 14. As a consequence, the horizontal and rotational stiffnesses of the test specimen at the CAA stage, as listed in Table 1 can be quantified through linear regression (marked by the dotted line in Fig. 13 and 14). It is worth noting that the connection gap and free rotation of the end column stub did not incorporate into the FE model.

A rigid rectangular plate was modeled to simulate the pinned connection at the bottom of the side column. The constraint between the plate and concrete (contacted with the plate) was set as tie, and a reference point 13 (RP13) coupled with the plate was established to restrain its vertical displacement. Similarly, RP15 was built for the convenience of exerting the vertically enforced displacement on the top of the steel plate. Two rigid plates were used to model the anchorage devices of the UPSs at each side column, and the contact constraints between the plates and concrete and UPSs were created as tie. Moreover, the perfect bonding between reinforcing bars and concrete was assumed in the FE model through the embedded constraint. A method was employed to simulate the interactions between the UPSs and concrete.[43] The method is that the nodes of the UPSs located in the concrete elements were coupled with the nodes of the concrete, and their free degrees in the x- and y-directions were limited. The friction action between the UPSs and their sheaths was neglected. The initial post-tensioning force was

imposed on the UPSs with help from the temperature-lowing method.

The truss element (T3D2) was used for the reinforcement cage and UPSs, whereas the reduced integration element (C3D8R) was used for all the other components in the test specimen. The mesh sizes of the reinforcement cage, the UPSs, and the concrete were approximately 25, 90, and 30 mm (0.98, 3.54, and 1.18 in.), respectively; the ideal elastic-plastic model was chosen for the reinforcement cage and UPSs. The ductile damage was introduced to simulate the rupture of longitudinal reinforcing bars in the double-span bridging beam.[44] The concrete-damaged plasticity (CDP) model was applied for modeling the concrete behavior. The constitutive relationships of tension and compression—developed by Mander et al.[45] and Guo and Zhang,[46] respectively—were adopted, as illustrated in Fig. 15. It should be noted that the tensile strength, f_t, of concrete could be determined by its compressive strength, f_{cp}.[41] The material properties of all the components in the FE model are the same as that of the test, as listed in Table 2.



(a) Compression (Mander et al.[45]) (b) Tension (Guo et al.[46])

Fig. 15—Stress-strain relationship of concrete material.

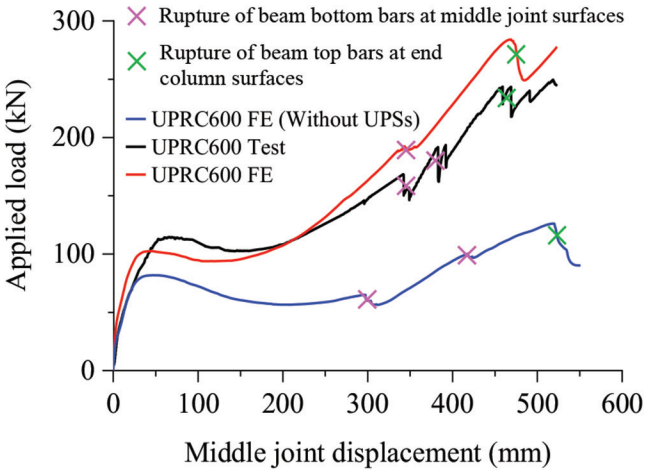


Fig. 16—Comparisons of applied load versus MJD curves between test and simulation results. (Note: 1 mm = 0.0394 in.; 1 kN = 0.225 kip.)

Validation of FE model

Figures 16 to 18 display the variation of the critical forces (namely, the vertical force, horizontal reaction force, and post-tensioning force of the UPSs) against MJD during the test. The CAA and CTA capacities of the specimen UPRC600, as well as its maximum horizontal compressive and tensile forces, are summarized in Table 3. Considering that the difference between the horizontal reaction forces at the A-frame and reaction wall is neglect (seen in Fig. 7), the horizontal reaction force at the A-frame was selected to compare with the simulation result. It should be noted that the vertical load versus MJD curve of the specimen UPRC600 without UPSs was also plotted in Fig. 16. It can be concluded from Fig. 16 that the CAA and CTA sustained

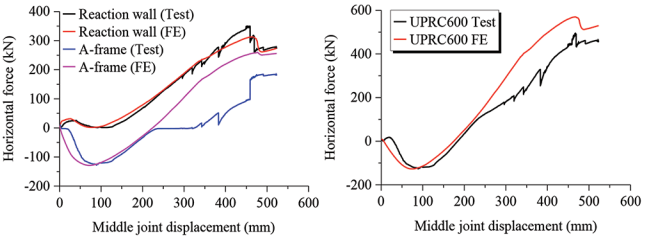


Fig. 17—Comparisons of horizontal reaction force versus MJD curves between test and simulation results. (Note: 1 mm = 0.0394 in.; 1 kN = 0.225 kip.)

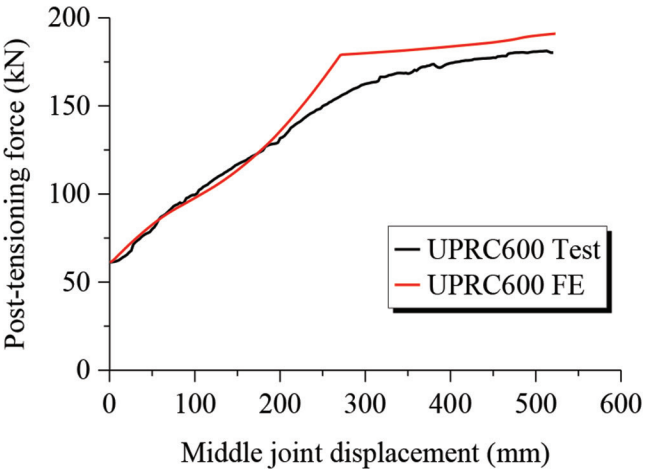


Fig. 18—Comparisons of post-tensioning force versus MJD curves between test and simulation results. (Note: 1 mm = 0.0394 in.; 1 kN = 0.225 kip.)

Table 2—Material properties

Material	Type	Elastic modulus, GPa	Yield strength, MPa	Yield strain, με	Ultimate strength, MPa	Elongation ratio, %
Reinforcements	T8	203.7	474.6	2330	631.7	22.1
	T12	205.8	445.4	2164	594.7	23.8
	T16	195.9	440.1	2247	604.7	21.7
UPS	T12.7	202.8	1816.2	—	1987.6	4.8
Concrete	Compressive strength f_{cp}, MPa			Secant modulus E_{cs}, GPa		
	63.9			36.4		

Table 3—Comparisons between experimental data and simulation results

Specimen	CAA capacity, kN		Maximum horizontal compressive force, kN		CTA capacity, kN		Maximum horizontal tensile force, kN	
	Test	FE	Test	FE	Test	FE	Test	FE
UPRC600	114.6	102.6	–126.5	–127	249.5	284.1	496.5	569.3

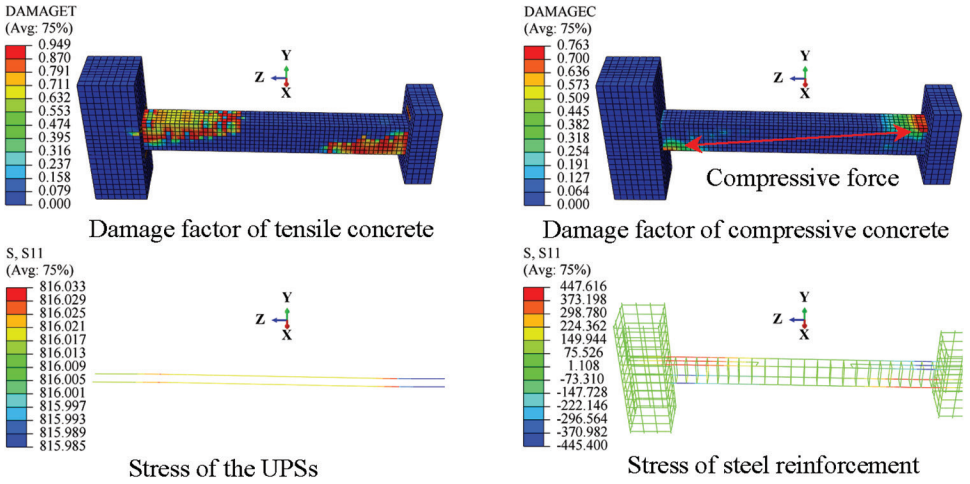


Fig. 19—Simulation results of UPRC600 at CAA strength.

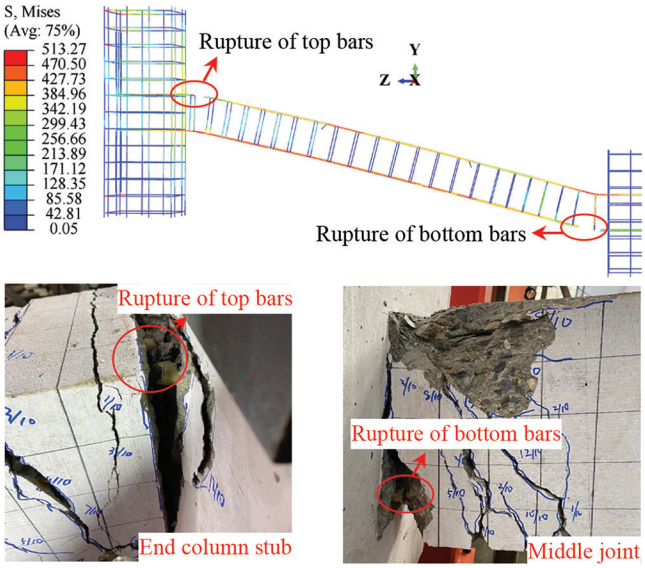


Fig. 20—Simulation results of reinforcing rupture in single bridging beam.

by the UPSs can be developed to enhance the load-bearing capacity of the UPRC subassemblage to defend against progressive collapse. However, the damage modes of specimen UPRC600 with and without UPSs were quite similar; namely, the sequential fractures were first observed in the beam bottom reinforcements adjacent to the middle joint, and then in the beam-top reinforcing bars close to the end-column stubs.

As can be seen from Fig. 16 and 17, the measured MJDs corresponding to the CAA capacity and maximum horizontal compressive force are marginally larger than those obtained by the simulation results. That is because the connection gap and free rotation of the end column stub were not considered in the FE model. The CAA strength of the tested substructure is slightly underestimated in the FE model and was reduced by 10% compared to the experimental result. However, the measured maximum horizontal compressive force is nearly the same as that of the FE model. Figure 19 gives the cloud charts of the test specimen at CAA capacity. It can be observed that, in this figure, the mechanical behavior of the UPRC subassemblage during the test could be accurately reflected by the FE model. Moreover, the FE model could also well simulate the reinforcing bar fracture (shown in Fig. 20). The calculated MJDs corresponding to the reinforcing rupture are similar to those of the test substructure with reasonably good accuracy (plotted in Fig. 16). At the CTA stage, CTA strength and maximum horizontal tensile force in the FE model were to a certain extent overestimated compared to the test results, and increased by 14% and 15%, respectively. This difference can be attributed to the fact that, during the test, a relative slip between the A-frame and floor was observed at the CTA stage, while in the FE model, this slip was not taken into consideration due to its undetermined value. Furthermore, the bottom restrains near the A-frame and reaction wall contributed an insignificant portion to total horizontal tension force at the CTA stage (presented in Fig. 6), but in the FE model, it played a critical role in developing CTA in the bridging beams. In conclusion, the simulation results of the load-displacement curve, crack pattern, and reinforcing rupture agreed well with the test results.

THEORETICAL MODEL FOR PREDICTING COLLAPSE-RESISTANT CAPACITY OF UPRC SUBASSEMBLAGES

Establishment of theoretical model

Figure 21 shows the simplified progressive collapse-resisting capacity curve of UPRC beam-column subassemblage. At the CAA stage, the analytical model proposed

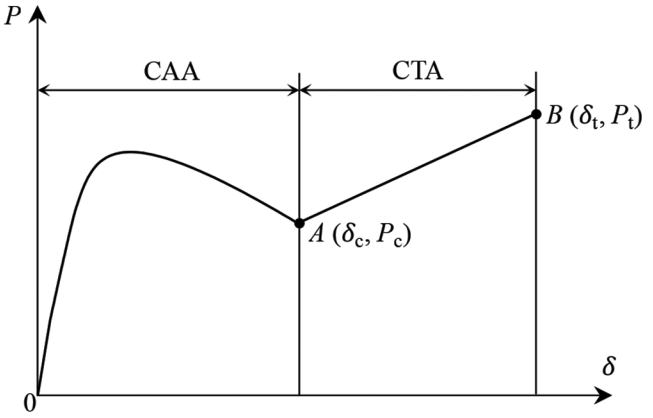


Fig. 21—Simplified collapse-resistant capacity curve of UPRC beam-column subassemblage.

by Xu and Wang[47] is adopted to predict collapse-resistant capacity of the UPRC subassemblage. After the CTA is mobilized in the UPRC subassemblage, a linear simplified model is developed to evaluate its load-carrying capacity. In this curve, the MJD and vertical force corresponding to characteristic points *A* and *B* can be determined as follows.

Based on the analytical model of Xu and Wang,[47] the vertical load-deflection relationship of UPRC subassemblage at the CAA stage can be obtained (seen in Fig. 21). It should be noted that when the horizontal reaction force of the subassemblage calculated through the method is initially transformed from compression to tension, the corresponding MJD and vertical load are regarded as the MJD δ_c and vertical load P_c of characteristic point *A*.

According to the specification of UFC 4-023-03,[7] a chord rotation of 0.2 rad between the column and beam is required for RC frame structures to prevent progressive collapse. However, the effect of UPSs upon the chord rotation of UPRC subassemblage is ignored for the purpose of simplifying the theoretical model to predict its collapse-resistant capacity at CTA stage. Hence, the MJD corresponding to the chord rotation of 0.2 rad is considered as the MJD δ_t of characteristic point *B*, as expressed in Eq. (1)

$$\delta_t = 0.2l \tag{1}$$

where *l* is the net span of the two-bay bridging beam.

From the test results of specimen UPRC600, it was found that when the MJD reached 342 mm (13.46 in.), the bottom reinforcing bars at the middle joint interfaces ruptured and a large gap occurred at the bean-column interfaces. Moreover, the crushing and spalling of concrete markedly occurred at the compression zone of the beam section. The compressive stress of beam top reinforcing bars near the middle joint interfaces changed into tensile stress due to subsequent development of CTA. Besides, the UPSs have reached their yielding stress state when the MJD reached 400 mm (15.75 in.) (presented in Fig. 10). Hence, the axial tension N_u on the beam section at characteristic point *B* was almost thoroughly sustained by the beam top reinforcements adjacent to the middle joint and the UPSs. The axial tension along the beam length is assumed to a constant, as

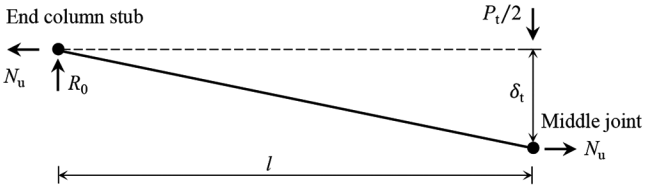


Fig. 22—Schematic diagram of force analysis for single-span beam at characteristic point B.

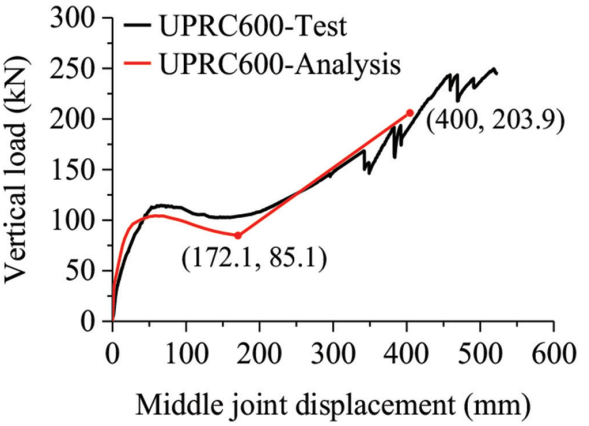


Fig. 23—Comparisons of experimental and calculated curves of vertical load against MJD. (Note: 1 mm = 0.0394 in.; 1 kN = 0.225 kip.)

expressed in Eq. (2). In this equation, the yielding strengths of the beam-top reinforcing bars close to the middle joint and the UPSs are used to calculate the axial tension force of the beam at characteristic point *B*

$$N_u = f_y' A_s' + f_{py} A_p \tag{2}$$

where f_y' and A_s' are the yield strength and cross-sectional area of the beam top reinforcing bars next to the middle joint, respectively; and f_{py} and A_p are the yield strength and cross-sectional area of the UPSs, respectively. Figure 22 illustrates the internal force equilibrium of the single-span beam at characteristic point *B*. According to force equilibrium condition, the vertical load P_t can be calculated from Eq. (3).

$$P_t = \frac{2N_u\delta_t}{l} \tag{3}$$

Validation of proposed theoretical model

Figure 23 plots the variation of applied vertical load with MJD. Comparisons between experimental data and analytical results demonstrated that the collapse-resistant capacity of specimen UPRC600 can be well predicted by the proposed theoretical model. Without considering the connection gap and free rotation of the side column in the model of Xu and Wang,[47] the vertical displacement corresponding with the CAA capacity measured from the tested substructure is appreciably larger than that calculated by the theoretical model. In comparison with the test results, the CAA and CTA strengths of the test specimen were slightly underrated by the model, and reduced by 9% and 18%, respectively.

Table 4—Dimension and reinforcement details of existing specimens available in literature

Specimens		Cross section, mm	Clear span, mm	Reinforcement at beam end		Reinforcement at beam middle span		Boundary condition			
				Top	Bottom	Top	Bottom	Axial stiffness $\times 10^5$, N/mm	Rotational stiffness $\times 10^4$, kN · m/rad	Connection gap, mm	Free rotation, rad
Yu and Tan[48,49]	S1	150 x 250	2750	1T13 + 2T10	2T10	2T10	2T10	1.06	1.0	0.5	0
	S2			3T10	2T10	2T10	2T10	1.06	1.0	1.2	
	S3			3T13	2T10	2T13	1T13 + 2T10	4.29	3.0	1.2	
	S4			3T13	2T13	2T13	2T13	4.29	3.0	1.0	
	S5			3T13	3T13	2T13	3T13	4.29	3.0	0.8	
	S6			3T16	2T13	2T16	2T13	4.29	3.0	0.8	
	S7		2150	3T13	2T13	2T13	2T13	4.29	3.0	1.2	
	S8		1550	3T13	2T13	2T13	2T13	4.29	3.0	0.8	
Kang and Tan,[50] Kang et al.[51]	MJ-B-0.52/0.35S	150 x 300	2750	3H10	2H10	2H10	2H10	1.51	2.14	1.1	0.005
	MJ-B-1.19/0.59	150 x 300		2H16 + H13	2H13	2H16	2H13	2.05	1.99	0.9	0.01

Notes: Distance between centroids of UPSs and beam section for all tested substructures is 80.5 mm (3.17 in.); 1 mm = 0.0394 in.; 1 kN = 0.225 kip.

In addition, the test results of conventional RC beam-column subassemblages available in published works[48-51] were employed to validate the reliability of their FE models developed by ABAQUS. The method to build the FE models of traditional RC subassemblages was the same as that of specimen UPRC600 (seen in Fig. 12), except for geometric dimension, reinforcement ratio, and UPSs. Detailed information on the existing substructures is given in Table 4. Figure 24 shows the variation of vertical load with MJD obtained from the results of the FE model. In comparisons between the experimental data and simulation results, it was identified that the load-carrying capacities of the RC subassemblages could be predicted by the FE model with reasonably good accuracy. Hence, two 12.7 mm (0.5 in.) UPSs with effective prestress levels of 620 MPa (89.92 ksi) were incorporated into the FE model. The simulation results of these UPRC subassemblages were adopted in this study to further verify the precision of the proposed theoretical model.

Table 5 summarizes the CAA and CTA capacities of these UPRC subassemblages. By comparison of numerical and calculated results, the proposed model was proven to be accurate for predicting the CAA and CTA strengths of the UPRC subassemblages. The mean ratio of CAA capacities of the FEM to the prediction is 1.02 with a coefficient of variation of 0.04. For the CTA strength, the average ratio is 1.02 with a coefficient of variation of 0.12. Moreover, Fig. 25 exhibits the variation of vertical load against MJD. From the comparisons between the numerical and analytical results, it can be concluded that the proposed model can also give a good precision to estimate the load-displacement curves of the UPRC subassemblages.

Table 5—Comparisons between numerical and analytical CAA and CTA capacities

Specimens			CAA capacity, kN	P_c, kN	CTA capacity, kN
Yu and Tan[48,49]	S1	FE	55.7	50.5	172.2
		Analysis	59.7	54.7	201.7
	S2	FE	53.2	49.4	233.8
		Analysis	57.1	51.4	191.0
	S3	FE	61.8	56.6	185.0
		Analysis	63.9	59.9	222.1
	S4	FE	70.6	66.1	234.4
		Analysis	73.2	66.7	222.1
	S5	FE	79.0	73.7	239.3
		Analysis	81.9	76.2	222.1
	S6	FE	77.7	73.0	239.3
		Analysis	79.3	77.5	267.2
	S7	FE	96.2	85.5	239.4
		Analysis	99.5	89.8	222.1
	S8	FE	144.8	121.9	227.7
		Analysis	145.1	129.0	222.1
Kang and Tan,[50] Kang et al.[51]	MJ-B-0.52/0.35S	FE	115.9	66.8	174.7
		Analysis	111.2	57.8	187.0
	MJ-B-1.19/0.59	FE	153.1	95.2	262.3
		Analysis	146.2	100.7	264.7
Mean ratio			1.02	1.03	1.02
Coefficient of variation			0.04	0.06	0.12

CONCLUSIONS

To investigate the effect of the unbonded post-tensioning strands (UPSs) (with a straight profile) on the collapse-resistant capacity of reinforced concrete (RC) frame structures, a static loading test of unbonded prestressed RC (UPRC) beam-column subassemblage under progressive collapse was performed. A high-fidelity finite element (FE) model of specimen UPRC600 was established by means of the FE software ABAQUS. Moreover, the theoretical model

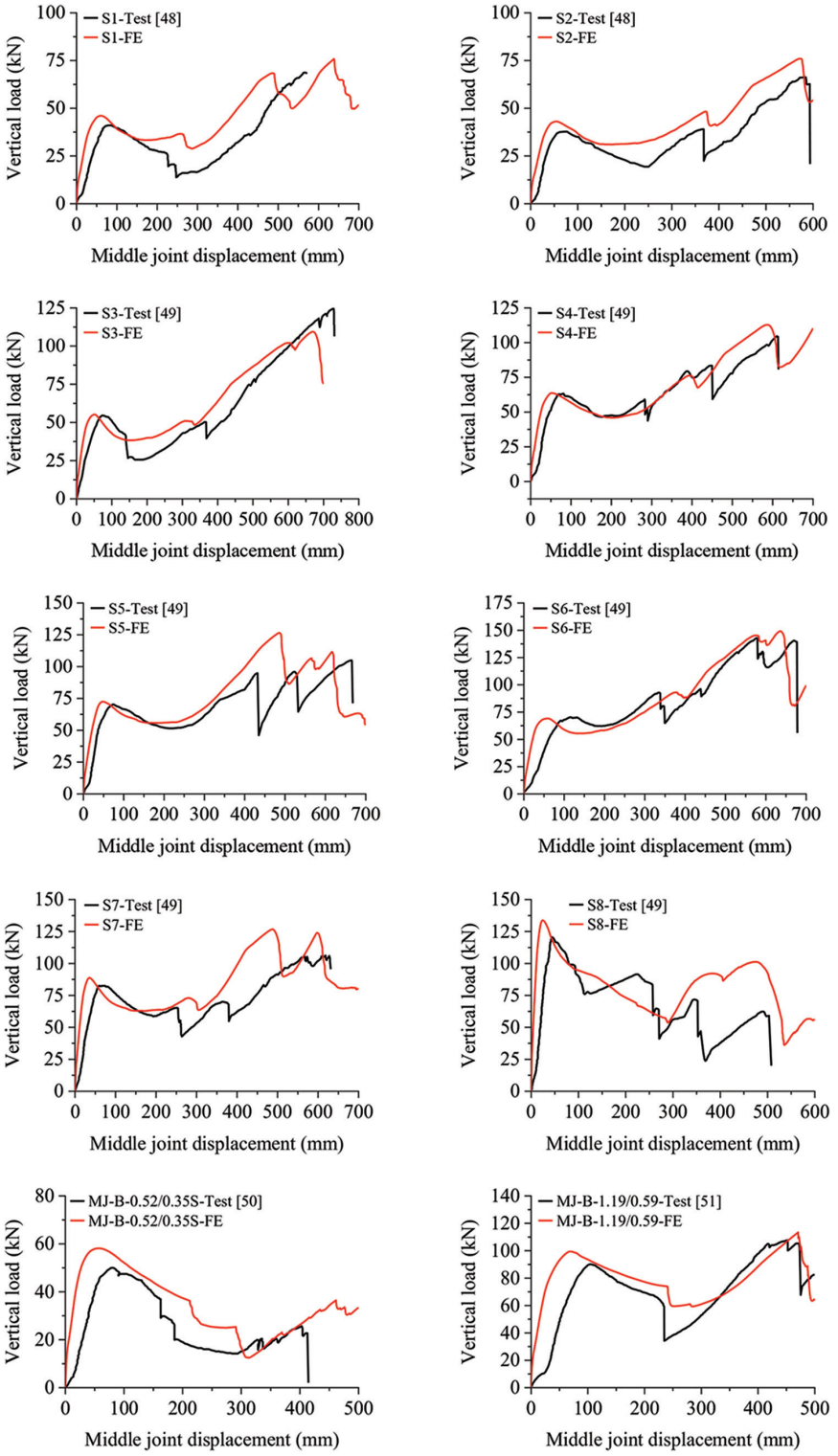


Fig. 24—Comparisons of vertical load versus MJD curves of RC subassemblages between test and simulation results. (Note: 1 mm = 0.0394 in.; 1 kN = 0.225 kip.)

was developed to predict the collapse-resistant capacity of UPRC subassemblage. The main conclusions are as follows:

- From the load-displacement curve of specimen UPRC600, it was observed that similar to conventional RC beam-column subassemblage, the compressive arch action (CAA) and catenary action (CTA) could also be activated in the specimen to mitigate structural progressive collapse.
- Based on the variation of post-tensioning force of the UPSs against middle joint displacement (MJD), it can be concluded that the CAA and CTA provided by the UPSs could be mobilized to increase the load-carrying capacity of the UPRC subassemblage to defend against progressive collapse.
- By comparing the experimental data and simulation results, it was validated that the developed FE model

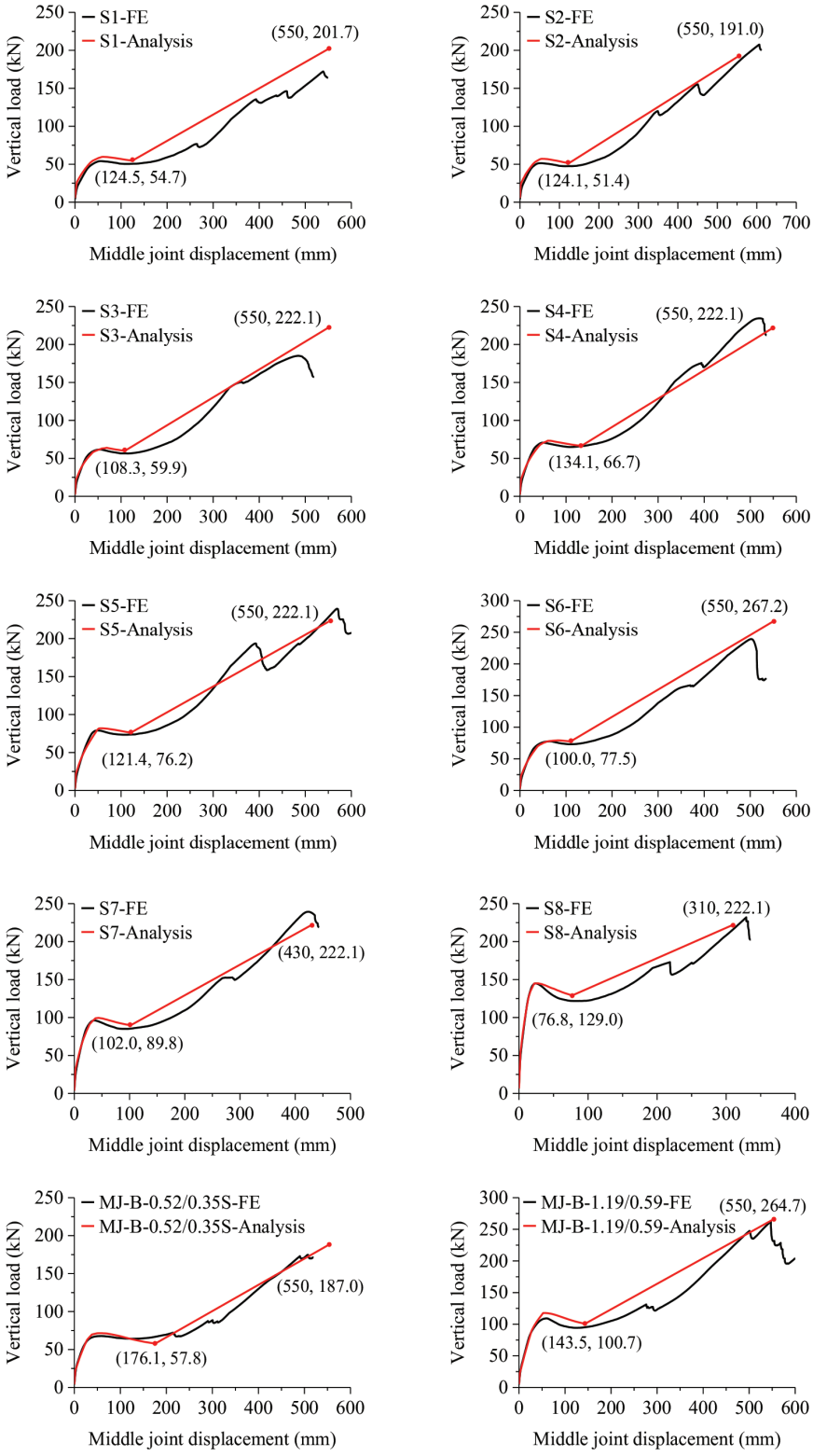


Fig. 25—Comparisons of load-displacement curves of UPRC subassemblages between numerical and calculated results. (Note: 1 mm = 0.0394 in.; 1 kN = 0.225 kip.)

can predict the variation of the critical forces (namely, the vertical force, horizontal reaction force, and post-tensioning force of the UPSs) against MJD with a good agreement. The crack pattern and reinforcing rupture of the UPRC subassemblages could also be accurately simulated.

- In comparison with the test results, the CAA and CTA capacities of the test specimen were slightly underrated by the proposed theoretical model and reduced by 9% and 18%, respectively. Besides, by comparing the results between the numerical and theoretical models of the UPRC subassemblages, it can be concluded that the mean ratio of the CAA strengths of the simulation

to the prediction is 1.02 with a coefficient of variation of 0.04, whereas for the CTA capacity, the average ratio is 1.02 with a coefficient of variation of 0.12. It demonstrated that the proposed model could give a reasonable prediction of the collapse-resistant capacity of UPRC subassemblages with good precision.

AUTHOR BIOS

Wen-Liu Xu *is a Lecturer in the School of City Construction at Jiangxi Normal University, Nanchang, Jiangxi, China. He received his BE from Wuhan University of Engineering Science, Wuhan, Hubei, China, in 2014; his MS from Guizhou University, Guiyang, Guizhou, China in 2017; and his PhD from Dalian University of Technology, Dalian, China, in 2022. His research interests include structural seismic and progressive collapse resistance design of reinforced concrete (RC) structures.*

Li-Cheng Wang *is a Professor at Dalian University of Technology, where he received his PhD in civil engineering in 2002. He received his BE in civil engineering from Shandong University of Technology, Jinan, Shandong, China, in 1997. His research interests include RC durability and structural seismic and progressive collapse resistance design of RC structures.*

Yong-Qin Liang *is a Lecturer in the School of Civil Engineering at Hebei University of Engineering, Handan, Hebei, China. He received his BE and PhD in civil engineering from Dalian University of Technology in 2013 and 2021, respectively. His research interests include RC durability and reinforcing bar corrosion.*

Fei-Fan Feng *is a Lecturer in the School of Civil Engineering at Hunan University of Science and Technology, Xiangtan, Hunan, China. He received his BS from Central South University, Changsha, Hunan, China, in 2015 and his PhD from Hunan University, Changsha, Hunan, China, in 2022. His research interests include structural performances under progressive collapse and impact loading.*

ACKNOWLEDGMENTS

The work was financially supported by the Natural Science Foundation of Liaoning Province (2020-MS-100). Its support is gratefully acknowledged.

REFERENCES

1. Pearson, C., and Delatte, N., "Ronan Point Apartment Tower Collapse and its Effect on Building Codes," *Journal of Performance of Constructed Facilities*, ASCE, V. 19, No. 2, 2005, pp. 172-177. doi: 10.1061/(ASCE)0887-3828(2005)19:2(172)

2. Lu, J. X.; Wu, H.; and Fang, Q., "Progressive Collapse of Murrah Federal Building: Revisited," *Journal of Building Engineering*, V. 57, Oct. 2022, p. 104939. doi: 10.1016/j.jobe.2022.104939

3. Le, J. L., and Bažant, Z. P., "Spontaneous Collapse Mechanism of World Trade Center Twin Towers and Progressive Collapse in General," *Journal of Structural Engineering*, ASCE, V. 148, No. 6, 2022, p. 04022065. doi: 10.1061/(ASCE)ST.1943-541X.0003342

4. Gross, J. L., and McGuire, W., "Progressive Collapse Resistant Design," *Journal of Structural Engineering*, ASCE, V. 109, No. 1, 1983, pp. 1-15. doi: 10.1061/(ASCE)0733-9445(1983)109:1(1)

5. Adam, J. M.; Parisi, F.; Sagaseta, J.; and Lu, X. Z., "Research and Practice on Progressive Collapse and Robustness of Building Structures in the 21st Century," *Engineering Structures*, V. 173, Oct. 2018, pp. 122-149. doi: 10.1016/j.engstruct.2018.06.082

6. NISTIR 7396, "Best Practices for Reducing the Potential for Progressive Collapse in Buildings," National Institute of Standards and Technology, Gaithersburg, MD, 2007.

7. UFC 4-023-03, "Design of Buildings to Resist Progressive Collapse," U.S. Department of Defense, Washington, DC, 2016.

8. ASCE/SEI 7-16, "Minimum Design Loads and Associated Criteria for Buildings and Other Structures," American Society of Civil Engineers, Reston, VA, 2016.

9. GSA, *Progressive Collapse Analysis and Design Guidelines for New Federal Office Buildings and Major Modernization Projects*, Office of Chief Architects, Washing, DC, 2016.

10. Marjanishvili, S., and Agnew, E., "Comparison of Various Procedures for Progressive Collapse Analysis," *Journal of Performance of Constructed Facilities*, ASCE, V. 20, No. 4, 2006, pp. 365-374. doi: 10.1061/(ASCE)0887-3828(2006)20:4(365)

11. Tsai, M. H., and Lin, B. H., "Investigation of Progressive Collapse Resistance and Inelastic Response for an Earthquake-Resistant RC Building Subjected to Column Failure," *Engineering Structures*, V. 30, No. 12, 2008, pp. 122-149. doi: 10.1016/j.engstruct.2008.05.031

12. Sasani, M.; Kazemi, A.; Sagiroglu, S.; and Forest, S., "Progressive Collapse Resistance of an Actual 11-Story Structure Subjected to Severe Initial Damage," *Journal of Structural Engineering*, ASCE, V. 137, No. 9, 2011, pp. 893-902. doi: 10.1061/(ASCE)ST.1943-541X.0000418

13. Sasani, M., and Sagiroglu, S., "Progressive Collapse Resistance of Hotel San Diego," *Journal of Structural Engineering*, ASCE, V. 134, No. 3, 2008, pp. 478-488. doi: 10.1061/(ASCE)0733-9445(2008)134:3(478)

14. Sasani, M., and Sagiroglu, S., "Gravity Load Redistribution and Progressive Collapse Resistance of 20-Story Reinforced Concrete Structure Following Loss of Interior Column," *ACI Structural Journal*, V. 107, No. 6, Nov.-Dec. 2010, pp. 636-644. doi: 10.14359/51664011

15. Qian, K., and Li, B., "Dynamic and Residual Behavior of Reinforced Concrete Floors Following Instantaneous Removal of a Column," *Engineering Structures*, V. 148, Oct. 2017, pp. 175-184. doi: 10.1016/j.engstruct.2017.06.059

16. Adam, J. M.; Buitrago, M.; Bertolesi, E.; Sagaseta, J.; and Moragues, J. J., "Dynamic Performance of a Real-Scale Reinforced Concrete Building Test Under a Corner-Column Failure Scenario," *Engineering Structures*, V. 210, Feb. 2020, p. 110414. doi: 10.1016/j.engstruct.2020.110414

17. Xiao, Y.; Zhao, Y. B.; Li, F. W.; Kunnath, S.; and Lew, H. S., "Collapse Test of a 3-Story Half-Scale RC Frame Structure," *Structures Congress*, Pittsburgh, PA, May 2013. doi: 10.1061/9780784412848.002

18. Izzuddin, B. A.; Vlassis, A. G.; Elghazouli, A. Y.; and Nethercot, D. A., "Progressive Collapse of Multi-Storey Buildings Due to Sudden Column Loss - Part I: Simplified Assessment Framework," *Engineering Structures*, V. 30, No. 5, 2008, pp. 1308-1318. doi: 10.1016/j.engstruct.2007.07.011

19. Orton, S. L., and Kirby, J. E., "Dynamic Response of a RC Frame Under Column Removal," *Journal of Performance of Constructed Facilities*, ASCE, V. 28, No. 4, 2014, p. 04014010. doi: 10.1061/(ASCE)CF.1943-5509.0000464

20. Yi, W. J.; He, Q. F.; Xiao, Y.; and Kunnath, S. K., "Experimental Study on Progressive Collapse-Resistance Behaviour of Reinforced Frame Structures," *ACI Structural Journal*, V. 105, No. 4, July-Aug. 2008, pp. 433-439. doi: 10.14359/19857

21. Shan, S. D.; Li, S.; Xu, S. Y.; and Xie, L. L., "Experimental Study on the Progressive Collapse Performance of RC Frames with Infill Walls," *Engineering Structures*, V. 111, Mar. 2016, pp. 80-92. doi: 10.1016/j.engstruct.2015.12.010

22. Li, S.; Shan, S. D.; Zhai, C. H.; and Xie, L. L., "Experimental and Numerical Study on Progressive Collapse Process of RC Frames with Full-Height Infill Walls," *Engineering Failure Analysis*, V. 59, July 2016, pp. 57-68. doi: 10.1016/j.engfailanal.2015.11.020

23. Qian, K., and Li, B., "Effects of Masonry Infill Wall on the Performance of RC Frames to Resist Progressive Collapse," *Journal of Structural Engineering*, ASCE, V. 143, No. 9, 2017, p. 04017118. doi: 10.1061/(ASCE)ST.1943-541X.0001860

24. Qian, K.; Lan, D. Q.; Fu, F.; and Li, B., "Effects of Infilled Wall Opening on Load Resisting Capacity of RC Frames to Mitigate Progressive Collapse Risk," *Engineering Structures*, V. 223, Aug. 2020, p. 111196. doi: 10.1016/j.engstruct.2020.111196

25. Su, Y.; Tian, Y.; and Song, X., "Progressive Collapse Resistance of Axially-Restrained Frame Beams," *ACI Structural Journal*, V. 106, No. 5, Sept.-Oct. 2009, pp. 600-607. doi: 10.14359/51663100

26. Choi, H., and Kim, J., "Progressive Collapse-Resisting Capacity of RC Beam-Column Sub-Assemblage," *Magazine of Concrete Research*, V. 63, No. 4, 2011, pp. 297-310. doi: 10.1680/macr.9.00170

27. Qian, K.; Li, B.; and Ma, J. X., "Load-Carrying Mechanism to Resist Progressive Collapse of RC Buildings," *Journal of Structural Engineering*, ASCE, V. 141, No. 2, 2015, p. 04014107. doi: 10.1061/(ASCE)ST.1943-541X.0001046

28. Ren, P. Q.; Li, Y.; Lu, X. Z.; Guan, H.; and Zhou, Y. L., "Experimental Investigation of Progressive Collapse Resistance of One-Way Reinforced Concrete Beam-Slab Substructures Under a Middle-Column-Removal Scenario," *Engineering Structures*, V. 118, July 2016, pp. 28-40. doi: 10.1016/j.engstruct.2016.03.051

29. Forquin, P., and Chen, W., "An Experimental Investigation of the Progressive Collapse Resistance of Beam-Column RC Sub-Assemblages," *Construction and Building Materials*, V. 152, Aug. 2017, pp. 1068-1084. doi: 10.1016/j.conbuildmat.2017.05.179

30. Qian, K.; Zhang, X. D.; Fu, F.; and Li, B., "Progressive Collapse Resisting Mechanisms of Planar Prestressed Concrete Frame," *ACI Structural Journal*, V. 116, No. 4, July-Aug. 2019, pp. 77-90. doi: 10.14359/51715567

31. Zhao, Z. D.; Liu, Y.; Li, Y.; Guan, H.; Yang, Z.; Ren, P.; and Xiao, Y., "Experimental and Numerical Investigation of Dynamic Progressive Collapse of Reinforced Concrete Beam-Column Assemblies Under

a Middle-Column Removal Scenario," *Structures*, V. 38, Feb. 2022, pp. 979-992. doi: 10.1016/j.istruc.2022.02.050

32. FarhangVesali, N.; Valipour, H.; Samali, B.; and Foster, S., FarhangVesali. "Development of Arching Action in Longitudinally-Restrained Reinforced Concrete Beams," *Construction and Building Materials*, V. 47, Oct. 2013, pp. 7-19. doi: 10.1016/j.conbuildmat.2013.04.050

33. Kim, J., and Choi, H., "Monotonic Loading Tests of RC Beam-Column Subassemblage Strengthened to Prevent Progressive Collapse," *International Journal of Concrete Structures and Materials*, V. 9, No. 4, 2015, pp. 401-413. doi: 10.1007/s40069-015-0119-2

34. Qian, K.; Liu, Y.; Yang, T.; and Li, B., "Progressive Collapse Resistance of Posttensioned Concrete Beam-Column Subassemblages with Unbonded Posttensioning Strands," *Journal of Structural Engineering*, ASCE, V. 144, No. 1, 2018, p. 04017182. doi: 10.1061/(ASCE)ST.1943-541X.0001940

35. Deng, X. F.; Li, Z.; Weng, Y. H.; Yu, X. H.; and Qian, K., "Experimental Study on Performance of Prestressed Concrete Beam-Column Substructure Against Progressive Collapse," *Journal of Building Structures*, V. 40, No. 8, Aug. 2019, pp. 71-78. doi: 10.14006/j.jzjgxb.2018.0117

36. Yang, T.; Chen, W. Q.; and Han, Z. Q., "Experimental Investigation of Progressive Collapse of Prestressed Concrete Frames After the Loss of Middle Column," *Advances in Civil Engineering*, V. 2020, No. 1, 2020, pp. 1-12. doi: 10.1155/2020/8219712

37. Zhang, W. S.; Zhang, L.; and Yang, T., "Dynamic Experiments on Post-Tensioned Beam-Column Substructures Following the Sudden Removal of a Single Interior Column," *Journal of Building Engineering*, V. 49, May 2022, p. 103876. doi: 10.1016/j.jobe.2021.103876

38. Qian, K.; Liang, S. L.; Fu, F.; and Fang, Q., "Progressive Collapse Resistance of Precast Concrete Beam-Column Sub-Assemblages with High-Performance Dry Connections," *Engineering Structures*, V. 198, Aug. 2019, p. 109552. doi: 10.1016/j.engstruct.2019.109552

39. Lin, K. Q.; Lu, X. Z.; Li, Y.; and Guan, H., "Experimental Study of a Novel Multi-Hazard Resistant Prefabricated Concrete Frame Structure," *Soil Dynamics and Earthquake Engineering*, V. 119, Apr. 2019, pp. 390-407. doi: 10.1016/j.soildyn.2018.04.011

40. Li, Z. X.; Liu, H. K.; Shi, Y. C.; Ding, Y.; and Zhao, B., "Experimental Investigation on Progressive Collapse Performance of Prestressed Precast Concrete Frames with Dry Joints," *Engineering Structures*, V. 246, Nov. 2021, p. 113071. doi: 10.1016/j.engstruct.2021.113071

41. GB50010-2010, "Code for Design of Concrete Structures," Ministry of Housing and Urban-Rural Development of the People's Republic of China, Beijing, China, 2010.

42. Xu, W. L., and Wang, L. C., "Experimental Study on the Collapse-Resistant Performance of Unbonded Prestressed PC Beam-Column Sub-Assemblages with Pinned Connections," *Engineering Structures*, V. 279, Feb. 2023, p. 115637. doi: 10.1016/j.engstruct.2023.115637

43. Zhang, S. L., "ABAQUS FEM Analysis Partially Bonded and Prestressed Concrete Beams," *Low Temperature Architecture Technology*, V. 31, No. 5, May 2009, pp. 40-42.

44. ABAQUS, *Abaqus Analysis User's Guide*, Dassault Systèmes Simulia Corp, 2019.

45. Mander, J. A. B.; Priestley, M. J. N.; and Park, R., "Theoretical Stress-Strain Model for Confined Concrete," *Journal of Structural Engineering*, ASCE, V. 114, No. 8, 1988, pp. 1804-1826. doi: 10.1061/(ASCE)0733-9445(1988)114:8(1804)

46. Guo, Z. H., and Zhang, X. Q., "Investigation of Complete Stress-Deformation Curves for Concrete in Tension," *ACI Materials Journal*, V. 84, No. 4, July-Aug. 1987, pp. 278-285. doi: 10.14359/1616

47. Xu, W. L., and Wang, L. C., "Analytical Models for Reverse Arch and Compressive Arch Action in Horizontally Restrained Unbonded Prestressed RC Beam-Column Sub-Assemblages," *Engineering Structures*, V. 228, Nov. 2021, p. 110529. doi: 10.1016/j.engstruct.2020.111529

48. Yu, J., and Tan, K. H., "Experimental and Numerical Investigation on Progressive Collapse Resistance of Reinforced Concrete Beam Column Sub-Assemblages," *Engineering Structures*, V. 55, Dec. 2013, pp. 90-106. doi: 10.1016/j.engstruct.2011.08.040

49. Yu, J., and Tan, K. H., "Structural Behavior of RC Beam-Column Subassemblages Under a Middle Column Removal Scenario," *Journal of Structural Engineering*, ASCE, V. 139, No. 2, 2013, pp. 233-250. doi: 10.1061/(ASCE)ST.1943-541X.0000658

50. Kang, S. B., and Tan, K. H., "Behaviour of Precast Concrete Beam-Column Sub-Assemblages Subject to Column Removal," *Engineering Structures*, V. 93, June 2015, pp. 85-96. doi: 10.1016/j.engstruct.2015.03.027

51. Kang, S. B.; Tan, K. H.; and Yang, E. H., "Progressive Collapse Resistance of Precast Beam-Column Sub-Assemblages with Engineered Cementitious Composites," *Engineering Structures*, V. 98, Sept. 2015, pp. 186-200. doi: 10.1016/j.engstruct.2015.04.034



ACI Foundation Seeks Research Needs, Industry Problem Statements, and Ideas for Innovation

aci Foundation
Building the Future

The ACI Foundation will evaluate, and prioritize submissions based on impact, relevancy, and urgency. There are a variety of ways the ACI Foundation can provide support, such as hosting stakeholder meetings, funding a road map, business plan, document development, or standard research.

We are interested in both small discreet needs or large-scale interdisciplinary projects and visionary topics. We value collaboration and strategic partnerships with ACI committees and industry stakeholders outside of the ACI community to fully leverage the ACI Foundation's resources.

The ACI Foundation is committed to impacting ACI and the concrete industry through concrete research and innovative initiatives.

We are seeking your ideas, research needs and problem statements that advance the knowledge and use of concrete materials, structures, and construction, as well as new technologies and innovations that provide solutions to industry issues.

Visit **acifoundation.org/research/solicitations** for additional information, the submission form, and detailed instructions

ACI STRUCTURAL JOURNAL TECHNICAL PAPER

Title No. 122-S68

Cyclic Loading Test for Precast Columns Using Slag-Based Concrete and Sleeve Splices

by H.-S. Moon, K.-W. Jo, H.-J. Hwang, C.-S. Kim, J.-H. Jeong, C.-K. Park, and H.-G. Park

Slag-based zero-cement concrete (ZC) of high strength (60 MPa [8.70 ksi]) was developed as an eco-friendly construction material. In the present study, to investigate the structural behavior of precast columns using ZC, cyclic loading tests were performed for five column specimens with reinforcement details of ordinary moment frames. Longitudinal reinforcement was connected by sleeve splices at the precast column-footing joint. The test parameters included the concrete type (portland cement-based normal concrete [NC] versus ZC), construction method (monolithic versus precast), longitudinal reinforcement ratio, and sleeve size. The test results showed that the structural performance (failure mode, strength, stiffness, energy dissipation, and deformation capacity) of the precast ZC columns was comparable to that of the monolithic NC and precast NC columns, and the tested strengths agreed with the nominal strengths calculated by ACI 318-19. These results indicate that current design codes for cementitious materials and sleeve splice of longitudinal reinforcement are applicable to the design of precast ZC columns.

Keywords: column; cyclic loading test; precast concrete; seismic performance; slag-based concrete; sleeve splice; zero-cement concrete.

INTRODUCTION

Recently, zero-cement concrete (ZC) has attracted more attention because it can reduce carbon emissions. In ZC, unlike normal concrete (NC), portland cement is not used. Instead, industrial by-products (such as ground-granulated blast-furnace slag [GGBS] or fly ash) are used as a binder along with an alkaline activator for chemical reaction.[1-3] Thus, ZC is also known as alkali-activated concrete.[4,5]

A large number of material studies have been conducted to develop various ZCs, especially since 2016.[6] However, it is difficult to quantify the generic material properties of ZC, as they vary greatly depending on its constituents and mixture proportions and are highly sensitive to curing conditions.[7,8] Meanwhile, there have also been various experimental studies on structural members using ZC, such as beams under flexure,[9-11] beams under shear,[12] columns under compression,[13] walls under compression or shear,[14,15] slabs under flexure or shear,[16-18] bond strength,[19,20] and interior and exterior beam-column joints under cyclic lateral load.[20-23] However, cyclic loading testing of ZC columns is very rare. Most of these studies reported that ZC members can be designed according to current design codes.

In the present research program, a new type of slag-based ZC of high strength (60 MPa [8.70 ksi]) was developed, and a series of tests were prepared to verify the structural performance of structural members using the new ZC. Note that ZC is more applicable for precast construction, as its mechanical properties are sensitive to curing conditions. Thus, this research program focused on the performance of precast ZC members.

For precast column connections, sleeve splices or grouted splice-sleeve connections are widely used. In existing studies, the structural performance of precast columns with sleeve splices was investigated through cyclic loading tests or shaking table tests. Haber et al.[24] reported that the ultimate displacement and ductility of a precast column with sleeve splices were 40% and 39% lower than those of a counterpart monolithic column, respectively, due to the early damage in the sleeve zone and the early fracture of longitudinal reinforcement. A similar observation can be found in Ameli et al.[25]: the ultimate displacement and ductility of a precast column with sleeve splices were 41% and 51% lower than those of the counterpart monolithic column, respectively. Damage patterns were also different: in the precast column with sleeve splices, most damage was localized at the joint between the column and footing, and gap-opening repeatedly occurred at the column-footing joint under reversed cyclic loading. As a result, slip of longitudinal reinforcement occurred in the splice sleeves at the joint, which caused pinching in the cyclic behavior. Ultimately, the column failed in the pullout of longitudinal reinforcement from the sleeves. In another study by Ameli et al.,[26] a precast column with sleeve splices showed 14% lower ultimate displacement and 39% lower ductility, and failed in the fracture of longitudinal reinforcement in the footing. Qu et al.[27] reported that in a precast column with sleeve splices, the ultimate displacement was decreased by 14% due to local damage and gap-opening at the joint. On the other hand, positive test results can also be found in the literature: Xin et al.[28] reported that a precast column with sleeve splices showed 16% greater ultimate displacement and 7% greater ductility, though damages were concentrated at the joint. The existing studies reported that insufficient grout-infill (that is, grouting defects) can cause bond-slip and gap-opening, leading to the degradation of strength, energy dissipation, and deformation capacity.[29,30] As such, the behavior of precast columns is strongly affected by the reinforcing bar connection method.

In the present study, to verify the structural performance of precast ZC columns with sleeve splices, cyclic lateral

ACI Structural Journal, V. 122, No. 5, September 2025.
MS No. S-2023-259.R1, doi: 10.14359/51746791, received February 6, 2024, and reviewed under Institute publication policies. Copyright © 2025, American Concrete Institute. All rights reserved, including the making of copies unless permission is obtained from the copyright proprietors. Pertinent discussion including author's closure, if any, will be published ten months from this journal's date if the discussion is received within four months of the paper's print publication.

Table 1—Mixture proportions of concrete and grout, kg/m³

Type	Cement	GGBS	Activator		W	S	CA	D	Calcium sulfate	Other
			CSA compound	NaOH						
NC	305	130	—	—	165	805	978	4	—	—
ZC	—	500	100	6	155	759	862	8.6	—	—
Grout	40 to 50%	—	—	—	—	40 to 50%	—	—	1 to 5%	1 to 5%

Note: S is sand; CA is coarse aggregate; and D is dispersant. 1 kg/m³ = 0.062 lb/ft³.

Table 2—Chemical composition of GGBS, %

Composition	SiO_2	CaO	Al_2O_3	MgO	Fe_2O_3	SO_3	K_2O
GGBS	35.64	41.30	14.73	5.18	0.41	2.16	0.39

loading tests were performed under constant axial load. Test parameters included the concrete type (NC versus ZC), construction method (monolithic versus precast), longitudinal reinforcement ratio, and sleeve size. Five full-scale column specimens were tested (a monolithic NC, a precast NC, and three precast ZC specimens). The structural performance of precast ZC columns was compared with that of monolithic and precast NC columns in terms of failure mode, strength, stiffness, energy dissipation, and deformation capacity. The test results were evaluated based on ACI 374.1-05[31] and AIJ Guidelines.[32]

RESEARCH SIGNIFICANCE

A new type of slag-based ZC was developed for carbon neutrality of concrete. In the present study, the structural performance of precast ZC columns with sleeve splices was investigated through quasi-static testing. The test results were compared with those of monolithic and precast NC columns, and the tested strength was compared with the nominal strength predicted by current design codes. The results of the present study can be used as evidence for the practical application of ZC columns.

CONCRETE MATERIAL

Mixture proportions

Table 1 shows the mixture proportions of ZC and NC used in the present study. In ZC, without using portland cement, GGBS (refer to Table 2) was used as a binder and a mixture of calcium sulfoaluminate (CSA) compound and solid sodium hydroxide (NaOH) was used as an activator. In NC, using portland cement, GGBS (30%) was used as a partial replacement of the cement.

All ZC and NC column specimens were steam-cured and the curing condition was carefully controlled, as the material properties of ZC are sensitive to the curing condition. First, the column specimens were cured at the temperature of 20°C (68°F) for 2 to 3 hours for preconditioning after casting. Then, in the case of ZC columns, the temperature was increased to 35°C (95.0°F) for 2 hours, and maintained for 8 hours. In the case of NC columns, the temperature was increased to 50 to 60°C (122 to 140°F) for 2 hours, and maintained for 6 hours. After the heating, the temperature was lowered to 20°C (68°F) for 2 hours, and then the specimens were kept at ambient conditions before column testing.

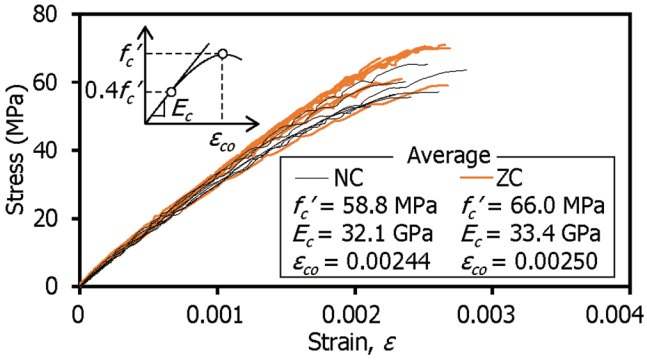


Fig. 1—Stress-strain relationships of NC and ZC. (Note: 1 MPa = 145 psi.)

Concrete cylinders, which were prepared to investigate the material strength on the day of column testing, were cured at the same conditions as the column specimens.

Stress-strain relationships

At the day of column testing (concrete age of 27 to 31 days), material (compression) testing was conducted for Ø100 x 200 mm (Ø3.94 x 7.87 in.) concrete cylinders. Figure 1 compares the stress-strain relationships of 10 ZC and eight NC cylinders, which were obtained from the compression tests. As shown in the figure, ZC shows a typical compressive behavior of concrete. The compressive strength (f_c') was measured to be 59.1 to 70.9 MPa (8.58 to 10.3 ksi) (66.0 MPa [9.58 ksi] on average) for ZC and 52.8 to 65.3 MPa (7.66 to 65.3 ksi) (58.8 MPa [8.53 ksi] on average) for NC at the day of testing. The modulus of elasticity (E_c) and strain at peak stress (ε_{co}) of ZC were similar to those of NC; E_c = 30.0 to 35.5 GPa (4352 to 5155 ksi) (33.4 GPa [4842 ksi] on average) for ZC and E_c = 30.2 to 35.5 GPa (4388 to 5153 ksi) (32.1 GPa [4655 ksi] on average) for NC; ε_{co} = 0.00218 to 0.00269 (0.00250 on average) for ZC and ε_{co} = 0.00212 to 0.00282 (0.00244 on average) for NC.

TEST PLAN

Test specimens

Table 3 summarizes the test parameters of column specimens (concrete type, construction method, longitudinal reinforcement ratio, and sleeve size). In specimen nomenclature, the first letters 'NC' or 'ZC' denote the concrete type (portland cement-based NC or slag-based ZC), the second letter 'M' or 'P' denotes the construction method (monolithic or precast), and the last letter 'R' or 'S' indicates the increase of longitudinal reinforcement ratio and the sleeve size, respectively. The sleeve size was increased to investigate the effect of grout-filling on sleeve splice performance.

Table 3—Test parameters and material properties

Specimen	Concrete type	Construction method	Longitudinal reinforcement ρ	Sleeve size	Concrete f_c', MPa	Grout f_c', MPa	Reinforcing bar	
							f_y, MPa	f_{yt}, MPa
NC-M	NC	Monolithic	8-D25 (1.62%)	—	59.5	75.0	661.1	620.0
NC-P	NC	Precast	8-D25 (1.62%)	D25	59.5	75.0	661.1	620.0
ZC-P	ZC	Precast	8-D25 (1.62%)	D25	69.4	83.7	646.4	571.3
ZC-P-R	ZC	Precast	8-D32 (2.54%)	D32	60.4	75.0	636.0	620.0
ZC-P-S	ZC	Precast	8-D25 (1.62%)	D29	70.5	83.7	646.4	571.3

Note: $\rho = A_s/bd$ is longitudinal reinforcement ratio (A_s is total cross-sectional area of longitudinal reinforcement, b is sectional width, and d is sectional effective depth); nominal diameter of longitudinal reinforcement is 25.4 mm (1 in.) for D25, 28.6 mm (1.125 in.) for D29, or 31.8 mm (1.25 in.) for D32; sleeve size is standard size of spliced bars; f_c' is cylindrical compressive strength of concrete or grout; f_y is yield strength of longitudinal reinforcement; and f_{yt} is yield strength of transverse reinforcement (D13: nominal diameter = 12.9 mm [0.51 in.]). 1 MPa = 145 psi.

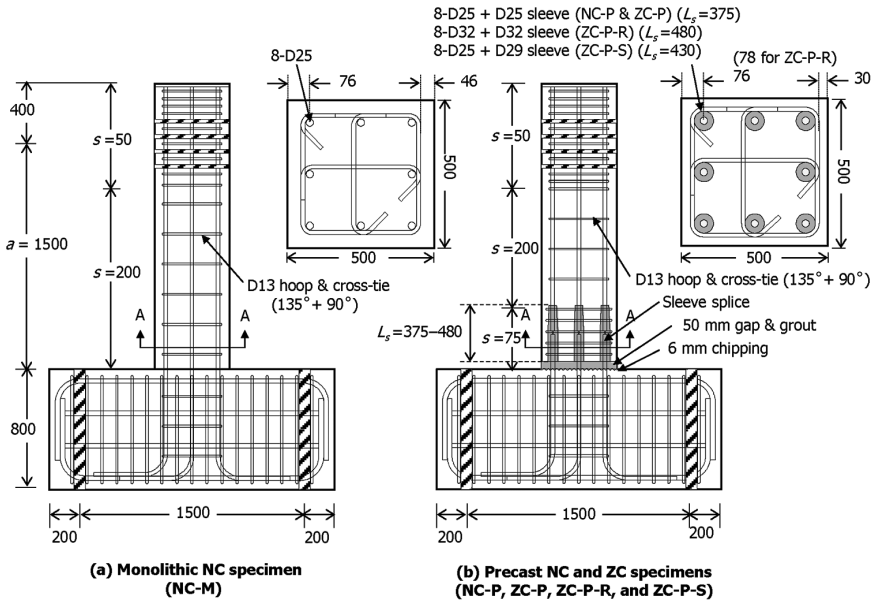


Fig. 2—Details of column specimens. (Note: Units in mm; 1 mm = 0.039 in.)

Figure 2 shows the details of the column specimens. For precast column connections, sleeve splices are frequently used for splicing of longitudinal reinforcement, as they can accommodate construction tolerance in vertical alignment of columns. However, sleeve splices are known to have limited seismic performance under cyclic loads.[24-27] For this reason, the column specimens were designed as a part of an ordinary moment frame. Each test specimen consisted of a column and an NC footing. The width (b), depth (h), and shear span (a is the column length from the bottom end to the lateral loading point) were the same for all the column specimens: b x h x a = 500 x 500 x 1500 mm (19.7 x 19.7 x 59.1 in.).

Figure 2(a) shows the details of the monolithic NC specimen (NC-M). The column and footing were cast monolithically. For longitudinal reinforcement, eight D25 bars (nominal diameter d_b = 25.4 mm [1.0 in.], yield strength f_y = 661.1 MPa [95.9 ksi], and reinforcement ratio ρ = 1.62%) of the column were extended and anchored to the footing. For transverse reinforcement (hoops and crossties), D13 bars (d_b = 12.9 mm [0.51 in.], and f_y = 620.0 MPa [89.9 ksi]) were placed at a spacing of 200 mm (7.87 in.) (approximately one-half of the effective depth), with 135-degree hook at one end and 90-degree hook at the other end.

Figure 2(b) shows the details of the precast specimens (NC-P, ZC-P, ZC-P-R, and ZC-P-S). For the precast specimens, the column (NC or ZC) and footing (NC) were cast separately (Fig. 3(a)), and then connected by sleeve splices (Fig. 3(b)). For longitudinal reinforcement, eight D25 (d_b = 25.4 mm [1.0 in.], f_y = 646.4 to 661.1 MPa [92.3 to 97.2 ksi], and ρ = 1.62%) or D32 (d_b = 31.8 mm [1.25 in.], f_y = 636.0 MPa [92.3 ksi], and reinforcement ratio ρ = 2.54%) bars were used. For splice of longitudinal reinforcement at the column-footing joint, typical sleeves were used along with high-strength non-shrink grout (refer to Tables 1 and 3). To replicate actual precast construction, the top surface of the footings was roughened by 6 mm (0.24 in.) chipping, and a 50 mm (1.97 in.) gap was provided between the column and footing for vertical alignment. Transverse reinforcement (d_b = 12.9 mm [0.51 in.], and f_y = 571.3 to 620.0 MPa [82.9 to 89.9 ksi]) in the precast specimens had the same details as in the monolithic specimen (NC-M), except the spacing around sleeves: in the region where sleeves were located, the spacing of transverse reinforcement was reduced to approximately 75 mm (2.95 in.) to prevent early loosening of transverse reinforcement.

At the day of column-testing (concrete age of 27 to 31 days), material (compression) testing was conducted

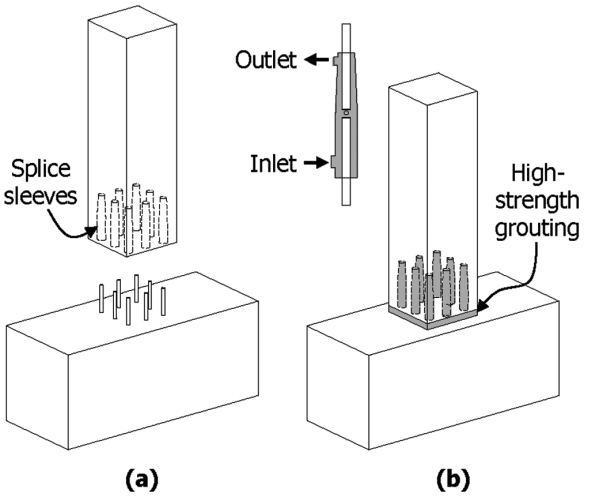


Fig. 3—Construction process of precast specimens.

for concrete and grout; a 40 x 40 x 160 mm (1.57 x 1.57 x 6.30 in.) prism[33] was used for grout specimens. The compressive strength (f_c') for each column specimen was measured to be 60.4 to 70.8 MPa (8.76 to 10.3 ksi) for ZC, 59.5 MPa (8.63 ksi) for NC, and 75.0 to 83.7 MPa (10.9 to 12.1 ksi) for grout. The measured material properties of concrete and grout are presented in Table 3, along with the properties of longitudinal and transverse reinforcement.

Test setup and measurement

Figure 4 shows the test setup for cyclic lateral loading under constant axial load. First, an axial load was applied on the top of the column using two hydraulic jacks, and then cyclic lateral loading was applied using an actuator. The magnitude of axial load was approximately 13% of the nominal axial strength of the column. The cyclic loading protocol was planned based on ACI 374.1-05[31]: loading steps corresponding to drift ratios of 0.25, 0.35, 0.5, 0.75, 1.0, 1.5, 2.0, 2.75, 3.5, 4.5, 6.0, and 8.0%. Three fully reversed load cycles were at each drift ratio. Structural damages were carefully checked at every loading step. In each specimen, the displacements of the column were measured by nine linear variable differential transformers (LVDTs), and the reinforcement strains were measured by eight strain gauges.

TEST RESULTS

Load-displacement relationships

Figure 5 shows the lateral load-displacement relationships (P-Δ). In the figure, the drift ratio ($\delta = \Delta/a$) and column moment ($M = P \times a$) are provided, and the envelope curves of hysteresis loops are also presented in Fig. 5(f) for comparison. The test results are summarized in Table 4.

Overall, the initial cyclic behavior up to the maximum load (occurring at the drift ratio of 1.47 to 2.73%) was similar for all the specimens. However, the post-peak behavior varied depending on the test parameters. Compared to the precast specimens (NC-P, ZC-P, ZC-P-R, and ZC-P-S), the monolithic specimen (NC-M) showed relatively brittle post-peak behavior. On the other hand, the precast specimens (NC-P, ZC-P, and ZC-P-S) showed more-ductile behavior, though pinching was pronounced at large drift ratios. Interestingly,

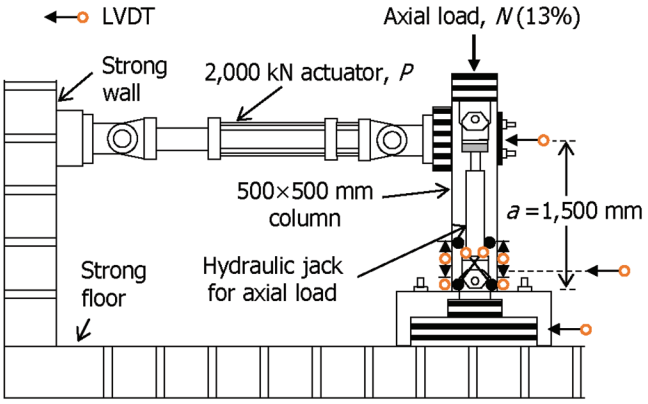


Fig. 4—Test setup and measurement plan. (Note: 1 kN = 0.225 kip; 1 mm = 0.039 in.)

ZC-P-R with a higher longitudinal reinforcement ratio (using D32 bars) showed the best performance in terms of energy dissipation and deformation capacity, as well as strength.

The effects of test parameters can be identified by comparing the envelope curves. In Fig. 6(a), the positive strength of ZC-P was comparable to that of NC-M. However, as shown in Fig. 6(b), strength degradation began to occur earlier in ZC-P than in NC-P. ZC-P-R using a higher longitudinal reinforcement ratio showed the greater strength and more ductile behavior than ZC-P (Fig. 6(c)). In ZC-P-S, using larger-sized sleeves, strength degradation was slightly less than in ZC-P (Fig. 6(d)).

Failure modes

Figure 7 shows the damage patterns at 2.0% drift ratio and at the end of tests. Figure 8 shows the ultimate failure modes. In all the specimens, flexural yielding occurred, followed by local failure depending on the test parameters.

More specifically, in the case of the monolithic NC specimen (NC-M), typical flexural failure occurred: flexural cracks, diagonal propagation of the cracks under reversed cyclic loading, concrete crushing, and steel yielding. Ultimately, local buckling of longitudinal reinforcement occurred and the load suddenly dropped, implying shear failure (at 3.5%; Fig. 8(a)). This failure mode of NC-M was mainly attributed to the greater spacing of transverse reinforcement, which resulted in low confinement and low shear capacity.

In the precast NC and ZC specimens (NC-P, ZC-P, and ZC-P-S), inherent discontinuities at the column-footing joint (that is, the interfaces between the grout and column concrete and between the grout and footing concrete) affected the damage patterns. From early loading steps, the two interfaces were repeatedly opened and closed under reversed cyclic loading. Further, due to the relatively rigid sleeves, most of early damages were concentrated in the 50 mm (1.97 in.) depth grout zone. The cracking patterns and steel strains in Fig. 7 and as shown later confirm this damage mode. Later, the concrete damage around sleeves became significant due to the bearing of the column concrete. In NC-P, there was a burst of sound on a sleeve splice in compression without apparent concrete damage, and then the load and the steel strain suddenly dropped, which implies that grout crushing

Table 4—Nominal strengths and tests results of column specimens

Specimen	Axial load ratio	P_n, kN	P_{max}, kN		δ at P_{max}, %		δ_y, %		δ_u, %		$\mu = \delta_u/\delta_y$	
			Pos.	Neg.	Pos.	Neg.	Pos.	Neg.	Pos.	Neg.	Pos.	Neg.
NC-M	13%	534	596	−585	1.50	−1.50	1.01	−0.97	2.41	−2.48	2.37	−2.54
NC-P		534	611	−583	2.70	−2.73	0.89	−0.85	4.18	−5.09	4.71	−6.02
ZC-P		566	593	−516	1.49	−1.38	1.03	−0.66	2.70	−3.17	2.62	−4.78
ZC-P-R		659	756	−755	2.69	−2.70	0.91	−1.00	5.99	−5.93	6.56	−5.92
ZC-P-S		570	585	−591	1.49	−1.47	0.89	−0.77	3.42	−4.16	3.85	−5.38

Note: Axial load ratio = $N/(0.85f_c'(A_g - A_s) + f_yA_s)$; N is axial load; P_n is lateral load corresponding to nominal flexural strength of column; P_{max} is measured lateral load strength; δ_y is yield drift ratio; δ_u is ultimate drift ratio; μ is displacement ductility; Pos. is positive; Neg. is negative. 1 kN-m = 0.735 kip-ft; 1 kN = 0.225 kip.

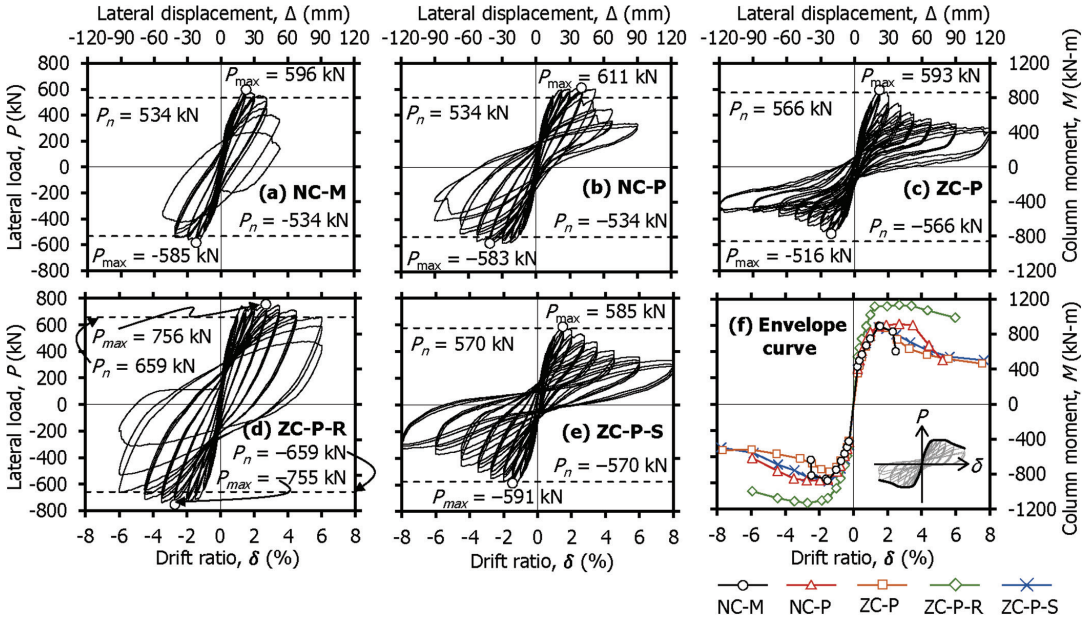


Fig. 5—Lateral load-displacement relationships. (Note: 1 kN = 0.225 kip; 1 mm = 0.039 in.; 1 kN-mm = 5.71 kip/in.)

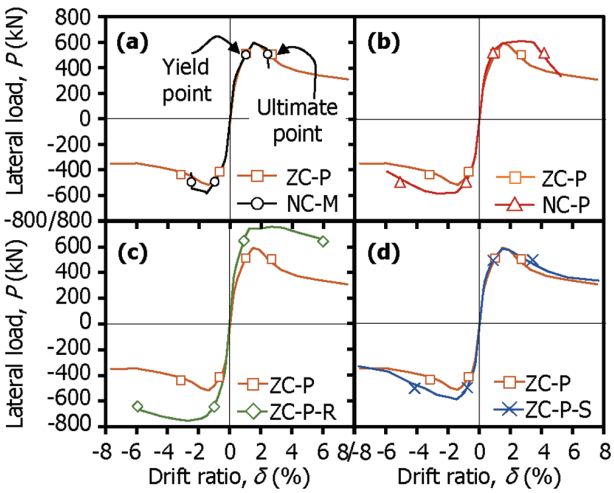


Fig. 6—Effects of test parameters. (Note: 1 kN = 0.225 kip.)

occurred inside the sleeve (Fig. 8(b)). In ZC-P and ZC-P-S, bond-slip between the longitudinal reinforcement and the grout in sleeves in tension was observed during the tests (Fig. 8(f)). This bond-slip significantly affected the structural behavior: unbalanced strength under positive and negative loadings, reduced energy dissipation and deformation capacity, and decreased strain of the reinforcement. Ultimately, ZC-P failed by rupture of a sleeve at very large drift ratio (8.0%) (Fig. 8(c)). In ZC-P-R with the higher longitudinal reinforcement ratio, the cyclic behavior was ductile until failure. At 6.0%, the load suddenly dropped with large diagonal cracks, which implies shear failure (Fig. 8(d)). In ZC-P-S, failure was caused by gradual concrete crushing in compression, and bond-slip in tension (Fig. 8(e)).

An existing study[21] on interior ZC beam-column joints reported that, in ZC specimens, cracks developed earlier, and more significant cracks occurred due to more microcracks of ZC compared to NC specimens. However, in the present study, crack patterns of the precast NC and ZC specimens (NC-P and ZC-P) did not show significant differences (Fig. 9). Overall, the damage pattern and failure mode of the precast ZC specimens (ZC-P, ZC-P-R, and ZC-P-S) were not significantly different from those of the precast NC specimen (NC-P) (Fig. 7 and 8). Rather, the grout-infill quality affected the failure mode. More specifically, grouting defects (uneven or insufficient filling), which resulted in bond slip, appeared to be the main cause of the differences in the cyclic behaviors of the precast NC specimen (NC-P) and the precast ZC specimens (ZC-P and ZC-P-S). The effect of the grout-infill quality can be confirmed by ZC-P-R (with relatively good quality of sleeve splices), showing the best performance despite the higher longitudinal reinforcement ratio.

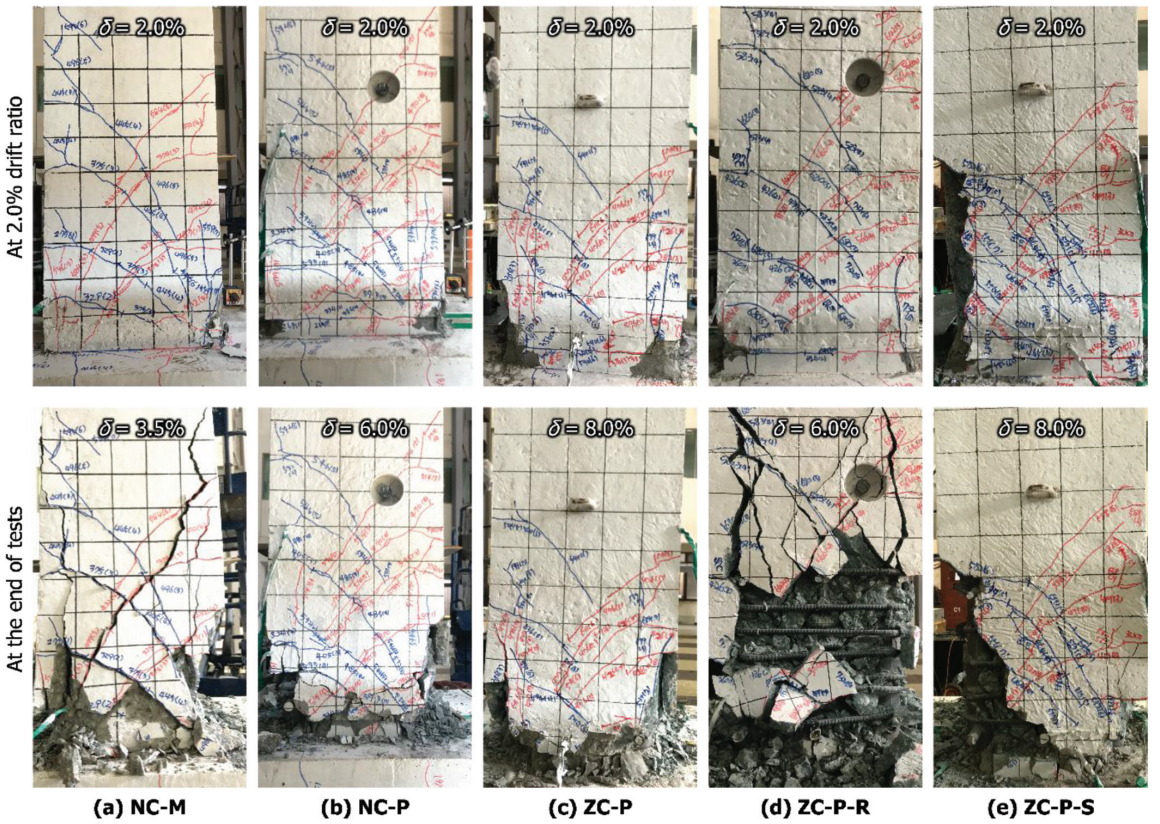


Fig. 7—Damage patterns (at 2.0% drift ratio and at end of tests).

Strains of longitudinal reinforcement

Figures 10 and 11 show the strains of longitudinal reinforcement. The strains were measured at the locations of 25 mm (0.98 in.) below the column-footing joint, 25 mm (0.98 in.) above the joint (or at the middle of the 50 mm [1.97 in.] depth grout zone in the precast specimens), and approximately 25 mm (0.98 in.) above the sleeves in the precast specimens (the distance from the joint was 450 mm [17.7 in.] for NC-M, NC-P, and ZC-P, 555 mm [21.9 in.] for ZC-P-R, or 505 mm [19.9 in.] for ZC-P-S; refer to L_s in Fig. 2). At some strain gauges, strains were not properly measured due to the malfunction or damage of embedded strain gauges.

In Fig. 10, the strains at 25 mm (0.98 in.) above the joint were significantly higher than those at the other locations in the precast specimens (NC-P, ZC-P, ZC-P-R, and ZC-P-S), which confirms that most damages were concentrated at the column-footing joint in the precast specimens. The strains in ZC-P were significantly unbalanced under positive and negative loadings, which indicates that bond-slip occurred in ZC-P due to grouting defects. The strains in ZC-P-S were also unbalanced under positive and negative loadings, which indicates the occurrence of bond-slip. Figure 11 shows the strain histories at 25 mm (0.98 in.) above the joint, which represent the overall behavior of longitudinal reinforcement. All tensile reinforcement yielded before the maximum load, which indicates that flexural yielding occurred in all the column specimens. After the maximum load, the tensile strains of NC-P suddenly dropped, but the tensile strains of ZC-P and ZC-P-S decreased gradually. This result indicates that bond-slip occurred in ZC-P and ZC-P-S. In ZC-P-R with the higher reinforcement ratio, the strain behavior was relatively stable, compared to the other specimens. This is because damages were well distributed in the plastic hinge zone (approximately 500 mm [19.7 in.] above the joint) in ZC-P-R, while most of damages were concentrated at the joint in the other precast specimens (Fig. 7 and 10).

Secant stiffness

To compare the stiffness degradations of NC and ZC, the secant stiffness was examined. Figure 12 shows the variation in secant stiffness, which was defined as the slope between the origin and the peak load at each drift ratio. In general, as the drift ratio increased, the secant stiffnesses decreased. However, the difference in stiffness degradation was marginal in all the column specimens.

Energy dissipation

Figure 13(a) shows the cumulative energy dissipation of the column specimens. The energy dissipation was defined as the area enclosed by the hysteresis loop in each cycle. The energy dissipation of the monolithic NC specimen (NC-M) is presented only to 3.5% due to the early failure. ZC-P showed relatively low energy dissipation due to its lower negative strength, and the energy dissipation of ZC-P-S was similar to that of NC-P. ZC-P-R showed the highest energy dissipation due to the higher longitudinal reinforcement ratio.

Figure 13(b) compares the energy dissipation ratios at each drift ratio. The energy dissipation ratio ($\kappa = E_D/E_{ep}$) was defined as the ratio of the area enclosed by the hysteresis loop for the third cycle (E_D) to the area enclosed by the idealized elasto-perfectly plastic parallelogram (E_{ep}).

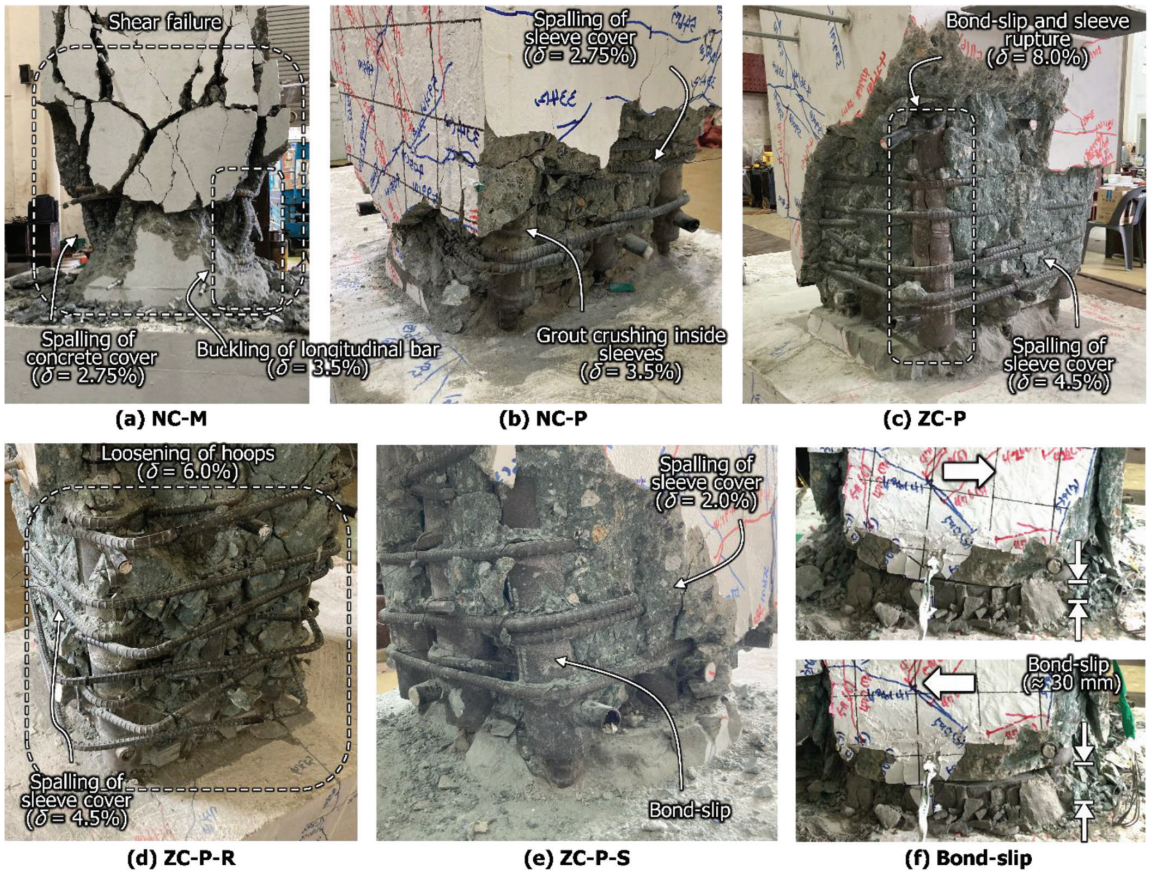


Fig. 8—Ultimate failure modes.

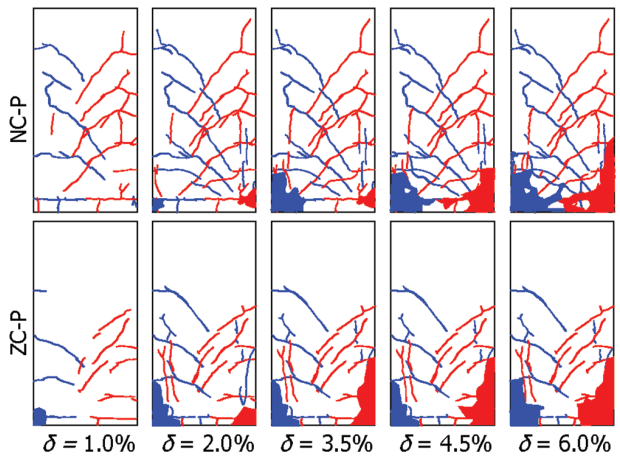


Fig. 9—Cracking patterns of NC-P and ZC-P.

Figure 13(b) shows that the energy dissipation ratios differed depending on the test parameters, and the difference became clearer as the drift ratio increased. The monolithic NC specimen (NC-M) showed the lowest energy dissipation ratio at 0.75 to 2.0%. The energy dissipation ratio of ZC-P was greater than that of NC-M, but lower than that of the other precast specimens (NC-P, ZC-P-R, and ZC-P-S). The lower energy dissipation of ZC-P is attributed to the bond-slip and sleeve rupture (Fig. 8, 10, and 11). ZC-P-R with the higher longitudinal reinforcement ratio showed the greatest energy dissipation ratio after 3.5%, and the energy dissipation ratio gradually increased until the failure at 6.0%. Overall, the energy dissipation ratio of the precast ZC specimens was similar to that of the precast NC specimen.

Deformation capacity

To compare the deformation capacities, the yield displacement (Δ_y), ultimate displacement (Δ_u), and displacement ductility ($\mu = \Delta_u/\Delta_y$) were evaluated from the envelope curves. The yield and ultimate points were determined by the definitions given in Fig. 14.[34,35] Table 4 summarizes the evaluated deformation capacities. For clear comparison, drift ratios are provided in the table, instead of displacements. Because there was no significant difference between the elastic moduli of NC and ZC, the elastic flexural stiffnesses of columns were similar, and as a result, all the column specimens reached the yield displacement at approximately 1.0%. However, the ultimate displacements were significantly different: the ultimate displacement was greater in the order of ZC-P-R > NC-P > ZC-P-S > ZC-P > NC-M. The lowest deformation capacity of the monolithic specimen (NC-M) was attributed to the larger spacing of transverse reinforcement. The deformation capacities of the precast specimens were mainly affected by the grout-infill quality.

EVALUATION BASED ON CURRENT DESIGN CODES

Strength evaluation based on ACI 318-19

To check the applicability of the current design codes to ZC, the test results were compared with the nominal strengths calculated by ACI 318-19.[36] Table 4 summarizes

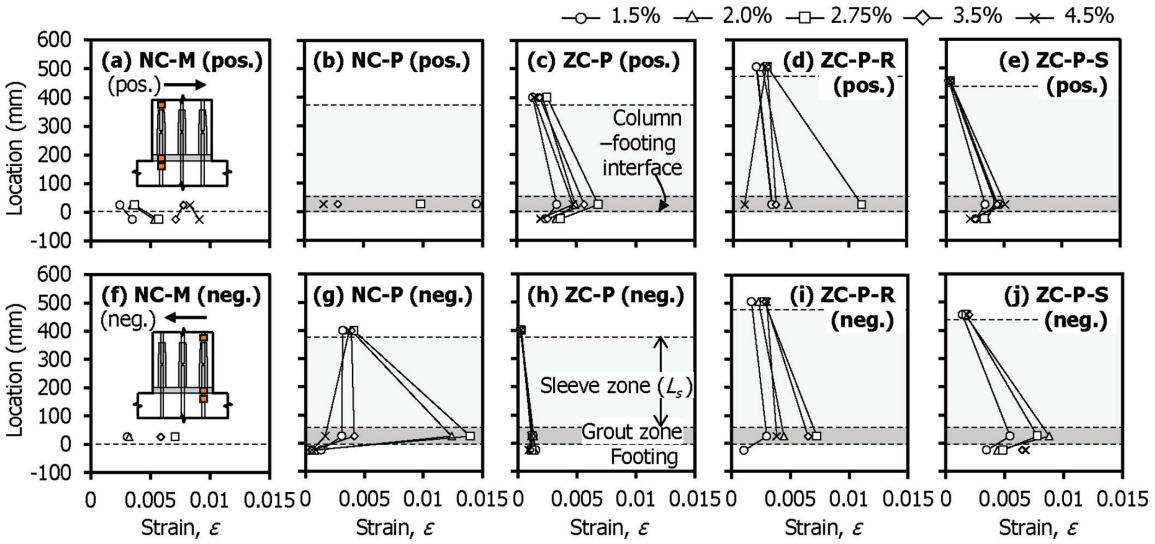


Fig. 10—Strains of longitudinal reinforcement. (Note: 1 mm = 0.039 in.)

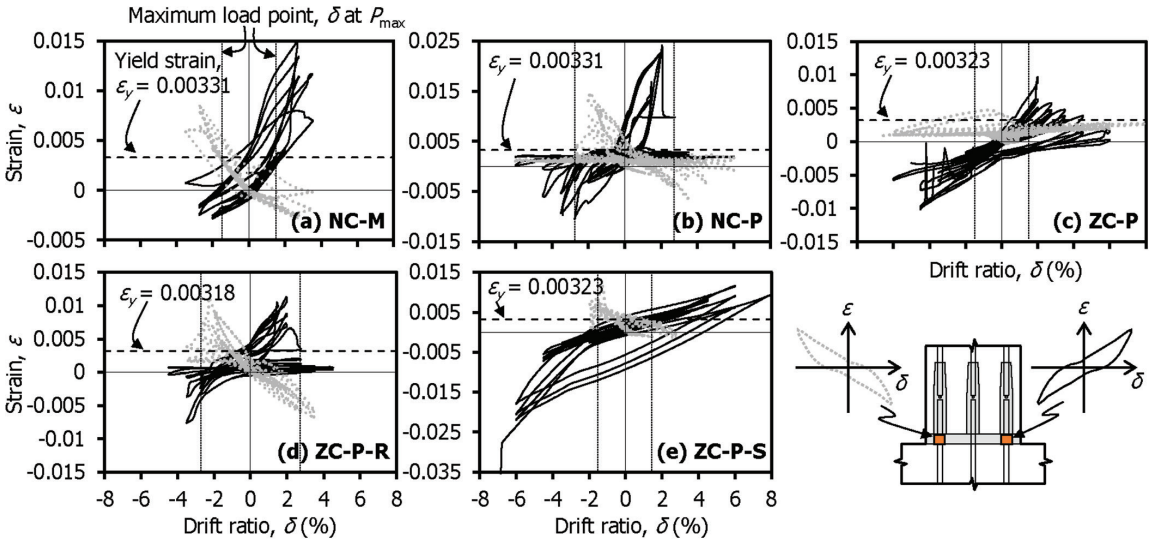


Fig. 11—Strain history of longitudinal reinforcement at joint.

the calculated nominal strengths (P_n), and the horizontal dashed lines in Fig. 5 represent the calculated nominal strengths. The nominal strength is defined as the lateral load ($P_n = M_n/a$) corresponding to the nominal flexural strength (M_n) obtained from the axial force-moment interaction relationship. In Table 4 and Fig. 5, all the measured maximum loads (P_{max}) were 3 to 15% greater than the calculated nominal strengths (P_n), except for ZC-P under negative loading. The lower negative strength of ZC-P was attributed to the grouting defects, and a similar result can be found in Xie et al.[30] The good agreement for lateral load strength implies that ACI 318-19[36] is applicable to the flexural design of ZC columns. The nominal shear strength (V_n) was also calculated by ACI 318-19.[36] The calculated nominal shear strength was in the range of 1056 to 1078 kN (237 to 242 kip), without considering the small spacing in the region of sleeves. The shear strengths (V_n) were 63 to 97% higher than the lateral loads (P_n) corresponding to the nominal flexural strengths. As a result, the flexural yielding preceded the shear failure in all the column specimens.

Seismic performance evaluation based on ACI 374.1-05

ACI 318-19[36] specifies that application of the design code to non-monolithic structures should be based on evidence provided by test results. In the present study, the seismic performance of the precast ZC specimens was evaluated based on ACI 374.1-05[31] (acceptance criteria for moment frames in regions of high seismic risk), though the specimens were designed as columns of ordinary moment frame. ACI 374.1-05[31] requires the following three criteria (for strength degradation, energy dissipation, and stiffness degradation) at the third load cycle at 3.5% drift ratio: (a) the peak load ($P_{3.5\%}$) should be not less than 75% of the maximum load ($0.75P_{max}$); (b) the relative energy dissipation ratio should be not less than 1/8; and (c) the secant stiffness ($K_{3.5\%}$) between the points of ±0.35% should be not less than 0.05 times the initial stiffness ($0.05K_i$).

Table 5 shows the evaluation results. Only ZC-P-R, with the higher longitudinal reinforcement ratio, satisfied all the criteria, while ZC-P and ZC-P-S did not satisfy criterion (a) for strength degradation. The precast NC specimen (NC-P)

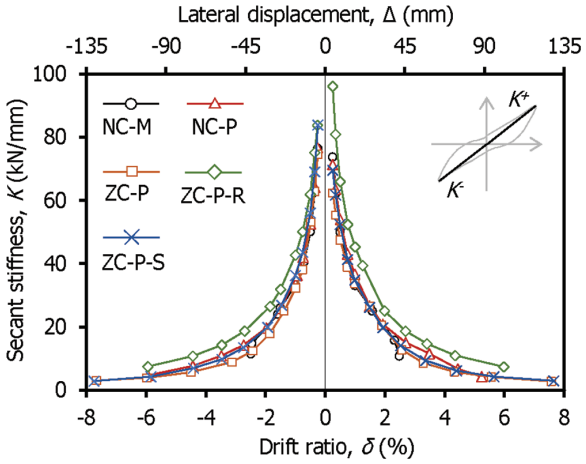


Fig. 12—Secant stiffness. (Note: 1 kN-mm = 5.71 kip/in.; 1 mm = 0.039 in.)

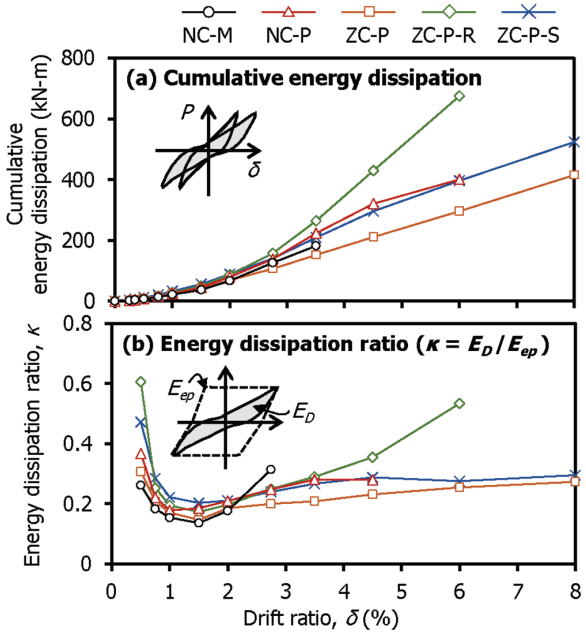


Fig. 13—Energy dissipation capacity. (Note: 1 kN-m = 0.735 kip-ft.)

also did not satisfy criterion (a). The monolithic NC specimen (NC-M) with the large spacing of transverse reinforcement did not satisfy criteria (a) and (c) due to the early failure.

Seismic performance evaluation based on AIJ Guidelines

The AIJ Guidelines[32] specify the acceptance criteria for the emulation evaluation of precast concrete structures, as follows: (a) and (b) the yield strength (P_y) and maximum strength (P_{max}) of a precast member should exceed those of a monolithic member; (c) the strength at the second cycle (P_{2nd}) to the 2% drift ratio should remain within 80% of the strength of the first cycle (P_{1st}); (d) the difference between the yield displacements (δ_y) of the precast and monolithic members should be less than 20%; and (e) the energy dissipation capacity ($E_{2\%}$) of the precast member at the second

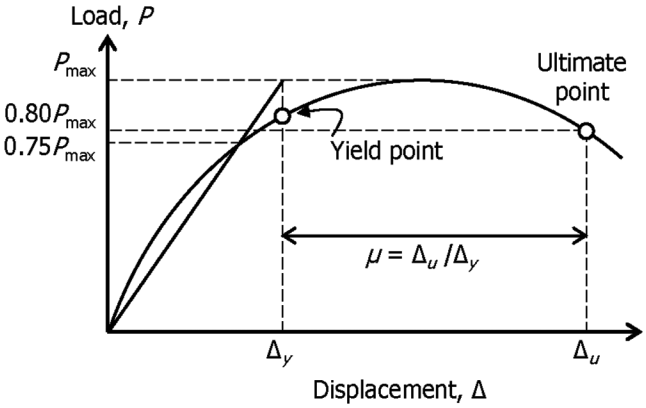


Fig. 14—Definition of deformation capacity.

cycle to the 2% drift ratio should exceed 80% of that of the monolithic member.

The AIJ Guidelines[32] require direct comparison between monolithic and precast specimens. Thus, the seismic performance of ZC-P and ZC-P-S was compared with that of the monolithic NC specimen (NC-M). ZC-P-R with higher longitudinal reinforcement ratio was not evaluated.

Table 6 shows the evaluation results. For clear evaluation, the performance ratios of the precast ZC specimens to NC-M are provided in the table. ZC-P satisfied all the criteria under positive loading, but did not satisfy criterion (a) for yield strength (ratio = 0.84 < 1.0), (b) for maximum strength (ratio = 0.88 < 1.0), and (d) for yield displacement (ratio = 0.68 < 0.8) under negative loading. The poor grout-infill quality was responsible for the low performance under negative loading. ZC-P-S also did not satisfy criterion (a) for yield strength under positive loading (ratio = 0.99 < 1.0), (b) for maximum strength under positive loading (ratio = 0.99 < 1.0), and (d) for yield displacement under negative loading (ratio = 0.79 < 0.8), but the differences were marginal.

CONCLUSIONS

In the present study, cyclic lateral loading tests were performed to investigate the structural performance of precast columns using a newly developed zero-cement concrete (ZC). Five full-scale column specimens were tested (a monolithic normal concrete [NC], a precast NC, and three precast ZC specimens), with reinforcement details of ordinary moment frames, and the test parameters included the concrete type, construction method, longitudinal reinforcement ratio, and sleeve size. The major findings are summarized as follows:

1. The material properties of ZC were comparable to those of NC in terms of peak strength, modulus of elasticity, and strain at peak stress.

2. In the column tests, the initial cyclic behavior up to the maximum load was similar for all the column specimens, but the post-peak behavior varied depending on the test parameters. In all the column specimens, flexural yielding occurred and the damage pattern and failure mode were similar, regardless of the concrete type. Rather, the performance of the precast specimens with sleeve splices was significantly affected by the performance of the reinforcing bar connections (that is, the grout-infill quality).

Table 5—Seismic performance evaluation based on ACI 374.1-05

Criterion		NC-M		NC-P		ZC-P		ZC-P-R		ZC-P-S	
		Pos.	Neg.	Pos.	Neg.	Pos.	Neg.	Pos.	Neg.	Pos.	Neg.
(a) Strength degradation, kN	$0.75P_{max}$	447	−439	458	−437	444	−387	567	−566	439	−443
	$P_{3.5\%}$	N/A	N/A	441	−498	363	−363	695	−686	402	−445
	Evaluation	NG	NG	NG	OK	NG	NG	OK	OK	NG	OK
(b) Energy dissipation, kN-m	Elastoplastic	86.8		68.4		68.4		124.0		79.4	
	Actual	24.4		14.5		14.5		34.8		21.2	
	Ratio	0.281		0.211		0.211		0.281		0.267	
	Evaluation	OK		OK		OK		OK		OK	
(c) Stiffness degradation, kN/mm	$0.05K_i$	3.70	3.82	3.57	—	3.07	3.73	4.81	4.28	3.42	4.20
	$K_{3.5\%}$	N/A	N/A	10.5	16.3	4.20	14.8	14.3	5.40	10.1	14.1
	Evaluation	NG	NG	OK	OK	OK	OK	OK	OK	OK	OK

Note: P_{max} is maximum lateral load strength; $P_{3.5\%}$ is strength at third cycle to 3.5% drift ratio; energy dissipation is energy dissipation at third cycle to 3.5% drift ratio; K_i is initial stiffness; and $K_{3.5\%}$ is secant stiffness between points of ±0.35% at third cycle to ±3.5% drift ratios. 1 kN = 0.225 kip; 1 kN-m = 0.735 kip-ft; and 1 kN/mm = 5.71 kip/in.

Table 6—Seismic performance evaluation based on AIJ Guidelines

Criterion		ZC-P		ZC-P-S	
		Pos.	Neg.	Pos.	Neg.
(a) Yield strength	P_y, kN	512	−415	495	−496
	Ratio	1.02	0.84	0.99	1.00
(b) Maximum strength	P_{max}, kN	593	−516	585	−591
	Ratio	1.00	0.88	0.98	1.01
(c) Strength degradation	P_{1st}, kN	579	−499	573	−574
	P_{2nd}, kN	491	−452	527	−543
	P_{2nd}/P_{1st}	0.85	0.91	0.92	0.94
(d) Yield displacement	δ_y, %	1.03	−0.66	0.89	−0.77
	Ratio	1.02	0.68	0.87	0.79
(e) Energy dissipation	$E_{2\%}$, kN-m	8.42		10.7	
	Ratio	0.96		1.22	

Note: Ratio is ratio of performance index to that of NC-M; P_y is yield strength; P_{max} is maximum load; P_{1st} is peak load at first cycle to 2% drift ratio; P_{2nd} is peak load at second cycle to 2% drift ratio; δ_y is yield drift ratio; $E_{2\%}$ is energy dissipation at second cycle to 2% drift ratio. 1 kN = 0.225 kip; 1 kN-m = 0.735 kip-ft.

3. The structural performance (strength, stiffness, energy dissipation, and deformation capacity) of the precast ZC specimens was comparable to that of the precast NC specimen. The tested strengths of the precast ZC columns exceeded the nominal strengths calculated by ACI 318-19, except for ZC-P under negative loading (due to the grouting defects). This result indicates that the current design codes for cementitious materials are applicable to the design of precast ZC columns.

4. The seismic performance of the precast ZC specimens did not satisfy some of the criteria of ACI 374.1-05 and AIJ Guidelines due to the poor grout-infill quality, but was comparable to that of the precast NC specimen. In the future, further studies are required for the grout-infill quality of sleeve reinforcing bar splices.

AUTHOR BIOS

Han-Se Moon *is a PhD Candidate in the Department of Architecture & Architectural Engineering at Seoul National University, Seoul, South Korea, where he received his BE and MS in architectural engineering.*

Kwang-Won Jo *is a PhD Candidate in the Department of Architecture & Architectural Engineering at Seoul National University, where he received his MS. He received his BE in architectural engineering at Chung-Ang University, Seoul, South Korea. His research interests include inelastic analysis and the seismic design of reinforced concrete (RC) structures.*

ACI member **Hyeon-Jong Hwang** *is an Associate Professor in the School of Architecture at Konkuk University, Seoul, South Korea. He received his BE, MS, and PhD in architectural engineering from Seoul National University. He is a member of Joint ACI-ASCE Committees 352, Joints and Connections in Monolithic Concrete Structures, and 408, Bond and Development of Steel Reinforcement. His research interests include inelastic analysis and seismic design of RC and composite structures.*

Chang-Soo Kim *is a Professor in the School of Architecture (Architectural Engineering Program) at Seoul National University of Science and Technology, Seoul, South Korea. He received his BS in architectural engineering from Pusan National University, Busan, South Korea, and his MS and PhD in structural engineering from Seoul National University. His research interests include structural design and performance evaluation of composite and precast concrete structures.*

Jae-Hong Jeong *is a Principal Researcher at the Institute of Construction Technology, Samsung C&T Corporation, Seoul, South Korea. He received his BS and MS from Seoul National University in 1995 and 1997, respectively. His research interests include carbon-reducing concrete, eco-friendly cement, concrete pumpability, and fiber-reinforced concrete.*

Chan-Kyu Park *is a Master Researcher at the Institute of Construction Technology, Samsung C&T Corporation. He received his PhD from Korea Advanced Institute of Science and Technology, Daejeon, South Korea, in 1997. His research interests include carbon-reducing concrete, concrete pumpability, and hydration control of mass concrete.*

Hong-Gun Park, *FACI, is a Professor in the Department of Architecture & Architectural Engineering at Seoul National University, where he received his BE and MS in architectural engineering. He received his PhD in civil engineering from The University of Texas at Austin, Austin, TX. His research interests include inelastic analysis and the seismic design of RC structures.*

ACKNOWLEDGMENTS

This research was supported by Samsung C&T Corporation; a grant (RS-2022-00143493) from Digital-based Building Construction and Safety Supervision Technology Research Program funded by the Ministry of Land, Infrastructure and Transport of Korean Government; the BK21 FOUR (Fostering Outstanding Universities for Research) Project in 2022 (No. 4120200113771); and National Research Foundation of

Korea (NRF) grants funded by the Korea government (MSIT) (No. NRF-2022R1A4A3026883). The authors are grateful to the authorities for their support.

REFERENCES

1. Mo, K. H.; Alengaram, U. J.; and Jumaat, M. Z., "Structural Performance of Reinforced Geopolymer Concrete Members: A Review," *Construction and Building Materials*, V. 120, May 2016, pp. 251-264. doi: 10.1016/j.conbuildmat.2016.05.088

2. Vashistha, P.; Park, S.; and Pyo, S., "A Review on Sustainable Fabrication of Futuristic Cementitious Binders based on Application of Waste Concrete Powder, Steel Slags, and Coal Bottom Ash," *International Journal of Concrete Structures and Materials*, V. 16, No. 1, 2022, pp. 1-28. doi: 10.1186/s40069-022-00541-9

3. Bakhoum, E. S., and Mater, Y. M., "Decision Analysis for the Influence of Incorporating Waste Materials on Green Concrete Properties," *International Journal of Concrete Structures and Materials*, V. 16, No. 1, 2022, pp. 1-16. doi: 10.1186/s40069-022-00553-5

4. Aldred, J., and Day, J., "Is Geopolymer Concrete a Suitable Alternative to Traditional Concrete?" *Proceedings of the 37th Conference on Our World in Concrete & Structures*, Singapore, Aug. 2012, pp. 29-31.

5. Srividya, T.; PR, K. R.; Sivasakthi, M.; Sujitha, A.; and Jeyalakshmi, R., "A State-of-the-Art on Development of Geopolymer Concrete and Its Field Applications," *Case Studies in Construction Materials*, V. 16, June 2022, p. e00812.

6. Ma, C. K.; Awang, A. Z.; and Omar, W., "Structural and Material Performance of Geopolymer Concrete: A Review," *Construction and Building Materials*, V. 186, Oct. 2018, pp. 90-102. doi: 10.1016/j.conbuildmat.2018.07.111

7. Amran, Y. M.; Alyousef, R.; Alabduljabbar, H.; and El-Zeadani, M., "Clean Production and Properties of Geopolymer Concrete; A Review," *Journal of Cleaner Production*, V. 251, Apr. 2020, p. 119679. doi: 10.1016/j.jclepro.2019.119679

8. Patil, A. A.; Chore, H.; and Dodeb, P., "Effect of Curing Condition on Strength of Geopolymer Concrete," *Advances in Concrete Construction*, V. 2, No. 1, 2014, pp. 29-37. doi: 10.12989/acc.2014.2.1.029

9. Du, Y.; Wang, J.; Shi, C.; Hwang, H. J.; and Li, N., "Flexural Behavior of Alkali-Activated Slag-based Concrete Beams," *Engineering Structures*, V. 229, Feb. 2021, p. 111644. doi: 10.1016/j.engstruct.2020.111644

10. Shibayama, A., and Nishiyama, M., "Flexural Strength and Load−Deformation Relationship of Fly-Ash Based Geopolymer Concrete Beams," *Japan Architectural Review*, V. 6, No. 1, 2023, p. e12331. doi: 10.1002/2475-8876.12331

11. Alex, A. G.; Gebrehiwet Tewele, T.; Kemal, Z.; and Subramanian, R. B., "Flexural Behavior of Low Calcium Fly Ash Based Geopolymer Reinforced Concrete Beam," *International Journal of Concrete Structures and Materials*, V. 16, No. 1, 2022, p. 40. doi: 10.1186/s40069-022-00531-x

12. Wu, C.; Hwang, H. J.; Shi, C.; Li, N.; and Du, Y., "Shear Tests on Reinforced Slag-Based Geopolymer Concrete Beams with Transverse Reinforcement," *Engineering Structures*, V. 219, Sept. 2020, p. 110966. doi: 10.1016/j.engstruct.2020.110966

13. Saranya, P.; Nagarajan, P.; and Shashikala, A. P., "Behaviour of GGBS-Dolomite Geopolymer Concrete Short Column Under Axial Loading," *Journal of Building Engineering*, V. 30, July 2020, p. 101232. doi: 10.1016/j.jobe.2020.101232

14. Ganesan, N.; Indira, P. V.; and Santhakumar, A., "Prediction of Ultimate Strength of Reinforced Geopolymer Concrete Wall Panels in One-Way Action," *Construction and Building Materials*, V. 48, Nov, 2013, pp. 91-97. doi: 10.1016/j.conbuildmat.2013.06.090

15. Cárdenas-Pulido, J.; Reyes, J. C.; Carrillo, J.; and Ramírez, F., "Shear Behavior of Geopolymer Concrete Panels Under Diagonal Tensile Stresses," *Engineering Structures*, V. 212, June 2020, p. 110518. doi: 10.1016/j.engstruct.2020.110518

16. Huang, J. Q.; Kumar, S.; and Dai, J. G., "Flexural Performance of Steel-Reinforced Geopolymer Concrete One-Way Slabs: Experimental and Numerical Investigations," *Construction and Building Materials*, V. 366, Feb. 2023, p. 130098. doi: 10.1016/j.conbuildmat.2022.130098

17. Mohmmad, S. H.; Gülşan, M. E.; and Çevik, A., "Punching Shear Behaviour of Geopolymer Concrete Two-Way Slabs Reinforced by FRP Bars Under Monotonic and Cyclic Loadings," *Advances in Structural Engineering*, V. 25, No. 3, 2022, pp. 453-472. doi: 10.1177/13694332211052349

18. Chen, C.; Zhang, X.; and Hao, H., "Investigation on The Impact Resistance of Reinforced Geopolymer Concrete Slab," *Journal of Cleaner Production*, V. 406, June 2023, p. 137144. doi: 10.1016/j.jclepro.2023.137144

19. Zhang, H. Y.; Kodur, V.; Wu, B.; Yan, J.; and Yuan, Z. S., "Effect of Temperature on Bond Characteristics of Geopolymer Concrete," *Construction and Building Materials*, V. 163, Feb. 2018, pp. 277-285. doi: 10.1016/j.conbuildmat.2017.12.043

20. Mao, Y.; Hwang, H. J.; Du, Y.; Su, J.; Hu, X.; Liu, Y.; and Shi, C., "Bond and Anchorage Performance of Beam Flexural Bars on Beam−Column Joints Using Slag-based Geopolymer Concrete and Their Effect on Seismic Performance," *Engineering Structures*, V. 273, Dec. 2022, p. 115062. doi: 10.1016/j.engstruct.2022.115062

21. Mao, Y.; Du, Y.; Hwang, H. J.; Su, J.; Hu, X.; Liu, Y.; and Shi, C., "Seismic Performance of Interior Beam−Column Joints Using Reinforced Slag-Based Geopolymer Concrete," *Earthquake Engineering & Structural Dynamics*, V. 52, No. 2, 2023, pp. 285-307. doi: 10.1002/eqe.3760

22. Ngo, T. T.; Tran, T. T.; Pham, T. M.; and Hao, H., "Performance of Geopolymer Concrete in Monolithic and Non-Corrosive Dry Joints Using CFRP Bolts Under Cyclic Loading," *Composite Structures*, V. 258, Feb. 2021, p. 113394. doi: 10.1016/j.compstruct.2020.113394

23. Saranya, P.; Nagarajan, P.; and Shashikala, A. P., "Seismic Performance of Geopolymer Concrete Beam−Column Joints Under Reverse Cyclic Loading," *Innovative Infrastructure Solutions*, V. 6, No. 2, June 2021, pp. 1-10. doi: 10.1007/s41062-021-00474-4

24. Haber, Z. B.; Saiidi, M. S.; and Sanders, D. H., "Seismic Performance of Precast Columns with Mechanically Spliced Column−Footing Connections," *ACI Structural Journal*, V. 111, No. 3, May-June 2014, pp. 639-650. doi: 10.14359/51686624

25. Ameli, M.; Parks, J. E.; Brown, D. N.; and Pantelides, C. P., "Seismic Evaluation of Grouted Splice Sleeve Connections for Reinforced Precast Concrete Column-To-Cap Beam Joints in Accelerated Bridge Construction," *PCI Journal*, V. 60, No. 2, 2015, pp. 80-103. doi: 10.15554/pcij.03012015.80.103

26. Ameli, M. J.; Brown, D. N.; Parks, J. E.; and Pantelides, C. P., "Seismic Column-to-Footing Connections Using Grouted Splice Sleeves," *ACI Structural Journal*, V. 113, No. 5, Sept.-Oct. 2016, pp. 1021-1030. doi: 10.14359/51688755

27. Qu, H.; Fu, J.; Li, T.; Wu, C.; Sun, X.; Wei, H.; and Wang, Z., "Experimental and Numerical Assessment of Precast Bridge Columns with Different Grouted Splice Sleeve Coupler Designs Based on Shake Table Test," *Journal of Bridge Engineering*, ASCE, V. 26, No. 8, 2021, p. 04021055. doi: 10.1061/(ASCE)BE.1943-5592.0001748

28. Xin, G.; Xu, W.; Wang, J.; Yan, X.; Chen, Y.; Yan, W.; and Li, J., "Seismic Performance of Fabricated Concrete Piers with Grouted Sleeve Joints and Bearing-Capacity Estimation Method," *Structures*, V. 33, Apr. 2021, pp. 169-186. doi: 10.1016/j.istruc.2021.04.047

29. Xiao, S.; Wang, Z.; Li, X.; Harries, K. A.; Xu, Q.; and Gao, R., "Study of Effects of Sleeve Grouting Defects on the Seismic Performance of Precast Concrete Shear Walls," *Engineering Structures*, V. 236, June 2021, p. 111833. doi: 10.1016/j.engstruct.2020.111833

30. Xie, L.; Wang, X.; Zhong, B.; Yang, C.; Chen, X.; Miao, Q.; and Liu, Q., "Full-Scale Experimental Investigation on the Seismic Performance of PC Columns Before and After Repair of Grouting Defects," *Journal of Building Engineering*, V. 58, Oct. 2022, p. 104996. doi: 10.1016/j.jobe.2022.104996

31. ACI Committee 374, "Acceptance Criteria for Moment Frames Based on Structural Testing and Commentary (ACI 374.1-05)," American Concrete Institute, Farmington Hills, MI, 2005, 9 pp.

32. AIJ, "Guidelines for the Design of Structural Precast Concrete Emulating Cast-in-Place Reinforced Concrete (AIJ Guidelines)," Architectural Institute of Japan, Tokyo, Japan, 2002.

33. Korean Standards Information Center, "Hydraulic-Cement Grout (Nonshrink) (KS F 4044)," Chungcheongbuk-do, Republic of Korea, 2019.

34. Park, R., "Evaluation of Ductility of Structures and Structural Assemblages from Laboratory Testing," *Bulletin of the New Zealand Society for Earthquake Engineering*, V. 22, No. 3, 1989, pp. 155-166. doi: 10.5459/bnzsee.22.3.155-166

35. Joint ACI-ASCE Committee 352, "Recommendations for Design of Beam-Column Connections in Monolithic Reinforced Concrete Structures (ACI 352R-02)," American Concrete Institute, Farmington Hills, MI, 2002, 38 pp.

36. ACI Committee 318, "Building Code Requirements for Structural Concrete (ACI 318-19) and Commentary (ACI 318R-19) (Reapproved 2022)," Farmington Hills, MI, American Concrete Institute, 2019, 624 pp.

ACI in Your Classroom

Integrate ACI into your classroom!

To support future leaders, ACI has launched several initiatives to engage students in the Institute's activities and programs – select programs that may be of interest to Educators are:

- **Free student membership –** encourage students to sign up
- **Special student discounts on *ACI 318 Building Code Requirements for Structural Concrete*, *ACI 530 Building Code Requirements and Specification for Masonry Structure*, & *Formwork for Concrete* manual.**
- **Access to *Concrete International* –** free to all ACI student members
- **Access to *ACI Structural Journal* and *ACI Materials Journal* –** free to all ACI student members
- **Free sustainability resources –** free copies of Sustainable Concrete Guides provided to universities for use in the classroom
- **Student competitions –** participate in ACI's written and/or team-based competitions
- **Scholarships and fellowships –** students who win awards are provided up to $15,000 and may be offered internships and paid travel to attend ACI's conventions
- **ACI Award for University Student Activities –** receive local and international recognition for your University's participation in concrete-related activities
- **Free access to the *ACI Collection of Concrete Codes, Specifications, and Practices* –** in conjunction with ACI's chapters, students are provided free access to the online ACI Collection
- **ACI online recorded web sessions and continuing education programs –** online learning tools ideal for use as quizzes or in-class study material

https://www.concrete.org/educatorsandresearchers/aciinyourclassroom.aspx

ACI STRUCTURAL JOURNAL TECHNICAL PAPER

Title No. 122-S69

Structural Assessment of Cracked Concrete Members by Digital Image Random Nonlinear Finite Element

by Abdalla Elhadi Alhashmi and Fadi Oudah

This paper presents a novel framework of analysis to assess the resistance of existing reinforced concrete (RC) members experiencing spatial variability of crack patterns and spatial variability of concrete mechanical properties. The spatial variabilities are considered by using digital image processing (DIP) to map crack patterns onto three-dimensional (3-D) nonlinear finite element (NFE) models, where the concrete mechanical properties (compressive strength, tensile strength, damage, and modulus of elasticity) are spatially varied using random fields (RFs) to form random NFE (RNFE) models. The framework was developed and applied to assess a corroded RC beam (to determine the distribution of the resistance) and column (to determine the reliability of the column at the ultimate limit state [ULS]). Research findings indicate improved accuracy in assessing the resistance of the corroded members up to 20%, and the adaptivity of the developed framework for performing reliability analysis of existing RC structures.

Keywords: digital image processing (DIP); random finite element (RFE) method; reinforced concrete (RC); structural assessment; structural degradation.

INTRODUCTION

Practicing engineers often use simplified methods of analysis to assess the safety of existing reinforced concrete (RC) structures subjected to active deterioration, which may yield unnecessary repairs or overlook possible failure modes. These methods are fundamentally based on evaluating the limit state of interest (flexure, shear, and so on) using simplified capacity calculations that do not account for the spatial variation in the member's inherent mechanical properties (for example, strength and stiffness) and degradation (for example, corrosion and cracking).[1,2] The deterioration effect on the structural resistance is typically considered deterministically, in practice, by uniformly reducing the cross-sectional area of the corroded steel or conservatively using a reduced concrete compressive strength due to cracking based on limited field tests (destructive or nondestructive). The calculated structural resistance is subsequently used to calculate the demand-to-capacity ratio and compare it with a ratio of unity to determine the need for repair. The prescribed approach may not yield an accurate assessment of existing structures because it overlooks the spatial variation in the structural resistance (that is, variation in the member capacity along its geometric dimensions) caused by the spatial variation in material mechanical properties (material variability) and the spatial variability in degradation mechanisms, such as corrosion, cracking, and alkali-silica reactivity (geometric variability).

Random fields (RFs) have gained significant attention in recent years due to their ability to replicate potential patterns of material property fluctuations[3] using various discretization techniques, such as the midpoint method,[4] weighted integral method,[5] orthogonal series expansion (OSE),[6] Karhunen-Loève (KL) expansion,[7] and expansion optimal linear estimation (EOLE).[8,9] RFs were employed in the literature to model complex concrete structures by combining material variability with linear-elastic and nonlinear finite element (NFE) analysis in one-dimensional (1-D),[10] two-dimensional (2-D),[11-14] and three-dimensional (3-D) domains.[14-16]

For geometric variability, numerous research studies have analyzed the effect of degradation (that is, corrosion) on the ultimate resistance of concrete structures in reliability assessment frameworks that use random NFE (RNFE) analysis.[17-21] These studies focused on the mechanical and geometrical variability of reinforcing bars and neglected geometrical changes in the concrete medium (that is, cracks). Existing literature on concrete cracks and damage mostly focuses on the micromechanical examination of heterogeneous and inhomogeneous materials.[22-32] Research integrated the use of laser scanning with 3-D point cloud data to transform damaged real physical objects to 3-D FE models[33,34] and used computer vision techniques such as digital image processing (DIP) to acquire the crack dimensions to update the existing FE model. Zhang and Lin[35] developed an automated methodology to update the FE mesh for steel structures with fatigue cracks using computer vision techniques. The computer vision techniques were employed to determine the shapes and dimensions of both structural components and damages. Geometric analyses were used to automate the deletion, generation, and splitting of components of shell elements in the FE models. Review of DIP-related research indicates the lack of work related to mapping cracks in RC members at the macroscale (as opposed to concrete microcracks). No research up to date has integrated both material and geometric variability (that is, crack patterns) to assess the reliability of RC structures in 3-D.

This paper proposes a novel framework of analysis to consider the spatial variability of material mechanical properties and crack patterns of existing RC structures by

ACI Structural Journal, V. 122, No. 5, September 2025.

MS No. S-2024-008.R2, doi: 10.14359/51746792, received September 20, 2024, and reviewed under Institute publication policies. Copyright © 2025, American Concrete Institute. All rights reserved, including the making of copies unless permission is obtained from the copyright proprietors. Pertinent discussion including author's closure, if any, will be published ten months from this journal's date if the discussion is received within four months of the paper's print publication.

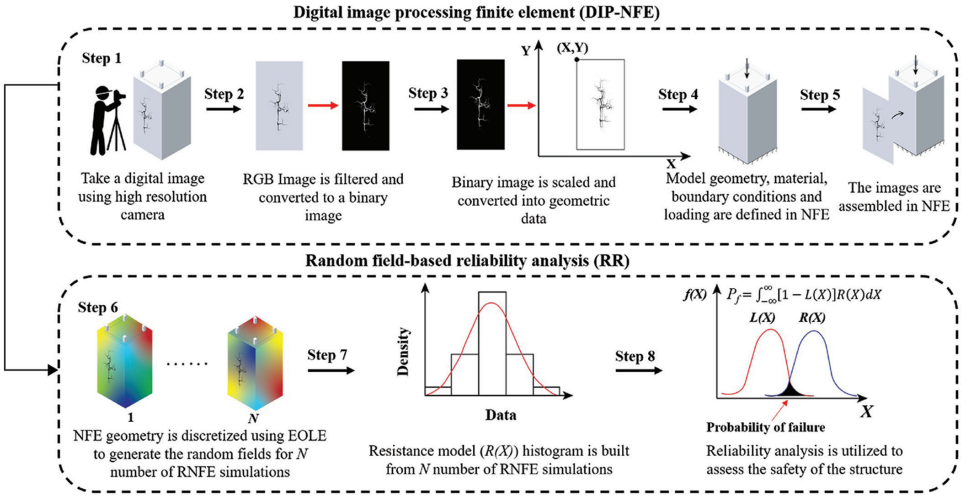


Fig. 1—General framework of DIP-FE-RR.

integrating DIP with RFs to perform 3-D RNFE analysis. The functionality of the proposed framework is validated against two practical examples of corroded RC members, where the developed DIP-RNFE framework is applied to determine the resistance distribution due to the spatial variability in cracks and concrete mechanical properties.

RESEARCH SIGNIFICANCE

This research presents a novel framework of analysis for assessing the safety of RC structures by integrating DIP and RNFE. It addresses current code limitations by considering the spatial material and geometrical variabilities in the structural assessment. Real-life images are used to develop NFE models, while RFs depict material property variations. The proposed approach enhances reliability estimation by reducing uncertainties in concrete crack patterns and steel corrosion processes. It aids engineers in making informed decisions about retrofitting or replacing structural members, often based on subjective or limited assessments.

DESCRIPTION OF PROPOSED FRAMEWORK OF ANALYSIS (DIP-RNFE)

Overview

The general framework of analysis for DIP-RNFE is illustrated in Fig. 1. The general procedure of the proposed framework is reviewed herein, while details are included in the subsequent sections. The proposed framework integrates three analyses: DIP, RNFE, and reliability estimation. For DIP, the digital image of the assessed structure is processed, filtered, and scaled using the MATLAB Image Processing Toolbox[36] and DigiSim software[37] to be transferred to FE software as geometric data. The direct use of digital images in numerical simulations such as FE is not feasible. Because FE models are often constructed based on geometric data, three main image formats exist, each representing a rectangular matrix of image pixels, including colored images, grayscale images, and binary images. In colored images, each pixel is denoted by three integer values ranging from 0 to 255, whereas grayscale images use a single integer value to represent each pixel. Finally, for a binary image, the integer value is restricted to either 0 or 1 (refer to the section "Digital image processing (DIP)").

The image is then assembled into an NFE software depending on the user's needs; for this research, the commercial software ABAQUS[38] was used. From there, the appropriate constitutive models, boundary conditions, and mesh density are defined. To account for the spatial variation in the mechanical properties (concrete strength, stiffness, and reinforcing bar cross-sectional loss due to corrosion), the structure was discretized using the EOLE method to form an RNFE mesh (refer to the "Random nonlinear finite element (RNFE)" section for details). N number of RNFE simulations of the DIP-generated model are generated (each with a different pattern of spatial variation of the material mechanical properties) and performed to build a resistance frequency histogram. The generated histogram is used to determine the characteristics of the resistance model: mean, standard deviation, coefficient of variation (COV), and the type of distribution (normal, uniform, Weibull, lognormal, and so on) to perform reliability analysis using Monte Carlo simulation (MCS) for a given load model and limit state (refer to the "Application 2: Overview of computational framework" section).

Digital image processing (DIP)

The digital image of a structural element is converted from red, green, and blue (RGB, called true color) to a grayscale image using the MATLAB Image Processing Toolbox.[36] An image contrast enhancement technique (that is, histogram equalization) is applied to enhance the contrast between the crack pattern and the concrete background. In this method, the contrast of the image is increased. This allows the pixel's intensity values (T) of the gray-level image to be distributed so that the intensity values are equal among the brightness range. Moreover, the cracks from the concrete background are separated, and the grayscale image is converted to a binary image. A binary image is represented by an X × Y logical matrix, where pixel values are 1 (black) or 0 (white). An image thresholding using Otsu's method is then employed.[26] If the threshold limit is larger than T, the value in the binary matrix will change to 0 (cracks). Otherwise,

it will be 1 (concrete). Local graph cut is used to select the needed parts in the image using regions of interest (ROIs). The image segmentation process is then refined using image morphology. The crack pattern in the image is adjusted by using a specific structural element (that is, a circle, diamond, or line) to connect any crack discontinuities and accommodate the user's needs. The image is further refined and filtered using image region thresholding.[27] The purpose of this step is to filter out all noise in the image by calculating the actual area of each white area. The threshold area eliminates all small white areas and keeps the larger ones in the binary image matrix. Figure 2 summarizes the conversion procedure of the digital image to a binary image. The approach employed for DIP herein may differ across users, contingent upon the specific problem being examined and the quality of the image being analyzed. Finally, the segmented binary image is mapped to ABAQUS[38] using DigiSim software.[37]

DigiSim[37] is a digital-image-based numerical simulation tool developed to study the microstructure features of digital images obtained by advanced digital cameras. It consists of three parts: bitmap vectorization, geometric statistics computation, and numerical model generation. Bitmap vectorization, often referred to as raster-to-vector conversion, is a DIP methodology employed to transform bitmap pictures, also known as raster, into vector graphics. Bitmap pictures consist of individual pixels, each containing a specific color value, and are particularly well-suited for displaying complex and visually appealing visuals, such as images. Nevertheless, the quality of the images diminishes as their size is reduced or scaled. On the other hand, vector graphics comprise pathways that are determined by mathematical equations, enabling them to be scaled indefinitely without any decrease in quality. The process of vectorization entails the conversion of a pixel-based picture into a geometric representation, wherein individual pixels are substituted with shapes, lines, and curves.

The binary image is read first and saved as a matrix; concrete parts have pixel values of 1, while other parts have a value of 0 (cracks). A boundary refinement algorithm is implemented to make the boundary polygon smoother with fewer points. Geometry scaling is applied to obtain the real size using a zoom factor. After vectorization of the digital image, geometric information (including the area, minimum bounding rectangle [MBR], and direction of axis) is calculated, and statistical analysis is performed. Geometric information is output in the "DXF" format in AutoCAD. Scripts for creating FE meshes with the help of Gmsh or ABAQUS[38] are then generated.

Random nonlinear finite element (RNFE)

To account for the inherent uncertainty in the spatial distribution of strength properties in materials such as concrete, it is necessary to incorporate RFs into the simulation process. This is due to the heterogeneous nature of concrete as a material. Sudret and Der Kiureghian[8] conducted research to evaluate the accuracy of three approaches, namely EOLE, KL, and OSE, in representing the field. The study evaluated the mean error of these methods and found that the EOLE and KL methods exhibited superior accuracy in field representation compared to the OSE method. The study found a minimal mean error between KL and EOLE. Therefore, the EOLE approach was used in this study.

The first step in generating RFs involves creating a virtual mesh of the structural geometry. The RF mesh density must be equal to or less than the conventional FE mesh. Let M_{RF} represent an n-dimensional array containing all RF vectors. $M_{RF} = \{RF^{(1)}, RF^{(2)},\ldots RF^{(N_{mesh})}\}$, where N_{mesh} is the number of the discretized mesh points, and $RF^{(i)}$ is the i-th vector representing a point in 3-D space;

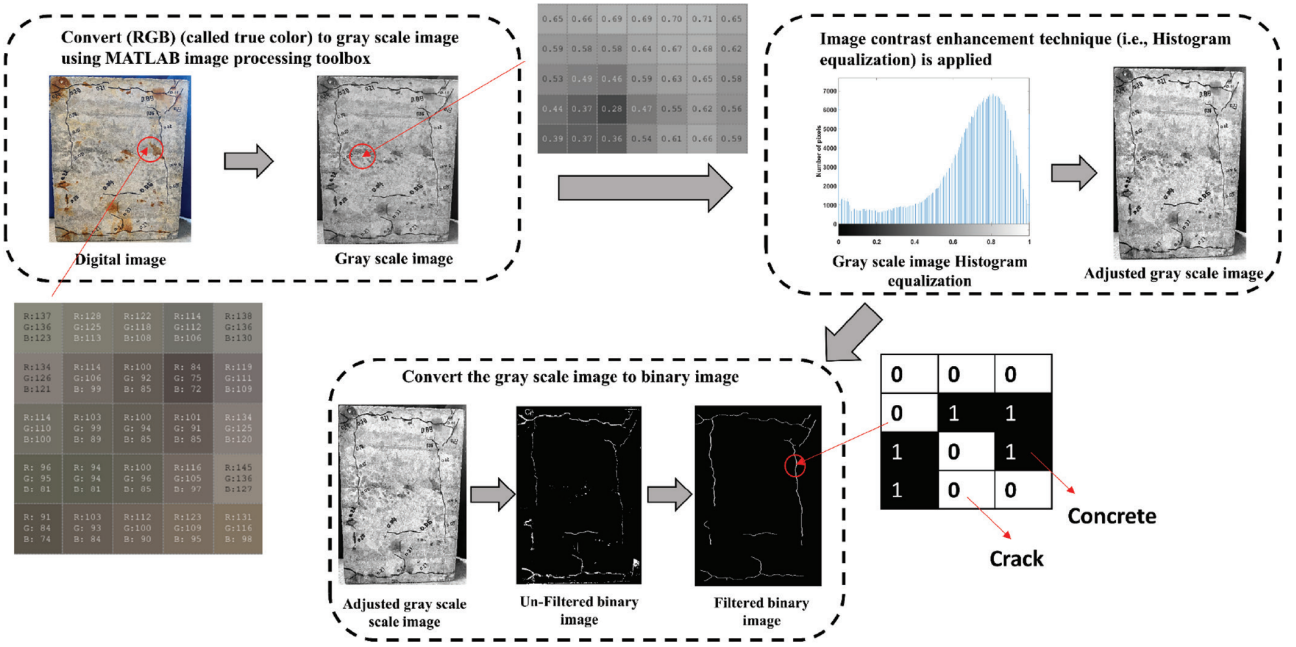


Fig. 2—Schematic illustrating DIP process employed in this research to transform digital image into binary image. (Note: Digital image adapted from Ma et al.[39])

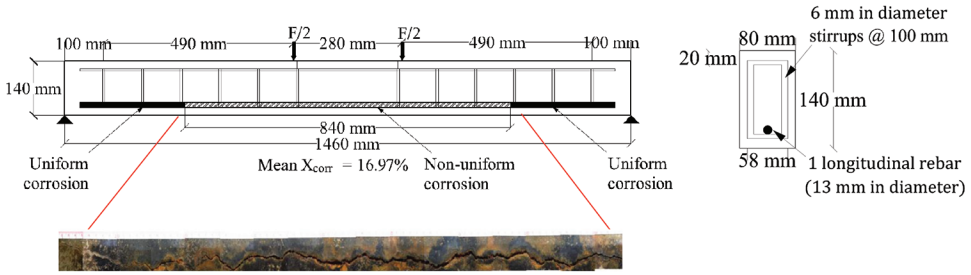


Fig. 3—Schematic illustration of experimental RC beam Lim et al.[20] used for this study: Application 1. (Note: 1 mm = 0.039 in.)

$RF^{(i)} = (X_{RF_i}, Y_{RF_i}, Z_{RF_i})$. The mean, standard deviation, and correlation matrix are assessed at the centroid of each point in the M_{RF} data set. Once the mean value has been calculated for each point in the mesh, the standard deviation is assessed by multiplying the mean by the COV of the field. Linear interpolation is a commonly employed technique in which the values and coordinates included in the M_{RF} are used to estimate the values of points that have unknown values in the real FE mesh. An automated MATLAB-Python code was developed to generate the input parameters required for the concrete properties for the RFE model. Stress-strain curves for tension and compression, and associated damage curves, were generated in MATLAB for specific nodes (that is, RF mesh) at the specified geometry (refer to the "DIP-NFE model development and verification" section). These nodes represent points in a predefined field that contains the RF. The predefined field contains material properties at a specific coordinate in a geometry, which is defined as an analytical field, which is independent of the FE mesh; ABAQUS[38] internally interpolates material properties assigned to the specified nodes to find corresponding material properties for a specific FE element based on its centroid.

A lognormal distribution is used to represent the correlation between points in space, using a Gaussian correlation function. The equation representing the covariance matrix in 3-D space is provided in Eq. (1)

$$C_{\hat{H}G}(i,j) = \sigma_i \sigma_j \rho_{ij};\ \rho_{ij} = \prod_{k=1}^{n} \exp\left\{-\frac{(X_{RFi} - X_{RFj})^2}{l_x^2} - \frac{(Y_{RFi} - Y_{RFj})^2}{l_y^2} - \frac{(Z_{RFi} - Z_{RFj})^2}{l_z^2}\right\} \quad (1)$$

where $C_{\hat{H}G}$ is the correlation matrix; σ_i and σ_j are the standard deviations; and ρ_{ij} is the correlation function between two consecutive points in space, $RF^{(i)}$ and $RF^{(j)}$. The terms l_x, l_y, and l_z represent the correlation lengths in the respective directions (that is, it measures the zone in which two points are correlated in space).

Petrie and Oudah[16] examined the influence of the correlation length (l_k) on the ultimate behavior of RC beams. l_k was found to have a minimal influence on the response of the concrete structure, and they recommended a value of 150 mm. A Nataf transformation[40-42] is required for the EOLE method, as presented in Eq. (2), to transform the lognormal correlation matrix to a Gaussian matrix because the EOLE method is based on a standard normal distribution.

$$\rho_{ij}' = x\rho_{ij} = \frac{\ln(1 + \rho_{ij} v_i v_j)}{\rho_{ij}\sqrt{\ln(1 + v_i^2)\ln(1 + v_j^2)}}\rho_{ij} \quad (2)$$

where ρ_{ij}' is the correlation for the standard normal field between two points, $RF^{(i)}$ and $RF^{(j)}$, in the RF mesh; x is a factor converting ρ_{ij} to ρ_{ij}' (that is, converting from lognormal to Gaussian); and v_i and v_j are the COV of the i-th and j-th point in the mesh, $RF^{(i)}$ and $RF^{(j)}$, respectively. After converting the field to a standard normal distribution, the realization of the specified random variables (that is, concrete strength) can be obtained using Eq. (3) and (4)

$$\hat{H}_G(RF^{(i)}, \theta) = \mu_{\ln y} + \sigma_{\ln y} \sum_{j=1}^{M} \frac{\xi_j}{\sqrt{\lambda_j}} \psi_j^T C_{\hat{H}G_j} \quad (3)$$

$$\mu_{\ln y} = \ln(\mu_y) - \frac{1}{2}\sigma_{\ln y}^2;\ \sigma_{\ln y} = \sqrt{\ln\left(1 + \frac{\sigma_y^2}{\mu_y^2}\right)} \quad (4)$$

where $\mu_{\ln y}$ is the mean of $\hat{H}_G$; $\sigma_{\ln y}$ is the standard deviation of $\hat{H}_G$; M is the considered number of eigenvalues of the covariance matrix; ξ_j is the j-th standard normal random variable; λ_j is the j-th eigenvalue; ψ_j^T is the j-th vector of the eigenvector matrix; and $C_{\hat{H}G_j}$ is the j-th vector of the correlation matrix (between all points in the RF mesh and the desired point Z).

The realizations of the field can be converted from normal to lognormal by applying Eq. (5)

$$\hat{H}_{LN}(RF^{(i)}, \theta) = \exp\{\hat{H}_G(RF^{(i)}, \theta)\} \quad (5)$$

where $\hat{H}_{LN}(RF^{(i)}, \theta)$ is the lognormal field value.

APPLICATION 1: CORRODED RC BEAM

Description

The developed DIP-RNFE framework was applied to build a resistance distribution of a corroded steel RC beam tested by Lim et al.[20] The beam details (ID II-1 in Lim et al.[20]) are schematically shown in Fig. 3. The beam was subjected to uniform and nonuniform corrosion by immersing it in an electrolytic solution to simulate an accelerated corrosion process on the longitudinal reinforcing bar. The spatial weight reduction of steel over the length of a reinforcing bar was determined using X-ray and DIP techniques. The mean weight reduction in the nonuniform corrosion region

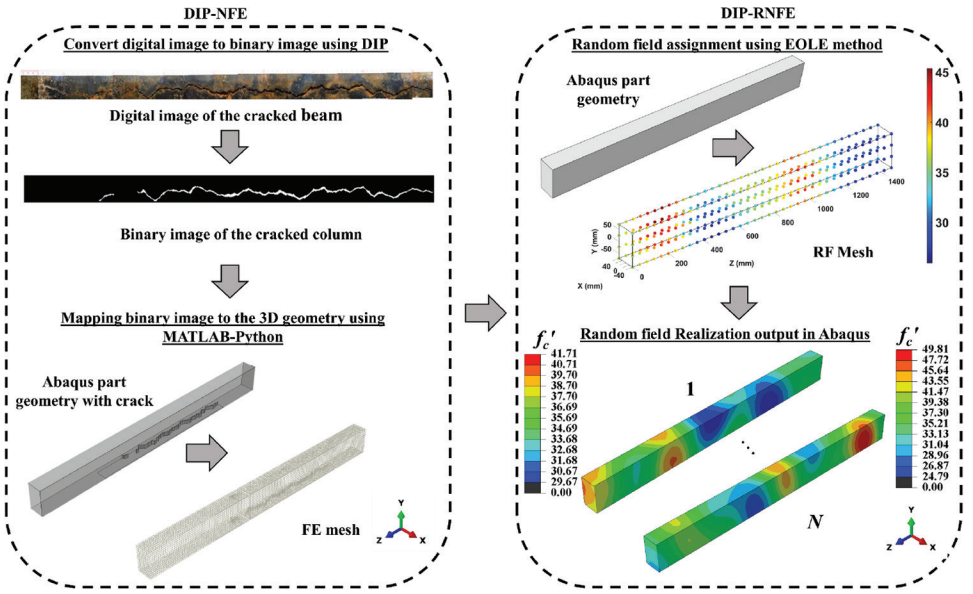


Fig. 4—Schematic presenting holistic overview of computational framework of analysis: Application 1.

(X_{corr}) was 16.97%. A longitudinal corrosion-induced crack was formed, running parallel to the flexural reinforcement, as shown in Fig. 3. The beam was tested monotonically in a four-point bending setting to determine the effect of corrosion on the ultimate resistance. The methodology of applying the DIP-RNFE framework and the analysis results of the resistance distribution are described in the following section. First, the development and validation of the DIP-NFE is presented, followed by augmenting it with RFs to build DIP-RNFE models. Finally, the distribution of the resistance is established.

Overview of computational framework

Figure 4 depicts the general steps to develop DIP-RNFE models of the examined beam using the developed framework. A base DIP-NFE model is developed and validated. Fifty unique 3-D RFs are then generated and applied to the base DIP-NFE model to generate 50 DIP-RNFE models. The DIP-RNFE models are loaded to failure, where the resistance at ultimate is extracted and used to generate a histogram, representing the distribution of beam resistance. The details about the development and validation of the DIP-NFE models and the analysis results of the DIP-RNFE models are presented in the following sections.

DIP-NFE model development and verification

Figure 5 presents the geometry, loading, and boundary conditions of the 3-D DIP-NFE model. Six-node linear triangular prism elements (C3D6) were used for the concrete volume. The steel cage (that is, longitudinal and transverse reinforcing bars) was modeled using beam elements. As presented in Fig. 5, the concrete crack was mapped to the beam geometry at the bottom of the beam using the methodology presented in the "Description of Proposed Framework of Analysis (DIP-RNFE)" section. The depth of the crack was considered to be equivalent to the concrete cover.

Figure 6 illustrates a comparison between the actual surface crack width obtained from the experiment and the

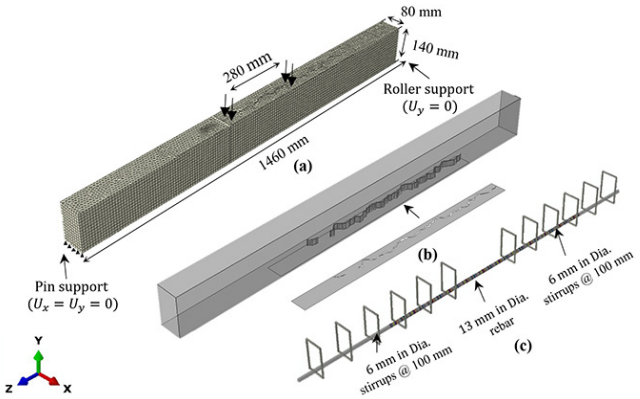


Fig. 5—FE model description: Application 1: (a) beam dimensions, support, and loading conditions; (b) beam with induced corrosion crack; and (c) reinforcement details. (Note: 1 mm = 0.039 in.)

DIP-NFE. The margin of error was quantified using the root mean square error (RMSE) expressed in Eq. (6). RMSE is used to assess the average magnitude of differences between expected (predicted) and observed (experimental) values. The obtained RMSE score of 0.515 mm suggests that the model's predictions exhibit an acceptable level of accuracy.

$$\text{RMSE} = \sqrt{\frac{1}{n}\sum_{i=1}^{n}(x_i - y_i)^2} \quad (6)$$

where n is the number of observations; x_i is the observed value; and y_i is the projected value.

The concrete was modeled using the concrete damage plasticity model (CDPM), while the steel reinforcement was modeled using a bilinear material model. The analytical models developed by the CEB-FIP Model Code 1990[43] and Cornelissen et al.[44] were used to generate the compression and tension stress-strain curves for the CDPM, respectively. Table 1 summarizes the material parameters used for the CDPM. The embedded region constraint was set to define

the host (concrete) and embedded regions (steel) in the model. Two deteriorating mechanisms were considered in the FE model: concrete cracks generated by corrosion, and steel corrosion.

The longitudinal reinforcing bar cross-sectional area and the steel-concrete bond strength were spatially reduced to account for the corrosion effect. The reduction in cross-sectional area was accounted for by assuming uniform and nonuniform corrosion regions (pitting corrosion). For the uniform corrosion region, the mean value of the cross-section reduction was used, X_{corr} = 16.97%. Figure 7 demonstrates the spatial variation in cross-sectional area throughout the length of the reinforcing bar for the nonuniform cross-sectional area.

Three methods exist in the literature for modeling the effect of corrosion on the steel-concrete bond-slip model in FE analysis: use of interface elements,[45] spring elements,[46] and simplified analytical models.[47-50] The former two methods are associated with computational inefficiencies and convergence issues.[48,49] The latter approach was proven to yield reliable results with efficient convergence and thus was used in this research. The constitutive model of steel reinforcement, including the modulus of elasticity, hardening modulus, and yield strength, was modified to account for the corrosion effect on the bond-slip relationship following the analytical models by Dehestani and Mousavi[50] and BaniAsad and Dehestani.[47] The model can be divided into two main components: the modified reinforcement model and the corrosion model. In the modified reinforcement model, the steel stiffness, E_s', and effective yield stress, $\hat{f}_y$, must be defined as presented in Eq. (7) to (12). Table 2 summarizes the material parameters used for the bilinear steel model.

Table 1—Material input parameters used for CDPM: Application 1

Concrete material parameters				
Compressive strength f_c', MPa (ksi)	Tensile strength f_t, MPa (ksi)	Young's modulus E_c, MPa (ksi)	Poisson's ratio v	
35 (5.1)	3.2 (0.464)	34,960 (5071)	0.2	
CDPM parameters				
Dilation angle Ψ, deg	Eccentricity ϵ	f_{b0}/f_{c0}*	K_c†	Viscosity μ
30	0.1	1.16	0.667	0.005

*f_{b0}/f_{c0} represents ratio of biaxial to uniaxial compressive strength; f_{b0} and f_{c0} are biaxial and uniaxial compressive yield strengths, respectively.

†K_c value represents ratio of deviatoric stress magnitudes in uniaxial tension and compression. It varies between 0.5, which corresponds to Rankine yield surface, and 1, which corresponds to von Mises yield surface.

$$\frac{\hat{f}_y}{f_y} = \left(0.93 - 2\frac{(f_{cr}/f_y)^{\frac{3}{2}}}{\rho_1}\right) \tag{7}$$

$$E_s' = \frac{\hat{f}_y}{\varepsilon_s + \left(\frac{\delta}{l}\right)} \tag{8}$$

$$\delta = \frac{0.7315 + K}{5.176 + 0.3333K} \tag{9}$$

$$K = \frac{c}{d_0} + 33\frac{A_{st}}{c \cdot s_{st}} \tag{10}$$

$$l = \frac{0.67}{2}s_{rm} \tag{11}$$

$$s_{rm} = \frac{2}{3}\frac{d_0 A_s}{3.6A_{c,Eff}} \tag{12}$$

where $\hat{f}_y$ is the modified embedded longitudinal reinforcing bar yield strength; f_y is the steel yield strength; ρ_1 is the longitudinal reinforcing bar reinforcement ratio; f_{cr} is the concrete tensile strength corresponding to a 0.00008 cracking strain, taken as $0.31\sqrt{f_c'}$ based on Belarbi and Hsu[51]; ε_s is the strain corresponding to the stress of the modified $\hat{f}_y$; l is the transmission length of the bond between the reinforcing bar and the surrounding concrete; K is a confinement factor (confinement by the concrete cover and the stirrups); δ is the peak

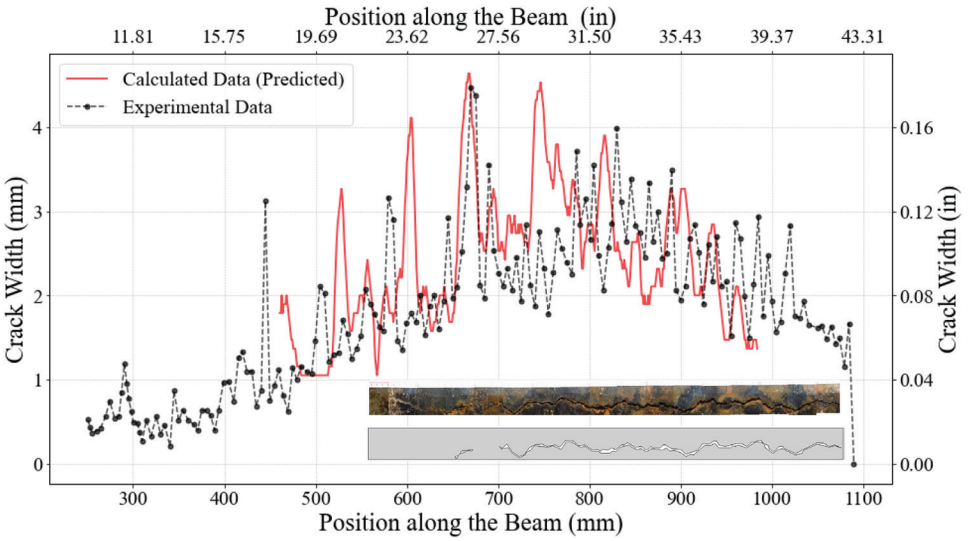


Fig. 6—Comparison between spatial variation of crack width in experimental test by Lim et al.[20] and FE model: Application 1.

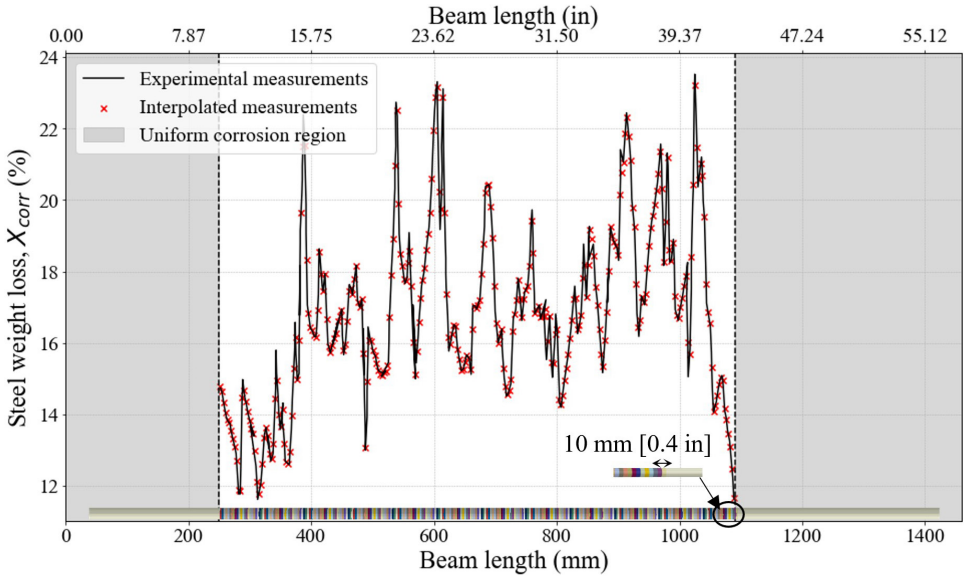


Fig. 7—Spatial variation in steel weight loss used in FE model depicted from Lim et al.[20]: Application 1.

Table 2—Steel properties used in FE model: Application 1

Steel material parameters	Longitudinal reinforcing bar	Stirrups
Young's modulus E_s, MPa (ksi)	200,000 (29,008)	200,000 (29,008)
Yield strength f_y, MPa (ksi)	345 (50)	345 (50)
Ultimate strength f_u, MPa (ksi)	490 (71)	490 (71)
Diameter d_0, mm (in.)	13 (0.512)	6 (0.236)
Modified yield strength $\hat{f}_y$, MPa (ksi)	303.52 (44)	—
Mean X_{corr}, %	16.97	—
Modified Young's modulus E_s', MPa (ksi)	44,113 (6398)	—
Modified yield strain ε_{sy}'	0.0069	—
Modified ultimate strain ε_{su}'	0.0931	—

slip at the maximum bond stress based on Wu and Zhao[48]; c is the concrete cover; d_0 is the reinforcing bar diameter; A_{st} is the area of one of the stirrup legs; s_{st} is the stirrups spacing; s_{rm} is the average spacing of flexural cracks according to the CEB-FIP Model Code 1990[43]; and $A_{c,Eff}$ is the effective cross-sectional area in tension.

In the corrosion model, it is assumed that the mechanical characteristics of the steel reinforcing bar undergo degradation as a result of pitting corrosion, as outlined in Eq. (13) and (14)

$$f_{sy}' = \frac{A_{sn}}{A_s}\hat{f}_y,\ A_{sn} = (1 - X_{Corr})A_s \tag{13}$$

$$\varepsilon_{sy}' = \frac{f_{sy}'}{E_s} \tag{14}$$

where f_{sy}' is the degraded yield strength of the reinforcing bar due to corrosion; A_s is the steel area of the non-corroded reinforcing bar; A_{sn} is the reduced steel area of the corroded reinforcing bar; X_{Corr} is the percentage mass or area loss of the steel due to corrosion; and ε_{sy}' is the yield strain of the corroded reinforcing bar. To account for reinforcing bar ductility, the ultimate strain of the corroded reinforcing bar, ε_{su}', must also be modified through Eq. (15)

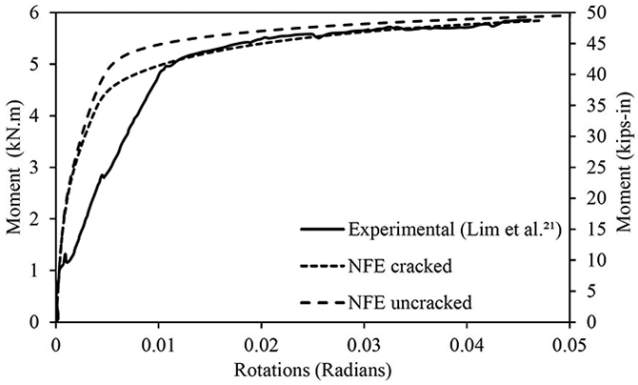


Fig. 8—Moment-rotation response comparison between NFE model and experimental results from Lim et al.[20]: Application 1.

$$\varepsilon_{su}' = (1 - 0.05X_{Corr})\varepsilon_{su} \tag{15}$$

The DIP-NFE modeling technique was validated against the experimental test by Lim et al.[20] and compared to ACI 318-19[1] and CSA A23.3:24.[2] Figure 8 presents a moment-rotation response comparison between the experimental results and damage scenarios (cracked and uncracked) using DIP-NFE. The failure was defined as the occurrence of either concrete crushing, denoted as M_{cu}, or steel yielding, denoted as M_u. The failure was defined to be the 0.0035 strain limit, as stipulated by the CSA A23.3,[2] for the concrete crushing, and 0.001725 for reinforcement yielding. Table 3 presents a capacity comparison between the NFE model and the experimental results at the ultimate loads (M_u and M_{cu}). The experimental results recorded the

Table 3—Capacity comparison between DIP-NFE model and experimental results conducted by Lim et al.[20] at ultimate loads: Application 1

Case	M_u, kN·m (kip·in.)	Percentage difference, %	M_{cu}, kN·m (kip·in.)	Percentage difference, %
Exp.	4.72 (41.77)	—	5.66 (50.09)	—
FE cracked	4.64 (41.06)	1.69	5.49 (48.59)	3.02
FE uncracked	5.08 (44.96)	7.08	5.57 (49.29)	1.61

moment capacity of the beam to be 4.72 kN·m (41.77 kip·in.) at reinforcement yielding and 5.66 kN·m (50.09 kip·in.) at concrete crushing. Comparison indicates that the NFE model with cracked concrete and corrosion is the most accurate for predicting the ultimate capacity of the corroded RC beam, which is governed by the corrosion effect as opposed to concrete cracking (that is, considering concrete cracking marginally affects the ultimate strength), which is expected for a bending member governed by flexure.

Figure 8 reveals a marginal discrepancy in the stiffness between the DIP-NFE models and the experimental results. This discrepancy in the stiffness is not expected to impact the reliability assessment because it is predominantly concerned with ultimate limit state (ULS). Moreover, both ACI 318-19[1] and the *fib* Model Code 2020[52] acknowledged the difficulties and uncertainties associated with NFE models.[53] To account for these uncertainties, RNFE models have been developed, as discussed in the next section.

For the Code calculations, the nominal moment capacity of the beam was found to be 4.48 kN·m (39.65 kip·in.) for the undamaged condition and 3.19 kN·m (28.23 kip·in.) for the damaged condition. The corrosion effect in the damaged section was determined by reducing the reinforcing bar's steel area by 16.97%, as reported by Lim et al.[20] The Code equation underestimates the experimental moment capacity of the damaged beam, showing an approximately 32% discrepancy compared to the experimental results.

DIP-RNFE models and analysis results

As opposed to DIP-NFE, DIP-RNFE models incorporate the inherent randomness and variability in the material properties (that is, RFs) and geometry (that is, cracks), leading to more accurate and reliable predictions. RFs were incorporated in the validated DIP-NFE model to model the spatial variability of material properties in concrete, namely E_c, f_c', f_t, and their associated damage parameters d_c and d_t (refer to the "Random nonlinear finite element (RNFE)" section). E_c, f_t, d_c, and d_t were assumed to be fully correlated to f_c', with a bias of 1.145, a COV of 0.05, and a lognormal distribution, as presented in Nowak and Szerszen.[54] The steel yield strength (f_y) was considered as a random variable with a bias of 1, a COV of 0.13, and a lognormal distribution.[55] Fifty DIP-RNFE models were generated, each with a unique set of spatial distribution of concrete properties and randomly generated steel yield strength. The models were loaded monotonically to failure, followed by extracting the ultimate resistance. Figure 9 shows the histogram of the ultimate resistance, fitted normal distribution, and the statistical

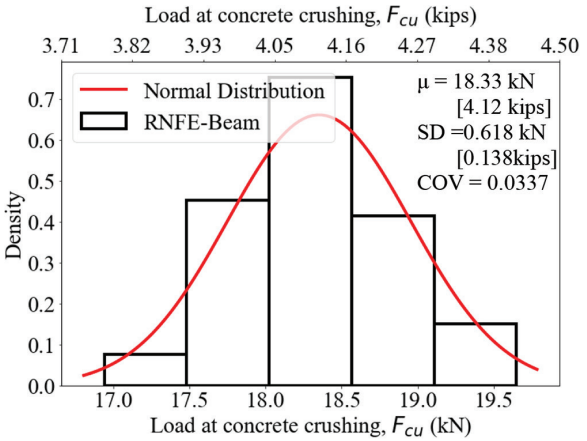


Fig. 9—Distribution of ultimate resistance of beam using DIP-RNFE: Application 1.

parameters. The COV of the fitted distribution is consistent with the findings of other studies of RC structures.[16]

APPLICATION 2: CORRODED RC COLUMN

Description

The developed DIP-RNFE framework was applied to assess the reliability of a corroded steel RC column tested by Ma et al.[39] for a prescribed range of applied dead loads (DLs) and live loads (LLs) (Column ID A3-2 in Ma et al.[39]). The corrosion of transverse reinforcements was simulated under controlled conditions by immersing test specimens in an electrochemical solution containing sodium chloride. The corrosion damage was observed to be uniform across stirrups, with a corrosion level of X_{corr} = 14%. To prevent concrete spalling resulting from corrosion expansion, the test specimens were enclosed by steel frames with a thickness of 5 mm (0.2 in.). Figure 10 illustrates the column dimensions and geometry used for this study.

Overview of computational framework

Figure 11 shows the general procedure to develop DIP-RNFE models of the examined column using the developed framework. A base DIP-NFE model was developed and validated. Fifty unique 3-D RFs were then generated and applied to the base DIP-NFE model to generate 50 DIP-RNFE models. Ultimate capacity was extracted to determine the distribution of the column resistance, $R_{FE}(X)$, to evaluate the structural safety at the ULS. The performance function, denoted as $G(X)$, corresponds to the difference between $R_{FE}(X)$ and the load model, denoted as $Q(X)$, as expressed in Eq. (16)

$$G(X) = m_f \cdot R_{FE}(X) - Q(X) < 0 \quad (16)$$

where m_f is a model factor that accounts for uncertainties or errors associated with calculations or the method of analysis; and X represents a vector consisting of random variables and fields that characterize the spatial variability in the FE model material properties.

The vector $Q(X)$ comprises three random variables that correspond to the moment or axial stress caused by the DL, the moment caused by the LL, and the transformation of

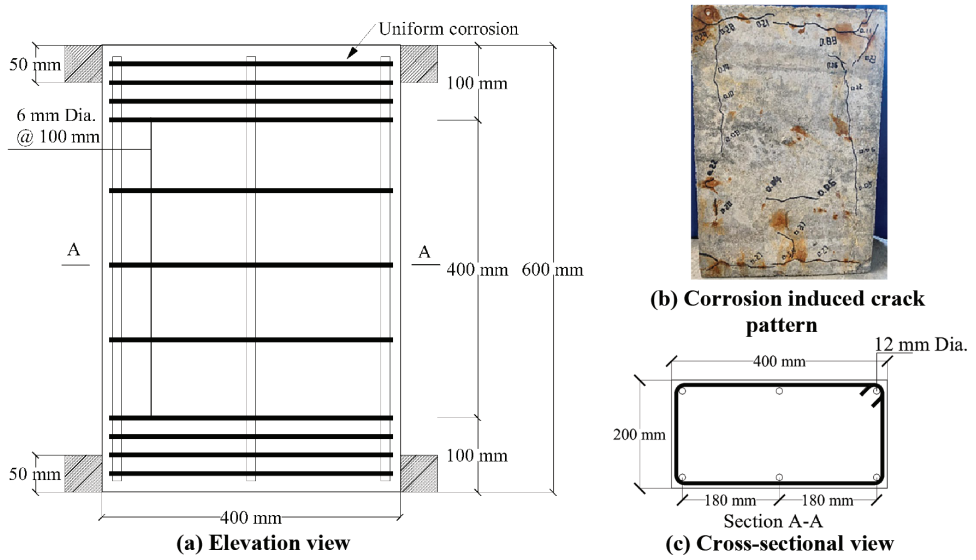


Fig. 10—Schematic illustration of experimental RC column tested by Ma et al.[39] used for this study: Application 2. (Note: 1 mm = 0.039 in.)

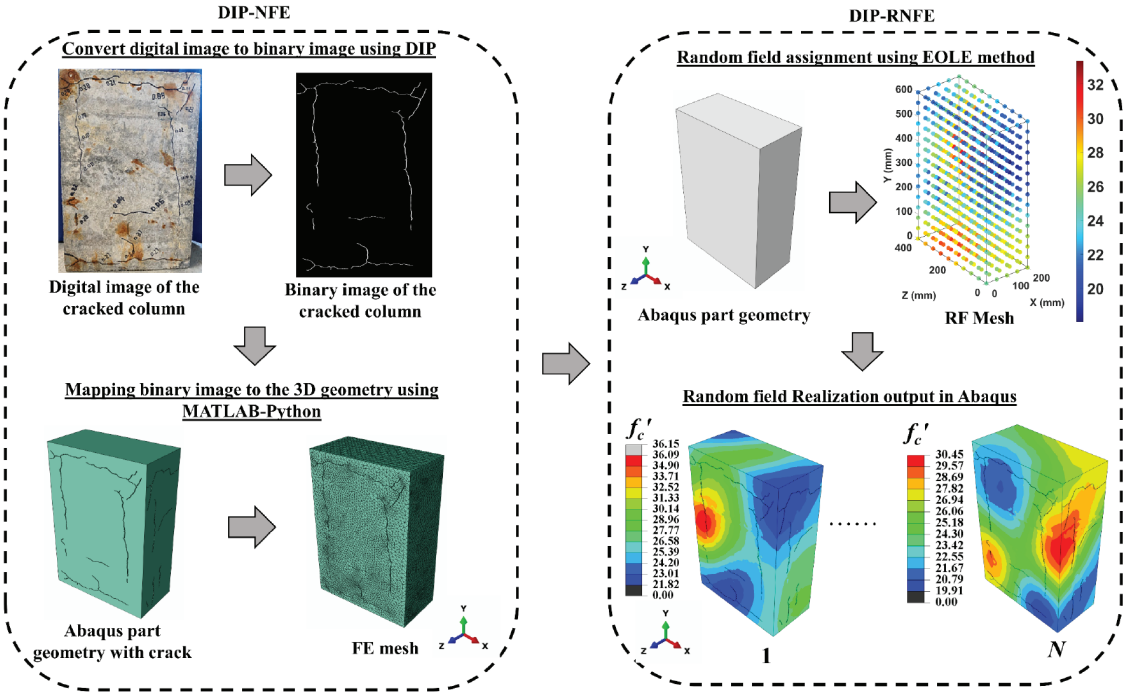


Fig. 11—Schematic presenting holistic overview of computational framework of analysis: Application 2.

the LL to the load effect (T2L). Table 4 shows the statistical parameters used for this study for the resistance model.

DIP-NFE model development and verification

The details of the DIP-NFE model, including geometry, boundary conditions, and loading, are shown in Fig. 12. The crack depth was equal to the thickness of the concrete cover. The concrete continuum was modeled using 10-node quadratic tetrahedral elements (C3D10) based on sensitivity analysis recommendations and due to the complex geometry of crack patterns, while the reinforcement was modeled using truss elements. Boundary conditions were implemented to effectively replicate the effect of the steel frame, as seen in Fig. 12(c). The CDPM was used to model the concrete material behavior using the confined concrete stress-stress material model by Mander et al.[58] The steel reinforcement was modeled using a linear-elastic perfectly plastic material model. The modulus of elasticity for concrete and steel was recorded as 24.96 GPa (3620 ksi) and 200 GPa (29,008 ksi), respectively. The Poisson's ratio for concrete and steel was 0.2 and 0.3, respectively. The concrete compressive and tensile strengths were 25 MPa (3.625 ksi) and 2.56 MPa (0.363 ksi), respectively. The steel yield strength was 460.8 MPa (66.83 ksi) for the longitudinal reinforcement and 325.8 MPa (47.25 ksi) for the transverse reinforcement. Uniform corrosion was applied on the transverse reinforcements by reducing the reinforcing bar cross-sectional area

Table 4—Summary of statistics and assumed variability used for resistance and load models: Application 2

Random variable	Bias	COV	Distribution	Reference
Resistance model				
f_y	1.145	0.05	Lognormal	Nowak and Szerszen[54]
f_c'	1	0.13	Lognormal	Bartlett[55]
m_f	1.10	0.12	Normal	Castaldo et al.[56]
Load model				
Dead load	1.05	0.1	Lognormal	Bartlett et al.[57]
Live load (50-year maximum load)	0.9	0.17	Gumbel	
Transformation to load effect	1	0.206	Normal	

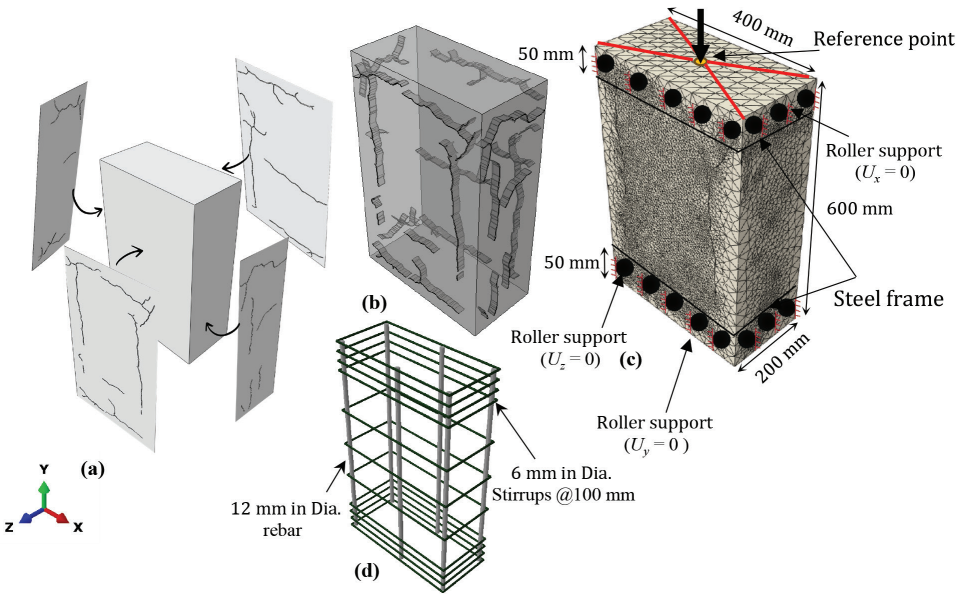


Fig. 12—FE model details: Application 2: (a) crack assembly on concrete block faces; (b) column with corrosion-induced cracks; (c) column dimensions, support, and loading conditions; and (d) reinforcement details. (Note: 1 mm = 0.039 in.)

uniformly (X_{corr} = 14%) and modifying the yield strength using Eq. (17), suggested by Vu et al.[59]

$$f_{yc} = (1 - \alpha_s X_{Corr}) f_y \quad (17)$$

where f_{yc} is the modified corroded steel yield strength; and α_s is the reduction factor, taken as 0.005.

Four variations of the DIP-NFE model were developed, loaded to failure, and compared with experimental test results, as included in Table 5. The variations include models with and without mapped corrosion-induced cracks and with and without steel corrosion. Comparison of the DIP-NFE models and the experimental test results indicates that the ultimate resistance of the column is governed by the corrosion-induced cracks and less by the reduction in the reinforcing bar cross-sectional area due to corrosion. This is evident in the approximately same percentage difference between models DIP-NFE-a and DIP-NFE-c. Also, mapping the cracks onto the NFE model was found to increase the accuracy in the ultimate resistance prediction by 22% by comparing the error associated with DIP-NFE-a and DIP-NFE-b. Therefore, the DIP-NFE analysis is validated.

DIP-RNFE models and analysis results

RFs were incorporated into the validated DIP-NFE-a model to form 50 DIP-RNFE models where the concrete properties were modeled to vary spatially within the column volume, and the steel yield strength was considered as a random variable. The distribution of the ultimate resistance of the 50 models is shown in Fig. 13 ($R_{FE}(X)$ in Eq. (16)). The reliability of the column was assessed at ULS following the performance function expressed in Eq. (16), the statistics (material variability parameters) included in Table 4, and the statistics of $R_{FE}(X)$ shown in Fig. 13. MCS was used to perform reliability analysis. The reliability analysis findings are depicted in Fig. 14. The 3-D surface plot is depicted as a mathematical function involving three variables: mean DL/R, mean LL/R, and target reliability index (β_T). Here, R represents the structural capacity. The plot can be used by practicing engineers to obtain the allowable LL based on a prescribed β_T.

CONCLUSIONS

A novel computational framework for the evaluation of existing reinforced concrete (RC) structures was developed

Table 5—Comparison between four variations of DIP-NFE models and test results from Ma et al.[39]: Application 2

	Exp	DIP-NFE-a	DIP-NFE-b	DIP-NFE-c	DIP-NFE-d
Corrosion	Yes	Yes	Yes	No	No
Cracked	Yes	Yes	No	Yes	No
Maximum stress σ_u, MPa (ksi)	26.5 (3.84)	31.6 (4.58)	37.6 (5.45)	31.7 (4.59)	37.9 (5.49)
Percentage error, %*	—	19.2	41.9	19.6	43.0

*With respect to Exp-C for corroded DIP-NFE models and Exp-NC for uncorroded DIP-NFE models.

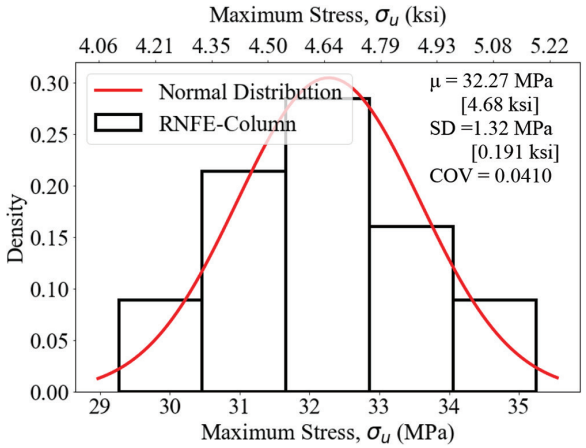


Fig. 13—Distribution of ultimate resistance of column using DIP-RNFE: Application 2.

in this research by integrating digital image processing (DIP) in generating random nonlinear finite element (RNFE) models. The framework is useful for determining the distribution of the resistance of existing structures experiencing considerable spatial variation in the concrete material properties and cracks due to structural or environmental effects (such as corrosion-induced cracks). The DIP method was used to convert RGB digital imagery into binary formats. Subsequently, binary matrix data were converted and integrated into nonlinear finite element (NFE) models as geometric information using MATLAB-Python scripts, where random fields (RFs) generated using the expansion optimal linear estimation (EOLE) were integrated into the analysis to generate DIP-RNFE models.

The developed framework was applied to assess a corroded RC beam and a column experiencing corrosion-induced cracks, as tested in the literature. DIP-NFE models were first developed and compared with the experimental tests to validate the DIP component of the developed framework, followed by integrating the models with RFs to generate 50 DIP-RNFE models, each with a unique set of spatial variation of concrete mechanical properties (compressive strength, tensile strength, modulus of elasticity, damage to compressive strength, and damage to tensile strength). Resistance distributions were generated to determine the mean and coefficient of variation (COV) of the examined members. To demonstrate the application of the framework in reliability analysis, the reliability of the corroded RC column was quantified using the resistance distribution for a range of live-to-dead load ratios. The research findings can be summarized as follows:

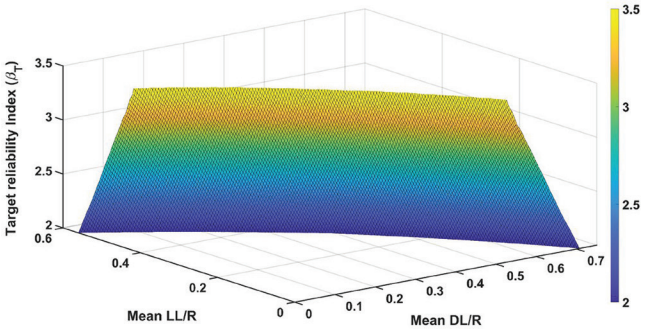


Fig. 14—Reliability analysis results of column using DIP-RNFE: Application 2.

- Mapping the corrosion-induced cracks from real-life images to the NFE models using DIP yielded improved accuracy up to 20% compared with NFE models without simulating the cracks.
- The resolution of the crack geometry in the DIP-NFE models was sensitive to the crack width quality of the image and the implemented DIP techniques. The use of machine learning techniques, such as convolutional neural networks (CNNs) or equivalent anomaly detection methods, can be used to improve the accuracy of crack mapping.
- The resistance distributions of the corroded RC beam and column yielded approximately the same COV (ranging from 3 to 4%). The range of COV was consistent with RNFE analysis of non-corroded beams found elsewhere in the literature.
- The integration of the framework with Monte Carlo simulation (MCS) in the corroded column analysis demonstrates the use of the framework for real-life reliability analysis of existing RC structures.

The developed framework does not encompass the analysis of residual stresses that may arise in loaded existing structural elements. The accuracy of the method can be further improved if the crack propagation is included in the underlying FE analysis method.

AUTHOR BIOS

ACI member **Abdalla Elhadi Alhashmi** *is a PhD Student in the Department of Civil and Resource Engineering at Dalhousie University, Halifax, NS, Canada, and a Mathematics of Information Technology and Complex Systems (MITACS) Intern at Norlander Oudah Engineering Ltd. (NOEL) in Calgary, AB, Canada. He received his BSc from United Arab Emirates University, Al Ain, UAE, and his MESc from the University of Western Ontario, London, ON, Canada, in 2016 and 2020, respectively. His research interests include proposing novel methods and tools for retrofitting existing reinforced concrete structures.*

ACI member **Fadi Oudah** *is an Associate Professor in the Department of Civil and Resource Engineering at Dalhousie University. He is a member of ACI Committee 215, Fatigue of Concrete, and ACI Subcommittee 440-J, FRP Stay-in-Place Forms. His research interests include assessment and retrofit of buildings and bridges using structural reliability, advanced composites, and smart materials.*

ACKNOWLEDGMENTS

The authors wish to acknowledge the financial contributions of Dalhousie University, the Mathematics of Information Technology and Complex Systems (MITACS) program, and Norlander Oudah Engineering Ltd. (NOEL).

REFERENCES

1. ACI Committee 318, "Building Code Requirements for Structural Concrete (ACI 318-19) and Commentary (ACI 318R-19) (Reapproved 2022)," American Concrete Institute, Farmington Hills, MI, 2019, 624 pp.

2. CSA A23.3:24, "Design of Concrete Structures," CSA Group, Toronto, ON, Canada, 2024, 342 pp.

3. Botte, W.; Vereecken, E.; and Caspeele, R., "Random Field Modelling of Spatial Variability in Concrete – A Review," *Structure and Infrastructure Engineering*, V. 21, No. 6, 2025, pp. 1047-1060.

4. Der Kiureghian, A., and Ke, J.-B., "The Stochastic Finite Element Method in Structural Reliability," *Probabilistic Engineering Mechanics*, V. 3, No. 2, June 1988, pp. 83-91.

5. Deodatis, G., "Weighted Integral Method. I: Stochastic Stiffness Matrix," *Journal of Engineering Mechanics*, ASCE, V. 117, No. 8, Aug. 1991, pp. 1851-1864. doi: 10.1061/(ASCE)0733-9399(1991)117:8(1851)

6. Zhang, J., and Ellingwood, B., "Orthogonal Series Expansions of Random Fields in Reliability Analysis," *Journal of Engineering Mechanics*, V. 120, No. 12, Dec. 1994, pp. 2660-2677. doi: 10.1061/(ASCE)0733-9399(1994)120:12(2660)

7. Spanos, P. D., and Ghanem, R., "Stochastic Finite Element Expansion for Random Media," *Journal of Engineering Mechanics*, ASCE, V. 115, No. 5, May 1989, pp. 1035-1053. doi: 10.1061/(ASCE)0733-9399(1989)115:5(1035)

8. Sudret, B., and Der Kiureghian, A., "Stochastic Finite Element Methods and Reliability: A State-of-the-Art Report," Report No. UCB/SEMM-2000/08, University of California, Berkeley, Berkeley, CA, Nov. 2000, 189 pp.

9. Li, C.-C., and Der Kiureghian, A., "Optimal Discretization of Random Fields," *Journal of Engineering Mechanics*, ASCE, V. 119, No. 6, June 1993, pp. 1136-1154. doi: 10.1061/(ASCE)0733-9399(1993)119:6(1136)

10. Stewart, M. G., and Suo, Q., "Extent of Spatially Variable Corrosion Damage as an Indicator of Strength and Time-Dependent Reliability of RC Beams," *Engineering Structures*, V. 31, No. 1, Jan. 2009, pp. 198-207. doi: 10.1016/j.engstruct.2008.08.011

11. Hajializadeh, D.; OBrien, E. J.; and Stewart, M. G., "The Sensitivity of Bridge Safety to Spatial Correlation of Load and Resistance," *Structures*, V. 5, Feb. 2016, pp. 23-34. doi: 10.1016/j.istruc.2015.07.002

12. Most, T., and Bucher, C., "Probabilistic Analysis of Concrete Cracking Using Neural Networks and Random Fields," *Probabilistic Engineering Mechanics*, V. 22, No. 2, Apr. 2007, pp. 219-229. doi: 10.1016/j.probengmech.2006.11.001

13. Geyer, S.; Papaioannou, I.; Kunz, C.; and Straub, D., "Reliability Assessment of Large Hydraulic Structures with Spatially Distributed Measurements," *Structure and Infrastructure Engineering*, V. 16, No. 4, 2020, pp. 599-612. doi: 10.1080/15732479.2019.1652331

14. Liu, P.; Chen, J.; Fan, S.; and Xu, Q., "Uncertainty Quantification of the Effect of Concrete Heterogeneity on Nonlinear Seismic Response of Gravity Dams Including Record-to-Record Variability," *Structures*, V. 34, Dec. 2021, pp. 1785-1797. doi: 10.1016/j.istruc.2021.08.098

15. Hariri-Ardebili, M. A., "Safety and Reliability Assessment of Heterogeneous Concrete Components in Nuclear Structures," *Reliability Engineering & System Safety*, V. 203, Nov. 2020, Article No. 107104.

16. Petrie, C., and Oudah, F., "Stochastic Finite Element Approach to Assess Reliability of Fiber-Reinforced Polymer-Strengthened Concrete Beams," *ACI Structural Journal*, V. 120, No. 6, Nov. 2023, pp. 193-204.

17. Zhang, M.; Song, H.; Lim, S.; Akiyama, M.; and Frangopol, D. M., "Reliability Estimation of Corroded RC Structures Based on Spatial Variability Using Experimental Evidence, Probabilistic Analysis and Finite Element Method," *Engineering Structures*, V. 192, Aug. 2019, pp. 30-52. doi: 10.1016/j.engstruct.2019.04.085

18. Srivaranun, S.; Akiyama, M.; Masuda, K.; Frangopol, D. M.; and Maruyama, O., "Random Field-Based Reliability Updating Framework for Existing RC Structures Incorporating the Effect of Spatial Steel Corrosion Distribution," *Structure and Infrastructure Engineering*, V. 18, No. 7, 2022, pp. 967-982. doi: 10.1080/15732479.2021.1995445

19. Srivaranun, S.; Akiyama, M.; Bocchini, P.; Christou, V.; Frangopol, D. M.; Fukushima, H.; and Masuda, K., "Effect of the Interaction of Corrosion Pits Among Multiple Tensile Rebars on the Reliability of RC Structures: Experimental and Numerical Investigation," *Structural Safety*, V. 93, Nov. 2021, Article No. 102115.

20. Lim, S.; Akiyama, M.; and Frangopol, D. M., "Assessment of the Structural Performance of Corrosion-Affected RC Members Based on Experimental Study and Probabilistic Modeling," *Engineering Structures*, V. 127, Nov. 2016, pp. 189-205. doi: 10.1016/j.engstruct.2016.08.040

21. Gu, X.; Guo, H.; Zhou, B.; Zhang, W.; and Jiang, C., "Corrosion Non-Uniformity of Steel Bars and Reliability of Corroded RC Beams," *Engineering Structures*, V. 167, July 2018, pp. 188-202. doi: 10.1016/j.engstruct.2018.04.020

22. Li, J.; Li, S.; Gu, G.; Li, H.; Liu, Q.; Fan, Z.; Chen, H.; Han, X.; Zhao, Y.; and Zhang, P., "A Novel Method Based on Digital Image Processing Technique and Finite Element Method for Rapidly Modeling Optical Properties of Actual Microstructured Optical Fibers," *IEEE Photonics Journal*, V. 8, No. 6, Dec. 2016, Article No. 7102314. doi: 10.1109/JPHOT.2016.2614780

23. Bai, X.; Mi, X.; Xie, H.; Shi, K.; Xiong, F.; Zhang, Y.; and Guo, L., "An Image-Based Double-Smoothing Cohesive Finite Element Framework for Particle-Reinforced Materials," *Mathematics*, V. 8, No. 4, Apr. 2020, Article No. 543. doi: 10.3390/math8040543

24. Razmjoo, A., "Application of Image Processing and Finite Element Analysis in Modeling Chloride Diffusion in Concrete," PhD dissertation, Clemson University, Clemson, SC, 2013, 118 pp.

25. Guldberg, R. E.; Hollister, S. J.; and Charras, G. T., "The Accuracy of Digital Image-Based Finite Element Models," *Journal of Biomechanical Engineering*, V. 120, No. 2, Apr. 1998, pp. 289-295. doi: 10.1115/1.2798314

26. Huang, W.; Zhang, X.; and Yin, Y., "An Image-Based Finite Element Approach for Simulating Viscoelastic Response of Asphalt Mixture," *Advances in Materials Science and Engineering*, V. 2016, No. 1, 2016, Article No. 7428623.

27. Yue, Z. Q.; Chen, S.; and Tham, L. G., "Finite Element Modeling of Geomaterials Using Digital Image Processing," *Computers and Geotechnics*, V. 30, No. 5, July 2003, pp. 375-397. doi: 10.1016/S0266-352X(03)00015-6

28. Chen, S.; Yue, Z. Q.; and Tham, L. G., "Digital Image Based Approach for Three-Dimensional Mechanical Analysis of Heterogeneous Rocks," *Rock Mechanics and Rock Engineering*, V. 40, No. 2, Apr. 2007, pp. 145-168. doi: 10.1007/s00603-006-0105-8

29. Xu, W.-J.; Yue, Z.-Q.; and Hu, R.-L., "Study on the Mesostructure and Mesomechanical Characteristics of the Soil–Rock Mixture Using Digital Image Processing Based Finite Element Method," *International Journal of Rock Mechanics and Mining Sciences*, V. 45, No. 5, July 2008, pp. 749-762. doi: 10.1016/j.ijrmms.2007.09.003

30. Zhang, L.; Ren, Z.; and Lu, Q., "Simulation of Mesofracture Process of Asphalt Mixture Using Digital Image Processing and Extended Finite-Element Method," *Journal of Testing and Evaluation*, V. 45, No. 1, 2017, pp. 281-293. doi: 10.1520/JTE20160143

31. Zhang, H.; Huang, Y.-J.; Guo, F.-Q.; and Yang, Z.-J., "A Meso-Scale Size Effect Study of Concrete Tensile Strength Considering Parameters of Random Fields," *Engineering Fracture Mechanics*, V. 269, June 2022, Article No. 108519.

32. Roubin, E.; Colliat, J.-B.; and Benkemoun, N., "Meso-Scale Modeling of Concrete: A Morphological Description Based on Excursion Sets of Random Fields," *Computational Materials Science*, V. 102, May 2015, pp. 183-195. doi: 10.1016/j.commatsci.2015.02.039

33. Ghahremani, K.; Khaloo, A.; Mohamadi, S.; and Lattanzi, D., "Damage Detection and Finite-Element Model Updating of Structural Components through Point Cloud Analysis," *Journal of Aerospace Engineering*, ASCE, V. 31, No. 5, Sept. 2018, p. 04018068. doi: 10.1061/(ASCE)AS.1943-5525.0000885

34. Zhang, Y.; Xia, B.; and Taylor, S., "High-Resolution 3-D Geometry Updating of Digital Functional Models Using Point Cloud Processing and Surface Cut," *Computer-Aided Civil and Infrastructure Engineering*, V. 39, No. 1, Jan. 2024, pp. 3-19.

35. Zhang, Y., and Lin, W., "Computer-Vision-Based Differential Remeshing for Updating the Geometry of Finite Element Model," *Computer-Aided Civil and Infrastructure Engineering*, V. 37, No. 2, Feb. 2022, pp. 185-203. doi: 10.1111/mice.12708

36. The MathWorks, Inc., "Image Processing Toolbox: 9.4 (R2022a)," Natick, MA, 2022.

37. Meng, Q.-X.; Xu, W.-Y.; Wang, H.-L.; Zhuang, X.-Y.; Xie, W.-C.; and Rabczuk, T., "DigiSim — An Open Source Software Package for Heterogeneous Material Modeling Based on Digital Image Processing," *Advances in Engineering Software*, V. 148, Oct. 2020, Article No. 102836.

38. Dassault Systèmes, "ABAQUS," Vélizy-Villacoublay, France, 2021.

39. Ma, J.; Yu, L.; Li, B.; and Yu, B., "Stress–Strain Model for Confined Concrete in Rectangular Columns with Corroded Transverse Reinforcement," *Engineering Structures*, V. 267, Sept. 2022, Article No. 114710.

40. Nataf, A., "Determination des Distribution dont les Marges sont Donnees," *Comptes Rendus de l'Académie des Sciences*, V. 225, 1962, pp. 42-43.

41. Liu, P.-L., and Der Kiureghian, A., "Multivariate Distribution Models with Prescribed Marginals and Covariances," *Probabilistic Engineering Mechanics*, V. 1, No. 2, June 1986, pp. 105-112. doi: 10.1016/0266-8920(86)90033-0

42. Melchers, R. E., and Beck, A. T., *Structural Reliability Analysis and Prediction*, third edition, John Wiley & Sons Ltd., Chichester, UK, 2018, 528 pp.

43. *fib*, "CEB-FIP Model Code 1990," International Federation for Structural Concrete, Lausanne, Switzerland, 1993, 460 pp.

44. Cornelissen, H. A. W.; Hordijk, D. A.; and Reinhardt, H. W., "Experimental Determination of Crack Softening Characteristics of Normalweight and Lightweight Concrete," *HERON*, V. 31, No. 2, 1986, pp. 45-56.

45. Murcia-Delso, J., and Shing, P. B., "Bond-Slip Model for Detailed Finite-Element Analysis of Reinforced Concrete Structures," *Journal of Structural Engineering*, ASCE, V. 141, No. 4, Apr. 2015, p. 04014125. doi: 10.1061/(ASCE)ST.1943-541X.0001070

46. Bai, G., and Liu, B., "Nonlinear Finite Element Analysis of Bond-Slip Performance of Recycled Aggregate Concrete Filled Circular Steel Tube," *Journal of Adhesion Science and Technology*, V. 33, No. 12, 2019, pp. 1294-1319. doi: 10.1080/01694243.2019.1602913

47. BaniAsad, E., and Dehestani, M., "Incorporation of Corrosion and Bond-Slip Effects in Properties of Reinforcing Element Embedded in Concrete Beams," *Structures*, V. 20, Aug. 2019, pp. 105-115. doi: 10.1016/j.istruc.2019.03.004

48. Wu, Y.-F., and Zhao, X.-M., "Unified Bond Stress–Slip Model for Reinforced Concrete," *Journal of Structural Engineering*, ASCE, V. 139, No. 11, Nov. 2013, pp. 1951-1962. doi: 10.1061/(ASCE)ST.1943-541X.0000747

49. Yuan, W.; Guo, A.; and Li, H., "Equivalent Elastic Modulus of Reinforcement to Consider Bond-Slip Effects of Coastal Bridge Piers with Non-uniform Corrosion," *Engineering Structures*, V. 210, May 2020, Article No. 110382.

50. Dehestani, M., and Mousavi, S. S., "Modified Steel Bar Model Incorporating Bond-Slip Effects for Embedded Element Method," *Construction and Building Materials*, V. 81, Apr. 2015, pp. 284-290. doi: 10.1016/j.conbuildmat.2015.02.027

51. Belarbi, A., and Hsu, T. T. C., "Constitutive Laws of Concrete in Tension and Reinforcing Bars Stiffened by Concrete," *ACI Structural Journal*, V. 91, No. 4, July-Aug. 1994, pp. 465-474.

52. *fib*, "*fib* Model Code for Concrete Structures (2020)," International Federation for Structural Concrete, Lausanne, Switzerland, 2023, 720 pp.

53. Prado, F. S.; Meneghetti, L. C.; and Stucchi, F. R., "Confinement Effect of Two-Way Beam-and-Slab System on the Effective Compressive Strength of Interior Concrete Columns," *Structural Concrete*, V. 24, No. 6, Dec. 2023, pp. 6872-6896. doi: 10.1002/suco.202200991

54. Nowak, A. S., and Szerszen, M. M., "Calibration of Design Code for Buildings (ACI 318): Part 1—Statistical Models for Resistance," *ACI Structural Journal*, V. 100, No. 3, May-June 2003, pp. 377-382.

55. Bartlett, F. M., "Canadian Standards Association Standard A23.3-04 Resistance Factor for Concrete in Compression," *Canadian Journal of Civil Engineering*, V. 34, No. 9, Sept. 2007, pp. 1029-1037. doi: 10.1139/l07-034

56. Castaldo, P.; Gino, D.; and Mancini, G., "Safety Formats for Non-linear Finite Element Analysis of Reinforced Concrete Structures: Discussion, Comparison and Proposals," *Engineering Structures*, V. 193, Aug. 2019, pp. 136-153. doi: 10.1016/j.engstruct.2019.05.029

57. Bartlett, F. M.; Hong, H. P.; and Zhou, W., "Load Factor Calibration for the Proposed 2005 Edition of the National Building Code of Canada: Statistics of Loads and Load Effects," *Canadian Journal of Civil Engineering*, V. 30, No. 2, Apr. 2003, pp. 429-439. doi: 10.1139/l02-087

58. Mander, J. B.; Priestley, M. J. N.; and Park, R., "Theoretical Stress-Strain Model for Confined Concrete," *Journal of Structural Engineering*, ASCE, V. 114, No. 8, Sept. 1988, pp. 1804-1826.

59. Vu, N. S.; Yu, B.; and Li, B., "Stress-Strain Model for Confined Concrete with Corroded Transverse Reinforcement," *Engineering Structures*, V. 151, Nov. 2017, pp. 472-487. doi: 10.1016/j.engstruct.2017.08.049

CALL FOR ACTION

ACI Invites You To...

Share your expertise

Do you have EXPERTISE in any of these areas?

- BIM
- Chimneys
- Circular Concrete Structures Prestressed by Wrapping with Wire and Strand
- Circular Concrete Structures Prestressed with Circumferential Tendons
- Concrete Properties
- Demolition
- Deterioration of Concrete in Hydraulic Structures
- Electronic Data Exchange
- Insulating Concrete Forms, Design, and Construction
- Nuclear Reactors, Concrete Components
- Pedestal Water Towers
- Pipe, Cast-in-Place
- Strengthening of Concrete Members
- Sustainability

Then become a REVIEWER for the *ACI Structural Journal* or the *ACI Materials Journal*.

Become a Reviewer for the ACI Journals

How to become a Reviewer:

1. Go to: **http://mc.manuscriptcentral.com/aci**;
2. Click on "Create Account" in the upper right-hand corner; and
3. Enter your E-mail/Name, Address, User ID and Password, and Area(s) of Expertise.

Update your Manuscript Central user account information

Did you know that the database for MANUSCRIPT CENTRAL, our manuscript submission program, is separate from the ACI membership database?

How to update your user account:

1. Go to **http://mc.manuscriptcentral.com/aci**;
2. Log in with your current User ID & Password; and
3. Update your E-mail/Name, Address, User ID and Password, and Area(s) of Expertise.

QUESTIONS?

E-mail any questions to Journals.Manuscripts@concrete.org.

American Concrete Institute

Always advancing

ACI STRUCTURAL JOURNAL TECHNICAL PAPER

Title No. 122-S70

Behavior of Exterior Beam-Column Connections with Headed Bars under Nonreversible Cyclic Loading

by Gustavo J. Parra-Montesinos and Jacob Zeuske

Two large-scale exterior beam-column connections with beam longitudinal headed bars were tested to evaluate their susceptibility to breakout failures. The specimens were designed following the strength and transverse reinforcement detailing provisions in Chapter 15 of ACI 318-19. The variable investigated was the headed bar embedment length, which was determined based on either Chapter 25 of ACI 318-19 or recent research at The University of Kansas, the latter leading to a 22% shorter embedment length. Both specimens exhibited beam flexural yielding, but the specimen with the shorter bar embedment length experienced significantly more connection damage, followed by a concrete breakout failure. Based on the limited test results, it is recommended that nominal joint shear strength be calculated based on a joint effective depth equal to the headed bar embedment length and a shear stress of $1.0\lambda\sqrt{f_c'}$ MPa ($12\lambda\sqrt{f_c'}$ psi). A method for calculating headed bar group anchorage strength in exterior beam-column connections was proposed, which led to reasonable and conservative strength estimates in the test specimens.

Keywords: anchorage; bar groups; breakout strength; development length; joints; shear.

INTRODUCTION

Exterior beam-column joints designed in accordance with the strength and reinforcement detailing provisions of Chapters 15 and 25 of ACI 318-19 (ACI Committee 318 2019) are assumed to exhibit adequate performance under gravity loads, wind, and minor earthquake motions (Seismic Design Category A). The design joint shear strength of exterior joints with continuous columns in Chapter 15 of ACI 318-19 is calculated as follows

$$\phi V_n = 1.25\lambda\sqrt{f_c'}A_j \text{ (SI)} \quad (1a)$$

$$\phi V_n = 15\lambda\sqrt{f_c'}A_j \text{ (U.S.)} \quad (1b)$$

where ϕ is a strength reduction factor (0.75); λ is a factor that accounts for the use of lightweight concrete (1.0 for joints with normalweight concrete); f_c' is the specified concrete compressive strength; and A_j is the effective joint area.

Minimum transverse reinforcement for exterior joints consists of two layers of ties, hoops, or spirals over the depth of the shallowest beam framing into the joint. Further, transverse reinforcement must be provided over the depth of the deepest beam framing into the joint at a spacing not greater than 200 mm (8 in.). Chapter 15 of ACI 318-19 also requires that beam longitudinal reinforcement terminating at the joint be embedded to satisfy the development length provisions in Chapter 25 for either straight bars, hooked bars, or headed bars, as applicable.

During the 2025 ACI 318 Code cycle, in light of breakout failures observed in column-footing connections subjected to lateral load reversals (Worsfold et al. 2022; Worsfold and Moehle 2023a,b; Cheng et al. 2025), breakout strength provisions for connections where reinforcement is terminated were proposed by ACI Subcommittee 318-1R and are currently under consideration by ACI Committee 318. Exempted from breakout strength calculations, however, are exterior beam-column joints designed in accordance with Chapter 15 (and Chapter 18, if applicable), given the history of satisfactory performance of exterior joints constructed in the past several decades.

In most exterior beam-column joints, beam longitudinal reinforcement is anchored in the column with standard 90-degree hooks. The use of headed longitudinal reinforcement, while allowed since ACI 318-08, is still a relatively recent innovation, and thus, evidence of adequate behavior is not as extensive as that for exterior joints with hooked bars. Further, most laboratory tests of beam-column connections with headed bars have focused on well-confined joints and columns such as those of special moment frames (SMFs), for which the potential of breakout failures in the connection is significantly less than that in connections of non-seismic or ordinary moment frames (OMFs). Two large-scale exterior beam-column connection subassemblies were thus tested to evaluate the behavior of exterior beam-column connections of non-seismic or OMFs with longitudinal beam reinforcement terminated by heads.

RESEARCH SIGNIFICANCE

Most research on exterior beam-column connections with headed bars has focused on those of SMFs (for example, Kang et al. 2009; Lee et al. 2024) for which confinement requirements make concrete breakout failures highly unlikely. Laboratory test data are thus needed to better understand the behavior of lightly confined connections, such as those of non-seismic or OMFs, including their susceptibility to breakout failures. This paper contains new information for researchers and structural designers regarding the behavior of connections of non-seismic or OMFs under nonreversible

ACI Structural Journal, V. 122, No. 5, September 2025.

MS No. S-2024-041.R1, doi: 10.14359/51746793, received August 18, 2024, and reviewed under Institute publication policies. Copyright © 2025, American Concrete Institute. All rights reserved, including the making of copies unless permission is obtained from the copyright proprietors. Pertinent discussion including author's closure, if any, will be published ten months from this journal's date if the discussion is received within four months of the paper's print publication.

cyclic loading, with a focus on anchorage strength of headed bar groups and joint shear behavior.

LABORATORY TEST PROGRAM

Overall specimen configuration and test setup

The laboratory test program consisted of testing two large-scale, exterior beam-column connection subassemblies under nonreversible (half) lateral load cycles, followed by a monotonically increased lateral load. Figure 1 shows a drawing of the test specimen and test setup. As shown in the figure, each specimen consisted of a column extending approximately half a story above and below the beam, and a beam extending approximately a third of its assumed length. The column and beam ends were pinned to simulate inflection points. Lateral displacements/forces were applied near the top of the column through a hydraulic actuator, while an axial compressive force was applied to the column through rods and hydraulic jacks.

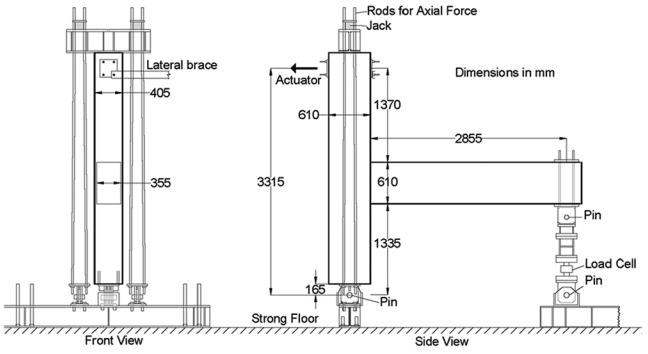


Fig. 1—Exterior beam-column connection test specimen and setup.

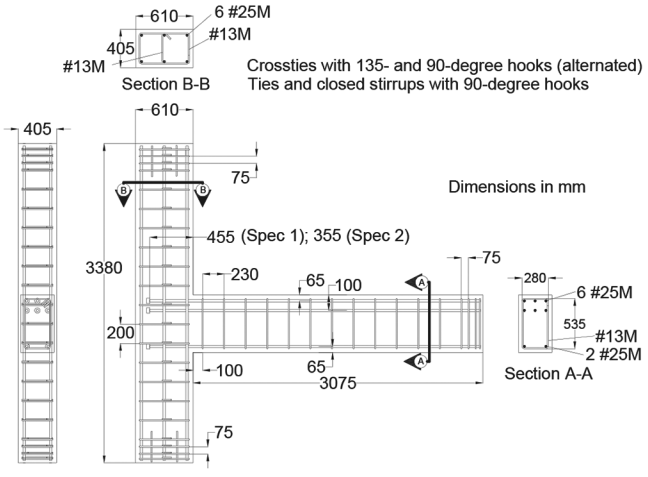


Fig. 2—Reinforcement detailing for test specimens.

Specimen design

Both specimens were designed such that beam flexural yielding would occur prior to column yielding. This is typical for exterior beam-column connections of frame structures given that only one beam frames into the column. ASTM A615 Grade 420 (Grade 60) steel was used for all reinforcement, while the specified concrete compressive strength was 27.6 MPa (4000 psi). Figure 2 shows the reinforcement detailing for the two specimens, while Fig. 3 shows a photograph of the connection reinforcement in Specimen 1.

The only difference between the design of Specimens 1 and 2 was the embedment (effective) length of the beam longitudinal headed bars, measured from the face of the column. The head bearing area was equal to four times the bar area. Table 1 shows the calculated nominal flexural and shear strengths for the columns and beam. Also shown in Table 1 are the probable flexural strength of the beam, based on a longitudinal steel stress of 1.25 times the nominal yield strength f_y, as well as the associated maximum column moment and beam and column shear forces.

Embedment length for the headed bars in Specimen 1 was determined in accordance with Chapter 25 of ACI 318-19. Section 25.4.4.2 of ACI 318-19 requires calculation of development length for headed bars, l_{dt}, as follows



Fig. 3—Connection reinforcement cage of Specimen 1.

Table 1—Nominal and probable strengths and associated actions for test specimens

$M_{n,b}$, kN·m (kip·in.)	$M_{n,c}$, kN·m (kip·in.)	$V_{n,b}$, kN (kip)	$V_{n,c}$, kN (kip)	$V_{n,j}$, kN (kip)	$M_{pr,b}$, kN·m (kip·in.)	$M_{u,c}$, kN·m (kip·in.)	$V_{u,b}$, kN (kip)	$V_{u,c}$, kN (kip)	$V_{u,j}$, kN (kip)
550 (4880)	465 (4130)	385 (86.5)	430 (96.5)	1620 (364)	670 (5940)	305 (2720)	235 (52.9)	225 (50.4)	1355 (305)

Note: $M_{n,b}$ is nominal beam flexural strength; $M_{n,c}$ is nominal column flexural strength; $V_{n,b}$ is nominal beam shear strength; $V_{n,c}$ is nominal column shear strength (neglecting axial load); $V_{n,j}$ is nominal joint shear strength; $M_{pr,b}$ is probable beam flexural strength; $M_{u,c}$ is maximum column moment corresponding to beam reaching probable flexural strength; $V_{u,b}$ is beam shear corresponding to beam reaching probable flexural strength; $V_{u,c}$ is column shear corresponding to beam reaching probable flexural strength; and $V_{u,j}$ is joint shear corresponding to beam reaching probable flexural strength.

$$l_{dt} = \frac{f_y \psi_e \psi_p \psi_o \psi_c}{31\sqrt{f_c'}} d_b^{1.5} \text{ (SI)} \quad (2a)$$

$$l_{dt} = \frac{f_y \psi_e \psi_p \psi_o \psi_c}{75\sqrt{f_c'}} d_b^{1.5} \text{ (U.S.)} \quad (2b)$$

where l_{dt} shall not be taken less than 150 mm (6 in.) or eight times the bar diameter, d_b; ψ_e is a modification factor for epoxy-coated bars (1.0); ψ_p is a parallel tie reinforcement modification factor (1.6); ψ_o is a location modification factor (1.0); and ψ_c is a concrete strength modification factor (0.87). For f_y = 414 MPa (60,000 psi), f_c' = 27.6 MPa (4000 psi), and d_b = 25.4 mm (1 in.), l_{dt} = 450 mm (17.5 in.). The embedment length provided for the headed bars in Specimen 1 was thus 455 mm (18 in.).

Embedment length for the headed bars in Specimen 2 was calculated based on recommendations in Banaeipour et al. (2023) as follows

$$l_{dt} = \frac{f_y \psi_e \psi_p \psi_o}{94(f_c')^{0.25}} d_b^{1.5} \text{ (SI)} \quad (3a)$$

$$l_{dt} = \frac{f_y \psi_e \psi_p \psi_o}{780(f_c')^{0.25}} d_b^{1.5} \text{ (U.S.)} \quad (3b)$$

where, for No. 35 (No. 11) bars and smaller, ψ_p is the lesser of

$$2 - \frac{s}{8d_b} \geq 0.85 \quad (4)$$

and

$$1.6 - \frac{2A_{tt}}{A_{hs}} \geq 0.85 \quad (5)$$

where s is the center-to-center spacing of headed bars; A_{tt} is the total cross-sectional area of tie reinforcement parallel to the headed bars and within $8d_b$ from the centerline of the headed bars toward the middle of the joint; and A_{hs} is the total cross-sectional area of headed bars being developed. For Specimen 2, s = 115 mm (4.5 in.), A_{tt} = 515 mm^2 (0.8 in.^{2}), A_{hs} = 3060 mm^2 (4.74 in.^{2}), ψ_p = 1.26, and l_{dt} = 310 mm (12.2 in.). The embedment length provided for the headed bars in Specimen 2 was 355 mm (14 in.).

Loading protocol

Beam-column connections of non-seismic or OMFs are not expected to experience reversals of moment under combined gravity and lateral loading. The loading protocol applied to Specimen 1 thus consisted of three nonreversible (half) cycles at target drift ratios of 0.25, 0.5, 0.75, and 1%, followed by a monotonic increase in applied load until the beam exhibited significant flexural yielding (Fig. 4). For Specimen 2, the applied cycles were targeted at the same lateral forces as those applied to Specimen 1, also shown in Fig. 4, rather than drift ratio. Prior to application of the lateral loads, an axial compressive force of 670 kN (150 kip) was applied to the column, which was approximately 10% of the product of the column gross cross-sectional area A_g and

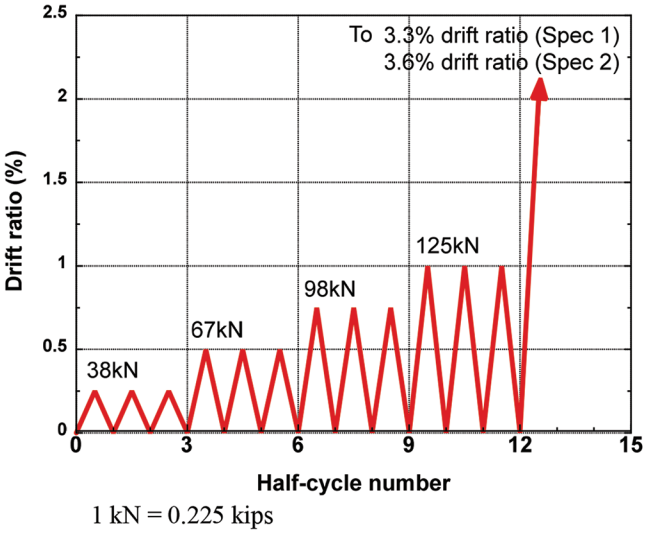


Fig. 4—Loading protocol with column axial force.

the specified concrete compressive strength. After significant flexural yielding, the specimens were unloaded, the column axial load was removed, and the specimens were reloaded monotonically until failure. The reason for removing the column axial force was to evaluate in a single test, to the extent possible, the effect of column axial compression on connection behavior.

Specimen instrumentation

Strain gauges were installed on select top longitudinal bars in the beam at the column face, mid-embedment length, and near the bearing face of the head. Strain gauges were also attached to the transverse reinforcement in the joint region and in the column above and below the joint. Optical markers were attached to one lateral face of the specimen, in the connection region, for calculation of joint, column, and beam deformations based on measured displacements. Applied lateral loads and displacements were monitored through a load cell and a linear variable differential transformer (LVDT) attached to the hydraulic actuator. A string potentiometer was used at the base of the column to track any sliding displacements of the test setup.

Material properties

Concrete compressive strength was obtained from tests of three 150 x 300 mm (6 x 12 in.) cylinders in accordance with ASTM C39/C39M-21 (2021) within 1 day of the specimen test date. The cylinders were cured at 70% relative humidity until the test day. The average cylinder compressive strength was 40.0 and 37.6 MPa (5800 and 5450 psi) for Specimens 1 and 2, respectively. Mill certificates for the headed bars and column longitudinal reinforcement indicated a yield strength of 449 and 455 MPa (65.2 and 66.0 ksi) for the bars in Specimens 1 and 2, respectively, and an ultimate strength of 717 and 723 MPa (104 and 105 ksi). No laboratory tests could be conducted to corroborate the properties reported in the mill certificates. ASTM A615 Grade 420 (Grade 60) steel was used for all the transverse reinforcement, but the yield and ultimate strengths for this reinforcement were not available.

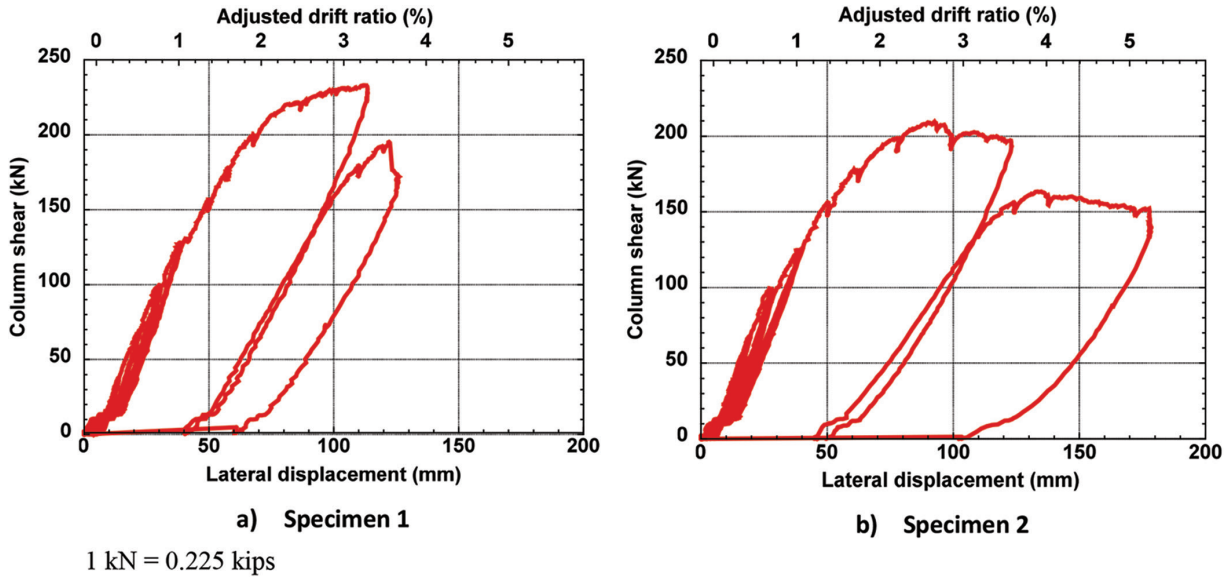


Fig. 5—Column shear versus lateral displacement response.

TEST RESULTS

Column shear versus lateral displacement response and damage progression

Figure 5 shows the column shear versus lateral displacement response for the two test specimens. The lower stiffness for loads below approximately 15 kN (3.4 kip) was caused by the flexibility of the connections between the various components of the vertical arm supporting the end of the beam. The applied displacement was thus adjusted by removing the component associated with the flexibility of the vertical arm support, and the drift ratio was calculated accordingly, as shown in the top x-axis of both plots. Drift ratio is equal to the relative lateral displacement between the column at the level of the actuator and the bottom pin (inflection points), divided by the distance between the column inflection points (3315 mm [130.5 in.]).

The two specimens exhibited an approximately linear-elastic response up to approximately two-thirds of the peak load. A few flexural cracks developed in the beam near the column face during the first cycle at a 0.5% drift ratio (67 kN [15 kip] of column shear). A distinct change in stiffness was observed at approximately a 1% drift ratio for Specimen 1 (125 kN [28 kip] of column shear) and a 0.75% drift ratio for Specimen 2 (100 kN [22 kip] of column shear), which was associated with additional flexural cracking in the beam as well as some joint inclined cracking.

Strain gauge data indicated that yielding in the top layer of beam longitudinal reinforcement started at a column shear close to 170 kN (38 kip) in both specimens (approximately at a 1.5% drift ratio), which led to a gradual decrease in the slope of the column shear versus lateral displacement response. At a 3.3% drift ratio, the column shear applied to Specimen 1 was 233 kN (52.4 kip), and damage in the connection region was moderate (Fig. 6(a)), characterized by some joint diagonal cracks and a 4 mm (0.15 in.) wide crack at the beam-column interface. Some cracks associated with a breakout mechanism were also identified near the front top corner of the joint, as well as the vertical turning of some of the joint diagonal cracks. The peak column shear applied to Specimen 2 was 208 kN (46.7 kip) (89% of that for Specimen 1) at an adjusted drift ratio of approximately 2.5%, followed by a gradual loss of strength. This specimen was displaced to an adjusted drift ratio of approximately 3.6%. At this stage, damage in Specimen 2 was severe and consisted of several wide joint diagonal cracks, bulging of the joint concrete, a nearly 6 mm (0.25 in.) wide crack at the beam-column interface, and a clear cracking pattern associated with a breakout mechanism (Fig. 7(a)). Both specimens were then unloaded, and the column axial load was removed.

After unloading and removal of the column axial force, the two specimens were reloaded until failure. The peak force attained was significantly lower than before removal of the column axial force. Both specimens exhibited severe damage in the connection region. Although Specimen 1 did not develop a breakout failure, the cracking pattern suggested significant breakout-related damage (Fig. 6(b)). Also, a sudden drop in the load occurred following the peak force, which is believed to be associated with fracture of one of the ties in the joint. Specimen 2 did develop a clear breakout failure (Fig. 7(b)), with significant damage not only on the lateral faces of the connection but also on the front face of the column above the beam. It should be kept in mind that a breakout failure in Specimen 2 developed at drifts much larger than what would be anticipated in an ordinary moment-resisting frame. The test results nevertheless suggest that significant damage at lower drifts, and even a breakout failure, would be possible in joints required to anchor larger beam bar tensile forces than those calculated in the tests.

Strains in beam longitudinal reinforcement

Figure 8 shows plots of applied column shear versus bar strains for one top beam longitudinal bar for each specimen. Three strain gauge responses are shown on each plot: one at the column face, another at nearly mid-embedment length, and the third near the bearing face of the head.



a) At 3.3% drift ratio with column axial load



b) End of test

Fig. 6—Damage in connection of Specimen 1.



a) At 3.6% drift ratio with column axial load



b) End of test

Fig. 7—Damage in connection of Specimen 2.

Yielding in tension of the beam longitudinal reinforcement, as indicated by a significant change in slope of the applied shear versus strain response, started near the column face at approximately a 1.5% drift ratio and an applied shear of 170 kN (38 kip) for both specimens. In Specimen 1, yielding at approximately mid-embedment length occurred at an applied column shear of nearly 220 kN (50 kip). Peak strain for this bar was approximately 0.015 prior to removal of the column axial force. While no yielding was detected near the bearing face of the head, the peak strain was close to the yield strain, indicating that most of the tension force in the bar was transferred through bearing of the head once yielding extended into the joint. In Specimen 2, yielding near the mid-embedment length occurred at peak load. When the specimen was displaced further, the strains at the column face and mid-embedment length were nearly equal, and the bar strain near the head was close to the yield strain. Peak tensile strain for this bar was approximately 0.009 (during loading with a column axial force).

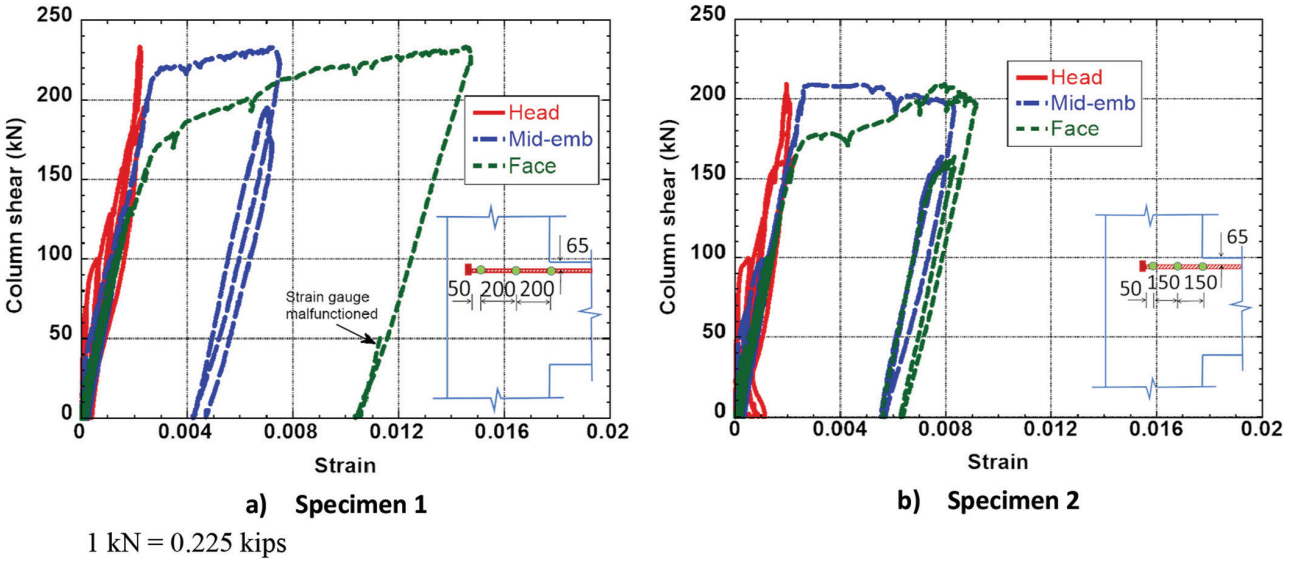


Fig. 8—Strains in top beam longitudinal bars.

Beam rotations

Figure 9 shows the column shear versus beam rotation responses for the two specimens. Three beam rotations were calculated: concentrated rotations at the column face, rotations between the column face and approximately 0.5 times the beam effective depth d, and between 0.5d and 0.9d from the column face. First yielding of the beam longitudinal reinforcement during lateral loading with axial compression in the column corresponded to a concentrated rotation of approximately 0.0025 to 0.003 rad for both specimens. The two specimens also exhibited a similar peak concentrated rotation prior to removal of column axial force (approximately 0.008 rad). During reloading after removal of the column axial force, peak interface rotation in Specimen 1 was only approximately 10% greater than that prior to removal of the column axial force (0.009 rad). For Specimen 2, on the other hand, the peak rotation increased by approximately 40% (0.011 rad). This significant increase in beam concentrated rotations in Specimen 2 is consistent with the severe joint shear and breakout-related damage, which led to further deterioration of the anchorage of the beam headed bars.

Rotations measured between the beam-column interface and approximately 0.5d indicate some spread of yielding away from the column face. Peak rotation for this beam region was 0.0065 and 0.003 rad in Specimens 1 and 2, respectively. The better rotation distribution exhibited by Specimen 1 is again consistent with the lesser joint shear and breakout-related damage observed in this specimen. Rotations between approximately 0.5d and 0.9d from the column face remained below approximately 0.002 rad. Some nonlinearities in the response can be observed in Specimen 1, suggesting that bar yielding spread beyond 0.5d from the column face for this specimen.

Joint shear distortions

Figure 10 shows a plot of average joint shear stress versus joint shear distortion response for each specimen. Joint shear force was calculated as the beam moment at the column face divided by (7/8)d (estimate of tensile force in beam headed bars) minus the applied column shear. Two joint shear stresses were calculated, one based on the overall column depth (ACI 318-19 provisions) and the other based on a joint effective depth equal to the effective (embedment) length of the headed bars, $h_{ef} = l_{dt}$. For the test specimens, the effective joint width was equal to the column width b_c.

As can be seen in Fig. 10, joint shear distortions were negligible up to an average joint shear stress of approximately $0.6\sqrt{f_c'}$ MPa ($7.2\sqrt{f_c'}$ psi) based on $A_j = b_c h_{ef}$, at which stress joint diagonal cracking first occurred. For Specimen 1, peak joint shear distortion during loading, including column axial force, was approximately 0.004 rad at a joint shear stress of either $1.2\sqrt{f_c'}$ MPa ($14\sqrt{f_c'}$ psi) based on $A_j = b_c h_{ef}$ or $0.8\sqrt{f_c'}$ MPa ($10\sqrt{f_c'}$ psi) based on the gross cross-sectional area of the column. At this stage, the joint of Specimen 1 exhibited moderate joint shear damage (Fig. 6(a)). Joint shear distortions were significantly larger in Specimen 2, as expected, given the shorter embedment length of the headed bars, which led to a smaller volume of concrete engaged in the joint. For this specimen, calculated peak joint shear stress was $1.3\sqrt{f_c'}$ MPa ($16\sqrt{f_c'}$ psi) based on $A_j = b_c h_{ef}$ and $0.8\sqrt{f_c'}$ MPa ($10\sqrt{f_c'}$ psi) based on the column gross cross-sectional area. Maximum shear distortion prior to removal of column axial force was 0.01 rad. At this stage, joint damage was significant (Fig. 7(a)).

The joints exhibited a significantly more flexible response when reloaded without axial compression in the column. For the case of Specimen 1, shear distortion was 0.009 rad at a shear stress of $0.9\sqrt{f_c'}$ MPa ($11\sqrt{f_c'}$ psi) based on $A_j = b_c h_{ef}$, at which point a sudden drop in applied load occurred. Peak joint shear distortion in this specimen was 0.01 rad. For Specimen 2, peak shear distortion during loading without column axial compression could not be determined due to unreliable marker data. The maximum shear distortion that could be calculated was 0.012 rad at a shear stress of $0.9\sqrt{f_c'}$ MPa ($11\sqrt{f_c'}$ psi) based on $A_j = b_c h_{ef}$. At the end of the test of Specimen 2, joint damage was excessive, as shown in Fig. 7(b).

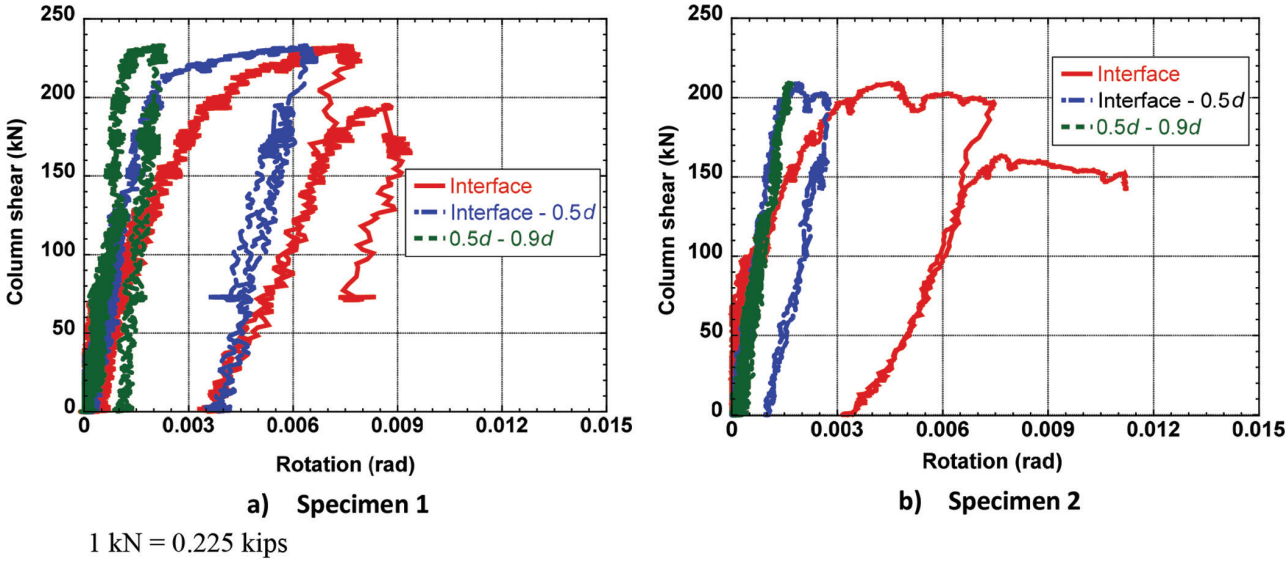


Fig. 9—Beam rotations.

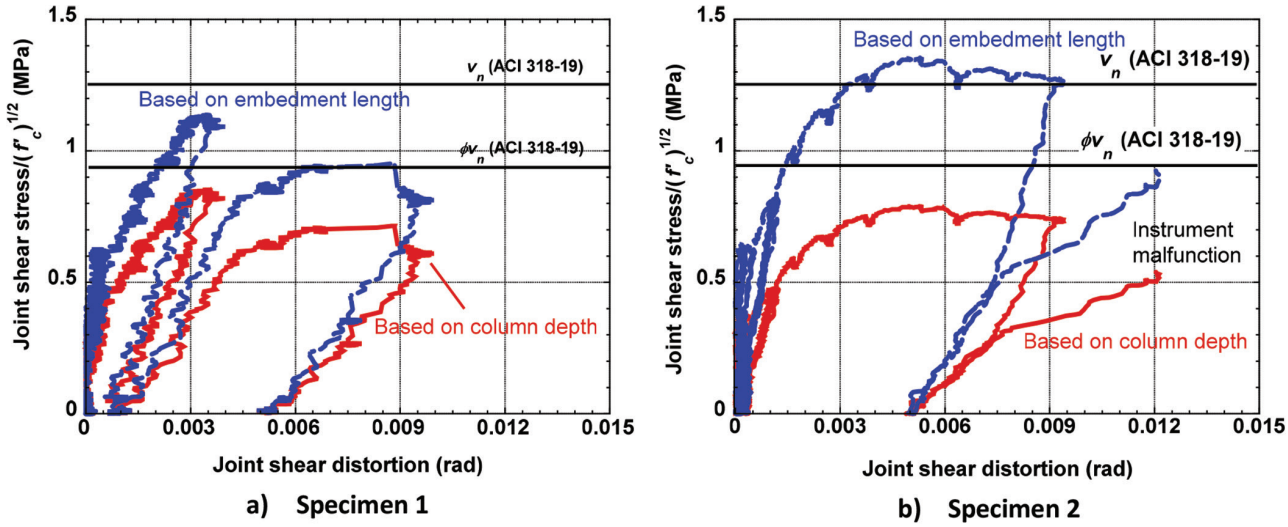


Fig. 10—Joint shear stress versus shear distortion response.

The severe joint damage exhibited by both test specimens at the end of the tests, given that the joint shear force was below the design strength calculated in accordance with Chapter 15 of ACI 318-19, is of concern. Based on the limited test results, it is recommended that the shear strength of exterior joints with beam longitudinal bars terminated with heads be determined using an effective joint depth equal to the embedment length as opposed to the overall column depth. It also seems reasonable to calculate the nominal shear strength based on a joint shear stress of $1.0\sqrt{f_c'}$ MPa ($12\sqrt{f_c'}$ psi).

Strains in column transverse reinforcement

Figure 11 shows the column shear versus strain response for various column ties in the connection region. In both specimens, significant yielding of the tie reinforcement within the joint (T5 and T6) took place during loading while the column was under axial compression. In Specimen 1, the tie immediately above the joint (T4) remained elastic, with a peak strain slightly below 0.002. For Specimen 2, however, this tie exhibited significant yielding, which is consistent with the more visible breakout-related damage.

During loading after removal of the column axial force, further yielding took place in Ties T5 and T6 of Specimen 1, while Tie T4 remained elastic. A large jump in strain in Ties T5 and T6 was recorded at the point where a sudden loss of strength occurred, which was likely due to fracture of Tie T6. The strain gauges attached to Tie T4 of Specimen 2 failed during loading without column axial compression, while the strain gauges on Ties T5 and T6 failed before removal of the column axial compression. All other instrumented ties (T1 through T3, and T7 and T8) remained elastic.

Yielding of the transverse reinforcement within the joint was consistent with the extensive joint diagonal cracking in both specimens. The significantly larger strains in the tie just above the joint (T4) compared to the ties further away from the joint (T1 through T3) are an indication of the more important role this tie played in resisting breakout-related tensile forces.

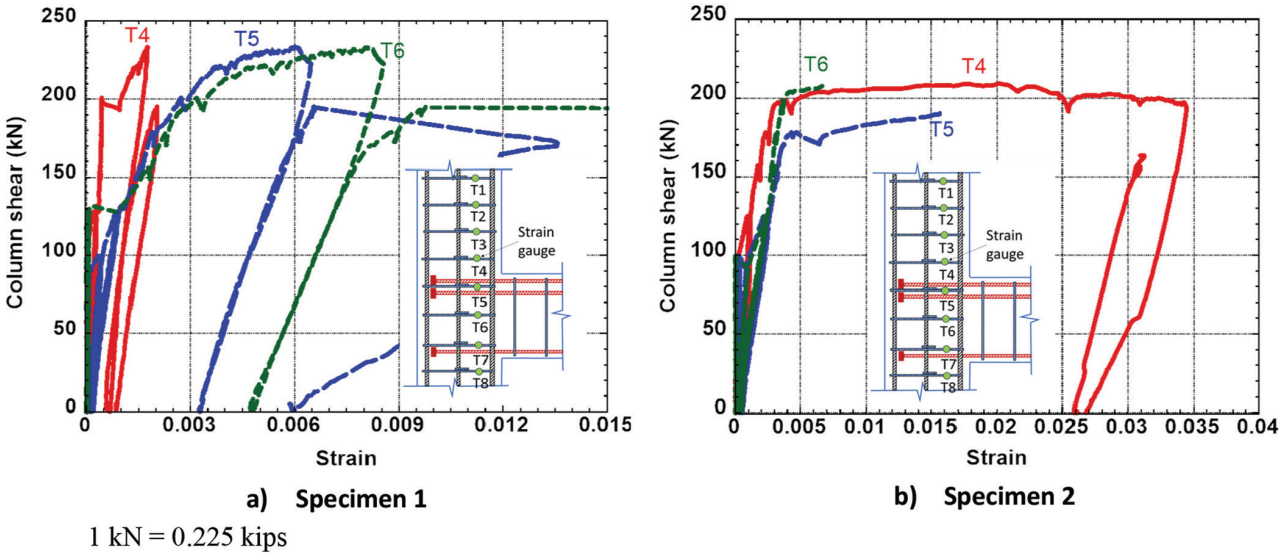


Fig. 11—Strains in column transverse reinforcement in connection region.

Evaluation of breakout strength

Evaluation of breakout strength based on proposal by ACI Subcommittee 318-1R—Breakout strength and detailing provisions for concrete connections where a group of bars is terminated were proposed by ACI Subcommittee 318-1R during the 2025 Code cycle. In the proposed provisions, the nominal breakout strength of a group of headed bars is calculated as the summation of a "concrete" contribution, N_{cbg}, and a transverse reinforcement contribution, N_s. The concrete contribution N_{cbg} is calculated following the same equation used for anchors in Chapter 17 of ACI 318-19 as follows

$$N_{cbg} = \frac{A_{Nc}}{A_{Nco}}\psi_{ec,N}\psi_{ed,N}\psi_{c,N}\psi_{cp,N}N_b \quad (6)$$

where A_{Nc} and A_{Nco} are the projected concrete failure areas for the anchor group and a single anchor, respectively; $\psi_{ec,N}$ is the eccentricity modification factor; $\psi_{ed,N}$ is the edge-effect modification factor; $\psi_{c,N}$ is the concrete cracking modification factor; $\psi_{cp,N}$ is the breakout splitting factor; and N_b is the basic single-anchor breakout strength. For the test specimens, A_{Nc}/A_{Nco} = 0.32 (Specimen 1) and 0.42 (Specimen 2); $\psi_{ed,N}$ = 0.74 (Specimen 1) and 0.75 (Specimen 2); and $\psi_{ec,N} = \psi_{c,N} = \psi_{cp,N} = 1$.

For a group of headed bars with embedment (effective) length between 280 and 635 mm (11 and 25 in.), the basic single-anchor concrete breakout strength in tension, N_b, can be calculated using Eq. (17.6.2.2.3) of ACI 318-19 increased by a factor of 5/3. Thus

$$N_b = 3.9\left(\frac{5}{3}\right)\lambda_a\sqrt{f_c'}h_{ef}^{5/3} \text{ (SI)} \quad (7a)$$

$$N_b = 16\left(\frac{5}{3}\right)\lambda_a\sqrt{f_c'}h_{ef}^{5/3} \text{ (U.S.)} \quad (7b)$$

where λ_a is a factor that accounts for the use of lightweight concrete; and h_{ef} is the effective embedment length. The 5/3 factor is meant to take the calculated strength from a 5% fractile, as targeted in Chapter 17 of ACI 318-19, to a median strength (4/3 increase) and to account for cracking conditions under service loads in the connection (5/4 increase). The steel contribution to breakout strength is calculated assuming the transverse reinforcement within $0.75h_{ef}$ on each side of the bar group, above and below, is effective in resisting breakout-induced forces. For a group of headed bars placed in two layers, as in the test specimens

$$N_s = \frac{(1.5h_{ef} + s_{hb})}{s_{tie}}A_{tie}f_{yt} \quad (8)$$

where s_{hb} is the spacing between the two layers of headed bars (100 mm [4 in.]); s_{tie} is the spacing of column ties (200 mm [8 in.]); A_{tie} is the cross-sectional area of the legs of a tie parallel to the headed bars (260 mm^2 [0.4 in.^{2}]); and f_{yt} is the nominal yield strength of the transverse steel (414 MPa [60 ksi]).

The calculated breakout strength for the test specimens ($N_{cbg} + N_s$), using the cylinder compressive strength and f_{yt} = 414 MPa (60 ksi), was 676 and 556 kN (152 and 125 kip) for Specimen 1 and Specimen 2, respectively. Given that the forces that developed in the headed bar groups were greater than that corresponding to the yield strength of the bars (approximately 1380 kN [310 kip]), it seems that the breakout strength equations are very conservative when applied to beam-column connections with headed bars. This is believed to be due to the contribution of the diagonal strut in the joint to concrete breakout strength within the joint, as discussed next.

Proposed method for calculating breakout strength in exterior beam-column connections—In a beam-column joint with a beam headed bar embedment length greater than or equal to approximately the beam effective depth/1.5, the joint shear is primarily resisted by a diagonal strut (Fig. 12). Assuming that the joint shear demand is less than the joint shear strength, the formation of such a strut prevents a breakout failure from developing within the joint, and thus, a breakout failure could only develop above the joint region. If

the joint shear stress is greater than the joint shear strength, on the other hand, the initiation of a joint shear failure would likely trigger a breakout failure within and above the joint. The breakout strength of the headed bar group anchorage would thus be the lesser of the tensile force corresponding to the joint shear strength and that corresponding to the breakout strength above the joint.

From equilibrium of horizontal forces in the joint, the horizontal joint shear force V_j can be calculated in terms of the tensile force in the headed bar group as follows

$$V_j = T - V_{col} = \frac{M_b}{jd} - V_{col} \quad (9)$$

where T is the tensile force in the headed bar group; V_{col} is the shear force in the column above the joint; M_b is the beam moment at the face of the column; and jd is the internal lever arm in the beam at the column face. The ratio between M_b and V_{col} depends on the location of inflection points in the column above and below the joint and in the beam. For the test specimens

$$M_b = \frac{V_{col}L_c}{L_b}\left(L_b - \frac{h_c}{2}\right) \quad (10)$$

and

$$V_j = V_{col}\left[\left(L_c - \frac{h_cL_c}{2L_b}\right)\frac{1}{jd} - 1\right] \quad (11)$$

where L_c is the distance between inflection points in the column (3315 mm [130.5 in.]); L_b is the distance from the center of the column to the beam inflection point (3160 mm [124.4 in.]); and h_c is the column depth (610 mm [24 in.]); refer to Fig. 1 for specimen dimensions. Taking jd = 7/8 of the effective beam depth (495 mm [19.5 in.]) results in an internal lever arm of 435 mm (17.1 in.) and the following relationship between the joint shear and the column shear.

$$V_j = 5.9V_{col} \quad (12)$$

The tensile force in the headed bar group associated with the nominal shear strength of the joint, T_j, can be calculated combining Eq. (9) and (11) and setting the joint shear V_j equal to the nominal joint shear strength $V_{n,j}$.

$$T_j = V_{n,j}\left[1 + \frac{1}{\left[\left(L_c - \frac{h_cL_c}{2L_b}\right)\frac{1}{jd} - 1\right]}\right] = 1.17V_{n,j} \quad (13)$$

As discussed earlier, it is recommended that joint shear stress in exterior beam-column joints be calculated based on a joint effective depth equal to the effective (embedment) length of the headed bars, h_{ef}. It is also recommended that for exterior joints of non-seismic or OMFs with headed bars, the joint shear stress at nominal strength be taken as $1.0\lambda\sqrt{f_c'}$ MPa ($12\lambda\sqrt{f_c'}$ psi). Thus

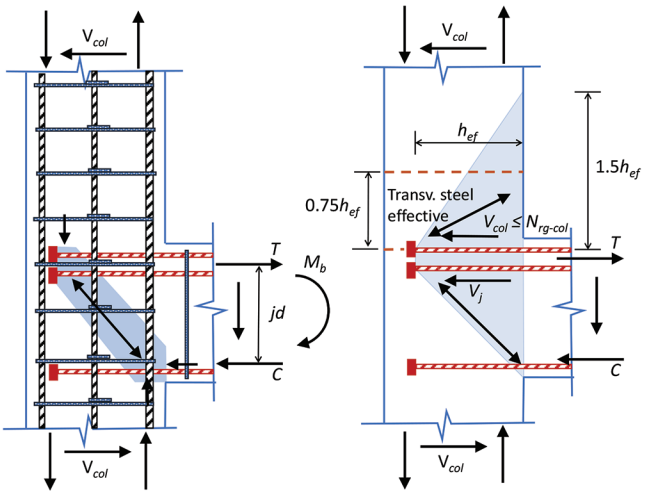


Fig. 12—Joint diagonal strut and assumed breakout-induced forces and failure surface in beam-column connection (not all forces shown).

$$V_{n,j} = 1.0\lambda\sqrt{f_c'}b_jh_{ef}\,(\text{SI}) \quad (14a)$$

$$V_{n,j} = 12\lambda\sqrt{f_c'}b_jh_{ef}\,(\text{U.S.}) \quad (14b)$$

where b_j is the effective joint width calculated in accordance with Chapter 15 of ACI 318-19.

The tensile force in the headed bar group associated with the breakout strength above the joint, $T_{bf\text{-}col}$, can be calculated by combining Eq. (9) and (12) and setting the column shear V_{col} equal to the breakout strength above the joint (Eq. (15))

$$T_{bf\text{-}col} = 6.9N_{rg\text{-}col} \quad (15)$$

where $N_{rg\text{-}col}$ is the breakout strength above the joint, taken as the summation of a concrete contribution $N_{cbg\text{-}col}$ and a steel contribution $N_{s\text{-}col}$. The concrete contribution to breakout strength above the joint, $N_{cbg\text{-}col}$, can be calculated as half of the calculated breakout strength obtained using Eq. (6) and assuming a failure developing from the center of the top layer of beam longitudinal bars (Fig. 12). This can be done by taking the A_{Nc}/A_{Nco} ratio in Eq. (6) as follows.

$$\frac{A_{Nc}}{A_{Nco}} = \frac{b_c}{6h_{ef}} \quad (16)$$

The contribution from the transverse reinforcement to breakout strength above the joint, $N_{s\text{-}col}$, is calculated assuming the reinforcement over a distance $0.75h_{ef}$ from the center of the top layer of beam longitudinal bars is effective in resisting breakout-induced forces.

$$N_{s\text{-}col} = \frac{(0.75h_{ef})}{s_{tie}}A_{tie}f_{yt} \quad (17)$$

The tensile strength of the headed bar group anchorage, T_n, would thus be the lesser of the tensile force associated with the joint shear strength (Eq. (13)) and that associated with the breakout strength above the joint (Eq. (15)).

Table 2—Calculated anchorage strength of headed bar group in test specimens

Specimen	h_{ef}, mm (in.)	f_c', MPa (psi)	$V_{n,j}$, kN (kip)	$N_{cbg\text{-}col}$, kN (kip)	$N_{s\text{-}col}$, kN (kip)	$N_{rg\text{-}col}$, kN (kip)	T_j, kN (kip)	$T_{bf\text{-}col}$, kN (kip)	T_n, kN (kip)	T_{max}, kN (kip)	T_n/T_{max}
1	455 (18)	40.0 (5800)	1175 (264)	122 (27.5)	180 (40.5)	302 (68.0)	1375 (309)	2087 (469)	1375 (309)	1611 (362)	0.85
2	355 (14)	37.6 (5450)	881 (198)	102 (22.9)	140 (31.5)	242 (54.4)	1028 (231)	1669 (375)	1028 (231)	1433 (322)	0.72

Table 2 lists the calculated strength contributions and the estimated peak tensile force in the headed bar group during the tests. The peak tensile force in the headed bar group was estimated as the maximum beam moment at the column face divided by 7/8 times the beam effective depth. As shown in Table 2, the calculated headed bar group anchorage strength was 85% and 72% of the calculated maximum tensile force in the headed bar group for Specimens 1 and 2, respectively. In both cases, the calculated anchorage strength was governed by the proposed nominal joint shear strength, which is consistent with the joint damage observed in the tests. Although significant breakout-related cracking above the joint was evident in Specimen 2 prior to the removal of the column axial force, it was only until severe joint damage developed that a breakout failure above the joint occurred. Additional data, however, are needed to further validate the proposed method, particularly for joints with a lower ratio between V_j and V_{col}, for which the calculated breakout capacity above the joint may govern the calculated strength of the headed bar group anchorage.

CONCLUSIONS

Based on the test results from two exterior beam-column connections and analyses conducted, the following conclusions can be drawn.

- Specimen 1, with a headed bar embedment length calculated based on the development length provisions of Chapter 25 of ACI 318-19, exhibited substantial beam flexural yielding with only moderate breakout-related cracking above the joint at the end of the test during loading with column axial force. Specimen 2, with a 22% shorter headed bar embedment length, calculated as proposed in Banaeipour et al. (2023), also exhibited beam flexural yielding, but with significantly greater breakout-related and joint shear damage.
- During loading of Specimen 1 after removal of the column axial force, severe joint damage developed, along with what could be considered moderate-to-significant breakout-related cracking. Specimen 2, on the other hand, exhibited a breakout failure above the joint, likely triggered by the excessive damage in the joint region.
- Once yielding in tension of the headed bars initiated, an increasing percentage of the bar tensile force was transferred over the back half of the embedment length and through the bearing of the head on the adjacent concrete. At tensile strains greater than approximately 0.008 at the column face, most of the bar tensile force was transferred through bearing of the head on the concrete.
- The formation of a diagonal strut in the joint between the bar heads and the joint corner corresponding to the beam and column flexural compression zones indicates that it is not possible to separate a breakout failure within the joint from a joint shear failure. The cracking pattern and severe damage in the joints at the end of the tests indicates that nominal joint shear strength should be calculated based on a joint effective depth equal to the headed bar embedment length and not the overall column depth. It is also recommended that for exterior joints of non-seismic or ordinary moment frames (OMFs), nominal joint shear strength be calculated using a stress of $1.0\lambda\sqrt{f_c'}$ MPa ($12\lambda\sqrt{f_c'}$ psi).
- The proposed method for calculating breakout strength in exterior beam-column joints led to reasonable and conservative strength estimates. Additional laboratory test data are needed to further validate this method, particularly for joints with ratios between joint shear and column shear lower than that in the test specimens.

AUTHOR BIOS

Gustavo J. Parra-Montesinos, *FACI, is a Professor of structural engineering at the University of Wisconsin–Madison, Madison, WI. He received his PhD from the University of Michigan, Ann Arbor, MI, in 2000. He is a member of ACI Committees 318, Structural Concrete Building Code, and 318S, Spanish Translation; ACI Subcommittees 318-C, Safety, Serviceability, and Analysis, and 318-H, Seismic Provisions; and Joint ACI-ASCE Committee 352, Joints and Connections in Monolithic Concrete Structures. His research interests include the inelastic behavior of reinforced concrete members and structures.*

Jacob Zeuske *is a Faculty Associate in the Department of Civil and Environmental Engineering and Manager of the Structures and Materials Testing Laboratory at the University of Wisconsin–Madison, where he received his master's degree in mechanical engineering in 2011.*

ACKNOWLEDGMENTS

Financial support for this research was provided by the ACI Foundation and the Jun and Sandy Lee Structural Research Fund at the University of Wisconsin–Madison. The support provided by nVent ERICO through the donation of headed bar and column reinforcement used in the test specimens is greatly appreciated. The findings and conclusions presented in this paper are those of the authors and do not necessarily reflect the views of the sponsors.

The authors would like to acknowledge the contributions from E. S. Thomas, M. Bajwa, and O. Carrillo—all students at the University of Wisconsin–Madison—for the construction, instrumentation, and testing of the test specimens. The valuable discussions with J. Silva (Hilti Corporation) and Professors M. Kreger (The University of Alabama), J. P. Moehle (University of California, Berkeley), B. Worsfold (University of Minnesota), and R. Lequesne (The University of Kansas) related to this research are greatly appreciated.

REFERENCES

ACI Committee 318, 2019, "Building Code Requirements for Structural Concrete (ACI 318-19) and Commentary (ACI 318R-19) (Reapproved 2022)," American Concrete Institute, Farmington Hills, MI, 624 pp.

ASTM C39/C39M-21, 2021, "Standard Test Method for Compressive Strength of Cylindrical Concrete Specimens," ASTM International, West Conshohocken, PA, 8 pp.

Banaeipour, A.; Darwin, D.; O'Reilly, M.; Lequesne, R. D.; Lepage, A.; and Blessent, M., 2023, "Development of Large High-Strength Reinforcing Bars with Standard Hooks and Heads," SM Report No. 153, The University of Kansas Center for Research, Inc., Lawrence, KS, July 2023, 428 pp.

Cheng, M.-Y.; Chen, P.-J.; Chen, C.-H.; Worsfold, B. L.; Parra-Montesinos, G. J.; and Moehle, J. P., 2025, "Effect of Reinforcement

Detailing on Cyclic Behavior of Reinforced Concrete Column-Footing Connections," *ACI Structural Journal*, V. 122, No. 4, July, pp. 19-34.

Kang, T. H.-K.; Shin, M.; Mitra, N.; and Bonacci, J. F., 2009, "Seismic Design of Reinforced Concrete Beam-Column Joints with Headed Bars," *ACI Structural Journal*, V. 106, No. 6, Nov.-Dec., pp. 868-877.

Lee, H.-J.; Yu, F.-C.; Lin, K.-C.; Wang, J.-C.; Worsfold, B. L.; and Silva, J. F., 2024, "High-Strength Headed Bars in Joints of Special Moment Frames under Cyclic Loading," *ACI Structural Journal*, V. 121, No. 6, Nov., pp. 105-120.

Worsfold, B. L., and Moehle, J. P., 2023a, "Shear-Reinforced Concrete Breakout Design Methodology for Moment Transfer at Column-Foundation Connections," *Engineering Structures*, V. 283, May, Article No. 115783.

Worsfold, B. L., and Moehle, J. P., 2023b, "Moment Transfer at Column-Foundation Connections: Analytical Studies," *ACI Structural Journal*, V. 120, No. 2, Mar., pp. 205-216.

Worsfold, B. L.; Moehle, J. P.; and Silva, J. F., 2022, "Moment Transfer at Column-Foundation Connections: Physical Tests," *ACI Structural Journal*, V. 119, No. 5, Sept., pp. 95-110.

ARE YOU A RESEARCHER?

SIGN UP FOR ORCID TODAY!



ORCID provides a digital identifier that distinguishes you from every other researcher and, through integration in key research workflows such as manuscript and grant submission, supports automated linkages between you and your professional activities, ensuring that your work is recognized.

ORCID services are FREE and it's as easy as **1-2-3**.

WWW.ORCID.ORG

ACI STRUCTURAL JOURNAL TECHNICAL PAPER

Title No. 122-S71

Tensile Cracking and Flexure-Shear Capacity of Recycled Aggregate Concrete

by Sourav Chakraborty and Kolluru V. L. Subramaniam

The reduction in shear capacity when using recycled coarse aggregate (RCA) made from crushed concrete is evaluated in terms of tensile cracking and fracture-surface characteristics. An experimental investigation into the fracture and flexure-shear behaviors of recycled aggregate concrete (RAC) is presented. Replacing natural aggregate in concrete proportioned for 30 MPa (4350 psi) compressive strength with RCA results in lower compressive and tensile strengths. The tensile fracture-surface characteristics vary between RAC and natural aggregate concrete (NAC). While the surface area created in the tensile fracture of RAC is larger than that of NAC, the fracture surface profile in RAC has a smaller roughness than NAC. In the flexure-shear response of reinforced concrete beams, the dilatancy determined from the slip and crack opening displacements measured across the shear crack is smaller in RAC than in NAC. The failure in the reinforced beam is due to the frictional stress transfer loss across the primary shear crack. There is a larger decrease in the shear capacity with the use of RAC than indicated by the reduction in compressive strength. The reduced shear capacity of reinforced RAC is due to the combined influences of reduced tensile strength and crack surface roughness. The design provisions require calibration for crack surface roughness when using RAC in structural applications.

Keywords: aggregate interlock; fracture; recycled aggregate concrete (RAC); recycled coarse aggregate (RCA); shear capacity.

INTRODUCTION

Aggregate contributes 70% of the volume of concrete, the world's most-used manufactured material. The inevitability of demolishing old structures creates the need for dumping and recycling waste material. On the other hand, the production and transportation of natural aggregate (NA) cause carbon emissions and environmental effects. The depleting stocks of NA and the need to effectively use material from old structures have inspired using recycled aggregate in concrete construction. The use of recycled coarse aggregate (RCA) derived from crushing old concrete is regulated by the codes of practice. Indian Code of Practice IS 383:2016[1] allows 25% replacement of NA with RCA for plain concrete and 20% for reinforced concrete up to a strength of 25 MPa (3626 psi). European Code of Practice BS EN 206:2013[2] allows a replacement of 50% for concrete with no risk of corrosion and 30% when carbonation-induced corrosion is possible. American Code of Practice ACI 318-14[3] does not specify any absolute limit and is determined by the type and susceptibility to freezing and thawing.

RCA is produced from concrete collected from demolished buildings, broken pavements, and crushed laboratory samples.[4-11] Steel, wood, and brick are segregated from debris before further processing. Similar ingredients are combined to minimize this segregation process.[12] The rest of the production process mainly consists of several rounds of crushing the larger pieces into smaller sizes suitable for use as aggregate and sorting them according to requirements.

RCA extracted from concrete has two phases: parent aggregate and old residual mortar. The surfaces of the RCA consist of fracture planes created through the parent concrete. The fracture planes are generated during manufacturing, which involves disintegration and crushing. The fracture planes pass through the mortar and aggregate in the old concrete. The production process also creates internal fractures within the aggregate phase of RCA.[13-15] The aggregate-mortar interface in the RCA is quite strong, having survived the production process.[13-15]

In recycled aggregate concrete (RAC), NA is replaced with RCA. In the RAC, the RCA is surrounded by a new mortar matrix. When RCA is placed inside a new mortar matrix, two new interfaces are created: between the new mortar and the aggregate and mortar phases in the RCA.[16] A porous interfacial transition zone (ITZ) is formed between the old and new mortar interfaces in the RAC.[15] The pores in the ITZ absorb water, reducing the workability and lowering the strength of concrete.[17-19] In the early ages, water absorption by the porous ITZ and the rough texture of RCA can produce faster setting and gain quicker strength in RAC.[20]

Interfaces in concrete made with RCA play a critical role in determining the tensile fracture in the RAC.[13,14] Due to the complex interface structure, RAC's cracking and tensile strength are determined by the weak planes formed by new mortar interfaces and preexisting fractures in the aggregate. The weak planes tend to decrease the tensile stress for cracking and cause an overall decrease in the tensile strength of RAC compared to natural aggregate concrete (NAC).[13-15] The cracking in RAC starts at a lower stress than in NAC, and more splitting cracks are produced.[4] There is also a decrease in the tensile fracture energy in the RAC up to 40% due to the increased porosity at the new mortar interface.[5,21] Existing models suggest that RAC is more brittle, and the critical crack opening for RAC is smaller than that of NAC.[5,18]

ACI Structural Journal, V. 122, No. 5, September 2025.

MS No. S-2024-055.R3, doi: 10.14359/51746815, received December 25, 2024, and reviewed under Institute publication policies. Copyright © 2025, American Concrete Institute. All rights reserved, including the making of copies unless permission is obtained from the copyright proprietors. Pertinent discussion including author's closure, if any, will be published ten months from this journal's date if the discussion is received within four months of the paper's print publication.

Table 1—Physical properties of NA and RCA

	10 mm (0.4 in.) NA	20 mm (0.8 in.) NA	10 mn (0.4 in.) RCA	20 mm (0.8 in.) RCA
Specific gravity	2.64	2.66	2.34	2.47
Impact resistance, %*	11.26	5.56	25.73	13.73
Water absorption, %	0.3	0.5	6.88	2.04

*Should be <30%[1] for use in structural applications.

Table 2—Mass proportions for 1.0 m³ of concrete mixture

Fine aggregate	20 mm (0.8 in.) coarse aggregate	10 mm (0.4 in.) coarse aggregate	Fly ash	Cement	Water
836 kg (1843 lb)	610 kg (1345 lb)	499 kg (1100 lb)	108 kg (238 lb)	252 kg (556 lb)	180 kg (397 lb)

The shear capacity of reinforced RAC has also been evaluated for developing structural applications. The shear capacity of reinforced RAC depends on many factors, such as the source of the RCA, the strengths of the old and new mortars in RAC, and even the mixing procedure. Although the mode of shear failure does not change with RCA replacement, changes have been observed in the shear crack's angle and shape.[6,22] The available data in the literature on shear capacity and the flexure-shear behavior of reinforced concrete beams made with RAC is inconclusive. Most studies show a shear strength decrease between 12 and 18% with full replacement of NA with RCA.[22-27] For beams without shear reinforcement, an even larger reduction in shear capacity of up to 28% has been observed.[28] However, some studies indicated similar shear strength from RAC and NAC.[6,27,29-31] Depending on the mixing process, some studies have also shown a slight improvement in the shear strength.[10,32] Fundamental insights into the reasons for variation in the results are not yet available in the literature. While it is acknowledged that the flexure-shear load response of reinforced concrete beams is intimately related to the tensile cracking in the concrete, the formation and propagation of flexure-shear cracks in reinforced RAC beams have not been explored. The nature of the flexure-shear cracking in RAC beams and its influence on the shear capacity is also not fully understood. A comparative evaluation of the flexure-shear cracking in NAC and RAC is required to provide a basis for the observed changes in the shear capacities of reinforced concrete.

The tensile stress primarily forms flexure-shear cracks in concrete. With the formation of shear cracks, a load-resistance mechanism in a reinforced concrete beam supported by shear transfer across the shear crack develops.[33] Shear cracks are dilatant.[34] The shear resistance is mobilized as the rough crack surfaces slip past each other. Simultaneously, there is an opening of the shear crack.[35] The shear resistance mobilized across the crack depends on the fracture surface of the shear crack formed under tensile stresses.[36] A fundamental evaluation of the shear capacity requires an assessment of the tensile fracture and the post-cracking shear stress transfer across the tensile fracture surfaces formed in shear. The shear failure in reinforced concrete is produced by a loss of shear stress transfer across the critical shear crack.[33,37-42] The nature of the tensile fracture surfaces is crucial to the shear transfer and the load capacity.[41]

RESEARCH SIGNIFICANCE

This study aims to understand the flexure-shear behavior of reinforced RAC beams related to crack propagation and failure mechanisms in reinforced concrete beams. The NAC and RAC are made using an identical matrix composition to study the influence of coarse aggregate. Flexure-shear cracking is evaluated in reinforced NAC and RAC beams. Observations about the nature of tensile fracture surfaces are related to the post-cracking response of reinforced beams up to the shear capacity. The influence of tensile fracture-surface characteristics on the shear failure mechanism in reinforced concrete beams is evaluated. A comparative evaluation of tensile and shear cracking in NAC and RAC is performed to provide a basis for the observed differences in shear capacity. Additionally, this study explores the shortcomings in the current code provisions in predicting the shear capacity of RAC beams. It provides solutions by exploring the possibility of integrating crack roughness into shear capacity predictions. This will help better understand and predict the shear capacity of RAC beams, resulting in easier incorporation of RCA in engineering practices.

EXPERIMENTAL PROGRAM

Two distinct coarse aggregate fractions of 10 and 20 mm (0.4 and 0.8 in.) were used. The physical properties of NA and RCA were evaluated according to IS 2386-4:1963[43] and are shown in Table 1. The proportions by mass of the concrete formulated with conventional aggregate are outlined in Table 2. The aggregate masses provided in the table pertain to the saturated surface-dry (SSD) state. Within this context, NAC and RAC serve as alternative designations for concrete made using only NA or RCA, respectively, as the coarse aggregate. Concrete mixture designs were prepared for a characteristic strength of 30 MPa (4350 psi) and a target mean strength of 38.25 MPa (5548 psi) using NA, as explained in IS 10262:2009.[44] In the RAC, the matrix composition was identical to that of the NAC, but the NA was replaced with RCA while keeping all other proportions identical. This allowed for the evaluation of the influence of aggregate on fracture and shear behaviors while keeping the matrix composition consistent between NAC and RAC.

A drum mixer was used to mix the concrete. Before adding water, the dry components were mixed for 2 minutes. The aggregate was place into the oven in a dry state and mixed with half the water for 2 minutes. Cement was added

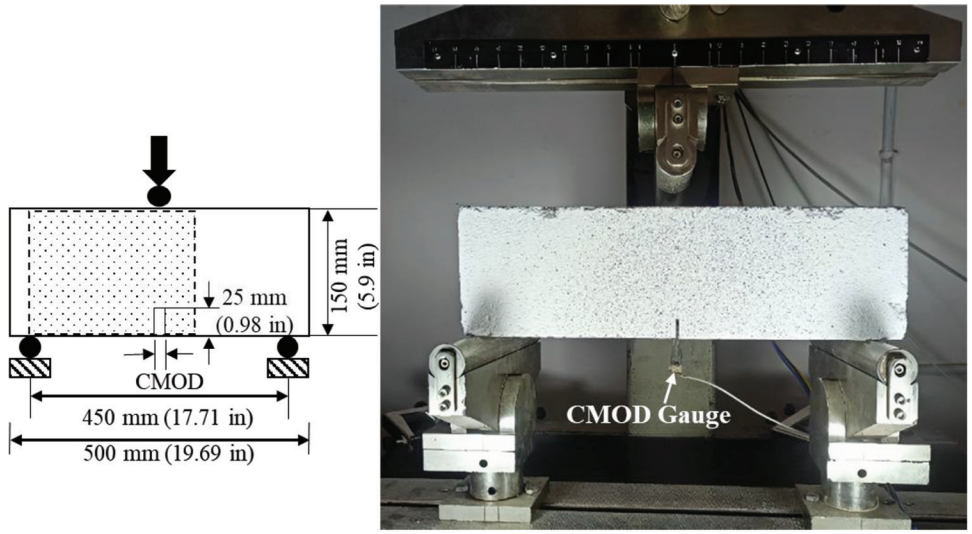


Fig. 1—Fracture test setup: (a) typical arrangement of CMOD measurement; and (b) photograph of test setup.

to the mixer, and mixing continued for 2 minutes while the remaining water was added. Water corresponding to the absorption capacity of concrete was added to ensure an SSD condition of the aggregate in the concrete. After mixing, the concrete was placed into the forms in three layers. Each layer was tamped, and after the final layer, the mold was vibrated on a table vibrator. The specimens were demolded at 24 hours and moist-cured at 27°C (80.6°F) for 28 days. For NAC and RAC, the 28-day compressive strengths obtained from 150 mm (5.9 in.) cubes were 42.8 and 32.0 MPa (6207 and 4641 psi), respectively. There is, therefore, a 21.6% decrease in the compressive strength when replacing NAC with RAC in the concrete.

Fracture testing

Fracture testing was conducted on notched beams subjected to flexural testing under center-point loading following EN 14651:2005.[45] The tests were conducted using a servo-hydraulic closed-loop test system. Prismatic beams measuring 500 mm (19.9 in.) in length and having a cross section of 150 x 150 mm (5.9 x 5.9 in.) were used. A notch was cut in every beam before the testing. The dimensions of the notch were 25 mm (1 in.) in depth and 2 mm (0.08 in.) in thickness. A circular wet saw was used to cut the notch. These notched beams were tested over an effective length of 450 mm (17.7 in.). A crack mouth opening displacement (CMOD) gauge was installed across the notch on the soffit of the beam. A CMOD control rate of 0.05 mm/min (0.002 in./min) was adopted to control the tests. The schematic diagram and photograph of the fracture test setup are shown in Fig. 1.

Flexure-shear testing

Reinforced concrete beams were tested for shear in a conventional three-point flexure testing configuration with a shear span-depth ratio of 2.25. Prismatic beams with dimensions measuring 125 mm (4.92 in.) in width, 250 mm (9.84 in.) in depth, and 1000 mm (39.4 in.) in length were tested. The concrete beams were reinforced in flexure using a pair of 16 mm (0.63 in.) diameter steel reinforcing bars. Steel reinforcement with a yield stress of 500 MPa (72.5 ksi), conforming to IS 1786:2008,[46] was used. Flexure-shear cracking was ensured on one side of the beam by providing shear stirrups on one side of the beam. Closed stirrups measuring 8 mm (0.31 in.), spaced at 110 mm (4.33 in.) intervals, were used as shear reinforcement.

A servo-hydraulic test system with a loading setup that met the requirements of EN 14651:2005[45] was used. The load-displacement response was tracked throughout the testing procedure, and full-field surface displacements were measured using the digital image correlation (DIC) technique. Linear variable displacement transducers (LVDTs) were securely fixed to stationary frames positioned outside the beams to gauge deflections at the midpoint of the span and over the supports. A schematic illustrating the shear beam configuration and an image showing the test equipment can be observed in Fig. 2.

Digital image correlation

Surface displacements were determined from the digital images of the specimen taken during the loading using a correlation between the images in the deformed state and the reference image taken in the undeformed state. The methodology derives surface displacements by comparing the initial image of an object with its subsequent images. The strain fields were calculated from the gradients of the displacement fields. The test setup for the image acquisition consisted of a 5-megapixel camera placed at a 1 m (3.28 ft) distance from the test specimen. The digital images captured during the test were stored for analysis. The images underwent a process of physical calibration, and the inherent random error associated with measurements was determined to be approximately 0.02 pixels. Regarding measurement resolution, the most conservative estimates were identified at 1.54 μm (6.1×10^{-5} in.) for displacement and 4 με for strain.[47,48]

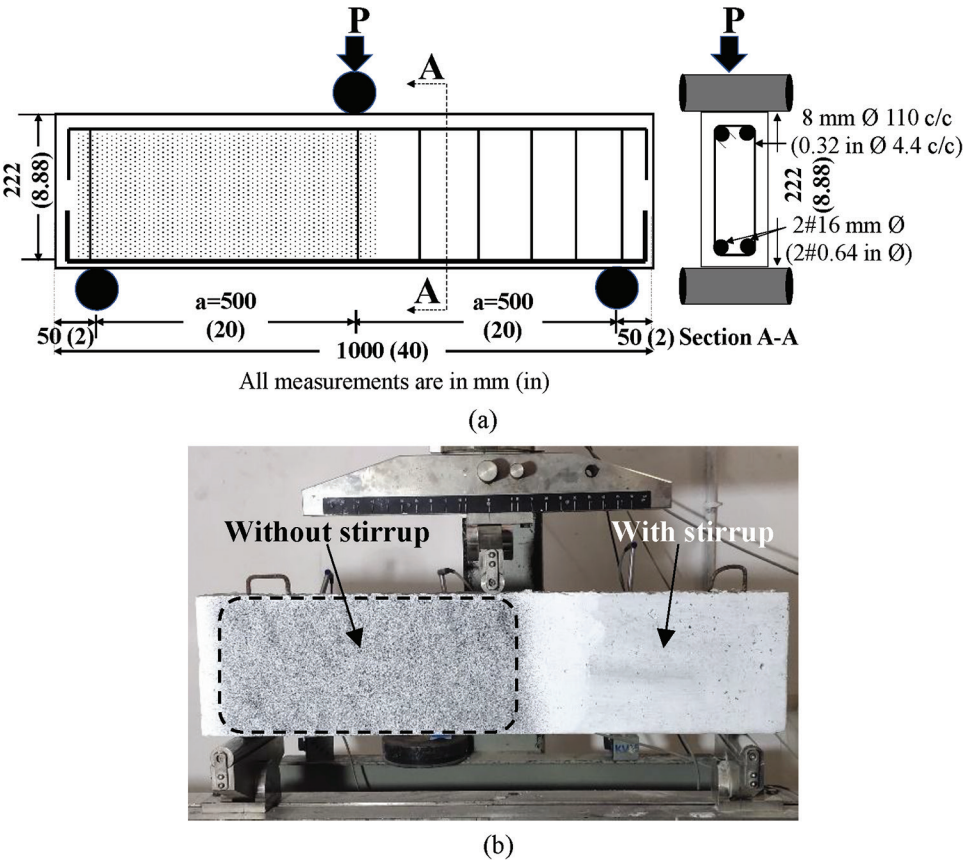


Fig. 2—(a) Illustration of shear beam and loading configuration; and (b) photograph of test setup.

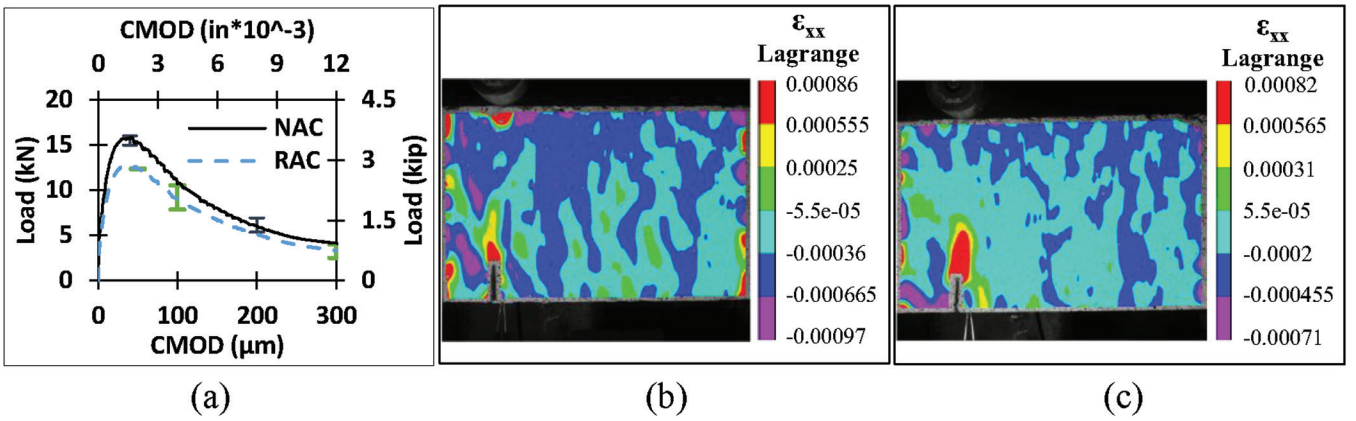


Fig. 3—(a) Fracture responses of NAC and RAC; longitudinal strain contour for specimens at peak load of: (b) NAC; and (c) RAC.

EXPERIMENTAL RESULTS AND ANALYSIS

Figure 3(a) displays the fracture test responses of the NAC and RAC beams. The load-CMOD responses are plotted as an average of four specimens each, and the scatter is represented with error bars, showing the maximum variation observed among the four specimens tested for each case. There are differences in the pre- and post-peak fracture responses recorded from the beams made with natural coarse aggregate (NCA) and RCA. RAC beams had smaller pre-peak stiffness and attained a lower peak load in the flexural response. The peak load in RCA beams was 19% lower than in NCA beams. This reduction is consistent with the decrease in compressive strength, where the cube strength decreased from 42.8 to 32 MPa (6207 to 4641 psi).

The contours of strain (ε_{xx}) at the peak load in the fracture response are plotted in Fig. 3(b) and (c). There was an intense localization of strain contours above the notch, which was produced by the crack. The localization of strain was used to follow the nucleation and propagation of the crack along the depth of the beam. At the peak load, RAC had a larger crack advancement than NAC. At the peak load in the fracture response, the crack propagated a significant portion along the beam depth in RAC.

The fracture response in flexure was used to determine the cohesive stress response of the concrete using a

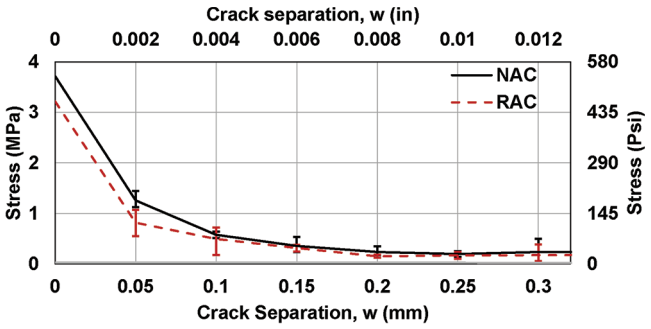


Fig. 4—Cohesive stress-crack opening relationship obtained using inversion procedure.

cracked-hinge idealization of the beam with a crack. The tensile strength and the cohesive stress as a function of the crack opening were obtained using an inversion procedure developed previously.[49,50] The nonlinearity produced by the crack is represented as a nonlinear hinge centered on the crack. The moment-rotation response of the hinge was derived for cracks of different lengths. The beam equilibrium response was traced by progressively increasing the cohesive crack length within the hinge.[49,51,52] For any crack length within the hinge, the crack tip was identified with the tensile strength of the concrete. The stress in the cohesive crack below the crack tip was obtained for the assumed cohesive stress relationship. The cohesive stress across the crack opening established equilibrium at the crack location. The moment-rotation relationship for the cracked hinge was previously derived for a general multi-linear form of cohesive stress-crack separation (σ-w) relationship.[49]

The load response of the beam with the nonlinear hinge was determined by increasing the rotation of the hinge in small increments. The hinge length was assumed to be 40 mm (1.57 in.).[49] The crack opening at the bottom of the beam corresponding to the increasing hinge rotation was also calculated. The load response was derived from the combined deflections of the elastic beams at the ends of the hinge and the hinge. The load response of the beam was traced by increasing the rotation of the hinge portion. An initial σ-w relationship was assumed when deriving the load response. In the assumed σ-w relationship, initial guesses were taken for the stresses (σ_i) corresponding to the predefined values of crack openings (w_i). An inverse analysis process was adopted to determine the values of σ_i of the beams by comparing the predicted and experimental load-CMOD responses. The cohesive σ-w relationship parameters were iterated systematically to minimize the error function and match the predicted and experimental load responses. The cohesive stress (σ) was determined at predefined crack separation values (w) through a numerical minimization of residuals.

The method of multi-variable optimization was employed to determine the cohesive relationship in the form of stresses (σ_i) corresponding to predefined crack separation (w_i).[51,52] Determination of σ_i was performed in multiple stages. In the first step, the elastic modulus of the beam was optimized for further calculation of the rest of the variables by minimizing an objective function defined as the least-squares residual between the measured and predicted load responses

$$\text{Norm} = \frac{1}{n}\sqrt{\sum_{i=1}^{n}\left(P_i^{experimental} - P_i^{theoretical}\right)^2} \quad (1)$$

where $P_i^{experimental}$ and $P_i^{theoretical}$ refer to the i-th loads in the experimental and numerically predicted load responses in the initial linear load response; and n refers to the number of points considered in the analysis. Then, the tensile strength (f_t) and the initial softening portion of the σ-w response were derived using the load response up to a CMOD of 0.1 mm (0.004 in.). The objective function selected for this optimization stage is given in Eq. (2)

$$\text{Norm} = \left|\left(P_u^{experimental} - P_u^{theoretical}\right)\right| + \frac{1}{n}\sqrt{\sum_{i=1}^{n}\left(P_i^{experimental} - P_i^{theoretical}\right)^2} \quad (2)$$

where $P_u^{experimental}$ represents the peak load in the experimental test response; $P_u^{theoretical}$ signifies the peak load determined by numerical analysis; $P_i^{experimental}$ and $P_i^{theoretical}$ refer to the i-th loads at specified CMOD values in the experimental and numerically predicted load responses; and n denotes the number of CMOD load points considered up to 0.1 mm (0.004 in.).

In the last stage of the inversion, the coordinates of the cohesive stresses at predetermined crack opening values of up to 0.3 mm (0.12 in.) were determined to be optimized by minimizing the least-squares residual of the form given by Eq. (1). A flattening of the response was observed in the load-CMOD responses beyond 0.3 mm (0.12 in.) CMOD. The values of stress were very small, nearly zero. The analysis for residual stress was not followed for crack openings larger than 0.3 mm (0.12 in.).

Figure 4 shows the cohesive stress crack opening relationships for the NAC and RAC given in terms of crack closing stresses, σ_i, at predefined crack separation w_i. The σ-w responses were obtained from the individual fracture beams, and the average values are shown with the scatter bars indicating the ranges. The tensile strengths, f_t, obtained from the inversion for the NAC and RAC were 3.71 and 3.21 MPa (538 and 466 psi), respectively. For reference, NAC and RAC's compressive strengths were 42.8 and 32 MPa (6208 and 4641 psi), respectively. The tensile strength of concrete is less sensitive to using RCA than the compressive strength. The f_t corresponds to the stress at the initiation of the crack. The tensile strength of RAC is lower than that of NAC, causing the crack initiation at a lower stress.

At any given crack separation, w_i, the cohesive σ_i in NAC is higher than in RAC. The σ for crack separation values larger than 0.15 mm (0.006 in.) were very similar. The stress decreased to an insignificant value for crack separation larger than 0.15 mm (0.006 in.). The stress σ with increasing crack separation w indicated a very rapid decrease initially. The rate of initial stress loss in RAC was quicker than in NAC. There was also a significantly larger area under the σ-w curve for the NAC than for the RAC, indicating larger energy absorption for creating crack surface area.

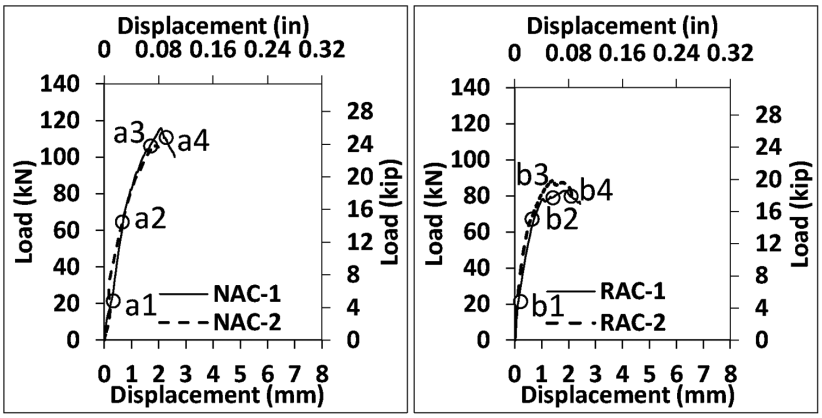


Fig. 5—Load responses obtained from flexure-shear testing: (a) NAC; and (b) RAC.

FLEXURE-SHEAR RESPONSE AND ANALYSIS

Figures 5(a) and (b) illustrate the load-displacement behaviors of steel-reinforced concrete beams of NAC and RAC, respectively. Although the load responses from the NAC and RAC beams show nominal similarity, a discernible reduction in the maximum load was observed in the RAC beams compared to the NAC counterparts. Notably, RAC beams exhibited a lower ultimate shear capacity than NAC beams. Load-displacement responses among the NAC and RAC beams demonstrated good consistency. The failure occurred immediately after reaching the peak load, accompanied by a sudden widening of the shear crack at midheight. All the beams experienced brittle failure, and even in the displacement control mode of testing, post-peak load response could not be effectively controlled. The average peak loads of the NAC and RAC beams were 112 and 82 kN (25.2 and 18.4 kip), respectively. There is, therefore, a 26% decrease in the flexure-shear capacity when replacing NAC with RAC in reinforced concrete beams. The decrease in the shear capacity is higher than the reduction in the compressive strength with the use of RAC.

The crack formation and propagation during the load responses of the beams were evaluated using the DIC data. Four points from both NAC and RAC beams were selected, as marked in Fig. 5, to analyze and further understand the crack initiation and growth. Figures 6 and 7 show the longitudinal strain (ε_{xx}) contours at the marked points in the load-displacement response. There is an intense localization of strain contours leading up to the formation of a crack. The localization in strains occurs before physical separation produced by a crack is visible. Therefore, the formation of cracking can be evaluated very accurately using the DIC technique. Cracks were identified in the part of the beam where shear reinforcement was not provided. Several flexural cracks formed in the early part of the load-displacement curve. These cracks were formed in a 40 to 60 kN (9 to 13.5 kip) load range in NAC beams. The same pattern was observed in the load range between 20 and 50 kN (4.5 and 11.2 kip) in RAC beams. Shear cracks emerged from the flexural cracks and propagated toward the neutral axis. In NAC beams, shear cracks developed at a load exceeding 60 kN (13.5 kip); in RAC beams, the same happened at a lower load of approximately 50 kN (11.2 kip). The primary shear crack started growing with increasing load and was fully developed at peak load. Close to the peak load, the primary shear crack extended from the level of flexural reinforcement up to the load point. The creation of a wedge at the top and a splitting crack beneath the flexural reinforcing bar caused the failure. The primary shear crack was approximately 45 degrees to the horizontal. An abrupt opening of the shear crack was observed at the peak load, followed by a drop in the load resistance.

The comparison of the cracking patterns inferred from strain contours reveals a generally similar trend in both RAC and NAC beams. When analyzing Fig. 6(b) and 7(b), it was observed that in NAC, only flexural cracks formed for a comparable load, while in RAC, the development of shear cracks initiated from the flexural crack. Analysis of the images indicates that cracks that initiate as flexural cracks away from the center of the beam ultimately evolve into shear cracks. Figures 6(c) and 7(c) depict fully cracked sections, with the primary shear crack fully established between the tensile reinforcement and the load application point. However, the cracking pattern indicated by the strain contours in RAC beams occurs at a significantly lower load than in NAC. Figures 6(d) and 7(d) demonstrate that the angle of cracking and the pattern of crack formation closely resemble each other in both NAC and RAC beams at the respective points of failure. The formation of these shear cracks is complete before reaching the peak load, leading to a brittle failure caused by an abrupt opening of the primary shear crack. This opening across the primary shear crack is evident as a clear discontinuity. Fully formed shear cracks are oriented at a 45-degree angle in RAC and NAC beams. The breakdown of load resistance across the crack results in a loss of load-carrying capacity and leads to failure.

The contour plots of longitudinal displacement (U_x) are presented in Fig. 8(a). Physical cracks are identified from the discontinuities in the displacement contours. These contours help determine relative movement across the crack. The relationship between crack slip and crack opening displacement is termed dilatancy.[35,36] Crack slip refers to the relative displacement of the two sides of the crack along the crack direction (U_S). The corresponding crack opening is the relative displacement perpendicular to the crack direction (U_w). These values were calculated from horizontal and vertical

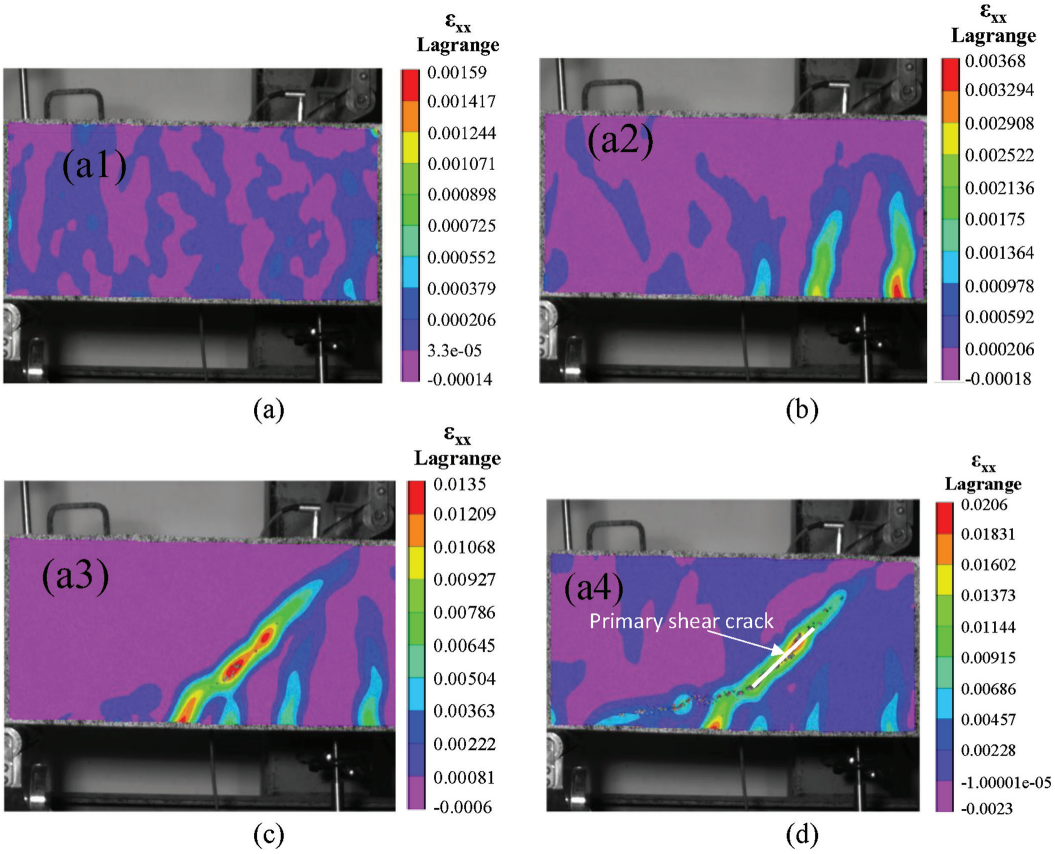


Fig. 6—Longitudinal strain contours for NAC-1 at points marked in load response: (a) a1 (23.4 kN [5.26 kip]); (b) a2 (67.2 kN [15.1 kip]); (c) a3 (110 kN [24.7 kip]); and (d) a4 (112.3 kN [25.2 kip]).

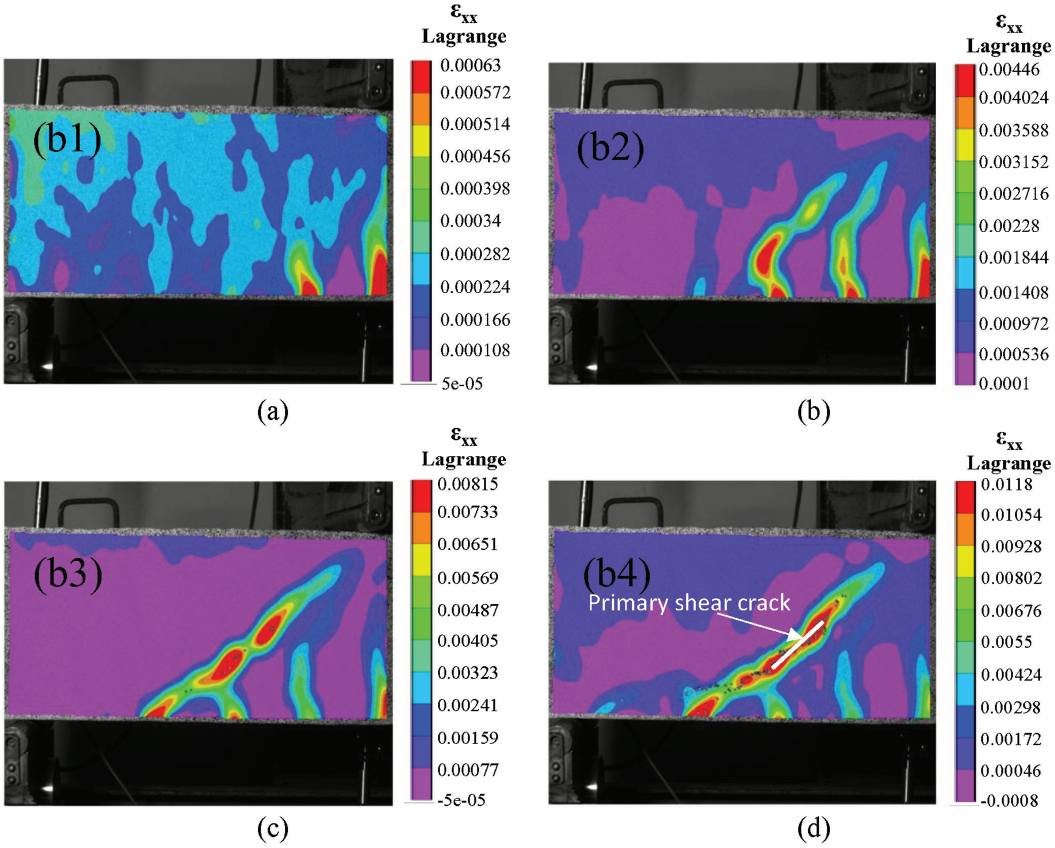
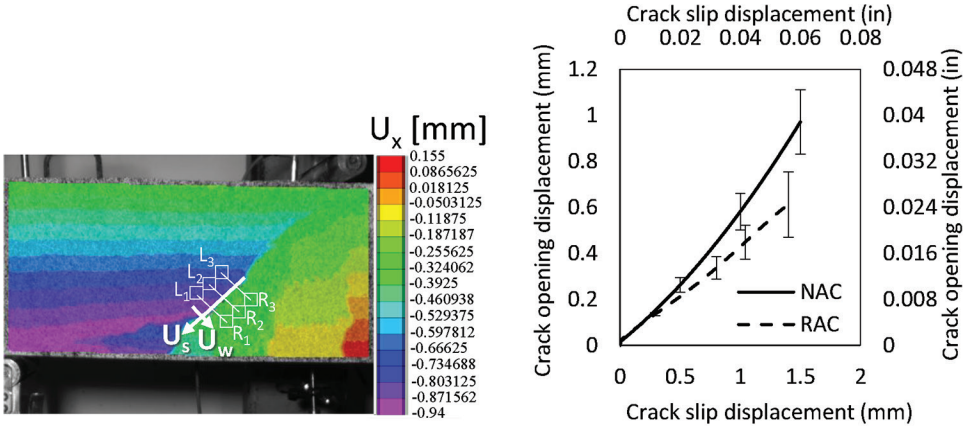


Fig. 7—Longitudinal strain contours for RAC-1 at points marked in load response: (a) a1 (23.4 kN [5.26 kip]); (b) a2 (67.2 kN [15.1 kip]); (c) a3 (80 kN [18 kip]); and (d) a4 (77.6 kN [17.5 kip]).



(a) (b)

Fig. 8—(a) Contour plot of U_x from NAC beam; and (b) measured dilatancy in terms of crack opening corresponding to given slip across primary shear crack in NAC and RAC beams.

displacements at matching points on either side of the primary shear crack within specified boxes. The procedure developed previously for accurately determining relative displacements along and across the crack was adopted.[35] The continuous increase in slip and crack opening with loading is evident from the measurements. Notably, the dilatant response differs between RAC and NAC. The measurements from NAC beams indicate a larger crack opening displacement for a given slip compared to RAC. As slip increases, the gap between the crack opening displacement measured from NAC and RAC widens.

DISCUSSION

Comparing Fig. 6(a) and 7(a), it is evident that cracks initiate at a lower load in RAC beams than in NAC beams. Figure 6(a) displays no initial signs of crack development, while Fig. 7(a) indicates strain concentration suggestive of flexural crack formation. This disparity can be attributed to the lower tensile strength inherent in RAC, which results in cracking at reduced load levels in RAC beams. When subjected to loads of similar magnitudes, the advancement of shear cracking in RAC beams is noticeably more pronounced than in NAC beams. This heightened progression of shear cracking in RAC is attributed to its lower tensile strength, which promotes the early initiation and spreading of shear cracks at lower load levels. Significantly, the development of the shear crack between the flexural reinforcement and the load application point occurs at an earlier load in RAC beams compared to NAC beams. Despite resemblances in the visual appearance of cracks, the marked disparity in tensile strength characteristics of RAC substantially affects the pattern of flexure-shear crack formation in reinforced beams.

The final capacity in shear is determined by the equilibrium established across the shear crack.[34,36] The resistance generated by the rough crack faces contributes to the load capacity of reinforced concrete in shear. Aggregate interlock contributes significantly to shear load resistance.[13,34,36] The load resistance derived from the shear transfer across the shear crack depends on the nature of surfaces in contact and the tensile flexural reinforcement. The failure of stress transfer across the rough cracks is due to the loss of aggregate interlock.[36] The brittle failure due to loss of aggregate interlock produces a large opening of the shear crack at shear failure in beams. Some indication of the rough surfaces in contact is obtained from the dilatancy measured during the relative slip between the two crack faces. The higher dilatancy indicates a rougher crack interface in the NAC. The crack trajectory of the shear crack indicates that it is produced by tensile cracking. An analysis of the tensile fracture surface created in the fracture tests is essential to develop an understanding of the shear resistance and capacity in reinforced concrete beams.

Figure 9 shows the fracture surfaces in NAC and RAC beams from the fracture test in flexure. In the case of NAC, no aggregates were found to be broken across the fracture plane formed in the beam. The failure plane in NAC passed through the new ITZ, leaving some adhered mortar in the aggregate. Most of the aggregates were broken across the fracture plane formed in RAC. Some aggregates and their counterparts are marked in Fig. 9. The same shapes have been used to indicate counterparts in the two fracture surfaces. Solid shapes mark unbroken aggregates, and dashed-line ones indicate broken aggregates.

The creation of these different kinds of fracture surfaces shows a change in the fracture mechanism due to the incorporation of RCA. The surface created by the tensile fracture was further analyzed using a laser-based profile measurement system. The surface profile of a 50 mm (2 in.) square area of the fracture surface was scanned using a laser displacement sensor. Data were collected at 0.1 mm (0.004 in.) intervals in both directions. Test setup and typical scanned areas are shown in Fig. 10. The surface profile was measured with an accuracy of 2 µm (0.008×10^{-5} in.). The movement speed of the platform was 600 mm/min (23.6 in./min). In the surface profile plot, the x- and y-coordinates refer to locations along the width (along the notch) and depth (along the direction of crack growth) of the fracture beam, respectively. A typical scan showing the surface profile in terms of the measured height at the different locations given by x- and y-coordinates within the 50 mm (2 in.) square area is shown in Fig. 10(b). The normalized surface area, defined

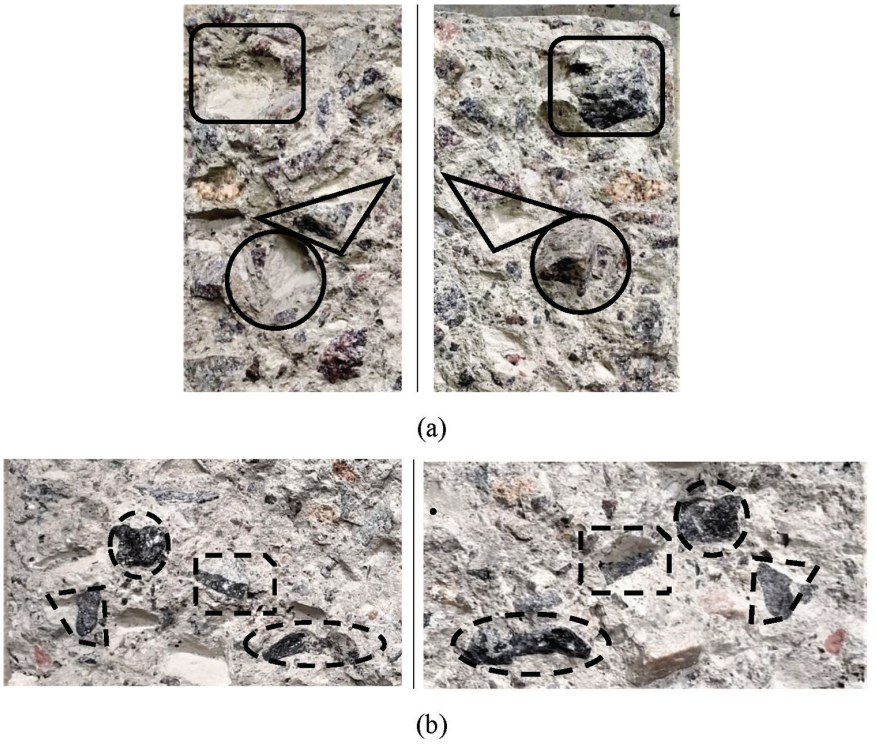


Fig. 9—Counterpart surfaces created by tensile fracture from: (a) NAC; and (b) RAC, where solid and dashed lines correspond to unbroken and broken aggregates, respectively.

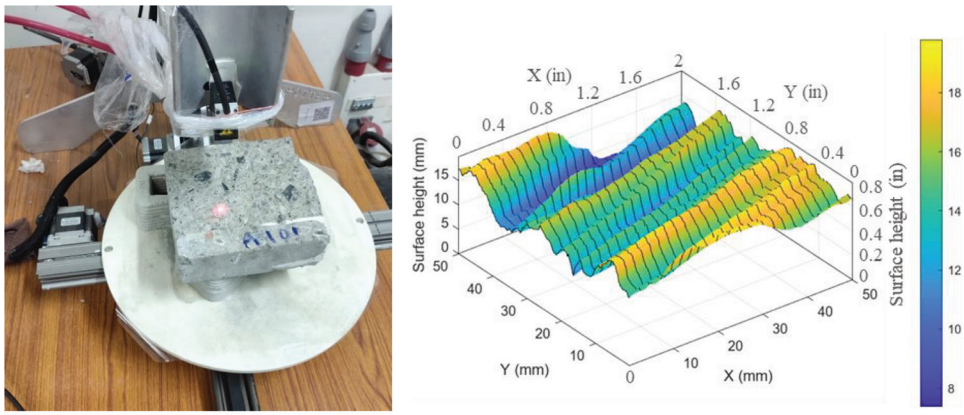


Fig. 10—(a) Photograph of experimental setup for laser displacement sensor; and (b) representative scanned area.

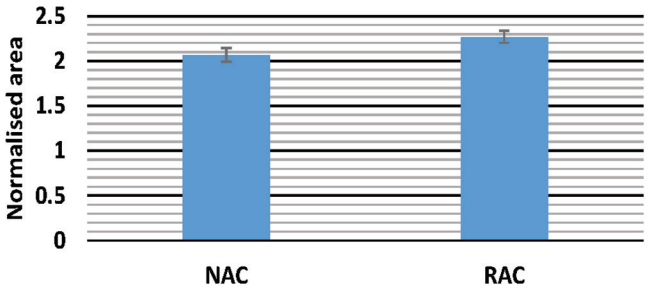


Fig. 11—Normalized tensile fracture surface areas from RAC and NAC.

as the ratio of the actual surface area to the projected planar surface area from the fracture surfaces in NAC and RAC, is plotted in Fig. 11. The measurements in Fig. 11 indicate that a larger surface area is created by a tensile fracture in RAC compared to NAC. The larger surface area in RAC has previously been shown to be due to weak planes in the RAC identified with preexisting cracks in the RCA and the weak interfaces of RCA with new mortar.[13]

Measurements indicate that RAC creates a larger fracture surface area than NAC. Visual observations, however, indicated differences in the surface profiles of the fracture surfaces in the NAC and RAC. The fracture surface formed in the RAC looked smoother than in the NAC. A more detailed analysis of the fracture surface profiles was performed to evaluate the surface roughness created by tensile fracture. Typical scanned profiles from the tensile fracture surfaces with varying y-coordinates along lines of constant x are shown in Fig. 12(a) and (b) for NAC and RAC, respectively. The surface undulations are shown as variations in the surface profile about the mean. A visual examination reveals

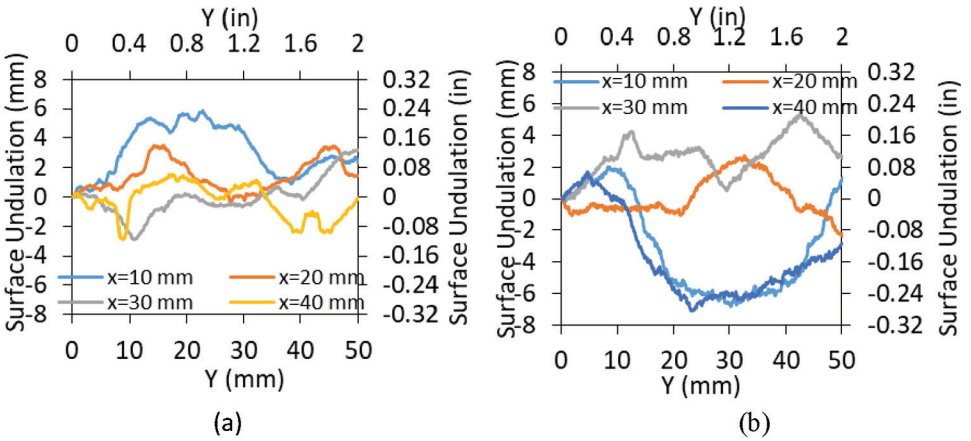


Fig. 12—Typical surface profiles from tensile fracture in: (a) NAC; and (b) RAC.

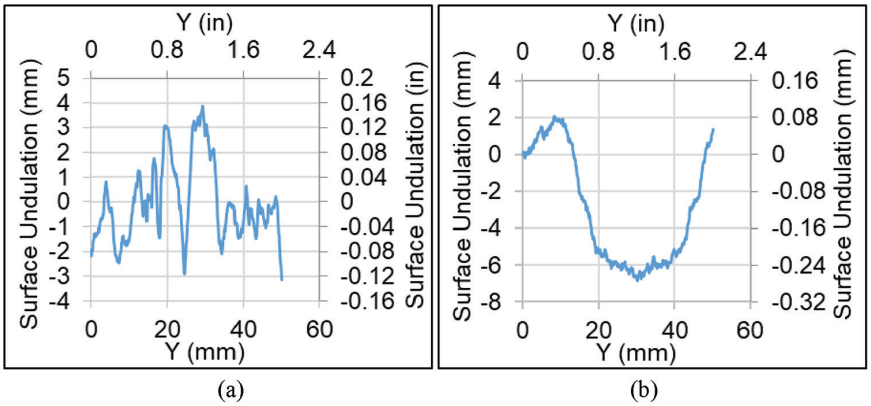


Fig. 13—Undulations in typical profiles of fracture surfaces in: (a) NAC; and (b) RAC.

more peaks in NAC than in RAC. There is also a difference in the length scale of the variations in the tensile fracture surfaces. The differences between the peaks and valleys in the RAC are on a larger scale, giving it an overall increase in the true area. Even visually, the fracture surface formed in RAC appeared to be smoother between larger undulations over the larger length scale.

The surface roughness analysis was performed using the measured profiles from the fracture surfaces, shown in Fig. 12. The average and the root-mean-square (RMS) values of the roughness are presented in the table. The average and RMS roughness are the average absolute and RMS deviations of the surface profile from the profile mean line, respectively. Skewness and kurtosis are the third and fourth central moments of the amplitude density function for the surface profile, respectively. The statistical parameters were calculated from the measured undulations about the mean as an average of 10 consecutive lines spaced 0.1 mm (0.004 in.) apart. Averaging for 10 consecutive lines reduces the variation and instrumental errors. From each fracture specimen, the statistical measures shown in Table 3 were taken from two areas of 50 x 50 mm (2 x 2 in.) dimensions, and in each area, lines were taken along the x-coordinate at three locations. The average and RMS of the undulations on the fracture surfaces in RAC are higher than the corresponding surfaces in NAC. The mean and the RMS measures of the undulations essentially coincide with the larger surface area measured from the RAC fracture surface compared to the NAC fracture surface. The average and RMS deal with the values of the frequency distribution, not the order of the distribution, and provide a reliable indication of surface roughness if the frequency distribution of the undulations about the mean follows the perfectly normal (or Gaussian) distribution with zero skewness and a kurtosis value of 3.

Table 3—Statistical parameters derived from deviations about mean (undulations) from measured surface profiles

	Average	RMS	Skewness	Kurtosis
NAC	1.86 (0.27)	2.42 (0.24)	–0.23 (0.09)	3.14 (0.76)
RAC	2.5 (0.28)	3.02 (0.34)	0.55 (0.24)	2.64 (0.08)

The applicability of the normal distribution to the undulations measured from the fracture surface areas is illustrated using typical surface profiles from NAC and RAC. Figure 13 shows the undulations along a y-coordinate from typical surface profiles of one scanned line from the fracture surfaces in NAC and RAC. These lines may not represent the entire surface but provide good visual evidence of the disparity between the number of peaks and valleys in NAC and RAC beams for the same given measurement length. The corresponding frequency distributions of the deviation of the surface profiles about the means from the fracture surface profiles from NAC and RAC are shown in Fig. 14. The frequency histograms of the measured deviation about

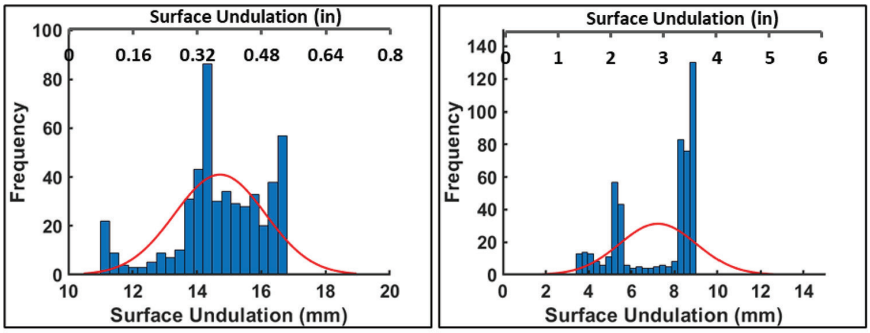


Fig. 14—Frequency distribution and Gaussian histogram fit to undulations in measured surface profiles: (a) NAC; and (b) RAC.

the mean appear bimodal, and the Gaussian distribution does not provide a good fit.

The frequency distribution of the deviation in the surface profile about the mean indicates the presence of two length scales in the measurement. The bimodal distribution indicates prominent peaks at two different length scales: the short and long length scales. Fundamental differences in the distribution of the undulations at the length scales contribute differently to surface area and roughness. Because the undulations lack conformity with the normal distribution, kurtosis is a parameter that can indicate surface roughness. Kurtosis is the fourth moment of the frequency distribution function, measured over the sampling length. From Fig. 15, higher kurtosis values result from rougher surfaces with more peaks and valleys, and lower kurtosis values indicate surfaces with undulations over a larger length scale. The kurtosis determined from the measured surface profiles in the tensile fracture surface of RAC and NAC are shown in Table 3. The kurtosis value from RAC is smaller than 3.0, while the corresponding value from NAC is larger than 3.0. A smaller kurtosis in RAC indicates fewer peaks and valleys and an overall smoother surface compared to NAC. The kurtosis confirms the visual observations in the measured undulations on the fracture surface. The fracture surface in NAC is rougher, with more peaks and valleys. The fracture surface in RAC has a significant variation on the larger length scale but smaller variations on the smaller scale. This contributes to lower roughness in the crack surface created by tensile fracture in RAC compared to NAC.

The roughness of the crack surface positively influences the ability of stress transfer across a crack—cracks exhibiting greater roughness produce a more pronounced dilatant response. In the context of NAC, failure is characterized by a larger crack opening at the point of failure due to its larger roughness, which produces a more significant dilation with slip. Consequently, it implies that the load transfer across the primary shear crack is sustained over a larger crack opening displacement in reinforced NAC beams than in RAC beams. The comparatively smaller roughness of the tensile crack in RAC promotes easier sliding between the sections on either side of the primary shear crack. As a result, there is a reduction in the shear capacity due to the relatively easier sliding between the faces. The reduced roughness further leads to a dilatant response, featuring a smaller opening for a given slip along the shear cracks in RAC.

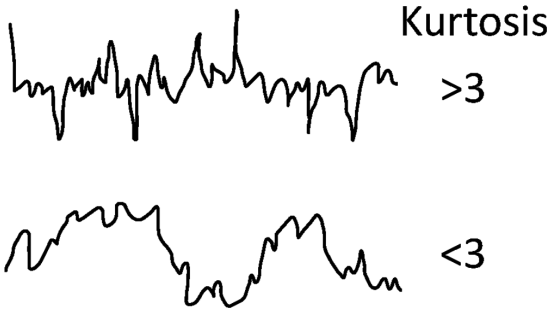


Fig. 15—Profiles and their size distributions showing effect of kurtosis.

The shear capacity of concrete is intimately linked with the tensile fracture characteristics. The tensile strength determines the load at which the shear crack is fully established. The shear capacity depends on the roughness of the tensile crack formed in shear. Using RCA decreases the shear capacity by reducing the tensile strength and crack roughness. There is a compounding of the influences of tensile strength and tensile crack roughness that contribute to lower shear capacity. The lower tensile strength leads to the shear crack formation at a lower load in reinforced RAC beams.

Additionally, the smaller roughness of the shear crack formed under tensile stress leads to a lower capacity of the crack to transmit shear. In conventional design, the influence of tensile strength on shear capacity is included in empirical formulations with a term that includes the influence of tensile strength using a square root of compressive strength term. A comparison of the shear capacities predicted by the different code equations for reinforced NAC and RAC beams is shown in Table 4. As a general observation, the code equation predictions are conservative compared to the experimental values. However, predicted values from the code equations are more conservative for the NAC than for the RAC. The compounded influences of reduced tensile strength and roughness are not captured in a single parameter derived from the compressive strength of concrete. Therefore, using RAC in structural applications requires careful calibration of the code equations to maintain the same margin of safety.

Typical equations of shear capacity are empirical and are of the form

Table 4—Experimental and predicted shear capacities of reinforced NAC and RAC beams

	Shear strength for sections without shear reinforcement		
	NAC	RAC	Code prediction
Experimental	1.96 + 0.11 MPa (284.27 ± 15.95 psi)	1.51 + 0.08 MPa (218.92 ± 11.60 psi)	—
Eurocode[53]	1.39 MPa (201 psi)	1.32 MPa (191 psi)	$V_{Rd,c} = [0.18k(100\rho_l f_{ck})^{1/3}]b_w d$
ACI 318-14[3]	1.14 MPa (165.74 psi)	1.07 MPa (155.59 psi)	$v_c = \left(1.9\sqrt{145.04f_c'} + 2500\rho\frac{Vd}{M}\right)\left(\frac{1}{145.04}\right) \le 3.5\sqrt{145.04f_c'}$

Note: $k = 1 + \sqrt{200/d} \le 2.0$; $\rho_l = (A_s/b_w d) \le 0.02$.

$$v_c = f\left(\sqrt{f_c}, k_1, k_2, k_3, k_4\right) \quad (3)$$

where the influence of the concrete compressive strength is accounted for in terms of its tensile strength using the square root (compressive strength); and k_1, k_2, k_3, and k_4 are factors to account for the lightweight aggregate, size of the aggregate, percentage of longitudinal reinforcement, and shear span-depth ratio.

The conventional design criteria that were derived from the compressive strength of concrete, while conservative, were found to provide an inconsistent margin of safety in predicting shear capacity. Understanding the fracture-surface characteristics and the factors that control the tensile fracture in RAC is therefore important to develop rational design procedures for shear design using RCA. It is proposed that a modification to the equation be considered by introducing an additional term that accounts for the roughness of the fracture surface.

$$v_c = f\left(\sqrt{f_c}, k_1, k_2, k_3, k_4, r\right) \quad (4)$$

The term r would account for the roughness of the tensile fracture surface. The change in shear capacity from NAC to RAC is a function of aggregate and matrix strength. Based on data available for different sources of RCA, their strength, and the strength of the concrete they are incorporated into, a partial safety factor can be included in the existing code provisions. For the shear capacity-predicting models, the crack surface's roughness must be considered an input variable. As measuring the roughness can be difficult every time, it can be made a function of the aggregate strength from the tensile testing and the grade of concrete. A fracture-based failure criterion could be developed that provides a better design prediction in shear with uniform consistency.

CONCLUSIONS

The tensile fracture in natural aggregate concrete (NAC) and recycled aggregate concrete (RAC) was evaluated and related to reinforced concrete beams' shear cracking and capacity. The tensile fracture in concrete was evaluated using a flexure test. The surface created by tensile fracture was evaluated for roughness. Shear cracking in reinforced shear beams was evaluated and related to observations of tensile fracture. The following summarizes the study's conclusions.

1. Tensile fracture in RAC occurs at a lower tensile strength than in NAC. The cohesive stress crack separation relation shows that the initial decrease in residual stress is faster in RAC than in NAC. This results in lower peak load and fracture energy measured from RAC compared to NAC.

2. Scanning of fracture surfaces reveals that the crack in RAC has a larger surface area than in NAC. However, the undulations in the fracture surface indicate that a rougher surface is formed in NAC than in RAC. The fracture surfaces in RAC and NAC are fundamentally different, considering undulations over different length scales. The number of peaks and valleys for the same length is lower in RAC than in NAC. Hence, rougher fracture surfaces are created in NAC despite having a lower fracture surface area.

3. All the beams tested in shear failed just after reaching the peak load. At the time of failure, shear cracks were fully established. The shear cracks primarily formed in the direction of the principal tension. Failures in shear were sudden and triggered by loss of stress transfer across the crack.

4. RAC beams tested in flexure-shear cracked at a lower applied load than NAC, just like fracture beams, due to the lower tensile strength of RAC. As a result of a smoother surface, reduced crack dilatancy is observed across the shear crack in RAC. Reduced crack dilatancy allows the crack's opposite sides to slide against each other without much resistance. The combined effect of lower tensile strength and reduced dilatancy causes the crack in RAC beams to start early and grow faster, causing more advanced cracks compared to NAC at comparable loads.

5. Inferior shear performance in RAC is due to the combined effect of tensile strength degradation and reduction in the aggregate interlock capacity of the tensile shear crack.

6. Current code provisions do not account for the impact of crack roughness on the shear capacity of concrete beams. The roughness of cracks significantly affects shear transfer, yet this factor remains inadequately addressed in current standards.

7. A separate partial safety factor should be designed for RAC, considering the crack roughness to predict the shear capacity better.

AUTHOR BIOS

Sourav Chakraborty *is a Postdoctoral Fellow at the Indian Institute of Technology (IIT) Madras, Chennai, Tamil Nadu, India. He received his PhD in civil engineering from IIT Hyderabad, Sangareddy, Telangana, India. His research interests include recycled aggregate concrete, the shear response of reinforced concrete, and experimental fracture mechanics.*

Kolluru V. L. Subramaniam, *FACI, is a Professor in the Department of Civil Engineering at IIT Hyderabad. He received his BTech from IIT Delhi, New Delhi, Delhi, India, and his PhD from Northwestern University, Evanston, IL. He is a member of ACI Committees 123, Research and*

Current Developments, and 215, Fatigue of Concrete; and Joint ACI-ASCE Committee 446, Fracture Mechanics of Concrete.

REFERENCES

1. IS 383:2016, "Coarse and Fine Aggregate for Concrete—Specification (Third Revision)," Bureau of Indian Standards, New Delhi, India, 2016.

2. BS EN 206:2013+A1:2016, "Concrete - Specification, Performance, Production and Conformity," British Standards Institution, London, UK, 2016.

3. ACI Committee 318, "Building Code Requirements for Structural Concrete (ACI 318-14) and Commentary (ACI 318R-14)," American Concrete Institute, Farmington Hills, MI, 2014, 520 pp.

4. González-Fonteboa, B.; Martínez-Abella, F.; Martínez-Lage, I.; and Eiras-López, J., "Structural Shear Behaviour of Recycled Concrete with Silica Fume," *Construction and Building Materials*, V. 23, No. 11, 2009, pp. 3406-3410. doi: 10.1016/j.conbuildmat.2009.06.035

5. Ghorbel, E., and Wardeh, G., "Influence of Recycled Coarse Aggregates Incorporation on the Fracture Properties of Concrete," *Construction and Building Materials*, V. 154, 2017, pp. 51-60. doi; 10.1016/j.conbuildmat.2017.07.183

6. Ignjatović, I. S.; Marinković, S. B.; and Tošić, N., "Shear Behaviour of Recycled Aggregate Concrete Beams with and without Shear Reinforcement," *Engineering Structures*, V. 141, 2017, pp. 386-401. doi: 10.1016/j.engstruct.2017.03.026

7. Adams, M. P.; Fu, T.; Cabrera, A. G.; Morales, M.; Ideker, J. H.; and Isgor, O. B., "Cracking Susceptibility of Concrete Made with Coarse Recycled Concrete Aggregates," *Construction and Building Materials*, V. 102, Part 1, 2016, pp. 802-810. doi: 10.1016/j.conbuildmat.2015.11.022

8. Ceia, F.; Raposo, J.; Guerra, M.; Júlio, E.; and de Brito, J., "Shear Strength of Recycled Aggregate Concrete to Natural Aggregate Concrete Interfaces," *Construction and Building Materials*, V. 109, 2016, pp. 139-145. doi: 10.1016/j.conbuildmat.2016.02.002

9. Waseem, S. A., and Singh, B., "Shear Transfer Strength of Normal and High-Strength Recycled Aggregate Concrete – An Experimental Investigation," *Construction and Building Materials*, V. 125, 2016, pp. 29-40. doi: 10.1016/j.conbuildmat.2016.08.022

10. Arezoumandi, M.; Smith, A.; Volz, J. S.; and Khayat, K. H., "An Experimental Study on Flexural Strength of Reinforced Concrete Beams with 100% Recycled Concrete Aggregate," *Engineering Structures*, V. 88, 2015, pp. 154-162. doi: 10.1016/j.engstruct.2015.01.043

11. Arezoumandi, M.; Smith, A.; Volz, J. S.; and Khayat, K. H., "An Experimental Study on Shear Strength of Reinforced Concrete Beams with 100% Recycled Concrete Aggregate," *Construction and Building Materials*, V. 53, 2014, pp. 612-620. doi: 10.1016/j.conbuildmat.2013.12.019

12. Pantini, S., and Rigamonti, L., "Is Selective Demolition Always a Sustainable Choice?" *Waste Management*, V. 103, 2020, pp. 169-176. doi: 10.1016/j.wasman.2019.12.033

13. Chakraborty, S., and Subramaniam, K. V. L., "Fracture and Shear Behaviours of Recycled Aggregate Concrete," *Building for the Future: Durable, Sustainable, Resilient: Proceedings of the* fib *Symposium 2023 – Volume 1*, A. Ilki, D. Çavunt, and Y. S. Çavunt, eds., Springer Nature Switzerland, Cham, Switzerland, 2023, pp. 468-475

14. Chakraborty, S., and Subramaniam, K. V. L., "Influences of Matrix Strength and Weak Planes on Fracture Response of Recycled Aggregate Concrete," *Theoretical and Applied Fracture Mechanics*, V. 124, 2023, Article No. 103801. doi: 10.1016/j.tafmec.2023.103801

15. Chakraborty, S., and Subramaniam, K. V. L., "Evaluation of Cracking and Cohesive Fracture Response in Recycled Aggregate Concrete," *Materials and Structures*, V. 56, No. 7, 2023, Article No. 130. doi: 10.1617/s11527-023-02193-x

16. Behera, M.; Bhattacharyya, S. K.; Minocha, A. K.; Deoliya, R.; and Maiti, S., "Recycled Aggregate from C&D Waste & Its Use in Concrete – A Breakthrough Towards Sustainability in Construction Sector: A Review," *Construction and Building Materials*, V. 68, 2014, pp. 501-516. doi: 10.1016/j.conbuildmat.2014.07.003

17. Dhir, R. K.; de Brito, J.; Silva, R. V.; and Lye, C. Q., "Properties and Composition of Recycled Aggregates," *Sustainable Construction Materials: Recycled Aggregates*, Woodhead Publishing, Sawston, UK, 2019, pp. 89-141.

18. Musiket, K.; Rosendahl, M.; and Xi, Y., "Fracture of Recycled Aggregate Concrete under High Loading Rates," *Journal of Materials in Civil Engineering*, ASCE, V. 28, No. 6, 2016, p. 04016018. doi: 10.1061/(ASCE)MT.1943-5533.0001513

19. Thomas, C.; de Brito, J.; Cimentada, A.; and Sainz-Aja, J. A., "Macro- and Micro- Properties of Multi-Recycled Aggregate Concrete," *Journal of Cleaner Production*, V. 245, 2020, Article No. 118843. doi: 10.1016/j.jclepro.2019.118843

20. Biswal, U. S., and Dinakar, P., "A Mix Design Procedure for Fly Ash and Ground Granulated Blast Furnace Slag Based Treated Recycled Aggregate Concrete," *Cleaner Engineering and Technology*, V. 5, 2021, Article No. 100314. doi: 10.1016/j.clet.2021.100314

21. Fallahnejad, H.; Davoodi, M. R.; and Nikbin, I. M., "The Influence of Aging on the Fracture Characteristics of Recycled Aggregate Concrete through Three Methods," *Structural Concrete*, V. 22, No. S1, 2021, pp. E74-E93. doi: 10.1002/suco.202000119

22. Arabiyat, S.; Abdel Jaber, M.; Katkhuda, H.; and Shatarat, N., "Influence of Using Two Types of Recycled Aggregates on Shear Behavior of Concrete Beams," *Construction and Building Materials*, V. 279, 2021, Article No. 122475. doi: 10.1016/j.conbuildmat.2021.122475

23. Choi, H. B.; Yi, C. K.; Cho, H. H.; and Kang, K. I., "Experimental Study on the Shear Strength of Recycled Aggregate Concrete Beams," *Magazine of Concrete Research*, V. 62, No. 2, 2010, pp. 103-114. doi: 10.1680/macr.2008.62.2.103

24. Liu, B.; Feng, C.; and Deng, Z., "Shear Behavior of Three Types of Recycled Aggregate Concrete," *Construction and Building Materials*, V. 217, 2019, pp. 557-572. doi: 10.1016/j.conbuildmat.2019.05.079

25. Xiao, J.; Xie, H.; and Yang, Z., "Shear Transfer across a Crack in Recycled Aggregate Concrete," *Cement and Concrete Research*, V. 42, No. 5, 2012, pp. 700-709. doi: 10.1016/j.cemconres.2012.02.006

26. Schubert, S.; Hoffmann, C.; Leemann, A.; Moser, K.; and Motavalli, M., "Recycled Aggregate Concrete: Experimental Shear Resistance of Slabs without Shear Reinforcement," *Engineering Structures*, V. 41, 2012, pp. 490-497. doi: 10.1016/j.engstruct.2012.04.006

27. Sagheer, A. M.; Tabsh, S. W.; and Yehia, S., "The Structural Behavior of Reinforced Concrete Beams Made with Locally Produced Recycled Aggregate in the UAE," *Buildings*, V. 13, No. 10, 2023, Article No. 2597. doi: 10.3390/buildings13102597

28. Trindade, J. C.; Garcia, S. L. G.; Lacerda, T. N.; and Resende, T. L., "Analysis of the Shear Behavior of Reinforced Recycled Aggregate Concrete Beams Based on Shear Transfer Mechanisms," *Engineering Structures*, V. 293, 2023, Article No. 116616. doi: 10.1016/j.engstruct.2023.116616

29. Zhang, H.; Calvi, P. M.; Lehman, D.; Kuder, K.; and Roeder, C., "Response of Recycled Coarse Aggregate Concrete Subjected to Pure Shear," *Journal of Structural Engineering*, ASCE, V. 146, No. 5, 2020, p. 04020075. doi: 10.1061/(ASCE)ST.1943-541X.0002620

30. Fathifazl, G.; Razaqpur, A. G.; Isgor, O. B.; Abbas, A.; Fournier, B.; and Foo, S., "Shear Capacity Evaluation of Steel Reinforced Recycled Concrete (RRC) Beams," *Engineering Structures*, V. 33, No. 3, 2011, pp. 1025-1033. doi: 10.1016/j.engstruct.2010.12.025

31. Setkit, M.; Leelatanon, S.; Imjai, T.; Garcia, R.; and Limkatanyu, S., "Prediction of Shear Strength of Reinforced Recycled Aggregate Concrete Beams without Stirrups," *Buildings*, V. 11, No. 9, 2021, Article No. 402. doi: 10.3390/buildings11090402

32. Anike, E. E.; Saidani, M.; Ganjian, E.; Tyrer, M.; and Olubanwo, A. O., "Evaluation of Conventional and Equivalent Mortar Volume Mix Design Methods for Recycled Aggregate Concrete," *Materials and Structures*, V. 53, No. 1, 2020, Article No. 22. doi: 10.1617/s11527-020-1457-3

33. Collins, M. P.; Bentz, E. C.; and Sherwood, E. G., "Where is Shear Reinforcement Required? Review of Research Results and Design Procedures," *ACI Structural Journal*, V. 105, No. 5, Sept.-Oct. 2008, pp. 590-600.

34. Gali, S., and Subramaniam, K. V. L., "Influence of Cohesive Stresses on Shear Capacity of Reinforced SFRC Beams without Stirrups: A Discrete Crack Approach," *Engineering Fracture Mechanics*, V. 206, 2019, pp. 218-232. doi: 10.1016/j.engfracmech.2018.11.035

35. Gali, S., and Subramaniam, K. V. L., "Investigation of the Dilatant Behavior of Cracks in the Shear Response of Steel Fiber Reinforced Concrete Beams," *Engineering Structures*, V. 152, 2017, pp. 832-842. doi: 10.1016/j.engstruct.2017.09.050

36. Gali, S., and Subramaniam, K. V. L., "Improvements in Fracture Behavior and Shear Capacity of Fiber Reinforced Normal and Self Consolidating Concrete: A Comparative Study," *Construction and Building Materials*, V. 189, 2018, pp. 205-217. doi: 10.1016/j.conbuildmat.2018.08.194

37. Fenwick, R. C., and Paulay, T., "Mechanisms of Shear Resistance of Concrete Beams," *Journal of the Structural Division*, ASCE, V. 94, No. 10, 1968, pp. 2325-2350. doi: 10.1061/JSDEAG.0002092

38. Park, R., and Paulay, T., *Reinforced Concrete Structures*, John Wiley & Sons, Inc., New York, 1975.

39. Taylor, H. P. J., "Shear Strength of Large Beams," *Journal of the Structural Division*, ASCE, V. 98, No. 11, 1972, pp. 2473-2490. doi: 10.1061/JSDEAG.0003376

40. Sato, Y.; Tadokoro, T.; and Ueda, T., "Diagonal Tensile Failure Mechanism of Reinforced Concrete Beams," *Journal of Advanced Concrete Technology*, V. 2, No. 3, 2004, pp. 327-341. doi: 10.3151/jact.2.327

41. Walraven, J. C., "Aggregate Interlock: A Theoretical and Experimental Analysis," PhD thesis, Delft University of Technology, Delft, the Netherlands, 1980, 210 pp.

42. Walraven, J. C., and Reinhardt, H. W., "Concrete Mechanics. Part A: Theory and Experiments on the Mechanical Behavior of Cracks in Plain and Reinforced Concrete Subjected to Shear Loading," NASA STIRecon Technical Report 82, 1981.

43. IS 2386-4:1963, "Methods of Test for Aggregates for Concrete - Part 4: Mechanical Properties (Reaffirmed 2002)," Bureau of Indian Standards, New Delhi, India, 1963.

44. IS 10262:2009, "Concrete Mix Design Proportioning—Guidelines (First Revision)," Bureau of Indian Standards, New Delhi, India, 2009.

45. EN 14651:2005, "Test Method for Metallic Fibered Concrete – Measuring the Flexural Tensile Strength (Limit of Proportionality (LOP), Residual)," European Committee for Standardization, Brussels, Belgium, 2005.

46. IS 1786:2008, "High Strength Deformed Steel Bars and Wires for Concrete Reinforcement — Specification (Fourth Revision)," Bureau of Indian Standards, New Delhi, India, 2008.

47. Bruck, H. A.; McNeill, S. R.; Sutton, M. A.; and Peters, W. H. III, "Digital Image Correlation Using Newton-Raphson Method of Partial Differential Correction," *Experimental Mechanics*, V. 29, No. 3, 1989, pp. 261-267. doi: 10.1007/BF02321405

48. Schreier, H. W., and Sutton, M. A., "Systematic Errors in Digital Image Correlation Due to Undermatched Subset Shape Functions," *Experimental Mechanics*, V. 42, No. 3, 2002, pp. 303-310. doi: 10.1007/BF02410987

49. Chiranjeevi Reddy, K., and Subramaniam, K. V. L., "Analysis for Multi-Linear Stress-Crack Opening Cohesive Relationship: Application to Macro-Synthetic Fiber Reinforced Concrete," *Engineering Fracture Mechanics*, V. 169, 2017, pp. 128-145. doi: 10.1016/j.engfracmech.2016.11.015

50. Olesen, J. F., "Fictitious Crack Propagation in Fiber-Reinforced Concrete Beams," *Journal of Engineering Mechanics*, ASCE, V. 127, No. 3, 2001, pp. 272-280. doi: 10.1061/(ASCE)0733-9399(2001)127:3(272)

51. Bhogone, M. V., and Subramaniam, K. V. L., "Early-Age Tensile Constitutive Relationships for Steel and Polypropylene Fiber Reinforced Concrete," *Engineering Fracture Mechanics*, V. 244, 2021, Article No. 107556. doi: 10.1016/j.engfracmech.2021.107556

52. Gali, S., and Subramaniam, K. V. L., "Multi-Linear Stress-Crack Separation Relationship for Steel Fiber Reinforced Concrete: Analytical Framework and Experimental Evaluation," *Theoretical and Applied Fracture Mechanics*, V. 93, 2018, pp. 33-43. doi: 10.1016/j.tafmec.2017.06.018

53. EN 1992-1-1:2004, "Eurocode 2: Design of Concrete Structures – Part 1-1: General Rules and Rules for Buildings," European Committee for Standardization, Brussels, Belgium, 2004.

ACI STRUCTURAL JOURNAL TECHNICAL PAPER

Title No. 122-S72

Lightweight Alternative Machine Learning Model for Automating Concrete Crack Image Classification

by Sang Min Lee, Hyeon-Sik Choi, Chanho Kim, and Thomas H.-K. Kang

In this study, the challenge of automating concrete crack image classification by developing a lightweight machine learning model that balances accuracy with computational efficiency was addressed. Traditional deep learning models, while accurate, suffer from high computational demands, limiting their practicality in on-site applications. This study's approach used the random forest (RF) classifier combined with histogram of oriented gradients (HOG) and local binary patterns (LBP) for feature extraction, offering a more feasible alternative for real-time structural health monitoring. Comparative analysis with the convolutional neural network (CNN) model highlights this model's significantly reduced size and inference times, with only a marginal compromise in accuracy. The results demonstrated that the RF models, particularly RF with LBP, are well-suited for integration into resource-constrained environments, paving the way for their deployment in portable, on-site diagnostic systems in civil engineering. This study contributed a novel perspective to the field, emphasizing the importance of efficient machine learning solutions in practical applications of structural health monitoring.

Keywords: concrete crack image; convolutional neural network (CNN); histogram of oriented gradients (HOG); local binary patterns (LBP); random forest (RF).

INTRODUCTION

Concrete structures, fundamental to modern infrastructures, are susceptible to cracking, which, if significant, may compromise their structural integrity and serviceability. The early and accurate detection of these cracks and their propagation is paramount for ensuring structural health and safety. Traditional methods for crack detection, predominantly manual inspections, are not only time-consuming but also subject to human error, leading to potential oversights and inaccuracies. The advent of machine learning and artificial intelligence (AI) technologies has brought a paradigm shift in this domain, offering solutions that are not only more accurate but also significantly more efficient. Meng (2021) highlights how these advancements have revolutionized automated crack detection, making it a more reliable and swift process.

The application of machine learning in crack detection has seen considerable progress in recent years. However, deploying such methods in low-resource environments, where computational efficiency and energy use are critical, remains a challenge. Researchers have delved into various deep neural network models, particularly focusing on semantic segmentation of crack images. Advanced architectures like ResNet and VGG have been employed for pixel-wise detection, offering a more nuanced and detailed analysis of crack patterns (Huyan et al. 2022). Moreover, the concept of transfer learning has been instrumental, where pre-trained models are adapted to the specific task of crack detection. This approach leverages the vast amount of learning from other domains, making the models more robust and efficient in crack detection scenarios (Islam et al. 2022). The success of these methods, especially in accurately classifying images into crack and non-crack categories, underscores the potential of deep learning in practical engineering applications, as noted by Rajadurai and Kang (2021). Dais et al. (2021) demonstrated the effectiveness of convolutional neural networks (CNNs) combined with transfer learning for automatic crack classification and segmentation on masonry surfaces, achieving high accuracy even in complex real-world conditions. Kim et al. (2019) proposed a machine learning-based method for identifying cracks on concrete surfaces. By using image binarization to extract crack candidate regions and employing classification models based on CNN, their approach effectively distinguished cracks from non-crack noise patterns such as shadows and stains, achieving robust performance in complex scenarios. Zhou et al. (2022) introduced YOLOv4-ED, an enhanced deep learning-based model designed to address challenges in tunnel lining defect detection, such as low accuracy and poor anti-interference ability. By incorporating EfficientNet as the backbone for improved accuracy and depth-wise separable convolution blocks for higher efficiency, YOLOv4-ED achieved superior performance metrics. The model demonstrated robust and automated defect detection capabilities, even under complex lighting and background conditions.

However, despite these advancements, a critical challenge in deploying deep learning models for concrete crack detection in real-world scenarios lies in the balance between model complexity and practical utility (Yu et al. 2022). Traditional deep learning models, while offering high accuracy, often come with substantial computational costs associated with large model sizes and prolonged inference times, which can be prohibitive in resource-constrained environments (Ali et al. 2021). In contrast, the proposed methods cater to scenarios where such constraints necessitate alternative solutions. This poses a significant hurdle for their application

ACI Structural Journal, V. 122, No. 5, September 2025.

MS No. S-2024-074.R2, doi: 10.14359/51746755, received December 13, 2024, and reviewed under Institute publication policies. Copyright © 2025, American Concrete Institute. All rights reserved, including the making of copies unless permission is obtained from the copyright proprietors. Pertinent discussion including author's closure, if any, will be published ten months from this journal's date if the discussion is received within four months of the paper's print publication.

in on-site scenarios, where rapid and efficient processing is crucial. The emphasis on accuracy has led to the development of increasingly complex models, such as those based on deep CNNs, which require substantial computational resources for training and inference (Maalej et al. 2022). These models, characterized by their deep architectures and extensive number of parameters, necessitate powerful hardware and considerable memory, making them less viable for deployment in resource-constrained environments. For instance, models based on architectures like ResNet and VGG, though highly accurate, are often too cumbersome for practical applications where immediate results are necessary, such as real-time structural health monitoring.

Furthermore, the focus on leveraging pre-existing, large-scale data sets through transfer learning, while beneficial for model robustness, does not always translate into efficient performance in specific tasks like crack detection. The adaptation of these models to specialized tasks often requires fine-tuning with additional layers or retraining, which further adds to the computational load. The discrepancy between the resource-intensive nature of these models and the practical requirements of crack detection tasks presents a significant gap in the current approach to the automated crack analysis.

In light of these challenges, there is a growing need for developing lightweight alternative machine learning models that maintain high accuracy while significantly reducing computational demands. Fu et al. (2023) introduced StairNet, a lightweight CNN designed for concrete crack detection, which demonstrated superior efficiency and accuracy compared to models such as EfficientNetV2, GoogLeNet, and ResNet34. Their extended Faster R-Stair model, validated on real-world data sets, further underscores the potential for deploying efficient models in practical scenarios such as real-time structural health monitoring. The aim of this study is to design models that are not only effective in identifying and classifying concrete cracks but also efficient in terms of model size, memory use, and inference time. Such models would be more suitable for practical applications, particularly in scenarios requiring real-time analysis and decision-making. Therefore, this study focuses on the development of a lightweight machine learning model tailored for the automated classification of concrete cracks. By optimizing the model architecture and employing innovative techniques to reduce computational complexity, this study aims to bridge the gap between high accuracy and practical applicability. The proposed model endeavors to provide a solution that is not only technically robust but also feasible for real-time, on-site crack detection in various concrete structures.

RESEARCH SIGNIFICANCE

This study innovatively addresses the critical balance between computational efficiency and accuracy in automating concrete crack image classification, specifically targeting low-resource environments. By integrating a lightweight machine learning model using random forest (RF) classifiers with histogram of oriented gradients (HOG) and local binary patterns (LBP) for feature extraction, it provides a pragmatic solution surpassing the limitations of conventional deep learning models in scenarios such as remote monitoring stations or resource-constrained internet of things (IoT) devices. This approach not only demonstrates a significant reduction in model size and inference times but also maintains commendable accuracy, proving particularly advantageous for deployment in resource-constrained, on-site diagnostic systems within civil engineering. This study's emphasis on efficient, practical machine learning applications marks a valuable contribution to the field, setting a precedent for future advancements in infrastructure safety and maintenance.

CONCRETE CRACK IMAGE DATABASE

Crack image collection

The concrete crack image database used in this study is an extensive open-source collection, comprising a total of 40,000 images, offering diverse conditions such as varying lighting, shadowing, and surface textures (Özgenel 2018). Additionally, the adaptability of the proposed methods to larger images is ensured by segmenting these images into smaller patches for analysis, with results aggregated across patches. This database is evenly divided, with 20,000 images depicting surfaces without cracks and the remaining 20,000 showcasing various forms of cracks. Each image in the database is an RGB color image with dimensions of 227 x 227 pixels, providing a detailed view suitable for deep learning or machine learning analysis. The methodology for creating these smaller-sized images from high-resolution sources is critical for the effectiveness of the model. This process follows the approach outlined by Zhang et al. (2016), ensuring that the integrity and characteristics of the cracks are accurately represented in the reduced-size images. The original high-resolution images, from which these samples were derived, consist of 458 RGB color images, each with dimensions of 4032 x 3024 pixels. These images were meticulously collected from several campus buildings at Middle East Technical University, offering a diverse range of real-world scenarios and crack patterns. This diversity is crucial for training a model that is robust and effective across various concrete structures and conditions. Figure 1 shows five examples of non-cracked concrete images and Fig. 2 shows another five examples of cracked concrete images.

Manual preprocessing

Manual preprocessing was performed on all 40,000 original image data. As a result, out of the 20,000 images classified as negative, two images with cracks, 132 images with fine cracks, 92 images that were difficult to judge as negative due to varying colors, and 104 images that were difficult to read due to other contaminants were selected. Similarly, of the 20,000 images classified as positive, 43 images were difficult to judge due to varying colors and 80 images were difficult to determine due to other contaminants. Therefore, 330 of the 20,000 negative images were excluded as shown in Fig. 3, resulting in a total of 19,670 images, and 123 of the 20,000 positive images were excluded as shown in Fig. 4, resulting in a total of 19,877 images, as shown in Table 1. The total number of images after manual filtering was 39,547. All data sets consisted exclusively of images

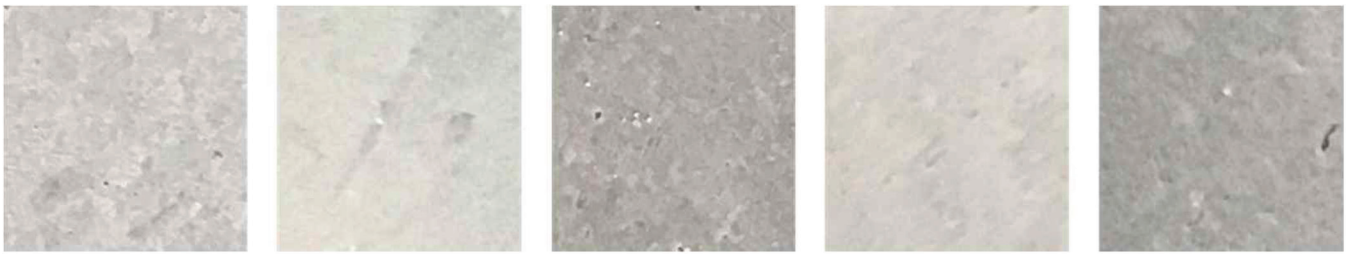


Fig. 1—Examples of non-cracked concrete images.

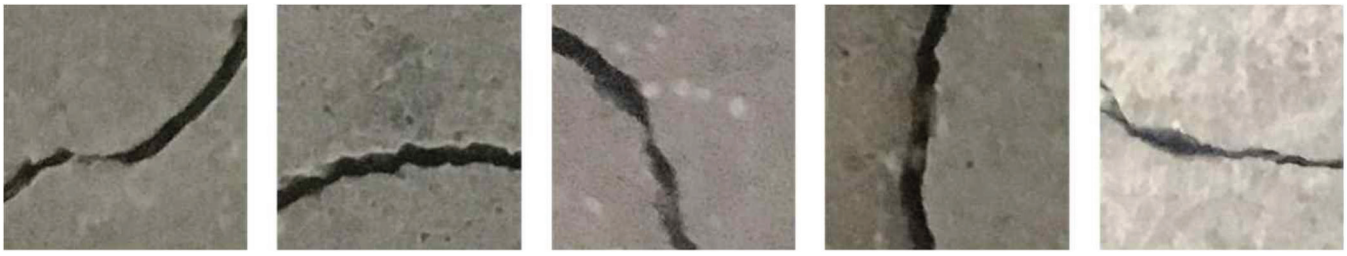


Fig. 2—Examples of cracked concrete images.



Fig. 3—Filtered examples from data set classified as negative.

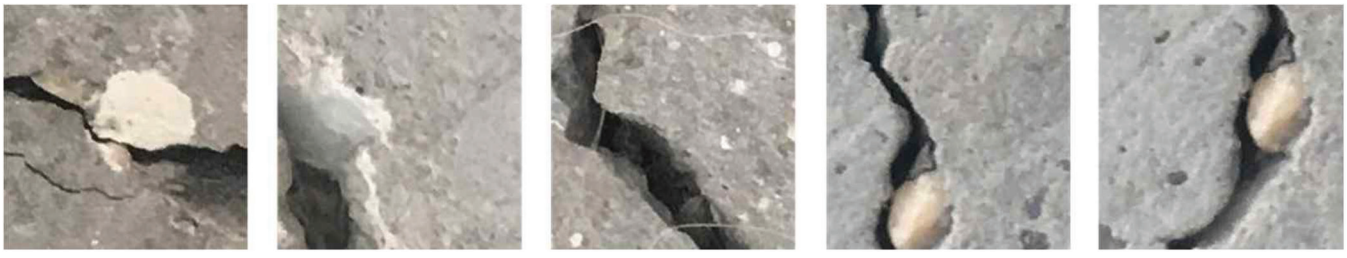


Fig. 4—Filtered examples from data set classified as positive.

Table 1—Label and number of images before and after manual preprocessing

Image type	Label	Number of images (before filtering)	Number of images (after filtering)
Negative (without crack)	0	20,000	19,670
Positive (with crack)	1	20,000	19,877

captured under uniform illumination conditions, ensuring the absence of any cast shadows.

CONVOLUTIONAL NEURAL NETWORK FOR DEEP LEARNING

To compare the accuracy, model capacity, and inference time of the lightweight alternative machine learning model proposed in this study, a CNN, which is known to perform well in image analysis, was trained and used as a baseline deep learning model. The CNN consists of an input layer, several hidden layers, and an output layer. Hidden layers typically include convolutional layers, pooling layers, fully connected layers, and normalization layers. The convolutional layers, which are central to the network, employ filters to create feature maps that capture spatial features such as edges and textures. This is followed by the application of a nonlinear activation function, typically the rectified linear unit (ReLU), to introduce complexity into the model. Pooling layers then reduce the dimensionality of each feature map, maintaining essential information, while fully connected layers near the end of the network integrate these features. The output layer, often using a softmax function, yields the classification results. In image analysis, CNNs undergo a process of feature learning and

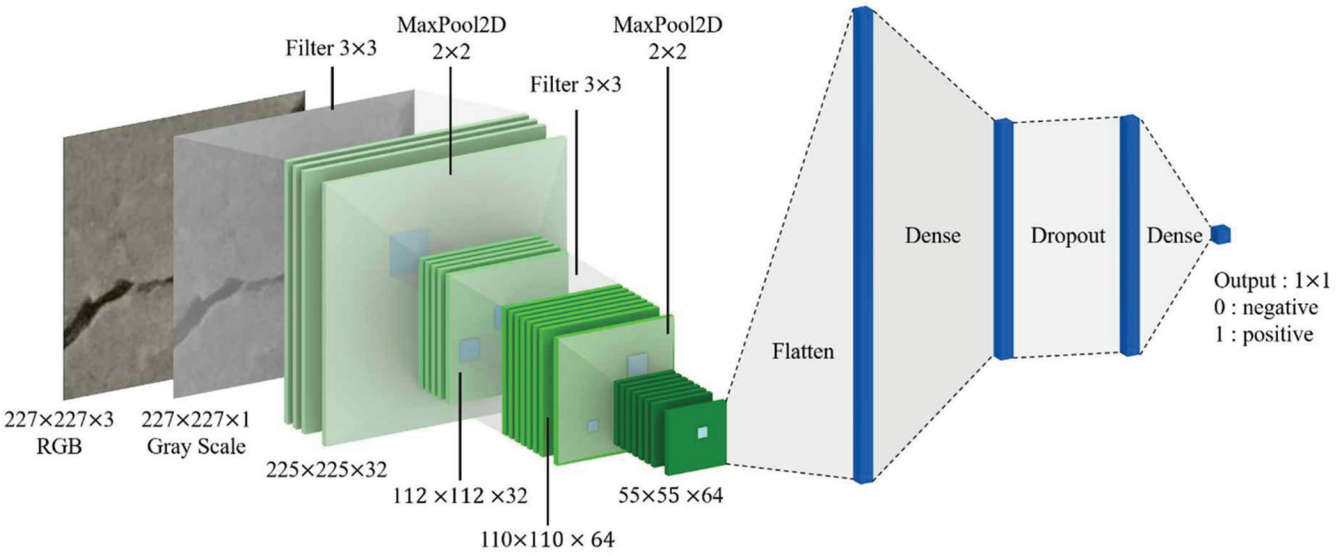


Fig. 5—CNN architecture for concrete crack image classification.

integration. During the forward propagation, an image is processed through layers that identify and integrate various features with backpropagation and optimization algorithms such as Adam or stochastic gradient descent, fine-tuning the model's weights for accuracy. Once trained, CNNs can efficiently process and classify new images, making them ideal for tasks such as crack detection in concrete. In this study, the CNN was used as a baseline model against which the performance of a proposed lightweight machine learning model was compared, particularly in terms of accuracy, model capacity, and inference time, to highlight the efficiency and effectiveness of the proposed model in practical applications.

The intricate structure of the CNN model is depicted in Fig. 5, a visualization of the end-to-end neural network architecture. The input initially converted from an RGB image with dimensions of 227 x 227 x 3 to a grayscale image with dimensions of 227 x 227. This model applies a 2 x 2 size MaxPool2D twice in a row on a 3 x 3 convolution filter. The features of the image data set are extracted using this procedure, and the multidimensional feature map is then flattened into a one-dimensional vector by applying the Flatten layer. Subsequently, the Dense layers are stacked one after the other with a 0.5 dropout ratio in between the Dense layers to prevent overfitting. Until it reaches the final layer, the activation function employs the ReLU. The ReLU function adds nonlinearity and alleviates the gradient loss problem. The final layer is the Dense layer, which employs the sigmoid activation function to convert the final output into probabilities ranging from 0 to 1, allowing the network to solve the binary classification problem. In this model, two output classes are assumed and the division of "0: normal" and "1: crack" to detect cracks is used.

FEATURE EXTRACTION FOR MACHINE LEARNING

Histogram of oriented gradients

The HOG is an essential feature descriptor widely used in computer vision and image processing, especially for detecting objects like pedestrians. HOG's main principle is to depict an object's shape and appearance in a localized area of an image by analyzing the spread of edge directions or intensity gradients.

In HOG's methodology, an image is divided into small sections called cells, and each cell compiles a histogram based on the orientation of gradients. The process starts with transforming the image into a grayscale format to highlight structures and edges. Subsequently, the image's gradients, which emphasize contours, edges, and textures, are calculated as shown in Fig. 6. Each cell's gradient orientation is then categorized into a histogram, with orientations typically divided into nine bins spanning 0 to 180 degrees. As shown in Fig. 7, the HOG changes depending on the position of the cell. The upper example in Fig. 7 shows the result for a cell at position [5, 6], which is a histogram with a larger gradient magnitude at orientations between 0 and 20 degrees. However, the example below shows the result for the cell at [5, 5], and the histogram has a large gradient magnitude for orientations between 160 and 180 degrees.

These histograms effectively capture the prevalence of gradient directions in each cell. However, histograms for cells alone can be overly sensitive to lighting and contrast variations. To mitigate this, HOG uses block normalization, where adjacent cells are grouped into larger, overlapping blocks. The histograms from all cells in a block are combined and normalized, reducing the impact of lighting and shadow differences. The final feature vector is created by joining the normalized histograms from all blocks, forming a comprehensive descriptor of the image. This vector is then used as input for a machine learning algorithm trained to identify classes of an image.

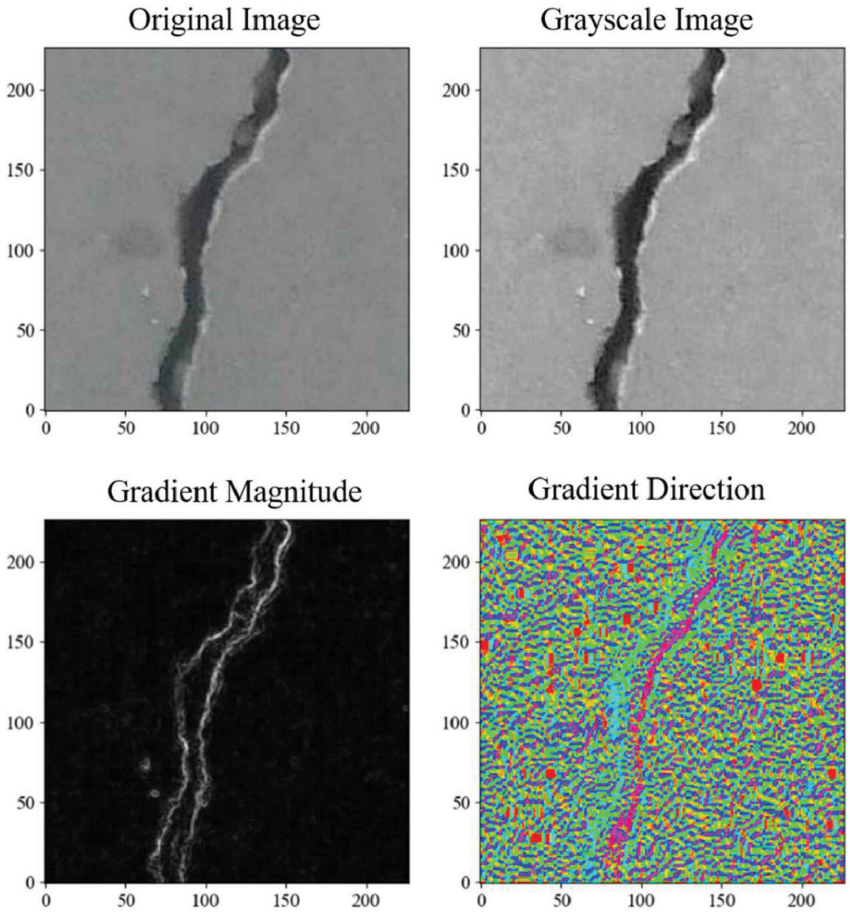


Fig. 6—Gradient magnitude and direction example from raw and grayscale images.

Local binary patterns

LBP are a straightforward yet potent method for texture analysis in image processing. The essence of LBP lies in its ability to efficiently encapsulate the local structural patterns of a grayscale image. It operates by comparing the intensity of each pixel with that of its neighboring pixels, encoding this comparison into a binary number. These binary values from the surrounding pixels are concatenated to form a binary string, often converted into a decimal value for simplicity. The selection of the neighborhood can vary, typically involving an 8-pixel neighborhood in a 3 x 3 grid, but it can be expanded to capture larger textures by adjusting the radius and the number of neighboring points. Notably, uniform LBP, a popular variant, focuses on binary patterns with minimal transitions, significantly reducing feature space dimensionality and enhancing noise resistance.

As shown in Fig. 8, the core output of LBP is a histogram of these binary patterns, serving as a feature vector that characterizes the image's texture. This histogram effectively captures various local elements like edges and spots. Predominantly used in facial recognition, LBP excels in identifying features such as lines and skin texture. It was also employed in texture classification across diverse fields like medical imaging and environmental modeling. One of LBP's primary advantages is its computational efficiency, making it well-suited for real-time applications. Additionally, its relative measurement approach offers robustness against variations in lighting conditions. However, LBP primarily focuses on textural information and may struggle in uniformly textured regions or in capturing high-level semantic content. Despite these limitations, LBP remains a popular choice for texture and pattern recognition tasks due to its effectiveness in capturing detailed local textural information.

TRAINING AND EVALUATION PROCESS OF PROPOSED MODEL

In machine learning, RF is a robust ensemble learning method, particularly effective for classification tasks. It operates by constructing a multitude of decision trees during the training phase and outputs the class that is the mode of the classes predicted by individual trees. This ensemble approach not only improves the predictive accuracy but also controls overfitting, a common issue in complex models. The strength of an RF classifier lies in its diversity. Each tree in the forest is trained on a random subset of the data and features, making the overall model more resilient to noise and variance in the data set. By aggregating the decisions of multiple trees, RF reduces the risk of erroneous predictions, leading to a more reliable and stable performance.

In the proposed model, leveraging the RF model and algorithm for crack detection in concrete structures, the choice of hyperparameters plays a pivotal role in optimizing performance. Two key feature extraction techniques, HOG and

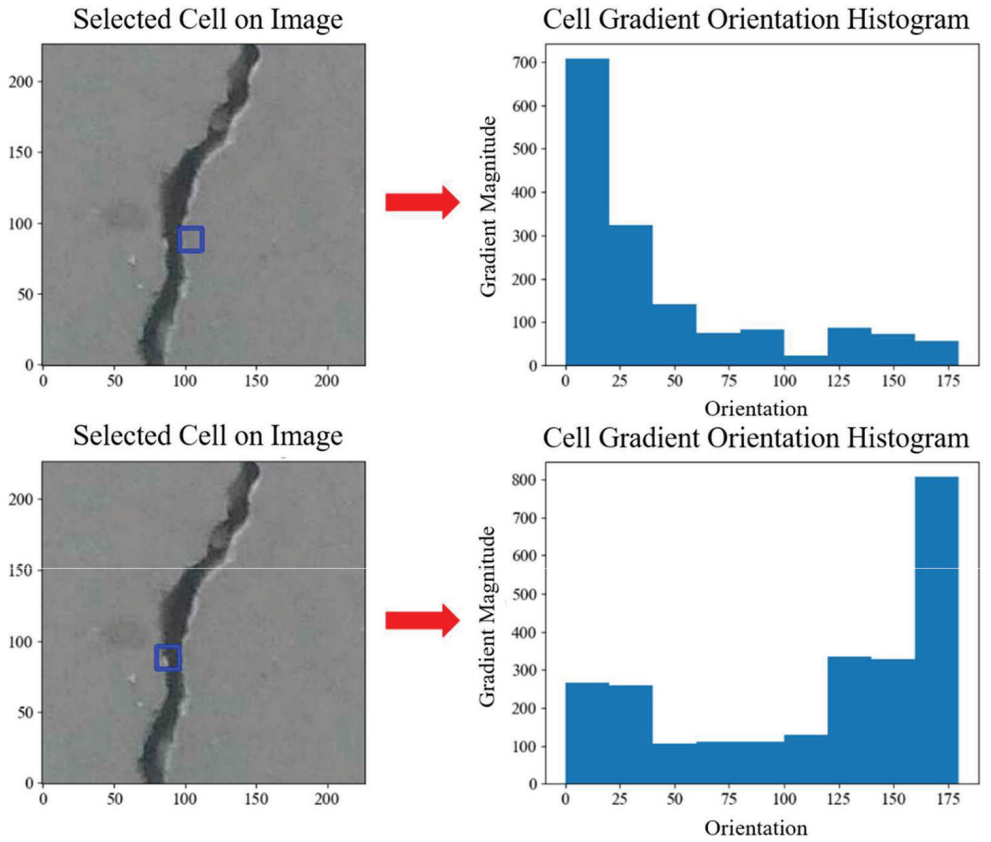


Fig. 7—HOG from selected cell: (above) example of cell position [5, 6]; and (below) example of cell position [5, 5].

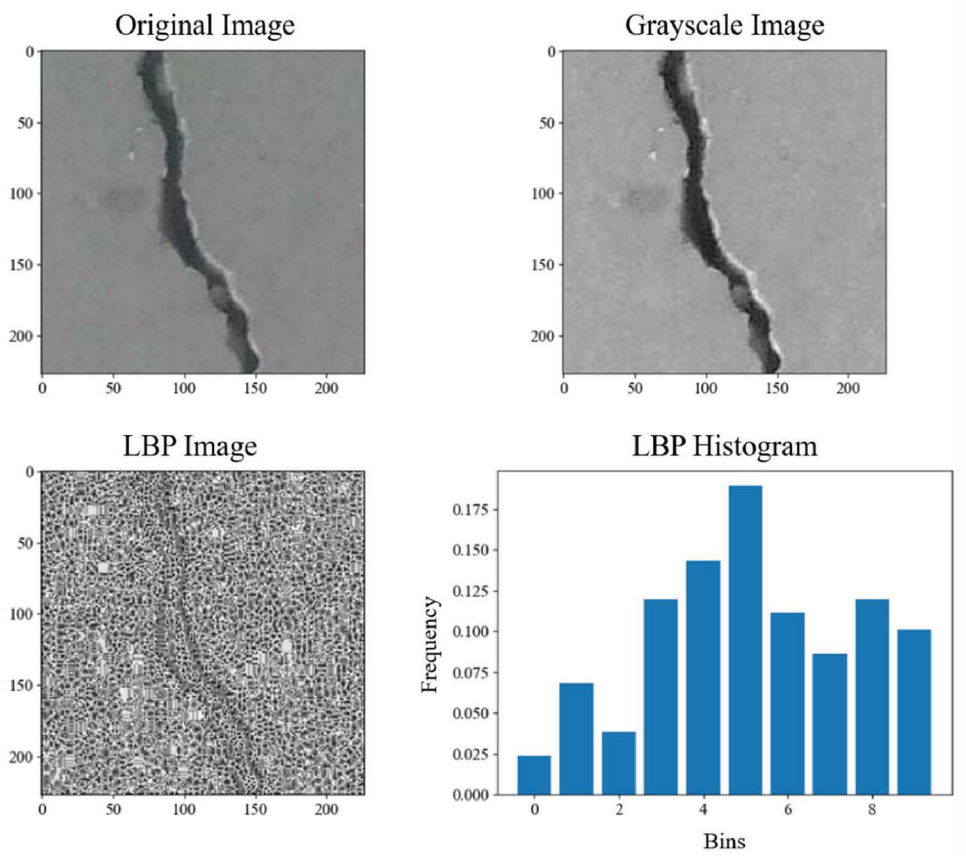


Fig. 8—LBP image processing and histogram.

LBP, are employed. The HOG descriptor captures edge and texture information by quantifying gradient orientations in localized portions of the image, while LBP encodes local texture by comparing each pixel with its neighbors. Critical hyperparameters for the RF include the number of decision trees and the maximum depth of these trees. For the HOG feature extraction, parameters such as the number of orientation bins and the size of the cells and blocks are vital. In contrast, for LBP, the radius of the neighborhood and the number of points considered around each pixel are key. These hyperparameters are meticulously tuned to ensure that the model extracts the most relevant and discriminatory features from the images, which is crucial for accurately distinguishing between cracked and non-cracked surfaces.

The training process involves feeding the HOG and LBP features of the images into an RF classifier. This is followed by splitting the data set into the training and testing sets to validate the model's performance. The evaluation process uses metrics such as the accuracy score and the generation of confusion matrixes to assess the model's effectiveness. The accuracy score provides a straightforward measure of how often the model correctly classifies images, while the confusion matrix offers deeper insights into the types of errors made by the classifiers, such as false positives and false negatives. The use of these evaluation techniques ensures a comprehensive understanding of the model's capabilities and limitations, allowing for further refinements and adjustments to enhance its performance in real-world crack detection scenarios. By integrating robust feature extraction methods with a finely tuned RF classifier, the proposed model aims to deliver high accuracy in crack detection while maintaining reasonable computational efficiency, making it suitable for practical applications in structural health monitoring.

The specifications of the workstation which was used in this study are described in Table 2. The training and evaluation of machine learning models were conducted on a high-performance computing workstation equipped with advanced hardware and software components to ensure efficient processing and accurate results. The core of the workstation is powered by the 32-core processor that provides exceptional computational speed and multitasking capabilities, crucial for handling complex machine learning algorithms. For graphical processing, the workstation used a commercial-level graphics processing unit (GPU), known for its high-end performance in processing large data sets and accelerating computational tasks, especially in image-related machine learning processes. The system is bolstered by a substantial memory capacity of 256 GB, facilitating rapid data access and efficient handling of large-scale data sets, a typical requirement in deep learning models. For storage, it is equipped with a 2 TB solid-state drive (SSD), offering fast data read and write speeds, which significantly reduces the data loading and model training time. The workstation operates on Windows 10.

Regarding software, Python 3.8 was chosen for its widespread popularity and support in the data science community, coupled with a suite of powerful machine learning libraries. This includes scikit-learn for implementing the RF classifier, skimage for image processing, NumPy for numerical operations, pandas for data manipulation, seaborn for advanced data visualization, and matplotlib for creating comprehensive charts and graphs. These libraries were integral in developing, training, and evaluating the machine learning model that is proposed in this study. The combination of this sophisticated hardware and comprehensive software toolkit provided an optimal environment for conducting this study, ensuring both efficiency and reliability in the model development and evaluation processes.

Table 2—Specification of workstation used in training and evaluation of model

Component	Specification
Central processing unit	32 cores
Graphics processing unit	RTX6000
Random access memory	DDR4 256 GB
Storage	SSD 980 M.2 NVMe 2280 2TB
Operating system	Windows 10
Python version	3.8
Machine learning libraries	scikit-learn, Skimage, TensorFlow, Keras, NumPy, pandas, Seaborn, matplotlib

RESULTS AND DISCUSSION

Figure 9 shows the confusion matrix of the three models trained on the unfiltered data set. This was done with 8000 testing data sets that were never used for training. The testing data set is 20% of the total data and was randomly selected. The horizontal axis is the result predicted by the trained model and the vertical axis is the ground truth. The CNN model correctly classified 3994 out of 4014 negatives labeled 0 as uncracked cases, and 3925 out of 3986 positives labeled 1 as cracked cases. As shown in Table 3, the accuracy of the CNN model was 98.99%, the most accurate of the three models. However, the size of the trained model was approximately 142 MB, which is almost 10 times larger than the other two models, and the inference time to infer the result for one image data was approximately 105 ms, which is approximately 685 times longer than RF with HOG and 6819 times longer than RF with LBP.

The RF with HOG correctly classified 3870 out of 4014 negatives labeled 0 as uncracked cases, and 3820 out of 3986 positives labeled 1 as cracked cases. The prediction accuracy was approximately 96.13%, and the model size was 16.6705 MB, the smallest of the three models. The inference time was 0.1533 ms. It can be considered to be close to real-time analysis. For RF with LBP, 3488 out of 4014 labeled 0 were correctly classified as uncracked cases, and 3689 out of 3986 positives labeled 1 were correctly classified as cracked cases. The prediction accuracy was approximately 89.71%, the least accurate of the three models. The model capacity was 19.7158 MB, which is higher than RF with HOG. However, the inference time was 0.0154 ms, which is approximately 10 times faster than RF with HOG.

Figure 10 shows the confusion matrix of the three models trained on the filtered data set. The CNN model correctly classified 3910 out of 3916 negatives labeled 0 as uncracked cases, and 3797 out of 3995 positives labeled 1 as cracked

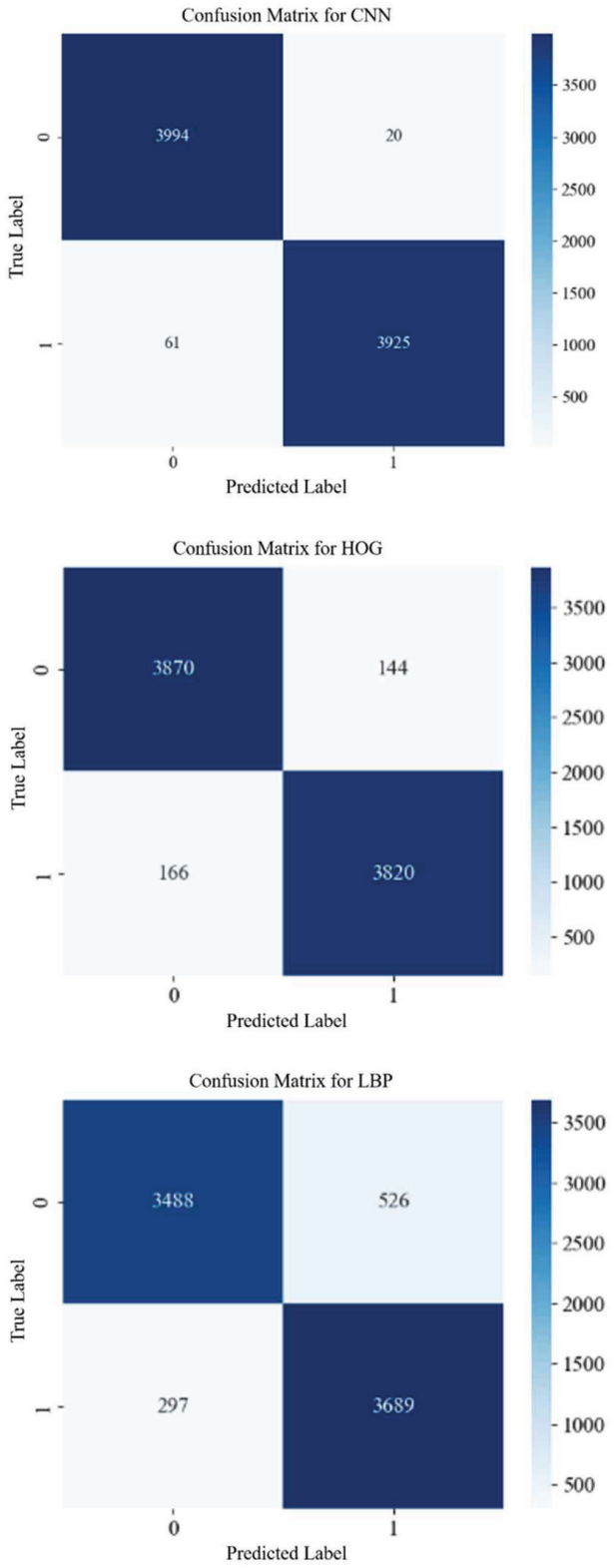


Fig. 9—Confusion matrixes with unfiltered data set: (top) CNN model; (middle) RF model with HOG; and (bottom) RF model with LBP.

cases. As shown in Table 4, the accuracy of the CNN model is 97.42%, which is approximately 1% lower than the accuracy of the unfiltered data set. The size of the trained model was 142 MB, which is almost 10 times larger than the other two models, and it was found that the overall performance

Table 3—Performance comparison with unfiltered data set

Model type	Accuracy	Trained model capacity, MB	Inference time, ms
CNN	0.9899	142.0561	105.0231
RF with HOG	0.9613	16.6705	0.1533
RF with LBP	0.8971	19.7158	0.0154

of the CNN model was the same before and after manual preprocessing. The inference time was 100 ms, which is approximately 650 times longer than RF with HOG and approximately 6411 times longer than RF with LBP.

The RF with HOG correctly classified 3775 out of 3916 cases labeled 0 as uncracked, and 3815 out of 3995 positive cases labeled 1 as cracked. The accuracy was 95.94%, which is approximately 1.5% lower than the CNN model, but the model size was reduced by 10 times and the inference time was 650 times faster. For RF with LBP, 3430 out of 3916 labeled 0 were correctly classified as uncracked cases, and 3700 out of 3995 positive labeled 1 were correctly classified as cracked cases. The accuracy was approximately 90.13%, the lowest of the three models, and the model size was 3.5 MB larger than RF with HOG, but the inference time was 10 times faster.

Among all training and testing results, only the RF with HOG model performed on the filtered data set had a model capacity of 16 MB or less. The reason for setting the model capacity as 16 MB is that the microcontrolling unit (MCU) used in the manufacturing of edge devices for the future study has an additional memory capacity of 16 MB. The overall results showed that the CNN model was the most accurate both before and after manual preprocessing, but the trained model was the heaviest and had the longest inference time. When comparing RF with HOG and RF with LBP, the model capacities were almost similar. While RF with LBP has slightly lower accuracy, its inference time is 10 times shorter, which indicates that RF with LBP is more suitable for real-time applications than RF with HOG, even at the cost of slightly lower accuracy.

CONCLUSIONS

The primary objective of this study was to devise a computationally efficient, yet accurate, machine learning model for the classification of concrete crack images, particularly for non-critical or preliminary screening applications. While the random forest (RF) with local binary patterns (LBP) model exhibits lower accuracy than convolutional neural networks (CNNs), its rapid inference time and lightweight nature make it well-suited for environments with strict computational constraints. These attributes allow the model to serve as a complementary tool to CNNs in workflows requiring both efficiency and detailed accuracy. Recognizing the limitations inherent in traditional deep learning models—principally their high computational cost and extensive inference times—this study embarked on developing a more streamlined and practical alternative. To this end, this study focused on the integration of RF classifiers with two distinct

Table 4—Performance comparison with filtered data set

Model type	Accuracy	Trained model capacity, MB	Inference time, ms
CNN	0.9742	142.0561	100.0230
RF with HOG	0.9594	14.5030	0.1538
RF with LBP	0.9013	17.9908	0.0156

feature extraction techniques: histogram of oriented gradients (HOG) and LBP.

Quantitative analysis of the results underscored the superiority of the CNN model in terms of accuracy, achieving a remarkable 98.99% accuracy on the unfiltered data set and 97.42% on the filtered data set. However, this high accuracy came at the expense of a significant computational burden, as evidenced by the model's substantial size of approximately 142 MB and an inference time of approximately 100 to 105 ms. In contrast, the RF models, particularly when combined with HOG and LBP, exhibited a notable reduction in both model size and inference time. The RF with HOG model demonstrated an accuracy of 96.13% on the unfiltered data set and 95.94% on the filtered data set, with a reduced model size of approximately 16 to 17 MB and an inference time of 0.1533 ms. While this accuracy is slightly lower than CNNs, the significantly reduced model size and inference time highlight its suitability for edge devices and low-cost internet of things (IoT) applications. The RF with LBP model, while presenting the lowest accuracy among the models at 89.71% and 90.13% for the unfiltered and filtered data sets, respectively, boasted the shortest inference time at approximately 0.0154 ms, and a model size of approximately 17 to 20 MB.

This study's findings are pivotal in two key aspects. First, the trade-off between model accuracy and computational efficiency is not only feasible but also advantageous in practical applications such as real-time structural health monitoring. Second, the reduced model sizes and inference times of the RF with HOG and RF with LBP models demonstrated their potential for deployment in resource-constrained environments, particularly in embedded systems or edge artificial intelligence (AI) devices. In summary, this study successfully addresses the gap in the existing literature by providing an alternative machine learning approach for concrete crack image classification that is both computationally efficient and reasonably accurate. The RF models developed in this study, especially when integrated with HOG and LBP feature extraction methods, present a viable solution for real-world applications in the field of civil engineering, especially in structural health monitoring.

The data set used in this study encompassed a diverse range of crack patterns observed in various building structures, ensuring a representative depiction of structural damage commonly encountered in practice. However, additional consideration may be required for other types of concrete infrastructure, such as pavements, bridges, piers, abutments, and foundations, which exhibit distinct structural behaviors and loading conditions.

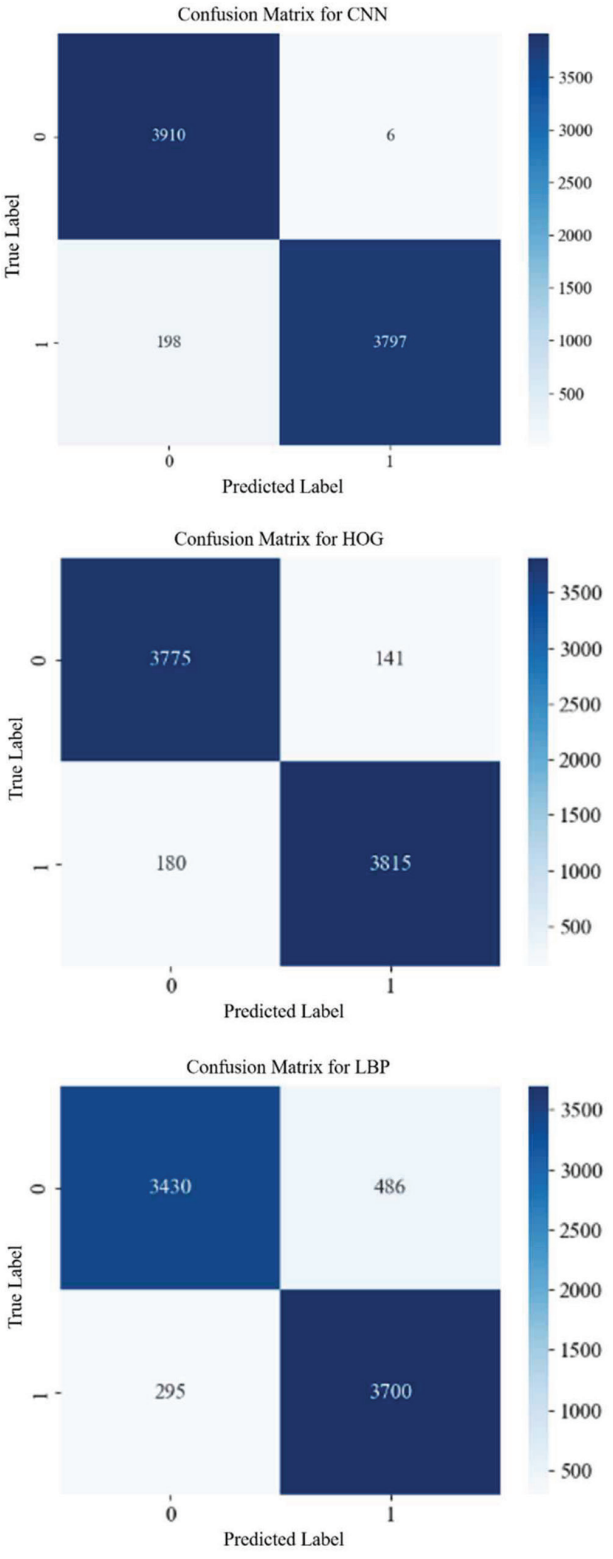


Fig. 10—Confusion matrixes with filtered data set: (top) CNN model; (middle) RF model with HOG; and (bottom) RF model with LBP.

Nonetheless, the proposed model focuses primarily on the localized geometry and texture of cracks rather than macroscale stress conditions, effectively minimizing the influence of structural and loading variations on its performance. As a result, the model demonstrates strong potential for detecting visible cracks across a wide array of concrete surfaces.

Future studies could further enhance the model's generalization capabilities by expanding the training data set to include images from a broader spectrum of concrete infrastructures.

AUTHOR BIOS

ACI member **Sang Min Lee** *is a PhD Student of the Interdisciplinary Program in Artificial Intelligence of Seoul National University, Seoul, Korea, where he received his BS and MS. His research interests include the application of artificial intelligence to structural engineering.*

ACI member **Hyeon-Sik Choi** *is a PhD Student of structural engineering at Seoul National University, where he received his BS. His research interests include the analysis and design of prestressed concrete structures under impact or blast loads.*

ACI member **Chanho Kim** *is a PhD Student in the Interdisciplinary Program in Artificial Intelligence at Seoul National University, where he received his BS and MS. His research interests include structural wind engineering with artificial intelligence and machine learning.*

Thomas H.-K. Kang, *FACI, is a Professor of structural engineering and the Interdisciplinary Program in Artificial Intelligence at Seoul National University. He is a member of Joint ACI-PTI Committee 320, Post-Tensioned Structural Concrete Code; Joint ACI-ASCE Committees 352, Joints and Connections in Monolithic Concrete Structures, and 423, Prestressed Concrete; and Joint ACI-ASME Committee 359, Concrete Containments for Nuclear Reactors. He received the ACI Wason Medal for Most Meritorious Paper in 2009 and the T. Y. Lin Award jointly from ASCE, ACI, PCI, and PTI in 2025. His research interests include the design and behavior of reinforced, prestressed, and post-tensioned concrete structures, as well as artificial intelligence applications.*

ACKNOWLEDGMENTS

This work was supported by Institute of Information & communications Technology Planning & Evaluation (IITP) grant funded by the Korea government (MSIT) [No.RS-2021-II211343, Artificial Intelligence Graduate School Program (Seoul National University)] and by Seoul National University. The authors would like to acknowledge J. Seo (deceased) for his willing discussion on the topic while he visited Seoul National University.

REFERENCES

Ali, L.; Alnajjar, F.; Jassmi, H. A.; Gocho, M.; Khan, W.; and Serhani, M. A., 2021, "Performance Evaluation of Deep CNN-Based Crack Detection and Localization Techniques for Concrete Structures," *Sensors*, V. 21, No. 5, p. 1688. doi: 10.3390/s21051688

Dais, D.; Bal, I. E.; Smyrou, E.; and Sarhosis, V., 2021, "Automatic Crack Classification and Segmentation on Masonry Surfaces Using Convolutional Neural Networks and Transfer Learning," *Automation in Construction*, V. 125, p. 103606. doi: 10.1016/j.autcon.2021.103606

Fu, R.; Cao, M.; Novak, D.; Qian, X.; and Alkayem, N. F., 2023, "Extended Efficient Convolutional Neural Network for Concrete Crack Detection with Illustrated Merits," *Automation in Construction*, V. 156, p. 105098. doi: 10.1016/j.autcon.2023.105098

Huyan, J.; Ma, T.; Li, W.; Yang, H.; and Xu, Z., 2022, "Pixelwise Asphalt Concrete Pavement Crack Detection via Deep Learning-Based Semantic Segmentation Method," *Structural Control and Health Monitoring*, V. 29, No. 8, p. e2974. doi: 10.1002/stc.2974

Islam, M. M.; Hossain, M. B.; Akhtar, M. N.; Moni, M. A.; and Hasan, K. F., 2022, "CNN Based on Transfer Learning Models Using Data Augmentation and Transformation for Detection of Concrete Cracks," *Algorithms*, V. 15, No. 8, p. 287. doi: 10.3390/a15080287

Kim, H.; Ahn, E.; Shin, M.; and Sim, S.-H., 2019, "Crack and Noncrack Classification from Concrete Surface Images Using Machine Learning," *Structural Health Monitoring*, V. 18, No. 3, pp. 725-738. doi: 10.1177/1475921718768747

Maalej, M.; Cherif, R.; Yaddaden, Y.; and Khoumsi, A., 2022, "Automatic Crack Detection on Concrete Structure Using a Deep Convolutional Neural Network and Transfer Learning," *2022 International Conference on Advanced Electrical Engineering (ICAEE)*, Constantine, Algeria. doi: 10.1109/ICAEE53772.2022.9962029

Meng, X., 2021, "Concrete Crack Detection Algorithm Based on Deep Residual Neural Networks," *Scientific Programming*, V. 2021, p. 3137083. doi: 10.1155/2021/3137083

Özgenel, Ç. F., 2018, "Concrete Crack Images for Classification," Mendeley Data. doi: 10.17632/5y9wdsg2zt.1

Rajadurai, R.-S., and Kang, S.-T., 2021, "Automated Vision-Based Crack Detection on Concrete Surfaces Using Deep Learning," *Applied Sciences*, V. 11, No. 11, p. 5229. doi: 10.3390/app11115229

Yu, Y.; Rashidi, M.; Samali, B.; Mohammadi, M.; Nguyen, T. N.; and Zhou, X., 2022, "Crack Detection of Concrete Structures Using Deep Convolutional Neural Networks Optimized by Enhanced Chicken Swarm Algorithm," *Structural Health Monitoring*, V. 21, No. 5, pp. 1-15. doi: 10.1177/14759217211053546

Zhang, L.; Yang, F.; Zhang, Y. D.; and Zhu, Y. J., 2016, "Road Crack Detection Using Deep Convolutional Neural Network," *2016 IEEE International Conference on Image Processing (ICIP)*, Phoenix, AZ, pp. 3708-3712. doi: 10.1109/ICIP.2016.7533052

Zhou, Z.; Zhang, J.; and Gong, C., 2022, "Automatic Detection Method of Tunnel Lining Multi-Defects via an Enhanced You Only Look Once Network," *Computer-Aided Civil and Infrastructure Engineering*, V. 37, No. 6, pp. 762-780. doi: 10.1111/mice.12836

ACI STRUCTURAL JOURNAL TECHNICAL PAPER

Title No. 122-S73

Efficient Seismic-Resistant Vertical Dry Connections in Precast Walls

by A Selva Ganesa Moorthi and G. Appa Rao

Prefabricated structural wall buildings exhibit superior strength, stiffness, and ductility under seismic loading effects. Segmental wall construction is popular due to easy transportation and on-site assembly. The present study deals with the performance of precast wall elements connected through welded plates vertically subjected to seismic loading conditions. The study proposes welded plates with varying thickness to connect two structural walls on one or both faces. Full-scale quasi-static load tests were performed to analyze the seismic behavior of the connections. A conventional foundation with loading beams at top and bottom, to test the structural walls, was replaced with a special steel shoe setup, achieving real conditions, to minimize the testing cost. It was observed that the connections using mild steel plates achieve the most desirable characteristics such as plate yielding, energy dissipation, and ductility. High-strength steel plates failed in brittle mode with poor post-peak response, indicating precautions in selecting the type of connecting steel plates in precast construction. The proposed connecting plates improve the ductility and post-peak response for easy retrofitting of the precast wall system. The study brings out improvement in the seismic performance, selection of materials, and connection detailing for resilient precast structures.

Keywords: ductile connection; experimental study; precast structural wall; quasi-static test; reinforced concrete (RC); seismic resistant; welded joint.

INTRODUCTION

Prefabricated construction has garnered significance in civil and structural engineering practices due to several advantages such as savings in construction time, economy, improved quality control, and site safety. It also looks like a sustainable construction approach[1] due to minimum wastage[2] and noise control. Precast construction is predominantly encountered in bridges and industrial buildings, and now is popular in mid- and high-rise buildings as well. Precast concrete structural walls resist lateral loads due to wind or seismic forces. Numerous studies demonstrate that the addition of structural walls enhance a structure's lateral resistance.[3-5] However, a challenge with precast structural walls lies in their size and weight, making transportation limited from the fabrication yard to the construction site. To address this issue, precast structural walls are segmented and assembled on-site using suitable connection methods.[6] When wall panels are designed to transfer loads, it is important to consider the additional loads developed to design the connection.[7] The connections between precast wall segments are crucial for the overall performance of the structure in terms of energy dissipation and structural integrity during extreme loading effects.[8-10]

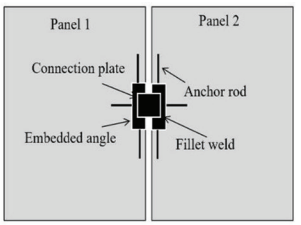
Connections between structural components may play multiple roles beyond merely transferring shear forces from lateral loads. For instance, weld plates in flanged components often help distribute concentrated loads and adjust the differences in camber. Similarly, grout keys are provided in joints to aid in load distribution.[11]

Observations from past earthquakes[12-16] revealed that connections are the weak links in precast buildings, with deficient detailing as a major factor for poor performance. Failures were predominantly observed in the connection location, mainly due to low ductility of the connections. Specific guidelines for designing and detailing vertical connections in prefabricated structural wall systems are lacking.

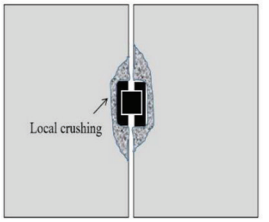
Wet connections use fresh concrete to connect precast segments, and prolong construction time as the concrete needs to cure before other construction activities can proceed. The delay potentially disrupts the construction schedule. The complexity of creating formwork for wet connections increases the construction cost and time. Additionally, wet connections develop voids, honeycombing, and inadequate compaction, which can lead to challenging tasks, resulting in changes in integrity and overall performance. Wet connections behave as a monolithic structure.[17]

Dry connections are steel connections in precast structural walls that offer several key advantages over wet connections,[17,18] such as no curing, which leads to a shorter overall construction schedule. Additionally, the fabrication process is easier and more accessible, resulting in more predictable and reliable connection performance. The main vertical dry connections include field welding and a combination of bolting and welding.[19] Moreover, dry connections are lighter, more compact, and cost-effective, which also facilitates easier handling and installation on site. Furthermore, their customizability allows for greater design flexibility to meet specific project requirements. In terms of sustainability, dry connections produce less construction waste and require fewer on-site resources, leading to more environmentally friendly construction processes. Another significant advantage is the ductility of dry connections, which allows for inclusion of inelastic deformation within the connection itself if designed and detailed properly. The ductility is an important property under earthquake loads, which absorbs

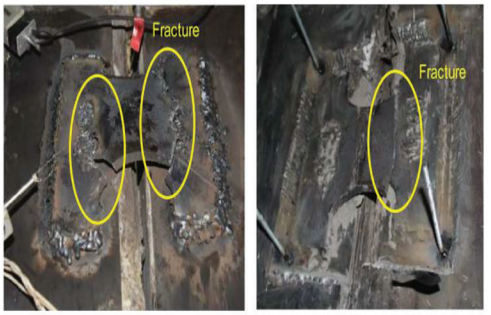
ACI Structural Journal, V. 122, No. 5, September 2025.
MS No. S-2024-076.R3, doi: 10.14359/51746816, received January 3, 2025, and reviewed under Institute publication policies. Copyright © 2025, American Concrete Institute. All rights reserved, including the making of copies unless permission is obtained from the copyright proprietors. Pertinent discussion including author's closure, if any, will be published ten months from this journal's date if the discussion is received within four months of the paper's print publication.



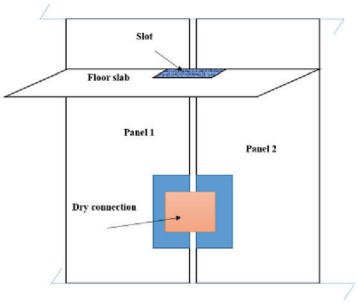
a) Welded loose plate connection



b) Local crushing of concrete



c) Fracture near slot weld [24]



d) Slotted floor slab system

Fig. 1—Welded plate connection.

energy and reduces the risk of brittle failure. The ease of replacement of dry connections after an earthquake further enhances their appeal in seismic-resistant constructions. These benefits favor dry and ductile connections in intermediate precast structural wall construction in Seismic Design Categories A, B, and C.

Contemporary dry connections in precast construction use mechanical bolts, threaded rods, dowel bars, welded connections, or specialized connectors.[20-23] These connectors avoid wet concrete, expediting construction and ensuring better quality control. Their ability to absorb deformation enhances the resilience in seismic zones. The selected vertical connection must exhibit elastic-plastic behavior, maintain a stable hysteretic response during reversed cyclic loading, accommodate larger deformations, dissipating more energy than the cast-in-place monolithic structural walls, and fulfilling its functions without complete collapse. The vertical bolted connections in precast reinforced concrete (RC) shear wall assembly primarily function to transfer vertical shear forces between adjacent walls when subjected to lateral loads. If designed effectively, these connections allow the lateral load behavior of the precast shear wall to approximate that of a monolithic RC shear wall.[24]

The connection consists of a rectangular steel plate with a concentric circular perforation for coupling precast structural walls.[25] The baseline welded stitch plate (WSP) connections tested were the weakest and most flexible among the grouted panel packet connection and post-tensioned corbel connections. Their strength relied heavily on the strength and arrangement of the cast-in shear studs. In contrast, the stiffness of the connection was influenced by the configuration of these studs.[26]

Welded loose-plate connections consist of angle sections tested under quasi-static loading in the laboratory as shown in Fig. 1(a). The experimental results show that these connections resist high lateral forces and transfer shear forces effectively. However, these connections fail in brittle mode, leading to local crushing of concrete around the embedded region due to inadequate embedment techniques, as shown in Fig. 1(b).[27] To prevent local crushing, the use of anchoring techniques for plate embedment needs to be modified.

The steel shear key connection proposed consists of H-shaped plates, on which the experimental study was carried out, under quasi-static loading. The experimental results showed that the walls with steel shear keys performed better than the monolithically constructed walls, with high lateral strength, energy dissipation, and ductility.[28,29] Fracture near the plug weld was observed, as shown in Fig. 1(c). The failure of the weld in the connection area seems to be brittle, so it needs to be avoided. Conventional cast-in-place RC structural walls often lack ductility and are prone to cracking due to their low height-to-width ratio. In contrast, the RC precast structural walls with welded plate connections are divided into smaller segments, which improves deformability of the structural wall system, reduces damage to the wall elements, and improves overall performance of the structure. To enhance the energy dissipation, two precast walls were separated with a gap.

However, conventional floor slabs exhibit concentrated deformation in the narrow gap between two wall panels. This shearing deformation can lead to damage and limits the application of precast shear key walls. A slotted floor system possesses a gap (slot) between the wall panel and the floor slab at the slab level as shown in Fig. 1(d). In these systems, the slot makes it so the floor slab is not directly connected to the wall panels, and it is filled with polystyrene.[30-32] The slot provided at the floor slab allows for release of concentrated deformation in the floor slab and enables the

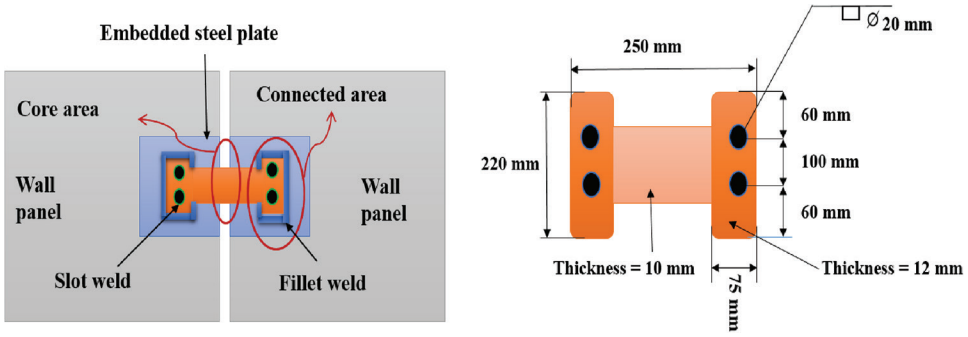


Fig. 2—Proposed connection and detailing.

migration of shear failure by increasing the proportion of bending deformation. Additionally, it helps to reduce mutual damage between the floor slab and wall panels. Based on this background, two walls were separated with 30 mm gaps, which is based on the serviceability criteria and avoids the crushing of panels hitting each other during the application of lateral load. Between the upper wall panels, a plastic pad was inserted between the panels during testing. Using a steel shoe as a replacement for the foundation beam significantly reduced the experimental testing cost.[33]

RESEARCH SIGNIFICANCE

This study proposes an improved detailed connection system using steel plates of varying thickness to prevent brittle weld failure and to encourage yielding in the unconnected region of the plate. Additionally, it explores a novel comparison between single-faced and dual-faced connections and examines the effect on the yield strength of the connection plate. These insights offer significant refinement in connection design, improving structural performance and resilience. The hysteretic response, mode of failure, and state of strain in the connecting plates of structural walls with vertical connections were verified under quasi-static reversed cyclic loading. An improved anchoring method for minimizing local crushing due to stress concentration near the embedded plate region was adopted for all specimens.

PROPOSED CONNECTION AND SPECIMEN PREPARATION

Three different welded plate connections in structural wall panels with the same reinforcement detailing and anchoring techniques with embedded steel plates were tested to study their performance. The connection consisted of two individual RC structural wall panels measuring 3850 x 850 x 200 mm with embedded steel plates at midheight. For testing the connected RC structural wall panels, the bottoms of the wall panels were erected in a steel shoe and fixed to a strong floor, with the top ends reflecting the free end similar to real wall conditions in a building. A steel shoe at the top connected to the loading beam for transferring the dead loads. The use of steel shoes for fixing and transferring the loads significantly reduces the cost of testing and mimics casting in a prefabrication yard.[33] Horizontal panel casting is also easier than vertical casting.

The seismic behavior of full-scale precast structural wall panels connected with the ductile welded steel plate connections was studied experimentally. A steel plate was embedded into a precast wall panel during the casting stage and another H-shaped steel plate was connected to the structural wall panels after they were erected as a vertical welded plate connection. This connection is very similar to that of coupled structural walls, except for the difference of the load transfer mechanism. The coupled beam transfers both the shear force and bending moment from one wall to another, whereas the welded steel plate connection transfers only the shear force, similar to a shear key.

The proposed design philosophy for this ductile connection emphasizes that welding should be intact, without failure, as it is catastrophic and should be avoided under dynamic loading conditions. Therefore, the strength of the weld should be much higher than the strength of the unconnected plates. The size and length of the weld and the thickness of the connecting plate are directly related to the strength of the weld. Because fillet welding is performed around the perimeter of the flange area, the available weld length depends on the perimeter of the flange area. To achieve the same strength of connection, a rectangular configuration would require a thicker connecting plate, or a larger plate size compared to an H-shape, which is not economical.

This study proposes an H-shaped improved ductile connection, in which the connecting plate is designed to yield prior to failure of the structural wall panel and weld. This connection promotes ductile failure and enables sufficient energy dissipation. An improved tapered connecting steel plate is proposed, consisting of two distinct sectional parts: the connected part and the unconnected part (core area), as shown in Fig. 2. The connected part has a thickness of 12 mm, providing the necessary shear strength to the connection, as it is directly influenced by the strength and size of the weld and the plate thickness. On the other hand, the unconnected part has a thickness of 10 mm, which acts as a weaker section, possessing sufficient ductility and energy dissipation capacity. To ensure ductile behavior, the design aims at yielding the connection first. This necessitates maintaining a specific distance between the two wall panels. If the wall panels are positioned closely, they contact each other, causing concrete crushing in the wall panel due to collision of the wall panels. Then, the connection does not transfer the load, wall panel collision under lateral loading is not acceptable; therefore, a 30 mm gap is provided between the wall panels.

Detailing of connection

The welded plate connection consists of two forms of welds: peripheral fillet welds and circular slot welds, as shown in Fig. 2. Fillet welds provide a highly efficient lap joint, and are easy to fabricate, modify, and join at different locations. Slot welds transfer the shear force between steel plates and prevent the connecting plate from out-of-plane buckling under dynamic loads. The connecting plate is designed to ensure yielding of the connecting plate before failure of the wall panel. The welded connections were designed as per AWS D1.1/D1.1M:2020.[34] A 10 mm fillet weld was adopted along the periphery. As per AWS D1.1/D1.1M:2020, the minimum size of a fillet weld is 5 mm (for plate thicknesses varying between 6 and 12 mm) and the maximum size of the fillet weld is equal to the thickness minus 2 mm (for thicknesses greater than 6 mm). The minimum length of the weld is at least four times the nominal size of the weld as per the code (4 × 10 = 40 mm). To avoid out-of-plane buckling of the connecting plate, a 20 mm diameter slot weld at 100 mm center-to-center spacing was used, as shown in Fig. 2. The minimum size of the slot weld is its thickness plus 8 mm (10 + 8 = 18 mm), and the minimum center-to-center spacing of slot weld is at least four times the hole diameter (4 × 20 = 80 mm). Material characterization was carried out to understand its properties, to be adopted in casting and testing.

Concrete

Before casting prefabricated wall panels, the properties of cement, sand, coarse aggregate, and water were determined. Concrete mixture design was carried out and the average 28-day compressive strength of the concrete on standard 150 mm cubes was observed to be 40.68 MPa, as shown in Table 1. During the casting process, 80 mm fresh concrete slump was found to ensure good workability using a water-cement ratio (*w*/*c*) of 0.44. The concrete mixture proportion of 1:1.438:2.61 was used for casting wall panels.

Reinforcing steel

For all wall elements, Fe 550D grade steel reinforcing bars of 8 and 16 mm diameter were used. The bars were tested in the laboratory using a universal testing machine (UTM). The modulus of elasticity, yield and ultimate strengths, and strain in the reinforcing bar were determined. The stress-versus-strain response as obtained is shown in Fig. 3.

Connection steel plate

For connecting two wall panels, a 12 mm thick mild steel plate was adopted in one case and an 8 mm thick high-strength steel plate was adopted in another case. Tension coupon testing was performed on these steel plates to obtain the yield strength and yield strain, which are shown in Table 2. The stress-strain variation in the mild steel (MS) and high-strength steel (HS) plates are shown in Fig. 4.

Grout

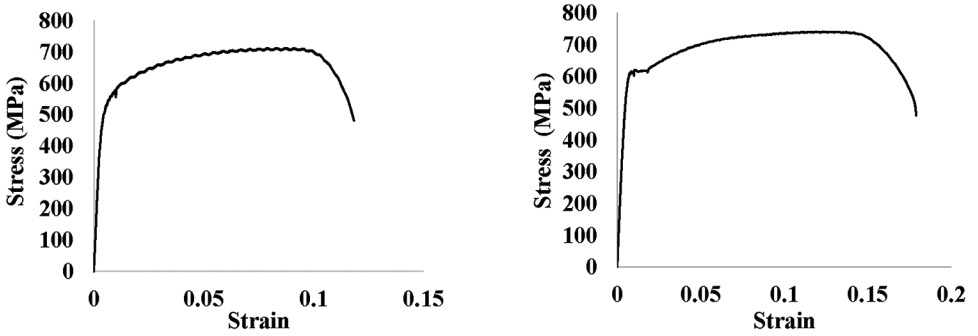
After erecting the structural wall panels in the bottom steel shoe, they were locked with four anchoring rods. The gaps between the wall panel and the steel shoe base and side faces were filled with a high-strength grout. To improve the bond between the wall panel and the steel shoe, the concrete surface was roughened by chipping the concrete surface. Commercially available grout powder with a compressive

Table 1—Concrete mixture and compressive strength

Mixture ratio	*w*/*c*	Average compressive strength, MPa	
		7 days	28 days
1:1.438:2.61	0.44	27.18	40.68

Table 2—Stress-strain details for connection plate

Specimen code	Connecting plate			Connection detail
	Yield strength, N/mm^2	Yield strain, με	Dimensions, mm	
PSW1 MS	231	2050	250 x 220 x 12 (varying thickness)	One face
PSW2 MS	231	2050	250 x 220 x 12 (varying thickness)	Both faces
PSW1 HS	390	3000	210 x 180 x 8 (constant thickness)	One face



a. 8mm Reinforcing bar

b. 16mm Reinforcing bar

Fig. 3—Stress-strain curve for reinforcing bars.

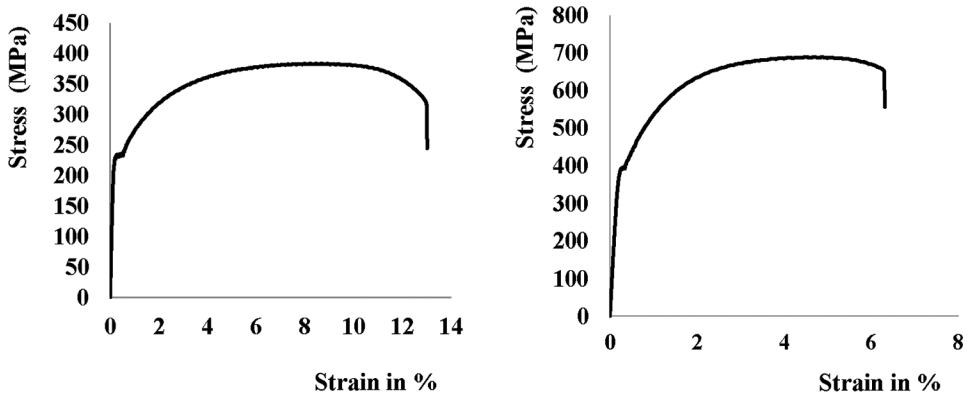


Fig. 4—Stress-strain curve from tension coupon test.

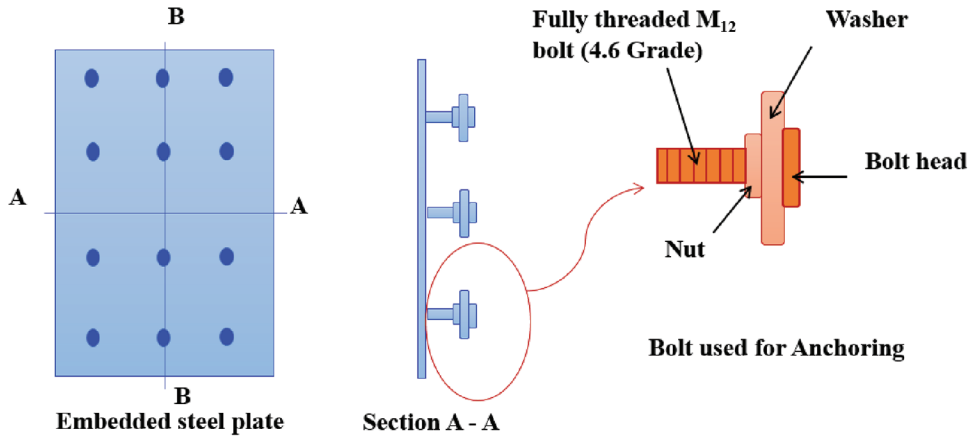


Fig. 5—Embedded steel plate with M12 bolts.

Table 3—Average compressive strength for grout

Description	Water-powder ratio	Flow	Compressive strength, MPa		
			3 days	7 days	28 days
GP2	0.17	Flowable	52	62	73

strength of 73 MPa at 28 days was used. It could sustain the static and dynamic loads. The water-powder ratio was 0.17. The grout was mixed gently to flow consistently. A flow test was carried out to observe the flow of the grout. Also prepared were 70 x 70 x 70 mm cubes to determine the grout's compressive strength, as shown in Table 3.

Fabrication process

The test specimens comprised prefabricated RC wall panels that were embedded with steel plates, the top steel shoe for applying the axial load, and a bottom steel shoe to fix to the strong floor. The preparation of these wall specimens involves several processes such as fabrication of the embedded steel plate, the reinforcement cage in the wall panel, casting of the concrete, and then lifting and stocking of the wall panels. It also includes the fabrication of the top and bottom steel shoes.

Fabrication of embedded steel plates

The steel plates were embedded in the structural wall panels during casting. The effective embedment was achieved by various mechanisms such as bonding, interlocking, and confining reinforcement. Pullout tests were carried out to study the bond strength between concrete and anchors. The results showed that a fully threaded bolt with a washer-nut arrangement achieved higher bond strength and displayed superior post-peak response than the other traditional anchors such as threaded rods or studs. Enhanced mechanical interlocking exhibited the higher interface fracture energy in the fully threaded washer-nut arrangement.[35] An embedded plate of 480 x 260 x 10 mm was adopted across all structural wall panels wherever connections were designated. The steel plates were anchored through fully threaded M12 bolts of 4.6 grade with a washer-nut system as shown in Fig. 5. Mild steel plates were adopted due to the advantages of their mechanical properties such as low-temperature performance, plasticity, ductility, and weldability. The fabrication of the embedded steel plates included marking the hole location, drilling the holes, threading in the hole, fixing the bolts, and tack welding, as demonstrated in Fig. 6(a) to (d). Direct tack welding of the bolts on the plate is not safe under cyclic loading. For that, a hole is made and the bolt is tightened, then tack welding is provided. Each plate was accommodated with 18 bolts on the rear face for anchoring purposes, with 80 mm center-to-center spacing.



a. Drilling hole



b. Threading in hole



c. Fixing bolts



d. Tack welding

Fig. 6—Process involved in making embedded plate.

Reinforcement detailing of specimen

When the wall panel is intended to act as a structural element, it might need to support gravity loads, withstand bending and shear forces, or be designed as a structural wall. All RC structural wall panels were designed and detailed according to IS 1893 (Part 1):2016 and IS 13920:2023 for ductile detailing; in this study, the same reinforcement detailing was adopted for all the panels.[36,37] The boundary elements of each structural wall panel were reinforced with two 16 mm diameter reinforcing bars on each face, with confining reinforcement of 8 mm stirrups at a center-to-center spacing of 200 mm. In the middle of the structural wall, vertical and horizontal bars of 8 mm diameter were placed at center-to-center spacing of 200 mm, with additional links of 8 mm bars positioned as shown in Fig. 7.

Casting, lifting, and stocking of panels

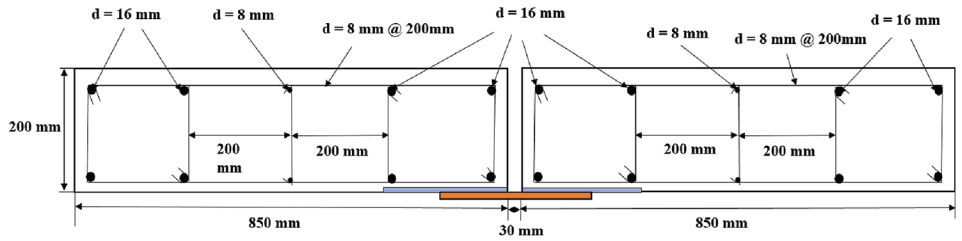
Fabrication of the RC structural walls[38] included mold preparation; reinforcement caging; strain gauge mounting; and mixing, placing, compaction, finishing, and curing of concrete, as shown in Fig. 8(a) to (f). The mold was prepared using steel channel sections and plywood sheets. After preparation of the specimen mold, plaster of paris was applied in the gaps between the edges and corners of the mold. Subsequently, the inner surfaces of the wooden planks were lubricated for easy demolding. Then the reinforcement cage was positioned in the mold with three lifting hooks. Electrical-resistant strain gauges, 10 mm in size, were mounted at specified locations to monitor the strain during testing of the specimen. The strain gauges mounted to the reinforcing bars were wrapped with a flexible material to minimize damage to the strain gauges during casting and compaction of concrete. Embedded steel plates along with the reinforcing bars were placed in the mold with spacer blocks for achieving minimum cover all-around. The concrete-making materials were weighed and mixed in a machine mixer. The concrete was placed, compacted using a needle vibrator, and the surface was finished using a leveling bar. Curing of walls was done by covering the specimen with canvas bags and sprinkling with water for 7 days. Then the specimen was lifted out of the casting mold using a forklift and stocked for the remaining proposed curing period.

Fabrication of top and bottom steel shoe

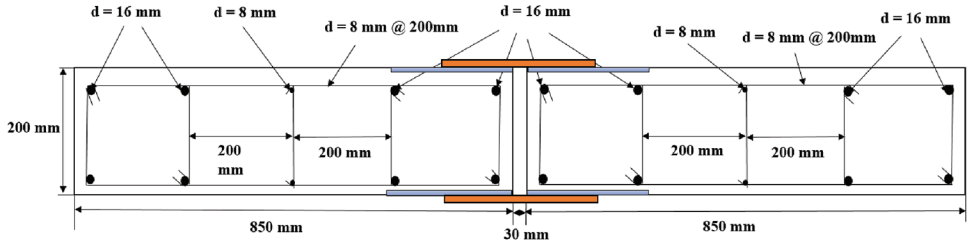
For transferring the axial compression uniformly to the structural wall, the top steel shoe was fabricated, and the bottom steel shoe was fabricated to position the structural wall panel and connect with the strong floor. The bottom plate of the foundation shoe is fixed to the strong floor using eight anchor bolts, while the wall panel is locked with the foundation shoe through vertical plates using four anchor bolts, as shown in Fig. 8(g). Additional stiffeners were provided to resist the reaction moment during testing. The clearance between the faces of the steel shoe and concrete wall panel was filled with grout. The connecting plate was welded layer by layer, in a time gap of 1 hour between each layer to allow the temperature to cool down.

EXPERIMENTAL INVESTIGATION

After curing for 28 days, two precast wall panels, measuring 3850 x 850 x 200 mm, were positioned on a horizontal concrete floor and aligned with the locking system



a) PSW1 MS and PSW1 HS (Connection on one face)



b) PSW2 MS (Connection on both faces)

Fig. 7—Reinforcement detailing of specimens.

using four strong steel channel sections for lifting by a crane. The lifted structural wall panels were then positioned in the specially prepared bottom shoe, which was aligned with four symmetrically positioned anchoring rods. While testing the structural wall, the boundary conditions reflect the cantilever wall with fixed support at the bottom by anchoring the steel shoe to the strong floor; the top end was free. Specimen designation was as follows: the single-sided mild steel plate connection at the midheight location was PSW1 MS; the two-sided mild steel plate connection at the midheight location was PSW2 MS; and the single-sided high-strength steel plate connection at the midheight location was PSW1 HS.

Loading condition

Quasi-static reversed cyclic loading was applied on structural walls under simulated seismic or wind loads to study their performance. ASTM E2126[39] was adopted for seismic assessment to measure the shear resistance of vertical elements of the lateral force-resisting systems. This method yields initial stiffness, shear strength, energy dissipation capacity, and ductility of the wall panels. To replicate the real-life building scenario, a constant axial load of 650 kN was applied through two 500 kN capacity hydraulic jacks, on top of the steel shoe, as shown in Fig. 9. Initially, five fully reversed single cycles of 1.25, 2.5, 5.0, 7.5, and 10 mm were adopted, followed by three fully reversed cycles of 20, 40, 60, 80, 100 and 120 mm through a 1000 kN actuator. For free lateral movement with less friction due to the applied axial load, a bearing arrangement was made consisting of a hinge with stainless steel plates, frictionless polytetrafluorethylene sheets, and lubricant. Throughout testing, data from load cells, linear variable differential transformers (LVDTs), strain gauges, and actuators were continuously monitored through a data-acquisition system. The front and side views of the experimental setup are shown in Fig. 10.

Instrumentation

The instrumentation required for obtaining the required data at various critical locations throughout testing of walls is shown in Fig. 11. Axial load was applied through two hydraulic jacks and reading was monitored using two 1000 kN load cells. Lateral load was applied through displacement-controlled cycles using a 1000 kN actuator. The lateral load and other data were recorded in a data-logging system throughout the experimentation. Strains were measured at several critical locations in steel reinforcing bars and on the concrete surface throughout the testing. To determine the state of stress and strain at a point in reinforcing bars or concrete surface, a strain gauge rosette with three strain gauges oriented at 0, 45, and 90 degrees was positioned in the middle of the connecting plate. These steel plates were mounted with 5 mm length strain gauges to measure the strain along three directions. For obtaining the strains due to flexure and position of neutral axis depth, 10 and 5 mm strain gauges were mounted just above the bottom steel shoe in the vertical reinforcement. The embedded steel plate in concrete causes stress concentration, where the strain gauges were located closely. To measure the strains on the concrete surface near the corners of the steel plate, a 60 mm strain gauge was mounted to measure the strain along the diagonal direction. To estimate the story drift, five LVDTs were fixed at heights of H, $3H/4$, $H/2$, $H/4$, and 0. During testing, it was proposed to measure the displacements in the push and pull directions of walls along the centerline of the actuator; two LVDTs were positioned. To measure the out-of-plane deformation on each wall panel, two LVDTs were provided. To measure the rocking and uplift movement of the wall, two LVDTs were positioned. To measure the lateral movement of the bottom shoe, two LVDTs were provided. To measure the deformation in the connection region, two LVDTs were placed diagonally. To monitor the opening and closing of the gap between the wall panel, two LVDTs were provided at heights of $3H/4$ and $H/4$.



a. Strain gauge fixing



b. Mould



c. Plate position



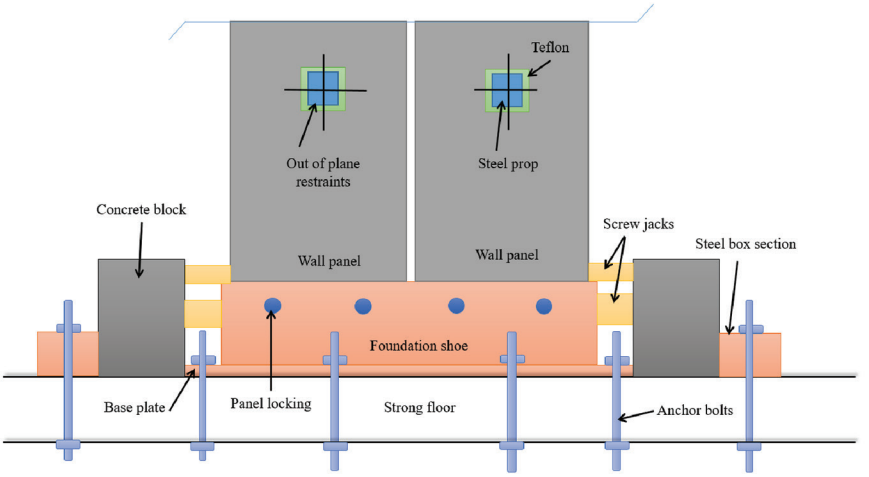
d. Slump test



e. Compaction



f. Stocking of panels



g. Locking arrangement

Fig. 8—Casting, lifting, and stocking of panels.

EXPERIMENTAL RESULTS AND DISCUSSION

This section presents experimental findings and data analysis, including the hysteresis and backbone curves, stiffness reduction, energy dissipation capacity, hysteresis damping coefficient, strain variations in the wall panels, the state of strain in the connecting steel plate, crack patterns in the wall panels, and failure of the connecting steel plate. The experimental results observed during testing of the wall panels are shown in Table 4.

Hysteretic behavior

During seismic loading, structures experience cyclic loading and unloading through ground shaking. The hysteretic response reflects how a structure behaves under cyclic loading and unloading, which helps to design the structure for earthquake loading with minimum damage. The reversed cyclic load-displacement response of PSW1 MS (connection on one face) exhibited hysteretic behavior, as shown in Fig. 12(a). The hysteric curve reached saturation without flattening up to a cyclic displacement of 24 mm. However,

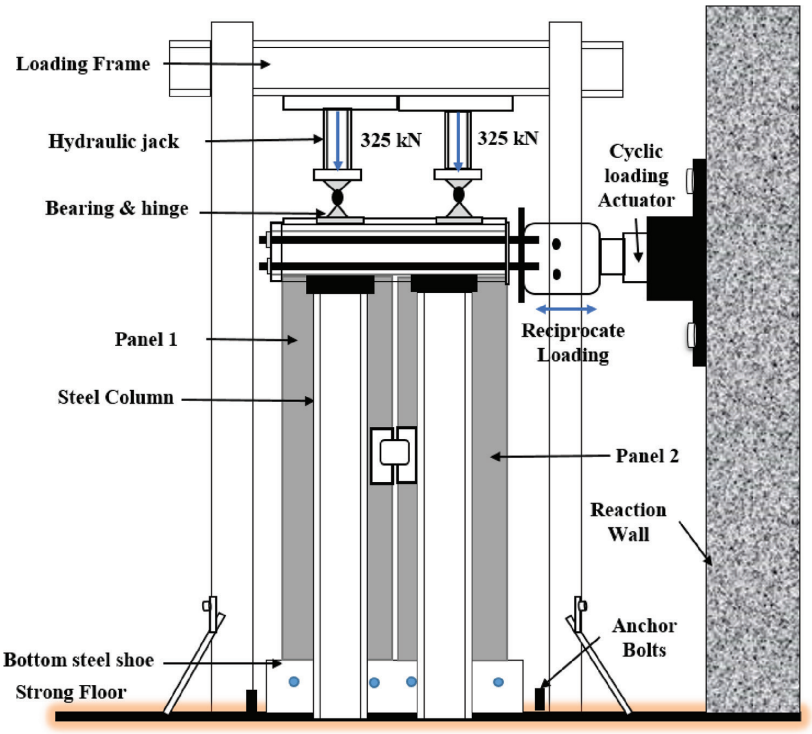


Fig. 9—Experimental setup for quasi-static loading.



Fig. 10—Front and side view of experimental setup.

at a displacement cycle of 48 mm, plumber hysteresis was observed, which occurs commonly in hybrid connections within precast wall system. The measurements observed from the LVDTs show that the wall panels were rocking slightly due to interface failure between the grout and concrete wall panel due to an inadequate locking system. Such a rocking mechanism could be prevented in the other two wall specimens by strengthening the locking arrangements. Yielding was observed at a load of 206 kN with a drift of 1/240, while the ultimate load was recorded at a load of 315 kN with a drift of 1/42. The hysteresis response is shown in Fig. 12(b) for the PSW2 MS specimen, which had connections on both faces. It displayed a consistent and broader hysteresis area compared to the PSW1 MS plate, which had a connection on one face. Notably, there was no pinching and rocking effect. The wall specimen exhibited yielding at a load of 342 kN, accompanied by a drift of 1/176. Furthermore, the ultimate load reached 427.1 kN at a drift of 1/85. Figure 12(c) shows the hysteretic behavior of PSW1 HS, which had a single-face connection with high-strength steel plate. This connection exhibited a poorer hysteresis curve than that of PSW2 MS without pinching and rocking effects. The connecting steel plate reached the yield strain at a displacement of 1/470 at the lowest yield load of 101.25 kN. The ultimate load of

Table 4—Experimental results

Specimen code	Initial stiffness, kN/mm	Drift at yield strain	Load at yield strain, kN	Peak load, kN	Ultimate displacement, mm	Failure in connecting plate
PSW1 MS	18.62	1/240	206.32	314.7	120	Yielding of connecting plate
PSW2 MS	36.67	1/176	342.16	427.1	100	Yielding of connecting plate
PSW1 HS	19.19	1/470	101.25	234.7	60	Fracture of connecting plate

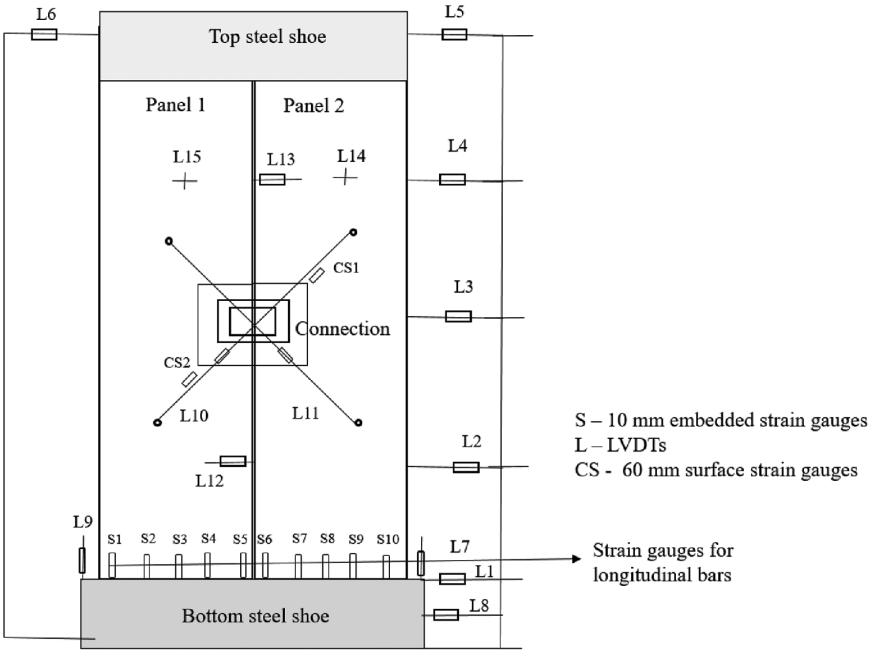


Fig. 11—Instrumentation details.

234.7 kN was observed at a drift of 1/58, with significant brittle failure due to fracture of the connecting steel plate at the weld location. From the hysteresis curves, PSW2 MS exhibited good and broader hysteretic response with better post-peak response with gradual failure due to symmetry of connections at two locations, with connecting steel plates on both faces of the wall. In comparison, PSW1 MS, with a single connecting plate, showed good post-peak behavior without fracture of connecting plate, while its hysteresis curve exhibited a different pattern due to rocking of the wall panels. This rocking effect was minimized in both PSW2 MS and PSW1 HS configurations by improved locking arrangements. The PSW2 MS specimen exhibited higher yield load and displacement. This occured as the two steel plates exhibited yielding in PSW2 MS at a load of 1.65 and 3.47 times that of PSW1 MS and PSW1 HS, respectively.

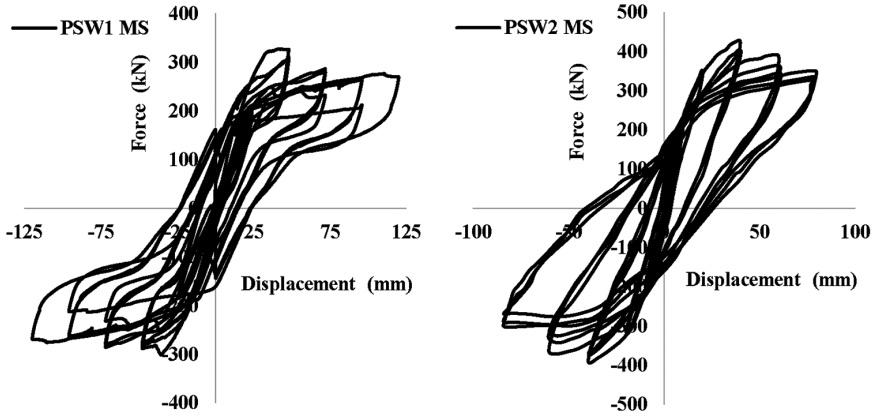
Stiffness degradation

Under reversed cyclic loading, precast RC structural walls exhibit stiffness degradation soon after cracking initiates in wall panels, yielding of steel plates, and plate rupture. Stiffness degradation was observed during both positive and negative load cycles in all structural walls. The stiffness degradation curves observed in the precast walls are shown in Fig. 13. In specimen PSW1 MS, which was connected on one face of the wall only, the initial stiffness during the positive load cycle was observed to be 18.62 kN/mm. However, with a connecting plate on the other face in PSW2 MS, the initial stiffness was observed to be doubled, equal to 36.69 kN/mm during the positive cycles. During the negative load cycles, the initial stiffness was observed to be lower than that of the positive cycle. In PSW1 MS, the stiffness was observed to be 16.19 kN/mm, whereas with PSW2 MS, the stiffness was observed to be 33.2 kN/mm. In PSW2 MS specimen, the connecting plate was attached to both faces, which doubled the stiffness compared to that of the single-face connection in PSW1 MS. Remarkably, once the yielding displacement cycle was surpassed, both connections PSW1 MS and PSW2 MS demonstrated comparable secant stiffness values, which was followed by yielding of the connection. The initial stiffness of 19.18 kN/mm was observed in connection PSW1 HS, which was almost same as that in PSW1 MS. The degrading trend during the positive and negative load cycles was the same in both PSW1 MS and PSW1 HS connections.

$$\text{Secant stiffness } K_i = \frac{\text{Force corresponding to the cycle } (F_{i\text{-th cycle}})}{\text{Displacement corresponding to the cycle } (u_{i\text{-th cycle}})}$$

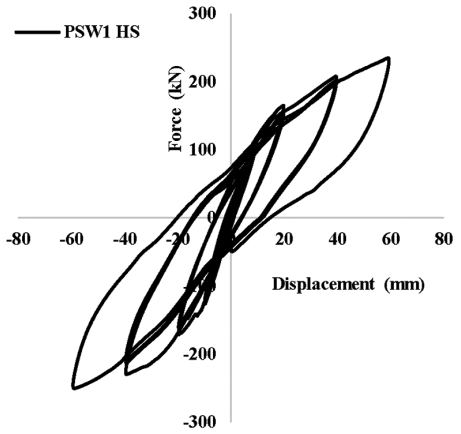
Backbone curve

The backbone curve is the simplified representation of the hysteresis curve, which shows the overall behavior of the precast structural wall connection. This backbone curve is developed by joining peak load points corresponding to the displacement cycles under both positive and negative loading. The backbone curve is influenced by the structural system stiffness, strength, and material properties of the



a) Hysteresis for PSW1 MS

b) Hysteresis for PSW2 MS



c) Hysteresis for PSW1 HS

Fig. 12—Hysteretic curves in various connections.

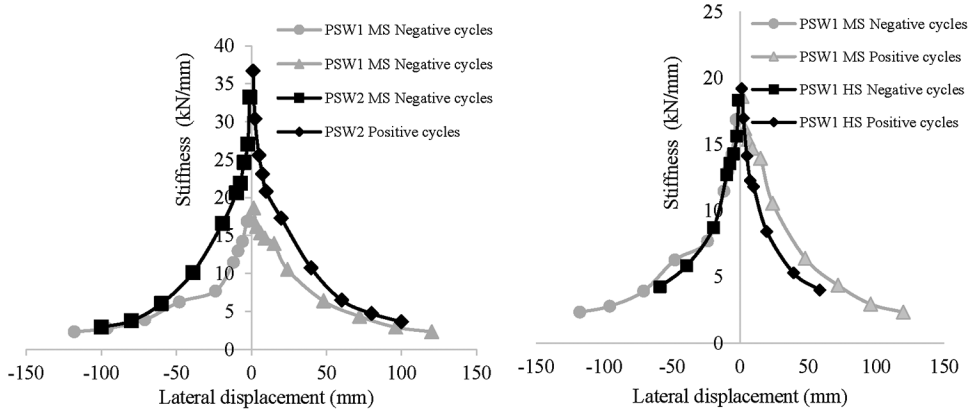


Fig. 13—Stiffness degradation.

building components. Figure 14 demonstrates the backbone curves for connections PSW1 MS and PSW2 MS, where the connecting plates in both walls yielded at displacements of 14.65 and 20 mm, respectively. But PSW2 MS exhibited a load of 1.65 times that of PSW1 MS. Furthermore, PSW2 MS achieved an ultimate load that was 36% higher than that of the PSW1 MS connection. In contrast, the connecting plate in PSW1 HS yielded at a displacement of 7.5 mm, with a corresponding yield load of 101.25 kN, which was much lower than the other two connections. Due to 8 mm thickness, the high-strength steel plate underwent yielding at lower displacement compared to the other two. In the PSW1 HS connection, the ultimate load of 234.7 kN was attained at a displacement of 60 mm, where sudden brittle fracture of the connecting plate occurred, indicating reduced post-peak behavior. This observation suggests that the use of high-strength plates does not effectively transfer the shear force from one wall panel to another. Thus, it is not worth connecting the system with a high-strength steel plate in a vertical connection between precast wall panels. Due to the

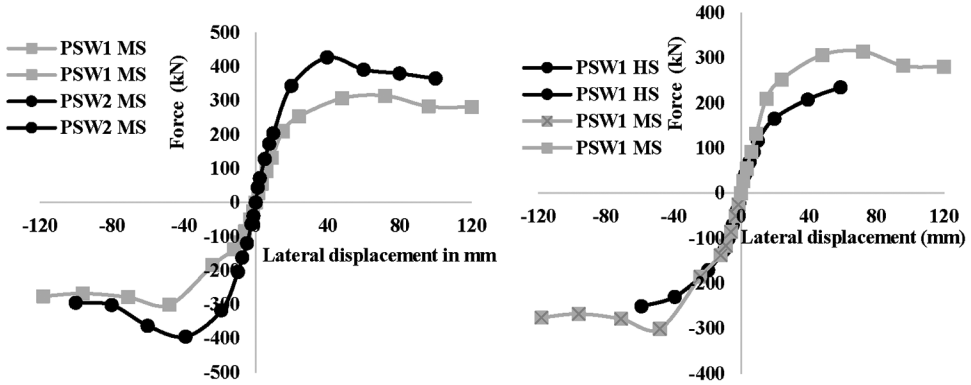


Fig. 14—Backbone curve.

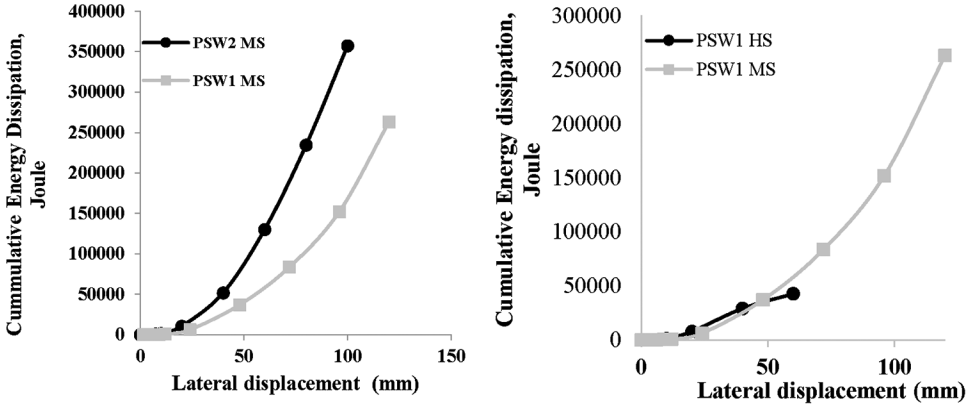


Fig. 15—Cumulative energy dissipation.

limitation of the 125 mm displacement of the actuator head, in both the push and pull directions, the backbone curves were drawn up to 120 mm in wall panels with connections PSW1 MS and 100 mm in PSW2 MS. Notably, none of the connections experienced complete failure; instead, yielding of the connecting plate took place, except in PSW1 HS.

Energy dissipation

Under quasi-static loading conditions, energy dissipation can be estimated by measuring the area under the load versus the displacement curve. To calculate the dissipated energy, it needs integration of the area under the load-displacement curve. The integral represents the sum of the products of load and displacement over the entire range of the test. Energy absorption capacity is the qualitative measure for plastic deformation and for the better seismic performance of precast structural wall connection. The cumulative energy dissipation in a precast structural wall subjected to cyclic loading refers to the total energy absorbed and dissipated by the structure as it undergoes repeated loading and unloading cycles represented in Fig. 15. This dissipation occurs due to internal damping mechanisms within the structure, which converts the mechanical energy from the applied loads into non-recoverable forms such as heat. Structures with high energy dissipation capacity can absorb seismic energy and withstand the effects of earthquakes with reduced damage. It was seen that PSW2 MS (both face connections) exhibited higher energy dissipation of 357 kJ than PSW1 MS and PSW1 HS. The cumulative energy dissipated by PSW2 MS was 35% more than PSW1 MS. PSW1 HS exhibited very low cumulative energy dissipation of 42.6 kJ because of the brittle failure of the connecting plate at a low displacement of 60 mm. Up to 40 mm displacement cycles, both PSW1 MS and PSW1 HS showed similar energy dissipation. Thereafter, PSW1 MS dissipated energy due to yielding of the connection plate. Energy dissipation was observed to be very low during the initial displacement amplitudes as the response is elastic. This energy dissipation capacity is the important parameter to estimate the hysteretic damping coefficient.

Hysteretic damping ratio

Kelvin-Voigt's viscoelastic model (Eq. (1)) has been used for studying the damping of real structure in the elastic range, which consists of a dashpot and spring connected in parallel.[40,41] From this model, the force P required to produce u-displacement is the sum of spring force and damping force. At a fast-loading rate, higher force is developed to produce same displacement, so that the viscous portion is complicated in terms of velocity (deformation rate) and it is approximately equal to $c\dot{u}$.

$$P = P_e + P_d = ku + c\dot{u} \quad (1)$$

Assuming that the system undergoes vibration in sinusoidal wave form in Eq. (2), the forcing function, Eq. (3), has two components in Eq. (1), and the P-u function represents an ellipse. The area under the elliptic curve is the energy dissipated by viscoelastic damping.

Vibration function and the corresponding forcing function:

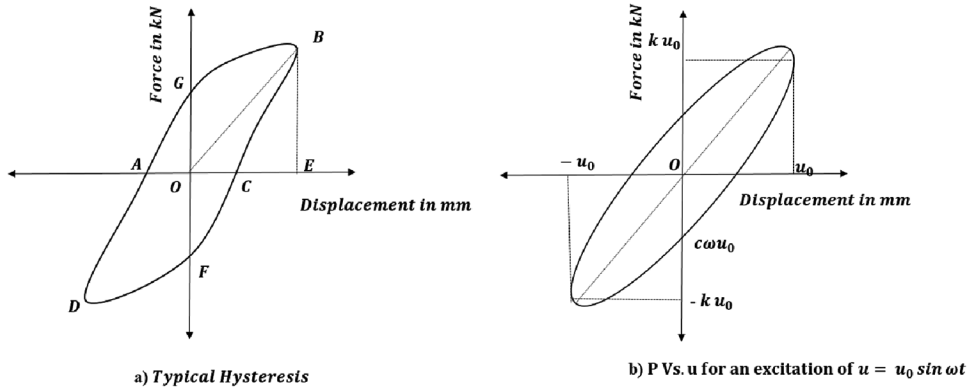


Fig. 16—Hysteresis curve—comparison.

$$u = u_0 \sin\omega t \tag{2}$$

$$P = ku_0 \sin\omega t + c\omega u_0 \cos\omega t \tag{3}$$

Maximum potential energy by considering as elastic:

$$U_e = \frac{1}{2} k u_0^2 \tag{4}$$

The energy dissipated by the viscoelastic component is the area under the loop calculated by integrating in Eq. (5)

$$\Delta W = \int_{T}^{T+2\pi\omega} P(t) \frac{du}{dt} dt = \pi c\omega u_0^2 \tag{5}$$

$$\frac{\text{Eq. (5)}}{\text{Eq. (4)}}$$

$$\frac{\Delta W}{U_e} = \frac{\pi c\omega u_0^2}{\frac{1}{2} k u_0^2} = \frac{2\pi c\omega}{k} \tag{6}$$

Damping can be written in terms of viscous damping ratio and c_{cr}

$$c = \varepsilon_e c_{cr} = 2M\omega\varepsilon_e$$

$$\varepsilon_e = \frac{c}{2M\omega} = \frac{c\omega^2}{2k\omega} = \frac{2\pi c\omega}{k} \frac{1}{4\pi}$$

$$\varepsilon_e = \frac{1}{4\pi} \frac{\Delta W}{U_e} \tag{7}$$

Inelastic deformation is observed during earthquake loading. The hysteretic behavior is more significant under dynamic loading conditions. By comparing Fig. 16(a) and (b), hysteretic damping may be approximately written as[42]

$$\text{Hysteretic damping ratio } \varepsilon_{hyst} = \frac{1}{4\pi} \frac{\Delta W_{hyst}}{U_e} = \frac{1}{4\pi} \frac{S_{ABC} + S_{ADC}}{S_{OBE}} \tag{8}$$

Hysteretic damping is a qualitative indicator of energy dissipation per cycle loading and it is an important parameter for the displacement-based design of structures. The hysteretic damping coefficient directly reflects the amount of energy dissipation in a system and is not affected by the specimen's characteristics or the loading procedure. A higher damping coefficient indicates a greater capacity of dissipating energy. This coefficient is derived from Eq. (8), which considers the area enclosed by a hysteresis loop ($S_{ABC} + S_{ADC}$) for a specific displacement cycle, as well as the area of the triangles (S_{OBE}) representing purely elastic behavior, as shown in Fig. 16(a). In the final displacement cycle, the equivalent hysteretic damping coefficients were 0.183, 0.198, and 0.077 for PSW1 MS, PSW2 MS, and PSW1 HS, respectively, from Fig. 17. At the ultimate displacement, PSW1 MS and PSW2 MS exhibited nearly the same hysteretic damping coefficient. However, at a displacement cycle of 60 mm, the hysteretic damping coefficient for PSW2 MS (0.2) was 60% higher than that of PSW1 MS (0.2) due to yielding of the plate on both faces. At 60 mm displacement cycle, PSW1 HS had only 0.077, which is 38.5% less than PSW1 MS.

Strain variation in panels

Strain gauges were strategically attached to the vertical reinforcements in the wall panels, positioned 150 mm above the lower steel shoe. Figure 18 illustrates the strain variation in precast structural wall panel corresponding to the 35 mm push cycle. In both PSW1 MS and PSW1 HS, the right wall panel experienced tension to roughly 95% of its extent. This indicates a relatively flexible connection link that imparts more bending in the wall panel, while transferring shear force from the right panel to the left. The neutral axis for the left panel is close to the midpoint of the left panel. This wall features a connection on one face, while lacking it on the opposing side, resulting in a marked distinction between the front and rear faces of the connection. This discrepancy arises from the inherent asymmetry of the connection configuration. Conversely, within PSW2 MS, the neutral axis precisely aligned with the midpoint of both the right and left wall panels. This precise alignment signifies a more robust connection link, creating a state of equilibrium, where one half-segment of the panel is subjected to tensile forces and the other half experiences compressive forces. It is noteworthy that both the anterior and posterior facets of the panel displayed analogous trends due to symmetrical arrangement of the connection.

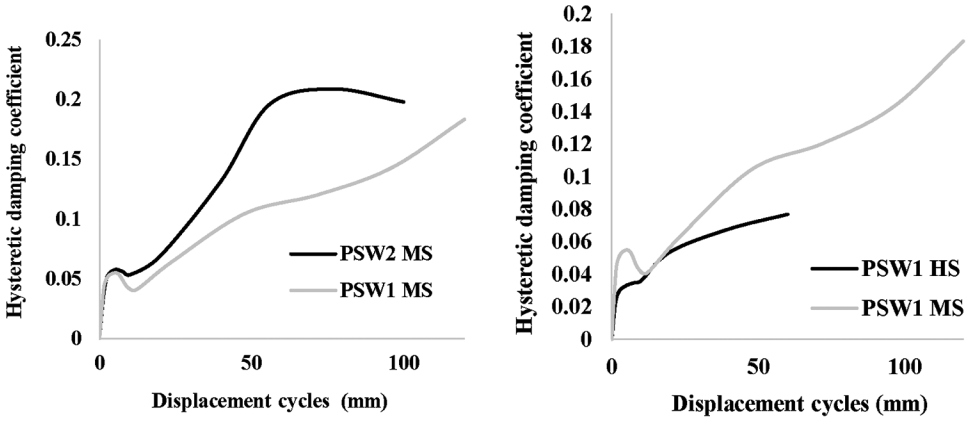


Fig. 17—Hysteretic damping coefficient.

State of strain in connecting plate

It is essential to monitor the strain state throughout testing to determine the yield strain and study the behavior of the connecting plate. A strain rosette of 0, 45, and 90 degrees was mounted on to the connecting plate to measure the maximum shear strain and major principal strain, and estimate the failure plane. The strain state corresponding to the yield point and ultimate point are given in Table 5. During the 96 mm cycle of PSW1 MS, a strain gauge got disturbed, and was unable to measure the strain at ultimate displacement. The observed variation in the failure plane ranges from +43 to –43 degrees for all specimens, indicating that the connecting plate primarily acts as a shear key, transferring shear force among wall panels. In PSW2 MS, both the front and rear side plates exhibited similar strain and trends due to the symmetric connection. The PSW1 HS plate reached its yield strain at a minimal displacement of 7.5 mm due to its lesser thickness compared to the other two. In both PSW1 MS and PSW2 MS, the connecting plate did not show a brittle fracture up to 120 mm displacement. However, the connecting plate in PSW1 HS fractured during 60 mm displacement cycle, leading to no post-peak behavior and rendering it unsuitable for dynamic loading conditions.

Failure mode

In PSW1 MS and PSW2 MS, the connecting plates yielded and the wall panels exhibited cracking, without collapse of the panel or rupture of the plate. Figure 19(a) shows the cracking of the wall panel, while Fig. 19(b) depicts yielding of the connecting plate. Initially, the cracks began as flexure cracks during the 24 mm displacement cycle and progressed into flexure-shear cracks in subsequent cycles. In PSW1 HS, the connecting plate failed due to a brittle fracture during the 64 mm displacement cycle without post-peak behavior. Therefore, using the high-strength connecting plate in welded plate connections is not advisable. The plate cracking originated at the junction of flange and web, then extended to connecting area, but stopped upon reaching the slot weld before fracturing, as shown in Fig. 19(c).

CONCLUSIONS

To study the performance of welded plate connections on one or both faces using mild steel and high-strength steel

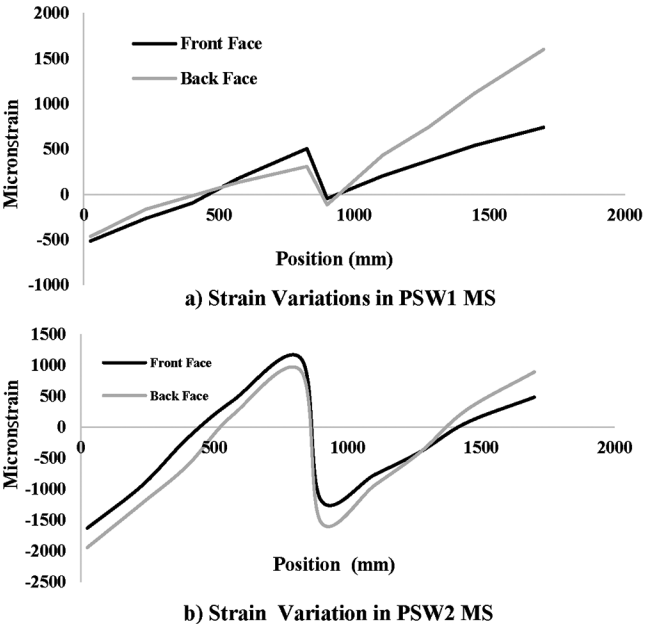


Fig. 18—Strain variation in panels.

connecting plates, quasi-static tests have been conducted. The experimental findings have been analyzed. From the experimental investigations, the following conclusions have been drawn:

1. PSW2 MS (two-faced connection with a mild steel plate) exhibited higher lateral stiffness than the single-face connection because the connection was made on both faces, making the structural wall stiffer and symmetric. It is important to note that the lateral stiffness of the specimen was almost double that of the one-faced connection.

2. In the case of mild steel plates, both single- and two-faced connections reached their yield strain at the story drift of 0.42% and 0.57%, respectively. In contrast, the specimen with a high-strength plate (PSW1 HS) yielded at a significantly lower story drift of 0.21%, which is half of the yield displacement of PSW1 MS.

3. The failure plane in all specimens was observed to range between 40 and 43 degrees, indicating that the connecting plate predominantly transfers the shear force from the loading panel to the adjacent panel and acts like a shear key.

4. At the ultimate displacement, the equivalent hysteretic damping coefficient was 0.183, 0.198, and 0.077 for PSW1

Table 5—State of strain for connecting plate

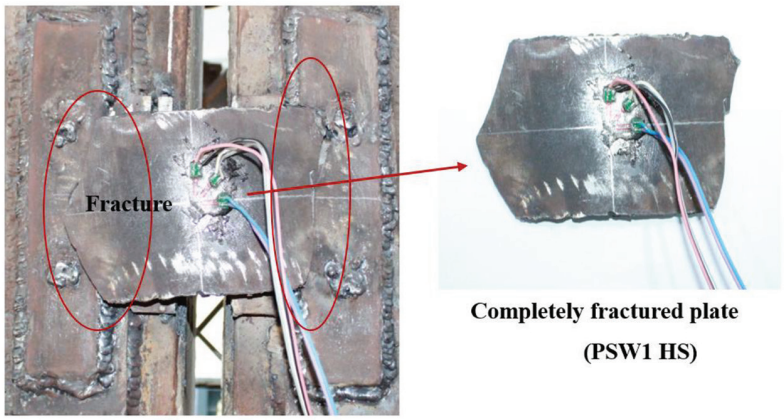
Specimen code	State of strain corresponding to yield point			Max. shear strain at ultimate displacement, μm/m
	Max. shear strain, μm/m	Failure plane angle	Failure plane variation	
PSW1 MS	2067	40.86	–40.5 to +40.5	—
PSW2 MS	2067	39.81	–41.3 to +39.5	20,569
PSW1 HS	3012	42.93	–42.5 to +43	16,440



a) Cracking in the panel



b) Yielding of connecting plate in PSW1 MS



c) Fracture of connecting plate in PSW1 HS

Fig. 19—Connection plate failure.

MS, PSW2 MS, and PSW1 HS, respectively. This suggests that the specimen with the high-strength plate exhibited very low energy dissipation capacity and is not advisable to use in earthquake-resistant prefabricated structures.

5. When the connection is on one face only, causing eccentricity to the connection, the neutral axis aligns with the edge of the panel instead of at the midpoint. Conversely, within PSW2 MS, the neutral axis aligns precisely with the midpoint of the right wall panel.

6. Connections with mild steel plates exhibit good ductility, while connections with high-strength steel plates fail suddenly due to rupture without post-peak response and should be avoided in connections.

AUTHOR BIOS

ACI member **A Selva Ganesa Moorthi** *is a Prime Minister's Research Fellow in the Structural Engineering Laboratory, Indian Institute of Technology Madras, Chennai, India. His research interests include precast reinforced concrete structures, dry connections, and structural concrete.*

ACI member **G. Appa Rao** *is a Professor at the Indian Institute of Technology Madras. He received his ME and PhD in structural engineering from the Indian Institute of Science, Bangalore, India. He is a member of Joint ACI-ASCE Committees 352, Joints and Connections in Monolithic Concrete Structures; 408, Bond and Development of Steel Reinforcement; and 447, Finite Element Analysis of Reinforced Concrete Structures. His research interests include reinforced concrete, connections, structural materials, fracture mechanics, and earthquake-resistant design of structures.*

ACKNOWLEDGMENTS

The authors are grateful for the financial support from the Prime Minister's Research Fellowship, Government of India, which was crucial in completing this research.

NOTATION

c = damping component
c_{cr} = critical damping coefficient
k = spring constant
m = system mass
P_d = damping force
P_e = spring force
u = displacement function
$\dot{u}$ = velocity function
ω = forcing frequency

REFERENCES

1. VanGeem, M., "Achieving Sustainability with Precast Concrete," *PCI Journal*, V. 51, No. 1, 2006, pp. 42-61. doi: 10.15554/pcij.01012006.42.61

2. Jaillon, L.; Poon, C.-S.; and Chiang, Y. H., "Quantifying the Waste Reduction Potential of Using Prefabrication in Building Construction in Hong Kong," *Waste Management*, V. 29, No. 1, 2009, pp. 309-320. doi: 10.1016/j.wasman.2008.02.015

3. Lefas, I. D., and Kotsovos, M. D., "Behaviour of Reinforced Concrete of Structural Walls: A New Interpretation," *Proceedings, IABSE Colloquium on Computational Mechanics of Concrete Structures—Advances and Applications*, Delft, the Netherlands, 1987, pp. 455-462.

4. Ozkul, T. A.; Kurtbeyoglu, A.; Borekci, M.; Zengin, B.; and Kocak, A., "Effect of Shear Wall on Seismic Performance of RC Frame Buildings," *Engineering Failure Analysis*, V. 100, 2019, pp. 60-75. doi: 10.1016/j.engfailanal.2019.02.032

5. Solak, A.; Tama, Y. S.; Yılmaz, S.; and Kaplan, H., "Experimental Study on Behavior of Anchored External Shear Wall Panel Connections," *Bulletin of Earthquake Engineering*, V. 13, No. 10, 2015, pp. 3065-3081. doi: 10.1007/s10518-015-9748-8

6. *fib*, "Seismic Design of Precast Concrete Building Structures: State-of-the-Art Report," *fib* Bulletin No. 27, International Federation for Structural Concrete, Lausanne, Switzerland, 2003.

7. ACI Committee 533, "Guide for Precast Concrete Wall Panels (ACI 533R-11)," American Concrete Institute, Farmington Hills, MI, 2011, 48 pp.

8. Kurama, Y. C.; Sritharan, S.; Fleischman, R. B.; Restrepo, J. I.; Henry, R. S.; Cleland, N. M.; Ghosh, S. K.; and Bonelli, P., "Seismic-Resistant Precast Concrete Structures: State of the Art," *Journal of Structural Engineering*, ASCE, V. 144, No. 4, 2018, p. 03118001. doi: 10.1061/(ASCE)ST.1943-541X.0001972

9. Singhal, S.; Chourasia, A.; Chellappa, S.; and Parashar, J., "Precast Reinforced Concrete Shear Walls: State of the Art Review," *Structural Concrete*, V. 20, No. 3, 2019, pp. 886-898. doi: 10.1002/suco.201800129

10. Hemamalini, S.; Vidjeapriya, R.; and Jaya, K. P., "Performance of Precast Shear Wall Connections Under Monotonic and Cyclic Loading: A State-of-the-Art Review," *Civil Engineering*, V. 45, No. 3, 2021, pp. 1307-1328. doi: 10.1007/s40996-020-00530-6

11. PCI, *PCI Design Handbook: Precast and Prestressed Concrete*, eighth edition, Precast/Prestressed Concrete Institute, Chicago, IL, 2017.

12. Finetti, I.; Russi, M.; and Slejko, D., "The Friuli Earthquake (1976–1977)," *Tectonophysics*, V. 53, No. 3-4, 1979, pp. 261-272. doi: 10.1016/0040-1951(79)90070-2

13. Fajfar, P., "The Behaviour of Buildings and Other Structures during the Earthquakes of 1979 in Montenegro," Institute of Structural and Earthquake Engineering, 1981.

14. Bonacina, G.; Indirli, M.; and Negro, P., "Northridge Earthquake—Report to the Sponsor: Earthquake Engineering Field Investigation Team," *Special Publication No. I.94.14*, 1994, Ispra, Italy.

15. Saatcioglu, M.; Mitchell, D.; Tinawi, R.; Gardner, N. J.; Gillies, A. G.; Ghobarah, A.; Anderson, D. A.; and Lau, D., "The August 17, 1999, Kocaeli (Turkey) Earthquake Damage to Structures," *Canadian Journal of Civil Engineering*, V. 28, No. 4, 2001, pp. 715-737.

16. Yin, Y.; Wang, F.; and Sun, P., "Landslide Hazards Triggered by the 2008 Wenchuan Earthquake, Sichuan, China," *Landslides*, V. 6, No. 2, 2009, pp. 139-152. doi: 10.1007/s10346-009-0148-5

17. Arthi, S., and Jaya, K. P., "Seismic Performance of Precast Shear Wall–Diaphragm Connection: A Comparative Study with Monolithic Connection," *International Journal of Civil Engineering*, V. 18, No. 1, 2020, pp. 9-17. doi: 10.1007/s40999-019-00444-z

18. Conley, J.; Sritharan, S.; and Priestley, M. J. N., "Precast Seismic Structural Systems PRESSS-3: The Five-Story Precast Test Building, V. 3-5: Wall Direction Response," *Report No. SSRP-99/19*, University of California, San Diego, La Jolla, CA, July 2002, 157 pp.

19. Vaghei, R.; Hejazi, F.; Taheri, H.; Jaafar, M. S.; and Aziz, F. N. A. A., "Development of a New Connection for Precast Concrete Walls Subjected to Cyclic Loading," *Earthquake Engineering and Engineering Vibration*, V. 16, No. 1, 2017, pp. 97-117. doi: 10.1007/s11803-017-0371-3

20. Biondini, F.; Dal Lago, B.; and Toniolo, G., "Role of Wall Panel Connections on the Seismic Performance of Precast Structures," *Bulletin of Earthquake Engineering*, V. 11, No. 4, 2013, pp. 1061-1081. doi: 10.1007/s10518-012-9418-z

21. Dal Lago, B.; Biondini, F.; and Toniolo, G., "Friction-Based Dissipative Devices for Precast Concrete Panels," *Engineering Structures*, V. 147, 2017, pp. 356-371. doi: 10.1016/j.engstruct.2017.05.050

22. Metta, S., "Thin Precast Wall Panel Construction," U.S. Patent 3,131,514, 1964.

23. Pall, A. S.; Marsh, C.; and Fazio, P., "Friction Joints for Seismic Control of Large Panel Structures," *PCI Journal*, V. 25, No. 6, 1980, pp. 38-61. doi: 10.15554/pcij.11011980.38.61

24. Sun, J.; Qiu, H.; and Jiang, H., "Lateral Load Behaviour of a Rectangular Precast Shear Wall Involving Vertical Bolted Connections," *Advances in Structural Engineering*, V. 22, No. 5, 2019, pp. 1211-1224. doi: 10.1177/1369433218807685

25. Crisafulli, F. J., and Restrepo, J. I., "Ductile Steel Connections for Seismic Resistant Precast Buildings," *Journal of Earthquake Engineering*, V. 7, No. 4, 2003, pp. 541-553. doi: 10.1080/13632460309350463

26. Menegon, S. J.; Wilson, J. L.; Lam, N. T. K.; and Gad, E. F., "Experimental Testing of Innovative Panel-to-Panel Connections for Precast Concrete Building Cores," *Engineering Structures*, V. 207, 2020, p. 110239. doi: 10.1016/j.engstruct.2020.110239

27. Hofheins, C. L.; Reaveley, L. D.; and Pantelides, C. P., "Behavior of Welded Plate Connections in Precast Concrete Panels under Simulated Seismic Loads," *PCI Journal*, V. 47, No. 4, 2002, pp. 122-133. doi: 10.15554/pcij.07012002.122.133

28. Shen, S.-D.; Pan, P.; Miao, Q.-S.; Li, W.-F.; and Gong, R.-H., "Test and Analysis of Reinforced Concrete (RC) Precast Shear Wall Assembled Using Steel Shear Key (SSK)," *Earthquake Engineering & Structural Dynamics*, V. 48, No. 14, 2019, pp. 1595-1612. doi: 10.1002/eqe.3215

29. Shen, S.-D.; Pan, P.; Ye, B.-B.; Ren, J.-Y.; and Gong, R.-H., "Design, Simulation and Test on the Shape Optimization of a Steel Shear Key (SSK)," *Measurement*, V. 151, 2020, p. 107127.

30. Shen, S.-D.; Cui, Y.; Pan, P.; Gong, R.-H.; Miao, Q.-S.; and Li, W.-F., "Experimental Study of RC Prefabricated Shear Walls with Shear Keys Affected by a Slotted Floor Slab," *Journal of Aerospace Engineering*, ASCE, V. 32, No. 3, 2019, pp. 1-9. doi: 10.1061/(ASCE)AS.1943-5525.0001000

31. Shen, S.-D.; Pan, P.; Miao, Q.-S.; Li, W.-F.; and Gong, R.-H., "Behaviour of Wall Segments and Floor Slabs in Precast Reinforced Concrete Shear Walls Assembled Using Steel Shear Keys (SSKW)," *Structural Control and Health Monitoring*, V. 26, No. 10, 2019, p. e2418. doi: 10.1002/stc.2418

32. Shen, S.-D.; Pan, P.; He, Z.-Z.; Ye, B.-B.; and Wang, Z.-K., "Development of an H-Shaped Shear Key for Mutually Perpendicular Precast Shear Walls," *Measurement*, V. 168, 2021, p. 108271. doi: 10.1016/j.measurement.2020.108271

33. Poluraju, P., and Appa Rao, G., "Performance of Squat 3D Sandwich Walls with Longitudinal Reinforcement and Boundary Elements under Lateral Cyclic Loading," *The Journal of Sandwich Structures & Materials*, V. 20, No. 8, 2018, pp. 946-973. doi: 10.1177/1099636216682546

34. AWS D1.1/D1.1M:2020, "Structural Welding Code—Steel," American Welding Society, Miami, FL, 2020.

35. Moorthi, A. S. G., and Rao, G. A., "Study on Interface Fracture and Failure Modes in Steel Plate and Concrete Embedment," *11th International Conference on Fracture Mechanics of Concrete and Concrete Structures (FraMCoS-11)*, J. M. Chandra Kishen, A. Ramaswamy, S. Ray, and R. Vidyasagar, eds., Bangalore, India, 2023.

36. IS 1893 (Part 1):2016, "Criteria for Earthquake Resistant Design of Structures - Part 1 General Provisions and Buildings," Bureau of Indian Standards, New Delhi, India, 2016, 39 pp.

37. IS 13920:2023, "Ductile Detailing of Reinforced Concrete Structures Subjected To Seismic Forces—Code of Practice," Bureau of Indian Standards, New Delhi, India, 2023, 16 pp.

38. ACI Committee 318, "Building Code Requirements for Structural Concrete (ACI 318-19) and Commentary (ACI 318R-19) (Reapproved 2022)," American Concrete Institute, Farmington Hills, MI, 2019, 624 pp.

39. ASTM E2126-19, "Standard Test Methods for Cyclic (Reversed) Load Test for Shear Resistance of Vertical Elements of the Lateral Force Resisting Systems for Buildings," ASTM International, West Conshohocken, PA, 2019, 15 pp.

40. Penelis, G., and Penelis, G., *Concrete Buildings in Seismic Regions*, CRC Press, Boca Raton, FL, 2018.

41. Housner, G. W.; Martel, R. R.; and Alford, J. L., "Spectrum Analysis of Strong-Motion Earthquakes," *Bulletin of the Seismological Society of America*, V. 43, No. 2, 1953, pp. 97-119. doi: 10.1785/BSSA0430020097

42. Jacobsen, L. S., "Damping in Composite Structures," *Proceedings of the Second World Conference on Earthquake Engineering (2WCEE)*, Tokyo and Kyoto, Japan, 1960, pp. 1029-1044.

ACI STRUCTURAL JOURNAL TECHNICAL PAPER

Title No. 122-S74

Novel Post-Tensioning Anchorage Solution with Ultra-High-Performance Concrete for Seismic Retrofit of Nonductile Reinforced Concrete Walls

by Sumedh Sharma, Sriram Aaleti, and Pinar Okumus

This study introduces a new anchorage strategy using ultra-high-performance concrete (UHPC) to attach unbonded post-tensioning (PT) strands to existing foundations. This solution complements a seismic retrofit scheme investigated by the authors, which transforms nonductile cast-in-place reinforced concrete (RC) shear walls into unbonded PT rocking shear walls following concepts of selective weakening and self-centering. In the proposed PT anchorage scheme, mild steel reinforcements are inserted through the shear wall thickness and into the foundation. Subsequently, UHPC is cast around the wall base, forming a vertical extension connected to the foundation, which is used to anchor the unbonded PT strands. The feasibility and performance of the anchorage scheme was investigated through a combination of laboratory testing and numerical simulations. Pullout testing on four scaled-down anchorage specimens was conducted in the laboratory. Hairline cracks were observed in the UHPC during testing. Additionally, three-dimensional (3-D) finite element (FE) models were created, validated, and used to study the performance of the proposed anchorage scheme under lateral loading. The simulation results support the effectiveness of the proposed anchorage strategy.

Keywords: anchorage of post-tensioning; experimental testing; reinforced concrete (RC) shear walls; seismic retrofit; selective weakening; self-centering; ultra-high-performance concrete (UHPC).

INTRODUCTION

The increasing demand for swift recovery in the aftermath of seismic events has prompted stakeholders toward the development of low-damage retrofit solutions for structurally deficient buildings.[1] This urgency is underscored by the arduous reconstruction process after recent earthquakes, most notably following the 2011 Christchurch earthquake.[2,3] In response to the push toward immediate occupancy of buildings after a seismic event, researchers, including the authors, have investigated a low-damage retrofit solution for nonductile reinforced concrete (RC) shear walls based on selective weakening and self-centering concepts.[4-11]

The basic steps in the retrofit scheme are shown in Fig. 1. Initially, a controlled cold joint was introduced at the wall-foundation interface to soften the structure (selective weakening), altering the load-resisting mechanism of the wall from flexural plastic hinging to rocking behavior and reducing the tensile stresses in concrete under lateral loads. Selected longitudinal reinforcements, typically closer to the center of the wall, were left uncut to provide energy dissipation. Alternatively, all the wall longitudinal reinforcements can be cut, and energy dissipation can be provided using external energy-dissipating (ED) elements. External unbonded post-tensioning (PT) elements were installed to anchor the wall to the foundation, enabling self-centering and partially restoring the flexural strength lost due to cutting of the longitudinal reinforcements. The external ED elements also contributed to the flexural capacity of the wall. When necessary, the boundary elements of the existing RC shear wall were provided with additional confinement to protect against localized damage. In essence, the retrofit scheme converted a nonductile RC shear wall into a rocking shear wall. As part of the broader research effort, the authors carried out laboratory testing of a deficient RC shear wall specimen, which served as the benchmark, and four retrofitted RC shear wall specimens based on the scheme shown in Fig. 1.[10,11] In general, the retrofitted RC shear walls exhibited minimal cracking and crushing in the wall panel, delay in yielding of shear reinforcement, improved drift capacities, and reduced residual drift compared to the benchmark RC shear wall.

RESEARCH SIGNIFICANCE

Despite promising results, past studies on the wall retrofit scheme based on selective weakening and self-centering concepts have focused on the lateral load performance of the shear wall and did not investigate the anchoring of externally provided PT elements.[4-11] This study aims to address this gap by proposing a novel PT anchorage scheme using ultra-high-performance concrete (UHPC). The scope of this study includes evaluating the proposed PT anchorage scheme under the assumption that the foundation has sufficient capacity to sustain the demand due to the anchoring of PT forces. As such, the primary focus is on the damage progression in the anchorage and probable impact of the anchorage scheme on lateral load performance of the shear wall. The performance of the foundation or retrofits of existing deficient foundations are outside the scope of this study. Although the anchorage system is developed for the shear wall retrofit scheme described previously, the results presented herein are relevant for other concrete structural elements that have PT added after construction,

ACI Structural Journal, V. 122, No. 5, September 2025.

MS No. S-2024-150.R1, doi: 10.14359/51746817, received December 21, 2024, and reviewed under Institute publication policies. Copyright © 2025, American Concrete Institute. All rights reserved, including the making of copies unless permission is obtained from the copyright proprietors. Pertinent discussion including author's closure, if any, will be published ten months from this journal's date if the discussion is received within four months of the paper's print publication.

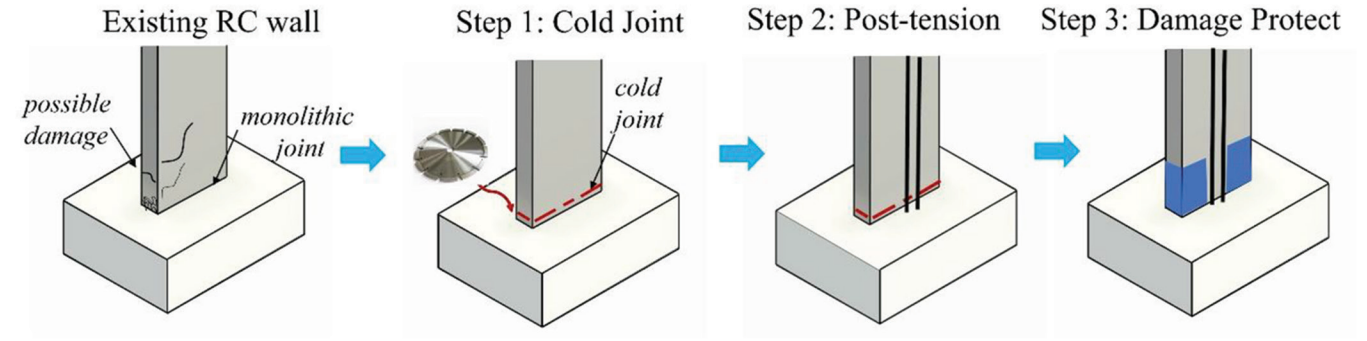


Fig. 1—Schematic of proposed retrofit method for non-code-performing RC shear walls.

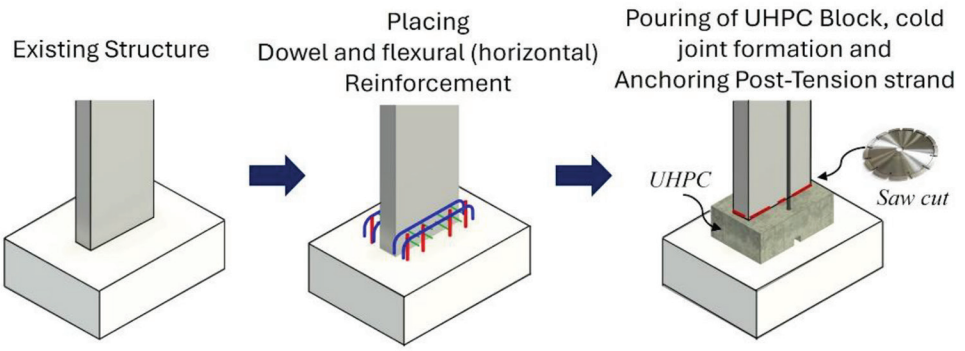


Fig. 2—Schematic of anchorage scheme used to anchor external PT elements into existing foundation using UHPC.

such as strengthening of concrete beams with external post-tensioning.

PROPOSED FOUNDATION RETROFIT SCHEME FOR ANCHORING EXTERNAL PT ELEMENTS

The proposed PT anchorage scheme is schematically presented in Fig. 2. The scheme involves embedding vertical and horizontal reinforcing bars (dowels) into the foundation and wall panel, respectively, a common construction step used in the retrofitting of RC structures.[12,13] UHPC is then placed around the base of the wall, which encases the exposed embedded bars. The externally provided PT is anchored inside the UHPC block. A cut is made across the wall panel just above the UHPC block to form a cold joint. Depending on the desired performance of the retrofitted shear wall, all or selected wall longitudinal reinforcements are cut. This specific cutting location is recommended as the UHPC block provides additional surface area beneath the wall base, which may accommodate slipping of the wall panel during lateral loading. This anchoring process is expected to provide reliable attachment of PT elements to the existing foundation, thereby maintaining the structural integrity and performance of the retrofit scheme.

UHPC's tensile strength is expected to minimize damage and enhance the transfer of anchorage force compared to normal-strength concrete (NC). The development length for U.S. Grade 60 (yield stress of 413.7 MPa [60 ksi]) mild steel reinforcements in UHPC is $10d_b$ (d_b is bar diameter) for a clear cover of $2d_b$.[14] This reduced development length of reinforcement compared to NC minimizes the size of the UHPC block encasing the reinforcement. Additionally, UHPC, when applied as a thin layer around NC members, has been reported to enhance confinement.[15] Thus, UHPC block is expected to provide confinement to the portion of NC wall below the cold joint, helping to mitigate the damage due to the stresses exerted during rocking motion of the wall panel. As an additional benefit, UHPC offers better resistance to corrosion and degradation compared to NC, thus improving the durability of the anchorage.[16]

RESEARCH METHODOLOGY

The research methodology, as illustrated in Fig. 3, integrates laboratory testing and finite element (FE) simulations. The study involved four small-scale anchorage specimens undergoing pullout testing. In these tests, PT force was applied to the UHPC block's anchorage location through axially loaded PT bars, aiming to investigate damage progression and the influence of embedded reinforcements and surface preparation on anchorage performance. FE models for the anchorage specimens were calibrated using the experimental results. Following this, FE modeling of a retrofitted shear wall specimen that had been tested as part of a broader study[10,11] was used to further investigate the performance of proposed anchorage scheme under lateral loading.

EXPERIMENTAL PROGRAM

Design of test specimens

The typical dimensions of the small-scale PT anchorage specimens are shown in Fig. 4(a). Four specimens were tested, with variables including the UHPC-NC interface texture, size of the dowel reinforcement, and size of the interface reinforcement. The design of the test specimens and the anchorage details were based on the PT forces

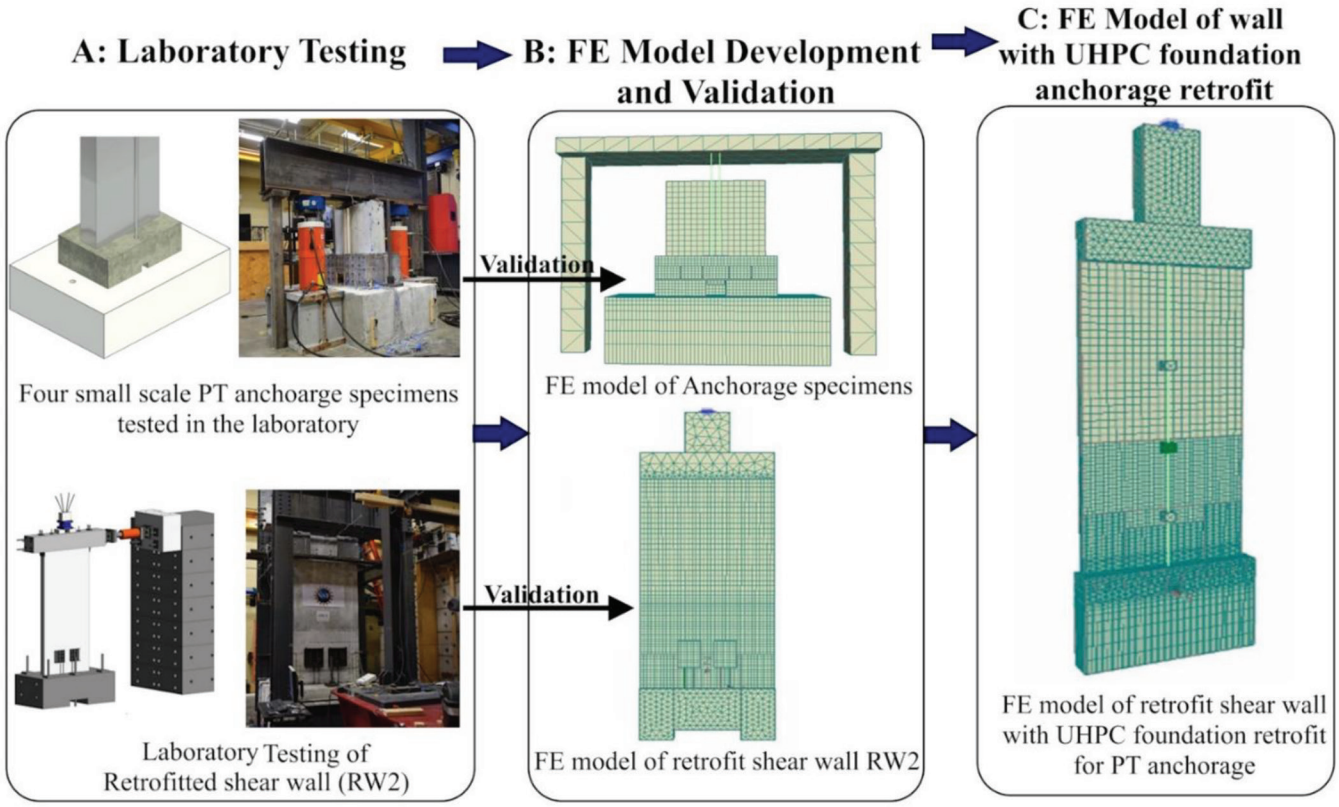


Fig. 3—Schematic of research methodology.

recorded during lateral load tests on RC shear walls retrofitted using the proposed retrofit method.[10,11] The peak PT force observed during the testing of retrofitted shear wall specimens that were 1524 mm (60 in.) wide and 152.4 mm (6 in.) thick was 1112.1 kN (250.0 kip).[10,11] Consequently, the target PT force for the anchorage test specimens was set at approximately 444.8 kN (100 kip) (two-fifths of peak PT force in retrofitted wall specimens), corresponding to the dimensions of the NC wall in these specimens, which were 610 mm (24 in.) long and 152.4 mm. (6 in.) thick. The height of the NC wall panel was kept at 812.8 mm (32 in.) from the foundation top to provide sufficient development length for the wall reinforcements. This was done to investigate the impact of the anchorage scheme on the longitudinal wall reinforcement that remained uncut during the retrofit process.

The UHPC block surrounding the NC wall was sized based on the development length and clear cover required for the embedded mild steel reinforcement.[14] Three pairs of longitudinal wall reinforcement were used (Fig. 4(b)). Vertical dowel reinforcements in the UHPC block (Fig. 4(c)), were designed assuming a uniform distribution of anchorage force among the dowels. The contribution of the wall longitudinal reinforcement to resisting anchorage forces was neglected. To remain conservative, the dowel bars were designed such that stresses resulting from design PT force were kept below 50% of nominal yield stress. Thus, eight Grade 60, U.S. size No. 6 (d_b = 19.1 mm [0.75 in.]) or No. 7 reinforcement (d_b = 22.2 mm [0.875 in.]) were provided as vertical dowels with design stress of 195.8 MPa (28.40 ksi) and 143.4 MPa (20.8 ksi), respectively.

The interface roughness and reinforcement were designed based on recommendations from pushoff tests on UHPC-NC composites[17] and ACI 318-19 provisions.[18] The interface was designed with a combination of surface roughness of 5.1 mm (0.2 in.) and U.S. size No. 3 interface reinforcement and surface roughness of 2 mm (0.08 in.) and U.S. size No. 4 interface reinforcement. Figures 4(d) and (e) show the standard form liners with roughness texture used at the interface, and Fig. 5 provides the reinforcement details used in the specimens. The name and combination of the design variables used in the test specimens are listed in Table 1. The specimens were denoted as SPx-xx-Dx, where SPx represents specimen No., xx represents the surface preparation at UHPC block-to-NC wall interface, and Dx represents U.S. size of the dowel reinforcements.

Specimen fabrication

The specimens were fabricated at The University of Alabama's Large-Scale Structures Laboratory; the fabrication process is shown in Fig. 6. Initially, the reinforcement cages for wall and foundation were fabricated and placed into the foundation formwork. To simplify the construction process, the dowel and interface bars were installed in the formwork prior to concrete casting rather than embedded into hardened concrete, as typically done in practical applications (Fig. 6(b)). As mentioned earlier, the embedding of reinforcement into hardened concrete is a regular practice in the retrofitting of RC structures and has been investigated by other researchers.[12,13] Besides, rated anchors and adhesives are commercially available to serve as dowel reinforcement.[19] Standard form liners (Fig. 4(d) and (e)) were used to

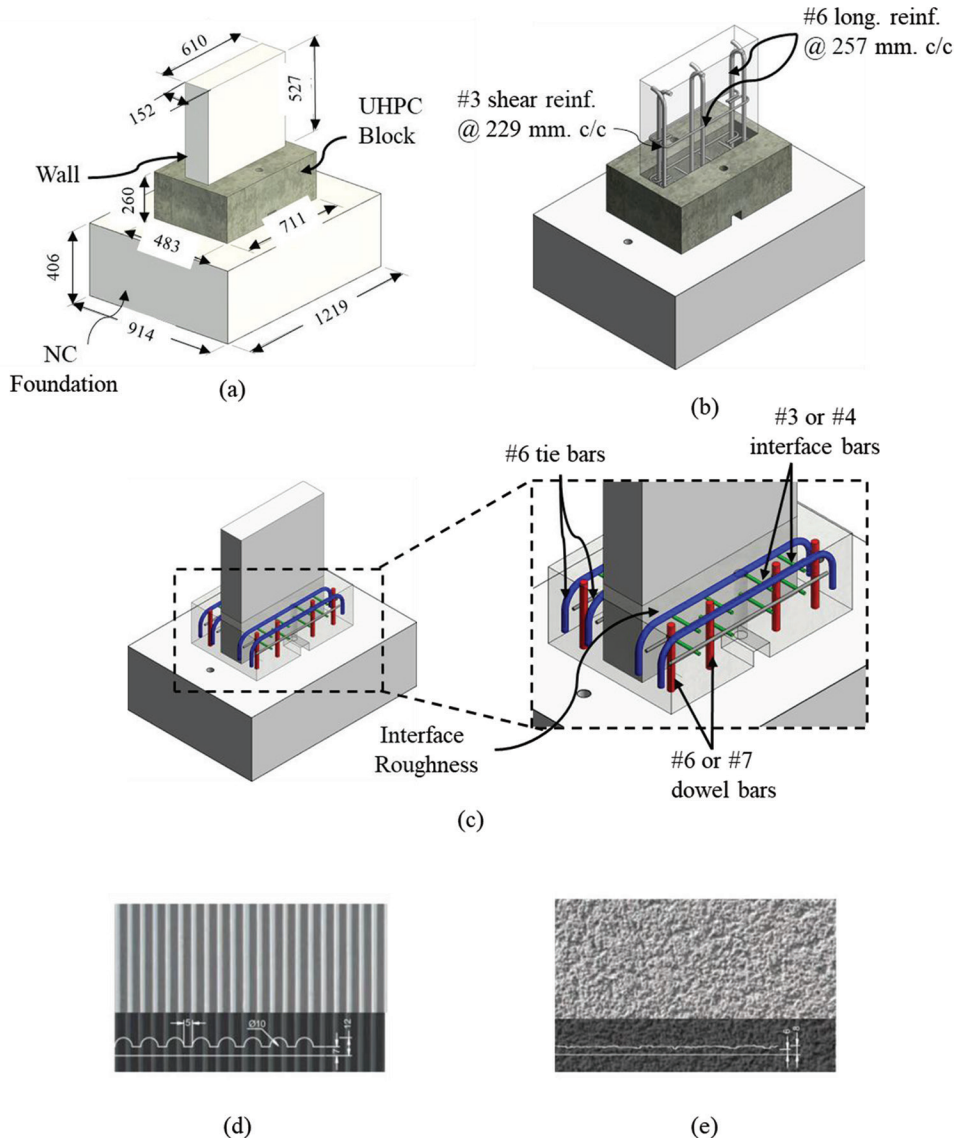


Fig. 4—Dimensions and detailing of PT anchorage specimens: (a) typical dimensions, in mm; (b) wall reinforcement; (c) close-up view of reinforcement inside UHPC block; interface roughness texture; (d) form liner—Wisla texture (5 mm); and (e) form liner—Parana texture (2 mm). (Note: 1 mm = 0.04 in.)

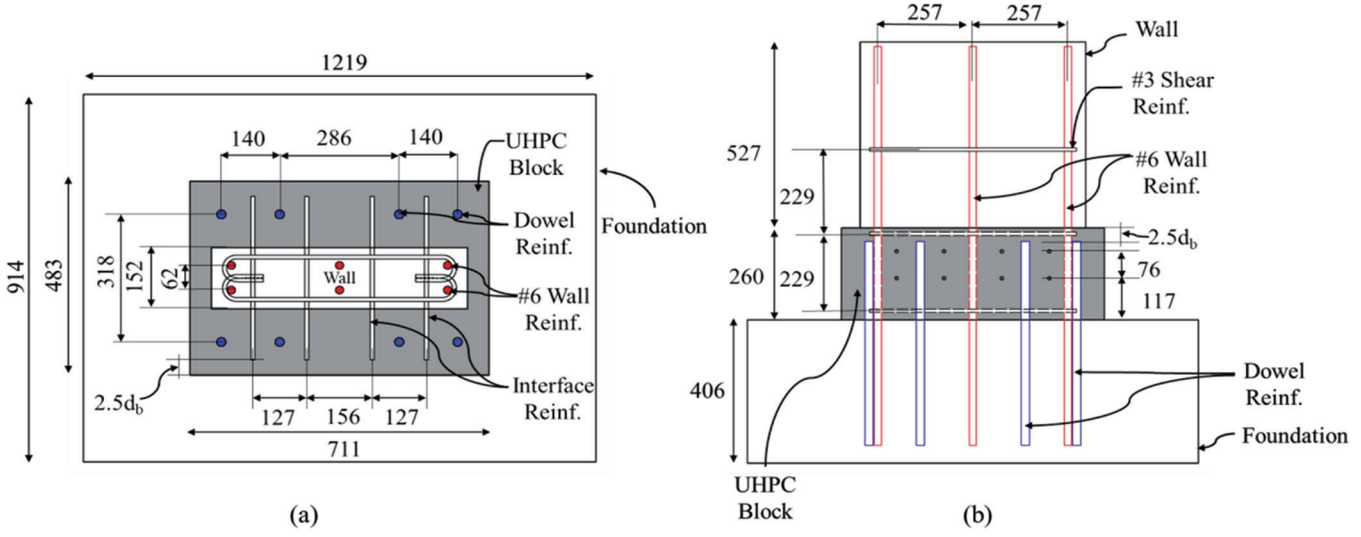


Fig. 5—Typical details of reinforcements used in anchorage specimens: (a) plan; and (b) elevation. (Note: Tie reinforcements used in UHPC block and foundation reinforcements not shown for clarity; units in mm; 1 mm = 0.04 in.)

Table 1—Labels and design variable used in anchorage specimens

Specimen name	Interface texture, roughness depth, mm (in.)	U.S. size of dowel reinforcement, diameter, mm (in.)	U.S. size of interface reinforcement, diameter, mm (in.)
SP1-WI-D7	Wisla, 5.1 (0.2)	No. 7, 22.2 (0.875)	No. 3, 9.5 (0.375)
SP2-PA-D7	Parana, 2 (0.08)	No. 7, 22.2 (0.875)	No. 4, 12.7 (0.5)
SP3-WI-D6	Wisla, 5.1 (0.2)	No. 6, 19.1 (0.75)	No. 3, 9.5 (0.375)
SP4-PA-D6	Parana, 2 (0.08)	No. 6, 19.1 (0.75)	No. 4, 12.7 (0.5)

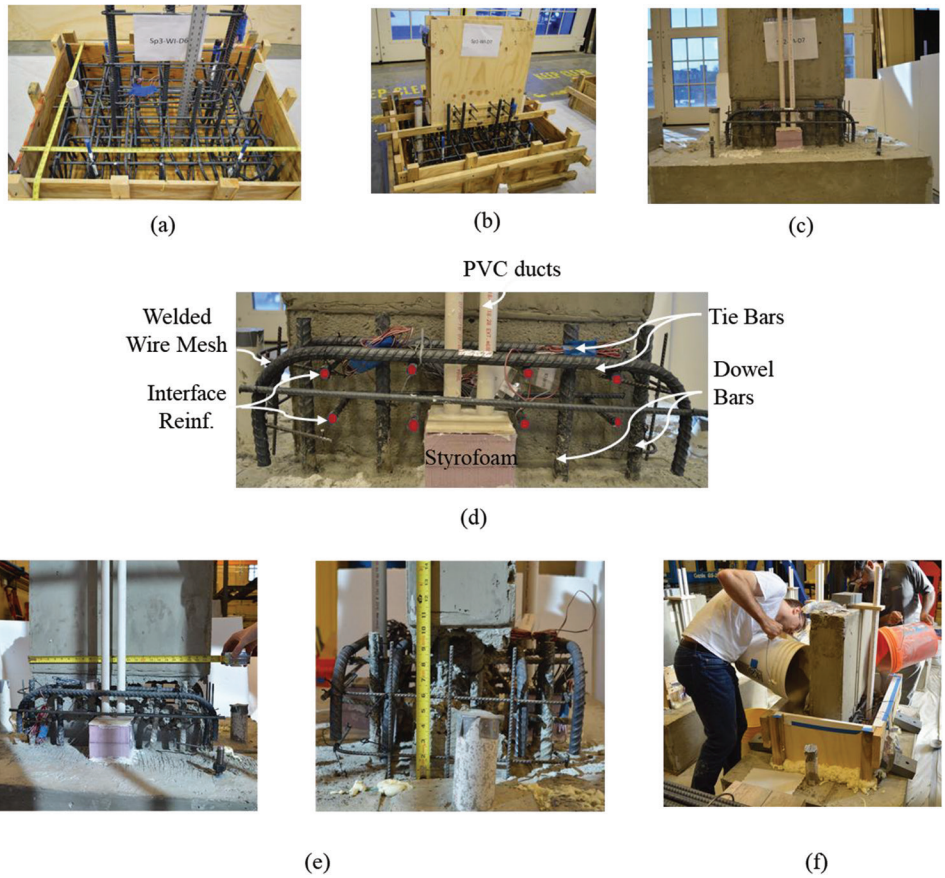


Fig. 6—Fabrication of anchorage specimens: (a) foundation and wall reinforcement cage inside foundation formwork; (b) specimen before placement of normal concrete; (c) preparation before UHPC placement; (d) close-up view of selected portion of specimen before UHPC placement; (e) Specimen SP4-PA-D6 before UHPC placement; and (f) placing of UHPC.

create roughness at UHPC-NC interface. The NC portion of specimens and foundations were cast simultaneously using a standard 27.6 MPa (4 ksi) concrete mixture with 12.7 mm (0.5 in.) aggregate, achieving a 152.4 mm (6 in.) slump. After 3 days, formwork was removed and specimens cured for 28 days in ambient lab conditions (23°C [73.4°F], 50% humidity). Before UHPC placement, tie bars were installed in the UHPC block and blockouts were created using polystyrene for anchoring of PT bars. Two polyvinyl chloride (PVC) ducts were also embedded in UHPC to enable placement of PT bars. Previous research by Ronanki and Aaleti[15] noted cracking at the corners of external UHPC confinement around rectangular sections due to poor fiber distribution and stress concentration. To mitigate this, welded wire reinforcement of 101.6 x 101.6 mm (4 x 4 in.) grid and diameter of 6.4 mm (0.25 in.) was installed around the corners of the UHPC block, as shown in Fig. 6(d).

In specimen SP4-PA-D6, a void formed across the thickness of the wall (nearly 254 mm [10 in.] high from the top of foundation and 304.8 mm [12 in.] long from the edge of the wall) due to faulty placement of NC (Fig. 6(e)). This resulted in a partial monolithic connection between UHPC layers on either side of the NC wall, which should be considered while comparing the performance of Specimen SP4-PA-D6 with other test specimens. A commercial UHPC mixture[20] was used for UHPC block in all the specimens except SP4-PA-D6, which used another commercial UHPC mixture.[21] Following UHPC casting, specimens were covered with plastic shrink-wrap and a tarp for 3 days. The specimens were air-cured in ambient laboratory conditions for more than 28 days.

Test setup and instrumentation

The test setup and instrumentation used for testing the anchorage specimens are shown in Fig. 7. The foundation block was secured to the strong floor using two 50.8 mm

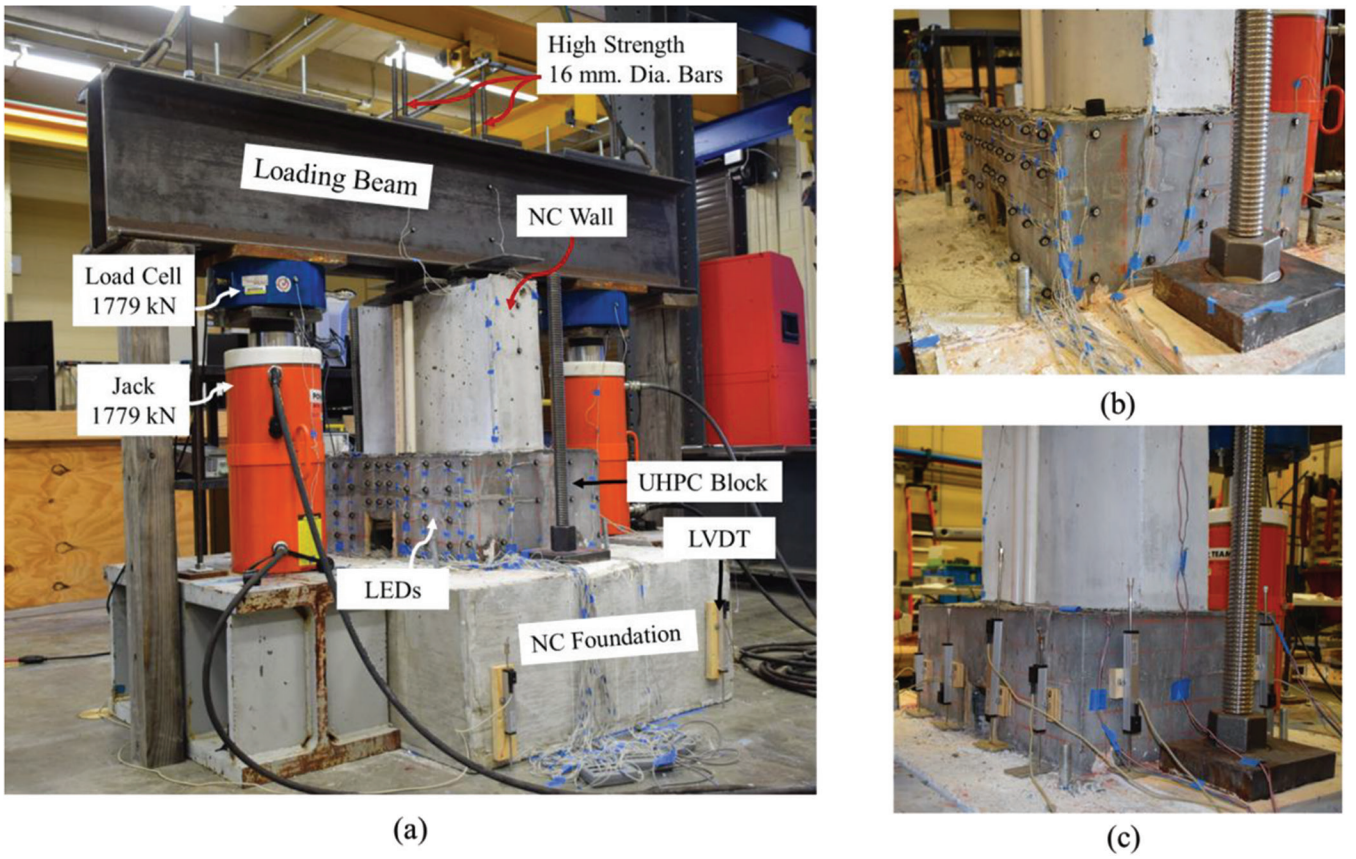


Fig. 7—(a) Setup used for testing of PT anchorage specimens; (b) distribution of LED markers on UHPC block surface; and (c) LVDTs used at UHPC block-NC foundation interface.

(2 in.) diameter high-strength threaded bars. Four 15.9 mm (0.625 in.) diameter high-strength all-thread bars with nominal yield strength of 724 MPa (105 ksi) were used to apply the design PT force on the test specimens. These bars were placed symmetrically on both sides of the wall. The bars were anchored to the UHPC block and bolted to the top of the steel loading crossbeam. The loading beam was subjected to vertical displacement using two manually operated hydraulic jacks, each with a capacity of 1779.3 kN (400 kip), and the applied force was monitored using load cells of the same capacity.

Surface displacements of the UHPC block were measured using an optical three-dimensional (3-D) motion-tracking system with light-emitting diode (LED) markers. LED markers were placed on the UHPC block in a 63.5 mm (2.5 in.) square grid pattern (Fig. 7(b)). Four linear variable differential transformers (LVDTs) were used to monitor the vertical displacement of the UHPC block relative to the NC foundation on the side inaccessible to the optical 3-D motion-tracking system (Fig. 7(c)). Additional LVDTs were used to monitor the vertical displacement of the NC foundation with respect to the laboratory's strong floor. Strain gauges were installed at locations corresponding to UHPC block-to-NC foundation interface on vertical dowel reinforcements, UHPC block-to-NC wall interface on interface reinforcements, and NC wall-to-NC foundation interface on vertical wall reinforcements. The readings from strain gauges, load cells, and LVDTs were recorded using a data acquisition system.

The test specimens were loaded monotonically until 489.3 kN (110 kip), corresponding to 85% of yield strength of threaded bars in increments of 44.5 kN (10 kip). After reaching peak force, all test specimens were subjected to three load cycles at the peak force except the first specimen, which was subjected to two load cycles. The loading protocol was chosen to investigate the effects of load reversal on the test specimens, and the number of repetitions was chosen to be consistent with the loading protocol used in testing of the benchmark retrofitted walls.[10,11] The specimens were inspected for damage at every 89 kN (20 kip) load increment.

Test observations and measured results

Material properties—The test-day compressive strengths of UHPC and NC were determined using 50.8 mm (2 in.) cube and standard 101.6 x 203.2 mm (4 x 8 in.) cylinder specimens, respectively. The UHPC cube strengths were multiplied by a factor of 0.96 to obtain the equivalent UHPC cylinder compressive strength.[22] The compression tests on NC cylinders were performed in accordance with ASTM C39/C39M procedure.[23] The measured compressive strength values for UHPC and NC in the wall specimens are presented in Table 2. The tensile testing of mild steel reinforcement was performed following ASTM E8/E8M procedure[24] and the measured tensile properties are presented in Table 3.

Retrofitted foundation anchorage specimens—

Damage progression:

The damage progression was consistent across all the test specimens, as shown in Fig. 8. Initial microcracking became

evident in the UHPC block at the approximate PT load of 177.9 kN (40.0 kip), primarily limited to the anchorage region and the locations of vertical dowel bars. As the load increased, existing microcracks extended and new microcracks formed. These microcracks in the UHPC blocks were only visible after applying acetone on the concrete surface and are identified in Fig. 8 for clarity. The minimal observed damage in the UHPC block highlights the benefits of superior mechanical properties of UHPC and indicates proper distribution of anchorage forces across the UHPC block. Typically, no new cracks were formed during the subsequent load cycles at the peak load, which is an attractive characteristic for seismic applications. The NC portion of the specimens were free of visible damage, as expected.

UHPC block:

The calculated vertical surface strain in the UHPC block, between adjacent LED markers, was less than 0.0005 mm/mm (0.0005 in./in.) for all the test specimens. The vertical displacements of the UHPC block, with respect to the NC foundation, as determined through LVDT measurements, were in range of 0.25 to 0.51 mm (0.01 to 0.02 in.) across all the test specimens, indicating excellent bond behavior between the UHPC block and NC foundation.

Behavior of reinforcement:

Dowel reinforcement—The measured PT force versus strain relationship and the location of gauges in dowel bars are shown in Fig. 9. The strain gauges were installed at the NC foundation-to-UHPC block interface. The strain gauge on the edge dowel reinforcement malfunctioned in specimen SP2-PA-D7 and is excluded from Fig. 9. As expected, specimens with smaller dowel bar sizes exhibited higher strains. In Specimens SP1-WI-D7 and SP4-PA-D6, the measured strains in the edge and the center dowel bars are identical at peak PT force, while in SP3-WI-D6, the measured strains in the edge dowel bar were 1.5 times greater than the center dowel bar at the peak PT force. In general, the measured strain in the edge and the center dowel bars indicates near uniform distribution of PT anchorage force in the dowel reinforcements. Moreover, the difference in dowel bar strains observed in SP3-WI-D6 could be due to softening of local cohesive bond between the UHPC block and the foundation.

Wall reinforcement—The measured PT force versus strain relationship and the location of gauges in wall reinforcing bars are shown in Fig. 10. The strain gauges on the wall reinforcement in SP4-PA-D6 malfunctioned and are not reported here. Based on the measured strain, wall reinforcements at the center of the wall experienced higher strain compared to reinforcements closer to the edge of the wall. This is attributed to the concentration of interface shear stress transfer across the UHPC block-to-NC wall interface at the location close to PT anchorage, indicated by the higher tensile strain in interface reinforcements at the wall center compared to those at the wall edge, as reported in Sharma.[7] The tensile demand in the wall reinforcement decreased with lowering of surface roughness, as shown by the results in specimens SP1-WI-D7 and SP2-PA-D7. The strain demand in wall reinforcements increased with reduction of size of dowel bars, as shown by results in specimens SP1-WI-D7 and SP3-WI-D6.

Interface and tie reinforcements—The strains recorded in interface reinforcements across all test specimens were less than 300 με. This suggests that there was limited slipping at the UHPC block-to-NC wall interface. The tie reinforcements developed tensile strain up to 750 με during testing and were engaged in distributing the anchorage force. The measured PT force-versus-strain relationships and additional discussion for these reinforcements are reported in Sharma.[7]

Table 2—Mechanical properties of NC and UHPC used in test specimens

Specimen	Concrete	Test-day compressive strength, MPa (ksi)
SP1-W1-D7	UHPC[20]	159.3 (23.1)
	NC	42.7 (6.2)
SP2-PA-D7	UHPC[20]	146.1 (21.2)
	NC	42.7 (6.2)
SP3-WI-D6	UHPC[20]	142.7 (20.7)
	NC	42.7 (6.2)
SP4-PA-D6	UHPC[21]	88.3 (12.8)
	NC	42.7 (6.2)

NUMERICAL INVESTIGATION

The behavior of the anchorage scheme under lateral loading, accounting for the rocking behavior of the wall panel, is investigated using FE analysis. To this end, FE models of the anchorage test specimens and retrofitted shear walls were developed using commercial software ATENA[25] and validated using the measured response of the anchorage specimens presented in this paper and the retrofitted wall specimen RW2 tested as part of the main study.[10] The validated models were then used to investigate performance of the retrofitted walls with the proposed anchorage scheme under lateral loads.

Numerical modeling of anchorage specimens and validation

This section presents the numerical modeling of PT anchorage specimens with 'Wisla' UHPC-NC interface texture, SP1-WI-D7 and SP3-WI-D6 only, due to space limitations.

Table 3—Measured mechanical properties of mild steel reinforcements used in test specimens

Reinforcing bar size	Reinforcing bar area, mm^2 (in.^{2})	Modulus of elasticity, MPa (ksi)	Yield stress, MPa (ksi)	Ultimate stress, MPa (ksi)	Ultimate strain, mm/mm (in./in.)
U.S. size No. 3	71 (0.11)	199,782 (28,976)	471 (68.3)	705.3 (102.3)	0.112
U.S. size No. 6	283.9 (0.44)	204,374 (29,642)	406.1 (58.9)	679.1 (98.5)	0.102
U.S. size No. 7	387.1 (0.6)	206,732 (29,984)	468.1 (67.9)	728.1 (105.6)	0.116

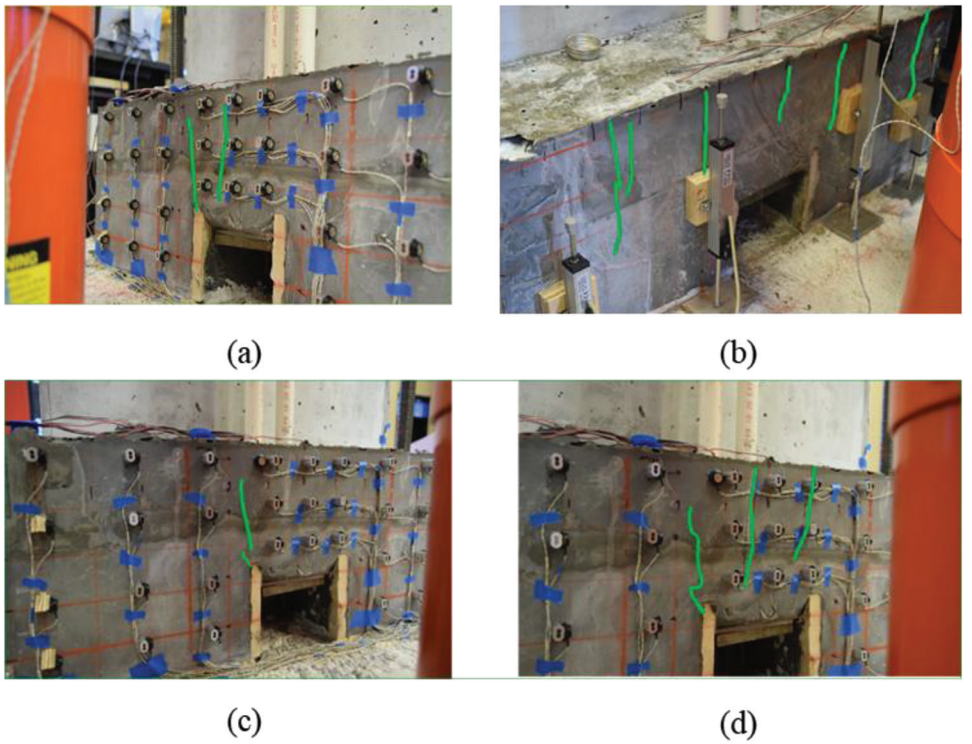


Fig. 8—Damage progression in anchorage specimens: (a) SP2-PA-D7 at 266.9 kN (60 kip); (b) SP2-PA-D7 at 444.8 kN (100 kip); (c) SP3-WI-D6 at 266.9 kN (60 kip); and (d) SP3-WI-D6 at 444.8 kN (100 kip).

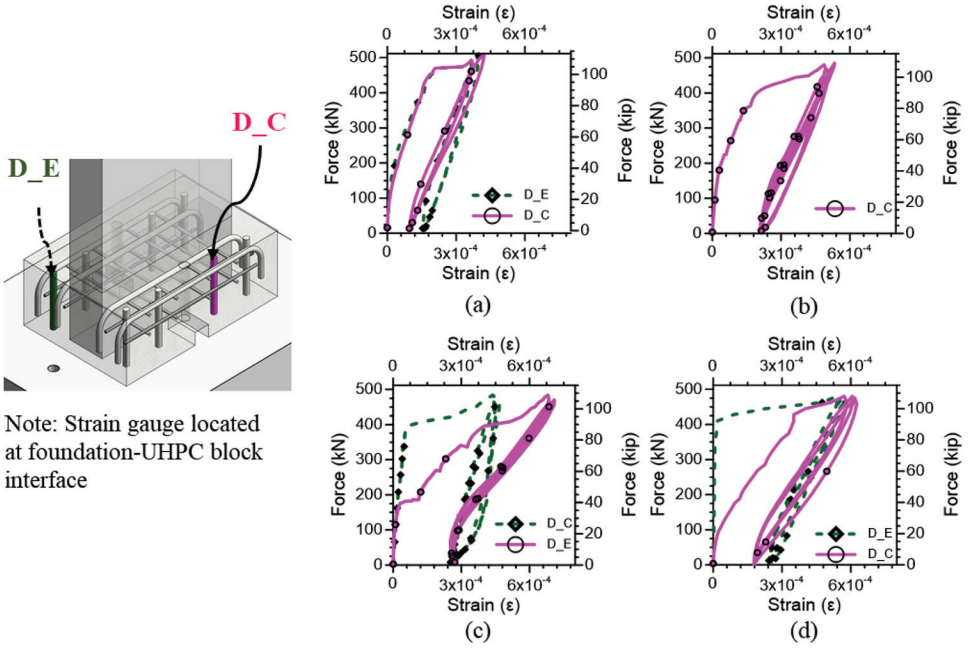


Fig. 9—Measured PT force versus strain relationship in vertical dowel bars: (a) SP1-WI-D7; (b) SP2-PA-D7; (c) SP3-WI-D6; and (d) SP4-PA-D6.

Model description—The general layout of the FE model used for simulating the foundation retrofit specimens is shown in Fig. 11(a). To minimize computational demands, only one half of the specimens, about the vertical plane of symmetry, was modeled. A finer mesh setting was used in the UHPC block, NC wall-UHPC interface, and the top surface of the foundation block. Eight-node 3-D brick elements were used for modeling the UHPC block and NC wall. The material behavior of UHPC and NC were represented using 'CC3DNonLinCementitious2', a nonlinear concrete constitutive model available in ATENA. The foundation and loading frame were modeled as elastic. The NC-to-UHPC block interface and the NC foundation-to-UHPC block interface were modeled using interface element 'CCIsoGap' with interface material model defined using 'CC3DInterface'. The material model parameters were defined using

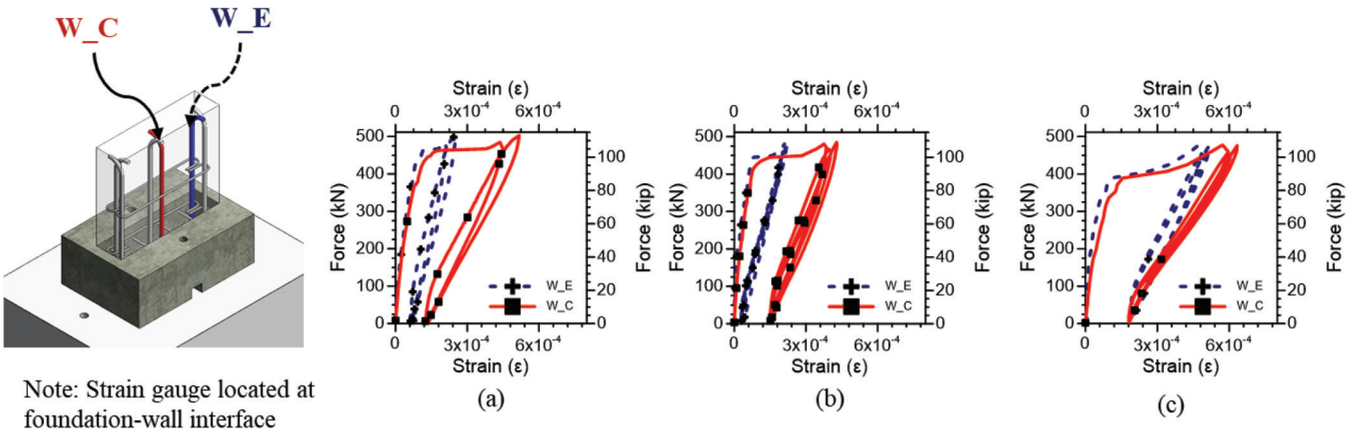


Fig. 10—Measured PT force versus strain relationship in vertical wall reinforcements: (a) SP1-WI-D7; (b) SP2-PA-D7; and (c) SP3-WI-D6.

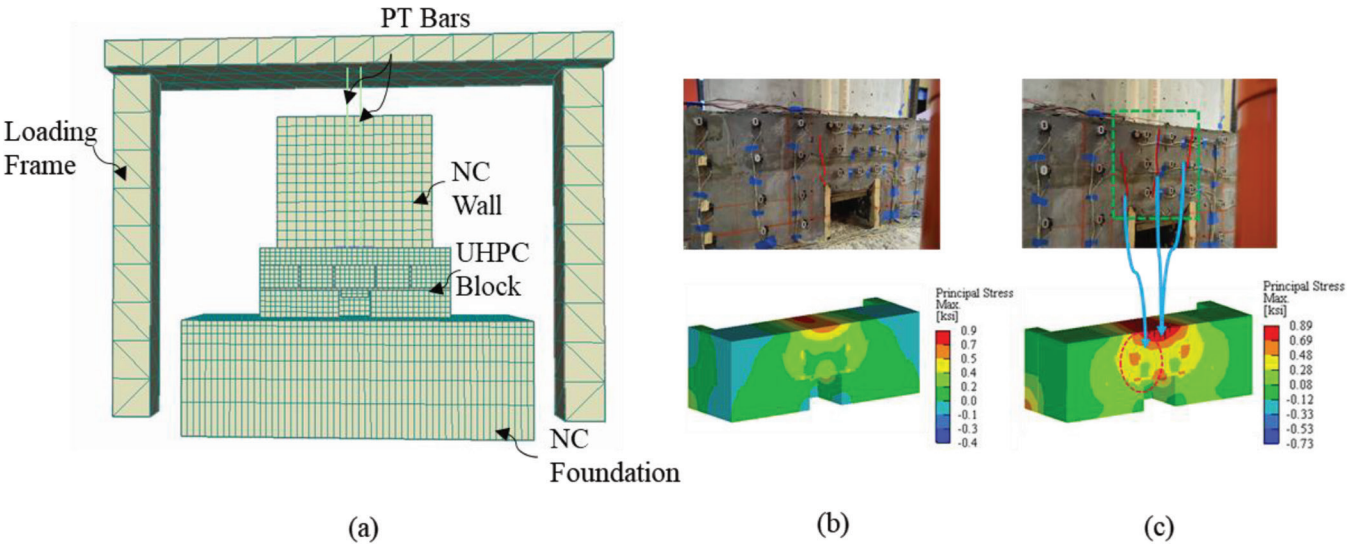


Fig. 11—(a) Schematic of numerical model of anchorage specimen used in ATENA 3D; comparison of damage progression between experimental and simulated response along with maximum principal stress distribution for UHPC block based on simulated response in specimen SP3-WI-D6; (b) at 266.9 kN (60 kip); and (c) 444.8 kN (100 kip).

interface shear tests on NC-UHPC composites by Sharma et al.[17] The interface reinforcement passing through UHPC block-wall interface was modeled using 3-D solid elements to account for the bending stiffness and dowel action. The rest of the mild steel reinforcement and PT bars were modeled as discrete truss elements with nonlinear material behavior defined using the measured mechanical properties. Additional details regarding mesh refinement, material models parameters, and the solver used in the FE analysis are presented elsewhere.[7] The displacements at the bottom surface of the foundation block were constrained in all directions. The specimen was also constrained in the out-of-plane direction along the vertical plain of symmetry. The specimens were loaded monotonically by applying prestressing load to the PT bars. A uniform load increment of 1.11 kN (0.25 kip) was applied at every load step.

Simulated response of anchorage specimens—The distribution of cracks (shown as red lines) observed at two different load levels during laboratory testing and the maximum principal stress in the UHPC block based on FE modeling of specimen SP3-WI-D6 are shown in Fig. 11(b) and (c). The FE model captured the crack and stress distribution around the anchorage region. The damage progression in the UHPC block based on the simulated response was similar in both the specimens SP3-WI-D6 and SP1-WI-D7, as observed during laboratory testing. The FE model also captured the behavior of the reinforcement, as shown by the comparisons of simulated and measured response of strain in dowel, wall, and interface reinforcements (Fig. 12) in specimens SP1-WI-D7 and SP3-WI-D6.

Numerical modeling of specimen RW2 and validation

Retrofitted shear wall specimen (RW2) details and testing—The dimensions and wall reinforcement layout of the retrofit wall specimen RW2 that was tested as part of the main study[10] and the measured responses are shown in Fig. 13. RW2 was anchored to the foundation with four 15.24 mm (0.6 in.) diameter Grade 270 low-relaxation unbonded PT strands. Eight U.S. Grade 60 reinforcements with milled cross-section areas of 200 mm^2 (0.31 in.^{2}) were used as ED reinforcement. The EDs were installed externally to the wall

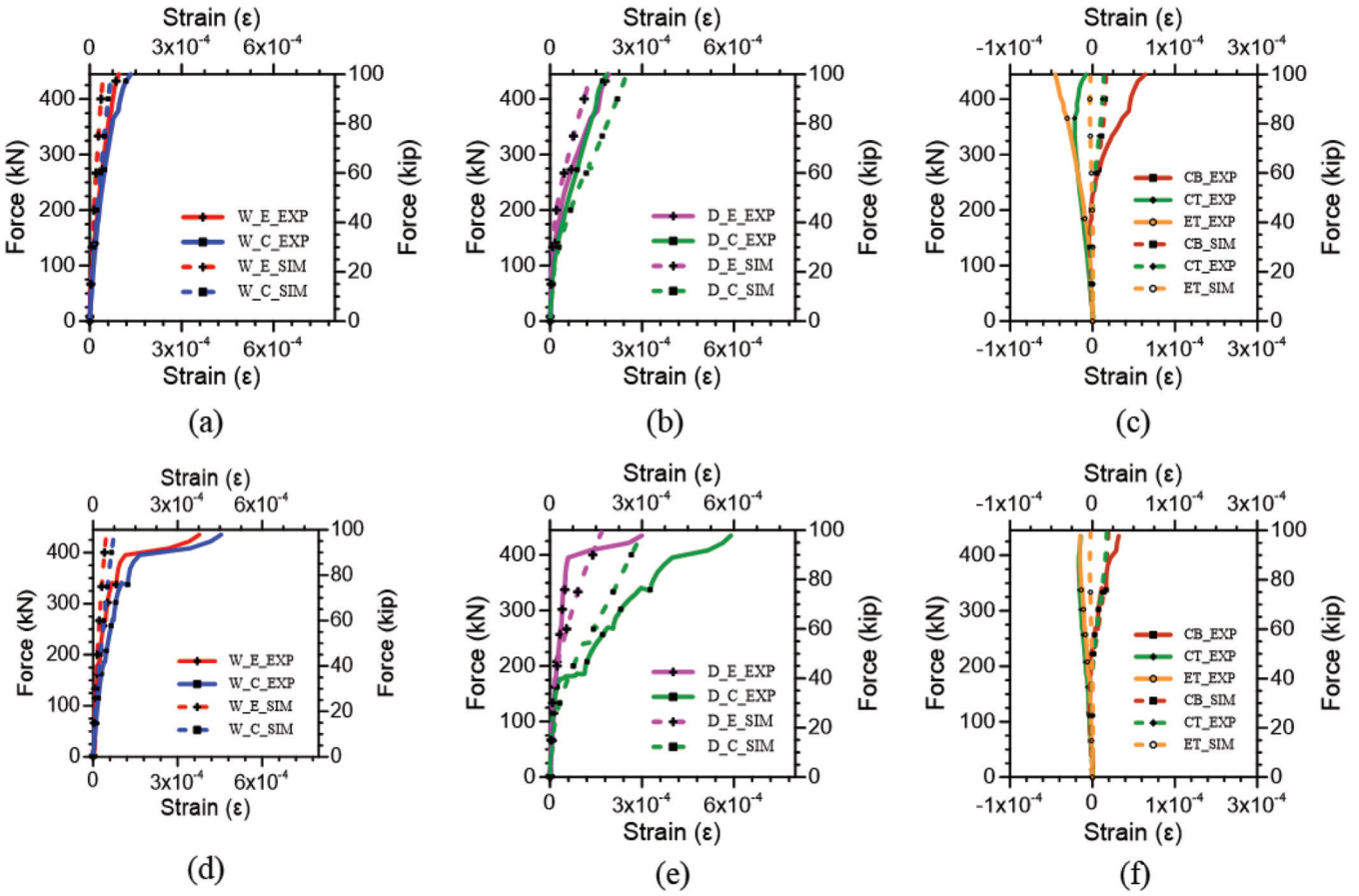


Fig. 12—Comparison of simulated and measured response of strains versus PT force in retrofitted foundation specimens: (a) SP1-WI-D7 wall reinforcement; (b) SP1-WI-D7 dowel reinforcement; (c) SP1-WI-D7 interface reinforcement; (d) SP3-WI-D6 wall reinforcement; (e) SP3-WI-D6 dowel reinforcement; and (f) SP3-WI-D6 interface reinforcement. (Legend: xx_EXP/SIM: xx is same as in Fig. 9 and 10, EXP is measured response, SIM is simulated response.)

panel. The proposed UHPC foundation retrofit was not used in anchoring the PT strands in the testing of RW2 specimen. The post-tensioning was placed in a standard rectangular PT duct inside the wall panel and was anchored in a top-block and a foundation block made of regular concrete. The rocking corners of the wall panel were replaced with UHPC to provide additional confinement. The retrofit specimen, RW2, was tested under quasi-static lateral loading in displacement control, following ACI 550.6-19.[26] The specimen exhibited negligible damage in the wall panel and the maximum measured residual drift was 0.06%. The detailed experimental observations and performance of retrofit shear wall specimen, RW2, are presented elsewhere.[10]

FE model description—The general layout of the FE model used for specimen RW2 is shown in Fig. 14(a) and (b). One half of the specimen, about the vertical plane of symmetry, was modeled to reduce computational demand. The mesh sensitivity study is detailed in a dissertation related to this study.[7] The wall panel components were modeled using eight-node 3-D brick elements and nonlinear concrete constitutive model 'CC3DNonLinCementitious2.' The foundation block, loading block, and PT anchors were modeled using four-node 3-D tetra elements with coarse mesh and elastic material. The wall reinforcements and PT reinforcements were modeled using discrete truss elements. To improve numerical stability, in wall panel regions with fine mesh, smeared reinforcement was provided based on recommendation by Lowes et al.[27] The material model used in the wall and PT reinforcement was defined using a bilinear stress-strain relationship based on the measured material properties. The ED reinforcement was modeled using eight 3-D node brick elements with fine mesh to capture the buckling response observed during the laboratory testing. Material model 'CC3DBilinearVonMisesSteel,' based on Von Mises plasticity, was used to model the ED reinforcement. The circular cross section of the ED reinforcement was modeled using an equivalent rectangle rather than an equivalent square cross section (Fig. 14(c)) to better capture the experimental response of ED bars. The comparison of simulated and measured responses of the ED reinforcement is shown in Fig 14(d), where measured axial force is plotted against applied axial displacement for the ED reinforcement under uniaxial loading conditions. The details about the setup and the loading protocol for the testing of ED reinforcements can be found in Sharma.[7]

The UHPC-NC interface at the rocking corners of the wall panel were modeled with a perfect bond, as negligible slip was measured at the interface during laboratory testing. The wall-to-foundation interface was modeled using the same approach as interfaces in the anchorage specimens. The coefficient of friction was set to 0.84, which is between the recommended values of 0.6 and 1.0 for various

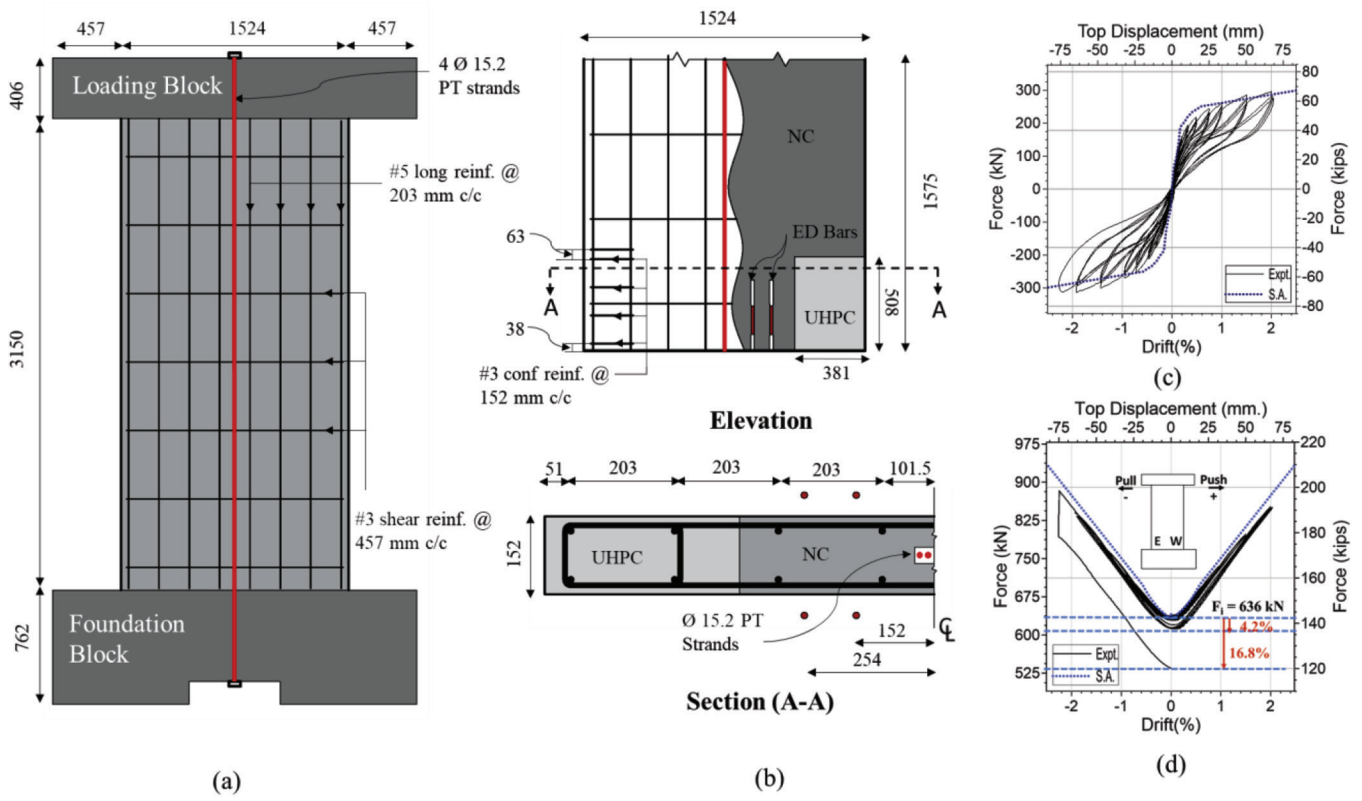


Fig. 13—(a) Specimen dimension and reinforcement layout of specimen RW2 (confinement details not shown); (b) reinforcement and confinement details of retrofitted walls; (c) measured force versus displacement response of RW2; and (d) measured PT force versus displacement in RW2.[10] (Note: Units in mm; 1 mm = 0.04 in.)

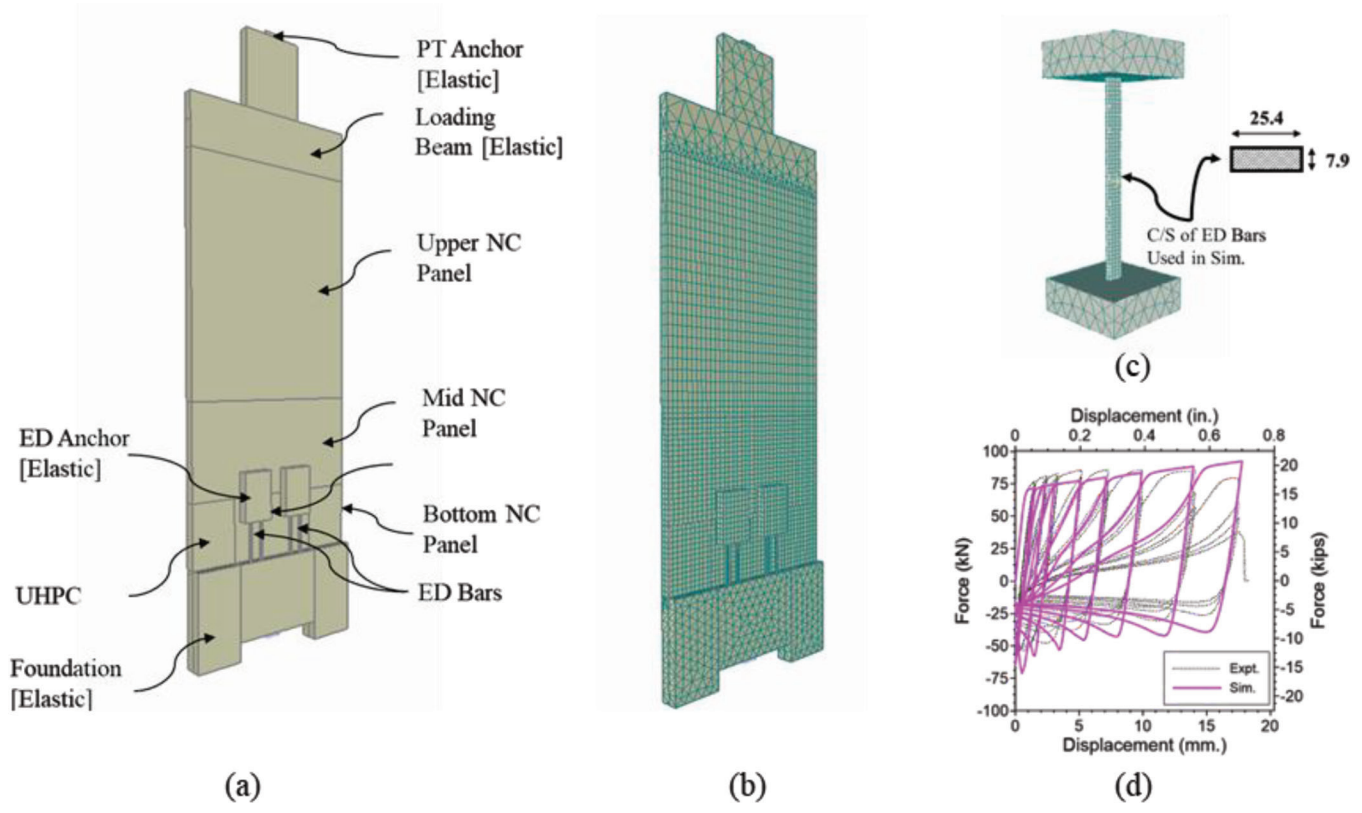


Fig. 14—Schematic of numerical model of retrofitted wall specimen RW2 in ATENA 3D: (a) different components in numerical model; (b) mesh distribution in numerical model; (c) schematic of FEM model used in calibration of ED reinforcements; and (d) comparison of measured and ATENA simulated response of ED reinforcements.

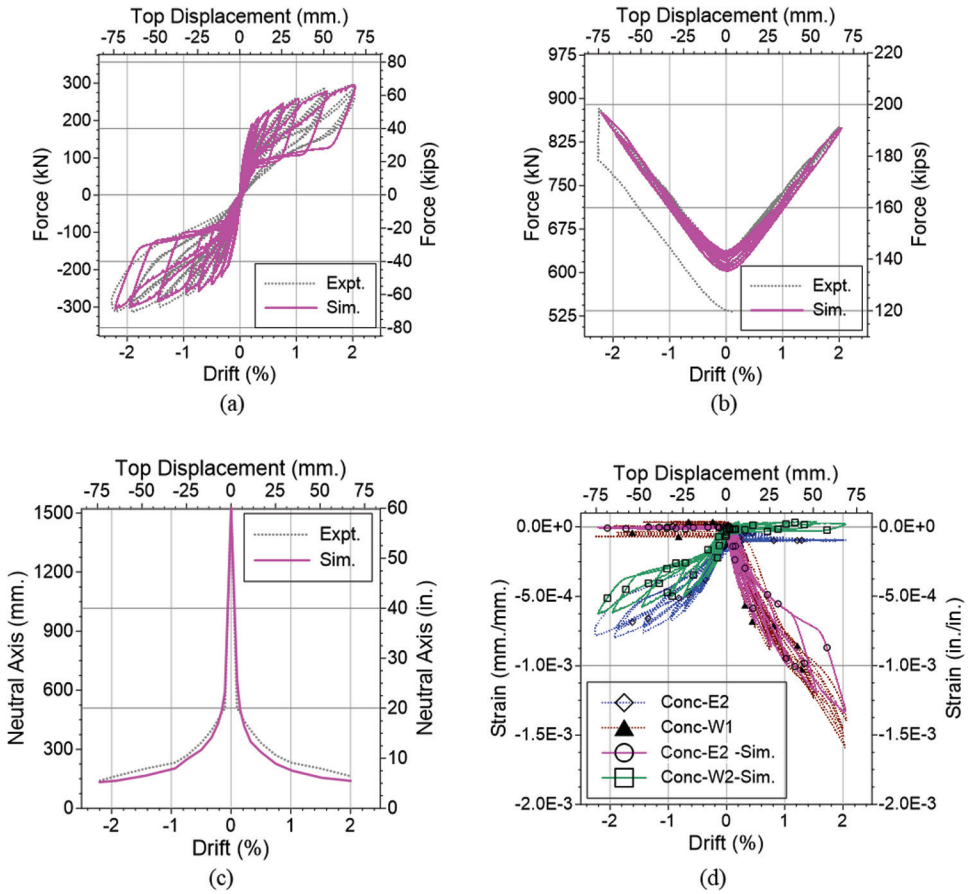


Fig. 15—Comparison of measured and FE model results for specimen RW2: (a) force versus drift; (b) PT force versus drift; (c) neutral axis depth versus drift; and (d) concrete strain versus drift. (Note: Units in mm; 1 mm = 0.04 in.)

surface preparations by ACI 318-19.[18] The input values for all the material models used in the FE model and additional descriptions can be found in Sharma.[7]

All degrees of freedom on the bottom surface of the foundation were constrained. The displacement of the wall panel and loading members were constrained in the out-of-plane direction due to the vertical symmetry imposed on the model. The numerical model was initially subjected to initial PT force distributed in 10 equal loading steps. The model also incorporated the self-weight of the concrete components. In the model, loading was simulated using displacement-controlled cyclic loading steps with a constant displacement loading step of 0.089 mm (0.0035 in.) applied to the loading beam at a height of 3352.8 mm (132 in.) from the wall base.

Comparison of measured and simulated response—Figure 15(a) illustrates the comparison between the FE model and measured force-displacement responses. The FE model closely matched the measured response, deviating by only 7% for lateral drifts exceeding 0.22% in the positive and 0.50% in the negative loading directions. The model successfully captured the self-centering behavior of the retrofitted shear wall, with a maximum residual drift of 0.06% in both simulated and measured results. The model accurately captured the measured PT force response, until one of the PT strands prematurely ruptured during testing, as seen in Fig. 15(b). The FE model neutral axis depth (Fig. 15(c)) was within 13% and 11% of the measured response in the positive and negative loading directions, respectively.

The comparison of measured and model predicted concrete strains at the rocking corners of the retrofitted wall are presented in Fig. 15(d). The measured strain labeled 'Conc-W1' was measured at a height of 64 mm (2.52 in.) from the wall base and at 64 mm (2.52 in.) from the west edge of the experimental wall specimen (RW2). The strain labeled 'Conc-E2' was measured at a height of 464 mm (18.27 in.) from the base of the wall and 83 mm (3.26 in.) from the east edge of the wall. The model-predicted strains corresponding to 'Conc-W1' at 1.0% drift and 2.0% drift were 6% and 10% lower than the measured strains, respectively. Similarly, predicted strains for 'Conc-E2' at 1.0% drift and 2.0% drift were 23% and 21% lower than the measured strains, respectively.

Investigation of UHPC foundation retrofit scheme for PT anchorage at full-scale under lateral loading

Design of full-scale PT anchorage—The full-scale anchorage scheme was designed based on the laboratory-tested anchorage specimen SP1-WI-D7 and retrofit wall specimen RW2, described previously. The height and width of the UHPC block, the PT anchorage location, and the embedment length of the dowel and interface reinforcements were kept the same as the laboratory-tested PT anchorage specimens. The length of the UHPC block was increased to surround the entire base of the wall. Additional dowel bars and interface bars were provided on either side of the center of the wall at the same spacing used in the

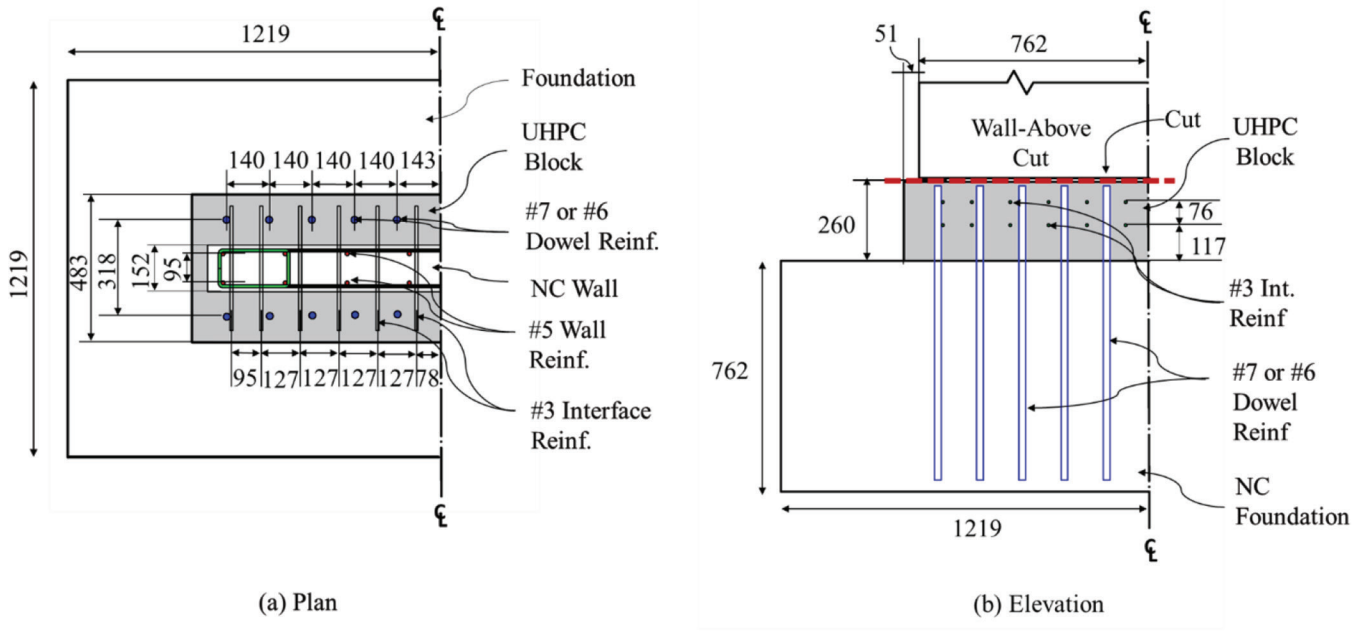


Fig. 16—Design of UHPC foundation retrofit for PT anchorage for full-scale specimen: (a) plan; and (b) elevation showing dimensions of UHPC block and details of dowel and interface reinforcements. (Note: Wall reinforcements not shown for clarity; units in mm; 1 mm = 0.04 in.)

laboratory-tested PT anchorage specimens. The retrofitted wall was assumed to be cut just above the UHPC block. The dimensions and the reinforcement details of PT anchorage for specimen RW2 are shown in Fig. 16. The details of the wall panel above the cut level, as indicated in Fig. 16(b), is the same as the wall specimen RW2.

FE model description—The general layout of the FE model used for modeling the full-scale anchorage scheme is shown in Fig. 17(a) and (b). The wall was modeled using the same elements, loading, mesh, and boundary conditions described previously for RW2 and the PT anchorage specimens. The wall was simulated under monotonic lateral loading, and the PT force and lateral loading were applied in a similar fashion as described previously in modeling RW2.

Simulated response of full-scale anchorage scheme—The simulated damage in the anchorage portion of the wall was limited to the UHPC block, and this damage was similar to the damage observed during laboratory testing of anchorage specimens (Fig. 17(c)). The cracking was limited to the anchorage region during application of the initial load. With increased drift, additional cracking was observed to propagate around the anchorage region. After 0.50% drift, the damage did not progress beyond the central region except for the cracking and accumulation of stress close to the wall compression region.

The comparison of measured and simulated force-displacement response and PT force-displacement response is shown in Fig. 18(a) and (b). After 0.50% drift, the force-displacement responses in both simulated specimens were within 15% of the measured response in specimen RW2. At the design drift of 0.60%, the lateral strength of the retrofitted shear wall obtained from the analysis was 251.8 kN (56.6 kip) compared to the design strength of 251.3 kN (56.5 kip). The PT force based on simulated results was within 5% of the measured PT force. The simulated strain demand in dowel and wall reinforcements is shown in Fig. 18(c) and (d). The dowel and wall reinforcements are labeled such that the one closest to the anchorage region is labeled as 1 and the reinforcements further away are labeled in increasing order. The dowel and wall reinforcements in the wall half consisting of compression zone are labeled as _C and the ones on the uplift side are labeled as _T. The demands on the dowel and wall reinforcements were lower than yielding. The tensile strain demands in the dowel and wall reinforcements were not uniform. The dowel and wall reinforcements closer to the anchorage region experienced (W1/D1_T/C) more than three times tensile demand compared to reinforcements closer to the wall edge (W4/D4_T and W4/D4_C).

Based on the simulated results, the proposed anchorage scheme was found to be sufficient in anchoring external PT force in retrofitted shear walls without affecting the global force-displacement response and with limited damage to the UHPC block. The performance of the anchorage scheme could be further improved by placing the dowel reinforcements close to the anchorage region and by increasing the size of UHPC block closer to the anchorage region and tapering it towards the edge of the wall.

CONCLUSIONS AND RECOMMENDATIONS

The following conclusions and recommendations are made based on the study:

- The proposed anchorage scheme with ultra-high-performance concrete (UHPC) was found suitable in anchoring external post-tensioning due to negligible damage observed in UHPC during testing and efficient

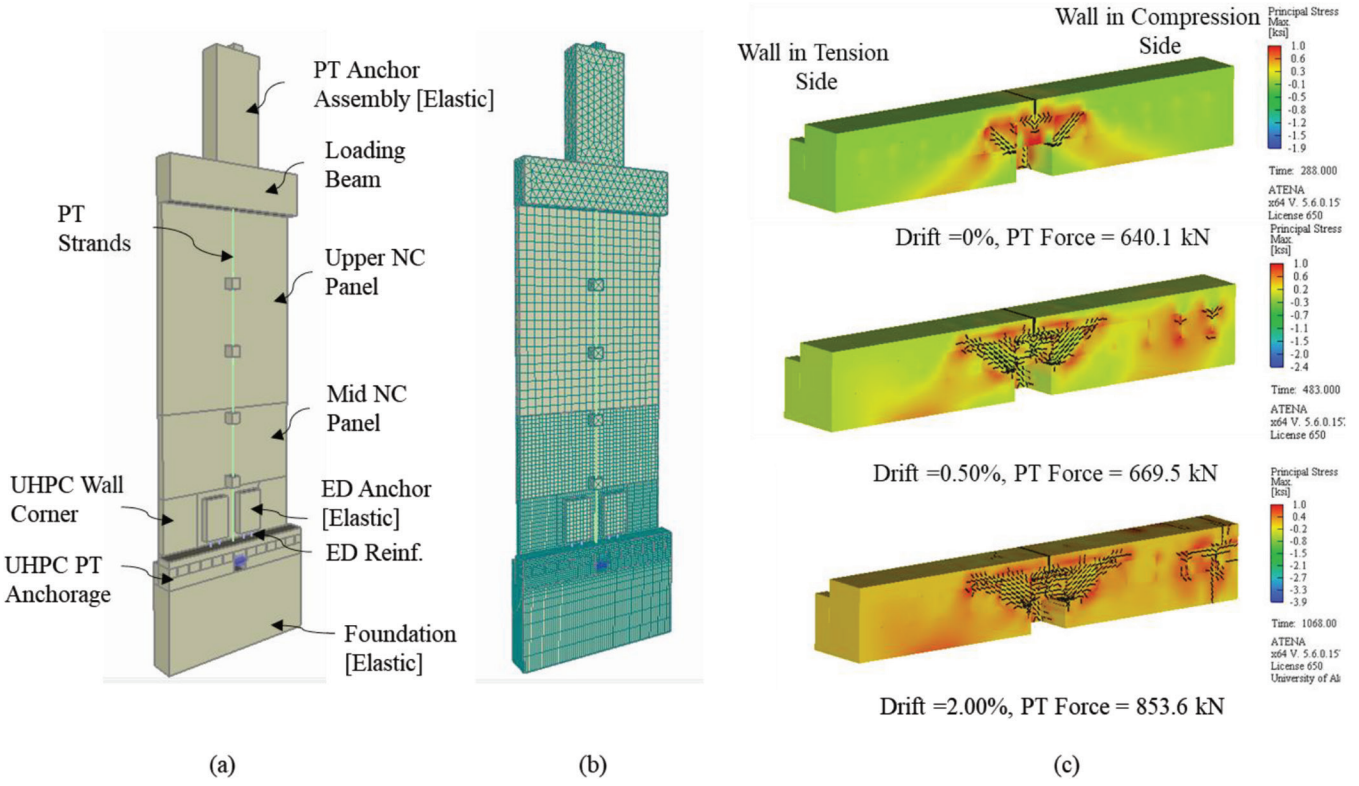


Fig. 17—Schematic of FE model used to investigate UHPC retrofit for PT anchorage scheme for full-scale wall in ATENA: (a) different components of FE model; (b) mesh distribution in FE model; and (c) simulated damage progression and distribution of maximum principal stress in UHPC block for PT anchorage at different wall drift levels. (Note: 1 kN = 0.225 kip.)

transfer of anchorage forces through engagement of dowel reinforcements.

- The mechanical characteristics of UHPC enabled the development of dowel bars with relatively small height of the UHPC block around the wall panel and supports the reduction in UHPC block height used in the post-tensioning (PT) anchorage scheme.
- Low tensile demand was measured in the normal-strength concrete (NC) wall-UHPC block interface reinforcement (measured strains were less than 300 με), indicating the surface roughness and the dowel bars were sufficient to limit the slip along that interface.
- The three-dimensional (3-D) finite element (FE) model of the PT anchorage specimen captured the damage progression in the UHPC region in the PT anchorage specimens and strain distribution in embedded reinforcements. Measured results from a broader range of specimen types are required to further refine and generalize the findings from the FE simulations.
- The 3-D FE model simulation of the retrofitted wall specimen, integrated with PT anchorage scheme using UHPC, indicates that the PT strands can achieve yield strength without causing significant damage to the anchorage region in the UHPC block. The dowel and wall reinforcements near the center of the anchorage region exhibited tensile strains nearly three times higher than those recorded in reinforcements closer to the wall's edge.
- FE simulation results suggest that positioning dowel reinforcements near the PT anchorage region and enlarging the UHPC block in this area, gradually tapering it towards the edge of the wall panel, could be advantageous. Based on the measured strains in the dowel bars in the laboratory-tested anchorage specimens, neglecting contribution from wall reinforcements, and limiting design stress in dowel bars to 50% of yield strength may result in overly conservative design. Thus, the design of dowel bars could be further optimized through additional experimental testing and numerical simulations.
- Additional crack control measures could be explored to minimize microcracking of UHPC block under application of PT anchorage forces to improve long-term durability of the anchorage.
- Additional parametric studies are needed to further refine and optimize the design of the anchorage region.

AUTHOR BIOS

ACI member **Sumedh Sharma** *is a Postdoctoral Research Fellow at Texas A&M University, College Station, TX. He received his BA from Kathmandu University, Dhulikhel, Nepal, and his MS and PhD from The University of Alabama, Tuscaloosa, AL. He is a member of ACI Subcommittee 564-B, Structural Design and Testing. His research interests include seismic-resistant design and retrofit of reinforced concrete structures, three-dimensional (3-D)-printed concrete structures, and ultra-high-performance concrete (UHPC).*

ACI member **Sriram Aaleti** *is a Professor at The University of Alabama. He received his BTech from the Indian Institute of Technology Madras, Chennai, Tamil Nadu, India, and his MS and PhD from Iowa State University, Ames, IA. He is a member of ACI Committee 239, Ultra-High-Performance Concrete, and ACI Subcommittee 318-D, Members. His research interests include the behavior of reinforced concrete structures under*

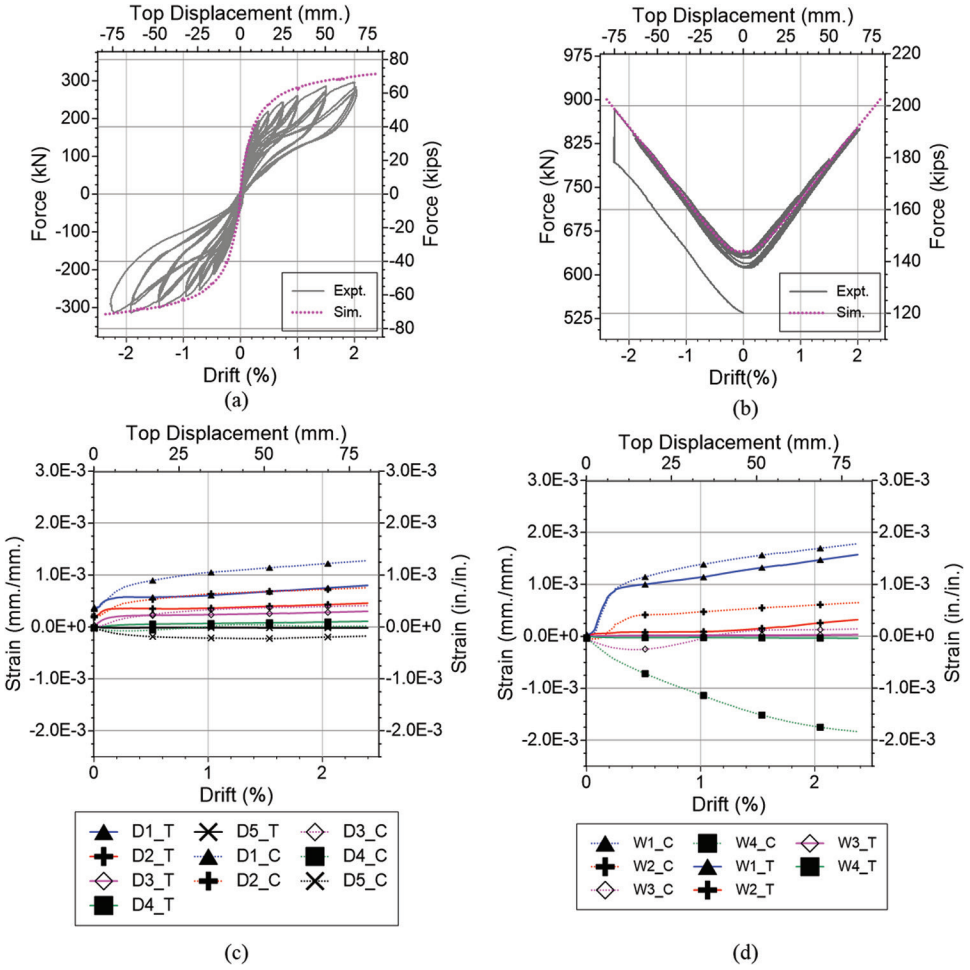


Fig. 18—Comparison of measured and simulated responses between specimen RW2 and full-scale anchorage specimen with No. 7 dowel reinforcements: (a) force-displacement; (b) PT force-displacement; results from simulated response of full-scale anchorage specimen with No. 7 dowel bars; (c) strain in dowel reinforcements versus displacement; and (d) strain in wall reinforcement versus displacement. (Note: 1 mm = 0.04 in.)

natural hazards, UHPC, large-scale testing, accelerated bridge construction, and finite element analysis.

ACI member **Pinar Okumus** *is an Associate Professor in the Department of Civil, Structural and Environmental Engineering at the University at Buffalo, Buffalo, NY. Her research interests include understanding the fundamental behaviors of reinforced concrete and prestressed concrete structures, analytical modeling, experimental testing, and accelerated bridge construction.*

ACKNOWLEDGMENTS

The study described in this paper was made possible by a grant from the National Science Foundation's Engineering for Natural Hazards (ENH) program, Grant No. 1662963. The opinions, findings, and conclusions in this paper are those of the authors and do not necessarily represent those of the sponsor. The authors are grateful to lab manager B. Battle; undergraduate students A. Cemalovic, H. Tzabari, and J. Beasley; and graduate students D. B. Valentim and G. Willis for their assistance in specimen fabrication and testing. The authors would also like to thank Nucor Steel in Birmingham, AL, and GTI USA for their generous donations of materials.

DATA SET

Aaleti, S., 2022 "Retrofit of Existing Foundation to Anchor External Post-Tensioning Using Ultra-High Performance Concrete," Seismic Retrofit of Deficient RC Shear Walls Using Selective Weakening and Self-Centering-(Foundation Retrofit), DesignSafe-CI. doi: 10.17603/ds2-kp1n-hs96

REFERENCES

1. Lin, R.-G. II, "California Earthquake Standard Designed to Save Lives but Not Buildings. There's a New Push to do Both," *Los Angeles Times*, Mar. 15, 2018.

2. Calvi, G. M.; Sullivan, T. J.; and Welch, D. P., "A Seismic Performance Classification Framework to Provide Increased Seismic Resilience, *Perspectives on European Earthquake Engineering and Seismology*, V. 34, 2014, pp. 361-400.

3. Craymer, L., "Christchurch Struggles with Shaky Recovery From 2011 Quake," *The Wall Street Journal*, July 10, 2015.

4. Pampanin, S., "Controversial Aspects in Seismic Assessment and Retrofit of Structures in Modern Times: Understanding and Implementing Lessons from Ancient Heritage," *Bulletin of the New Zealand Society for Earthquake Engineering*, V. 39, No. 2, 2006, pp. 120-133. doi: 10.5459/bnzsee.39.2.120-133

5. Kam, W. Y., and Pampanin, S., "Selective Weakening Techniques for Retrofit of Existing Reinforced Concrete Structures," The 14th World Conference on Earthquake Engineering, Beijing, China, 2008.

6. Pampanin, S., "Alternative Performance-Based Retrofit Strategies and Solutions for Existing RC Buildings, in Seismic Risk Assessment and Retrofitting: With Special Emphasis on Existing Low Rise Structures, A. Ilki, F. Karadogan, S. Pala, and E. Yuksel, eds., Springer, Dordrecht, the Netherlands, 2009, pp. 267-295.

7. Sharma, S., "Seismic Retrofit of Reinforced Concrete Shear Wall by Integrating Selective Weakening and Self Centering," PhD dissertation, The University of Alabama, Tuscaloosa, AL, 2022.

8. Basereh, S., "Resilient Seismic Retrofit of Reinforced Concrete Shear Walls Using Selective Weakening and Self-Centering," PhD dissertation, The State University of New York, Buffalo, NY, 2021.

9. Basereh, S.; Okumus, P.; and Aaleti, S., "Reinforced Concrete Shear Walls Retrofitted Using Weakening and Self-Centering: Numerical

Modelling," *Journal of Structural Engineering*, ASCE, V. 146, No. 7, 2020, p. 04020122. doi: 10.1061/(ASCE)ST.1943-541X.0002669

10. Sharma, S.; Aaleti, S.; and Okumus, P., "Experimental Testing of RC Shear Wall Seismic Retrofit Using Selective Weakening, Self-Centering and Ultra High Performance Concrete," *Resilient Cities and Structures*, V. 2, No. 1, 2023, pp. 76-90.

11. Basereh, S., "Testing and Predicting the Response of Reinforced Concrete Shear Walls Retrofitted for Recentering," *Engineering Structures*, V. 291, 2023, p. 116384.

12. Ruiz, M. F.; Muttoni, A.; and Kunz, J., "Strengthening of Flat Slabs Against Punching Shear Using Post-Installed Shear Reinforcement," *ACI Structural Journal*, V. 107, No. 4, July-Aug. 2010, pp. 434-442.

13. Breveglieri, M.; Aprile, A.; and Barros, J. A. O., "Shear Strengthening of Reinforced Concrete Beams Strengthened Using Embedded Through Section Steel Bars," *Engineering Structures*, V. 81, 2014, pp. 76-87. doi: 10.1016/j.engstruct.2014.09.026

14. Ronanki, V. S.; Aaleti, S.; and Valentim, D. B., "Experimental Investigation of Bond Behavior of Mild Steel Reinforcement in UHPC," *Engineering Structures*, V. 176, 2018, pp. 707-718. doi: 10.1016/j.engstruct.2018.09.031

15. Ronanki, V. S., and Aaleti, S., "Experimental and Analytical Investigation of UHPC Confined Concrete Behavior," *Construction and Building Materials*, V. 325, 2022, p. 126710. doi: 10.1016/j.conbuildmat.2022.126710

16. Russell, H. G., and Graybeal, B. A., *Ultra-High Performance Concrete: A State-of-the-Art Report for the Bridge Community*, Federal Highway Administration, Washington, DC, 2013.

17. Sharma, S.; Ronanki, V. S.; Aaleti, S.; and Okumus, P., "Experimental Investigation of Surface Preparation on Normal and Ultra High Performance Concrete Interface Behavior," *Journal of Bridge Engineering*, ASCE, V. 26, No. 4, 2021, p. 04021010. doi: 10.1061/(ASCE)BE.1943-5592.0001697

18. ACI Committee 318, "Building Code Requirements for Structural Concrete (ACI 318-19) and Commentary (ACI 318R-19) (Reapproved 2022)," American Concrete Institute, Farmington Hills, MI, 2019, 624 pp.

19. Hilti, "*HILTI*," Hilti Corporation, Schaan, Liechtenstein, 2022, https://www.hilti.com/. (last accessed Aug. 19, 2025).

20. Holcim, "*Ductal*®," LaFargeHolcim US, Chicago, IL, 2022, https://www.ductal.com/en. (last accessed Aug. 19, 2025).

21. DURA, "*DURA*®," DURA Concrete Canada Inc., Lakeshore, ON, Canada, 2022, https://www.duraconcrete.ca/. (last accessed Aug. 19, 2025).

22. Graybeal, B., and Davis, M., "Cylinder or Cube: Strength testing of 80 to 200 MPa (11.6 to 29 ksi) Ultra-High Performance Fiber-Reinforced Concrete," *ACI Materials Journal*, V. 105, No. 6, Nov.-Dec. 2008, pp. 603-609.

23. ASTM C39/C39M-20, "Standard Test Method for Compressive Strength of Cylindrical Concrete Specimens," ASTM International, West Conshohocken, PA, 2020.

24. ASTM E8/E8M-13, "Standard Test Methods for Tension Testing of Metallic Materials," ASTM International, West Conshohocken, PA, 2013.

25. Červenka, V., and Jendele, L. Č., J., *ATENA Program Documentation Part 1 Theory*, Červenka Consulting, Prague, Czech Republic, 2020.

26. ACI Committee 550, "Acceptance Criteria for Special Unbonded Post-Tensioned Precast Structural Walls Based on Validation Testing (ACI 550.6-19) and Commentary," American Concrete Institute, Farmington Hills, MI, 2019, 20 pp.

27. Lowes, L. N.; Lehman, D. E.; and Whitman, Z., "Investigation of Failure Mechanisms and Development of Design Recommendations for Flexural Reinforced Concrete Walls," *Engineering Structures*, V. 186, 2019, pp. 323-335. doi: 10.1016/j.engstruct.2019.01.122

ACI STRUCTURAL JOURNAL TECHNICAL PAPER

Title No. 122-S75

Stiffness Modifiers to Support Seismic Design of Reinforced Concrete Circular Columns

by Mario E. Rodriguez and José I. Restrepo

Linear structural analysis is the method of choice commonly used by practicing engineers to support the seismic design of a structure. The structural models are developed in commercial software and incorporate stiffness modifiers, which lower the stiffness of the members, in recognition of all the sources of flexibility that occur upon cracking of the concrete. This paper describes a mechanics-based model to compute the stiffness modifiers for columns with a circular cross section. The mechanics-based model accounts for five modes of deformation observed. Calibration of this model was performed with a database of tests reported in the literature on 22 circular-section columns that exhibited ductile response. The paper ends by describing a simplified method for use in design. The mechanics-based model and the design method yield an effective column lateral stiffness that closely aligns with the values obtained from the column database.

Keywords: circular columns; effective lateral stiffness; reinforced concrete; seismic analysis; stiffness modifiers; test.

INTRODUCTION

Most of the seismic designs for reinforced concrete structures rely on linear analysis. Various publications and design codes prescribe stiffness modifiers less than unity to compute the member's effective stiffness. The effective stiffness accounts for the reduced rigidity of columns caused by cracking and bar-bond slip. In a column, the stiffness modifier is defined as the ratio of the secant (or effective) stiffness to the initial stiffness, where the secant stiffness is measured after cracking and before the column's critical section reaches its flexural strength. The initial stiffness is typically based on calculations using gross-section properties.

Figure 1 depicts four parity plots comparing stiffness modifiers derived from column tests with those recommended in the literature for circular-section columns. A perfect model would align all points along the diagonal in a parity plot. However, the stiffness modifier prescribed in ACI 318-19 Code (Section 6.6.3.1.2) (ACI Committee 318 2019), ASCE/SEI 41-23 (2023), and AASHTO LRFD (AASHTO LRFD 2011) seismic design guide (Section 5.6.2, stiffness modifier estimation by slope of M-ϕ curve or Fig. 5.6.2.1) exhibit significant scatter. By contrast, the stiffness modifiers computed using the refined and simplified approaches proposed by Elwood and Eberhard (2009) demonstrate a stronger correlation between the test results and model predictions.

Most stiffness modifier recommendations in the literature pertain to members modeled using the Bernoulli beam-column formulation (Elwood and Eberhard 2009; AASHTO 2011; ACI 318-19). However, modern structural analysis software no longer offers the Bernoulli beam-column formulation as a modeling option. Instead, these programs adopt the Timoshenko beam-column formulation, which accounts for shear deformations. This shift has introduced ambiguity in the reinforced concrete design industry. Engineers often resolve this by adopting one of two approaches when applying Bernoulli-based stiffness modifiers in a Timoshenko beam-column model: 1) using an equal stiffness modifier for both flexure and shear; or 2) applying a stiffness modifier for flexure while setting the shear stiffness modifier to unity. Unfortunately, neither approach accurately represents the intended effective lateral stiffness.

This ambiguity becomes particularly relevant for elements with a short span or length-to-depth ratio of less than 3, a configuration commonly found in members of structures in high-seismic regions. Appendix A* illustrates that this ambiguity can be resolved by setting the shear area to infinity, effectively reducing the Timoshenko beam-column formulation to the Bernoulli formulation. In practice, this means that the stiffness modifiers derived for a Bernoulli beam-column model can be used in Timoshenko-based software by maximizing the shear area parameter and setting the shear stiffness modifier to unity. This paper examines a mechanics-based model for determining stiffness modifiers for columns with a circular cross section. Additionally, it introduces a simplified model calibrated against the mechanics-based model for practical use in design. The proposed stiffness modifiers are specifically intended for use in structural analysis, supporting the seismic design of reinforced concrete structures when columns are modeled with the Timoshenko beam-column formulation. The stiffness modifiers recommended herein must be equally applied to the gross-section moment of inertia and the shear area.

RESEARCH SIGNIFICANCE

Linear structural models are nearly always developed and used to support the seismic design of reinforced concrete structures. In these models, the reduction of the member

*The Appendix is available at **www.concrete.org/publications** in PDF format, appended to the online version of the published paper. It is also available in hard copy from ACI headquarters for a fee equal to the cost of reproduction plus handling at the time of the request.

ACI Structural Journal, V. 122, No. 5, September 2025.
MS No. S-2024-180.R2, doi: 10.14359/51746758, received March 11, 2025, and reviewed under Institute publication policies. Copyright © 2025, American Concrete Institute. All rights reserved, including the making of copies unless permission is obtained from the copyright proprietors. Pertinent discussion including author's closure, if any, will be published ten months from this journal's date if the discussion is received within four months of the paper's print publication.

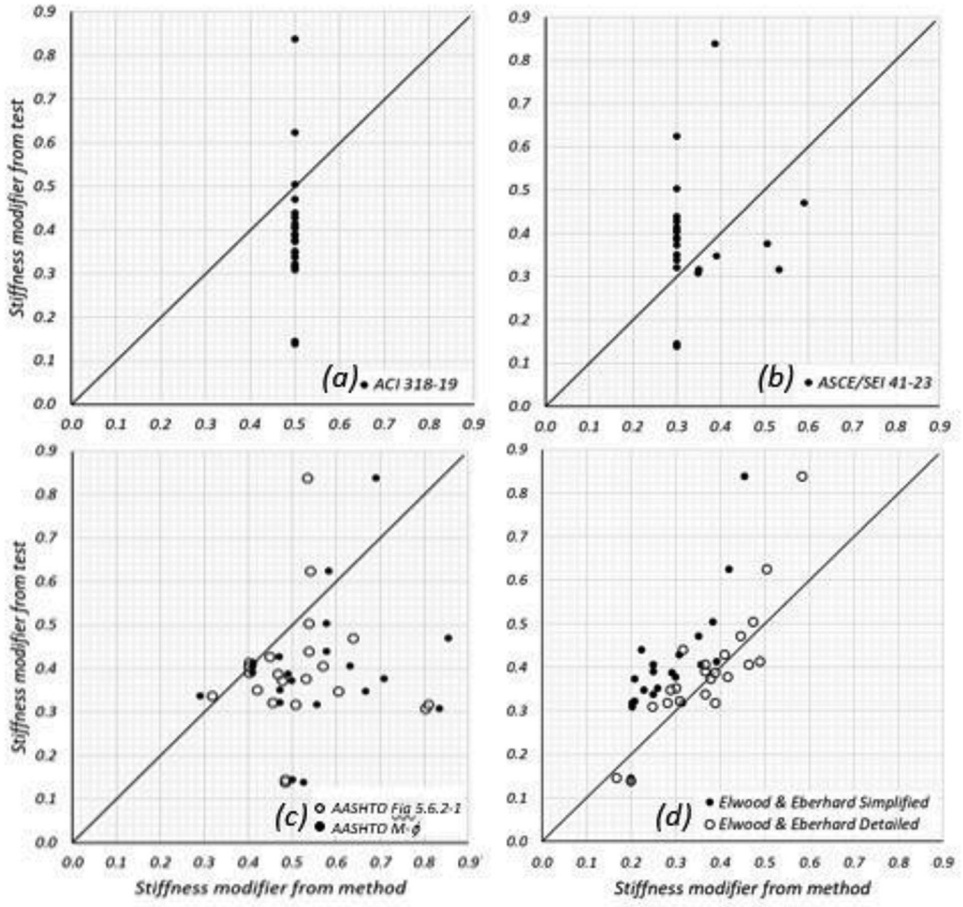


Fig. 1—Parity plots of stiffness modifiers derived from test columns and those recommended in literature for circular-section columns.

stiffness due to cracking and bar-bond slip is accounted for through the application of stiffness modifiers. The early commercial software used the Bernoulli beam-column formulation to model columns, leading to the development of stiffness modifier recommendations tailored specifically to that formulation. However, modern structural analysis software uses the Timoschenko beam-column formulation, which accounts for shear deformations. Despite this shift, many codes and guidelines continue to recommend stiffness modifiers developed for the Bernoulli model, creating a mismatch in their applicability.

This paper addresses the necessity for explicit stiffness modifiers that account for bending and shear when using Tymoshenko beam-column elements. Using simplified concrete mechanics and optimization, the authors present a method for deriving stiffness modifiers for circular columns compatible with the Timoschenko beam-column formulation. This approach extends the formulation derived by Restrepo and Rodriguez (2021) for rectangular columns. The paper concludes with recommendations for stiffness modifiers suitable for practical design applications.

DEFINITION OF STIFFNESS MODIFIER

This section provides a general definition of the stiffness modifier for a reinforced concrete element. Figure 2 plots the lateral force-displacement response of a reinforced concrete column configured as a cantilever under lateral loading. Initially, the force-displacement response is linear up to the cracking force, V_{cr}, with the corresponding lateral stiffness K_o defined as

$$K_o = \frac{3}{L^3}\frac{E_c I_t}{\chi} \tag{1}$$

according to a Timoschenko beam-column formulation.

In Eq. (1), E_c represents the modulus of elasticity of concrete; I_t denotes the moment of inertia of the transformed section of the column; and L is the column length, measured from its base to the point of inflection. The term $\chi = 1 + 0.51/(L/h)^2$ is a coefficient that accounts for shear deformations, derived using Cowper's (1966) shear coefficient for a circular cross section (refer to Appendix A).

The column shown in the inset of Fig. 2 exhibits a nonlinear response when the lateral force γV_{max} ranges between V_{cr} and V_i, with V_{max} defined as the maximum shear force resisted by the column. Force V_i corresponds to the ideal moment M_i at the column base, which is computed similarly to the nominal moment M_n defined in ACI 318-19 but using the measured or expected material properties (Restrepo and Rodriguez 2013). Unloading and reloading within this range of lateral force result in a nearly linear response characterized by an effective lateral stiffness K_e given by

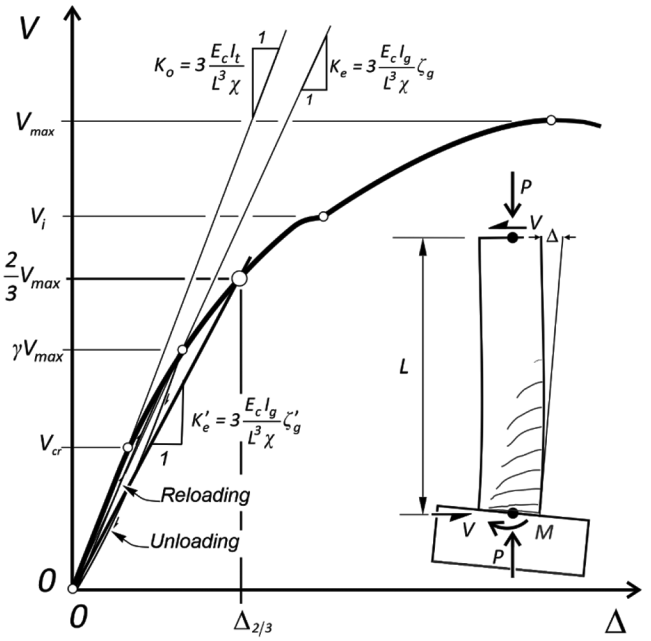


Fig. 2—Definition of effective lateral stiffness in cantilever column.

$$K_e = \frac{3}{L^3}\frac{E_c I_g}{\chi}\zeta_g \quad (2)$$

where ζ_g is a gross-section-based stiffness modifier that is less than or equal to unity. Using the stiffness modifier coefficient ζ_g implies that both flexural and shear stiffness degrade in the same proportion. This is a practical simplification due to the rarity of published test data that disaggregates the lateral displacement components. Such data would be necessary to calibrate separate stiffness modifiers for flexure and shear. For further details, the reader is referred to Appendix A, where the derivation of the equations and the simplification to a single stiffness modifier for flexure and shear are presented.

REVIEW OF PREVIOUS WORK

Existing methods for computing stiffness modifiers can be classified into two categories: 1) methods of analysis used to support the design of new structures; and 2) methods of analysis to support the assessment of existing structures. In the first category, the stiffness modifier is either a constant or depends on the axial load level. Examples of methods in this category are ACI 318-19, Paulay and Priestley (1992), Khuntia and Ghosh (2004), Kumar and Singh (2010), and ASCE/SEI 41-23. A second category includes methods incorporating parameters such as aspect ratio or longitudinal reinforcement ratio, which may require the longitudinal bar diameter to column depth ratio. Examples of methods in this category are Elwood and Eberhard (2009), AASHTO (2011), and Avsar et al. (2014). Based on the results of M-ϕ analyses, Avsar et al. (2014) proposed different stiffness modifiers for rectangular and circular columns.

Some methods use piecewise linear relationships and make $K_e \propto E_c\zeta_g \propto \sqrt{f'_c}(B_3 + B_4 P/(A_g f'_c))$, which, as shown in the following, might lead to contradictory results. For

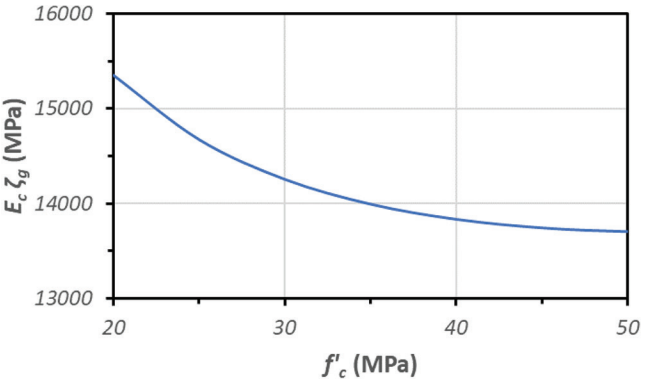


Fig. 3—Variation of stiffness $E_c\zeta_g$ *as function of* f_c' *for circular columns (*h *= 600 mm and* P *= 300 kN) computed by ASCE 41-23 when 0.2 <* $P/(A_g f_c') < 0.5$.

example, the stiffness modifier specified by ASCE/SEI 41-23 for columns having $0.1 < P/(A_g f'_c) < 0.5$ is $\zeta_g = 0.2 + P/(A_g f'_c)$, where ζ_g is the gross-section-based stiffness modifier. Figure 3 plots the values computed for $E_c\zeta_g$ as a function of f'_c for 600 mm diameter columns with $P = 300$ kN. In these columns, the axial load ratios vary within the range $0.2 < P/(A_g f'_c) < 0.5$. Figure 3 demonstrates that identical columns, differing only in the concrete compressive strengths and subjected to the same axial load in a relatively wide range of f'_c values (20 MPa $< f'_c <$ 50 MPa), a column with a higher concrete compressive strength exhibits a smaller effective lateral stiffness than a column with a lower concrete compressive strength. This result is paradoxical.

DATABASE

To support the calibration of the methods proposed herein and facilitate comparison with methods proposed by others, the authors compiled a database of 22 circular-section columns tested quasi-statically under reversed cyclic loading while maintaining a constant axial load; refer to Table 1. Only columns with at least a minimum dimension of 305 mm were included in the database. All columns developed and maintained a flexure plastic hinge throughout the end of the test. The 16- to 84-percentile range of values characterizing the database are as follows: column diameter h (457, 610 mm); concrete compressive strength $\hat{f}'_c$ (31.0, 38.0 MPa) indicating a relatively narrow variability in the strength; longitudinal reinforcement yield strength $\hat{f}_y$ (428, 475 MPa), indicating that all the longitudinal reinforcement is Grade 420; longitudinal reinforcement ratio ρ_l (1.7, 3.1; 20 columns tested under a compressive axial load ratio $P/A_g\hat{f}'_c$ [0.065, 0.189]), plus two columns tested under axial tension (shown with a negative sign in column 11 of Table 1(a)). Additional data include the ratio of column diameter to longitudinal bar diameter h/d_b (25, 38) (shown in column 5 of Table 1(b)) and the column shear span-depth ratio a_v/h [2, 7] (shown in column 6 of Table 1(b)).

MECHANICS-BASED MODEL

Figure 4 illustrates a circular cantilever column of length L, subjected to a lateral force $V = 2/3V_{max}$ and a constant axial load P. This figure also shows the corresponding

Table 1(a)—Relevant properties of circular test columns

Number	References	Designation	h, mm	L, mm	f_c', MPa	f_y, MPa	f_{yt}, MPa	ρ_l	I_t/I_g	$P/(A_g f_c')$
1	2	3	4	5	6	7	8	9	10	11
1	Vu et al. (1999)	VUNH2	457	910	39.2	427.5	430.2	0.0241	1.19	−0.10
2	Vu et al. (1999)	VUNH5	457	910	35.2	507.5	448.2	0.0241	1.20	−0.08
3	Moyer and Kowalsky (2003)	KOWALSU1	457	2438	32.7	565.0	434.0	0.0207	1.18	0.04
4	Stephan et al. (2003)	RES-U1	914	2896	64.1	426.0	413.7	0.0254	1.16	0.06
5	Stone and Cheok (1989)	NIST-F	1520	9140	35.8	475.0	493.0	0.0200	1.16	0.07
6	Stone and Cheok (1989)	NIST-S	1520	4570	34.3	475.0	435.0	0.0200	1.17	0.07
7	Lehman and Moehle (2000)	LEH1015	610	6096	31.0	462.0	607.0	0.0150	1.13	0.07
8	Lehman and Moehle (2000)	LEH407	610	2438	31.0	462.0	607.0	0.0075	1.07	0.07
9	Lehman and Moehle (2000)	LEH415	610	2438	31.0	462.0	607.0	0.0150	1.13	0.07
10	Lehman and Moehle (2000)	LEH430	610	2438	31.0	462.0	607.0	0.0303	1.26	0.07
11	Lehman and Moehle (2000)	LEH815	610	4877	31.0	462.0	607.0	0.0150	1.13	0.07
12	Calderone et al. (2000)	CAL328	610	1829	34.5	441.3	606.8	0.0273	1.23	0.09
13	Calderone et al. (2000)	CAL828	610	4877	34.5	441.3	606.8	0.0273	1.23	0.09
14	Calderone et al. (2000)	CAL1028	610	6096	34.5	441.3	606.8	0.0273	1.23	0.09
15	Kunnath et al. (1997)	KUN97A2	305	1372	29.0	448.0	434.0	0.0204	1.18	0.09
16	Vu et al. (1999)	VU98NH4	457	910	35.0	468.2	434.4	0.0521	1.43	0.15
17	Vu et al. (1999)	VU98NH3	457	910	39.4	427.5	430.2	0.0241	1.19	0.15
18	Chai et al. (1991)	CHAI-3	610	3657	32.6	315.1	351.6	0.0254	1.22	0.19
19	Wong et al. (1990)	WONG90U1	400	800	38.0	423.0	300.0	0.0320	1.26	0.19
20	Vu et al. (1999)	VU98NH1	457	910	38.3	427.5	430.2	0.0241	1.19	0.31
21	Vu et al. (1999)	VU98NH6	457	910	35.0	486.2	434.4	0.0521	1.43	0.33
22	Wong et al. (1990)	WONG90U3	400	800	37.0	475.0	300.0	0.0320	1.26	0.39
Mean			625	—	35.6	453.7	482.9	0.0255	1.21	0.11
Maximum			1520	—	64.1	565.0	607.0	0.0521	1.43	0.39
Minimum			305	—	29.0	315.1	300.0	0.0075	1.07	−0.10

first-order bending moment diagram, where the moment at the column base is $2/3M_{max}$ and M_{cr} is the cracking moment. The combination of bending and axial force causes cracking in the column over a length $y_{cr} + L_{sv}$, leaving an uncracked length L_{cr}.

For modeling purposes, the column, including its connection to the framing element or foundation, is discretized in five distinct regions, each characterized by a specific response mode. The column is divided into four regions, Regions 1 through 4, and the connection region is designated as Region 5. At the top of the column, the total lateral displacement, Δ is the sum of the contributions from these five regions.

The following sections describe the model used to characterize the response of each region. Regions 1, 4, and 5 are modeled using the same approaches described for rectangular columns by Restrepo and Rodriguez (2021). Consequently, this paper only briefly outlines the equations governing these regions. The descriptions are presented in the following order: Regions 1, 4, 5, 3, and 2. Region 2 is discussed last because its model relies on interpolation functions, which use boundary conditions determined for Region 1 and either Region 3 or 4.

The contribution of Region 5 to the lateral deformation of a column cannot be easily quantified using mechanics alone. Therefore, its contribution is determined in the final part of the paper through a multivariate optimization of an objective function supported by a database of test column lateral stiffness compiled from existing literature.

Regions 1, 4, and 5

Region 1 represents the uncracked portion of the column, where the bending moment at the lower end corresponds to the onset of flexural cracking, M_{cr} (refer to Fig. 4). This moment is given by

$$M_{cr} = S_{et}\left(f_r + \frac{P}{A_t}\right) \tag{3}$$

where S_{et} is the section modulus of the gross uncracked section transformed to concrete; f_r is the modulus of rupture for normalweight concrete in ACI 318-19 and is taken equal to $0.62\sqrt{f_c'}$ (MPa); P is the axial load applied at the column centroidal axis; and A_t is the area of the gross uncracked section transformed into concrete

The length of Region 1, L_{cr}, is given by

Table 1(b)—Relevant properties of circular test columns

Number	Designation	d_b, mm	d_{bt}, mm	h/d_b	a_v/h	f_{su}/f_y	$\rho_t(f_y/f_c')$	$\rho_s/\rho_{s,ACI}$	s/d_b	c_c, mm	V_{max}, kN
1	2	3	4	5	6	7	8	9	10	11	12
1	VUNH2	15.9	9.5	28.7	2.0	NR	0.26	1.04	3.8	24.8	279
2	VUNH5	15.9	9.5	28.7	2.0	NR	0.35	0.90	5.0	24.8	379
3	KOWALSU1	19.0	9.5	24.1	5.3	1.23	0.36	0.93	4.0	12.7	153
4	RES-U1	15.9	9.7	57.5	3.2	1.67	0.17	0.94	2.5	58.0	1485
5	NIST-F	43.0	15.9	35.3	6.0	NR	0.27	0.72	2.1	58.7	1480
6	NIST-S	43.0	19.1	35.3	3.0	NR	0.28	1.58	1.3	60.3	3300
7	LEH1015	16.0	6.4	38.1	10.0	1.36	0.22	1.15	2.0	22.2	98
8	LEH407	16.0	6.4	38.1	4.0	1.36	0.11	1.15	2.0	22.2	178
9	LEH415	16.0	6.4	38.1	4.0	1.36	0.22	1.15	2.0	22.2	285
10	LEH430	16.0	6.4	38.1	4.0	1.36	0.45	1.15	2.0	22.2	476
11	LEH815	16.0	6.4	38.1	8.0	1.36	0.22	1.15	2.0	22.2	151
12	CAL328	19.0	6.4	32.1	3.0	1.36	0.35	1.33	1.3	28.6	556
13	CAL828	19.0	6.4	32.1	8.0	1.36	0.35	1.33	1.3	28.6	204
14	CAL1028	19.0	6.4	32.1	10.0	1.36	0.35	1.33	1.3	28.6	190
15	KUN97A2	9.5	4.0	32.1	4.5	1.54	0.32	1.18	2.0	14.5	74
16	VU98NH4	19.0	12.7	24.1	2.0	NR	0.70	2.79	2.4	26.4	986
17	VU98NH3	16.0	9.5	28.6	2.0	NR	0.26	1.03	3.8	24.8	551
18	CHAI-3	19.0	6.4	32.1	6.0	1.58	0.25	0.16	6.7	20.0	239
19	WONG90U1	16.0	10.0	25.0	2.0	1.36	0.36	0.93	3.8	20.0	495
20	VU98NH1	15.9	9.5	28.7	2.0	NR	0.27	0.99	3.8	24.8	585
21	VU98NH6	19.0	12.7	24.1	2.0	NR	0.72	2.71	2.1	24.8	1100
22	WONG90U3	16.0	10.0	25.0	2.0	1.32	0.41	0.72	3.8	20.0	626
Mean				33	4.3	—	0.33	1.20	2.8	—	—
Maximum				57	10.0	—	0.72	2.79	6.7	—	—
Minimum				24	2.0	—	0.11	0.16	1.3	—	—

$$L_{cr} = \frac{3}{2}\frac{M_{cr}}{M_{max}}L \tag{4}$$

where M_{max} is the maximum moment resisted at the column base.

The lateral displacement at the column top Δ_1, contributed to by flexure and shear in Region 1 is

$$\Delta_1 = \frac{2}{3}\left(f_r + \frac{P}{A_t}\right)\frac{\chi_1 L_{cr}^2}{hE_c} \tag{5}$$

where $\chi_1 > 1$ is given by Eq. (A.11) of Appendix A when making $L = L_{cr}$, which leads to

$$\chi_1 = 1 + 0.51\left(\frac{h}{L_{cr}}\right)^2 \tag{6}$$

Region 4 is the portion of a column where the curvature is assumed constant; the length of this Region is L_{sv}, which is defined as

$$L_{sv} = \min(\xi x_c, L - L_{cr}) \geq 0 \tag{7}$$

where coefficient ξ is obtained from an optimization procedure described later. Parameter x_c is the distance between the compressive force resultant C and the extreme compressed fiber; refer to Fig. 5. The column section is assumed to satisfy Bernoulli's hypothesis of plane sections. Because L_{sv}/L is small, the curvature along the length L_{sv}, denoted as ϕ_M, is assumed to be constant. Additionally, because cracking occurs predominantly perpendicular to the axis of the element, the flexure-shear interaction can be ignored.

The free-body diagram of Region 4 depicted in Fig. 5 shows the strain profile within this region and the compressive and tensile force resultants C and T_e, respectively. These forces result from the bending moment $2/3M_{max}$ and the axial force P. As depicted in Fig. 5(b), the longitudinal strain ε_s is associated with the tensile force T_e in the equivalent longitudinal bar, the neutral axis depth c_o, and the curvature ϕ_M.

The forces C and T_e act with a lever arm jd. The distance $jd(1 - \alpha)$ represents the lever arm between the centroidal axis, where axial load P acts, and the compressive force C. Similarly, αjd is the lever arm between the axial load P and the tensile force T_e.

The curvature ϕ_M can be expressed in dimensionless form as

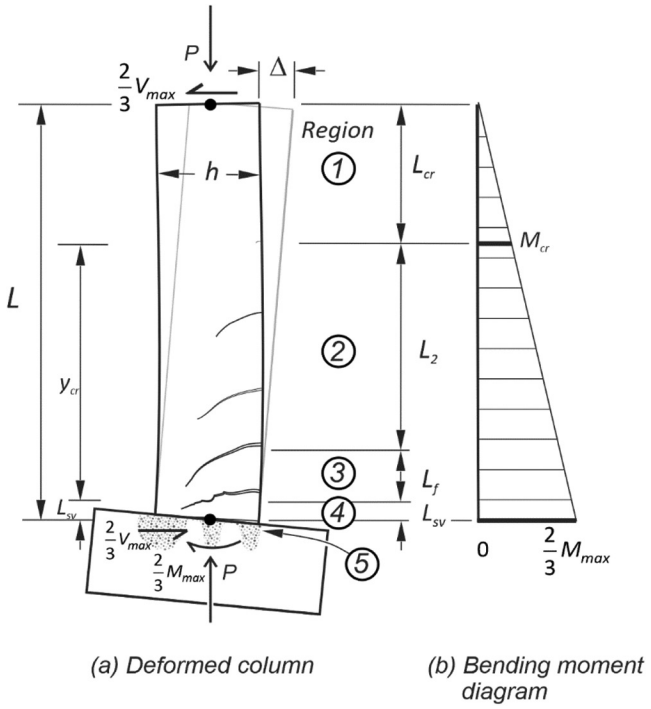


Fig. 4—Lateral displacement contribution regions in reinforced concrete column subjected to reversed cyclic lateral loading.

$$\phi_M h = \frac{\varepsilon_s}{\frac{jd}{h} + \frac{x_c}{h} - \frac{c_o}{h}} \tag{8}$$

To solve Eq. (8), a parametric analysis was conducted on circular columns to obtain empirical equations for $\phi_M h$, jd/h, x_c/h, c_o/h, $jd(1-\alpha)/h$, and $[T_e/(A_{st}f_y)](jd/h)$ for a bending moment of resistance at the column base equal to $2/3M_{max}$.

The contribution of Region 4 to the lateral displacement of the column at its top, Δ_4, is given by

$$\Delta_4 = \left(L - \frac{L_{sv}}{2}\right)\phi_M L_{sv} \tag{9}$$

Region 5 represents the column portion where the fixed-end rotation, θ_5, develops. This rotation arises from strain penetration or bar bond slip of the tensile and compressive longitudinal reinforcement extending beyond the column end. Restrepo and Rodriguez (2021) determined that for rectangular columns, θ_5 can be estimated using the following empirical equation

$$\theta_5 = \frac{1}{B_1\left(1 + B_2\frac{P}{A_g f_c'}\right)}\frac{d_b}{h}\frac{\rho_l f_y}{\sqrt{1\ \text{MPa}\cdot f_c'}} \tag{10}$$

The constants B_1 and B_2 in Eq. (10) were determined-through optimization using a database of columns, as described in the following sections.

The lateral displacement Δ_5 resulting from the fixed-end rotation θ_5 is given by

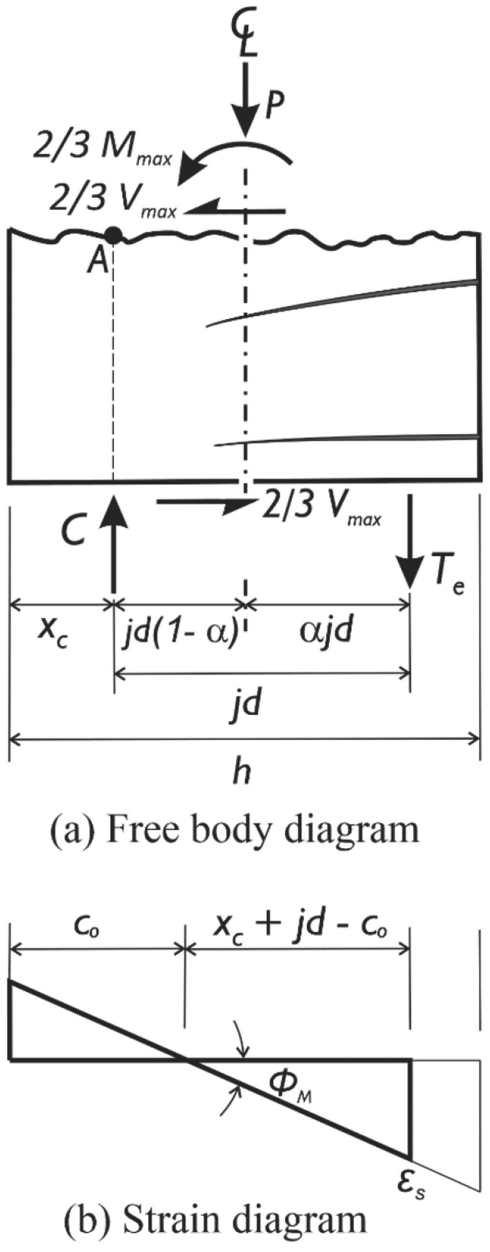


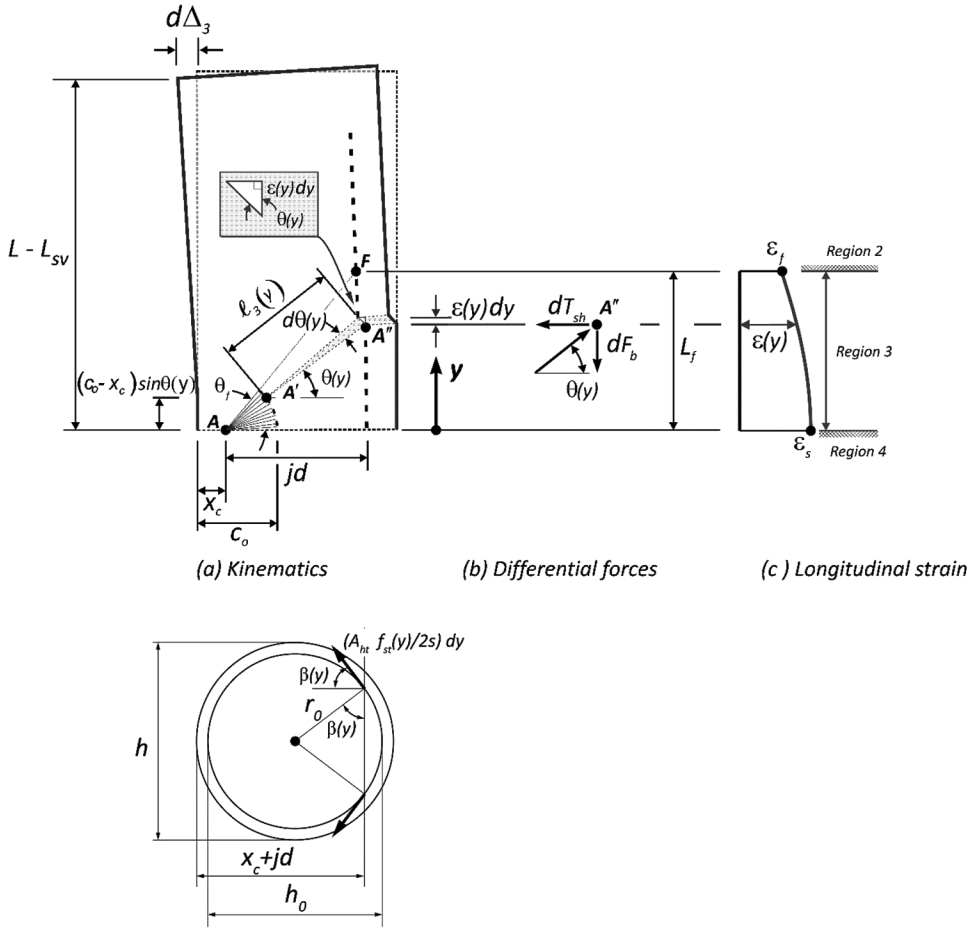
Fig. 5—Forces and longitudinal strain profile in Region 4 in differential column's length.

$$\Delta_5 = L\theta_5 \tag{11}$$

Region 3

Region 3, located between Regions 2 and 4, has a length $L_f = jd \tan\theta_f$ (refer to Fig. 6). A variable-angle compression stress field characterizes this Region, as shown in Fig. 4. At the boundary of Regions 3 and 4, cracks tend to form nearly perpendicular to the column's longitudinal axis. In contrast, at the boundary of Regions 2 and 3, cracks are inclined at an angle θ_f with the horizontal (refer to Fig. 6).

The procedure to calculate angle θ_f is described in Appendix B. The variable-angle stress field is assumed to radiate from point A, which coincides with the location of the compressive force resultant C in Region 4 (refer to Fig. 5(a) and 6). The point A' (refer to Fig. 6(a)) is defined as a point along an arc of a circle with a radius $c_o - x_c$ centered at point A with $0 \le \theta(y) \le \theta_f$.



d) Differential forces in transverse reinforcement at a column section at point A".

Fig. 6—Kinematics of Region 3 at differential of angle dθ(y)*, differential forces, and variation of equivalent longitudinal bar strain.*

In Region 3, the strain in the equivalent longitudinal bar, as previously defined in Region 4, varies from ε_s at the interface between Regions 3 and 4 to ε_f at the interface between Regions 3 and 2 (refer to Fig. 6(c)). This variation is due to the bond between the column longitudinal reinforcement and the concrete and the influence of the variable angle compressive stress field. Suppose the equivalent longitudinal bar is assumed to be located at $x_c + jd$ from the extreme compressed fiber (indicated by the dashed line in Fig. 6(a)). In that case, the change in the strain along the equivalent bar can be determined through equilibrium.

Differential tie force in Region 3

Figure 6(d) presents a cross section at point A'' of the equivalent longitudinal bar at ordinate y. The circular hoops or spirals, referred to as "hoops" hereafter in this paper, have a diameter h_o measured at the center of the hoop. The free-body diagram in Fig. 6(d) shows the force $[A_{ht}f_{st}(y)/2s]dy$ at each end of the hoop portion in this diagram, where A_{ht} denotes the cross-sectional area of the hoop; $f_{st}(y)$ is the tensile stress in the hoop at the ordinate y; and s is the spacing of this reinforcement.

At point A'' shown in Fig. 6(d), the effective transverse reinforcement area is $v_{e1}A_{sh}$, which resists a differential tie force dT_{sh} given by

$$dT_{sh} = \frac{v_{e1}A_{ht}f_{st}(y)}{s}dy \tag{12}$$

where v_{e1} is defined as $\cos\beta(y)$, as shown in Fig. 6(d). Additionally, from the geometry of the cross section in Fig. 6(d)

$$v_{e1} = \left[1 - \left(\frac{x_c + jd - 0.5h}{0.5\,h_o}\right)^2\right]^{1/2} \tag{13}$$

Contribution of Region 3 to column lateral displacement at top of column

The radial strut AA'' within the variable angle compression stress field inclines with the horizontal at an angle $\theta(y) = \arctan(y/jd)$. Equilibrium requires that the differential bond force dF_b acting on the equivalent longitudinal bar at point A'' (refer to Fig. 6(a), (b), and (d)) be equal to

$$dF_b = \frac{y}{jd}dT_{sh} = \frac{y}{jd}\frac{v_{e1}A_{ht}f_{st}(y)}{s}dy \tag{14}$$

At $2/3M_{max}$, the shear reinforcement in Region 3 is assumed to remain below its yield strength, for which stress $f_{st}(y)$ is unknown. The model assumes a linear variation of $f_{st}(y)$, where $f_{st}(y)$ is equal to 0 at $y = 0$, and equal to $f_{st}(L_f)$ at $y = L_f$, leading to

$$f_{st}(y) = \frac{y}{L_f} f_{st}(L_f) \tag{15}$$

Combining Eq. (14) and (15), the relationship for the differential bond force dF_b becomes

$$dF_b = \frac{y^2}{L_f jd} \frac{v_{e1} A_{ht} f_{st}(L_f)}{s} dy \tag{16}$$

The tensile force in the equivalent bar $T(y)$ at point A'' equals the difference between T_e, the force acting at the interface between Regions 3 and 4, and the integral of the bond force dF_b over the length y. This relationship is expressed as

$$T(y) = T_e - \int_0^y dF_b = T_e - \int_0^y \frac{y^2}{L_f jd} \frac{v_{e1} A_{ht} f_{st}(L_f)}{s} dy = T_e - \frac{v_{e1} A_{ht} f_{st}(L_f)}{s} \frac{1}{3 L_f jd} y^3 \tag{17}$$

for which the tensile strain $\varepsilon(y)$ in the equivalent bar at point A'' (refer to Fig. 6(a)) is

$$\varepsilon(y) = \varepsilon_s - \frac{v_{e1} A_{ht} f_{st}(L_f)}{s} \frac{\varepsilon_s}{T_e} \frac{1}{3 L_f jd} y^3 = \left[1 - \frac{v_{e1} A_{ht} f_{st}(L_f)}{s} \frac{1}{3 L_f jd} \frac{y^3}{T_e}\right] \varepsilon_s \tag{18}$$

The strain ε_f can be obtained by substituting $y = L_f$ into Eq. (18).

The strain ε_s at the bottom of Region 3 is associated with the tensile force in the equivalent longitudinal bar at that end, T_e. Similarly, strain ε_f at the upper end of Region 3 is associated with the tensile force in the equivalent longitudinal bar at that end, T_e'. In Eq. (17), making $T_e' = T(L_f)$ and $y = y_f$ results in

$$T_e - T_e' = \frac{v_{e1} A_{ht} f_{st}(L_f)}{3 jds} L_f^2 \tag{19}$$

Appendix B shows that Eq. (19) is used to derive the angle θ_f.

The axial deformation $\varepsilon(y)dy$ along the axis of the equivalent bar in the fan results in a differential angle $d\theta(y)$ (refer to Fig. 6(a)) given by

$$d\theta(y) = \frac{1}{l_3(y) \cos\theta(y)} \varepsilon(y) dy \tag{20}$$

where $l_3(y)$ is defined as (refer to Fig. 6(a))

$$l_3(y) = \sqrt{(jd)^2 + y^2} + x_c - c_o \tag{21}$$

The differential angle $d\theta(y)$ also results in a differential lateral displacement, $d\Delta_3$ (refer to Fig. 6), given by

$$d\Delta_3 = [L - L_{sv} - (c_o - x_c)\sin\theta(y)]\, d\theta(y) = \frac{L - L_{sv} - (c_o - x_c)\sin\theta(y)}{l_3(y)\cos\theta(y)} \varepsilon(y)\, dy \tag{22}$$

The differential displacement $d\Delta_3$ captures the flexure-shear interaction at a distance y in this column region. The lateral displacement, Δ_3 (refer to Fig. 6), is obtained by integrating Eq. (22) from $y = 0$ to $y = L_f$, resulting in

$$\Delta_3 = \int_0^{L_f} \frac{L - L_{sv} - (c_o - x_c)\sin\theta(y)}{l_3(y)\cos\theta(y)} \varepsilon(y)\, dy \tag{23}$$

Appendix C presents an approximate solution to Eq. (23) in closed form.

Region 2

Figure 4 shows that Region 2 is bounded between Region 1, which marks the onset of flexural cracking, and Region 3 at the end of the fan. Region 2 exists only when $y_{cr} > L_f$. Tension stiffening can significantly influence this Region, especially in lightly reinforced concrete columns. From Fig. 7

$$y_{cr} = L - (L_{cr} + L_{sv}) > L_f \tag{24}$$

In Region 2, a parallel-angle compressive stress field is inclined at an angle θ_f to the horizontal (refer to Fig. 7). This region is characterized by a variable neutral axis depth that transitions from c_{cr} at the interface between Regions 1 and 2 to c_f at the interface between Regions 2 and 3.

From linear theory, the neutral axis depth c_{cr} is given by

$$c_{cr} = h - \frac{f_r}{\phi_{cr} E_c} \tag{25}$$

The neutral axis depth c_f is assumed to be related to the neutral axis depth c at the base of Region 2 by the following geometrical relationship (refer to Fig. 7(a))

$$c_f = x_c + (c_o - x_c)\cos\theta_f \tag{26}$$

A function $c(z)$ must exist that relates the position of the neutral axis depth across the entire Region 2. The derivative $dc(z)/dy$ is assumed to be zero at Point B (refer to Fig. 7). Additionally, with z being a function of y, it can be shown (Restrepo and Rodriguez 2020) that at points C and B in Fig. 7

$$\left.\frac{dc(z)}{dy}\right|_{y=y_{cr}} = \tan\theta_c = \frac{P}{\frac{2}{3} V_{max}} \frac{I_t}{L_{cr}^2 A_t} \text{ and } \left.\frac{dc(z)}{dy}\right|_{y=L_f} = 0 \tag{27}$$

Equation (28) for the position of the neutral axis $c(z)$ is a continuous function used to interpolate the neutral axis depth between points B and C (refer to Fig. 7)

$$c(z) = c_f + (c_{cr} - c_f) \frac{z^2}{1 - \kappa_1 z (1 - z)} \tag{28}$$

where with known depths c_f and c_{cr} and known slopes at points B and C, it can be shown (Restrepo and Rodriguez 2020) that

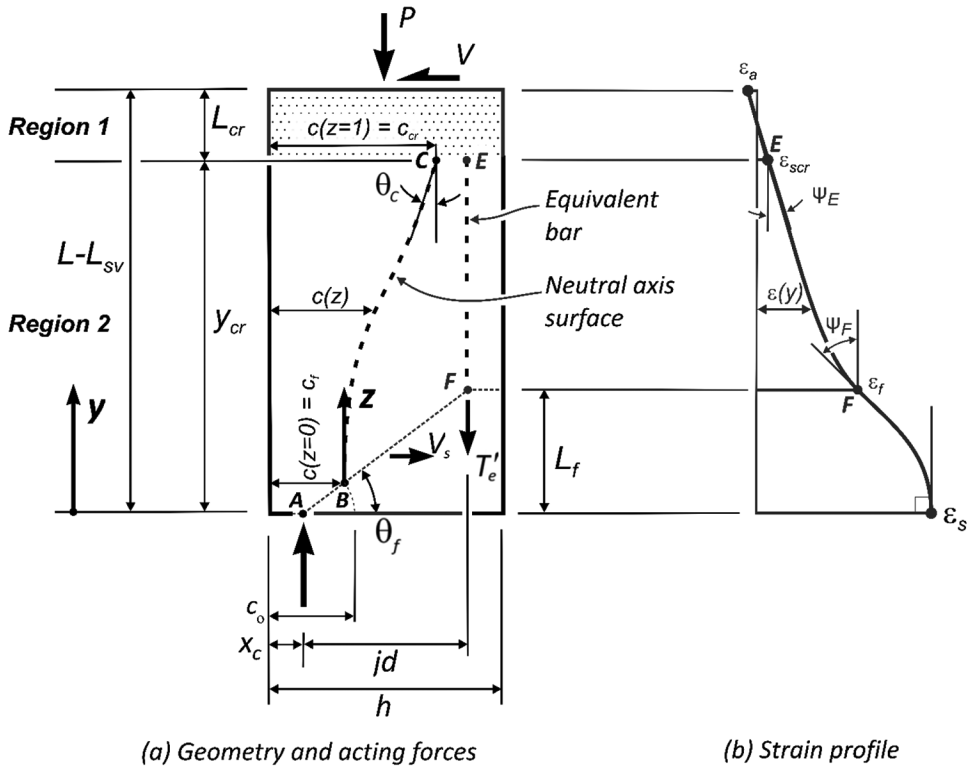


Fig. 7—(a) Region 2 geometry and acting forces; and (b) equivalent longitudinal bar strain profile.

$$z = \frac{y - L_f}{y_{cr} - L_f} \text{ and } \kappa_1 = 2 - \frac{y_{cr} - L_f}{c_{cr} - c_f}\tan\theta_c \tag{29}$$

In Region 2, the tensile strain in the equivalent bar varies from ε_f at point F to ε_{scr} at point E (refer to Fig. 7(b)) as a continuous function whose slopes at points F and E are given by $\tan\Psi_F$ and $\tan\Psi_E$, respectively.

$\tan\Psi_F$ is derived by differentiating Eq. (18) with respect to y and evaluating the derivative at $y = L_f$

$$\tan\Psi_F = \left|\frac{d\varepsilon(y)}{dy}\right|_{y=L_f} = -\frac{\varepsilon_s}{T_e}\frac{v_{e1}A_{ht}f_{st}(L_f)}{s}\frac{L_f}{jd} \tag{30}$$

From the linear strain variation in Region 1, refer to Fig. 8, $\tan\Psi_E$ is computed as

$$\tan\Psi_E = \frac{\varepsilon_{scr} - \varepsilon_a}{L_{cr}} = -\left(\frac{\varepsilon_{scr} + \dfrac{P}{A_t E_c}}{L_{cr}}\right) \tag{31}$$

where ε_{scr} is found from the strain profile shown in Fig. 8.

$$\varepsilon_{scr} = \left(\frac{jd + x_c - c_{cr}}{h - c_{cr}}\right)\varepsilon_{cr} \tag{32}$$

Similarly, the longitudinal strain, $\varepsilon(y)$ can be interpolated, forcing the following four boundary conditions: 1) $\varepsilon(L_f) = \varepsilon_f$; 2) $\varepsilon(y_{cr}) = \varepsilon_{scr}$; 3) $\left.\frac{d\varepsilon(y)}{dy}\right|_{y=y_{cr}} = \tan\Psi_E$; and 4) $\left.\frac{d\varepsilon(y)}{dy}\right|_{y=L_f} = \tan\Psi_F$ (Restrepo and Rodriguez 2020), as follows

$$\varepsilon(y) = \varepsilon_f - (\varepsilon_f - \varepsilon_{scr})\frac{\kappa_2 z + z^2}{1 + (\kappa_2 - \kappa_3)z + \kappa_3 z^2} \tag{33}$$

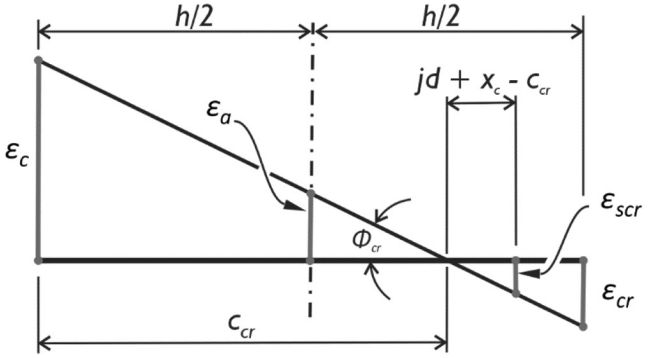


Fig. 8—Strain profile at lower end of Region 1.

where

$$\kappa_2 = \frac{y_{cr} - L_f}{\varepsilon_{scr} - \varepsilon_f}\tan\Psi_F$$

$$\kappa_3 = 2 - \frac{y_{cr} - L_f}{\varepsilon_{scr} - \varepsilon_f}(1 + \kappa_2)\tan\Psi_E \tag{34}$$

The differential lateral displacement $d\Delta_2$, in Region 2 (refer to Fig. 9), is given by

$$d\Delta_2 = L_3\, d\theta_f \tag{35}$$

where

$$L_3 = L - L_{sv} - y + (jd + x_c - c(z))\tan\theta_f \tag{36}$$

and where

$$d\theta_f = \frac{\varepsilon(y)dy}{\cos\theta_f}\frac{1}{\ell_2} = \frac{\varepsilon(y)dy}{jd + x_c - c(z)} \tag{37}$$

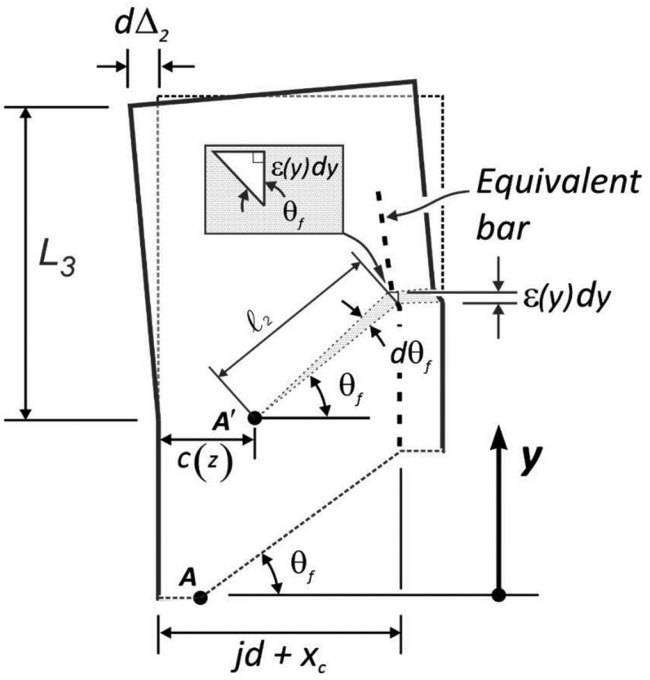


Fig. 9—Kinematics in Region 2 at differential angle $d\theta_f$.

Note that the term z is a function of the distance y and is given by Eq. (29).

The lateral displacement Δ_2 contributed by shear-flexure deformations in this region is computed by substituting Eq. (36) and (37) into Eq. (35) and integrating from $y = L_f$ to $y = y_{cr}$

$$\Delta_2 = \int_{L_f}^{y_{cr}} \left[L - L_{sv} - y + (jd + x_c - c(z))\tan\theta_f\right] \frac{\varepsilon(y)}{jd + x_c - c(z)}\, dy \tag{38}$$

Appendix C provides an approximate closed-form solution to Eq. (38).

CALIBRATION

The lateral displacement $\Delta_{2/3}$, at the top of the cantilever column caused by the lateral force $2/3V_{max}$ (refer to Fig. 4) is expressed as

$$\Delta_{2/3} = \sum_{i=1}^{5} \Delta_i \tag{39a}$$

Herein, Δ_1 through Δ_4 are determined using the equations described previously, while the empirical model for Δ_5 is derived from Eq. (10) and (11). In this model, $f_{st}(y)$, L_f, B_1 and B_2, and ξ (refer to Eq. (7)) are all unknown. These parameters are estimated by minimizing the following objective function

$$f = (\Delta_{2/3})_m - \sum_{i=1}^{5} \Delta_i \tag{39b}$$

where $(\Delta_{2/3})_m$ represents the measured lateral displacement at a given applied lateral force $2/3V_{max}$ in a test column.

The objective function f was subjected to the following two constraints, $f_{st}(y) \le f_{yt}$ and ξ ranging between 1.5 and 3.0. The first constraint recognizes that the longitudinal reinforcement must yield before the transverse reinforcement in columns designed to ensure the development of a flexural plastic hinge. Because in this study, the longitudinal column reinforcement was at or below yielding, the transverse reinforcement was also assumed to be at or below yielding. The second constraint was imposed based on the findings of Presland et al. (2001), who investigated this region. Minimization of the objective function f resulted in $B_1 = 18$, $B_2 = 0.9$, and $\xi = 2.0$ (Rodriguez and Restrepo 2024).

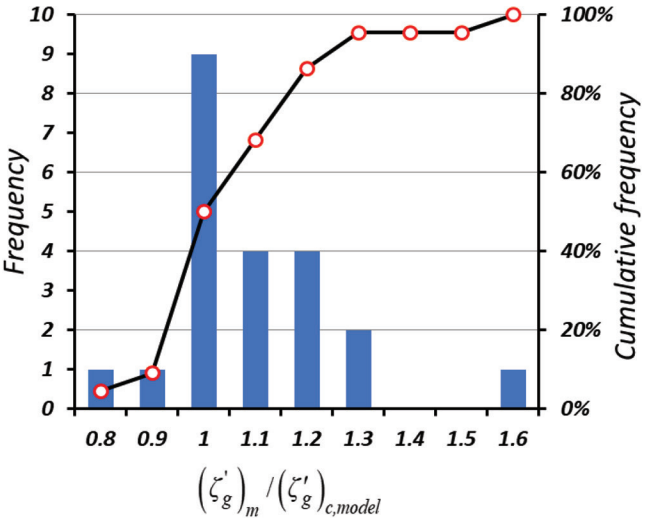


Fig. 10—Histogram and cumulative distribution of measured to calculated stiffness modifier ratio $(\zeta_g')_m/(\zeta_g')_{c,model}$.

The stiffness modifier ζ_t', defined at $2/3V_{max}$, is determined using the effective lateral stiffness, K_e', at this lateral force and is expressed as

$$\zeta_t' = \frac{K_e'}{K_o} \tag{40}$$

Table 2 presents the initial lateral stiffness K_o, the effective lateral stiffness $(K_e')_m$, and the stiffness modifiers $(\zeta_t')_m$ and $(\zeta_g')_m$ derived from the measured responses of the test columns. Table 3 provides the effective lateral stiffness $(K_e')_{c,model}$, the stiffness modifiers $(\zeta_t')_{c,model}$ and $(\zeta_g')_{c,model}$ computed from the model's output, and the ratio $(\zeta_g')_m/(\zeta_g')_{c,model}$. An analysis of residuals between the measured and model-predicted stiffness modifiers concerning the column axial load ratio, aspect ratio, reinforcement ratio, depth-to-bar diameter ratio, concrete compressive strength, and longitudinal reinforcement yield strength revealed no discernible trends (Rodriguez and Restrepo 2024).

Figure 10 plots the histogram of the ratio of measured-to-model stiffness modifiers $(\zeta_g')_m/(\zeta_g')_{c,model}$. The mean, median, and coefficient of variation are calculated for the $(\zeta_g')_m/(\zeta_g')_{c,model}$ ratios are 1.03, 1.00, and 16.6%, respectively.

DESIGN METHOD

The stiffness modifier ζ_t', derived in previous sections, involves several numerical integrations, making the model impractical for routine use in seismic design. Furthermore, the model requires detailed information about the reinforcement (number of bars and bar sizes), which is typically

Table 2—Measured lateral stiffness and stiffness modifiers

Number	Designation	K_o, kN/mm	$(K_e')_m$, kN/mm	$(\zeta_t')_m$	$(\zeta_g')_m$
1	2	3	4	5	6
1	VUNH2	248.92	28.94	0.116	0.138
2	VUNH5	240.94	29.12	0.121	0.145
3	KOWALSU1	13.28	3.97	0.299	0.351
4	RES-U1	156.44	50.31	0.322	0.373
5	NIST-F	31.64	11.63	0.368	0.428
6	NIST-S	239.76	66.03	0.275	0.322
7	LEH1015	2.57	0.94	0.366	0.414
8	LEH407	36.88	11.70	0.317	0.338
9	LEH415	39.15	13.51	0.345	0.390
10	LEH430	43.77	14.07	0.321	0.406
11	LEH815	5.01	1.79	0.358	0.405
12	CAL328	102.00	36.50	0.358	0.439
13	CAL828	5.64	2.32	0.411	0.504
14	CAL1028	2.90	1.47	0.508	0.624
15	KUN97A2	14.11	4.62	0.327	0.387
16	VU98NH4	287.10	61.95	0.216	0.309
17	VU98NH3	249.31	66.43	0.266	0.317
18	CHAI-3	12.90	8.89	0.689	0.839
19	WONG90U1	224.51	62.16	0.277	0.348
20	VU98NH1	247.16	78.11	0.316	0.377
21	VU98NH6	287.10	63.56	0.221	0.317
22	WONG90U3	222.82	83.29	0.374	0.471

unavailable during the initial analysis stage. Therefore, it is desirable to adopt a simplified equation for the gross-section-moment-of-inertia-based stiffness modifier ζ_g' defined as

$$\zeta_g' = \frac{I_t}{I_g}\zeta_t' \text{ where } \zeta_g' > \zeta_t' \tag{41}$$

This paper proposes an expression for the stiffness modifier ζ_g'. These stiffness modifiers were derived using a Monte Carlo simulation of the mechanics-based model. The range of values used in the simulation encompassed those commonly employed in practice. Results from these analyses indicate that the stiffness modifier ζ_g' can be expressed in terms of the three primary variables: the normalized axial load stress, the column aspect ratio, and the reinforcement yield strength, as follows

$$\zeta_g' = (\zeta_{AR}' + \zeta_P')\zeta_s' \tag{42a}$$

where

$$\zeta_{AR}' = \frac{a_v/h}{a_v/h + 8} \tag{42b}$$

$$\zeta_P' = 0.7\frac{P_u}{A_g f_c'}\frac{f_c'}{42\text{ MPa}} \tag{42c}$$

and

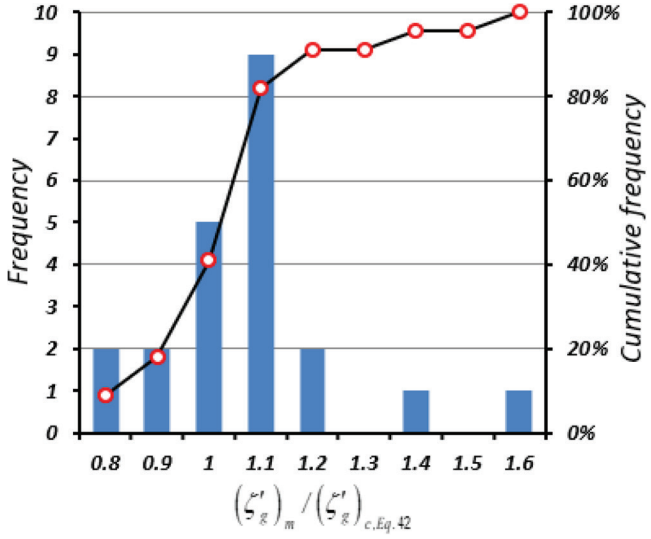


Fig. 11—Histogram of stiffness modifier ratio $(\zeta_g')_m/(\zeta_g')_{c,Eq.(42)}$.

$$\zeta_s' = 1.15 - \frac{f_y}{2760\text{ MPa}} \tag{42d}$$

Figure 11 shows the histogram of the ratio $(\zeta_g')_m/(\zeta_g')_{c,Eq.(42)}$, where $(\zeta_g')_{c,Eq.(42)}$ is the stiffness modifier calculated using Eq. (42). Table 3 summarizes the gross-section-based stiffness modifiers $(\zeta_g')_{c,Eq.(42)}$ and the ratio $(\zeta_g')_m/(\zeta_g')_{c,Eq.(42)}$. The mean, median, and coefficient of variation for this ratio are

Table 3—Measured and computed lateral stiffness and stiffness modifiers ratios

Number	Designation	$(K_e')_{c,model}$, kN/mm	$(\zeta_t')_{c,model}$	$(\zeta_g')_{c,model}$	$(\zeta_g')_m/(\zeta_g')_{c,model}$	$(\zeta_g')_{c,Eq.(42)}$	$(\zeta_g')_m/(\zeta_g')_{c,Eq.(42)}$
1	2	3	4	5	6	7	8
1	VUNH2	25.42	0.102	0.122	1.139	0.134	1.031
2	VUNH5	28.97	0.120	0.144	1.005	0.144	1.003
3	KOWALSU1	4.22	0.318	0.374	0.940	0.400	0.878
4	RES-U1	53.39	0.341	0.396	0.942	0.350	1.066
5	NIST-F	12.30	0.389	0.453	0.945	0.460	0.931
6	NIST-S	66.26	0.276	0.323	0.997	0.307	1.047
7	LEH1015	1.22	0.474	0.536	0.771	0.582	0.710
8	LEH407	10.40	0.282	0.300	1.125	0.364	0.928
9	LEH415	12.16	0.311	0.351	1.111	0.364	1.073
10	LEH430	14.58	0.333	0.421	0.965	0.364	1.117
11	LEH815	1.97	0.394	0.446	0.908	0.528	0.768
12	CAL328	29.66	0.291	0.357	1.231	0.322	1.366
13	CAL828	2.73	0.484	0.594	0.849	0.547	0.923
14	CAL1028	1.44	0.497	0.610	1.023	0.602	1.038
15	KUN97A2	5.02	0.356	0.421	0.920	0.401	0.967
16	VU98NH4	60.11	0.209	0.300	1.031	0.280	1.104
17	VU98NH3	62.68	0.251	0.299	1.060	0.296	1.070
18	CHAI-3	5.58	0.432	0.526	1.594	0.549	1.527
19	WONG90U1	55.16	0.246	0.309	1.127	0.319	1.090
20	VU98NH1	84.90	0.343	0.410	0.920	0.393	0.958
21	VU98NH6	70.27	0.245	0.351	0.905	0.383	0.827
22	WONG90U3	67.77	0.304	0.383	1.229	0.431	1.093
Mean					1.033	—	1.023
Stand. Dev.					0.172	—	0.177
Median					1.001	—	1.034
COV					0.166	—	0.173

1.02, 1.03, and 17.3%, respectively. These results suggest that the proposed stiffness modifier ζ_g' aligns well with the stiffness modifiers derived from the measured response of the test columns $(\zeta_g')_m$.

CONCLUSIONS

Stiffener modifiers are incorporated into linear structural models of reinforced concrete structures to account for the stiffness loss due to concrete cracking, bar bond slip, flexure-shear interaction, and other phenomena. This paper presented an analytical method that considers multiple sources of flexibility arising in circular columns subjected to lateral loads upon cracking of the concrete. The analytical model was calibrated against a database of large-size columns. However, the model's complexity makes it challenging for practicing engineers to use and implement in design codes. Consequently, this paper proposed a simplified method calibrated directly against the analytical model. The analytical and simplified models demonstrate acceptable predictive accuracy with minimal dispersion.

AUTHOR BIOS

Mario E. Rodriguez, *FACI, is a Professor of structural engineering at the Universidad Naciónal Autonoma de México (UNAM), Mexico City, Mexico. He received his BS in civil engineering from the Universidad Naciónal de Ingenieria, Lima, Peru, and his PhD from UNAM. He is a member of ACI Committees 369, Seismic Repair and Rehabilitation, and 374, Performance-Based Seismic Design of Concrete Buildings. His research interests include seismic design and evaluation of reinforced concrete structures.*

José I. Restrepo, *FACI, is a Professor of structural engineering at the University of California, San Diego, La Jolla, CA. He received his BS in civil engineering from the Universidad de Medellín, Medellín, Colombia, and his PhD from the University of Canterbury, Christchurch, New Zealand. He is a past recipient of the ACI Chester Paul Siess Award for Excellence in Structural Research. His research interests include reinforced and precast/prestressed concrete, particularly seismic design.*

NOTATION

A_g = gross area of concrete section
A_{ht} = spiral area
A_{st} = total area of longitudinal reinforcement
A_t = area of gross uncracked section transformed to concrete
A_v = shear area of concrete section
a_v = shear span
$B_1 \ldots B_4$ = constants
C = value of resultant compressive force in column section
c_c = clear cover of reinforcement

c_{cr} = neutral axis depth in column section at moment M_{cr}
c_f = smallest value of neutral axis depth in Region 2
$c(z)$ = neutral axis depth at distance z
c_o = neutral axis depth of Region 4 shown in Fig. 5 and 6
c_1 = parameter in Gauss-Lobatto numerical integration method
dF_b = differential of bond force shown in Fig. 6
dT_{sh} = differential tie force in Region 3 shown in Fig. 6
d_b = longitudinal bar diameter
d_{bt} = transverse reinforcement diameter
$d\theta(y)$ = differential of angle $\theta(y)$
E_c = concrete Young's Modulus
f = objective function
f_c' = specified compressive strength of concrete
$\hat{f}_c$ = measured compressive strength of concrete
f_r = modulus of rupture of concrete defined positive
$f_{st}(y)$ = tensile stress in transverse reinforcement at ordinate y
f_{yt} = yield strength of transverse reinforcement
f_y = specified yield strength of longitudinal reinforcement
$\hat{f}_y$ = measured yield strength of longitudinal reinforcement
G_c = shear modulus
h = overall thickness of column
h_0 = cross-sectional dimension of column core measured to center of transverse reinforcement
I_g = gross section moment of inertia
I_t = transformed section moment of inertia
jd = internal level arm between equivalent bar in tension T_e and resultant compression force in Region 4.
K_o = column lateral stiffness before cracking
K_e = column effective lateral stiffness at $V \in [V_{cr}, 2/3V_{max}]$
K_e' = column lateral stiffness at $V = 2/3V_{max}$
$(K_e')_m$ = effective lateral stiffness obtained from test columns' measured response
$(K_e')_{c,model}$ = effective lateral stiffness computed using model output
κ = shear coefficient
κ_1 = constant used in definition of $c(y)$
κ_2 = constant used in definition of $\varepsilon(y)$
κ_3 = constant used in definition of $\varepsilon(y)$
L = column shear span
L_{cr} = length of Region 1 representing extent of uncracked concrete in column
L_f = length of Region 3
L_{sv} = length of Region 4
L_2 = length of Region 2
L_3 = distance from crack at ordinate y in Region 2 to column upper end, as shown in Fig. 9
l_2 = length of diagonal compression field shown in Fig. 9
$l_3(y)$ = length of diagonal compressive field in Region 3 shown in Fig. 6(a)
M_{max} = maximum bending moment resisted at column end in reversed cyclic load test. M_{max} includes P-Delta moment whenever it is present
M_{cr} = bending moment at onset of flexural cracking
M_i = ideal moment strength
M_n = nominal moment as defined by ACI 318-19
M_{pr} = probable bending moment
m = parameter in Gauss-Lobatto numerical integration method
P = applied axial force in test column, defined as positive in compression and negative in tension
P_u = factored axial load for calculating effective stiffness, Eq. (42c), with load combination $0.9D$
r = radius defining rigid zone in Region 3
S_{et} = section modulus of gross uncracked section transformed to concrete
s = center-to-center spacing of transverse reinforcement
T_e = resultant of all forces in tension acting in column section
T_e' = tensile force in equivalent longitudinal bar at upper end of Region 3
$T(y)$ = tensile force in equivalent bar at ordinate y
V = shear force determined using first-order analysis
V_{cr} = shear force determined from first-order analysis at cracking moment
V_i = shear force at column base corresponding to ideal moment capacity M_i
V_{max} = M_{max}/L
V_{4R} = shear force resistance
x_c = distance from location of resultant compressive forces to extreme compressive fiber in column section within distance h_{sv} from column base
y = distance along longitudinal column axis
y_{cr} = length of cracked portion of column
z = parameter defining $c(y)$ and $\varepsilon(y)$
ajd = distance from T_e to column centerline
β = angle of force at end of hoop portion to horizontal
χ = shear deformation coefficient
χ_1 = ratio between sum of flexure and shear deformations to deformations due to flexure alone over length h_{cr}
Δ = column lateral displacement
$\Delta_{2/3}$ = displacement at top of cantilever column caused by lateral force $2/3V_{max}$
$(\Delta_{2/3})_m$ = measured lateral displacement at applied lateral force $2/3V_{max}$ in test column
Δ_1 = lateral displacement at column tip due to flexural moment and shear in Region 1
Δ_2 = lateral displacement at column tip due to flexural moment and shear in Region 2
Δ_3 = lateral displacement at column tip due to flexural moment and shear in Region 3
Δ_4 = lateral displacement at column tip due to flexural moment in Region 4
Δ_5 = lateral displacement at column tip due to tensile and compressive strain penetration of longitudinal column reinforcement in Region 5
ε_α = strain at upper end of Region 1
ε_{cr} = tensile strain at extreme concrete fiber at moment M_{cr}
ε_f = strain in equivalent bar in tension when it intersects first lower crack in Region 2
ε_{scr} = tensile strain in equivalent longitudinal bar at lower end of Region 1
ε_s = strain in equivalent bar in tension in Region 4
$\varepsilon(y)$ = strain in equivalent bar in tension at ordinate y shown in Fig. 6
ϕ_{cr} = curvature at cracking moment
ϕ_M = curvature in Region 4
γ = fraction of V_{max} in range V_{cr} to V_i
ν = Poissons' ratio
ν_{e1} = parameter defining effective spiral area when considering resultant of all forces in tension acting in circular column section
ν_{e2} = parameter defining the effective hoop area
θ_c = angle of slope of neutral axis profile to vertical at upper end of Region 2
θ_f = angle of stepper crack to horizontal axis in Region 3
$\theta(y)$ = angle of compressive field to horizontal axis in Region 3
θ_5 = rotation of Region 5 due to effect of fixed-end rotation that develops at column-to-elastic framing element
ρ_l = ratio of area of distributed longitudinal reinforcement to gross concrete area perpendicular to that reinforcement
ζ_{AR}' = variable used in calculation of stiffness modifier ζ_g' as function of a_v/h
ζ_P' = variable used in calculation of stiffness modifier ζ_g' as function of P/A_g
ζ_g = stiffness modifier when V ranges between V_{cr} and V_{max} and computed with I_g and effective lateral stiffness K_e
ζ_g' = stiffness modifier at $2/3V_{max}$ computed with I_g and effective lateral stiffness K_e'
$(\zeta_g')_{c,\text{Eq.(42)}}$ = calculated stiffness modifier using Eq. (42)
$(\zeta_g')_{c,model}$ = $I_t/I_g(\zeta_t')_{c,model}$
$(\zeta_g')_m$ = measured stiffness modifier obtained from column database
ζ_t' = stiffness modifier at $2/3V_{max}$ computed with I_t and effective lateral stiffness K_e'
$(\zeta_t')_{c,model}$ = calculated stiffness modifier using model computed with I_t and effective lateral stiffness K_e'
$(\zeta_t')_m$ = stiffness modifier obtained from test columns' measured response
ζ_s' = variable used in calculation of stiffness modifier ζ_g' as function of P/A_g and f_y
ξ = parameter for measuring extent of Region 4
Ψ_F = angle of slope of strain profile of equivalent bar at $y = y_f$
Ψ_E = angle of slope of strain profile of equivalent bar at $y = y_{cr}$

REFERENCES

AASHTO, 2011, "AASHTO Guide Specifications for LRFD Seismic Bridge Design," second edition, American Association of State Highway and Transportation Officials, Washington, DC, 23 pp.

ACI Committee 318, "Building Code Requirements for Structural Concrete (ACI 318-19) and Commentary (ACI 318R-19) (Reapproved 2022)," American Concrete Institute, Farmington Hills, MI, 2019, 624 pp.

ASCE/SEI 41-23, 2023, "Seismic Evaluation and Retrofit of Existing Buildings," American Society of Civil Engineers, Reston, VA.

Avsar, O.; Bayhan, B.; and Yakut, A., 2014, "Effective Flexural Rigidities for Ordinary Reinforced Concrete Columns and Beams," *Structural Design of Tall and Special Buildings*, V. 23, No. 6, pp. 463-482. doi: 10.1002/tal.1056

Calderone, A. J.; Lehman, D. E.; and Moehle, J. P., 2000, "Behavior of Reinforced Concrete Bridge Columns Having Varying Aspect Ratios and Varying Lengths of Confinement," PEER Report 2000-08, Pacific Earthquake Engineering Research Center, Berkeley, CA, 146 pp.

Chai, Y.; Priestley, N.; and Seible, F., 1991, "Seismic Retrofit of Circular Bridge Columns for Enhanced Flexural Performance," *ACI Structural Journal*, V. 88, No. 5, Sept.-Oct., pp. 572-584.

Cowper, G. R., 1966, "The Shear Coefficient in Timoshenko's Beam Theory," *Journal of Applied Mechanics*, V. 33, No. 2, pp. 335-340. doi: 10.1115/1.3625046

Elwood, K., and Eberhard, M., 2009, "Effective Stiffness of Reinforced Concrete Columns," *ACI Structural Journal*, V. 106, No. 4, July-Aug., pp. 476-484.

Khuntia, M., and Ghosh, S. K., 2004, "Flexural Stiffness of Reinforced Concrete Columns and Beams," *Experimental Verification*, V. 101, No. 3, pp. 364-374.

Kumar, R., and Singh, Y., 2010, "Stiffness of Reinforced Concrete Frame Members for Seismic Analysis," *ACI Structural Journal*, V. 107, No. 5, Sept.-Oct., pp. 607-615.

Kunnath, S.; El-Bahy, A.; Taylor, A.; and Stone, W., 1997, "Cumulative Seismic Damage of Reinforced Concrete Bridge Piers," Report NISTIR 6075, National Institute of Standards and Technology, Gaithersburg, MD, 136 pp.

Lehman, D., and Moehle, J., 2000, "Seismic Performance of Well-Confined Concrete Bridge Columns," PEER Report 1998/01, Pacific Earthquake Engineering Research Center, Berkeley, CA, 295 pp.

Moyer, M. J., and Kowalsky, M. J., 2003, "Influence of Tension Strain on Buckling of Reinforcement in Reinforced Concrete Bridge Columns," *ACI Structural Journal*, V. 100, No. 1, Jan.-Feb., pp. 75-85.

Paulay, T., and Priestley, M. J. N., 1992, *Seismic Design of Reinforced Concrete and Masonry Buildings*, John Wiley & Sons, Inc, New York.

Presland, R.; Restrepo, J.; and Park, R., 2001, "Seismic Performance of Retrofitted Reinforced Concrete Bridge Piers," Research Report 2001-3, Department of Civil Engineering, University of Canterbury, Christchurch, New Zealand, 513 pp.

Restrepo, J. I., and Rodriguez, M., 2013, "On the Probable Moment Strength of Reinforced Concrete Columns," *ACI Structural Journal,* V. 110, No. 4, July-Aug., pp. 681-690.

Restrepo, J. I., and Rodriguez, M., 2020, "Effective Lateral Stiffness in Reinforced Concrete Columns," Report SD60, Instituto de Ingenieria, Universidad Naciónal Autonoma de México, Mexico City, Mexico, 143 pp. (in Spanish)

Restrepo, J. I., and Rodriguez, M., 2021, "Stiffness Modifiers to Support the Seismic Design of Reinforced Concrete Rectangular Columns," *Journal of Structural Engineering*, ASCE, V. 147, No. 10. doi: 10.1061/(ASCE)ST.1943-541X.0003123

Rodriguez, M., and Restrepo, J. I., 2024, "Rigidez Lateral Effectiva de Columnas Circulares de Concreto Reforzado." doi: 10.31224/3704

Stephan, B.; Restrepo, J.; and Seible, F., 2003, "Seismic Behavior of Bridge Columns Built Incorporating MMFX Steel," Report No. SSRP-2003/09, Division of Structural Engineering, University of California, San Diego, La Jolla, CA, 31 pp.

Stone, W., and Cheok, G., 1989, "Inelastic Behavior of Full-Scale Bridge Columns Subjected to Cyclic Loading," *NIST Building Science Series*, National Institute of Standards and Technology, Gaithersburg, MD, 252 pp.

Vu, N.; Priestley, N.; Seible, F.; and Benzoni, G., 1999, "The Seismic Response of Well-Confined Circular Reinforced Concrete Columns with Low Aspect Ratios," Report No. SSRP-97/15, Division of Structural Engineering, University of California, San Diego, La Jolla, CA, 69 pp.

Wong, Y.; Paulay, T.; and Priestley, N., 1990, "Squat Circular Bridge Piers Under Multi-Directional Seismic Attack," Research Report 90-4, University of Canterbury, Christchurch, New Zealand, 264 pp.

ACI STRUCTURAL JOURNAL TECHNICAL PAPER

Title No. 122-S76

Behavior of Low-Carbon Fabric-Formed Reinforced Concrete Beams with Varying Shapes

by Jared Mason, Neil A. Hoult, Joshua E. Woods, Evan C. Bentz, Cody Somers, and John Orr

In this study, fabric formwork is used to cast I-shaped and non-prismatic tapered reinforced concrete (RC) beams that have up to a 40% reduction in concrete volume, resulting in lower embodied CO_2 than a rectangular prismatic beam. The primary aim of this research is to use distributed sensing to characterize the behavior of these shape-modified beams to an extent that was not previously possible and compare their behavior to that of a conventional rectilinear beam. Four RC beams (a rectangular control and three fabric-formed sections) were tested in three-point bending. Distributed fiber-optic strain sensors were used to measure strains along the full length of the longitudinal reinforcement, and digital image correlation (DIC) was used to acquire crack patterns and widths. The results indicate that fabric-formed RC beams can achieve the same load-carrying capacity as conventional rectilinear prismatic beams and meet serviceability requirements in terms of crack widths and deflections. The longitudinal reinforcement strains along the full length of the specimens were captured by Canadian concrete design equations, which account for the effects of both flexure and shear on reinforcement demand.

Keywords: digital image correlation (DIC); distributed fiber-optic sensing (DFOS); fabric formwork; low-carbon concrete; shape modification.

INTRODUCTION

An effective strategy for reducing embodied carbon in reinforced concrete (RC) beams is to minimize material use through shape modification. Prestressed I-girders are an example of RC members where the cross section has been modified to better match the structural demand, resulting in reduced concrete volumes, and they are common in practice for bridge construction. However, such modified sections are less widely used in the building sector due to the challenges associated with casting more complex sections and a lack of available data on their structural performance. Previous investigations have looked at non-prismatic beams (Hashemian 2012) and beams with variable depths (Orcutt et al. 2020), which can be used to reduce material volume. To form the complex geometry required to more efficiently meet structural demand, researchers have investigated the use of flexible fabric formwork, which can expand the possible form of RC members beyond what is possible using traditional formwork (Hawkins et al. 2016; Jayasinghe et al. 2021).

The challenge with modifying the shape to match the demand using fabric formwork is that, if the section has been modified efficiently, the critical section in terms of capacity can be anywhere along the beam. Thus, when testing beams with conventional instrumentation, such as strain gauges, the discrete nature of these sensors means that they may not be located at the critical section. The recent development of distributed sensing techniques, such as distributed fiber-optic sensing (DFOS) and digital image correlation (DIC), enables the behavior of these fabric-formed sections to be measured and analyzed in ways that were not possible even a decade ago.

This investigation involves testing a series of RC beams with both conventional prismatic rectilinear geometry and varying degrees of shape modification to reduce concrete demand. The novelty of the current study is that distributed sensing was used to capture crack patterns and longitudinal reinforcement strain/demand at all points in the section, enabling localized behavior and demand to be assessed. All beams were designed for the same loading conditions, instrumented with DFOS and DIC, and tested until failure. The objectives were to: 1) determine if the same capacity requirements can be met when the cross section is reduced; 2) investigate whether code equations can accurately predict the flexural and shear capacity of the beams; 3) evaluate the impact of shape modification on serviceability performance (that is, deflections, and crack widths and crack patterns from the DIC); and 4) compare measured distributed longitudinal strain behavior from the DFOS to that expected using theoretical models.

RESEARCH SIGNIFICANCE

Shape modification could lead to RC beams with lower embodied CO_2, but the structural performance of these members requires investigation because the critical cross section could occur at any point along the beam due to the combined effects of shear and moment. In this research, the shape-modified beams tested in three-point bending were found to have strength and serviceability performance comparable to that of a conventional rectilinear beam. Critically, the distributed strain measurements showed that both flexure and shear must be accounted for to provide accurate estimates of longitudinal reinforcement demand along the full length of shape-modified and rectilinear sections.

CARBON SAVINGS

Considering the potentially severe impacts of climate change, measures to reduce greenhouse gas (GHG) emissions

ACI Structural Journal, V. 122, No. 5, September 2025.
MS No. S-2024-223.R3, doi: 10.14359/51746818, received January 4, 2025, and reviewed under Institute publication policies. Copyright © 2025, American Concrete Institute. All rights reserved, including the making of copies unless permission is obtained from the copyright proprietors. Pertinent discussion including author's closure, if any, will be published ten months from this journal's date if the discussion is received within four months of the paper's print publication.

have become increasingly important. It is estimated that the concrete and steel industries contribute approximately 14% of total global anthropogenic CO_2 emissions, with approximately 7% for concrete (Van den Heede and De Belie 2012) and another 7% for steel (Chen et al. 2022). By comparison, the aviation industry accounts for only approximately 2% of anthropogenic CO_2 emissions (IEA 2024). As such, the carbon footprint of RC infrastructure needs to be reduced, but doing that will require various innovative methods for this multifaceted problem, depending on the structural system.

To achieve smart, sustainable structural design, one potential approach is the use of supplementary cementitious materials (SCMs), such as fly ash and slag, to partially replace the portland cement, the largest contributor to CO_2 emissions (Nie et al. 2022). Various commercially available lower-carbon concrete products are available, which provide CO_2 reductions of up to 90% for a given concrete volume (Amrize 2023). Another approach, as noted previously, is the use of shape modification (Hawkins et al. 2016; Jayasinghe et al. 2021). In the current work, low-carbon concrete was combined with shape modification to explore the impact of these approaches on beam performance.

DISTRIBUTED SENSING

DFOS provides thousands of strain readings along the length of the steel reinforcement within a beam or on the surface of a member (Barrias et al. 2018; Brault and Hoult 2019; Poldon et al. 2019). This allows for a more robust understanding of member behavior compared to traditional instrumentation techniques. DIC uses digital camera images taken before and after loading to facilitate the measurement of displacement and strain fields over the surface of a member. Using DFOS paired with DIC, a thorough analysis of the complex behavior of RC beams can be achieved. Poldon et al. (2019) demonstrated the combined use of DFOS bonded to the internal reinforcement and DIC surface measurements to create combined distributed measurement (CDM) plots, which provide a comprehensive picture of the beam behavior at a given load. Zhang et al. (2022) investigated beam-column connections using DFOS and DIC, and the measurements provided new insights regarding the connections' mechanical behavior. Thus, incorporating DFOS and DIC into the testing of fabric-formed beams can contribute to a more comprehensive understanding of the complex behavior that may occur.

EXPERIMENTAL PROGRAM

Four RC beam specimens with varying degrees of shape modification, from no reduction to 40% less concrete achieved using fabric formwork, were instrumented with DFOS on the longitudinal reinforcement. The specimens were then tested to failure in three-point bending.

Specimen geometry

Figure 1 shows a schematic of the fabricated beams, cross sections, and the configuration of the steel reinforcement in the more complex tapered beams. As noted previously, the four specimens were: 1) RC, the control specimen, where the "R" indicates that it is rectangular and the "C" indicates that it is the control; 2) IN, a prismatic I-beam; 3) TT, a non-prismatic tapered I-beam with a thin (75 mm [3 in.]) web; and 4) TW, a non-prismatic tapered I-beam with a wide (150 mm [6 in.]) web. Tapered beams with both a wide and narrow web were constructed to investigate the role of web width on shear capacity and cracking behavior. The width of the wide web was selected such that all three longitudinal reinforcing bars were within the web width (refer to Fig. 1(c)). The narrow web width was selected to provide 30 mm (1.2 in.) of concrete cover, the minimum allowed by CSA A23.3:19 (2019), on either side of the shear reinforcement in the web (refer to Fig. 1(b)).

All beams had an overall length of 3600 mm (141.7 in.), a midspan height of 500 mm (19.7 in.), a maximum width of 350 mm (13.8 in.), and a midspan effective depth of 450 mm (17.7 in.). The fabric-formed beams (IN, TT, and TW) had 200 mm (7.9 in.) long end blocks that were cast with traditional plywood formwork to create support blocks for the beams to rest on while testing and to represent other members that these beams might frame into (refer to Fig. 1). The fabric formwork technique uses a geotextile, which in this study was a polypropylene woven fabric, in place of traditional plywood formwork. Figure 2(a) shows a typical fabric formwork setup and a photo of the material used for the forms. The fabric formwork mold enables more complex geometries than traditional rigid formwork (Hawkins et al. 2016; Orr 2012; West 2016).

The web of the I-beam (IN) and the tapered beam (TT) at midspan had a nominal height of 200 mm (7.9 in.) and a width of 75 mm (3 in.), and the bottom flange height was 95 mm (3.75 in.). The tapered beam with a wide web (TW) had the same nominal web height of 200 mm (7.9 in.) at midspan but had a web thickness of 150 mm (6 in.) along the length of the beam. The tapered beams had a reduced overall depth of 300 mm (12 in.) at the interface with the support block, with an effective depth of 250 mm (9.8 in.). A fixed keel was used to control the member depth along the length, where the fabric freely rested on a support along the base of the beam. While this effectively controlled the depth of the member, it did allow for some ballooning of the fabric in the bottom flange of the member, resulting in some variability in the final dimensions of the fabric-formed beams, as shown in Fig. 2(b). As-built measurements taken using a cell-phone-based light detection and ranging (LiDAR) package verified against measurements taken using a measuring tape showed minor variations in other cross-section dimensions as a result of using the fabric formwork (shown in Fig. 2(b)), but these are within the tolerance of using traditional formwork on a construction site. These dimension changes did not affect the position of any reinforcing steel. Figure 2(c) shows beam TT after casting and demonstrates the complex geometries that can be created using the fabric formwork technique.

Flexure and shear design

The beams all had a flexural reinforcement ratio of 0.95% at midspan, which is a typical value for design, and this resulted in a nominal moment capacity for all members at

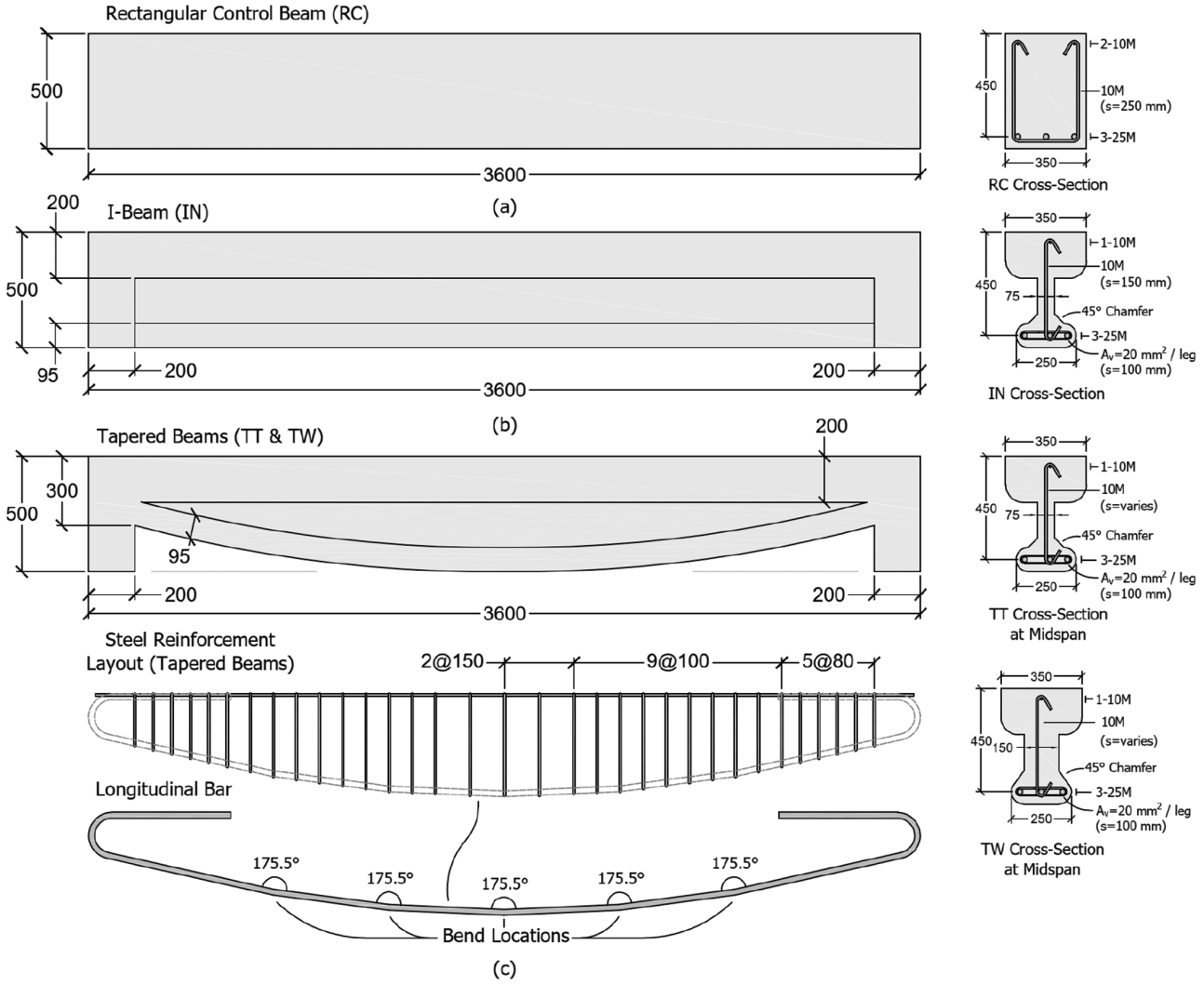


Fig. 1—Beam geometry: (a) RC; (b) IN; and (c) TT and TW. (Note: Dimensions in mm; 1 mm = 0.04 in.)

midspan of 314 kN·m (232 kip·ft) using the flexural design equations in CSA A23.3:19 and with material reduction factors set to unity. For the length between supports of the specimens (3.4 m [11.15 ft] on center), this moment capacity resulted in a point load of approximately 370 kN (83.2 kip) in three-point bending, corresponding to a required shear capacity of at least 185 kN (41.6 kip) to achieve flexural failure.

Each beam was designed such that the shear capacity calculated using the simplified shear design method in the Canadian code (CSA A23.3:19), with the material reduction factors set to unity, exceeded the expected shear at flexural failure (185 kN [41.6 kip]). The amount by which the required shear exceeded the shear at the expected moment capacity varied based on location and beam; this will be discussed in later sections. Beams with a narrower web would have a lower V_c and thus require a smaller stirrup spacing to compensate for a larger V_s. RC and IN had a constant stirrup spacing of 250 mm (9.8 in.) and 150 mm (6 in.), respectively, as shown in Fig. 1(a) and (b). The tapered beams (TT and TW) had varying stirrup spacing along their length to account for the reduction in effective shear depth (d_v) toward the supports. The spacing ranged from 150 mm (6 in.) at midspan to 80 mm (3.1 in.) at the supports, as per Fig. 1(c).

Reinforcement layout

All beams had three 25M longitudinal steel bottom bars (A_s = 1500 mm^2 [2.32 in.^{2}]), one 10M top bar (A_s' = 100 mm^2 [0.155 in.^{2}]), and a clear cover of 30 mm (1.2 in.) to the sides of the cross sections, with the exception of RC, which had two 10M top bars (A_s' = 200 mm^2 [0.31 in.^{2}]) to support the double-legged stirrups. The three 25M bars for the two tapered beams (TT and TW) had five 4.5-degree bends to create the desired tapered profile, as illustrated in Fig. 1(c).

All the stirrups were fabricated using 10M bars (A_v = 100 mm^2 [0.155 in.^{2}]). In addition to conventional shear reinforcement, all the fabric-formed beams had ties in the bottom flange that were made with 5 mm (0.2 in.) diameter bars (A_{bar} = 20 mm^2 [0.031 in.^{2}]). Figure 3 illustrates the design for shear for beam TT. The tie steel was provided to resist the shear stresses in the bottom flange caused by shear flow in an I-beam (Fig. 3(a)) and the vertical component of the flexural tension steel forces where the bars were bent (Fig. 3(b)). The shear was checked with a $V_c + V_s$ sectional approach, with the member width taken as the bottom flange thickness (refer to Fig. 3(a)), which enabled a first estimate of the amount of tie steel needed. The design for the vertical component of the flexural forces at the bar bend locations (Fig. 3(b)) was performed with the CSA-code strut-and-tie

model shown in Fig. 3(c). The fillet allowed a concrete strut (56.5 degrees) to transfer vertical forces from the outer tension bar to the web. The tie steel required for this strut-and-tie model (Fig. 3(c)) was added to that required to resist the shear flow (Fig. 3(a)). This combined tie steel was wrapped twice around the longitudinal reinforcement, resulting in four passes around the bottom flange tension bars as well as a 100 mm (4 in.) extension on either end for anchorage, resulting in a total effective tie area of A_{vtie} = 80 mm^2 (0.124 in.^{2}). The ties were spaced every 100 mm (4 in.) along the length of the fabric-formed beams.

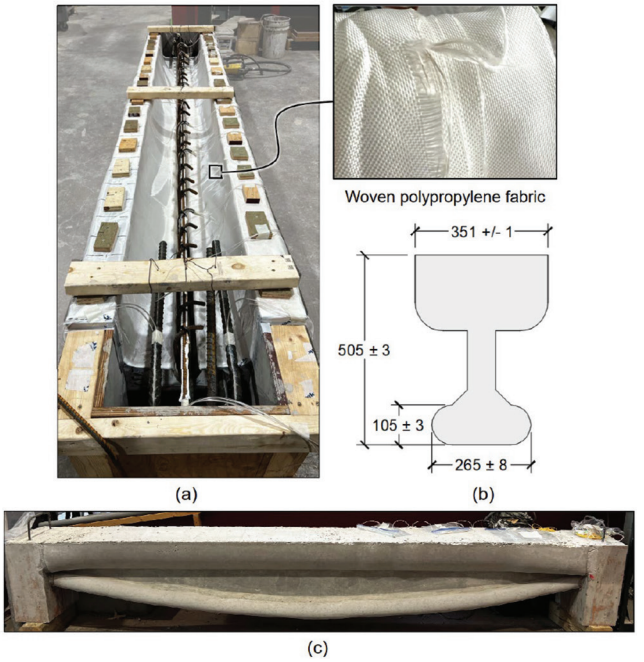


Fig. 2—Forming fabric-formed beams: (a) fabric formwork for specimen TT; (b) beam cross-section tolerances (all dimensions in mm; 1 mm = 0.04 in.); and (c) cast beam specimen TT.

Material properties

Three bar specimens were tested to get the average yield strength, which was 516 MPa (74.8 ksi) for the 25M bars, 492 MPa (71.4 ksi) for the 10M bars, and 550 MPa (79.8 ksi) for the 5 mm (0.2 in.) tie steel. The concrete for all beams was from a mixture of low-carbon concrete (Amrize 2023). This mixture had a slump of 100 mm (4 in.) and an air content of 6.5%, and the 28-day and 56-day strengths were 37.6 MPa (5450 psi) and 41.3 MPa (5990 psi), respectively. Though the beams were tested at various times after casting (43 days for RC, 51 days for IN, 56 days for TW, and 58 days for TT), the 56-day strength was used when evaluating the strength of each specimen using the code equations.

Test setup

Figure 4 shows the typical experimental setup for a beam tested in this study. A roller was used as the north support, and a captured roller was used as the south support to act as a pin. The beam had a span of 3.4 m (11.15 ft), measured from center-to-center of the support plates. The steel support plates were 100 mm (4 in.) long, 350 mm (13.8 in.) wide, and 25 mm (1 in.) thick.

Instrumentation

A single-mode nylon-coated fiber-optic cable was installed along the two outer bottom bars, as illustrated in Fig. 4(b). The instrumented bars had two passes of fiber-optic cable, one along each longitudinal rib of the reinforcing bar, so that the average strain could be calculated and the effects of local bending could be mitigated (Poldon et al. 2019).

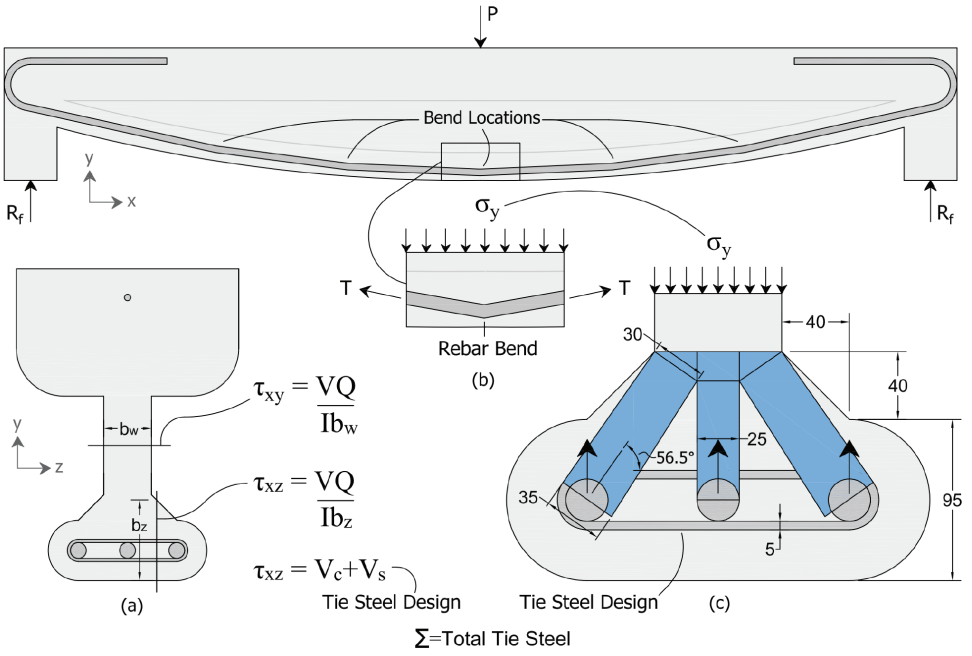


Fig. 3—Schematic illustration of shear design for bottom flange of specimen TT: (a) shear flow at bottom flange interface; (b) development of vertical force component in bent bars; and (c) fillet measurements and strut-and-tie dimensions in flange of fabric-formed beams. (Note: All measurements in mm; 1 mm = 0.04 in.)

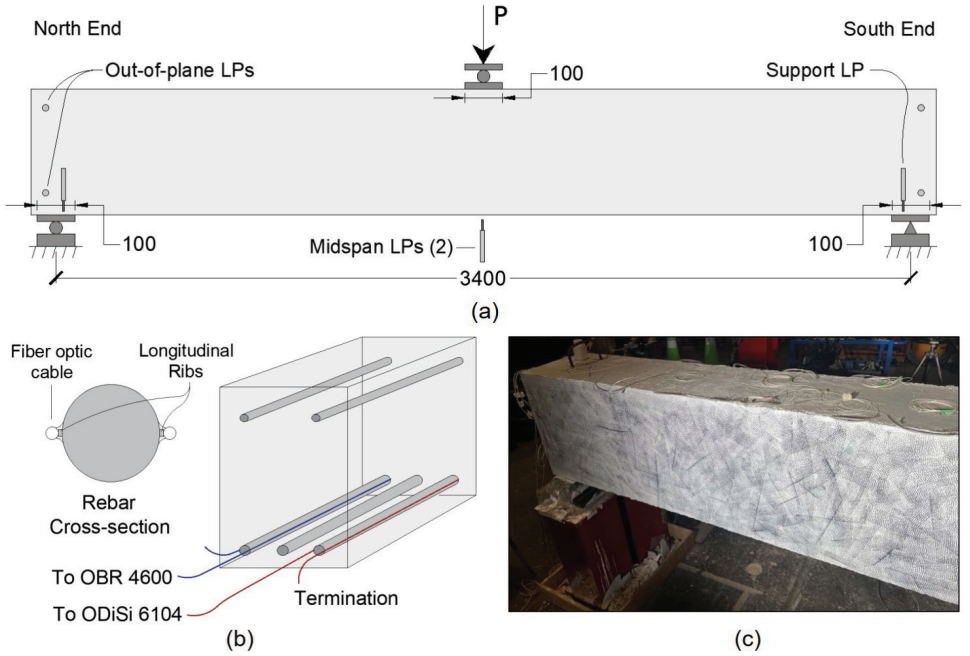


Fig. 4—Specimen test setup: (a) dimensions of test setup (beam RC shown); (b) location of fiber-optic cable on longitudinal reinforcement; and (c) speckle pattern for DIC (beam RC shown). (Note: Dimensions in mm; 1 mm = 0.04 in.)

Two DFOS analyzers were used to record strain data: 1) an optical backscatter reflectometer (OBR) recorded strain for one bottom bar at each load stage; and 2) an optical distributed sensor interrogator recorded strains for a second bottom bar continuously throughout the test. The process used to adhere the fiber-optic cables to the bars was the same as that used by Brault and Hoult (2019), where the longitudinal ribs along the length of the bar are ground smooth, sanded, and cleaned, and then the fiber is attached using a cyanoacrylate and protected with a layer of silicone that was approximately 5 mm (0.2 in.) thick. To prepare the beam for DIC, the west face of each beam was painted white, and then a dot-pattern roller was used to apply evenly spaced black dots on the face of the beam (Fig. 4(c)). The cameras used for DIC included a single digital camera at the south end of each beam, while the north end had a four-camera three-dimensional DIC system. A digital camera was used on the east face to record crack patterns. A load cell measured the applied load, and linear potentiometers (LPs) were used to record the beam displacement, as shown in Fig. 4(a). An LP was used at each support to measure support settlement. An additional two LPs were used at midspan to record displacement as well as rotations at the middle of the beam.

The beams were loaded at a displacement rate of 0.5 mm/min (0.02 in./min), and loading was paused every 20 kN (4.5 kip) to record DFOS data with the OBR system and measure crack widths on the east face of the beam. The east-face cracks were marked and measured at middepth of the beam and the depth of the bottom steel at select load stages throughout testing. The LPs, load cell, and optical distributed sensor interrogator analyzer recorded data at a rate of 1 Hz, while the DIC cameras recorded images at a rate of 0.2 Hz. The control beam was fully unloaded and reloaded at 160 kN (36 kip), and the two tapered beams were unloaded and reloaded at 60 kN (13.5 kip) to measure

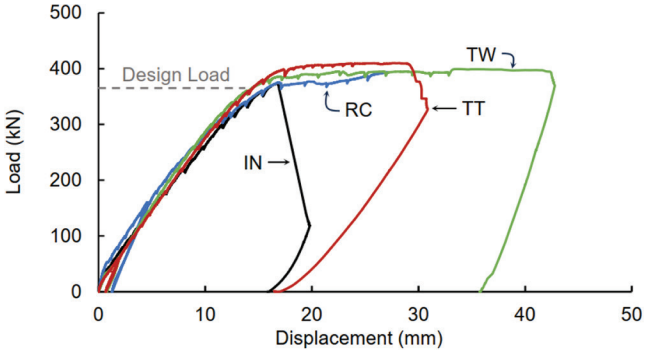


Fig. 5—Load-deflection behavior for all specimens. (Note: 1 mm = 0.04 in.; 1 kN = 0.22 kip.)

residual strains in the longitudinal reinforcement, although those results will not be discussed here. The I-beam was not unloaded during testing. Post-yielding, the displacement rate was increased to 1 mm/min (0.04 in./min), and the load stages were taken at every additional 2 mm (0.08 in.) of displacement. Cracks were not measured during the post-yield load stages, but OBR strain data were recorded.

RESULTS AND DISCUSSION

Load-deflection behavior

Figure 5 shows the load-deflection behavior for all beams compared to the predicted load with no safety factors, which was the capacity the beams were predicted to have using the Canadian code design equations (CSA A23.3:19), the material strengths obtained from testing, and with the material strength reduction factors set to unity. Table 1 summarizes the key response parameters for each beam, including the initial stiffness (K_i), cracking load (P_{cr}), cracked stiffness (K_{cr}), yield load (P_y), yield displacement (Δ_y), ultimate load (P_u), and the ultimate displacement (Δ_u). The control beam test (RC) was stopped due to the north support roller running

Table 1—Response parameters of each beam

Beam	K_i, kN/mm	P_{cr}, kN	K_{cr}, kN/mm	P_y, kN	Δ_y, mm	P_u, kN	Δ_u, mm	Failure mode
RC	89.8	46.8	27.5	375	17.1	393*	27.0*	—
IN	79.8	28.5	25.2	—	—	373	16.7	Shear
TT	50.1	33.6	28.5	397	17.2	399	33.8	Flexural crushing
TW	54.9	19.6	26.7	381	16.3	410	28.9	Flexural crushing

*Beam RC was not tested to failure, and P_u and Δ_u were recorded when test was stopped.

Note: 1 mm = 0.04 in.; 1 kN = 0.22 kip.

out of travel, and as such, an ultimate failure mechanism (for example, post-yield crushing of concrete) was not observed for this beam.

The maximum load-carrying capacity for each specimen ranged from 377 to 410 kN (84.8 to 92.2 kip). The results show that both tapered beams (TT and TW) had higher yield loads than the control beam (RC) and exhibited little to no strain hardening in the post-yield region. This is observed in Fig. 5 as TT and TW reach a relatively constant load after yield, while the control beam load plateaus initially, and then the load begins to increase after a displacement of approximately 21 mm (0.8 in.). One possible reason for this difference is the bend in the bars in the tapered beams (refer to Fig. 1), which required the steel to be plastically deformed at each bend location. This could have both increased the apparent yield strength at midspan and reduced the extent of the strain-hardening branch of the stress-strain curve, something that will be discussed in further detail later.

The cracking loads, shown in Table 1, ranged from 19.6 kN (4.4 kip) for TW to 46.8 kN (10.5 kip) for RC, with the higher cracking loads corresponding to the beams with a larger second moment of area, a result of increased concrete cross-sectional area. The expected cracking loads, based on the gross second moment of area (I_g) and distance to centroidal axis (y_t) calculated using the sectional analysis program Response-2000 (Bentz 2000, 2023), ranged from 54.2 kN (12.2 kip) for TW to 63.9 kN (14.4 kip) for RC. Although the theoretical cracking loads were higher than those observed in the laboratory (for example, RC had a cracking load that was 73% of the theoretical), the trend in the results matched the expected behavior in that the fabric-formed beams (with lower second moment of area) cracked at lower loads. The differences in cross sections also correlate with the precracked stiffness of the beams. The expected precracked stiffness (K_i) can be calculated as $48EI_t/L^3$, and because the transformed second moment of area (I_t) is lower in the beams with less concrete, so is the stiffness. In general, the results in Table 1 agreed with the theory, with RC being the specimen with the highest stiffness and TT, with the greatest concrete area reduction, having the lowest stiffness.

Post-cracking stiffness of the beams was measured as the average slope of the load displacement between the cracking load and the service load of 220 kN (49.5 kip) (taken as 60% of the lowest ultimate load of 373 kN [83.9 kip]). Beam IN had the lowest cracked stiffness of 25.2 kN/mm (144 kip/in.). RC and TW had stiffnesses of 27.5 kN/mm (157 kip/in.) and 26.7 kN/mm (152 kip/in.), respectively. TT had the highest cracked stiffness of 28.5 kN/mm (163 kip/in.), approximately 3.6% higher than the control (RC). This is unexpected as the control (RC) has a larger gross and cracked second moment of area, which should result in a higher stiffness. Overall, the maximum difference in stiffness was 3.3 kN/mm (18.8 kip/in.), and all beams were within 8.4% of the stiffness of the control beam up to the service load. All beams that yielded had similar deflections at first yield (Table 1) and were within 0.9 mm (0.035 in.) of each other. At the service load of 220 kN (49.5 kip), the displacements were 7.0 mm (0.28 in.) for RC, 7.4 mm (0.29 in.) for TT, 7.8 mm (0.3 in.) for TW, and 7.9 mm (0.31 in.) for IN. All beams satisfied a deflection limit of $L/300$ (11.3 mm [0.44 in.] for L = 3400 mm [134 in.]), although these deflections were based on the total load rather than the live load and do not include long-term creep.

The control beam (RC) was expected to begin yielding at a point load of 370 kN (83.2 kip) based on the material properties of the concrete and steel and the geometry of the cross section. During the experiment, the beam began yielding at 375 kN (84.3 kip), within 1% of the expected yield load. Beam IN was expected to have the same yield load of 370 kN (83.2 kip) but, although IN reached and surpassed the 370 kN (83.2 kip) load, it failed in shear at a load of 373 kN (83.9 kip), slightly before yielding based on the strain data and only 2 kN (0.5 kip) lower than the actual yield load of the control beam (RC). Based on the predicted shear capacity calculations excluding safety factors, IN was expected to have a shear capacity of 222 kN (49.9 kip) corresponding to a point load (P) of 444 kN (99.8 kip), so beam IN failed at 84% of the expected shear capacity. The 222 kN (49.9 kip) value was thought to be conservative because the Canadian code equations (CSA A23.3:19) for the concrete contribution to shear (V_c) use the minimum web width of 75 mm (3 in.). The material reduction factors were set to unity, and if they had instead been set to design values, the beam capacity and the predicted capacity would have been approximately the same (~185 kN [41.6 kip]). However, the partial factors on the load would still have ensured sufficient capacity.

Finally, the tapered beams had an average yield load of 398 kN (89.5 kip), which was approximately 7.6% higher than the expected value of 370 kN (83.2 kip) using the material strengths. As discussed previously, the capacity of these sections may have increased due to local strain hardening of the steel at midspan, resulting from bending of the longitudinal reinforcement, increasing the apparent yield strength of the steel. Because of the variable stirrup spacing, the end regions of TT, which had the same web width as IN of 75 mm (3 in.), had a nominal shear capacity of 216 kN (48.6 kip),

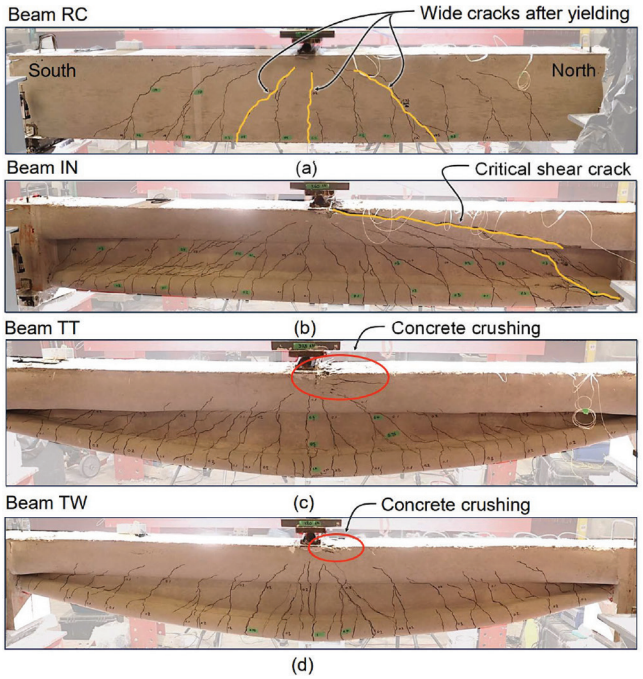


Fig. 6—Beams after testing: (a) RC with cracks that widened after yielding; (b) IN with critical shear crack; (c) TT with region of concrete crushing; and (d) TW with region of concrete crushing.

corresponding to a point load (P) of 432 kN (97.1 kip), and unlike IN, TT did not fail in shear.

Failure mechanisms

Figure 6 shows the failure mechanism for each beam. As noted earlier, RC was not tested to failure; however, the beam did reach the yield of the longitudinal reinforcement at midspan based on both the load-displacement response, where the load began to plateau (Fig. 5), and the measured strains, which exceeded the yield strain at midspan. Figure 6(a) shows the beam at the end of the test, where the three highlighted cracks had the largest visual width after the longitudinal reinforcement yielded. Beam IN failed in shear, as indicated by the rapid drop in load after reaching the peak load in Fig. 5, with the critical shear crack forming in the north span of the beam, extending from the loading plate to the support plate, as shown in Fig. 6(b). The inclination of the shear crack was steeper in the web and shallower in the top flange, where shear stress was lower. Similar changes in crack angle have been observed in previous tests on T-beams (Zararis et al. 2006). Beam TT failed due to concrete crushing on the north side of the loading plate, as shown circled in Fig. 6(c). Concrete crushing was deemed to be the cause of failure because of the sudden drop in load-carrying capacity that accompanied the development of localized crushing without any rapid increase in crack widths or rupture of the longitudinal reinforcement. Figure 6(d) shows that TW had a similar concrete crushing failure to TT at a higher load, which was to be expected because the web of this beam was wider.

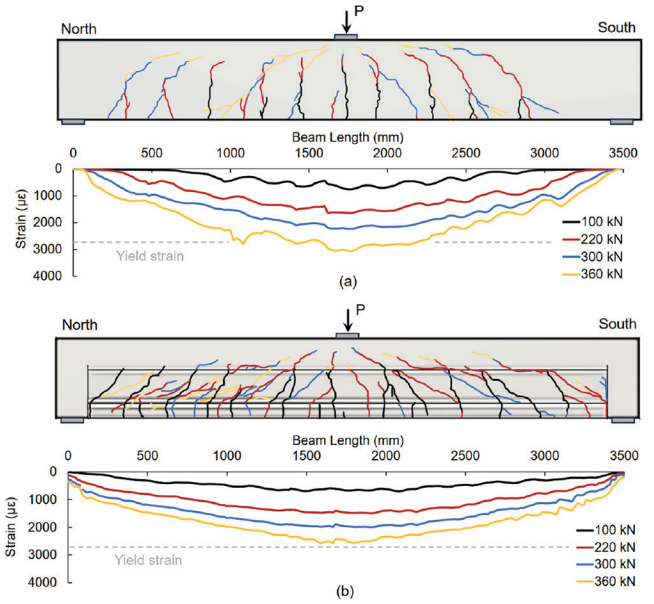


Fig. 7—Combined distributed measurement plots for beams: (a) RC; and (b) IN. (Note: 1 mm = 0.04 in.)

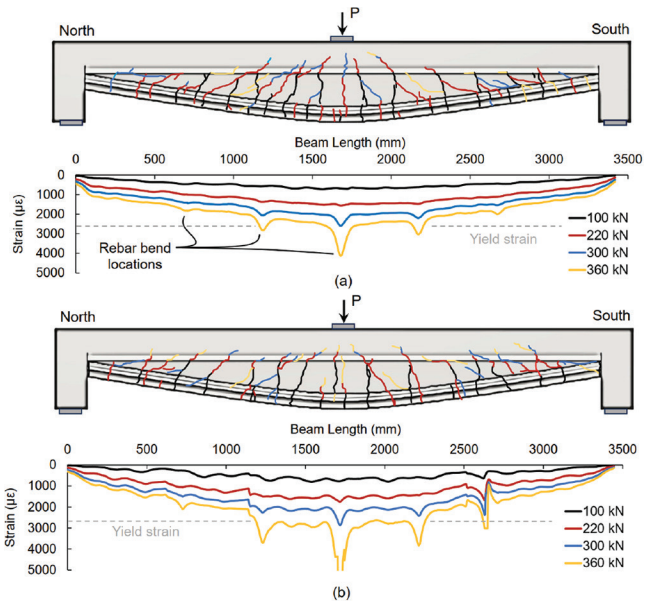


Fig. 8—Combined distributed measurement plots for beams: (a) TT; and (b) TW. (Note: 1 mm = 0.04 in.)

Longitudinal steel reinforcement strain distributions

Figures 7 and 8 show the CDM plots (as first introduced in Poldon et al. [2019]) for all four beams. These plots show the strains in the longitudinal steel reinforcement at select loads as well as the crack patterns for the corresponding loads. The RC beam strains (Fig. 7(a)) show localized peaks, most notably in the 100 kN (22.5 kip) strain profiles, which correspond with the location of cracks crossing the longitudinal reinforcement, as evident by the vertical alignment of the cracks with the peaks in the strain plot. The strains in the bottom bar reached above the yield strain (ε_y) of 2780 με, calculated as f_y/E, although the yield strain is affected by shrinkage, which can result in higher-than-expected yield strains. However, the strain offset method presented by

Poldon et al. (2022) was used on the midspan strain versus load data, and the beams were found to have no apparent restrained shrinkage strains. This is possible if the strain in the concrete due to shrinkage exceeded the cracking strain prior to testing, resulting in a release of shrinkage strain in the longitudinal bars. As such, in all the longitudinal strain figures presented, the strains are as measured, with compensation for shrinkage being zero. Because the control beam was prismatic, the strains were expected to be highest at midspan, then steadily decrease toward the supports following the moment demand, and the measured strains match this expectation.

Figure 7(b) shows the CDM for beam IN. The bottom bar strains show less localized peaks than RC, which could be a result of the increased amount of cracking. The IN crack diagram in Fig. 7(b) shows that the flexural cracks transitioned to shear cracks at a load of 220 kN (49.5 kip), a lower load than the control beam, which is likely a result of the reduced concrete contribution to shear strength (V_c). The tension strains for this beam peaked at approximately 2600 με, approximately 94% of the yield strain, indicating the beam was close to yielding when it failed in shear.

The tapered beam with the thin web (TT) showed different strain behavior than the previous two beams, as shown in Fig. 8(a). Five distinct peaks were present in the bottom steel reinforcement strain distribution, which became more pronounced as the load increased. These peaks aligned with the five bends in the tension bars. One possible explanation for this behavior is that the bend in the fiber-optic cable at these locations could cause a localized spike in the data as the cracks start to open and pull on the fiber. A second potential explanation is that the reinforcing bar began to straighten at these locations once cracks formed, resulting in localized yielding of the bar. In either case, the phenomenon appeared to be localized to the bend location and did not affect global behavior. Though the measured strains at midspan exceeded the yield strain (2780 με) at the 300 kN (67.4 kip) load stage, the beam load-deflection behavior (Fig. 5) was very similar to the two beams without bent longitudinal reinforcement (RC and IN), and in fact exceeded the load-carrying capacity of both beams.

Figure 8(b) shows the CDM plot for beam TW, which had identical geometry to TT but a larger web thickness (150 mm [6 in.] versus 75 mm [3 in.]). The same five peaks in the tension strain distributions are again observed, which correspond to the locations of the bends in the longitudinal reinforcement. Once again, the strain at midspan exceeded the yield strain prior to the beam yielding based on the load-deflection behavior, suggesting that the local strain peak is not indicative of overall beam behavior.

Calculated versus measured longitudinal strains

Figure 9 compares the measured strain distributions to the calculated strain distribution for RC at 220 kN (49.5 kip) (the serviceability load) and 360 kN (80.9 kip), which corresponds to a load near the ultimate load of all four beams. The calculated strains come from the method suggested by Poldon et al. (2022) and are composed of a flexural component and a shear component. The flexural component is

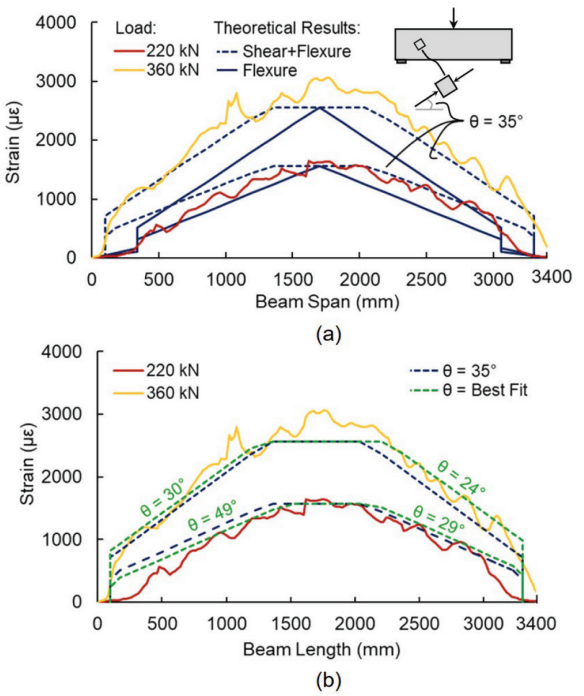


Fig. 9—Comparison between measured and calculated strain distribution for specimen RC at 220 kN (49.5 kip) (service load) and 360 kN (80.9 kip) (ultimate load): (a) measured versus theoretical strains for flexure and shear + flexure assuming compressive strut angle, θ, of 35 degrees; and (b) measured versus theoretical strains using concrete compressive strut angle, θ, of 35 degrees and based on best fit to strain data.

calculated using the moment in the beam at the location being evaluated; the transformed or cracked second moment of area, depending on whether cracking has occurred at that location along the beam; and the modulus of elasticity of the steel and the concrete. The shear and moment components are calculated based on Eq. (1), from the Canadian concrete code (CSA A23.3:19), and predict the strain in reinforcement at a crack due to moment and shear.

$$F_{lt} = \frac{M}{d_v} + (V - 0.5V_s)\cot\theta \quad (1)$$

where the longitudinal reinforcement must resist an axial force at a crack, F_{lt}, caused by the moment at the location being considered, M, divided by the effective depth in shear, d_v, and a portion of the total shear, V, modified by the stirrup component, V_s, which is determined by code equations at ultimate limit states, and the angle of the principal compressive stress, θ, also at ultimate limit state. The equation was then modified to calculate longitudinal reinforcement strain as per Eq. (2)

$$\varepsilon = \frac{My_{steel}}{E_s I} + \frac{(V - 0.5V_s)\cot\theta}{A_s E_s} \quad (2)$$

where y_{steel} is the distance from the neutral axis to the steel; E_s is the modulus of elasticity of the longitudinal steel; I is the transformed or cracked second moment of area, depending on the value of M relative to the cracking moment; and A_s is

the area of longitudinal steel. For lower loads, Poldon et al. (2022) proposed that the shear component at predicted shear failure $(V - 0.5V_s)\cot\theta$ be prorated by a factor, λ, equaling the ratio of the currently applied shear to the predicted shear capacity, to calculate the strain at lower loads. In the current work, the angle of principal compressive stress was evaluated in two ways. First, it was taken as 35 degrees, which is the recommended angle for design in the Canadian code (CSA A23.3:19). Second, the angle was iterated until the combined flexure and shear strain line was a best fit to the DFOS data, as seen in Fig. 9.

From Fig. 9(a), the results show that there is reasonable agreement between the measured strain distribution and the calculated strains using the method proposed by Poldon et al. (2022), and that including the shear component is required to capture the distributions of strain from the DFOS. The results in Fig. 9(b) show that assuming an angle of 35 degrees generally underestimates the strain in the bars, which indicates that the angle of principal compressive stress is lower in the actual specimen. The best-fit approach required a minimum angle of 24 degrees to match the measured strains, suggesting that the angle of principal compression may indeed be less than 35 degrees. It is difficult to confirm because the crack angles in the beam are generally steeper, although there are several cracks with shallower angles that formed at the level of the tension steel at higher loads (refer to Fig. 7(a)). Also, the principal compressive stress and crack angles are not necessarily the same.

Figure 10 provides the same comparison of measured to calculated longitudinal strains for IN, TT, and TW. In Fig. 10(a), the measured longitudinal strain distribution for IN was nonlinear and was not well estimated by the Poldon et al. method, which calculates strains based on the moment distribution, which is linear, and a constant shear force. The demand in the reinforcement does appear to be bounded by the best-fit approach at the supports, which uses an angle between 20 and 23 degrees at 360 kN (80.9 kip), and the approach using the code design angle of 35 degrees near the load point. This indicates that the angle of principal compression varies along the beam. There is evidence of that in the crack pattern, with some steeper cracks near the load point and shallower cracks near the supports, but the density and variability of the cracks (refer to Fig. 7(b)) make drawing definitive conclusions difficult.

The distributed longitudinal strain in the two tapered beams is captured by the Poldon et al. approach. There is little difference between using an assumed angle of 35 degrees and a best fit to the data. This suggests that the current Canadian code could be used to predict the behavior of the fabric-formed beams, including the reinforcement demand due to both shear and flexure.

Crack patterns and widths

Figure 11 shows the crack patterns at the service load of 220 kN (49.5 kip) for each beam, and Table 2 summarizes key crack parameters as measured by hand on the east face and with DIC on the west face of the beams. Although the hand and DIC measurements are similar, an exact comparison is difficult due to the crack data being recorded on

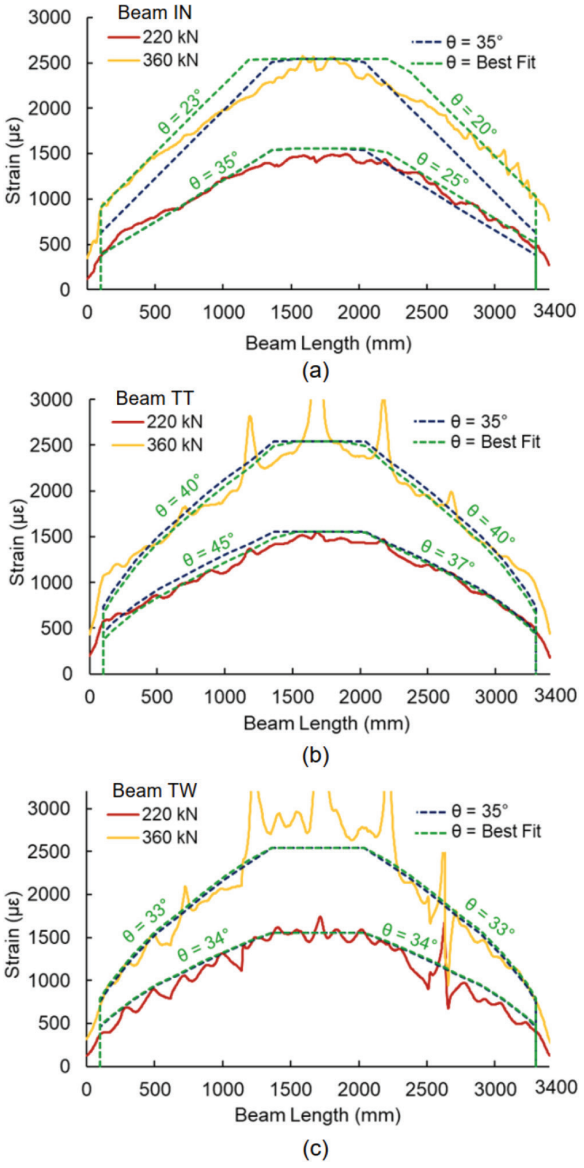


Fig. 10—Comparison between measured and calculated strains, using both 35 degrees and best fit to data angles, distribution for beams at applied loads of 220 kN (49.5 kip) (service load) and 360 kN (80.9 kip) (ultimate load): (a) IN; (b) TT; and (c) TW.

opposite faces of the beams. In general, the beams with reduced cross sections had more tightly spaced cracks with smaller widths than the control throughout testing. Although more cracks may be undesirable from an aesthetic point of view, the smaller average crack widths can be beneficial in terms of aggregate interlock, resulting in a larger concrete contribution to shear and better durability. The crack widths in the fabric-formed beams were smaller than those of the conventional rectilinear beam, suggesting that serviceability criteria can be met for these beams. Beams RC, TT, and TW had mostly flexural cracking at the service load, while IN had shear cracking, which was perhaps an early indication that it would fail in shear. Beams TT and TW both had three flexural cracks near midspan reaching into the top flange, while IN had approximately six shear cracks reaching up to halfway through the top flange.

Table 2—Key crack parameters for each beam as measured by hand and using DIC

Beam	Hand measurements			DIC measurements		Crack type at service
	w_{max} at service, mm ± 0.1	w_{max} at ultimate, mm ± 0.1	s at service, mm	w_{max} at service, mm ± 0.01	w_{max} at ultimate, mm ± 0.01	
RC	0.4	1.25	180 ± 40	0.21	1.55	Flexure
IN	0.3	0.75	105 ± 55	0.26	0.47	Shear
TT	0.3	1.0	95 ± 45	0.24	0.77	Flexure
TW	0.3	0.75	100 ± 50	0.13	0.49	Flexure

Note: w_{max} is the maximum crack width observed; s is the crack spacing; 1 mm = 0.04 in.

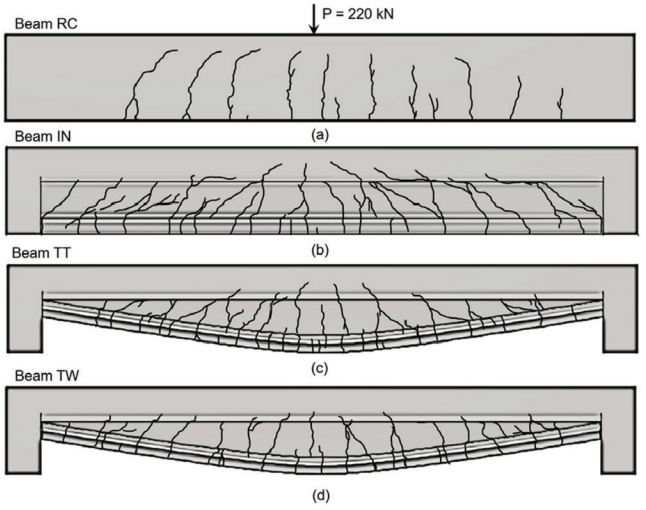


Fig. 11—Crack patterns at 220 kN (49.5 kip) service load for beam: (a) RC; (b) IN; (c) TT; and (d) TW.

For the beams that yielded (RC, TT, and TW), there were some differences in crack propagation near the ultimate load. RC had three dominant cracks near midspan (Fig. 6(a)) that widened during yielding. While TW had more cracks with smaller widths compared to RC, after yielding, again, three flexural cracks showed the most growth. On the other hand, TT had a single crack at midspan that increased in width during yielding. There is also a difference in tension strain peaks in Fig. 8(a) for TT versus Fig. 8(b) for TW at the 360 kN (80.9 kip) load. These results indicate that, for specimens where flexure governs, there does not appear to be a significant difference in the failure mechanism, with the caveat that RC was not taken to failure.

Carbon savings of current specimens

The reduction in the amount of concrete required for each beam when compared to the rectilinear control beam (RC), was 37% for the prismatic I-beam (IN), 41% for the non-prismatic tapered I-beam with a thin web (TT), and 35% for the non-prismatic tapered I-beam with a wide web (TW). In terms of CO_2e reductions from using low-carbon concrete (Amrize 2023), RC had a 55% reduction versus a similar beam using portland cement (415 kgCO_2 versus 187 kgCO_2), IN had a 72% reduction (415 kgCO_2 versus 116 kgCO_2), TT had a 73% reduction (415 kgCO_2 versus 111 kgCO_2), and TW had a 71% reduction (415 kgCO_2 versus 122 kgCO_2). It should be noted that the CO_2e reductions were for the concrete only and did not include the steel used, which was similar across the specimens.

CONCLUSIONS

This paper investigated the structural behavior of a series of beams designed using smart, sustainable structural design with varying degrees of shape modification, leading to concrete volume reduction using fabric formwork. The beams were instrumented with distributed fiber-optic sensing (DFOS) and digital image correlation (DIC) and tested in three-point bending. The conclusions from this work include:

1. Tapered sections were able to achieve higher capacities than the rectilinear prismatic control, likely due to strain hardening in the tension reinforcement due to the bends in the bars (although the control beam test was ended prematurely after yielding of the longitudinal bars).

2. Decreasing the beam cross-sectional area led to an increase in the number of cracks, although these cracks had lower widths on average. The lower cross-section area also corresponded to an increase in deflections at service loads, with up to 13% more deflection.

3. Current CSA A23.3:19 code calculations were able to predict flexural capacities of all beams to within 7%. The shear capacity of most sections was designed to be higher than the flexural capacity, and this proved to be true, except for the case of IN, where the tested capacity was 84% of the design capacity. It is worth noting that material reduction factors were not used, and if they had been, the predicted capacity and tested capacity would have been similar.

4. The strains in the longitudinal reinforcement were estimated using an approach that accounts for both flexural and shear demand. In general, lower principal compressive stress angles were required to estimate strains in prismatic beams, but the angle suggested by the Canadian code provided accurate estimates for tapered sections. This can be important for predicting anchorage forces.

5. Fabric-formed reinforced concrete (RC) beams with concrete volume reductions of up to approximately 40% and CO_2e reductions of approximately 70% compared to a rectilinear section using ordinary portland cement concrete can achieve the same load-carrying capacity as a rectilinear prismatic beam.

AUTHOR BIOS

Jared Mason *is a Project Associate at Sense Engineering, Toronto, ON, Canada. He received his BASc and MASc from Queen's University,*

Kingston, ON, Canada. His research interests include experimental testing and behavior of reinforced concrete beams.

ACI member **Neil A. Hoult** *is a Professor in the Department of Civil Engineering at Queen's University. He received his BASc and MASc from the University of Toronto, ON, Canada, and his PhD from the University of Cambridge, Cambridge, UK. His research interests include the behavior of reinforced concrete structures and the monitoring of infrastructure.*

Joshua E. Woods *is the Mitchell Professor in Intelligent Infrastructure Monitoring at Queen's University. He received his BEng, MASc, and PhD from Carleton University, Ottawa, ON, Canada. His research interests include the behavior of reinforced concrete structures, hybrid simulation, and advanced sensing technologies for condition assessment of structures.*

Evan C. Bentz, *FACI, is a Professor in the Department of Civil & Mineral Engineering at the University of Toronto. He received his BASc from the University of Waterloo, Waterloo, ON, Canada, and his PhD from the University of Toronto. His research interests include the shear and torsion design of reinforced concrete and the use of novel instrumentation.*

Cody Somers *is an MASc Candidate at Queen's University, where he received his BASc. His research interests include the use of fiber-optic sensors to assess the behavior of simply supported and continuous beams.*

John Orr *is Professor of structural engineering at the University of Cambridge. He received his MEng(hons) in civil engineering and his PhD from the University of Bath, Bath, UK, in 2009 and 2012, respectively. His research interests include sustainable design and reinforced concrete structures.*

ACKNOWLEDGMENTS

The authors thank the Natural Sciences and Engineering Research Council of Canada, Mitacs, Arup, KPMB Architects, and Lafarge [Lafarge Canada is now Amrize] for their financial support of this research, as well as the support of the City of Kingston, Aecon, and the Cement Association of Canada. The authors would also like to thank E. Batty, J. Bennett, J. Cherepacha, J. Goodwin, J. Matymish, H. Stephens, and J. Yager for their assistance with the fabrication and testing.

REFERENCES

Amrize, 2023, "Lafarge ECOPact Brochure," Amrize, Chicago, IL, https://www.lafarge.ca/en/ecopact. (last accessed July 3, 2025)

Barrias, A.; Casas, J. R.; and Villalba, S., 2018, "Embedded Distributed Optical Fiber Sensors in Reinforced Concrete Structures—A Case Study," *Sensors*, V. 18, No. 4, Apr., Article No. 980. doi: 10.3390/s18040980

Bentz, E. C., 2000, "Sectional Analysis of Reinforced Concrete Members," PhD thesis, University of Toronto, Toronto, ON, Canada, 316 pp.

Bentz, E. C., 2023, "Hadrian Software Works," Toronto, ON, Canada, https://www.hadrianworks.com/. (last accessed July 3, 2025)

Brault, A., and Hoult, N. A., 2019, "Distributed Reinforcement Strains: Measurement and Application," *ACI Structural Journal*, V. 116, No. 4, July, pp. 115-127. doi: 10.14359/51714483

Chen, W.; Zhang, Q.; Wang, C.; Li, Z.; Geng, Y.; Hong, J.; and Cheng, Y., 2022, "Environmental Sustainability Challenges of China's Steel Production: Impact-Oriented Water, Carbon and Fossil Energy Footprints Assessment," *Ecological Indicators*, V. 136, Mar., Article No. 108660. doi: 10.1016/j.ecolind.2022.108660

CSA A23.3:19, 2019, "Design of Concrete Structures," CSA Group, Toronto, ON, Canada, 301 pp.

Hashemian, F. K., 2012, "Structural Behaviour and Optimization of Moment-Shaped Reinforced Concrete Beams," PhD thesis, University of Manitoba, Winnipeg, MB, Canada, 391 pp.

Hawkins, W. J.; Herrmann, M.; Ibell, T. J.; Kromoser, B.; Michaelski, A.; Orr, J. J.; Pedreschi, R.; Pronk, A.; Schipper, H. R.; Shepherd, P.; Veenendaal, D.; Wansdronk, R.; and West, M., 2016, "Flexible Formwork Technologies – A State of the Art Review," *Structural Concrete*, V. 17, No. 6, Dec., pp. 911-935. doi: 10.1002/suco.201600117

IEA, 2024, "Aviation," International Energy Agency, Paris, France, https://www.iea.org/energy-system/transport/aviation. (last accessed July 3, 2025)

Jayasinghe, A.; Orr, J.; Ibell, T.; and Boshoff, W. P., 2021, "Minimising Embodied Carbon in Reinforced Concrete Beams," *Engineering Structures*, V. 242, Sept., Article No. 112590. doi: 10.1016/j.engstruct.2021.112590

Nie, S.; Zhou, J.; Yang, F.; Lan, M.; Li, J.; Zhang, Z.; Chen, Z.; Xu, M.; Li, H.; and Sanjayan, J. G., 2022, "Analysis of Theoretical Carbon Dioxide Emissions from Cement Production: Methodology and Application," *Journal of Cleaner Production*, V. 334, Feb., Article No. 130270. doi: 10.1016/j.jclepro.2021.130270

Orcutt, C.; Cook, W. D.; and Mitchell, D., 2020, "Response of Variable-Depth Reinforced Concrete Pier Cap Beams," *Journal of Bridge Engineering*, ASCE, V. 25, No. 6, June, p. 04020024. doi: 10.1061/(ASCE)BE.1943-5592.0001548

Orr, J. J., 2012, "Flexible Formwork for Concrete Structures," PhD thesis, University of Bath, Bath, UK, 544 pp.

Poldon, J. J.; Bentz, E. C.; and Hoult, N. A., 2022, "Assessing Beam Shear Behavior with Distributed Longitudinal Strains," *Structural Concrete*, V. 23, No. 3, June, pp. 1555-1571. doi: 10.1002/suco.202100730

Poldon, J. J.; Hoult, N. A.; and Bentz, E. C., 2019, "Distributed Sensing in Large Reinforced Concrete Shear Test," *ACI Structural Journal*, V. 116, No. 5, Sept., pp. 235-245. doi: 10.14359/51716765

Van den Heede, P., and De Belie, N., 2012, "Environmental Impact and Life Cycle Assessment (LCA) of Traditional and 'Green' Concretes: Literature Review and Theoretical Calculations," *Cement and Concrete Composites*, V. 34, No. 4, Apr., pp. 431-442. doi: 10.1016/j.cemconcomp.2012.01.004

West, M., 2016, *The Fabric Formwork Book: Methods for Building New Architectural and Structural Forms in Concrete*, Routledge, London, UK, 318 pp.

Zararis, I. P.; Karaveziroglou, M. K.; and Zararis, P. D., 2006, "Shear Strength of Reinforced Concrete T-Beams," *ACI Structural Journal*, V. 103, No. 5, Sept.-Oct., pp. 693-700.

Zhang, S.; Liu, H.; Darwish, E.; Mosalam, K. M.; and DeJong, M. J., 2022, "Distributed Fiber-Optic Strain Sensing of an Innovative Reinforced Concrete Beam–Column Connection," *Sensors*, V. 22, No. 10, May, Article No. 3957. doi: 10.3390/s22103957

ACI Faculty Network

Why Join the Faculty Network?

The Faculty Network is a support group for educators interested in ACI and the concrete industry. Members receive notifications about classroom resources, fellowships and scholarships, funding for research, online learning, and calls for papers and presenters.

Free 1-Year Educator Membership

ACI offers complimentary membership to teaching professionals who have not been an ACI member within the past 5 years.

Free Desk Copies

Faculty Network members can request a complimentary print or PDF copy of:

- ACI 318 PLUS (includes digital access to ACI CODE-318, ACI Reinforced Concrete Design Handbook, and ACI Detailing Manual)
- ACI CODE-318-25: Building Code for Structural Concrete—Code Requirements and Commentary (includes a free subscription to ACI 318 PLUS)
- ACI/PCI CODE-319-25: Structural Precast Concrete—Code Requirements and Commentary
- ACI/PTI CODE-320-25: Post-Tensioned Structural Concrete—Code Requirements and Commentary
- ACI CODE-323-24: Low-Carbon Concrete—Code Requirements and Commentary
- ACI CODE-562-25: Assessment, Repair, and Rehabilitation of Existing Concrete Structures—Code Requirements and Commentary
- ACI MNL-3(20): Guide to the Code for Assessment, Repair, and Rehabilitation of Existing Concrete Structures
- ACI MNL-5(19): Contractor's Guide to Quality Concrete Construction, 4th Edition
- ACI MNL-17(21): ACI Reinforced Concrete Design Handbook (available digitally with ACI 318 PLUS subscription)
- ACI SP-4: Formwork for Concrete

Networking

ACI hosts a Faculty Network Reception twice a year during the ACI Concrete Conventions, giving an opportunity to exchange ideas and network.

aci 318PLUS+ Faculty Network members receive a complimentary annual subscription that provides users with convenient digital interactive access to ACI CODE-318-25, ACI CODE-318-19, the ACI Detailing Manual, and the numerous design examples in the ACI Reinforced Concrete Design Handbook. The platform allows professors to create custom user notes that can be distributed to the students to view alongside the Code. Student members are provided 1-year access to ACI 318 PLUS when they purchase their printed copy of ACI 318-25 or ACI 318-19 at the student price of $105 (plus shipping).

aci Professors' Workshop
Materials | Pavements | Structures
Sponsor: aci Foundation

The Professors' Workshop is designed to provide instructors in civil engineering, architecture, architectural engineering, materials science, and construction management programs the tools to engage students in the latest developments in concrete design, construction, and materials.

aci Foundation
Building the Future

The Concrete Research Council (CRC) seeks concrete research projects that further the knowledge and sustainability of concrete materials, construction, and structures in coordination with ACI Committees. Annual Request for Proposals (RFP) are received annually between August 1 and December 1.

aci
American Concrete Institute
Always advancing

ADVANCE YOUR CLASSROOM WITH ACI

JOIN OR RENEW TODAY! concrete.org/educatorsandresearchers

ACI STRUCTURAL JOURNAL TECHNICAL PAPER

Title No. 122-S77

Geopolymer Composites: Potential as Repair and Strengthening Materials for Concrete Structures

by Giwan Noh, Uksun Kim, Myoungsu Shin, Woo-Young Lim, and Thomas H.-K. Kang

Geopolymer, an inorganic polymer material, has recently gained attention as an eco-friendly alternative to portland cement. Numerous studies have explored the potential of geopolymer as a primary structural material. This study aimed to examine the efficacy of geopolymer composites as repairing and strengthening materials rather than as structural materials. Data from 782 bond strength tests and 164 structural tests were collected and analyzed, including those on beams, beam-column connections, and walls. The analysis focused on critical factors affecting the bond strength of geopolymer composites with conventional cementitious concrete, and the structural behaviors of reinforced concrete members repaired or strengthened with these composites. The findings highlight the potential of geopolymer composites for enhancing the resilience and toughness of existing damaged or undamaged concrete structures. Additionally, they offer valuable insights into the key considerations for using geopolymer composites as repair or strengthening materials, providing a useful reference for future research in this field.

Keywords: bond strength; geopolymer; geopolymer concrete; rehabilitation; repair; strengthening.

INTRODUCTION

Geopolymer represents an emerging construction material attainable through the chemical interaction of inorganic constituents, obviating the necessity of portland cement.[1] The result of this chemical interaction yields an amorphous three-dimensional framework, where silicon and aluminum atoms form tetrahedral coordination linked by oxygen atoms, akin to the arrangement observed in zeolites.[2] While portland cement has had a significant impact on the construction industry, it is worth noting that, in light of environmental concerns—for example, approximately 1 ton of cement production results in the emission of 1 ton of carbon dioxide[3]—geopolymers have gained increasing prominence.

Concrete incorporating geopolymers, referred to as geopolymer concrete (GPC), is composed of water, aluminosilicate (that is, precursor), alkaline activators, and fine and coarse aggregates, as depicted in Fig. 1.[4] The primary distinction between GPC and ordinary portland cement concrete (OPC) lies in the composition of the cement paste. In the case of GPC, alkaline activators and aluminosilicates are used instead of conventional cement. Aluminosilicates, in this context, can comprise any substance containing amorphous Si and Al,[5] but, in consideration of environmental concerns, industrial waste materials such as fly ash (FA) and ground-granulated blast-furnace slag (GGBFS) are commonly used. Interestingly, the cement paste of GPC exhibits a rapid setting compared to that of OPC, which can either act as an advantage or a disadvantage depending on the construction site requirements.[6] Numerous studies have investigated the mechanical properties of geopolymer or GPC.[2,6-15] Hardjito and Rangan,[7] as well as Panias et al.,[8] analyzed the factors influencing the strength of geopolymer or GPC and confirmed that an increase in the content of sodium hydroxide (NaOH) and silicate (Na_2SiO_3) results in higher compressive strength. However, it was observed that there is a certain threshold beyond which further increments in these components lead to a reduction in f_c'.[8] Thomas and Peethamparan[11] and Noushini et al.[12] investigated the impact of curing temperature on f_c' and found that higher curing temperatures are associated with increased f_c'. Generally, the modulus of elasticity of GPC was lower than that of OPC,[2,6,7,9,12-15] while its tensile or flexural strengths were higher.[6,7,10,11,13,15] Additionally, GPC exhibited greater brittleness compared to OPC,[10-12] a characteristic attributed to a denser interfacial transition zone (ITZ).[10]

The mechanical properties of geopolymer are influenced by factors such as curing temperature and time, alkali dosage and modulus, and the type and properties of aluminosilicate[16]; therefore, specific determinations cannot be made. However, when comparing the overall mechanical properties of GPC and OPC, as mentioned earlier, GPC exhibits a lower modulus of elasticity, higher brittleness, and higher tensile and flexural strength. Additionally, from a sustainability and durability perspective, GPC excels in fire, chemical, and freeze and thaw cycling resistance compared to OPC.[17,18] It also makes use of industrial waste and does not require the use of cement, making it superior to OPC from an environmental standpoint. Owing to these advantages of GPC, to analyze whether GPC can replace OPC as a structural material, various structural tests[19-25] (for example, bond, flexural, and shear tests) have been conducted. These tests demonstrated that GPC has better bond strength than OPC,[19-21] and using design codes for OPC such as ACI 318[26] and EN 1992-1-1[27] on GPC posed no safety concerns.[22-25]

Concrete structures have endured extensive use over a prolonged period, withstanding both standard and harsh environmental conditions.[28] The deterioration of concrete over time arises from inherent material degradation, exposure to adverse external conditions, and significant mechanical

ACI Structural Journal, V. 122, No. 5, September 2025.
MS No. S-2024-325.R2, doi: 10.14359/51746719, received January 4, 2025, and reviewed under Institute publication policies. Copyright © 2025, American Concrete Institute. All rights reserved, including the making of copies unless permission is obtained from the copyright proprietors. Pertinent discussion including author's closure, if any, will be published ten months from this journal's date if the discussion is received within four months of the paper's print publication.

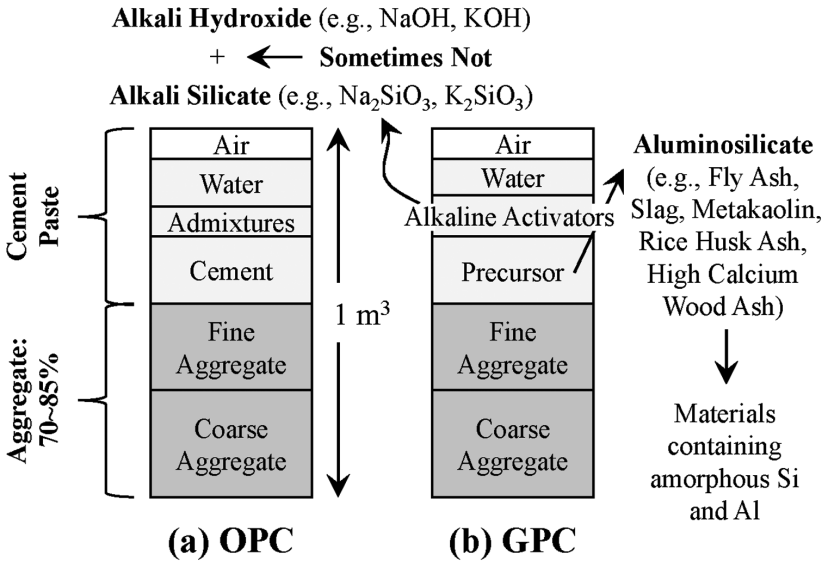


Fig. 1—Volumetric description (1 m³) for composition of OPC and GPC (redrawn from Li et al.[4]).

loads, resulting in issues such as concrete cracking, spalling, and steel corrosion.[29] Effective repair plays a pivotal role in the revitalization and restoration of reinforced concrete (RC) structures,[30] and the quest for cost-effective and efficient concrete repair materials highlights the promising potential of geopolymers.[31] Moreover, they will be effectively used for the strengthening of concrete members that require it due to reasons such as design errors or updates in codes. Although previous studies extensively reviewed and evaluated geopolymer as a fundamental structural material, there remains a lack of comprehensive research that systematically reviews and analyzes its potential as a repair and strengthening material. To address this gap, this study compiled all available test data related to bond strength tests of geopolymer composites, as well as large-scale experiments on structural members repaired or strengthened using these materials. A thorough analysis of their rehabilitation performance was then conducted to explore the potential of geopolymer in this context. The analysis focused on factors affecting the bond strength of geopolymer composites and the structural performance of large-scale members repaired or strengthened using these materials, providing a comprehensive assessment of geopolymer's potential as a repair and strengthening material across various scales.

RESEARCH SIGNIFICANCE

Geopolymers, a class of inorganic polymeric materials, represent a significant advancement in sustainable construction, especially as a potential substitute for portland cement, which is notorious for high carbon dioxide emissions. Previous research mainly examined the applicability of geopolymers as primary structural materials, along with their compatibility with existing design codes developed for OPC. In contrast, this study shifts the focus and evaluates the effectiveness of geopolymers specifically for the repair or strengthening of concrete structures. This comprehensive analysis synthesizes experimental data extensively gathered from the literature, offering new insights into the application of geopolymers. This paper will serve as a foundational reference for the novel use of geopolymers, highlighting their substantial potential as materials for enhancing structural resilience and toughness.

BOND PERFORMANCE AS REPAIR AND STRENGTHENING MATERIALS

Experimental data for bond strength

The methods for measuring the bond strength of repair and strengthening materials are diverse, as illustrated in Fig. 2.[32] This diversity enables the measurement of bond strength under various forms of loading conditions. To analyze the viability of geopolymers as repair and strengthening materials, the authors collected a total of 782 bond strength test data. Among these, there were 369 compressive shear tests,[28,29,33-52] 53 splitting tensile tests,[38,53,54] 110 pulloff tests,[29-31,35,46,51,55-59] 42 pure shear tests,[59-62] 193 bending tests,[29,36,38,43,51,63-69] and 15 direct tension tests.[70] Some of the specimens were made of portland cement composites or other commercially available repair materials for the purpose of comparison with geopolymer composites.

Evaluation of bond strength

Before assessing the bond strength of geopolymer composites as repair and strengthening materials, it is essential to understand the fundamentals of the underlying geopolymerization process, which is described in Appendix A.*

When geopolymer composites are applied to parts of a concrete structure requiring reinforcement, they integrate with OPC through the aforementioned geopolymerization process. The bond between OPC and geopolymer composites comes from a combination of chemical and mechanical interactions. These involve adhesion forces resulting from newly formed gels at the interface, Van der Waals forces, frictional forces associated with the surface condition,

*The Appendix is available at **www.concrete.org/publications** in PDF format, appended to the online version of the published paper. It is also available in hard copy from ACI headquarters for a fee equal to the cost of reproduction plus handling at the time of the request.

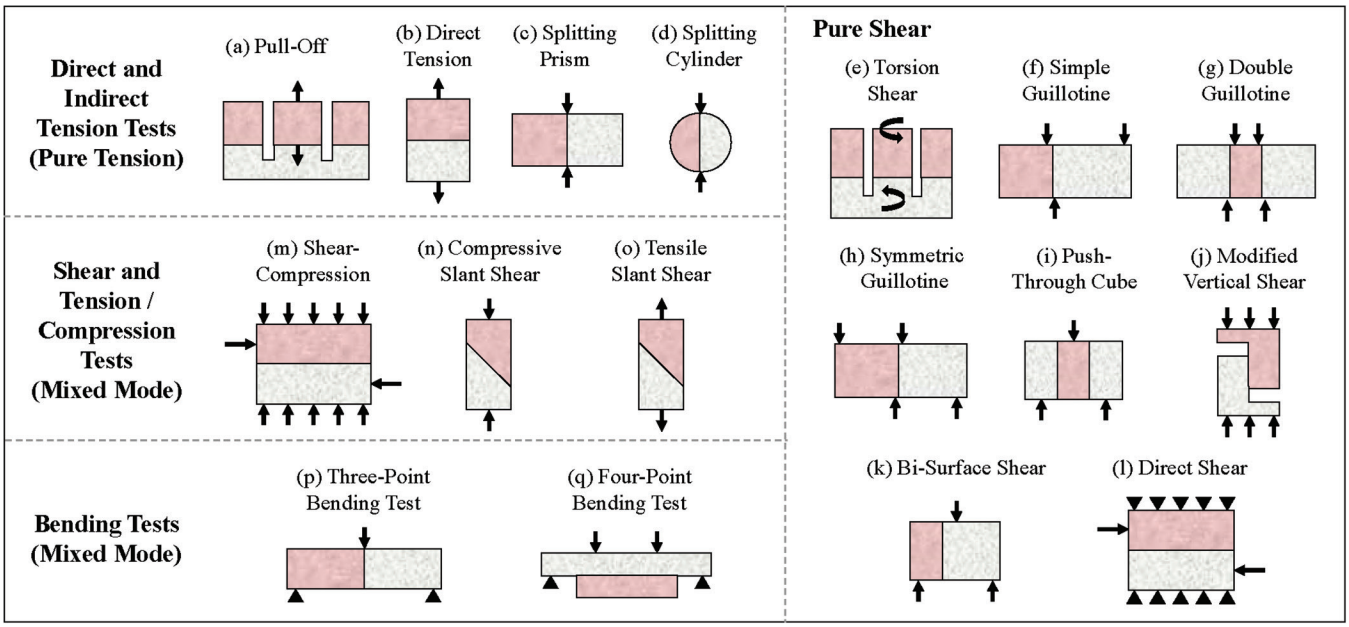


Fig. 2—Tests for assessing bond strength (redrawn from López-Carreño et al.[32]).

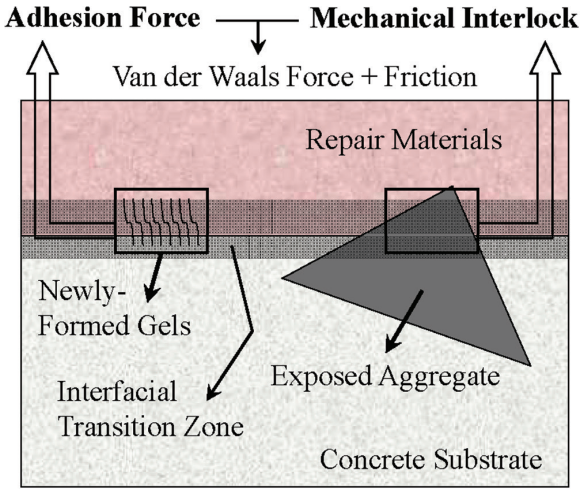


Fig. 3—Bonding mechanisms of interface between repair material and concrete substrate (redrawn from Wang et al.[29]).

and mechanical interlock induced by exposed aggregates (Fig. 3).[29,71]

A comprehensive evaluation of the bond strength of geopolymer composites based on a data set of 782 test results reveals the following:

Compressive strength of geopolymer composites—First, in the case of any bond strength, as can be seen in Fig. 4, it is observed to be proportional to f_c' of the repair material, which is consistent with the results of previous studies[29,31,38,42,44,45,47,49,52,66] (however, the experimental results of Kumar et al.[56] indicated that the bond strength is proportional to the modulus of elasticity of the repair material, rather than its f_c'). Note that in the compressive slant shear test (refer to Fig. 2(n)), the measured bond strength includes both shear bond strength (τ_s) and normal bond strength (σ_s), which are calculated as per Eq. (1) and (2), respectively. In Fig. 4, the shear bond strength of the compressive slant shear test refers to Eq. (1)

$$\tau_\sigma = (1/2)\cdot\sigma_o\cdot\sin 2\theta \quad (1)$$

$$\sigma_\sigma = \sigma_o\cdot\sin^2\theta \quad (2)$$

where σ_o is the maximum axial stress; and θ is the bond angle. It is a well-known fact that f_c' is closely related to the material's density, and as density increases, the number of voids and porosity decrease,[72] which naturally leads to an increase in bond strength. The mechanical strength of geopolymers is primarily attributed to the previously mentioned M-A-S-H, C-S-H, and/or C-A-S-H gels (refer to Appendix A). The formation of C-S-H and/or C-A-S-H gels is related to the amount of calcium used in the production of geopolymers, and notably, the influence of C-S-H and/or C-A-S-H gels was prominently observed in relation to bond strength. Several methods can be used to increase the calcium content in geopolymers. First, one can intentionally add high CaO content additives,[28,43] and the other can increase aluminosilicates with high calcium content, such as slag or GGBFS[29,36,38,48,54,63-65,67] or high-calcium FA[31,35] (note that in GGBFS-based GPC, increasing the proportion of low-calcium FA was found to decrease both compressive and bond strengths[39,45]). Here, an increase in the slag or GGBFS content was found to accelerate the geopolymerization process[53,64] and improve the microstructure of the geopolymer.[36,44,57] However, an excessively high slag or GGBFS content can form microcracks[64] or inhibit the formation of C-S-H, C-A-S-H, and M-A-S-H gels,[53] resulting in bond strength reduction.

As an additional note, an increase in the amount of C-S-H and/or C-A-S-H gels strengthens the bond at the ITZ and as shown in Table B1 of Appendix B, increases the adhesion coefficient (c).[31,35] The value of c can be calculated

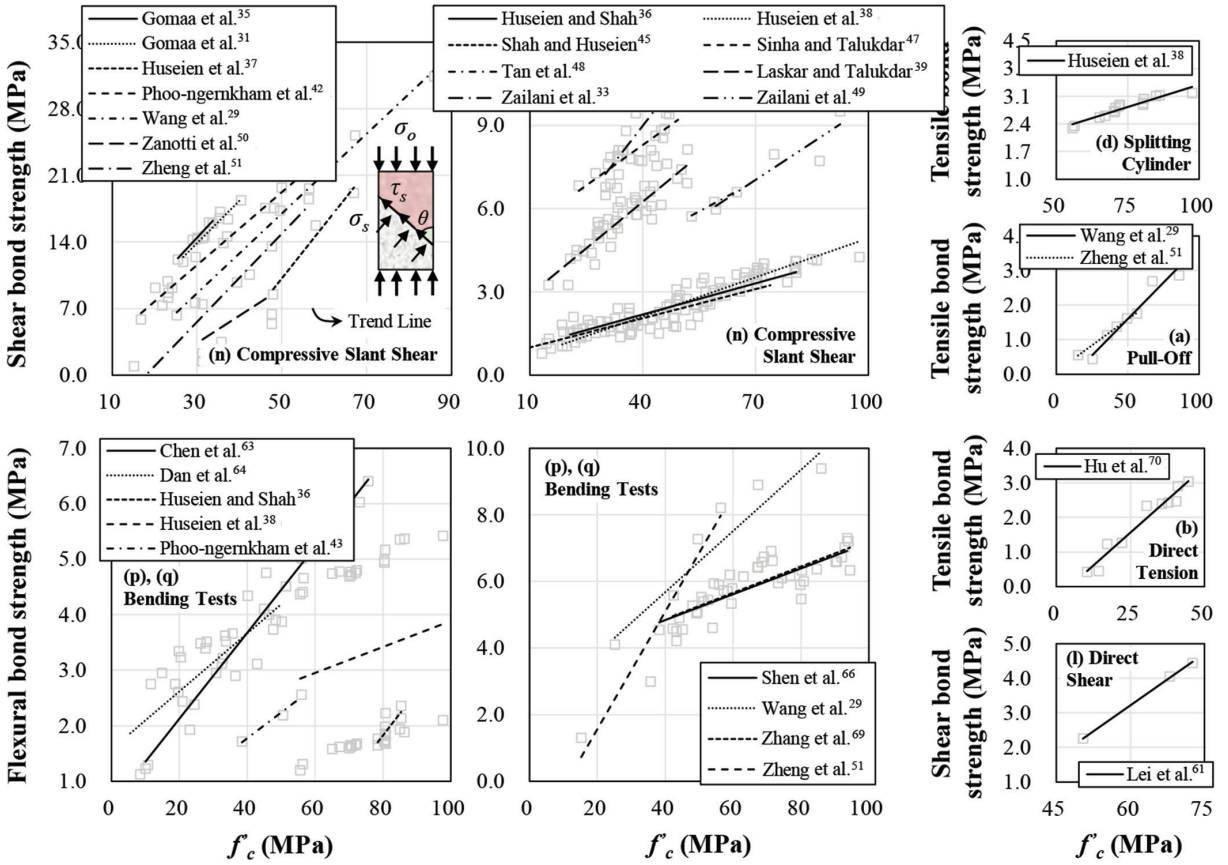


Fig. 4—Correlation between compressive strength of repair material and bond strength. (Note: Refer to Fig. 2 for test methods; geopolymer composites used in test data contained no fibers or portland cement.)

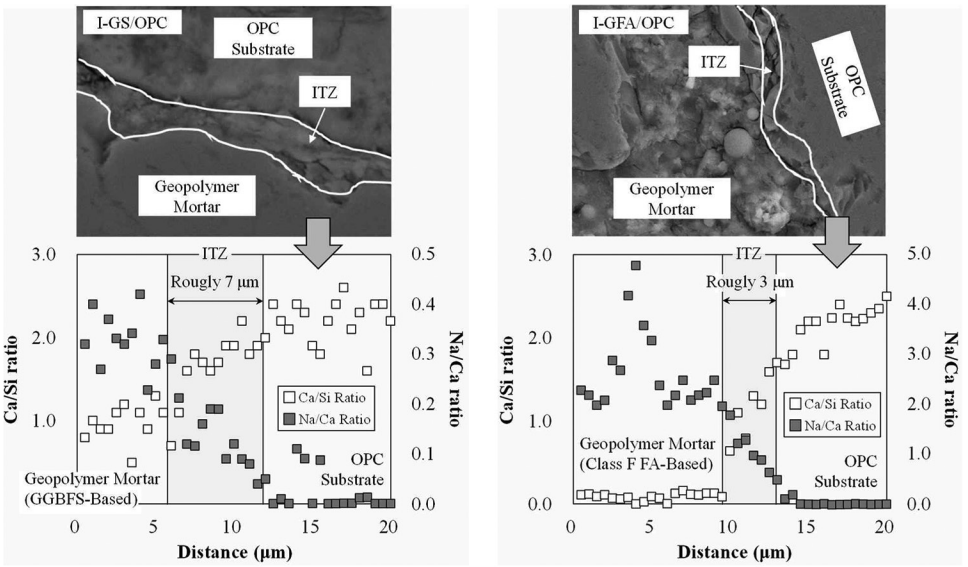


Fig. 5—Variations of Ca/Si and Na/Ca ratios at ITZs (adapted from Wang et al.[29]).

using Eq. (3). (where φ represents the internal friction angle)[31,35,50,73]

$$\tau_\sigma = \sigma_s \cdot \tan\varphi + c \quad (3)$$

This phenomenon can be explained by the fact that an increase in C-S-H and/or C-A-S-H gels leads to a widening of the ITZ, facilitating a smoother transition between the repair and substrate materials.[29] As shown in Fig. 5, the ITZ width in specimens reinforced with GGBFS-based geopolymer mortar (Fig. 5(a)) was wider than in those reinforced with low-calcium FA-based geopolymer mortar (Fig. 5(b)). Specifically, when comparing the Ca/Si ratio, indicative of C-S-H and/or C-A-S-H gels, the ratio near the ITZ was approximately 1.0 for GGBFS-based geopolymer mortar, while it was almost zero for Class F FA-based geopolymer

mortar. Consequently, the ITZ widths formed were approximately 7 and 3 μm, respectively. It is noteworthy that, as mentioned in Appendix A, Class F FA contributes to the formation of M-A-S-H gel in geopolymers. Consequently, as shown in Fig. 5(b), Class F FA-based geopolymer mortar had numerous points indicating a Na/Si ratio, which represents the sodium-aluminosilicate-hydrate (N-A-S-H) gels.

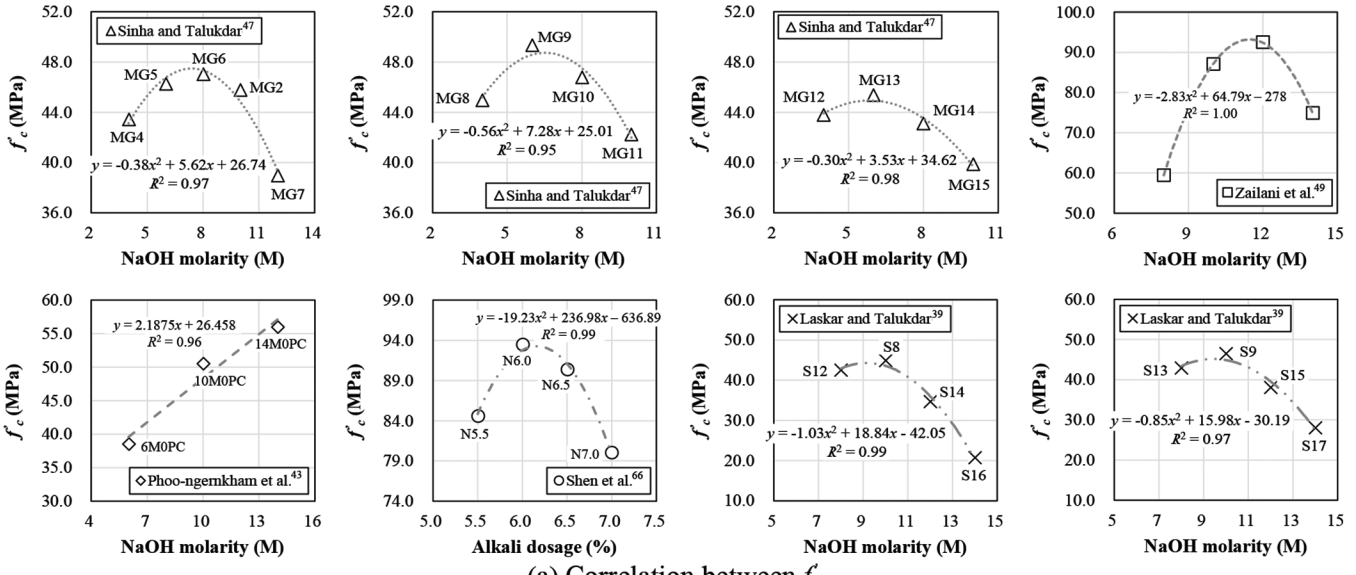
NaOH, as an alkaline activator, plays a critical role in decomposing aluminosilicate, thereby significantly influencing the geopolymerization process. Proper regulation of its content (for example, NaOH molarity, alkali dosage, or alkaline solution-binder ratio) is essential, as excessively high content of NaOH can negatively affect the f_c' of geopolymers, consequently leading to detrimental effects on their bond strength. The adverse effects that occur at high NaOH (or alkali) content are as follows:

- Precipitation of aluminosilicate gel during the early stage.[74]
- High NaOH concentration hindered calcium dissolution, resulting in fewer hydration products.[43]
- Increased porosity in geopolymer composites caused by reduced fluidity of the alkaline activator due to the addition of excessive solid NaOH pallets.[75]
- Formation of nonhomogenous geopolymer matrix due to loss of workability.[39]
- High pH enhances the stability of ions and reduces their mobility, ultimately delaying the formation of alkaline polymers.[76]
- At higher alkalinity, geopolymeric gels cannot form an integral matrix, leading to cracks and pores in the microstructure.[47]
- Reaction of a large number of Na^+ ions with carbon dioxide, forming sodium carbonate (commonly referred to as efflorescence), which impedes polymerization.[49,77-79]

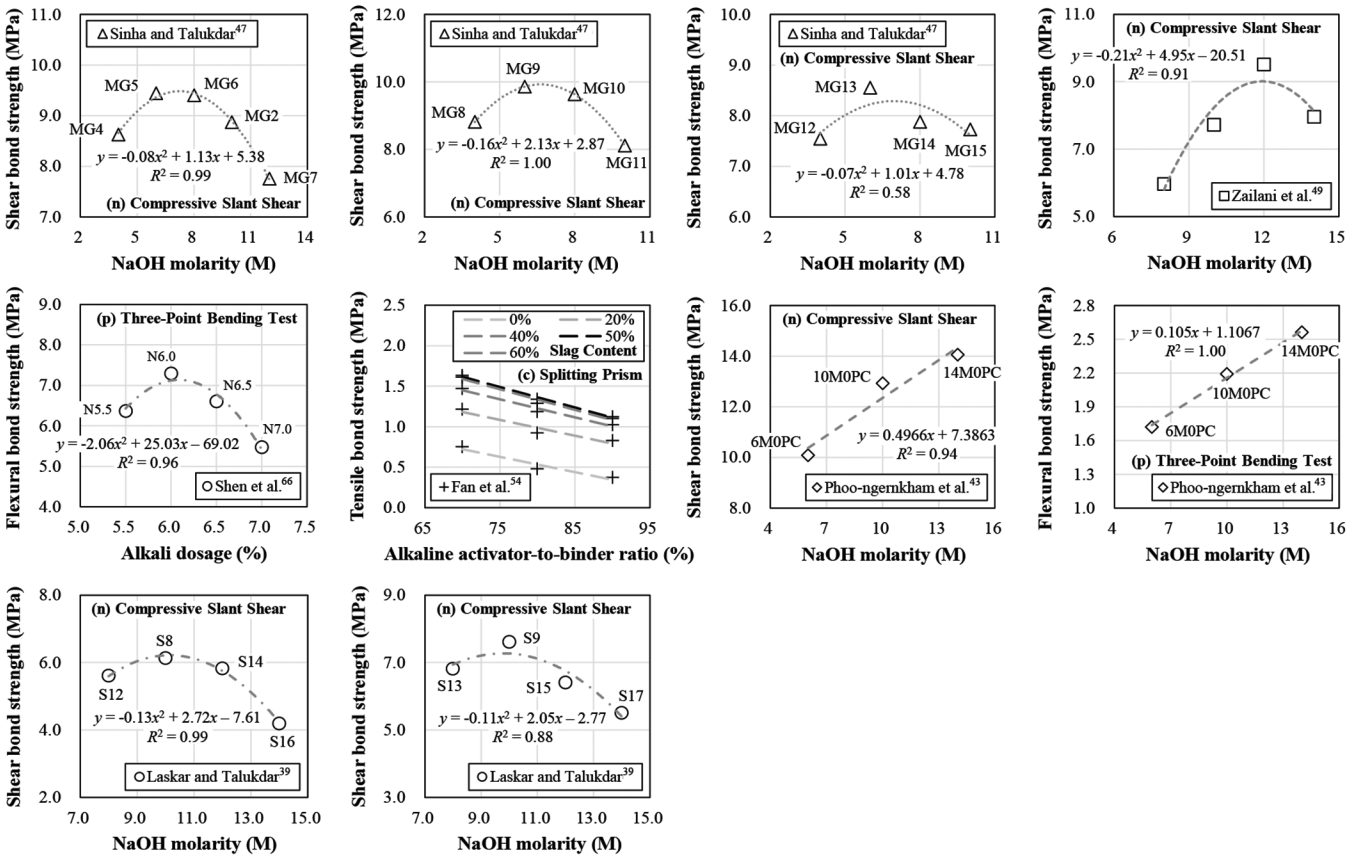
For these reasons, as shown in Fig. 6, a high NaOH content reduces f_c' of geopolymers, which in turn leads to a decrease in bond strength.

The composition of alkaline activators also significantly affects the strength of geopolymers. As mentioned in Appendix A, NaOH and Na_2SiO_3 are primarily used as alkaline activators because the intensity of geopolymerization can be enhanced more than when NaOH is solely used, leading to an improvement in mechanical properties. The experimental results of Phoo-ngernkham et al.[44,65] aptly demonstrate this, as shown in Fig. 7, where the highest f_c' was achieved when both NaOH and Na_2SiO_3 were used as alkaline activators (however, for the geopolymer paste with GGBFS at 28 and 60 days, no significant difference was observed between the cases where both NaOH and Na_2SiO_3 were used and where only Na_2SiO_3 was used). When examining geopolymer pastes in detail using scanning electron micrographs (SEM), the combination of NaOH and Na_2SiO_3 produced the densest composition.[44] The bond strength test data from Phoo-ngernkham et al.[44,65] and Zhang et al.[69] (Fig. 8) revealed that bond strength is not solely influenced by the f_c' of the repair material. It has been well-established through numerous experiments[28,29,31,35,36,38,43,44,48,63-65,69] that C-S-H and/or C-A-S-H gels positively influence the f_c' of geopolymer composites. Figure 8 also indicates that as the content of slag or GGBFS increases, more C-S-H and/or C-A-S-H gels form, resulting in higher f_c'. However, beyond a certain content level, the previously positive correlation between bond strength and f_c' becomes negative, indicating that factors other than just C-S-H and/or C-A-S-H gels also influence bond strength. In the study by Phoo-ngernkham et al.,[44] the decrease in bond strength despite the increase in f_c' was attributed to a deficiency in N-A-S-H gel. As mentioned in Appendix A, M-A-S-H gel, primarily formed by low-calcium FA, is responsible for the durability and mechanical properties of geopolymers. Using GGBFS alone, without FA, leads to the formation of relatively more C-S-H and/or C-A-S-H gels due to their high calcium content, resulting in a higher f_c' compared to geopolymers using both FA and GGBFS (refer to Fig. 8). However, this also leads to less formation of M-A-S-H gel, negatively impacting bond strength, as observed in Fig. 8(a) and (b). Furthermore, Phoo-ngernkham et al.[65] found that the absence of NaOH in the alkaline activator led to lower bond strength due to insufficient formation of C-S-H and/or C-A-S-H gels at the interface between OPC substrates and geopolymer mortar. This is because NaOH enhances the solubility of Si and Si-Al in the aluminosilicate, forming Si^{4+} and Al^{3+} ions, which then interact with calcium hydroxide on the surfaces of OPC substrates to form the gels.[65] This lack of bond strength was also reflected in the failure modes of the specimens, as can be seen in Fig. 9. Last, the experimental results of Zhang et al.[69] (Fig. 8(c)) suggest that excessive addition of slag in geopolymer mortar reduces fluidity and setting time due to accelerated geopolymerization, leading to an insufficient filling of the bonding surface with the OPC substrate, causing a reduction in bond strength.

Compressive strength of OPC substrate—Bonaldo et al.[80] conducted pulloff tests (Fig. 2(a)) to evaluate the bond strength between steel fiber reinforced concrete (SFRC) and OPC substrate. The experimental variables included: 1) f_c' of OPC substrate; 2) type of commercial bond agent; and 3) loading rate of pulloff strength. The results showed that in the pulloff test, an increase in the loading rate led to a higher bond strength, and an increase in the f_c' of OPC substrate led to an increase in bond strength (Fig. 10(a)). Especially where f_c' of OPC substrate was low to medium and bond agents P1 or P2 (epoxy resin-based adhesives) were used for interface with SFRC, there was a clear tendency for concrete substrate failure. This serves as evidence that tensile strength of OPC substrate directly influenced the bond strength, and it indicates that f_c' of OPC substrate affected the bond strength (typically, f_c' and tensile strength of concrete are in a proportional relationship). Robayo-Salazar et al.[58] also conducted pulloff tests with f_c' of OPC substrate as an experimental variable. Their approach differed in that they used geopolymer mortar as the repair material and did not include a separate bond agent between the repair material and the OPC substrate. The results showed that although the bond strength did not exceed the tensile strength of OPC substrate (implying, unlike the results of Bonaldo et al.,[80] that f_c' of OPC substrate did not directly influence bond strength), there was a trend of increasing bond strength with increasing



(a) Correlation between f'_c



(b) Correlation between bond strength

Fig. 6—Influence of alkaline activator concentration on f_c' *and bond strength. (Note: Refer to Fig. 2 for test methods; geopolymer composites used in test data contained no fibers or portland cement.)*

f_c' of OPC substrate (Fig. 10(a)). This may be attributed to the high content of calcium hydroxide, $Ca(OH)_2$, on OPC substrate surfaces, which interact with geopolymer-based binders. This interaction is driven by the need for positive ions, such as Ca^{2+}, to neutralize the negative charges of Al^{3+} ions,[34,41] consequently creating a chemical adherence.[58] As the f_c' of OPC substrate increases, this chemical adherence strengthens, affecting the bond strength. Abdullah et al.[34] also conducted bond strength tests between geopolymer mortar and OPC substrate, with the results indicating a positive correlation between f_c' of OPC substrate and bond strength (Fig. 10(a)).

Interfacial surface condition of OPC substrate—The interfacial surface condition of the OPC substrate is one of the key factors influencing bond strength and can be broadly categorized into bond angle and surface treatment. First, the impact of the bond angle on bond strength can be understood through compressive slant shear tests. As the bond angle

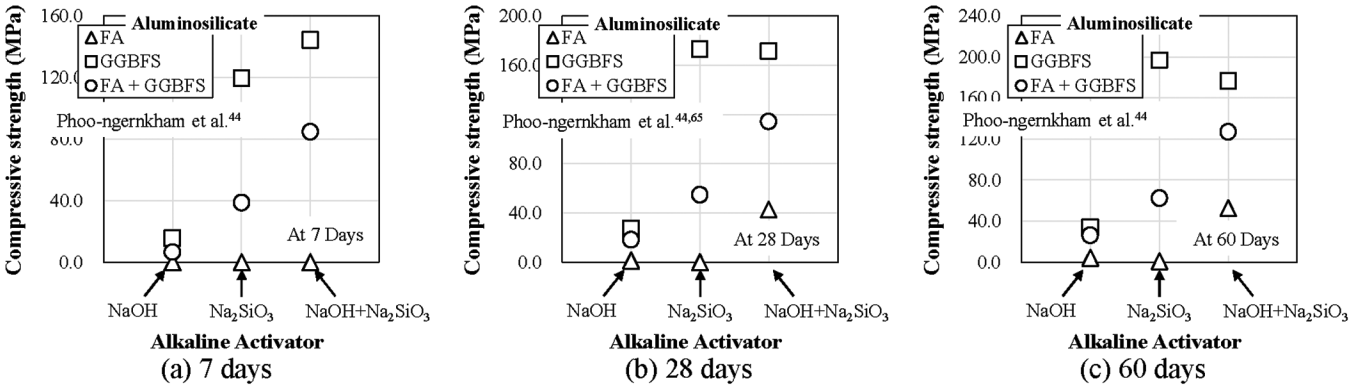
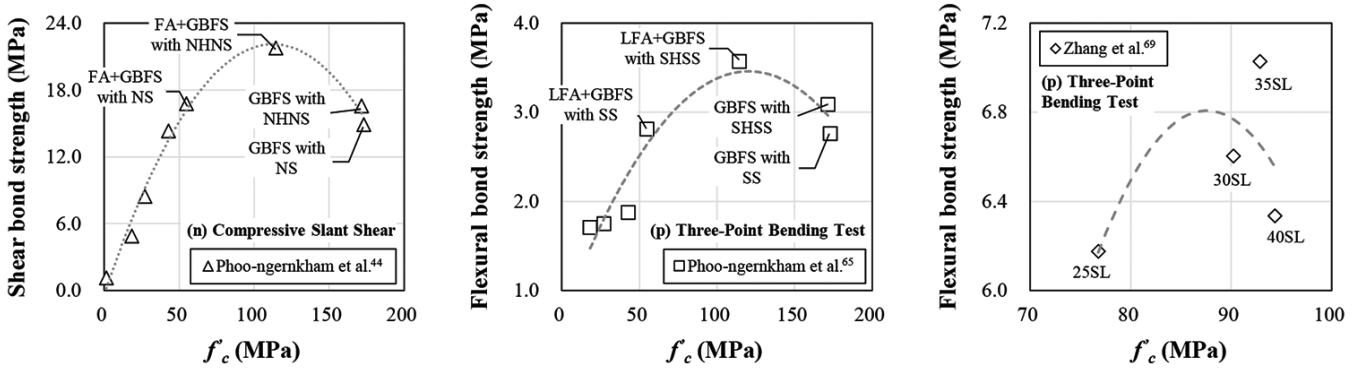


Fig. 7—Compressive strength of geopolymer composites.



ID	Aluminosilicate
FA + GBFS with NS	FA 50% + GGBFS 50%
FA + GBFS with NHNS	FA 50% + GGBFS 50%
GBFS with NHNS	GGBFS 100%
GBFS with NS	GGBFS 100%

(a)

ID	Aluminosilicate
LFA + GBFS with SHSS	FA 50% + GGBFS 50%
LFA + GBFS with SHSS	FA 50% + GGBFS 50%
GBFS with SHSS	GGBFS 100%
GBFS with SS	GGBFS 100%

(b)

ID	Aluminosilicate
25SL	FA 30% + Slag 25% + EFNS 45%
30SL	FA 30% + Slag 30% + EFNS 40%
35SL	FA 30% + Slag 35% + EFNS 35%
40SL	FA 30% + Slag 40% + EFNS 30%

(c)

Note: NH, SH = sodium hydroxide (NaOH); NS, SS = sodium silicate (Na_2SiO_3); and EFNS = electric furnace nickel slag.

Fig. 8—Factors affecting bond strength in geopolymers independent of f_c'. *(Note: Refer to Fig. 2 for test methods; geopolymer composites used in test data contained no fibers or portland cement.)*

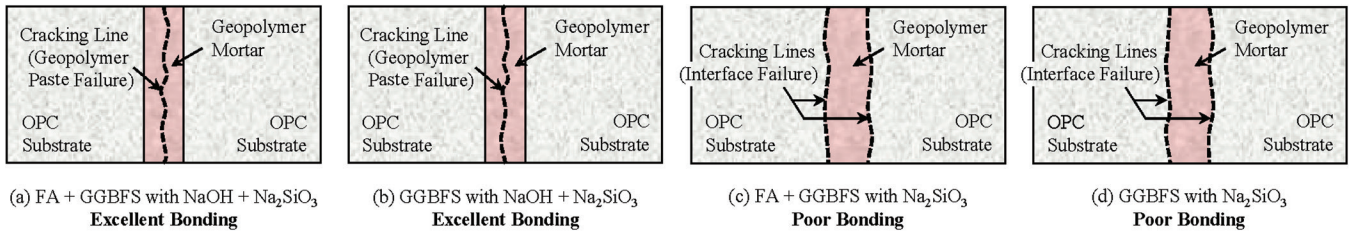


Fig. 9—Failure mode of specimens (redrawn from Phoo-ngernkham et al.[65]).

increases, the failure mode of concrete cylinders transitions from sliding along the interfacial surface (poor bonding) to compression failure (excellent bonding).[31,35] This indicates that a larger bond angle leads to a smaller shear-normal stress ratio (τ_s/σ_s; refer to Eq. (1) and (2)), implying that an increase in bond angle enhances bond strength,[31,35,50] as shown in Fig. 10(b). Second, regarding surface treatment, the experimental results of Wang et al.[59] showed that both pulloff and direct shear tests demonstrated an increase in bond strength with enhanced interface roughness, as shown in Fig. 10(b). The increase is likely due to the formation of a larger contact area between geopolymer composites and OPC substrate as the interface roughness increases, resulting in greater chemical, physical, and mechanical forces.[59] The pulloff test results by Asayesh et al.[55] and Gomaa et al.[31,35] also revealed that increasing the roughness of the OPC substrate led to an increase in bond strength. However, it was noted that geopolymer composites with strong adhesive properties (for example, tungsten mine waste mud-based) were less affected by interfacial treatment in terms of bond strength.[41] Note that applying epoxy resin to the contact area can effectively increase bond strength.[46] But using other commercial bonding agents may negatively impact bond strength.[31,35]

Additives for improving performance of geopolymer composites—Various additives have been incorporated to

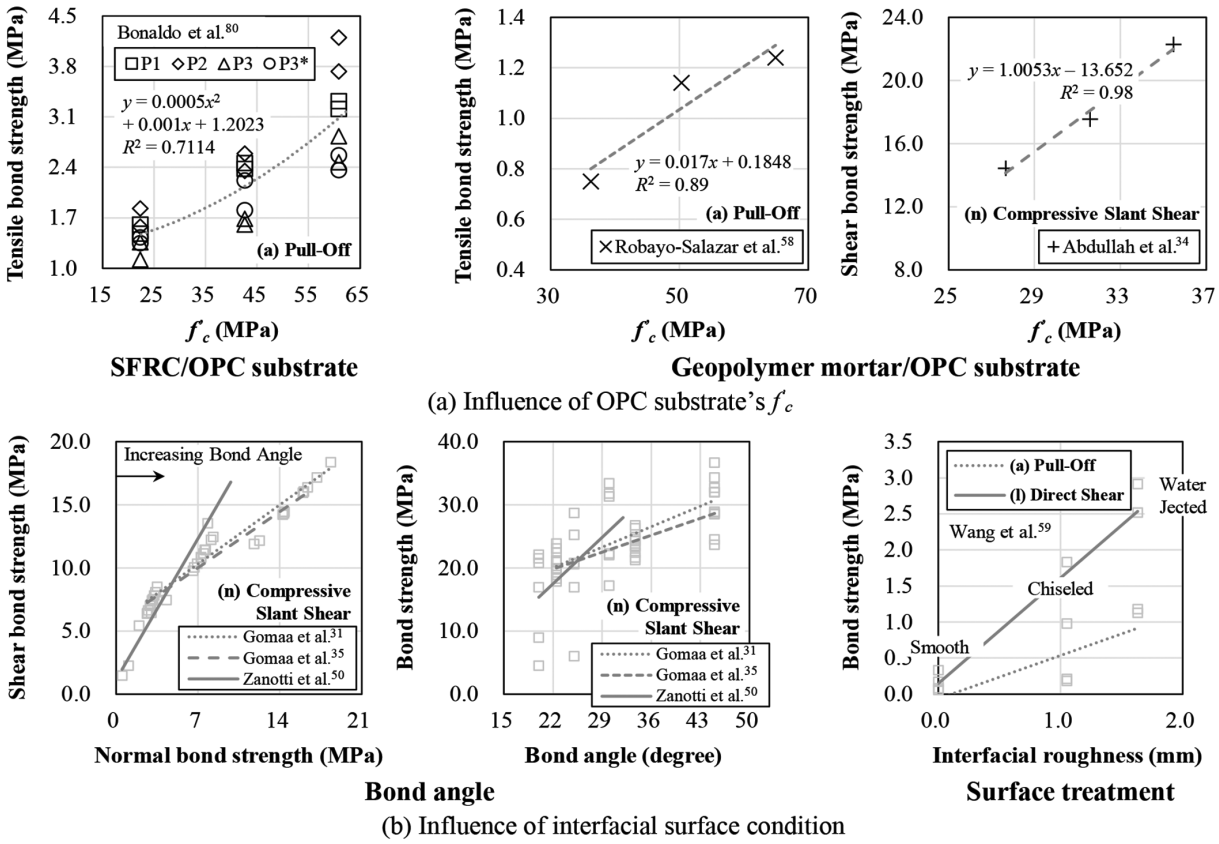


Fig. 10—External factors affecting bond strength in geopolymers. (Note: Refer to Fig. 2 for test methods; geopolymer composites used in test data contained no portland cement.)

enhance the bonding performance of geopolymer composites, and the results are as follows:

- Polyvinyl alcohol (PVA) fiber[30,50]: The inclusion of PVA fibers in geopolymer mortars improved cohesion regardless of curing temperatures (for example, heat or ambient). This resulted in enhanced bond strength not only at ambient temperatures but also at elevated temperatures.
- PVA fiber and nano-SiO_2[60]: Adding PVA fibers and nano-SiO_2 to geopolymer mortar in a certain amount improved its bond strength and synergistically increased its shear toughness.
- Rubber particles[62]: Replacing some fine aggregates with rubber particles increased the bond strength of geopolymer mortar. Additionally, it exhibited lower water absorption compared to OPC mortar, indicating superior durability.
- Epoxy resin[68]: The addition of epoxy resin enhanced the mechanical and bonding properties of geopolymer mortar by filling effects, which reduced the porosity without changing the main types of geopolymerization products. However, excessive additions adversely affected these properties.

Comparison between cementitious composites—To evaluate the potential of geopolymer composites as repair materials, it is essential to compare their bond strengths with those of conventional cementitious composites. Table B2 of Appendix B represents an assessment of geopolymer composites as repair and strengthening materials, and for a more accurate comparison of bonding performance, only specimens with similar f_c' of the repair materials were considered. As shown in Table B2, in cases where aluminosilicate is FA, it can be observed that the bond strength of geopolymer composites tends to be lower than that of cementitious composites under similar f_c'.[46] This outcome can be attributed to the previously discussed positive correlation between C-S-H and/or C-A-S-H gels and bond strength. It is important to note that FA (especially Class F) has a relatively lower CaO content compared to slag or GGBFS.

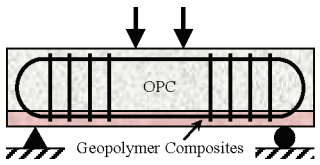
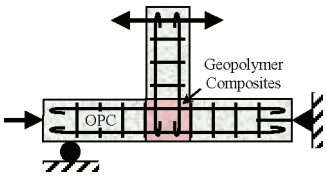
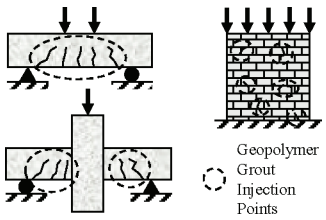
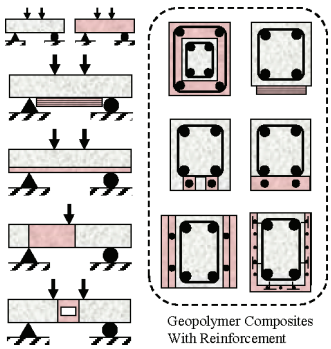
REPAIR AND STRENGTHENING PERFORMANCE

Experimental data for repair and strengthening performance

In this study, a total of 164 experimental data points[40,62,81-99] were collected to evaluate the repair and strengthening capabilities of geopolymer composites. This data set includes 46 reference plain specimens for benchmarking repair and strengthening outcomes, and 25 specimens for comparative analyses with cement composites or epoxy. The details of the collected experimental data are presented in Table 1, and the test specimens consist of 138 beams, 20 beam-column connections, and six walls. As shown in Table 1, most of the experiments used aluminosilicate containing slag or GGBFS, which enhances bond strength through the formation of C-S-H and/or C-A-S-H gels.

The test methods are divided into two approaches: one involves applying loads to repaired or strengthened undamaged specimens,[62,81,82,86,87,93,95-98] and the other to repaired or

Table 1—Collected test data for evaluating repair and strengthening performance

Source	Examples of repairing or strengthening method	Main components of geopolymer		
		Aluminosilicate	Alkaline liquid	Additive
Al-Majidi et al.[81]	 Note: Repair pattern varies depending on each specimen	FA + slag + SF	$KOH + K_2SiO_3$	PVA fiber
Al-Majidi et al.[82]		FA + slag + SF	$KOH + K_2SiO_3$	Steel or PVA fiber
Geraldo et al.[86]		Metakaolin + SF	NaOH	—
Guades et al.[87]		FA	$NaOH + Na_2SiO_3$	Steel and PVA fiber
Khalifa et al.[90*]		FA + GGBFS + SF	$KOH + K_2SiO_3$	Steel fiber
Laskar and Talukdar[91*]		FA + GGBFS	NaOH	—
Laskar et al.[40*]		GGBFS	NaOH	—
Zakeremamreza et al.[62]		GGBFS	$NaOH + Na_2SiO_3$	Rubber or not
Choudhury and Laskar[83,84*]		FA + GGBFS	NaOH	Steel fiber or not
Choudhury and Laskar[85*]		FA + GGBFS	NaOH	—
Kantarci and Maras[88*]		GGBFS	NaOH	$Ca(OH)_2$
Kantarci and Maras[89*]		GGBFS	NaOH	TiO_2
Maras[94*]		GGBFS	NaOH	Latex
Al-Majidi et al.[82]		FA + slag + SF	$KOH + K_2SiO_3$	Steel or PVA fiber
Khalifa et al.[90*]		FA + GGBFS + SF	$KOH + K_2SiO_3$	Steel fiber
Laskar and Talukdar[92*]		FA + GGBFS	NaOH	—
Mahmood et al.[93]		FA + GGBFS	$NaOH + Na_2SiO_3$	—
Menna et al.[95]		Metakaolin	$NaOH + Na_2SiO_3$	—
Peng et al.[96]		FA + slag	$Na_2CO_3 + Na_2SiO_3$	Steel, PVA fiber, or not
Peng et al.[97]		FA + slag	$Na_2CO_3 + Na_2SiO_3$	Steel fiber or not
Salman and Mansor[98]		FA + nano-silica	$NaOH + Na_2SiO_3$	Steel, carbon, or PP fiber
Sinha and Talukdar[99*]		FA + GGBFS	$NaOH + Na_2SiO_3$	Borate

*Contains experiments on specimens that were retested after being repaired or strengthened with geopolymer composites following damage.

Note: SF is silica fume; PVA is polyvinyl alcohol; and PP is polypropylene.

strengthened damaged specimens.[40,83-85,88-92,94,99] Additionally, the methods of repair or strengthening are categorized into those using only geopolymer composites[40,62,81-91,94] and those combining geopolymer composites with additional reinforcement.[82,90,92,93,95-99] Notably, the degree of pre-existing damage significantly impacted the performance of the structural members after repair or strengthening.[40,91,92] Ultimately, the use of geopolymer composites for the repair and strengthening of concrete members is recognized as an efficient method to swiftly restore the functionality,[92] owing to their rapid setting times.

Evaluation of repair and strengthening performance

The method for evaluating the repair or strengthening performance of geopolymer composites involves comparing the load-carrying capacity, yield stiffness, and ductility factor of repaired or strengthened specimens to those of plain, undamaged specimens when subjected to monotonic loading.[40,62,81,82,86-99] For cyclic loading,[40,83-85] additional metrics such as stiffness degradation ratio and cumulative energy absorbed (or dissipated) are also compared.

Load-carrying capacity, yield stiffness, and ductility factor—First, the load-carrying capacity refers to the maximum load or force a structure or structural element can withstand, commonly denoted as the ultimate load (P_u) on a load-displacement curve. These curves are divided into the pre-cracking zone, pre-yield stage, and post-yield stage. In the post-yield stage, which occurs after the yield point, cracks propagate, and the bottom steel reinforcement yields.[22] However, defining the yield point precisely is challenging due to the nonlinear behavior of materials, the fact that longitudinal bars at various depths within a RC section may yield at different moments, and so on.[100] Therefore, in this study, if the yield point of the collected experimental data was not indicated in the corresponding paper, it was

determined as the point on the load-displacement curves where the load reached $0.75P_u$, and the yield stiffness (K_y) was then calculated as the secant stiffness at this point. For experiments subjected to cyclic loading[40,83-85] and cases where a clear $0.75P_u$ point could not be discerned from the provided load-displacement curves,[90] the initial stiffness (K_i) was used.

The ductility factor (μ) is calculated by dividing the maximum (ultimate) deformation (Δ_u) by the deformation observed at the onset of yielding (Δ_y). However, it should be noted that in the case of cyclic loading tests for beam-column connection specimens,[83-85] the post-peak deflection at $0.75P_u$ was used instead of Δ_u. Table B3 of Appendix B shows the structural performance of repaired or strengthened RC members. K_y and μ were calculated using the aforementioned method, based on information from each paper; however, if needed, additional data were extracted from load-displacement curves. A summary of Table B3 and the key conclusions from various researchers includes the following:

- Al-Majidi et al.[81]: Repairing the lower tension side of beams with fiber-reinforced geopolymer mortar (FRGM) resulted in increases in P_u and K_y, but a decrease in μ was observed. Increasing the depth of the FRGM from 25 to 50 mm did not significantly aid in the increase of P_u and instead contributed to a reduction in K_y and μ. This suggests that increasing the depth of the FRGM, bringing it closer to the neutral axis, does not substantially affect the stress distribution on the tension side. However, corrosion resistance significantly improved.
- Al-Majidi et al.[82]: Three-side jacking of FRGM on RC beams increased P_u and K_y. However, applying FRGM only on the tension side also increased P_u and K_y but decreased μ (the greater increase in P_u compared to three-side jacking is attributed to the inclusion of additional reinforcement in the FRGM; for more detailed information, refer to Al-Majidi et al.[82]).
- Choudhury and Laskar[83-85]: In typical beam-column joints,[83] specimens repaired with geopolymer mortar exhibited improvements in P_u, K_i, and μ compared to plain specimens. This enhancement is attributed to the strong adhesion and strength properties of geopolymer mortar (both plain and geopolymer mortar [without fibers] repaired specimens experienced joint shear failure). However, in beam-column joints designed following the "strong-column and weak-beam" philosophy,[84,85] failure occurred due to plastic hinge formation in the beams, where repaired specimens (without fibers) showed beam failure accompanied by joint shear failure. Regardless of whether cement mortar or geopolymer mortar was used, detachment between the repair material and old concrete occurred due to diagonal cracks at the cold joints of the columns, with specimens repaired with cement mortar showing more severe detachment than those repaired with geopolymer mortar. As a result, specimens repaired with geopolymer mortar experienced less reduction in K_i and μ compared to those reinforced with cement mortar relative to plain specimens.[85] Furthermore, in both typical and "strong-column and weak-beam"-designed beam-column joints, specimens repaired with FRGM failed due to plastic hinge formation in the beams. This failure mode is believed to be caused by the bridging effect of steel fibers, which resist the opening of cracks around the embedded steel bars, thereby enhancing confinement.[83,84] In summary, reinforcing with FRGM can prevent brittle shear failure at the joint, regardless of whether the column is strong.
- Geraldo et al.[86]: Specimens repaired with geopolymer mortar, which rapidly exhibited strong strength and adhesion to concrete surfaces, generally showed enhanced P_u, K_y, and μ.
- Guades et al.[87]: Specimens reinforced on two or three sides with FRGM (S-2 J and S-3 J) exhibited improvements not only in flexural but also in shear performance.
- Kantarci and Maras[88,89]; Maras[94]: Geopolymer grout injection can rehabilitate the load-carrying capacity of damaged RC members; however, specific measures for K_y and μ seem necessary.
- Khalifa et al.[90]: Beams reinforced with steel fiber-reinforced geopolymer mortar (SFRGM) demonstrated increased P_u, K_i, and/or μ, and their failure modes were identical to those of plain specimens. No slippage or disintegration of SFRGC occurred at the interface throughout the process.
- Laskar et al.[40]; Laskar and Talukdar[91,92]: Specimens repaired or reinforced with geopolymer composites outperformed those repaired with cement composites in all aspects of P_u, K_y, and μ.
- Mahmood et al.[93]: Specimens strengthened with geopolymer paste exhibited similar strength and failure patterns to those strengthened with epoxy paste.
- Menna et al.[95]: The geopolymer matrix exhibited excellent adhesion to both concrete and steel cords, ensuring that no delamination took place. However, its adhesion to carbon was poor.
- Peng et al.[96]: As the slag content increased, the width of the ITZ expanded, indicating a stronger chemical reaction. The addition of fibers to geopolymer mortar effectively improved the reinforced beam's P_y (yield load), K_y, and μ but had little effect on P_u. Specimens reinforced with cast-in-place FRGM and those reinforced with epoxy-bonded FRGM displayed similar behaviors and failure modes, indicating superior bonding performance of geopolymer composites.
- Peng et al.[97]: Beams reinforced on two sides with geopolymer mortar had significantly higher P_u but lower μ compared to beams reinforced on one side.
- Salman and Mansor[98]: Detachment of the fiber-reinforced geopolymer paste did not occur until the strengthened specimen failed (both the newly added and existing steel reinforcing bars yielded).
- Sinha and Talukdar[99]: Beams repaired with geopolymer mortar demonstrated superior rehabilitation performance in terms of P_u, K_y, and μ compared to those repaired with cement mortar. This superior performance can be attributed to the rapid development of strength and enhanced bonding properties of geopolymer mortar, which resulted in improved adhesion to the

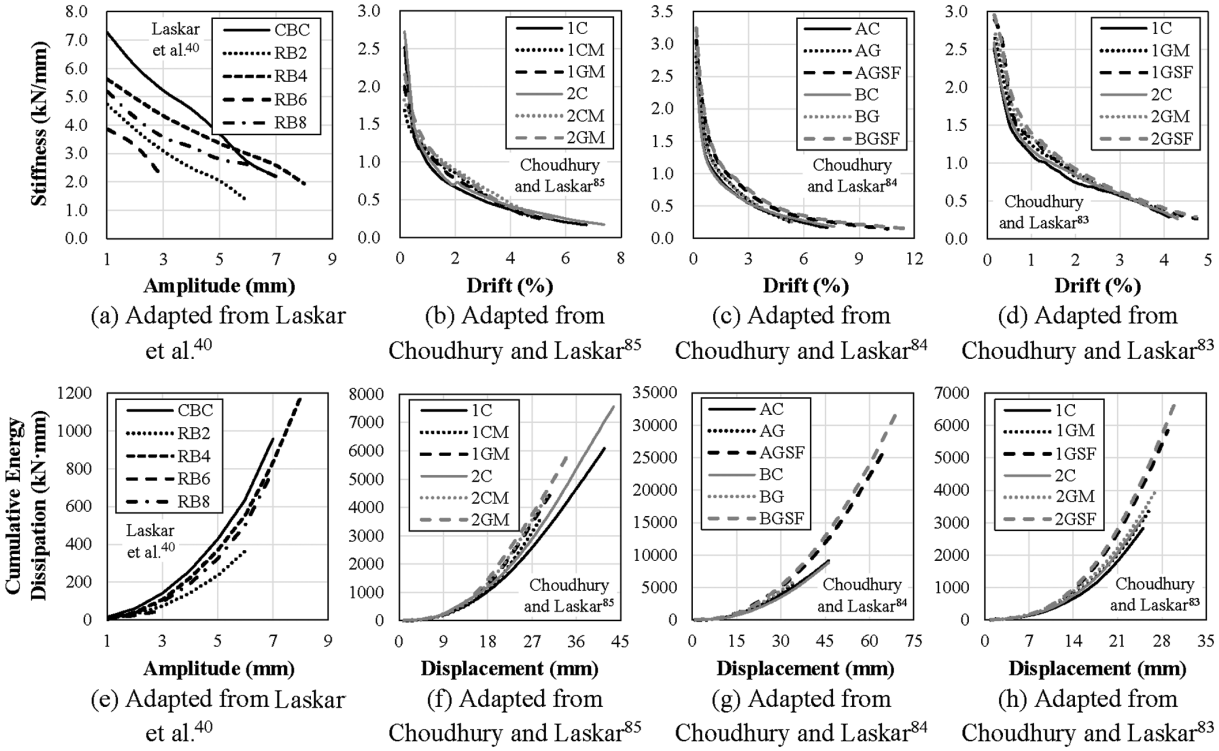


Fig. 11—Stiffness degradation and cumulative energy dissipation curves of repaired specimens.

beam specimen. Consequently, there was no occurrence of debonding or spalling of the repair material, issues commonly observed in beams repaired with cement mortar.

- Zakeremamreza et al.[62]: Rehabilitation performance of geopolymer mortar was superior to that of cement mortar, and the addition of rubber in geopolymer significantly enhanced K_y.

Stiffness degradation and cumulative energy dissipation—Stiffness reduction behavior reflects the damage index from cyclic loading, manifested through the spread of cracks and, occasionally, a reduced effective cross-sectional area due to the spalling of concrete.[40] Figures 10(a) to (d) show the stiffness degradation curves of repaired specimens, and the key conclusions from each figure are summarized as follows (refer to Table B3 for type of each specimen):

- Figure 11(a)[40]: Debonding occurred in areas repaired with cement mortar, with this phenomenon being more pronounced in fully damaged RC beams (RB6) compared to partially damaged ones (RB2). However, no such distinct occurrences were observed in RC beams repaired with geopolymer mortar (RB4 and RB8). Consequently, it can be seen in Fig. 11(a) that RB4 and RB8 exhibited superior stiffness degradation behavior than that of RB2 and RB6.
- Figure 11(b)[85]: Initially, K_i of specimens repaired with geopolymer mortar and cement mortar (1GM, 2GM, 1CM, and 2CM) was only 79 to 80% and 65 to 67%, respectively, compared to plain specimens (1C and 2C), which is attributed to the cold joint interface between the repair material and old concrete. At low drifts, the stiffness degradation of repaired specimens was lower than that of plain specimens due to the high strength of both geopolymer and cement mortar, which increased the resistance of diagonal cracks. However, at high drifts, there was significant stiffness degradation in repaired specimens, a consequence of the brittle nature of both geopolymer and cement mortar.
- Figure 11(c)[84]: Due to the bridging effect of steel fibers, as mentioned earlier, specimens repaired with FRGM (AGSF and BGSF) effectively resisted volumetric expansion at the joints. As a result, these specimens exhibited the lowest stiffness degradation among all tested.
- Figure 11(d)[83]: The stiffness degradation in specimens repaired with geopolymer mortar (1GM and 2GM) was lower than in plain specimens (1C and 2C), attributed to the high compressive strength of repair material, which led to fewer flexural and shear cracks. However, this applies to conventionally designed beam-column joints. In joints designed by "strong-column and weak-beam" philosophy,[84,85] a greater stiffness degradation was observed at higher drift levels due to the cold joint and the brittle nature of geopolymer mortar compared to plain specimens.

Energy dissipation is a crucial parameter for assessing the seismic performance of structures beyond the elastic range,[83] and the ability to dissipate a significant amount of energy is indicative of superior performance.[84] Figures 10(e) to (h) show the cumulative energy dissipation curves of repaired specimens, and the key findings from each depicted figure summarized as follows (refer to Table B3 for type of each specimen):

- Figure 11(e)[40]: Due to the superior bonding performance of geopolymer mortar, RC beams repaired with geopolymer mortar (RB4 and RB8) exhibited higher

straining capacity and μ than those repaired with cement mortar (RB2 and RB6), allowing them to absorb more energy.

- Figure 11(f)[85]: The presence of a cold joint and the yielding of hoop reinforcement within the joint restrained the full recovery of cumulative energy dissipation capacity. However, the superior μ of specimens repaired with geopolymer mortar (1GM and 2GM) resulted in greater cumulative energy dissipation compared to those repaired with cement mortar (1CM and 2CM).
- Figure 11(g)[84]: Steel fibers provided a bridging action that prevented the widening of microcracks, thereby increasing frictional forces, which subsequently improved both stiffness and μ of the specimens (AGSF and BGSF). This led to the highest cumulative energy dissipation observed.
- Figure 11(h)[83]: In typically designed beam-column joints, specimens repaired with geopolymer mortar (1GM and 2GM) exhibited higher K_i and μ values, resulting in greater cumulative energy dissipation compared to plain specimens (1C and 2C).

CONCLUSIONS

This study collected and analyzed data from a total of 782 bond strength tests and 164 large-scale tests to examine the potential of geopolymer composites as repair and strengthening materials for concrete structures. The findings and conclusions are as follows:

1. The bond strength of geopolymer composites is generally correlated with the compressive strength. Specifically, the formation of C-S-H and/or C-A-S-H gels was found to be proportional to the amount of calcium added in the geopolymerization process; a larger quantity of C-S-H and/or C-A-S-H gels expanded the interfacial transition zone (ITZ), enhancing bond strength. The calcium content can be increased by adding high CaO additives or high-calcium aluminosilicate materials such as slag. However, excessive use of slag may induce microcracks and hinder the formation of C-S-H, C-A-S-H, and M-A-S-H gels, and can also reduce fluidity and setting time, causing poor adherence and inadequate filling of the bonding interface with the ordinary portland cement concrete (OPC) substrate, which ultimately result in decreasing bond strength.

2. NaOH plays a critical role in decomposing aluminosilicate, and increasing its quantity enhances the geopolymerization process, positively affecting both compressive and bond strength of geopolymers. However, excessive NaOH can negatively impact these properties by precipitating aluminosilicate gel and suppressing calcium dissolution, and so on. Additionally, combining Na_2SiO_3 with NaOH as an alkaline activator may intensify the geopolymerization process and result in a denser geopolymer matrix.

3. In addition to the mechanical properties of geopolymer composites, the compressive strength of the OPC substrate and the condition of the interfacial surface influence the bond strength of geopolymer composites. Increased compressive strength of the OPC substrate enhances chemical adherence with the geopolymer composites at the ITZ. Furthermore, greater bond angles and appropriate surface treatments can further improve bond strength.

4. Geopolymer composites may exhibit either better or poorer bond performance than conventional cementitious composites with similar compressive strengths, depending on the CaO content of the aluminosilicate used. This variability is attributed to the relationship between C-S-H and/or C-A-S-H gel formation and bond strength. To address this issue, it is recommended to use high-CaO additives or high calcium aluminosilicates.

5. Large-scale tests demonstrated the exceptional capabilities of geopolymer composites, especially in reinforced concrete members where areas repaired or reinforced with geopolymer composites showed no noticeable debonding, unlike cementitious composites. Consequently, specimens repaired or strengthened with geopolymer composites generally exhibited superior load-carrying capacity, yield or initial stiffness, ductility factor, resistance to stiffness degradation, and ability to dissipate cumulative energy compared to those repaired with cementitious composites. However, due to the brittle nature of geopolymers, adding fibers can further enhance their performance as repair materials through the crack-bridging effect.

6. As the performance of repaired structures varies based on their damage condition, geopolymer composites with relatively fast setting times are considered effective materials for repairing or strengthening concrete structures.

AUTHOR BIOS

ACI member **Giwan Noh** *is a Master's Student of structural engineering at Seoul National University, Seoul, Korea. He received his BS from Pusan National University, Busan, Korea. His research interests include the design and behavior of reinforced, prestressed, and post-tensioned concrete structures.*

Uksun Kim *is a Professor and a past Chair of civil engineering at California State University, Fullerton, Fullerton, CA. He received his BS from Yonsei University, Seoul, Korea; his MS from Michigan State University, East Lansing, MI; and his PhD from the Georgia Institute of Technology, Atlanta, GA. His research interests include seismic design of building systems with steel joist girders, partially restrained connections and concrete-filled steel tubes, and seismic rehabilitation of prestressed building systems.*

ACI member **Myoungsu Shin** *is a Professor at Ulsan National Institute of Science and Technology (UNIST), Ulsan, Korea. He received his BS and MS from Seoul National University, and his PhD from the University of Illinois Urbana-Champaign, Urbana, IL. He is a member of ACI Committees 228, Nondestructive Testing of Concrete; 374, Performance-Based Seismic Design of Concrete Buildings; and 564, 3-D Printing with Cementitious Materials; and Joint ACI-ASCE Committees 352, Joints and Connections in Monolithic Concrete Structures, and 421, Design of Reinforced Concrete Slabs.*

Woo-Young Lim *is an Associate Professor of structural engineering at Wonkwang University, Iksan, Korea. He received his PhD from Seoul National University in 2012. His research interests include reinforced concrete members in shear and strengthening of concrete members using ultra-high-performance concrete (UHPC) jacketing.*

Thomas H.-K. Kang, *FACI, is a Professor of structural engineering and the Interdisciplinary Program of Artificial Intelligence at Seoul National University. He is a member of ACI Subcommittee 318-T, Post-Tensioned Concrete (Structural Concrete Building Code); Joint ACI-ASCE Committees 352, Joints and Connections in Monolithic Concrete Structures, and 423, Prestressed Concrete; Joint ACI-ASME Committee 359, Concrete Containments for Nuclear Reactors; and Joint ACI-PTI Committee 320, Post-Tensioned Concrete Code. He received the ACI Wason Medal for Most*

Meritorious Paper in 2009. His research interests include the design and behavior of reinforced, prestressed, and post-tensioned concrete structures.

ACKNOWLEDGMENTS

This research was supported by National Research Foundation of Korea (2021R1A5A1032433 and RS-2024-00399324), the Institute of Engineering Research at Seoul National University, and the Institute of Information & communications Technology Planning & Evaluation grant (RS-2021-II211343, MSIT). The views expressed are those of the authors, and do not necessarily represent those of the sponsors.

REFERENCES

1. Alanazi, H.; Yang, M.; Zhang, D.; and Gao, Z., "Bond Strength of PCC Pavement Repairs Using Metakaolin-Based Geoploymer Mortar," *Cement and Concrete Composites*, V. 65, 2016, pp. 75-82. doi: 10.1016/j.cemconcomp.2015.10.009

2. Diaz-Loya, E. I.; Allouche, E. N.; and Vaidya, S., "Mechanical Properties of Fly-Ash-Based Geoploymer Concrete," *ACI Materials Journal*, V. 108, No. 3, May-June 2011, pp. 300-306. doi: 10.14359/51682495

3. Davidovits, J., "High-Alkali Cements for 21st Century Concretes," *Concrete Technology: Past, Present, and Future*, SP-144, P. K. Mehta, ed., American Concrete Institute, Farmington Hills, MI, 1994, pp. 383-398. doi: 10.14359/452310.14359/4523

4. Li, N.; Shi, C.; Zhang, Z.; Wang, H.; and Liu, Y., "A Review on Mixture Design Methods for Geopolymer Concrete," *Composites. Part B, Engineering*, V. 178, 2019, p. 107490. doi: 10.1016/j.compositesb.2019.107490

5. Ma, C.-K.; Awang, A. Z.; and Omar, W., "Structural and Material Performance of Geopolymer Concrete: A Review," *Construction and Building Materials*, V. 186, 2018, pp. 90-102. doi: 10.1016/j.conbuildmat.2018.07.111

6. Sofi, M.; van Deventer, J. S. J.; Mendis, P. A.; and Lukey, G. C., "Engineering Properties of Inorganic Polymer Concretes (IPCs)," *Cement and Concrete Research*, V. 37, No. 2, 2007, pp. 251-257. doi: 10.1016/j.cemconres.2006.10.008

7. Hardjito, D., and Rangan, V., "Development and Properties of Low-Calcium Fly Ash-Based Geopolymer Concrete," *Research Report GC 1*, Curtin University of Technology, Perth, Australia, 2005.

8. Panias, D.; Giannopoulou, I. P.; and Perraki, T., "Effect of Synthesis Parameters on the Mechanical Properties of Fly Ash-Based Geopolymers," *Colloids and Surfaces. A, Physicochemical and Engineering Aspects*, V. 301, No. 1-3, 2007, pp. 246-254. doi: 10.1016/j.colsurfa.2006.12.064

9. Lee, N. K., and Lee, H. K., "Setting and Mechanical Properties of Alkali-Activated Fly Ash/Slag Concrete Manufactured at Room Temperature," *Construction and Building Materials*, V. 47, 2013, pp. 1201-1209. doi: 10.1016/j.conbuildmat.2013.05.107

10. Sarker, P. K.; Haque, R.; and Ramgolam, K. V., "Fracture Behaviour of Heat Cured Fly Ash Based Geopolymer Concrete," *Materials & Design*, V. 44, 2013, pp. 580-586. doi: 10.1016/j.matdes.2012.08.005

11. Thomas, R. J., and Peethamparan, S., "Alkali-Activated Concrete: Engineering Properties and Stress-Strain Behavior," *Construction and Building Materials*, V. 93, 2015, pp. 49-56. doi: 10.1016/j.conbuildmat.2015.04.039

12. Noushini, A.; Aslani, F.; Castel, A.; Gilbert, R. I.; Uy, B.; and Foster, S., "Compressive Stress-Strain Model for Low-Calcium Fly Ash-Based Geopolymer and Heat-Cured Portland Cement Concrete," *Cement and Concrete Composites*, V. 73, 2016, pp. 136-146. doi: 10.1016/j.cemconcomp.2016.07.004

13. Nath, P., and Sarker, P. K., "Flexural Strength and Elastic Modulus of Ambient-Cured Blended Low-Calcium Fly Ash Geopolymer Concrete," *Construction and Building Materials*, V. 130, 2017, pp. 22-31. doi: 10.1016/j.conbuildmat.2016.11.034

14. Nikoloutsopoulos, N.; Sotiropoulou, A.; Kakali, G.; and Tsivilis, S., "Physical and Mechanical Properties of Fly Ash Based Geopolymer Concrete Compared to Conventional Concrete," *Buildings*, V. 11, No. 5, 2021, p. 178 doi: 10.3390/buildings11050178

15. Farhan, N. A.; Sheikh, M. N.; and Hadi, M. N. S., "Investigation of Engineering Properties of Normal and High Strength Fly Ash Based Geopolymer and Alkali-Activated Slag Concrete Compared to Ordinary Portland Cement Concrete," *Construction and Building Materials*, V. 196, 2019, pp. 26-42. doi: 10.1016/j.conbuildmat.2018.11.083

16. Soutsos, M.; Boyle, A. P.; Vinai, R.; Hadjierakleous, A.; and Barnett, S. J., "Factors Influencing the Compressive Strength of Fly Ash Based Geopolymers," *Construction and Building Materials*, V. 110, 2016, pp. 355-368. doi: 10.1016/j.conbuildmat.2015.11.045

17. Sarker, P. K.; Kelly, S.; and Yao, Z., "Effect of Fire Exposure on Cracking, Spalling and Residual Strength of Fly Ash Geopolymer Concrete," *Materials & Design*, V. 63, 2014, pp. 584-592. doi: 10.1016/j.matdes.2014.06.059

18. Farooq, F.; Xin, J.; Javed, M. F.; Akbar, A.; Shah, M. I.; Aslam, F.; and Alyousef, R., "Geopolymer Concrete as Sustainable Material: A State of the Art Review," *Construction and Building Materials*, V. 306, 2021, p. 124762. doi: 10.1016/j.conbuildmat.2021.124762

19. Fernández-Jiménez, A. M.; Palomo, A.; and López-Hombrados, C., "Engineering Properties of Alkali-Activated Fly Ash Concrete," *ACI Materials Journal*, V. 103, No. 2, Mar.-Apr. 2006, pp. 106-112. doi: 10.14359/15261

20. Paswan, R.; Rahman, M. R.; Singh, S. K.; and Singh, B., "Bond Behavior of Reinforcing Steel Bar and Geopolymer Concrete," *Journal of Materials in Civil Engineering*, ASCE, V. 32, No. 7, 2020, p. 04020167. doi: 10.1061/(ASCE)MT.1943-5533.0003237

21. Sarker, P. K., "Bond Strength of Reinforcing Steel Embedded in Fly Ash-Based Geopolymer Concrete," *Materials and Structures*, V. 44, No. 5, 2011, pp. 1021-1030. doi: 10.1617/s11527-010-9683-8

22. Mamdouh, H.; Ali, A. M.; Osman, M. A.; Deifalla, A. F.; and Ayash, N. M., "Effects of Size and Flexural Reinforcement Ratio on Ambient-Cured Geopolymer Slag Concrete Beams under Four Point Bending," *Buildings*, V. 12, No. 10, 2022, p. 1554. doi: 10.3390/buildings12101554

23. Maranan, G. B.; Manalo, A. C.; Benmokrane, B.; Karunasena, W.; Mendis, P.; and Nguyen, T. Q., "Shear Behaviour of Geopolymer-Concrete Beams Transversely Reinforced with Continuous Rectangular GFRP Composite Spirals," *Composite Structures*, V. 187, 2018, pp. 454-465. doi: 10.1016/j.compstruct.2017.12.080

24. Maranan, G. B.; Manalo, A. C.; Benmokrane, B.; Karunasena, W.; Mendis, P.; and Nguyen, T. Q., "Flexural Behavior of Geopolymer-Concrete Beams Longitudinally Reinforced with GFRP and Steel Hybrid Reinforcements," *Engineering Structures*, V. 182, 2019, pp. 141-152. doi: 10.1016/j.engstruct.2018.12.073

25. Wu, C.; Hwang, H.-J.; Shi, C.; Li, N.; and Du, Y., "Shear Tests on Reinforced Slag-Based Geopolymer Concrete Beams with Transverse Reinforcement," *Engineering Structures*, V. 219, 2020, p. 110966. doi: 10.1016/j.engstruct.2020.110966

26. ACI Committee 318, "Building Code Requirements for Structural Concrete (ACI 318-19) and Commentary (318R-19) (Reapproved 2022)," American Concrete Institute, Farmington Hills, MI, 2019, 624 pp.

27. EN 1992-1-1, "Eurocode 2: Design of Concrete Structures - Part 1-1: General Rules and Rules for Buildings," European Committee for Standardization, Brussels, Belgium, 2004.

28. Chindaprasirt, P.; Sriopas, B.; Phosri, P.; Yoddumrong, P.; Anantakarn, K.; and Kroehong, W., "Hybrid High Calcium Fly Ash Alkali-Activated Repair Material for Concrete Exposed to Sulfate Environment," *Journal of Building Engineering*, V. 45, 2022, p. 103590 doi: 10.1016/j.jobe.2021.103590

29. Wang, Y.-S.; Peng, K.-D.; Alrefaei, Y.; and Dai, J.-G., "The Bond between Geopolymer Repair Mortars and OPC Concrete Substrate: Strength and Microscopic Interactions," *Cement and Concrete Composites*, V. 119, 2021, p. 103991. doi: 10.1016/j.cemconcomp.2021.103991

30. Albidah, A.; Abadel, A.; Alrshoudi, F.; Altheeb, A.; Abbas, H.; and Al-Salloum, Y., "Bond Strength between Concrete Substrate and Metakaolin Geopolymer Repair Mortars at Ambient and Elevated Temperatures," *Journal of Materials Research and Technology*, V. 9, No. 5, 2020, pp. 10732-10745. doi: 10.1016/j.jmrt.2020.07.092

31. Gomaa, E.; Gheni, A.; and ElGawady, M. A., "Repair of Ordinary Portland Cement Concrete Using Ambient-Cured Alkali Activated Concrete: Interfacial Behavior," *Cement and Concrete Research*, V. 129, 2020, p. 105968 doi: 10.1016/j.cemconres.2019.105968

32. López-Carreño, R.-D.; Pujadas, P.; Cavalaro, S. H. P.; and Aguado, A., "Bond Strength of Whitetoppings and Bonded Overlays Constructed with Self-Compacting High-Performance Concrete," *Construction and Building Materials*, V. 153, 2017, pp. 835-845. doi: 10.1016/j.conbuildmat.2017.07.136

33. Zailani, W. W. A.; Abdullah, M. M. A. B.; Zainol, M. R. R. M. A.; Razak, R. A.; and Tahir, M. F. M., "Compressive and Bonding Strength of Fly Ash Based Geopolymer Mortar," *AIP Conference Proceedings*, V. 1887, No. 1, 2017, p. 020058. doi: 10.1063/1.5003541

34. Abdullah, M. M. A. B.; Aziz, I. H. A.; Zailani, W. W. A.; Rahim, S. Z. A.; Yong, H. C.; Sandu, A. V.; and Peng, L. S., "Silica Bonding Reaction on Fly Ash Based Geopolymer Repair Material System with incorporation of Various Concrete Substrates," *Archives of Metallurgy and Materials*, V. 67, No. 4, 2022, pp. 1277-1281. doi: 10.24425/amm.2022.141052

35. Gomaa, E.; Gheni, A. A.; Kashosi, C.; and ElGawady, M. A., "Bond Strength of Eco-Friendly Class C Fly Ash-Based Thermally Cured Alkali-Activated Concrete to Portland Cement Concrete," *Journal of Cleaner Production*, V. 235, 2019, pp. 404-416. doi: 10.1016/j.jclepro.2019.06.268

36. Huseien, G. F., and Shah, K. W., "Performance Evaluation of Alkali-Activated Mortars Containing Industrial Wastes as Surface Repair

Materials," *Journal of Building Engineering*, V. 30, 2020, p. 101234. doi: 10.1016/j.jobe.2020.101234

37. Huseien, G. F.; Mirza, J.; Ismail, M.; Ghoshal, S. K.; and Ariffin, M. A. M., "Effect of Metakaolin Replaced Granulated Blast Furnace Slag on Fresh and Early Strength Properties of Geopolymer Mortar," *Ain Shams Engineering Journal*, V. 9, No. 4, 2018, pp. 1557-1566. doi: 10.1016/j.asej.2016.11.011

38. Huseien, G. F.; Hussein, Z. J.; Kubba, Z.; Nikolaevich, B. M.; and Mirza, J., "Improved Bond Strength Performance of Geopolymer Mortars: Role of High Volume Ground Blast Furnace Slag, Fly Ash, and Palm Oil Fuel Ash Incorporation," *Minerals*, V. 13, No. 8, 2023, p. 1096. doi: 10.3390/min13081096

39. Laskar, S. M., and Talukdar, S., "Preparation and Tests for Workability, Compressive and Bond Strength of Ultra-Fine Slag Based Geopolymer as Concrete Repairing Agent," *Construction and Building Materials*, V. 154, 2017, pp. 176-190. doi: 10.1016/j.conbuildmat.2017.07.187

40. Laskar, S. M.; Mozumder, R. A.; and Laskar, A. I., "Behaviour of RC Beam Repaired Using Alkali Activated Slag-Based Agent under Static and Cyclic Loading," *Structures*, V. 31, 2021, pp. 761-768. doi: 10.1016/j.istruc.2021.02.039

41. Pacheco-Torgal, F.; Castro-Gomes, J. P.; and Jalali, S., "Adhesion Characterization of Tungsten Mine Waste Geopolymeric Binder. Influence of OPC Concrete Substrate Surface Treatment," *Construction and Building Materials*, V. 22, No. 3, 2008, pp. 154-161. doi: 10.1016/j.conbuildmat.2006.10.005

42. Phoo-ngernkham, T.; Chindaprasirt, P.; Sata, V.; Hanjitsuwan, S.; and Hatanaka, S., "The Effect of Adding Nano-SiO_2 and Nano-Al_2O_3 on Properties of High Calcium Fly Ash Geopolymer Cured at Ambient Temperature," *Materials & Design*, V. 55, 2014, pp. 58-65. doi: 10.1016/j.matdes.2013.09.049

43. Phoo-ngernkham, T.; Sata, V.; Hanjitsuwan, S.; Ridtirud, C.; Hatanaka, S.; and Chindaprasirt, P., "High Calcium Fly Ash Geopolymer Mortar Containing Portland Cement for Use as Repair Material," *Construction and Building Materials*, V. 98, 2015, pp. 482-488. doi: 10.1016/j.conbuildmat.2015.08.139

44. Phoo-ngernkham, T.; Maegawa, A.; Mishima, N.; Hatanaka, S.; and Chindaprasirt, P., "Effects of Sodium Hydroxide and Sodium Silicate Solutions on Compressive and Shear Bond Strengths of FA-GBFS Geopolymer," *Construction and Building Materials*, V. 91, 2015, pp. 1-8. doi: 10.1016/j.conbuildmat.2015.05.001

45. Shah, K. W., and Huseien, G. F., "Bond Strength Performance of Ceramic, Fly Ash and GBFS Ternary Wastes Combined Alkali-Activated Mortars Exposed to Aggressive Environments," *Construction and Building Materials*, V. 251, 2020, p. 119088. doi: 10.1016/j.conbuildmat.2020.119088

46. Sharkawi, A.; Taman, M.; Afefy, H. M.; and Hegazy, Y., "Efficiency of Geopolymer vs. High-Strength Grout as Repairing Material for Reinforced Cementitious Elements," *Structures*, V. 27, 2020, pp. 330-342. doi: 10.1016/j.istruc.2020.06.001

47. Sinha, A. K., and Talukdar, S., "Mechanical and Bond Behaviour of High Volume Ultrafine-Slag Blended Fly Ash Based Alkali Activated Concrete," *Construction and Building Materials*, V. 383, 2023, p. 131368. doi: 10.1016/j.conbuildmat.2023.131368

48. Tan, J.; Dan, H.; and Ma, Z., "Metakaolin Based Geopolymer Mortar as Concrete Repairs: Bond Strength and Degradation when Subjected to Aggressive Environments," *Ceramics International*, V. 48, No. 16, 2022, pp. 23559-23570. doi: 10.1016/j.ceramint.2022.05.004

49. Zailani, W. W. A.; Bouaissi, A.; Abdullah, M. M. A. B.; Razak, R. A.; Yoriya, S.; Salleh, M. A. A. M.; Zainol, M. R. R. M. A.; and Fansuri, H., "Bonding Strength Characteristics of FA-Based Geopolymer Paste as a Repair Material When Applied on OPC Substrate," *Applied Sciences*, V. 10, No. 9, 2020, p. 3321. doi: 10.3390/app10093321

50. Zanotti, C.; Borges, P. H. R.; Bhutta, A.; and Banthia, N., "Bond Strength between Concrete Substrate and Metakaolin Geopolymer Repair Mortar: Effect of Curing Regime and PVA Fiber Reinforcement," *Cement and Concrete Composites*, V. 80, 2017, pp. 307-316. doi: 10.1016/j.cemconcomp.2016.12.014

51. Zheng, C.; Mao, Z.; Chen, L.; Qian, H.; and Wang, J., "Development of a Novel Rapid Repairing Agent for Concrete Based on GFRP Waste Powder/GGBS Geopolymer Mortars," *Journal of Building Engineering*, V. 71, 2023, p. 106542. doi: 10.1016/j.jobe.2023.106542

52. Ma, Z.; Dan, H.; Tan, J.; Li, M.; and Li, S., "Optimization Design of MK-GGBS Based Geopolymer Repairing Mortar Based on Response Surface Methodology," *Materials*, V. 16, No. 5, 2023, p. 1889. doi: 10.3390/ma16051889

53. Fan, J., and Zhang, B., "Repair of Ordinary Portland Cement Concrete Using Alkali Activated Slag/Fly Ash: Freeze-Thaw Resistance and Pore Size Evolution of Adhesive Interface," *Construction and Building Materials*, V. 300, 2021, p. 124334. doi: 10.1016/j.conbuildmat.2021.124334

54. Fan, L. F.; Chen, D. K.; and Zhong, W. L., "Effects of Slag and Alkaline Solution Contents on Bonding Strength of Geopolymer-Concrete Composites," *Construction and Building Materials*, V. 406, 2023, p. 133391. doi: 10.1016/j.conbuildmat.2023.133391

55. Asayesh, S.; Javid, A. A. S.; Ziari, H.; and Mehri, B., "Evaluating Fresh State, Hardened State, Thermal Expansion and Bond Properties of Geopolymers for the Repairing of Concrete Pavements under Restrained Conditions," *Construction and Building Materials*, V. 292, 2021, p. 123398. doi: 10.1016/j.conbuildmat.2021.123398

56. Kumar, S.; Sekhar Das, C.; Lao, J.; Alrefaei, Y.; and Dai, J.-G., "Effect of Sand Content on Bond Performance of Engineered Geopolymer Composites (EGC) Repair Material," *Construction and Building Materials*, V. 328, 2022, p. 127080. doi: 10.1016/j.conbuildmat.2022.127080

57. Nunes, V. A.; Borges, P. H. R.; and Zanotti, C., "Mechanical Compatibility and Adhesion between Alkali-Activated Repair Mortars and Portland Cement Concrete Substrate," *Construction and Building Materials*, V. 215, 2019, pp. 569-581. doi: 10.1016/j.conbuildmat.2019.04.189

58. Robayo-Salazar, R., and Jesús, C., Mejía de Gutiérrez, R., and Pacheco-Torgal, F., "Alkali-Activated Binary Mortar Based on Natural Volcanic Pozzolan for Repair Applications," *Journal of Building Engineering*, V. 25, 2019, p. 100785. doi: 10.1016/j.jobe.2019.100785

59. Wang, B.; Feng, H.; Huang, H.; Guo, A.; Zheng, Y.; and Wang, Y., "Bonding Properties between Fly Ash/Slag-Based Engineering Geopolymer Composites and Concrete," *Materials*, V. 16, No. 12, 2023, p. 4232. doi: 10.3390/ma16124232

60. Gao, Z.; Zhang, P.; Wang, J.; Wang, K.; and Zhang, T., "Interfacial Properties of Geopolymer Mortar and Concrete Substrate: Effect of Polyvinyl Alcohol Fiber and Nano-SiO_2 Contents," *Construction and Building Materials*, V. 315, 2022, p. 125735. doi: 10.1016/j.conbuildmat.2021.125735

61. Lei, M.; Wang, X.; Meng, H.; Yan, Z.; Lin, J.; and Wu, Z., "Study of Fly Ash-Slag Geopolymer Mortar as a Rapid Strengthening Agent for Concrete Structures," *Construction and Building Materials*, V. 394, 2023, p. 132147. doi: 10.1016/j.conbuildmat.2023.132147

62. Zakeremamreza, A.; Kianifar, M. E.; Chibuisi, C.; Ahmadi, E.; and Salami, M. R., "A High-Performance Rubberised Alkali-Activated Mortar for Repair of RC Beams," *Construction and Building Materials*, V. 400, 2023, p. 132610. doi: 10.1016/j.conbuildmat.2023.132610

63. Chen, K.; Wu, D.; Yi, M.; Cai, Q.; and Zhang, Z., "Mechanical and Durability Properties of Metakaolin Blended with Slag Geopolymer Mortars used for Pavement Repair," *Construction and Building Materials*, V. 281, 2021, p. 122566. doi: 10.1016/j.conbuildmat.2021.122566

64. Dan, H.; Ma, Z.; Li, M.; Ma, S.; and Tan, J., "Early Performance and Bonding Mechanism of Metakaolin (MK)-Ground Granulated Blast Furnace Slag (GGBFS) Based Geopolymer Road Repair Mortar," *The International Journal of Pavement Engineering*, V. 24, No. 1, 2023, p. 2252156. doi: 10.1080/10298436.2023.2252156

65. Phoo-ngernkham, T.; Hanjitsuwan, S.; Suksiripattanapong, C.; Thumrongvut, J.; Suebsuk, J.; and Sookasem, S., "Flexural Strength of Notched Concrete Beam Filled with Alkali-Activated Binders under Different Types of Alkali Solutions," *Construction and Building Materials*, V. 127, 2016, pp. 673-678. doi: 10.1016/j.conbuildmat.2016.10.053

66. Shen, Y.; Kang, S.; Cheng, G.; Wang, J.; Wu, W.; Wang, X.; Zhao, Y.; and Li, Q., "Effects of Silicate Modulus and Alkali Dosage on the Performance of One-Part Electric Furnace Nickel Slag-Based Geopolymer Repair Materials," *Case Studies in Construction Materials*, V. 19, 2023, p. e02224. doi: 10.1016/j.cscm.2023.e02224

67. Wang, J.; Huang, T.; Cheng, G.; Liu, Z.; Li, S.; and Wang, D., "Effects of Fly Ash on the Properties and Microstructure of Alkali-Activated FA/BFS Repairing Mortar," *Fuel*, V. 256, 2019, p. 115919. doi: 10.1016/j.fuel.2019.115919

68. Xiong, G.; Guo, X.; and Zhang, H., "Preparation of Epoxy Resin-Geopolymer (ERG) for Repairing and the Microstructures of the New-to-Old Interface," *Composites Part B: Engineering*, V. 259, 2023, p. 110731 doi: 10.1016/j.compositesb.2023.110731

69. Zhang, D.; Wang, X.; Kang, S.; Cheng, G.; and Wu, W., "The Effect of Slag and Fly Ash Content on the Properties of Electric Furnace Nickel Slag-Based Geopolymer Used for Repair Materials," *Case Studies in Construction Materials*, V. 19, 2023, p. e02284. doi: 10.1016/j.cscm.2023.e02284

70. Hu, S.; Wang, H.; Zhang, G.; and Ding, Q., "Bonding and Abrasion Resistance of Geopolymeric Repair Material Made with Steel Slag," *Cement and Concrete Composites*, V. 30, No. 3, 2008, pp. 239-244. doi: 10.1016/j.cemconcomp.2007.04.004

71. He, Y.; Zhang, X.; Hooton, R. D.; and Zhang, X., "Effects of Interface Roughness and Interface Adhesion on New-to-Old Concrete Bonding," *Construction and Building Materials*, V. 151, 2017, pp. 582-590. doi: 10.1016/j.conbuildmat.2017.05.049

72. Iffat, S., "Relation Between Density and Compressive Strength of Hardened Concrete," *Concretet Research Letters*, V. 6, No. 4, 2015, pp. 182-189.

73. Austin, S.; Robins, P.; and Pan, Y., "Shear Bond Testing of Concrete Repairs," *Cement and Concrete Research*, V. 29, No. 7, 1999, pp. 1067-1076. doi: 10.1016/S0008-8846(99)00088-5

74. Lee, W. K. W., and van Deventer, J. S. J., "The Effects of Inorganic Salt Contamination on the Strength and Durability of Geopolymer," *Colloids and Surfaces. A, Physicochemical and Engineering Aspects*, V. 211, No. 2-3, 2002, pp. 115-126. doi: 10.1016/S0927-7757(02)00239-X

75. Sinha, A. K., and Talukdar, S., "Enhancement of the Properties of Silicate Activated Ultrafine-Slag Based Geopolymer Mortar Using Retarder," *Construction and Building Materials*, V. 313, 2021, p. 125380. doi: 10.1016/j.conbuildmat.2021.125380

76. Alonso, S., and Palomo, A., "Alkaline Activation of Metakaolin and Calcium Hydroxide Mixtures: Influence of Temperature, Activator Concentration and Solids Ratio," *Materials Letters*, V. 47, No. 1-2, 2001, pp. 55-62. doi: 10.1016/S0167-577X(00)00212-3

77. Malkawi, A. B.; Nuruddin, M. F.; Fauzi, A.; Almattarneh, H.; and Mohammed, B. S., "Effects of Alkaline Solution on Propeties of the HCFA Geopolymer Mortars," *Procedia Engineering*, V. 148, 2016, pp. 710-717. doi: 10.1016/j.proeng.2016.06.581

78. Kani, E. N.; Allahverdi, A.; and Provis, J. L., "Efflorescence Control in Geopolymer Binders Based on Natural Pozzolan," *Cement and Concrete Composites*, V. 34, No. 1, 2012, pp. 25-33. doi: 10.1016/j.cemconcomp.2011.07.007

79. Barbosa, V. F. F.; MacKenzie, K. J. D.; and Thaumaturgo, C., "Synthesis and Characterisation of Materials Based on Inorganic Polymers of Alumina and Silica: Sodium Polysialate Polymers," *International Journal of Inorganic Materials*, V. 2, No. 4, 2000, pp. 309-317. doi: 10.1016/S1466-6049(00)00041-6

80. Bonaldo, E.; Barros, J. A. O.; and Lourenço, P. B., "Bond Characterization between Concrete Substrate and Repairing SFRC Using Pull-Off Testing," *International Journal of Adhesion and Adhesives*, V. 25, No. 6, 2005, pp. 463-474. doi: 10.1016/j.ijadhadh.2005.01.002

81. Al-Majidi, M. H.; Lampropoulos, A. P.; Cundy, A. B.; Tsioulou, O. T.; and Al-Rekabi, S., "A Novel Corrosion Resistant Repair Technique for Existing Reinforced Concrete (RC) Elements Using Polyvinyl Alcohol Fibre Reinforced Geopolymer Concrete (PVAFRGC)," *Construction and Building Materials*, V. 164, 2018, pp. 603-619. doi: 10.1016/j.conbuildmat.2017.12.213

82. Al-Majidi, M. H.; Lampropoulos, A. P.; Cundy, A. B.; Tsioulou, O. T.; and Alrekabi, S., "Flexural Performance of Reinforced Concrete Beams Strengthened with Fibre Reinforced Geopolymer Concrete under Accelerated Corrosion," *Structures*, V. 19, 2019, pp. 394-410. doi: 10.1016/j.istruc.2019.02.005

83. Choudhury, A. H., and Laskar, A. I., "Rehabilitation of Substandard Beam-Column Joint Using Geopolymer," *Engineering Structures*, V. 238, 2021, p. 112241 doi: 10.1016/j.engstruct.2021.112241

84. Choudhury, A. H., and Laskar, A. I., "Performance of Geopolymer Mortar and Steel Fiber Reinforced Geopolymer Mortar on Rehabilitation of Seismically Detailed BeamColumn Joint," *Journal of Earthquake Engineering*, V. 27, No. 6, 2023, pp. 1607-1628. doi: 10.1080/13632469.2022.2086187

85. Choudhury, A. H., and Laskar, A. I., "Rehabilitation of Exterior Beam-Column Joint by Geopolymer Mortar under Quasi-Static Loading," *ACI Structural Journal*, V. 120, No. 5, Sept. 2023, pp. 49-62. doi: 10.14359/51738835

86. Geraldo, R. H.; Teixeira, O. G.; Matos, S. R. C.; Silva, F. G. S.; Gonçalves, J. P.; and Camarini, G., "Study of Alkali-Activated Mortar Used as Conventional Repair in Reinforced Concrete," *Construction and Building Materials*, V. 165, 2018, pp. 914-919. doi: 10.1016/j.conbuildmat.2018.01.063

87. Guades, E. J.; Stang, H.; Schmidt, J. W.; and Fischer, G., "Flexural Behavior of Hybrid Fibre-Reinforced Geopolymer Composites (FRGC)-Jacketed RC Beams," *Engineering Structures*, V. 235, 2021, p. 112053. doi: 10.1016/j.engstruct.2021.112053

88. Kantarci, F., and Maras, M. M., "Fabrication of Novel Geopolymer Grout as Repairing Material for Application in Damaged RC Beams," *International Journal of Civil Engineering*, V. 20, No. 4, 2022, pp. 461-474. doi: 10.1007/s40999-021-00695-9

89. Kantarcı, F., and Maras, M. M., "Formulation of a Novel TiO_2-Modified Geopolymer Grout for Application in Damaged Beam-Column Joints," *Construction and Building Materials*, V. 317, 2022, p. 125929. doi: 10.1016/j.conbuildmat.2021.125929

90. Khalifa, A.; El-Thakeb, A. E.; El-Sebai, A.; and Elmannaey, A., "Innovative Flexural Repair Technique of Pre-Damaged T-Beams Using Eco-Friendly Steel-Fibre-Reinforced Geopolymer Concrete," *Fibers*, V. 12, No. 1, 2024, p. 3. doi: 10.3390/fib12010003

91. Laskar, S. M., and Talukdar, S., "A Study on the Performance of Damaged RC Members Repaired Using Ultra-Fine Slag Based Geopolymer Mortar," *Construction and Building Materials*, V. 217, 2019, pp. 216-225. doi: 10.1016/j.conbuildmat.2019.05.033

92. Laskar, S. M., and Talukdar, S., "Slag-Based Geopolymer Concrete as Reinforced Concrete Jacketing Agent," *Journal of Materials in Civil Engineering*, ASCE, V. 33, No. 7, 2021, p. 04021150. doi: 10.1061/(ASCE)MT.1943-5533.0003780

93. Mahmood, M.; Salman, W. D.; and Mubarak, H. M., "Effectiveness of Geopolymer in the Strengthening of RC Beams Using Bottom NSM Reinforcements," *Asian Journal of Civil Engineering*, V. 24, No. 7, 2023, pp. 2451-2465. doi: 10.1007/s42107-023-00654-w

94. Maras, M. M., "Experimental Behavior of Injected Geopolymer Grout Using Styrene-Butadiene Latex for the Repair and Strengthening of Masonry Walls," *Advances in Structural Engineering*, V. 24, No. 11, 2021, pp. 2484-2499. doi: 10.1177/13694332211001513

95. Menna, C.; Asprone, D.; Ferone, C.; Colangelo, F.; Balsamo, A.; Prota, A.; Cioffi, R.; and Manfredi, G., "Use of Geopolymers for Composite External Reinforcement of RC Members," *Composites Part B: Engineering*, V. 45, No. 1, 2013, pp. 1667-1676. doi: 10.1016/j.compositesb.2012.09.019

96. Peng, K.-D.; Huang, B.-T.; Xu, L.-Y.; Hu, R.-L.; and Dai, J.-G., "Flexural Strengthening of Reinforced Concrete Beams Using Geopolymer-Bonded Small-Diameter CFRP Bars," *Engineering Structures*, V. 256, 2022, p. 113992. doi: 10.1016/j.engstruct.2022.113992

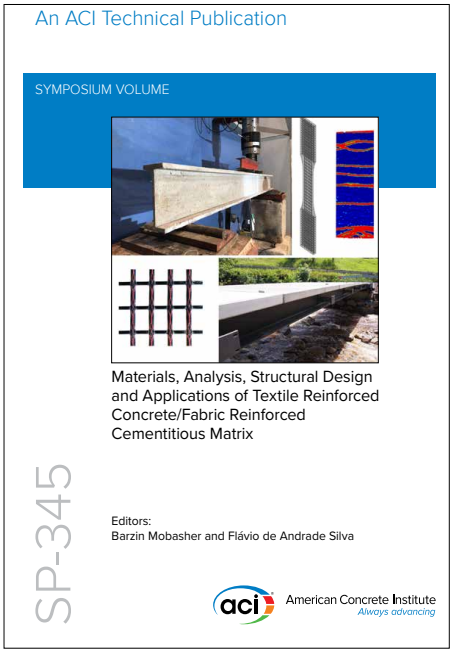
97. Peng, K.-D.; Huang, J.-Q.; Huang, B.-T.; Xu, L.-Y.; and Dai, J.-G., "Shear Strengthening of Reinforced Concrete Beams Using Geopolymer-Bonded Small-Diameter FRP Bars," *Composite Structures*, V. 305, 2023, p. 116513. doi: 10.1016/j.compstruct.2022.116513

98. Salman, W. D., and Mansor, A. A., "Fibrous Geopolymer Paste Composites for Near-Surface-Mounted Strengthening of Reinforced Concrete Beams in Flexure," *Case Studies in Construction Materials*, V. 14, 2021, p. e00529. doi: 10.1016/j.cscm.2021.e00529

99. Sinha, A. K., and Talukdar, S., "Repairing of Web Opening RC Beam with Ferrocement Laminates Using Alkali Activated Mortar," *Journal of Building Pathology and Rehabilitation*, V. 8, No. 1, 2023, p. 57. doi: 10.1007/s41024-023-00302-5

100. Park, R., "Ductility Evaluation from Laboratory and Analytical Testing," *Proceedings of Ninth World Conference on Earthquake Engineering*, V. 8, 1988, pp. 605-616.

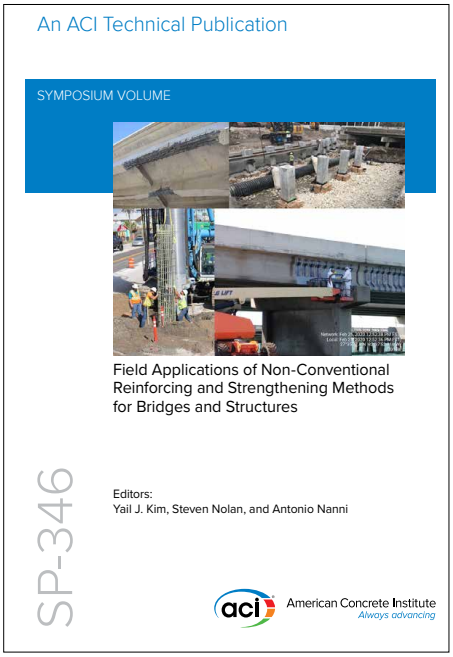
NEW Symposium Publications from ACI



SP-345: Materials, Analysis, Structural Design and Applications of Textile Reinforced Concrete/Fabric Reinforced Cementitious Matrix

Several state-of-the-art sessions on textile-reinforced concrete/fabric-reinforced cementitious matrix (TRC/FRCM) were organized by ACI Committee 549 in collaboration with RILEM TC MCC during the ACI Fall 2019 Convention in Cincinnati, OH, and the ACI Virtual Technical Presentations in June 2020. The forum provided a unique opportunity to collect information and present knowledge in the field of TRC and FRCM as sustainable construction materials.

Available in PDF format: $69.50
(FREE to ACI members)



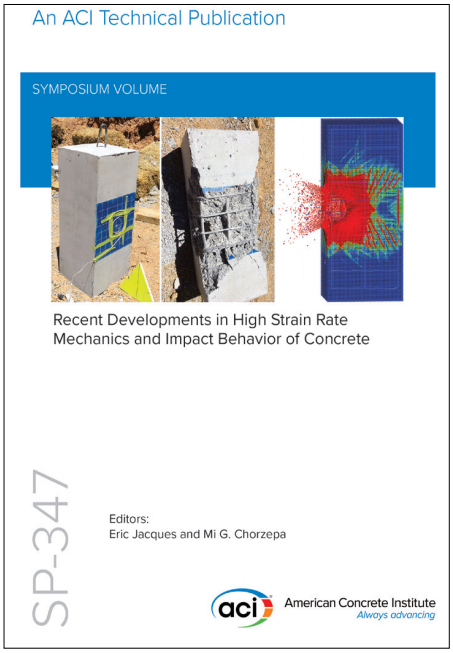
SP-346: Field Applications of Non-Conventional Reinforcing and Strengthening Methods for Bridges and Structures

A sustainable built environment requires a comprehensive process from material selection through to reliable management. Although traditional materials and methods still dominate the design and construction of our civil infrastructure, nonconventional reinforcing and strengthening methods for concrete bridges and structures can address the functional and economic challenges facing modern society.

Available in PDF format: $69.50
(FREE to ACI members)

American Concrete Institute
+1.248.848.3700 • www.concrete.org

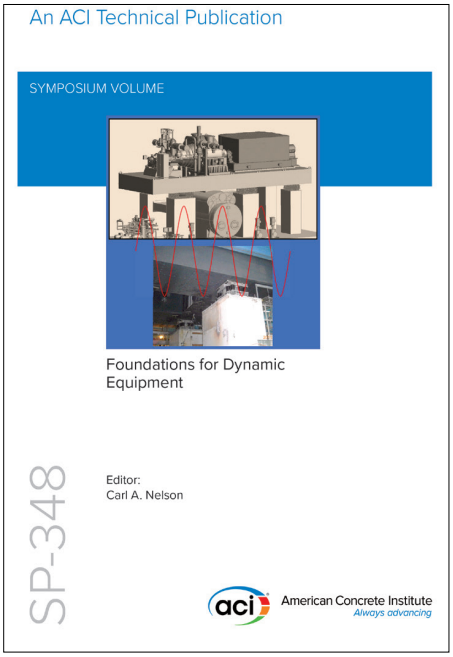
NEW Symposium Publications from ACI



SP-347: Recent Developments in High Strain Rate Mechanics and Impact Behavior of Concrete

This Symposium Volume reports on the latest developments in the field of high-strain-rate mechanics and behavior of concrete subject to impact loads. This effort supports the mission of ACI Committee 370, Blast and Impact Load Effects, to develop and disseminate information on the design of concrete structures subjected to impact, as well as blast and other short-duration dynamic loads.

Available in PDF format: $69.50
(ACI members: $39.00) ($30.50 savings)



SP-348: Foundations for Dynamic Equipment

This special publication grew out of the Technical Session titled “Application of ACI 351-C Report on Dynamic Foundations,” held at the ACI Spring 2019 Convention in Québec City, Québec. Following this event, ACI Committee 351 decided to undertake a special publication with contributions from those session participants willing to develop their presentations into full-length papers. Three papers included in the current publication were contributed by these presenters and their coauthors, with six additional papers provided by others.

Available in PDF format: $69.50
(ACI members: $39.00) ($30.50 savings)

American Concrete Institute
+1.248.848.3700 • www.concrete.org

ACI STRUCTURAL JOURNAL

The American Concrete Institute (ACI) is a leading authority and resource worldwide for the development and distribution of consensus-based standards and technical resources, educational programs, and certifications for individuals and organizations involved in concrete design, construction, and materials, who share a commitment to pursuing the best use of concrete.

Individuals interested in the activities of ACI are encouraged to explore the ACI website for membership opportunities, committee activities, and a wide variety of concrete resources. As a volunteer member-driven organization, ACI invites partnerships and welcomes all concrete professionals who wish to be part of a respected, connected, social group that provides an opportunity for professional growth, networking, and enjoyment.



American Concrete Institute